An investigation of crustal contamination through petrology and geochemisty

MCLEOD, CLAIRE,LOUISE

An investigation of crustal contamination through petrology and geochemistry.

Claire Louise McLeod

A THESIS SUBMITTED IN PARTIAL FULFILMENT OF THE
REQUIREMENTS FOR THE DEGREE OF DOCTOR OF PHILOSOPHY
AT DURHAM UNIVERSITY

Department of Earth Sciences
Durham University
2012

If we knew what it was we were doing, it would not be called research, would it?

Albert Einstein

Abstract

The contamination of mantle-derived magmas by the continental crust is an important process during petrogenesis of volcanic rocks at active continental margins e.g. The Andes. Investigating the evolution of continental arc magmas is, however, hampered by our limited knowledge of, and poor constraints on, the nature of the underlying crustal basement and the mechanisms of crustal anatexis. This thesis reports results from:

1) a whole rock geochemical and *in-situ* geochronological investigation of a suite of crustal xenoliths from the Bolvian Altiplano, Central Andes;
2) a whole rock geochemical study of the xenoiths' host lavas and;
3) detailed *in-situ* geochemical studies of crustal partial melts (quenched to glasses) trapped within their crustal progenitors from Bolivia, NE China and SE Spain.

Sampled crustal xenoliths from the Bolivan Altiplano provide a rare insight into the nature of the Central Andean continental basement and reveal lithological and geochemical heterogeneity exists at depth with $^{87}Sr/^{86}Sr$ values extending to 0.7368 which is more radiogenic than any Sr-isotopic signature exhibited by the recent (< 60 Ma) volcanic record. *In-situ* U-Pb dating of zircon separates reveal predominant age peaks at 1.7-1.9 Ga, 1.0-1.2 Ga and 495-380 Ma which correspond to periods of supercontinent formation and break-up e.g. construction of Rodinia.

Lavas erupted from monogenetic centres on the eastern Bolivian Altiplano show petrographic and geochemical evidence for crustal contamination. The geochemical heterogeneity exhibited by the lavas is, however, difficult to reconcile through simple two component crust-magma interaction models (bulk mixing, AFC and EC-AFC). Instead, contamination is inferred to have involved numerous crustal components. The geochemical signatures observed in lavas from monogenetic centres towards the active Andean arc (between ~18-21^{o}S) are distinct (e.g. lower $^{87}Sr/^{86}Sr$, higher Sr/Y, higher Ba/Nb at higher Zr/Nb) and may indicate a lower degree of crust-magma interaction, an increase in the contribution from slab-derived fluids and thinner crust arc-wards, the latter which has previously been inferred from geophysical studies.

In-situ analysis of anatectic melts reveals that Sr-isotopic disequilibrium between a crustal melt and its source can exist on the sub-millimetre scale. This is understood to reflect the melting of aged minerals with different Rb/Sr (and therefore $^{87}Sr/^{86}Sr$) more quickly than the isotopic composition can diffusively equilibrate between melt and minerals. Results suggest therefore that crustal anatexis can produce melts which are geochemically heterogeneous both spatially and temporally. This highlights the need for detailed microscopic investigations coupled with petrogenetic modelling in order to develop a more robust characterisation and well-constrained quantification of crustal contamination in open magmatic systems.

Declaration

I, Claire Louise McLeod, declare that this thesis, presented for the degree of Doctor of Philosophy at Durham University, is a result of my own original research and has not been previously submitted to Durham University or any other institution. I have clearly indicated, when appropriate, the contributions of colleagues and have made every effort to acknowledge all collaborative work.

Claire McLeod
Durham University
May 2012

Acknowledgements

It is with a little disbelief that I write these acknowledgements, the past three and a half years have had their ups and downs and without the following people, completion of this thesis would never have been possible.

My first thanks go to my long-suffering supervisors Jon Davidson and Geoff Nowell for being constant sources of inspiration throughout this project and providing continuous support and encouragement. I cannot thank you enough. I owe Jon, Bob, Yaoling and Claire my gratitude for believing in my passion for this project back in March 2008 and entrusting me with a studentship. Thanks go to NERC for providing the funding that has made all of this possible and taken me to some truly incredible corners of the world over the past few years. On this note, I extend a big thank you to Jon for allowing me to gallivant off around the globe on slightly more than one occasion. I have been extremely fortunate in being able to visit some truly fascinating countries and meet many wonderful people. I extend further thanks to Geoff for unwavering support throughout my time in the lab both during sample preparation and analysis. As additional thanks, I leave you with a full, clean set of (micro-Sr) Teflon beakers. As for the dirty whole rock beaker set, I believe they await some poor, naiive, unsuspecting 1st-year PhD student (with whom I can sympathise).

Shan de Silva (Oregon State University), my "unofficial" supervisor, I thank you for a constant supply of enthusiasm and for your guidance up, down and across the Bolivian Altiplano. Your breadth of knowledge and understanding of Central Andean geology is incredibly inspiring. My time with you and your students, Jamie, Jason and Rodrigo, out on the Bolivian Altiplano and into the Altiplano-Puna Volcanic Complex has been one of the highlights of this work. Thanks also to Jacqueline Malarkey and Graham Pearson for your support during my early days as a PhD student. Your guidance was invaluable. Further thanks to The Durham Volcanology Group (DVG) for extensive and thoroughly enjoyable (at times amusing) scientific discussions on a weekly basis. I hope the group goes from strength to strength and continues to grow. Wednesday lunchtimes will not be the same without the accompanying coffee and home-made cakes.

Thanks are owed to Nic Odling, Simon Harley and Chris Hayward at the University of Edinburgh for their support during XRF and EMP analysis and discussion throughout this project; Axel Schmitt and Rita Economos at the University of California, Los Angeles for SIMS analysis and Chris Ottley at Durham University for support and guidance throughout the use of the ICPMS instruments and to Dave Sales for sample preparation. Without your inputs this work would not have been possible.

Thanks also go to my family for their constant support throughout the past seven and a half years during my time at both Edinburgh and Durham. Without your encouragement from an early age it is unlikely I would be where I am today. A big thank you to all my fellow PhD students who without, this thesis would still be in draft format. The coffee breaks, the shopping trips, the fieldtrips, the holidays, the sleepovers, the late-night pizzas, the Glee-full nights, the hours spent playing Guitar Hero, the ice-filled mojitos at Popolos and the evenings spent watching MIC, it was all totes. Izzy, Yuanyuan, Pete, B-J and Scott, life in the bay would not have been the same without you. Special thanks to Alan. R, Amy, Ben. F, Chris, Claudia, Dave. A, Dave. D, Iona, Izzy, Kathy, Kirstie, Laura, Niamh, Pete, Dr. Sarah. C, Sarah. P, Sabina, Simon, Viv and Yuanyuan for their friendship and support during my time in Durham. And to Rich, I owe you a big thank you for keeping me grounded as this all came together and for being there to remind me that life can be still be fun and full of mischief even when there is a thesis to write.

Last, but by no means least, I extend a big thank you to my long-suffering, blonde ball of fun Raini who has always been there to remind me that a world exists outside this crazy geology bubble. At the end of the day I cannot disagree with you... it is “just rocks”. I owe you my sanity.

Finally, I hope you are all proud of what you have enabled me to achieve.

Contents

Dedication

To Dennis and Brenda Shephard

To Alec and Margaret McLeod

List of Figures

Chapter 1

Chapter 2

Chapter 3

Fig. 3.4 a-g Variations in major element compositions within the sampled xenolith suite.

Fig. 3.5 a-h Primitive-mantle normalised trace element multi element diagrams for the eight sampled xenolith lithologies. Normalising values of McDonough et al., (1991).

Fig. 3.6 a. Sr-Pb characteristics of the sampled xenolith suite. **b**. Sm-Nd signatures showing broad geochemical affinity to upper and middle crustal reservoirs. UCC, MCC and LCC: upper, middle and lower crust respectively (values from Rudnick and Gao, 2003). Symbols as in Fig. 3.4.

Fig. 3.7 a-h. Chondrite-normalised REE patterns for the eight sampled xenolith lithologies. Normalising values of Nakamura (1974).

Fig. 3.8. Sr-Nd isotopic compositions of sampled Bolivian xenoliths. Compositional fields for previously studied outcrops of crustal basement throughout the central Andes are also shown. Data sources: James, 1982; Lucassen et al., 1999; Lucassen et al., 2001 The Precambrian Charcani Gneiss of Peru plots outwith the compositional field shown at significantly lower $^{143}Nd/^{144}Nd$ (0.5115) and $^{87}Sr/^{86}Sr$ of 0.740.

Fig. 3.9 a. $^{206}Pb/^{204}Pb$ vs. $^{207}Pb/^{204}Pb$ for sampled crustal xenoliths. **b**. $^{206}Pb/^{204}Pb$ vs. $^{208}Pb/^{204}Pb$ for sampled crustal xenoliths. Geochron and upper crustal evolution lines (each tick at 100 Ma intervals) after Zartman and Haines, (1988); Rollinson (1993).

Fig. 3.10 a-c. CL images of zircons in the sampled xenolith suite. Note: these grains were not sampled for their U-Pb ages (see Figs. 3.11 a, b).

Fig. 3.11 a, b. Maps showing separated zircon grains and location of spot analyses. Images courtesy of Shan de Silva.

Fig. 3.12 a, b. U-Pb concordia plots for sampled cores and rims of zircons within BC10QSX107 and BC93PAX14.

Fig. 3.13 a, b. Calculated P-T pseudosections for xenoliths BC93PAX14 (a.) and BC93QSX04 (b.)

Fig. 3.14 a, b. Pb isotopic composition of sampled xenoliths plotted alongside the Northern, Central and Southern crustal domains of the Arequipa-Antofalla basement block. Domains are redrawn from Loewy et al., (2004).

Fig. 3.14 c. $^{206}Pb/^{204}Pb$ vs. $^{207}Pb/^{204}Pb$ for crustal xenoliths of this study and from previous studies of continental basement rocks in the Central Andes. All samples are distinct from the Laurentian crustal trend at μ of ~9.3. Fields redrawn from Wörner et al., (2000).

Fig. 3.15. Calculated T_{DM} ages of sampled xenoliths.

Fig. 3.16 a-c. U-Pb ages from *in-situ* analyses of zircon grains across the Andean Cordillera. For data sources see end of chapter.

Fig. 3.17 a Map showing the cratonic interior of the South America continent and its extent relative to the modern day Andean fold belt. **b**. Geological history of the South American Craton. Map and timescale are modified from de Almeida et al., (2000).

Fig. 3.18. Map showing reconstruction of the Rodinian supercontinent. The Grenvillian-aged belts (c. 1 Ga) are highlighted. The Andean inliers are also shown; SB: Sunsas belt; G: Grenville belt; c: Colombian Massifs; m: Mexican Massifs; a: Arequipa-Antofalla basement; cu: Cuyania terrane. Map is modified from Cordani et al., (2005).

Fig. 3.19. Map showing the separation of Laurentia and Gondwana by the Iapetus Ocean at 550 Ma. AA: Arequipa-Antofalla; AC: Amazonian Craton; AN: Arabian-Nubian Shield; ANT: Antarctica; AU: Australia; AV: Avalonia; C-SF: Congo-San-Francisco; C: Colombian basement; Cu: Cuyania; IN: India; K: Kalahari; LA: Laurentia; MB: Mozambique belt; RP: Rio de la Plata (see Fig. 3.1); U-N: Uweinat-Nile; WA: Western Africa. (Map modified from Cordani et al., 2005).

Fig. 3.20. Plot of SiO_2 vs. major oxides for all xenoliths of this study plotted alongside estimates for the lower, middle, upper and bulk continental crust (Data sources: Clarke, 1924; Pakiser and Robinson, 1966; Taylor and McLennan 1981; Weaver and Tarney, 1984; Taylor and McLennan, 1985; Shaw et al., 1986; Christensen and Mooney, 1995; Rudnick and Fountain, 1995; Wedepohl, 1995; Rudnick and Gao, 2003).

Fig. 3.21. SiO_2 vs. Eu anomalies for crustal reservoirs and sampled xenoliths.

Fig. 3.22. AFC modelling of lavas at Pampas Aullagas and Quillacas. The most primitive volcanic rock in the Central Andes (the Chiar Kkollu basalt, Davidson and de Silva, 1992; 1995) is used as the mantle end-member.

Fig. 3.23 a. Cross section at 21°S across the Central Andes. Modified from Schmitz, (1994). **b**. hypothetical vertical section through stacked crustal units.

Chapter 4

Fig. 4.9 a, b. La/Yb and Dy/Yb plotted for sampled lavas at PA and QL and the minor centres of Davidson and de Silva (1995, Yb data not given, symbols as in Fig. 4.7). **c**. Correlation between La/Yb and Dy/Yb indicative of garnet fractionation at depth.

Fig. 4.10 a. SiO_2 vs. Sr for PA and QL lavas. **b**. PA and QL data plotted alongside lavas of Davidson and de Silva (1995). Symbols as in Fig. 4.7.

Fig. 4.11. Sm/Yb vs. calculated Eu anomaly. Symbols as in Fig. 4.4.

Fig. 4.12 a. Sr-Nd isotopic compositions of sampled PA and QL lavas. Signatures are significantly enriched relative to $^{87}Sr/^{86}Sr$ of lavas erupted from recent monogenetic volcanic centres in the Central Andes. **b**. Inset graph showing the elevated $^{87}Sr/^{86}Sr$ exhibited by Central Andean volcanic rocks and the relatively depleted nature of volcanic rocks from the NVZ and SVZ. DM: Depleted Mantle, BSE: Bulk Silicate Earth. Fields for Andean volcanic rocks are derived from GEOROC data (http://georoc.mpch-mainz.gwdg.de) for volcanic rocks aged 60 Ma or younger (database accessed 07.11.11).

Fig. 4.12 c. Crustal contamination during magmatic differentiation beneath the PA and QL lavas.

Fig. 4.13 a. $^{206}Pb/^{204}Pb$ vs. $^{207}Pb/^{204}Pb$ for Bolivian lavas. Fields re-drawn from Davidson and de Silva, (1995). Symbols as in Fig. 4.12 a.

Fig. 4.13 b. Pb isotope domain showing the location of the PA and QL centres relative to the boundaries of inferred crustal provinces. Map modified from Aitcheson et al. (1995). **c**. Pb isotopic signatures in sampled volcanic rocks from minor centres on the Bolivian Altiplano. Symbols as in Fig. 4.12 a.

Fig. 4.14 a-c. Major element trends at PA and QL projecting back to Chiar Kkollu.

Fig. 4.15. REE abundances produced from melting **a**. garnet peridotite and **b**. spinel peridotite at F values of 0.005, 0.01, 0.05 and 0.1.

Fig. 4.16. Distinct Sr-Pb isotopic signatures in lavas sampled at PA and QL.

Fig. 4.17. bulk mixing between Chiar Kkollu and sampled crustal xenoliths.

Fig. 4.18 a-f. Graphs showing the effects of AFC (equations of De Paolo, 1981) on $^{87}Sr/^{86}Sr$ vs. Sr (ppm) between a Chiar Kkollu-type magma and the sampled crustal xenoliths (Chapter 3). AFC

parameters given in each figure. Each tick on the AFC curves represents melt left after assimilation (in 10% increments). Numbers correspond to xenoliths in Fig. 4.17. Where appropriate, numbers were omitted for clarity.

Fig. 4.19. Modelled EC-AFC curves for PA and QL lavas. Models shown are those which best fitted the data. Numbers correspond to model parameters presented in Appendix D.

Fig. 4.20 a. Contaminated nature of PA and QL lavas. **b**. Deep vs. shallow level differentiation. Lavas of Hoke and Lamb, (2007) also included.

Fig. 4.21 a-c. Geochemical changes in lava geochemistry from west (behind arc) to the east (PA, QL and the Eastern Altiplano). For discussion see text.

Fig. 4.22 a. K-h relationship highlighting higher K_2O contents in Eastern Altiplano (including PA and QL) lavas. **b**. Inference of thin and thick crust based on CaO at 6 wt. % MgO. See text for discussion.

Fig. 4.23 a. Summary cartoon of observed across arc changes from the active Andean arc to the Eastern Altiplano at ~18-21^{o}S.

Fig. 4.23 b. Seismic profile constructed from P-wave residuals at 21^{o}S. Earthquake hypocentres are represented by black circles. Profile is adapted from Heit et al., (2008).

Fig. 4.23 c. Average residual seismic velocities (after correction for topography and the Moho discontinuity) across a ~600 km transect from Chile through to central southern Bolivia at 21^{o}S. Areas recording fast seismic velocities are shown in blue, areas of slow seismic velocities are in red. Map is modified from Heit et al., (2008).

Chapter 5

Fig. 5.1 a, b. Quenched anatectic melts in sampled Bolivian crustal xenoliths.

Fig. 5.2 a, b. Crustal contamination in lavas at Pampas Aullagas (PA) and Quillacas (QL).

Fig. 5.3 EC-AFC modelling of PA and QL lavas. Numbers correspond to different EC-AFC models run, details are given in Appendix D.

Fig. 5.4. TAS plot for sampled anatectic melts. Source xenoliths are also shown (squares); BC93PAX12 at 79.8 wt. % SiO_2, QNX02 at 68.47 %, QNX03 at 68.67 %, BC10PAX138 at 70.27 %.

PAX08 was not analysed for its major element composition. For the full suite of xenolith major element compositions see Tables 2, 4 in Appendix B.

Fig. 5.5 a-h. Distinct geochemical nature of anatectic glasses with respect to major oxides.

Fig. 5.6 a-c. Geochemical heterogeneity at the micro-scale within sampled brown glass.

Fig. 5.7 a-d. Location maps of drill sites in two thick (100 μm) sections of xenolith BC93PAX12.

Fig. 5.8 a, b. Enrichment and depletion of sampled mafic anatectic melts relative to their source xenolith (BC93PAX12).

Fig. 5.9 a. Rb vs. $^{87}Sr/^{86}Sr_i$ for sampled mafic anatectic glasses, section BC93PAX12_a (Fig. 5.7 a, b). Compositions are age corrected for the Pliocene age of lava eruption (1.89 Ma). Time arrow infers the decreasing contribution from high Rb/Sr phases to the melt, for discussion see text.

Fig. 5.9 b. Rb vs. $^{87}Sr/^{86}Sr_i$ for sampled mafic anatectic glasses, section BC93PAX12_b (Fig. 5.7 c, d). Compositions are age corrected for the Pliocene age of lava eruption (1.89 Ma). Time arrow infers the decreasing contribution from high Rb/Sr phases to the melt, for discussion see text.

Fig. 5.9 c, d. Rb/Sr vs. $^{87}Sr/^{86}Sr_i$ for sampled mafic anatectic glasses, groundmass glass from within the same thick section and five whole rock analyses. All compositions are age corrected.

Fig. 5.10. Phase diagram for muscovite and biotite dehydration solidi. Adapted from Farina and Stevens, (2011). Shaded region represents potential temperature-pressure field for xenolith BC93PAX12. Dotted line: dehydration melting solidus from Peto (1976); dashed line (1): muscovite-schist solidus (Patiño Douce and Harris, 1998); dashed line (2) muscovite schist dehydration solidus (Patiño Douce and Harris, 1998); solid black lines: biotite dehydration at different biotite Mg# (in brackets) in the absence of muscovite (Vielzeuf and Montel, 1994; Patiño Douce and Beard, 1995, 1996); dashed line: phlogopite-quartz solidus (Vielzeuf and Clemens, 1992).

Fig. 5.11 a. Hypothetical melt evolution with respect to $^{87}Sr/^{86}Sr$ as a variable Rb/Sr phases breakdown during anatexis (compositions from Zeng et al., 2005).

Fig. 5.11 b. Schematic control of isotope systematics by disequilibrium melting. Initially, high Rb/Sr phases may contribute more radiogenic Sr to the melt (e.g. biotite). As anatexis proceeds, the breakdown of lower Rb/Sr phases may dominate (e.g. plagioclase feldspar, see also, Fig. 5.11 a). The bulk mixing line (shown at 10% intervals) indicates bulk mixing between the Chiar

Kkollu lava and the average composition of sampled anatectic glasses. Realistically however, the composition of the contaminant may change (see text for discussion). The solid black, and associated dashed black, trends illustrate the potential contamination pathways ascending mantle-derived magmas assimilating compositionally variable anatectic melts may have in terms of their Rb versus $^{87}Sr/^{86}Sr_i$ (based on bulk melt composition with Rb content used as a proxy for time, see Fig. 5.9). All compositions age corrected to eruption age (1.42 Ma for QL).

Fig. 5.12. The effects of crustal melting in Ba vs. Rb/Sr compositional space. Adapted from Whittington and Treloar, (2002). DH: dehydration, WS: water-saturated, HH(C): High Himalayan (Crystalline Series). Vectors show 10% change due to crystallisation of corresponding phase; F: melt volume fraction. For a detailed explanation on the controls governing melting and crystallisation see Whittington and Treloar (2002).

Fig. 5.13 a. Dihedral angle ≤ 60 forming an interconnected melt network. **b**. Dihedral angle ≥ 60 producing isolated melt pockets. Adapted from Laporte, (1994).

Fig. 5.13 c. Schematic illustrating how geochemical heterogeneity may arise in residual melt trapped within a crystal mush.

Chapter 6

Fig. 6.1. Geological map of the Wudalianchi region (modified from Xiao and Wang, 2009).

Fig. 6.2 a. Sphene in sampled basement granite.

Fig. 6.2 b. Granite modal mineralogy.

Fig. 6.3. Modal mineralogy of sampled lava and xenoliths.

Fig. 6.3 cont. Representative modal mineralogy of Xenolith 5d.

Fig. 6.4 a, b. Melt mixing within a lava pocket of partially melted granitic xenolith 3a. Photos courtesy of Lucy McGee.

Fig. 6.5 a, b. Partially-melted sphene.

Fig. 6.6. Sampled partially melted crustal xenoliths (Suite 5). Photos courtesy of Lucy McGee.

Fig. 6.7. **a**. 'Stranded' olivine crystal within silicic melt pockets and vesicles of partially melted granitic xenolith 5b. Olivine crystal is assumed to have been transferred from the enclosing basaltic magma to the xenolith when the two materials were partially molten and in contact, showing small-scale interaction**. b.** Lava-xenolith contact in sample 5b showing complex mixing zone between the silicic (colourless) and basaltic melts. Photos courtesy of Lucy McGee.

Fig. 6.8. SiO_2 vs. K_2O for sampled xenoliths.

Fig. 6.9. Chondrite normalised REE pattern for sampled lava, xenoliths and basement granite.

Fig. 6.10. Sr-Nd isotopic compositions of sampled lava, granite and xenoliths.

Fig. 6.11 a. Elemental budgets of sampled minerals in the basement granite.

Fig. 6.11 b. Trace elemental budgets of sampled glasses and plagioclase feldspars.

Fig. 6.11 c-e. REE patterns for sampled glasses normalised to their host xenolith bulk composition.

Fig. 6.11 f. Chondrite normalised REE patterns for sampled glasses and the basement granite. Normalising values of Nakamura, (1974).

Fig. 6.12. $^{87}Sr/^{86}Sr$ compositions of the basement granite, its constituent minerals and sampled glasses. Note: Trace element concentrations were determined on one glass separate only.

Fig. 6.13. Rb-Sr whole rock isochron for sample basement granite.

Fig. 6.14. Disequilibrium between source and melt.

Fig. 6.15. Phase diagram for muscovite and biotite dehydration solidi. Adapted from Farina and Stevens, (2011). Muscovite dehydration field is highlighted in blue.

Fig. 6.16. Graph showing SiO_2 plotted against $^{87}Sr/^{86}Sr$ for lavas in NE China. Wudalianchi data from this study and Basu et al., (1991); Kuandian data from Basu et al., (1991), WEK (Wudalianchi-Erkeshan-Keluo) data from Zhang et al., (1991); Heilongjiang from Peng et al., (1986, no location given).

Fig. 6.17. Interaction between an OIB-type source and the sampled melts would fail to reproduce the slightly enriched nature of the lava. OIB, MORB and primitive mantle values from Sun and McDonough, (1989).

Chapter 7

Fig. 7.1. Annotated Google Earth image showing the location of the El Joyazo volcanic centre relative to nearby major Spanish cities and neighbouring countries.

Fig. 7.2 a. Map showing location of the Betic cordillera orogen in south-eastern Spain and conjugate Rif orogen in north-western Africa (map is modified from Cesare et al., 2003). **b**. Map showing distribution of volcanic rocks throughout the Neogene Volcanic Province. Outcrop localities define a NE-SW trend from Almeria to Mar Menor (map is modified from Benito et al., 1999).

Fig. 7.3. Field photograph of the El Joyazo volcanic centre composed of three dacitic domes set in a circular depression rimmed by Messinian limestones. Photo taken looking north-north-east.

Fig. 7.4. a, b. Field photographs of Grt-Bt-Sill partially melted crustal xenoliths hosted in dacite.

Fig. 7.5 a. Thick section (100 μm) of a Grt-Bt-Sill xenolith containing characteristic garnet porphyroblasts (found as xenocrysts within the dacite host. **b**. intergrown needles of sillimanite and quenched anatectic melt ("mix").

Fig. 7.6. Graph showing Sr-isotopic variability between the different rock types sampled at El Joyazo (whole rock data sourced from Munksgaard, 1984; Benito et al., 1999; Turner et al., 1999; Perini et al., 2009).

Fig. 7.7. Variable $^{87}Sr/^{86}Sr$ signatures recorded in sampled "mix" (aggregate of sillimanite needles and quenched melt). Also shown is the relatively radiogenic nature of sampled biotite and un-radiogenic nature of plagioclase. Data is compared to $^{87}Sr/^{86}Sr$ values obtained by this study to those of Perini et al., (2009) on mix and mineral separates from the Grt-Bt-Sill xenolith suite. Whole rock values for Grt-Bt-Sill xenoliths from Munksgaard, (1984) and Perini et al., (2009).

Chapter 8

Fig. 8.1. U-Th decay scheme for isotopes used during U-series disequilibria studies in arc rocks. Note: not all decay products are shown.

Appendix E

Fig. E.1. Comparison of average measured concentrations of elements (in ppm) stated in Table E.3 of the international standards BIR-1, BCR, BEN and BHVO-1 by XRF to accepted values (Govindaraju, 1994).

Fig. E.2. Comparison of average measured concentrations of elements of the international standards W-2, BIR-1, AGV-1 and BHVO-1 (in ppm stated in Table E.4, measured by ICPMS, ELAN 6000) to accepted values.

Fig. E.3. Comparison of average measured concentrations of elements of international standards (in ppm, stated in Table E.5, measured by ICPMS, X-Series 2) to accepted values.

Fig. E.4. Graph showing reproducibility for the $^{87}Sr/^{86}Sr$ composition of NBS987 international standard during this study (during whole rock analyses, n=22, see Table E.6). Error bars show 2σ confidence. Shaded area represents accepted values as reported by Thirlwall, (1991). Dark shaded area represents 2 standard deviations on the average value of the NBS987 standard obtained by this study (n = 22).

Fig. E.5. Graph showing reproducibility for the $^{143}Nd/^{144}Nd$ composition of in-house J and M standard during this study (during whole rock analyses, n=16, see Table E.6). Error bars show 2σ confidence. Values are within 2σ of the average $^{143}Nd/^{144}Nd$ J and M standard value for the period June 2009-June 2011. Shaded area represents 2 standard deviations on the average value of the J and M standard obtained by this study (n= 30).

Fig. E.6. Graphs showing reproducibility for the ^{206}, ^{207} and $^{208}Pb/^{204}Pb$ composition of NBS981 international standard during this study (during whole rock analyses by PIMMS, n=48, see Table E.7). Error bars show 2σ confidence. Solid line represents average values, shaded region represent 2σ of this (n = 48).

Fig. E.7. Comparison of average measured concentrations of elements (in ppm) stated in Table E.9 of the international standard W-2 to USGS accepted values. 1-100 denotes dilution by a factor of 100, 1-1000 by 1000.

Fig. E.8. Graphs showing reproducibility on the $^{87}Sr/^{86}Sr$ composition of NBS987 international standard during this study (by TIMS, see Table E.10). Error bars show 2σ confidence. Shaded region represents range of accepted values (after Thirlwall, 1991). Solid line represents average value obtained during this work, dashed lines show 2σ on this value (0.710256 ± 0.000020).

Fig. E.9. Comparison of measured ages ($^{206}Pb/^{238}U$ and $^{207}Pb/^{235}U$, n = 21) on zircon standard AS3 at UCLA to the average value (and 2σ of, represented by the shaded region) presented in Schmitz et al., (2003) (n = 27).

Introduction 1

1.1 Thesis Rationale

This thesis aims to investigate the processes through which crustal contamination of mantle-derived magmas occurs. It is widely accepted that on route to the Earth's surface, these magmas interact with (and are contaminated by) the surrounding continental crust. However, the extent to which contamination overprints the characteristics of the primary mantle source is poorly constrained as too is the nature of the contaminants. Addressing these problems is crucial to furthering our understanding of mantle-crust interaction and the mass transfer between Earth's geochemical reservoirs (Fig. 1.1).

The crustal basement and the volcanic eruptives at continental arcs deserve study for three principal reasons:

1) the composition and structure of the continental crust dictates the potential effects on continental arc magmas as they ascend through, and differentiate within, the crust;

2) the nature and compositions of erupted lavas at the surface provide insights to the processes associated with magmatic differentiation and allows for evaluation of the relative importance of mantle and crustal reservoirs during arc-magma genesis;

3) the composition, age and structure of the crust are key factors in determining the geological and plate tectonic development of an active continental margin and its progenitors.

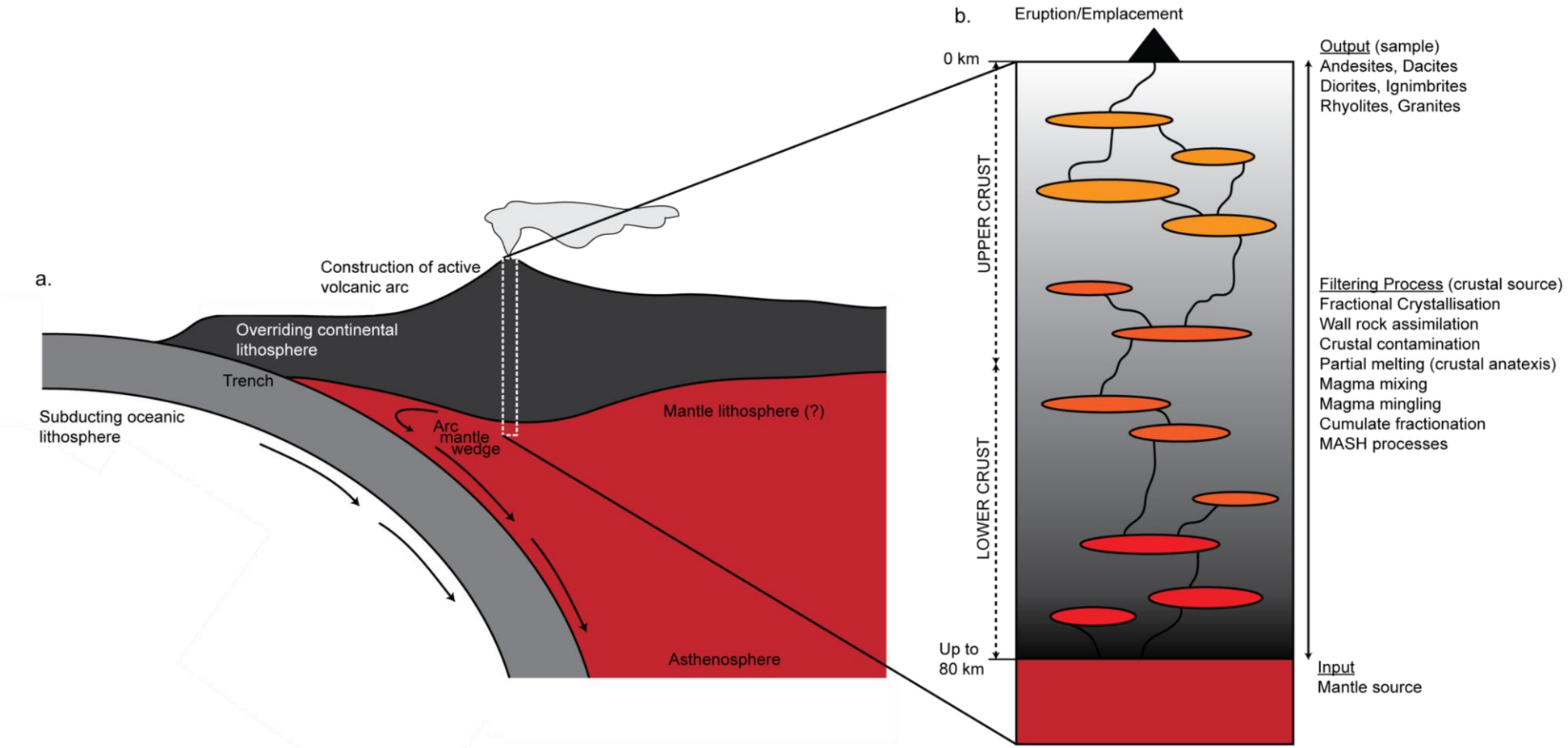

Fig. 1.1 a. The subduction factory: a cross section through a continent-ocean convergent margin. Oceanic sediments and crust are subducted beneath the overriding plate where they variably dehydrate and lower the melting temperature of the mantle wedge from which arc magmas are derived. **b**. Schematic cross section of the volcanic plumbing system where a hypothetical interconnected network of magma chambers is inferred to exist and through which ascending mantle-derived melts are filtered on route to the earth's surface. The volcanic (or plutonic) product which is then sampled can be used to acquire information regarding the processes occurring at depth.

Since the first plate tectonic models were developed over half a century ago, the Andes of South America have been considered a typical example of ocean-continent collision and a classic site of continental crust production on the modern earth. Despite the early realisation that the Andes provide a natural laboratory in which to study geochemical mass budgets and the transfer of these between earth's crust and mantle reservoirs, little is currently known about 1) the nature and history of the crustal basement upon which volcanic edifices of the active volcanic arc are constructed and 2) the degree to which its geochemical signatures influence the composition of volcanic (and plutonic) rocks sampled at the surface.

In light of the lack of knowledge regarding the components of this complex open magmatic plumbing system, the geochemical nature of lavas, erupted in the Central Andes from monogenetic volcanic centres on the Bolivian Altiplano-plateau, were investigated. Lavas from this region were chosen for study as they are hosts to a suite of variably partially melted crustal xenoliths and for this reason, are unique across the Central Andes. These xenoliths offer a rare insight into the nature of the crust on which the Central Andean Cordillera is built and provide key constraints as to the compositions of the crustal reservoirs involved during Central Andean magma petrogenesis. The concurrent existence of lavas and their potential crustal contaminants, the xenoliths, presents a fantastic chance to study the process of crustal contamination which has literally been "caught in the act". Furthermore, the occurrence of quenched crustal melts trapped within their protoliths offers a rare snapshot of the crustal anatexis process and presents an exceptional opportunity to assess and quantify, *in-situ*, the geochemical characteristics of anatectic melts which are potential contaminants to ascending mantle-derived magmas.

In addition to the suite of xenoliths sampled from Bolivian lavas, partially melted crustal xenoliths sampled from lavas in the Wudalianchi volcanic field in northeast China and at the El Joyazo volcanic centre in the southeast volcanic province of southern Spain provide the opportunity for comparative studies into the process of crustal anatexis and contamination.

A range of analytical methods were employed throughout this study. The details of each method can be found in Appendix E. Additionally, and where appropriate, the methods are summarised in each chapter and reported alongside results from the blanks and international standards run throughout each instrument session.

Chapter 2 presents a comprehensive review of the relevant literature pertaining to the geological setting and evolution of the Central Andean Cordillera. The development of the modern day arc front is discussed; the mechanisms through which the high Altiplano-Puna plateau has grown are examined and a regional geological summary provides context and reference for discussion in Chapters 3 and 4.

Chapter 3 focuses on the petrography and whole rock geochemistry of the sampled xenolith suite. The crustal xenoliths provide an important window into the architecture of the thickest crust at any subduction zone on Earth today. Through study of their geochemical compositions, particularly their Pb isotopes, the Central Andean basement in this region is characterised. Additional geochronological constraints from *in-situ* U-Pb age analyses of zircon separates yield constraints on the age and evolution of the Central Andean basement which subsequently has important implications for paleotectonic reconstructions and orogenesis.

Chapter 4 focuses on the petrography and whole rock geochemistry of the sampled lavas. The lavas are used to assess the degree to which the primary mantle-derived magmas have interacted with the continental crust on route to the surface. The sampled xenoliths (Chapter 3) are subsequently used to model crustal contamination during magma petrogenesis. The geochemical characteristics of the lavas are compared to lavas from the suite of monogenetic volcanic centres which exist across the Altiplano region from the active arc into the back-arc. From this, an attempt is made to constrain across-arc changes in the mantle melting regime and crustal thickness.

Chapter 5 presents the first case study of the geochemical characteristics of naturally occurring anatectic melts which will provide 1) a more robust characterisation and well-constrained quantification of potential crustal contaminants in open magmatic systems and 2) an insight into the compositions of crustal melts produced during anatexis. Study of these anatectic melts ultimately aims to examine the process of crustal contamination beyond the traditional whole rock perspective and to question the assumption that the crustal contaminant in open magmatic systems is a single composition both spatially and temporally. Results and inferences are then applied to the macro (outcrop and hand specimen) scale in order to assess the degree to which the observations at the micro scale can be applied to larger systems e.g. plutonism.

Chapter 6 focuses on the second case study of naturally occurring anatectic melts. Whole rock Sr-Nd and micro-Sr geochemistry for mineral separates and quenched anatectic melts (glass) from a suite of partially-melted crustal xenoliths from the Wudalianchi volcanic field in northeast China are presented. This data is used to assess the characteristics of naturally occurring crustal melts and compared to results presented in Chapter 5.

Chapter 7 focuses on the third case study of the geochemistry of quenched anatectic melts. Glasses from partially melted xenoliths hosted in lavas from the El Joyazo volcanic centre, southeast Spain are sampled *in-situ* for their Sr-isotope compositions. This relatively small dataset is used to assess the characteristics of naturally occurring crustal melts and is compared to results presented in Chapters 5 and 6.

The final chapter, **Chapter 8**, summarises the conclusions from each of the previous chapters in order to:

1) present a comprehensive and concise account of the nature and evolution of the Central Andean continental basement as inferred from whole rock geochemistry and *in-situ* U-Pb geochronology;
2) provide a detailed assessment of the role of crustal contamination in the petrogenesis of Central Andean lavas from the arc into the back arc region on the Bolivian Altiplano and;
3) present a consistent, succinct account of the crustal anatexis process and the geochemical implications this has for contamination of mantle-derived magmas in open magmatic systems.

Ideas and directions for future work are also presented.

1.2 Chapter Contributions

1.2.1 Chapter 2

I wrote this chapter in its entirety. This chapter aims to provide a comprehensive review of the Central Andean tectonic setting, evolution and regional geology which will be referred to in the chapters that follow. No new work is presented here.

1.2.2 Chapter 3

The work detailed here will be submitted as a paper to the *Geological Society of America (GSA) Bulletin*.

Claire McLeod: I carried out all of the whole rock analytical work on the suite of sampled crustal xenoliths. This involved the petrography, cutting and crushing of samples, chemistry, analysis of major elements, trace elements and Sr, Nd and Pb isotope ratios and data processing. The interpretations and conclusions drawn from the data set were my own and benefitted from discussions with Jon and Shan during fieldwork (which took place in October 2010) prior to collection of the full geochemical dataset. I wrote the manuscript and subsequently passed it on to co-authors. Following feedback, the structure of the paper changed in order to improve the flow of the discussion and present more concisely, the trace element data.

Jon Davidson: Jon provided the initial xenolith sample suite which was characterised and analysed prior to fieldwork. He also provided a dataset for the Sr-Nd isotopic composition for a sub-set of the suite. Jon provided discussion and constructive criticism throughout preparation of the manuscript.

Geoff Nowell: Geoff provided unwavering assistance and support during sample preparation and throughout sample analysis in the lab on the PIMMS instrument. He provided technical assistance and always thoroughly discussed any analytical problems that arose.

Shan de Silva: Shan provided invaluable assistance throughout the field season and constantly shared his in-depth knowledge of Central Andean geology. He arranged separation of the zircon fraction from the selected xenoliths at Oregon State University

(OSU) as no such facility exists at Durham University. Following this, he arranged the separates to be resin mounted and allocated a portion of his SIMS instrument time at the University of California, Los Angeles (UCLA) for U-Pb analysis of the Bolivian zircon separates.

Chris Ottley: Chris provided support throughout preparation and running of samples for trace elements on the ELAN and X-Series ICPMS. He was available for discussing data processing and assessing data quality.

Axel Schmitt: Following a SIMS short course for post graduate students at the University of California, Los Angeles (UCLA) in February 2011, He and Shan agreed to analyse a small number of zircon grains from the xenolith suite. He provided his instrument expertise throughout the analyses, ensured high data quality and provided constructive feedback during the later stages of manuscript preparation.

1.2.3 Chapter 4

The work detailed here will be submitted as a paper to the *Journal of Petrology*.

Claire McLeod: I carried out all of the whole rock analytical work on the suite of sampled lavas. This involved the petrography, cutting and crushing of samples, chemistry, analysis of major elements, trace elements and Sr, Nd and Pb isotope ratios and data processing. I carried out all the microsampling on the selected crustal xenolith samples. This involved major element analyses, chemistry and subsequent analysis for trace elements and Sr isotope ratios. The interpretations, discussion and conclusions drawn from the combined whole-rock and *in-situ* data set were my own and benefitted from discussions with Jon and Shan throughout preparation of the chapter. I arranged visits to the University of Edinburgh to use their XRF and electron probe facilities (with

Nic Odling and Chris Hayward respectively) as these facilities are not available at Durham.

Jon Davidson: Jon provided a suite of thin sections, rock samples and sample powders for the study prior to fieldwork. He also provided Sr, Nd and Pb isotope data for a small number of the samples. Jon assisted with refining the structure of the chapter and gave constructive feedback throughout.

Geoff Nowell: Geoff provided support during sample preparation and throughout sample analysis in the lab. He was available for technical assistance with the PIMMS and TIMS instruments and discussion of data quality.

Shan de Silva: Shan provided feedback and constructive reviews of chapter drafts and helped to develop the context of the discussion through his extensive knowledge of the field area.

Chris Ottley: Chris provided support throughout all the trace element analyses I undertook on the ELAN, X-Series and Element II ICPMS. He was available for discussion of data quality, processing of data and instrument method setup throughout the study.

1.2.4 Chapter 5

This is an extended version of a paper that has been accepted for publication in *Geology*, (to be published May 2012). A copy of the manuscript (and appropriate supplementary material) is included at the end of the chapter.

Claire McLeod: I carried out all of the *in-situ* analytical work on thick sections of the sampled xenoliths. This involved the petrography, microsampling, chemistry, analysis for major elements, trace elements, Sr isotope ratios and data processing. The data was modelled and interpreted by me. Conclusions drawn from the raw data set and subsequent models were aided by discussion with Jon and the Durham Volcanology Group. Constructive reviews from Antonio Acosta-Vigil (University of Granada) and one anonymous reviewer allowed the data collected, implications made and the discussion presented to be conveyed to a wider audience.

Jon Davidson: Jon provided constructive feedback throughout the preparation of the manuscript and helped me to refine my ideas so that they might be presented in a clearer, more coherent manner.

Geoff Nowell: Geoff provided assistance during initial microsampling in the lab and discussed the chemical separation method. He was available throughout the Sr-isotope analyses on the TIMS in order to address any instrument problems that arose.

Shan de Silva: Shan provided feedback on later drafts of the manuscript. He was available for discussion and used his Central Andean expertise to help provide a regional context to the implications the study presented.

1.2.5 Chapter 6

The work presented in this chapter builds on previous work by Lucy McGee (former Durham MSci student (2008), now at the University of Auckland) and will be submitted as a paper to *Contributions to Mineralogy and Petrology*.

Claire McLeod: I carried out the chemistry and analyses for whole rock Sr-Nd isotopes and the micro-Sr chemistry and analyses on the glass, biotite and plagioclase separates from four xenolith samples. I used this data in conjunction with the petrographic observations and the geochemical data set obtained by Lucy to support the interpretations made and conclusions drawn from my own data set in Chapter 5.

Lucy McGee: Lucy collected the major and trace element data for the glass and mineral separates. She characterised the samples through detailed petrographic work and modelled the elemental data. She was available for discussion as the isotope data was obtained and provided constructive comments on interpretations and conclusions drawn from the integration of the two geochemical data sets.

Jon Davidson: Jon provided useful discussion and guidance throughout. He assisted with data interpretation and provided useful comments on the direction the manuscript should take.

Geoff Nowell: Geoff provided assistance and support during sample preparation and analysis in the lab. He was available for discussion and ensured high data quality.

Yaoling Nui: Yaoling provided the sample suite this study was based on and helped conceive the original MSci project.

1.2.6 Chapter 7

The work presented in this chapter adds to extensive and thoroughly detailed previous work by Antonio Acosta-Vigil (University of Granada) and Bernardo Cesare (Padova University). The data set discussed is small and will not contribute to a manuscript on

its own but it is hoped it will be integrated into a publication in the future pending further data acquisition.

Claire McLeod: I carried out the microsampling, chemistry and analysis for Sr isotope ratios on glass and mineral phases in thick section. I interpreted the data and used the conclusions drawn to support the arguments presented in Chapters 5 and 6.

Antonio Acosta-Vigil: Antonio provided the samples from which the phases were microdrilled and which he has characterised thoroughly in previous studies. He provided useful, constructive comments and feedback on ideas and initial drafting of this chapter. He was available to provide his expert geochemical knowledge and understanding of the study area and assisted with how best to integrate the isotope results with previous work.

Bernardo Cesare: Bernardo provided useful assistance and discussion of results. He provided his textural expertise on the sample suite and helped greatly by adding context to the discussion of the isotope data.

Jon Davidson: Jon provided feedback on drafts of the chapter and advice on how best to present the integration of this work with interpretations and conclusions made in Chapters 4, 5 and 6.

Geoff Nowell: Geoff provided assistance and support throughout sample preparation and analysis in the lab. He was available for discussion and addressed any instrument problems that arose.

The Central Andean continental margin 2

2.1 Introduction

The Andes of South America constitute the longest continental mountain range on Earth and the highest outside of Asia reaching a maximum elevation of 6.96 km in Argentina. The volcanoes of the Andes are the highest in the world with the peak of Mount Chimborazo in Ecuador being the point on the earth's surface which is most distant from the centre of the Earth. The Andean Cordillera is one of the world's best (if not *the* best) examples of magmatism which has developed on a continental margin. The mountains extend for over 7500 km along the western margin of the South American continent and have long provided a particular fascination for geoscientific research. As early as the first half of the 19th century, Charles Darwin was exploring the fundamental characteristics of this extensive range, yet large areas still remain unexplored today.

2.2 A converging destructive margin

The processes associated with subduction orogeny are some of the most intensely studied throughout the field of Earth Science as they are natural laboratories at which the energy flux rates and mass transfer between Earths reservoirs can be investigated. Convergent continental margins affect the continental lithosphere's internal architecture, thermal and geochemical budgets and are sites of deformation, crustal growth and destruction, ore genesis, uplift, magmatism and 90% of the earth's seismic energy (Oncken et al., 2006). The Andes therefore provide an exceptional insight into the processes governing the evolution of an active, destructive margin on the earth today. The Andean Cordillera can be divided into four zones: the Northern Volcanic Zone (NVZ; 6^{o}N-3^{o}S) to the east of the Cocos Ridge, the Central Volcanic Zone (CVZ; 14-28^{o}S) to the east of the Peru-Chile trench (where the subducting Nazca Plate is *c*. 44 Ma), the Southern Volcanic Zone (SVZ; 33-46^{o}S) to the east of the Chile Rise and the Austral Volcanic Zone (AVZ; 49-55^{o}S) which extends south from the Patagonian

Volcanic Gap to the Tierra del Fuego archipelago (Fig. 2.1 a). The existence of the most southerly zone may be predominantly controlled by the convergence of the South American and Antarctic Plate, transcurrent faulting and ridge subduction (e.g. Stern et al., 1984) rather than the easterly subduction of the Nazca Plate. The NVZ, CVZ and SVZ are characterised by relatively steep subduction angles (25-30^{o}) and are separated by volcanically inactive segments characterised by shallower subduction angles (Sørensen and Holm, 2008 and references therein) i.e. magmatism throughout the Andean Cordillera is controlled by subduction zone geometry with the presence of an asthenospheric mantle wedge separating the overriding plate from the subducting plate, a prerequisite for volcanic activity (Thorpe et al., 1981). Of particular relevance to this study is the CVZ which changes strike southwards from northwest to north at the Arica bend (~ 18^{o}S, Fig. 2.1 b). At these latitudes, the arc can be seen to bend the wrong way. Sinistral shear to the north and dextral shear to the south has produced counter-clockwise and clockwise block rotation respectively (from palaeomagnetic data, e.g. Beck, 1988), geodynamic scenario which has previously attributed to two arms of a failed triple junction (Scanlan and Turner, 1992). More recent work by however attributes the uncharacteristic geometry (convex to the downgoing slab) of the Central Andean arc to differences in the degree of "mechanical coupling" between the Nazca and South American Plates i.e. the variability in the resistive force that each plate exerts on the other in the opposite direction of their movement (Iaffaldano et al., 2012). In this scenario the upper plate is modelled to resist overriding the lower plate and the Central Andean margin is seen to accommodate more shortening than the regions to the north and south of it.

Beneath the Central Andes subduction occurs at 30^{o} (flatter to the north and south) at a rate of 61 ± 3 mm a^{-1} at an azimuth of 79 ± 4^{o} (Delacour et al., 2007 and references therein).

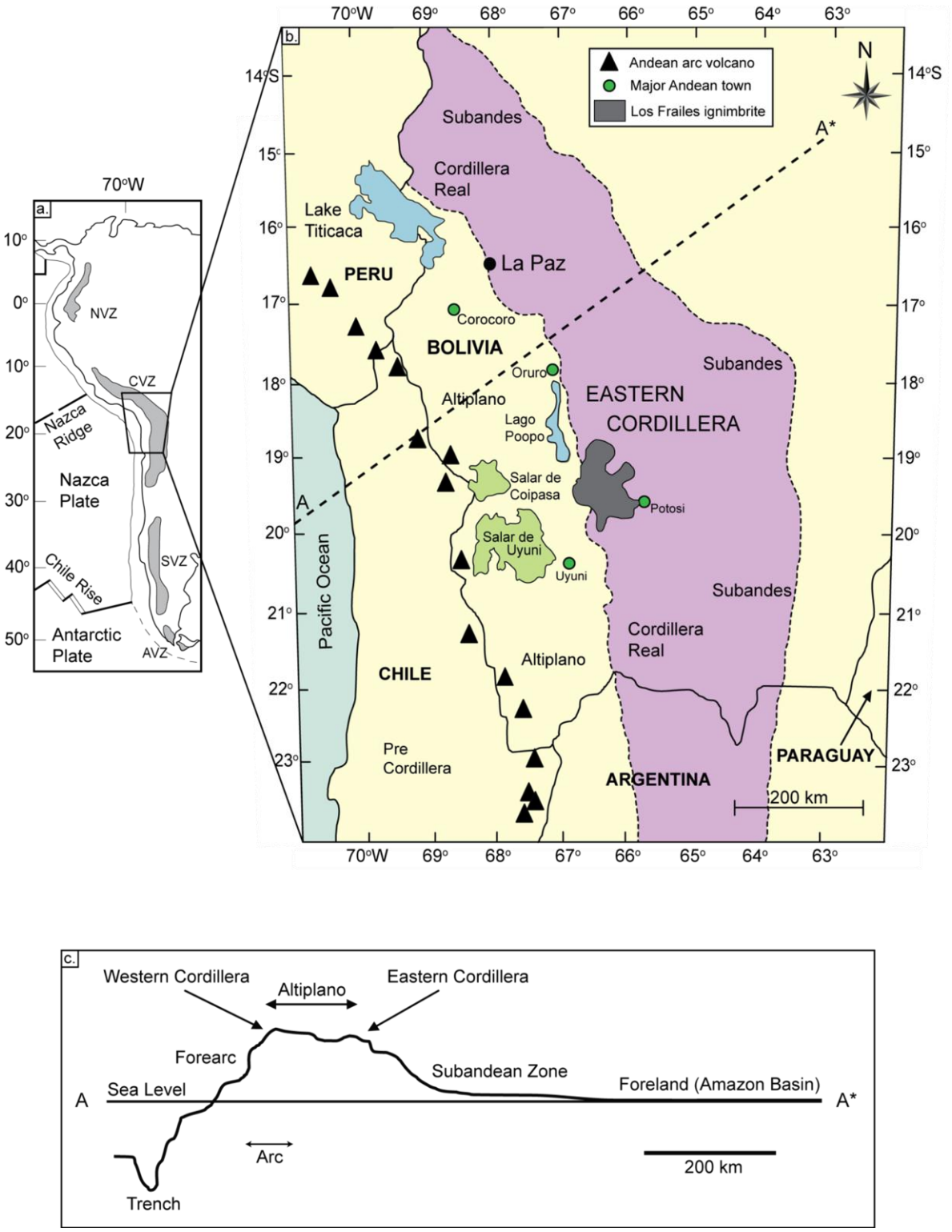

Fig. 2.1 a. The four main volcanic zones of the Andean Cordillera; the NVZ, CVZ, SVZ and AVZ. Map is modified from de Silva, (1989). **b**. Map showing the main features of the Central Andes including Salar de Uyuni, the world's largest salt flat (modified from Davidson and de Silva, 1995). The dashed dine (A-A*) corresponds to the profile in Fig. 2.1 c. **c**. Simplified E-W cross section highlighting Central Andean topography (adapted from Lamb et al., 1997).

This area is characterised by the active volcanic arc to the west, the Western Cordillera, which is arid with a few rivers draining to the west into the Pacific Ocean; a high plateau region to the east of the arc where the Andes are at their widest, the Altiplano-Puna Plateau at an average height of ~3.8 km, which is an extensive area of internal drainage with Salars (e.g. Salar de Uyuni) and freshwater lakes (e.g. Lake Titicaca) and an actively deforming foreland belt, the Eastern Cordillera, which reaches 5 km in height towards the Amazon Rainforest (Fig. 2.1 c).

The Peru-Chile Trench (also known as the Atacama Trench) lies ~70 km off the coast of western central South America with an estimated 14 km difference in altitude over 300 km from the deepest part of the trench at Richards Deep (8,065 m below sea level) to the highest point of the Western Cordillera at Ojos del Salado, Argentina which is the world's highest active volcano (6891 m).

2.3 Geological evolution of the Central Andes

The aim of this section is to present a regional framework for discussions presented later in this thesis on the genesis of Central Andean magmas and the nature of the underlying continental crust of this area. For detailed studies of Central Andean geology the reader is referred to the articles of Lucassen et al., (2000); McQuarrie, (2002); Jiménez and Lopez-Velásquez, (2008); Hoorn et al., (2010) and the reviews of Allmendinger et al., (1997) and Gregory-Wodzicki et al., (2000).

The geological evolution of the Central Andes has traditionally been divided into two orogenies; the "Hercynian Orogeny" (from ~550 to 220 my, Carlier et al., 1982) and the more recent "Andean Orogeny" (e.g. Sobolev and Babeyko, 2005). Metamorphism associated with early Hercynian deformation is understood to be low grade with rare high grade gneisses and schists (Bard et al., 1974; Laubacher and Mégard, 1985) and

minor associated magmatism. This early phase of Hercynian deformation was reactivated by Late Hercynian deformation (~ 270 my). A few workers have suggested that at this time, the Central Andes deformed in a transition zone between intra- and pericratonic regions during which subduction produced an active island arc which migrated westward through time (e.g. McNutt et al., 1975; Coira at el., 1982). However, Laubacher and Mégard, (1985) refuted this idea based on the lack of evidence for the existence of an island arc and its associated suture within the fold belt.

The nature and events of the Andean Orogeny are relatively better understood and constrained. The western margin of the South American continent has been defined by subduction since the early Jurassic and since subduction-related volcanism (and plutonism) began, the locus of the arc front has migrated by ~200 km eastward relative to its current position (Fig. 2.2 a). The Jurassic magmatic arc now makes up the Coastal Cordillera and the modern day fore arc which lies 50-150 km away from the trench (Trumbull et al., 2006). Over time the zone of magmatic activity has also broadened significantly especially since ~20 Ma (Oncken et al., 2006).

The Andean Orogeny can be divided into six main compressional stages, each of which lasted a few hundred thousand to a few million years (Mégard, 1984): the Mochica phase (following the work of Steinmann, 1929) which saw the folding of eugeosynclinal deposits in western Peru; the Peruvian phase (constrained to ~84 Ma) saw widespread deformation in the Central Andes (particularly Peru) which resulted in the formation of basins in western and eastern Peru in which continental red bed sedimentation took over from marine sedimentation; the Incaic phase spanning the mid to late Eocene which produced the deformed belt of the western Cordillera which was subsequently eroded and overlain by sediments and volcanic rocks ~ 40 Ma (Noble and Mégard, 1979); and Quechua phases 1, 2 and 3 which span ~14 million years from ~20 Ma to ~6 Ma. Deformation throughout these phases is understood to

have migrated progressively eastward into the Amazonian foreland throughout the Andean Orogeny (Mégard, 1984).

More recently, Lamb et al., (1997) recognised five main tectonic stages throughout the Cenozoic era (since ~65 Ma) specifically in Bolivia and northern Chile. These events are summarised below and schematically in Fig 2.2 a. They highlight the significant crustal shortening (Fig. 2.2 b) that has occurred, establishment of the modern day volcanic arc front and the rise of the Altiplano(-Puna) Plateau.

1) During the late Cretaceous and early Tertiary (Paleocene) a volcanic arc developed on the modern day fore arc. To the east a 400 km wide zone of subsidence existed at (or close to) sea level which was filled by material derived from the arc and easterly back arc regions. At the start of the Cenozoic, subduction of the Farallon Plate occurred beneath the South American Plate and following the break-up of the Farallon Plate ~23 Ma (Lonsdale, 2005) subduction beneath the South American continent has been defined by the Nazca Plate. The subduction history beneath the Central Andean margin prior to the Cenozoic is poorly understood but is thought to have been dominated by the accretion and subduction of oceanic terranes (e.g. Aspden et al., 1987).
2) During the Eocene (the Incaic phase of Mégard, 1984), the back arc basin that existed in the Cretaceous was inverted and uplifted in a narrow (<100 km) zone. This defines the western extent of the Eastern Cordillera today which at its time of formation was a few 100 km east of the active arc front. This uplift created a basin, the proto-Altiplano, which accumulated sediment from the arc and the uplifting eastern basin.

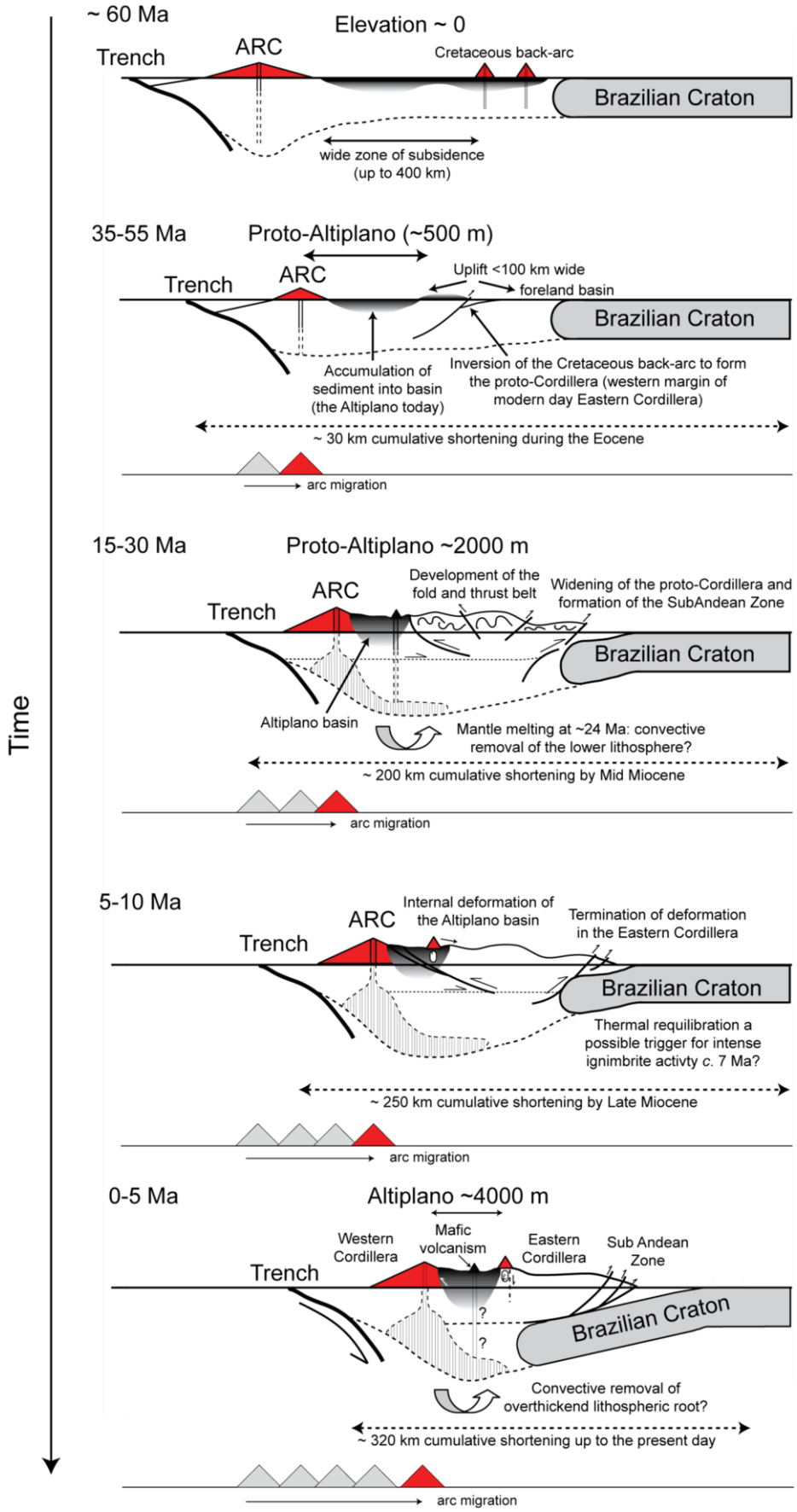

Fig. 2.2 a. Cartoon depicting the Cenozoic evolution of the Central Andes at 20°S (modified from Lamb et al., 1997)

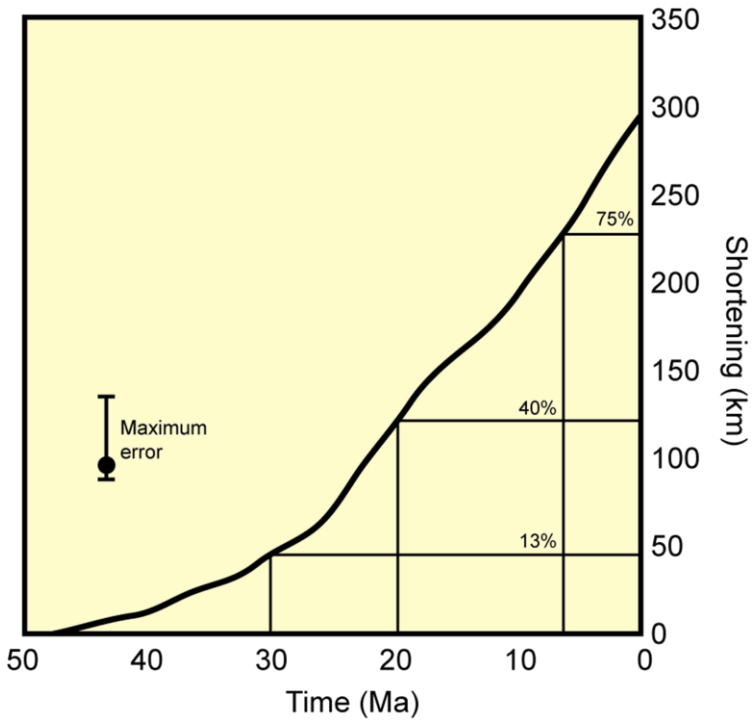

Fig. 2.2 b. Graph displaying the cumulative shortening (%) across the Central Andes (at 21°S) since 50 Ma (adapted from Oncken et al., 2006).

3) By ~25 Ma the zone of uplift had widened and deformation extended westwards towards the Altiplano as a fold and thrust belt and eastward in east-verging structures (Quechua phase 1, Mégard, 1984). At this time deformation is thought to have been thick-skinned, characterised by upright folds and high angle reverse faulting. Deformation in the east resulted in the development of a foreland basin (the Subandean zone today) and an initial phase of minor mafic volcanism occurred, possibly related to (partial?) loss of the lower lithosphere at depth.

4) Towards the end of the Miocene the style of deformation changed across the region. Deformation in the Eastern Cordillera stopped and was instead concentrated in the Altiplano which shortened internally from ~9 Ma to ~ 5 Ma. This cessation in deformation may have coincided with the eastward underthrusting of the Brazilian Craton and subsequent deformation in the Subandean Zone (Quechua phase 2, Mégard, 1984).

5) Prior to ~5 Ma, deformation was dominated by a west-verging component. Following ~5 Ma, deformation was east-verging (Quechua phase 3, 1984). A second phase of minor, mafic volcanism occurred at this time which has been attributed to removal of an overthickened lithospheric root as a result of Mid to Late Miocene shortening. Today the Altiplano is at a height of ~ 3.8 km and the region has accommodated ~ 400 km of horizontal shortening since ~ 60 Ma.

2.4 The Altiplano-Puna Plateau

The continental plateau of the Central Andes is one of the biggest tectonically active orogens on earth (Tibet being the largest). In spite of this, the evolution and construction of this defining topographical and morphological feature is poorly understood and continues to be an active research topic today (e.g. Barnes and Ehlers, 2009). Not only is the construction of the plateau of interest to geologists but the uplift history is of particular interest to climatologists as the plateau's height will have had (and has) direct effects on atmospheric circulation, seasonal precipitation and rates of weathering and erosion.

The Altiplano (Bolivia, Peru)-Puna (Argentina) Plateau covers a region over 500,000 km^2 at an average height of 3.8 km (Fig. 2.3 a) and is unique along the entire 60,000 km of the globe's convergent margins (Oncken et al., 2006). It exists as a geodynamical paradox; the production of a high plateau during crustal thickening and continuous subduction of an oceanic plate yet in the absence of continent-continent collision and terrane accretion. The existence of the high plateau has since been compared to the production of the Mesozoic-Cenozoic Cordillera of the western United States (the Laramide province) which is also referred to as an "Andean-type" margin (e.g. Burchfield and Davis, 1975) given the inference of eastward subduction beneath a

continental margin. Respectively, the plateaus represent eroded and active examples of the same orogenic system (Jordan et al., 1983).

The high, flat plateau is present only in the Central Andes from ~14 to ~29°S and is bound to the north and south by amagmatic regions which reflect the relatively flat subduction of the Nazca Plate at those latitudes. The easterly extent of the Altiplano plateau is marked by the Eastern Cordillera which is composed of the remnants of a magmatic arc which existed in the Late-Oligocene through to the Late Miocene.

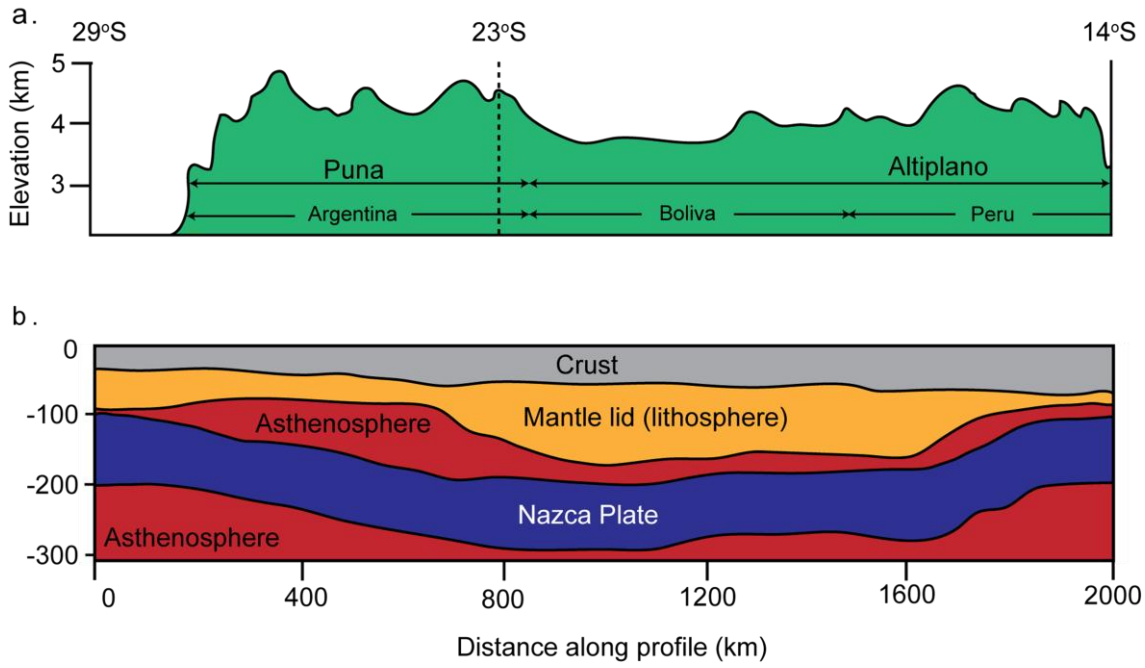

Fig. 2.3 a. North-South topographic profile along the Central Andean Cordillera (adapted from Whitman et al., 1996). **b**. Along-strike variations in lithospheric structure as inferred from seismic attenuation and the depth to the descending Nazca Plate between 14°S and 29°S (adapted from Whitman et al., 1996).

On the plateau's surface lie Salars, most notably Salar de Uyuni which at 10,583 km^2 is the world's largest salt lake and contains a significant concentration of lithium in its seasonal brines (Keating, 2009). Volcanic rocks from the Late Oligocene to recent are also present on the plateau's surface (e.g. Davidson and de Silva, 1995) alongside extensive Miocene to recent ignimbrite complexes e.g. Kari Kari and Los Frailes. The

plateau's western extent is marked by the rise of the Western Cordillera, the modern-day magmatic arc which is characterised by 44 potentially active composite volcanoes e.g. Tata Sabaya, Irruputunca and Ollagüe (de Silva and Francis, 1991).

Inferred along-strike variations from 14°S (Peru) to 29°S (Argentina) in the structure of the upper mantle correspond to topographic changes on the surface (Fig. 2.3 a, b; Whitman et al., 1993). There is a significant change south of 23°S where the lithosphere is interpreted to be thinner (by 50-100 km) and weaker, and the upper mantle is hotter. This coincides with the topographic change between the Altiplano and Puna regions of the Central Andean plateau. From Beck et al., (1996), estimates of crustal thickness (assuming Airy-type isostasy) revealed a close agreement between crustal thickness and topography across the Altiplano region at ~21°S (Fig. 2.4).

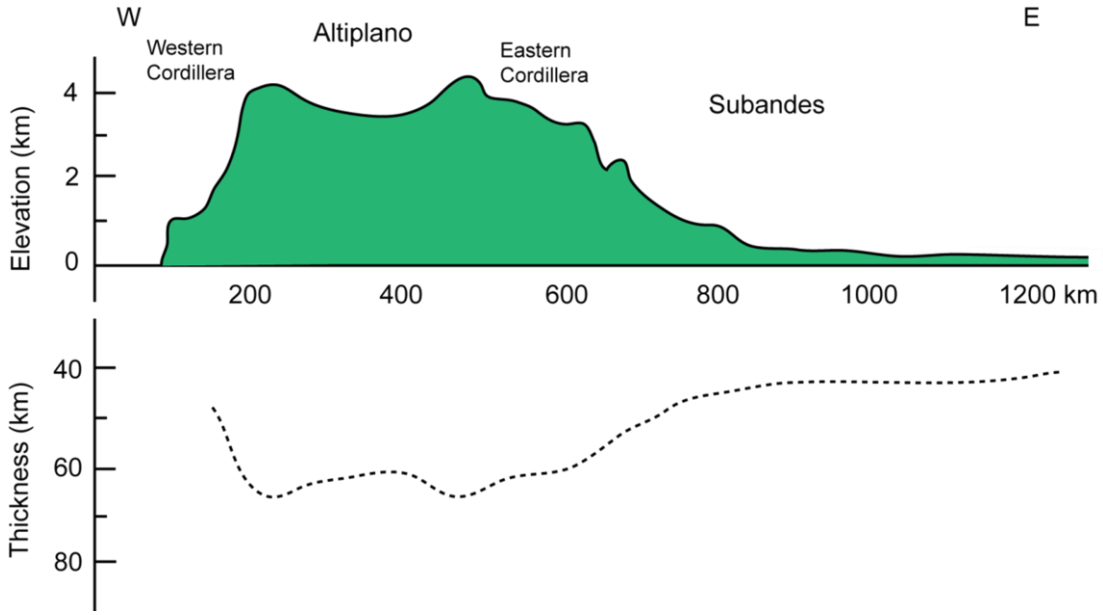

Fig. 2.4. An east-west topographic cross section of the Central Andes at 20°S and corresponding crustal thickness assuming Airy-type isostasy (modified from Beck et al., 1996).

Further constraints on the nature of the underlying lithospheric structure beneath the Altiplano Plateau come from seismological and gravimetric studies (e.g. Beck et al.,

1996; Schmitz et al., 1999; Romanyuk et al., 1999). The Central Andean crust is principally felsic in composition (i.e. quartzofeldspathic). It generally lacks a mafic lower crust where Fe-Mg minerals would be expected to dominate, with the exception of the Chilean coastal Cordillera (Lucassen et al., 2001). Seismic velocities show low values beneath the Central Andes inconsistent with the presence of mafic lithologies at depth. The absence of a velocity contrast between an upper felsic and lower mafic crust (as would be expected in a typical cross section through the continental crust), also suggests no high density lower crust exists beneath the Altiplano. No densities > 3.0 gcm^{-1} are inferred at depth again indicating the lack of mafic crust. Beneath the area of Bolivian Altiplano of this study a region of fast P wave velocities suggest the presence of lithospheric mantle (Myers et al., 1998; Barnes and Ehlers, 2009). The base of this high velocity layer is ~125-150 km and spans the Altiplano at ~19°S but to the south (~21°S) low seismic velocities encroach from the Eastern Cordillera. Upper mantle seismic parameters are therefore consistent with mantle lithospheric compositions from 18 to 20°S and the thinning of the mantle lithosphere to the south corresponds with the voluminous surface volcanism on the Altiplano-Puna complex south of ~21°S. This is supported by results from a bouguer and residual gravity study by Scheuber and Giese, (1999) which were interpreted as indicating the absence of lithospheric mantle beneath the Andean arc and Altiplano at 21°S with mantle asthenosphere inferred to be in contact with the base of the thickened continental crust.

The growth of the Altiplano-Puna plateau correlates with Cenozoic Andean arc magmatism both spatially and temporally but its uplift and extreme height is understood to be the result of significant crustal thickening due to horizontal shortening (Allmendinger et al., 1997) although it has been suggested that this shortening varies along strike (Kley and Monaldi, 1998). Various other models accounting for the plateau's extreme height and vertical extent have however been

proposed (see below and in Fig. 2.5; for detailed discussion as to the validity of these models, the reader is referred to the summary of Barnes and Ehlers, 2009 and references therein): 1) Crustal shortening (up to 80% of total shortening; Allmendinger et al., 1997); 2) Crustal flow (Husson and Sempere, 2003); 3) Delamination of an overthickened lithospheric root (Kay et al., 1994); 4) Magmatic addition to the base of the lower crust (Thorpe et al., 1981); 5) Cratonic underthrusting by the eastward subduction of the Brazilian craton (Lamb and Hoke, 1997); 6) Variations in space and time of erosion (Strecker et al., 2009); and 7) Variations in space and time of upper plate properties and the geometry of the subduction zone (Isacks, 1988; McQuarrie, 2002).

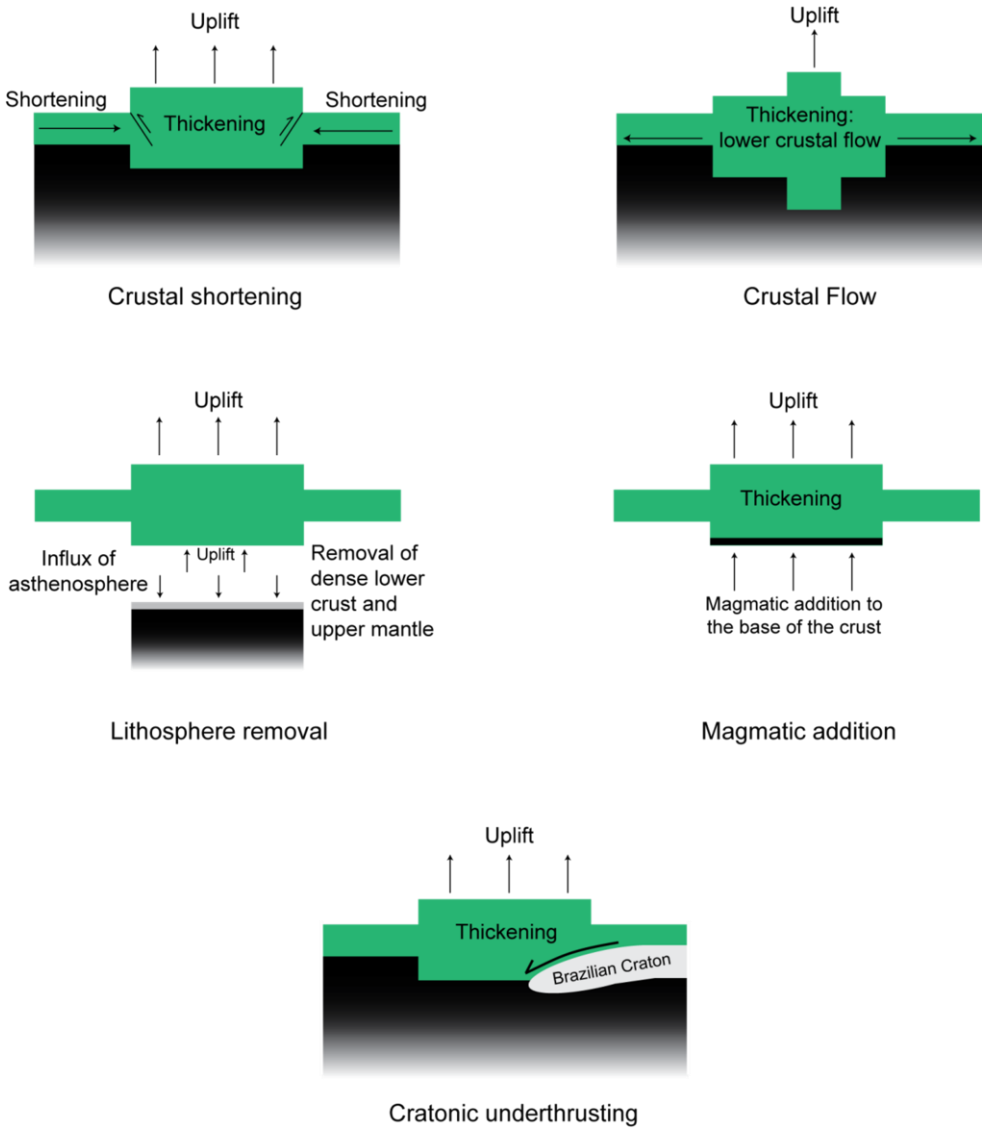

Fig. 2.5. Models proposed for the formation of the Altiplano-Puna Plateau.

The growth of the plateau through bulk shortening has recently been shown to have occurred over three distinct intervals: 45 to 30 Ma saw an increase in the bulk shortening rate from 0 to 8 mm/yr; 30 to 10 Ma saw a fluctuation between 6 and 10 mm/yr and 10 – 0 Ma has seen an increase to between 8 and 14 mm/yr with today's value estimated at an average 9 mm/yr (Oncken et al., 2006). Questions still remain however regarding how this shortening is spatially and temporally distributed, how the plateau has mechanically and thermally evolved and what the controls on topographic and structural geometries are. As a simple approach, Allmendinger and Gubbels, (1996) considered two end members: crustal shortening through simple shear and pure shear where the difference lies in the distribution of the shortening throughout the crustal column. Across the Central Andes the Altiplano Plateau of Bolivia accumulates more shortening than the southern Puna plateau, is underthrust by the cold, dense Brazilian Shield from the east and deforms thin-skinned in the Subandean foreland belt where the locus of upper crustal shortening is not located directly above the locus of lower crustal shortening (Fig. 2.6 a).

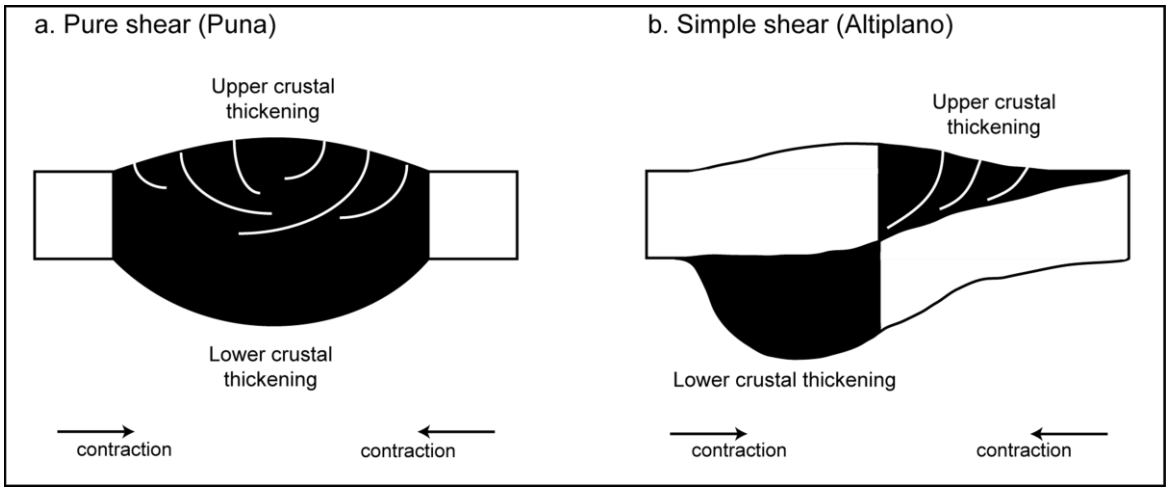

Fig. 2.6. End member models accounting for the crustal shortening observed across the Central Andes. **a**. Pure shear. **b**. Simple shear. Adapted from Barnes and Ehlers, (2009).

In comparison, the Puna Plateau of Chile and Argentina is narrower, on average ~1 km higher in elevation, has thinner lithosphere at depth and deforms thick-skinned in the Santa Barbara and Sierras Pampeanas foreland belts, where the locus of upper crustal shortening corresponds vertically to the locus of lower crustal shortening Fig. 2.6 b).

These observations are reconciled by models of crustal shortening through simple shear in the Altiplano and pure shear in the Puna (Allmendinger and Gubbels, 1996). The difference in elevation between the two plateau segments (and relative lack of a lithospheric root beneath the Puna plateau) has been attributed to the delamination of the lower lithosphere into the asthenospheric mantle and the subsequent return flow of less dense asthenosphere into the space (Kay and Kay, 1993).

The rate of plateau uplift can similarly be considered by two end member models; a slow and steady uplift (with concomitant deformation) of the plateau since ~40 Ma in contrast to a rapid uplift of 2.5-3.5 km between 10 and 6 Ma (Barnes and Ehlers, 2009). Supporting evidence for a rapid rise of the plateau during the Late Miocene comes from a notable change in the oxygen isotopic compositions of carbonate rocks to the north of the Altiplano between 10 and ~6.8 Ma (Garzione et al., 2006). Estimates of paleoaltimetry from the oxygen isotopic compositions of carbonate rocks (where $\delta^{18}O$ is empirically related to altitude) have been interpreted as demonstrating that between 11.5 and 10.3 Ma the plateau was at -700 ± 1000 m and 1700 ± 700 m compared to estimates of 3500 ± 500 m to 4200 ± 500 m by 6.8 Ma. A rapid uplift rate of 2.5-3.5 km in 4 Myrs requires an average vertical rate of 0.6 mm/yr (Garzione et al., 2006). These changes in paleoelevation are shown to be coincident with a ~30% decrease in the convergence rate between the South American and Nazca Plates and the magnitude of this uplift has been reconciled with the (rapid) removal of a dense (lower crustal) eclogitic root and mantle lithosphere (Garzione et al., 2006). Measurements of the

concentrations of ^{13}C-^{18}O bonds in paleosoils from the Altiplano have also been interpreted as recording a rapid plateau rise, in this case 1.03 ± 0.12 mm/yr from -400 to 0 m since ~10.3 Ma to its current elevation at ~6.7 Ma (Ghosh et al., 2006). Further estimates of paleoelevation have been derived from leaf physiognomy (Gregory-Wodzicki et al., 1998) which has been inferred to indicate that a 10.66 ± 0.66 Ma flora ($^{40}Ar/^{39}Ar$ dating) in the northern Altiplano grew at at an altitude of 590-1610 ± 1000 m. This is significatly lower than the plateau's current elevation. A significant rise in plateau elevation is therefore required to have occurred since ~10 Ma although no constraints on the rate of plateau uplift can be placed from this study. Additonal paleoaltimetry data from paleosols are interpreted as recording the plateau (at least parts thereof) at sea level as recently as ~11 Ma (Ghosh et al., 2006) which severely contradicts the widely held view that the Andean Orogeny began in modern-day western Bolivia at least 26 Ma (Sempere et al., 1990), with geomorphic evidence indicating the Western Cordillera of Bolivia to be at ~2 km as recently as 20 Ma (Sébrier et al., 1988). There are however problems with the studies discussed above. It has been suggested that the analysed paleosols have undergone burial metamorphism (and therefore potential recrystallisation) and that the paleoaltimetry method underestimates high altitudes (Sempere et al., 2006). Furthermore, the sampled carbonates are likely to have experienced oxygen isotope fractionation due to evaporation and therefore $\delta^{18}O$ enrichment (evaporative enrichment has been shown to potentially account for up to 2‰ shifts in $\delta^{18}O$, Ghosh et al., 2006).

Alternatively, it has been suggested that uplift was (and still is) steady and has been since at least ~40 Ma i.e. plateau uplift and deformation are concomitant. Recent results from the thermochronometer applied to apatite and zircon fission tracks indicates exhumation of the Eastern Cordillera commenced ~27 to 36 Ma and continued into the late Oligocene and early Miocene. Exhumation in the Interandean zone began ~19-22

Ma and is inferred to indicate the establishment of the modern day width of the Altiplano Plateau (with considerable crustal thickness) established by 15-20 Ma (Barnes et al., 2008). The plateau's shape is also thought to have been established by Paleogene times (Oncken et al., 2006). Additionally, between 2 and 2.5 km of elevation of the plateau is inferred to have occurred prior to 11 Ma (Rech et al., 2006; Picard et al., 2008) with significant crustal deformation and sedimentological regimes requiring thickened crust prior to ~ 25 Ma (Barnes and Ehlers, 2009).

In summary an uplift model of slow, steady rise since the late Eocene is shown to be more consistent with observations across the Altiplano-Puna Plateau (Barnes and Ehlers, 2009) with research into the mechanisms inherent to plateau construction on-going today. With the amount of crustal shortening observed across the Central Andes since construction of the plateau began, a mechanism that is removing/has removed the shortened mantle lithosphere (or part thereof) must exist at depth. The exact nature of this mechanism remains unconstrained but may involve one or more of the following: delamination (England and Houseman, 1988) and convective removal (Lamb et al., 1997).

2.5 Regional faulting

Cenozoic deformation within the Altiplano-Puna Plateau has been dominated by folding and thrusting (i.e. contraction). At the present day (and since the Neogene) however, activity on regional strike-slip domains and local normal faults along which orogen-parallel extension is accommodated is more important (Oncken et al., 2006).

The Central Andean Plateau is a region of well documented anomalously thick continental crust hence it is surprising that surface expressions of magmatism exist at all. In many volcanic provinces on Earth, magma ascent is driven primarily by

buoyancy as ascending magmas are less dense than their mantle source. However, in the Central Andes the overlying (and less dense) felsic crust prevents the ascent of mantle derived melts driven simply by buoyancy. That said, although primary mantle melts may not be buoyant locally within the continental crust they will at least initially have been less dense than their mantle source and therefore would have risen into the crust, i.e. the pressure gradient would have been sufficient enough to drive the magma into the crust just not sufficient enough to drive eruption.

An important observation made by Marrett and Emerman, (1992) was the correlation in space and time of monogenetic mafic volcanism and regional faulting in the Central Andes. This leads to the idea that the eruption of minor volcanic centres on the Altiplano-Puno Plateau is strongly linked to fault activity with fault planes acting as conduits to ascending mantle-derived melts. Fault kinematic studies across the Central Andean plateau reveal a distinct change in the nature of deformation from the Miocene-Pliocene into the Quaternary (e.g. Marrett and Emerman, 1992; Cladouhos et al., 1994). The older phase (the Quechua phase, 21.5 to 12.5 Ma after Mégard, 1984) is characterised by a regime of NW-SE shortening on dip-slip faults and vertical extension dominated by plateau parallel thrust faults and normal faults (?) respectively (Fig. 2.7 a). This Miocene shortening is thought to have reactivated normal faults associated with an intracratonic Cretaceous rift system in reverse. Dip-slip motion on these reverse faults strikes NNE-SSW (with minor N-S motion) implying a shortening direction of $120^{o} \pm 020^{o}$. Cessation of orogen perpendicular shortening is inferred to have occurred during the late Miocene as constrained by dating of a tuff at Pampa de Yavi in northern Argentina which covers reverse faults at 8.78 ± 0.17 Ma. This regime is in contrast to the more recent phase of deformation which occurs in a dominantly strike-slip regime (with minor normal faulting) with NE-SW to E-W shortening and NW-SE, N-S horizontal extension (Fig. 2.7 b).

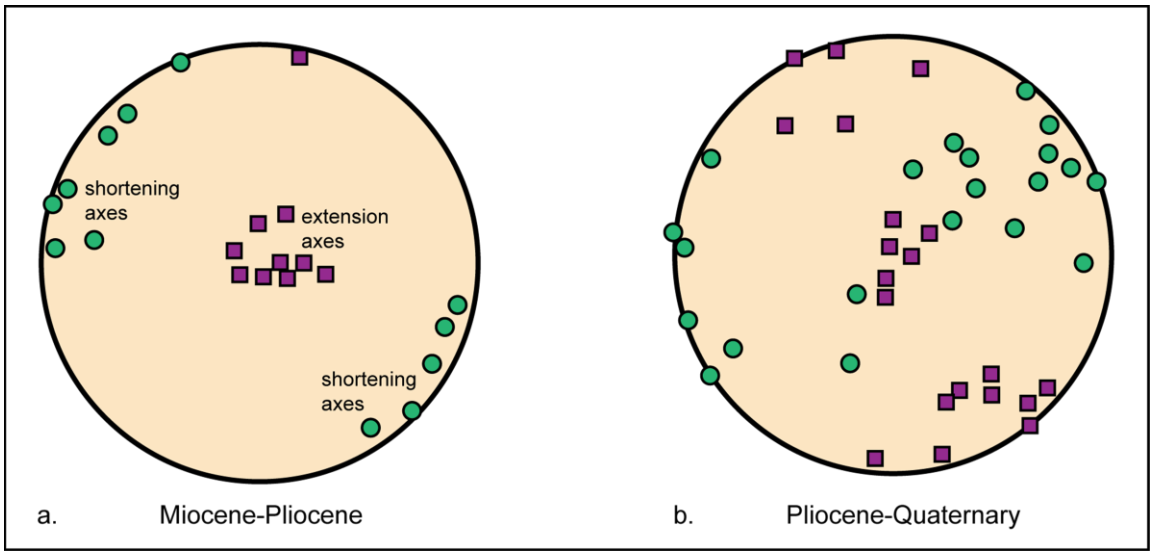

Fig. 2.7. Fault kinematics of **a**. Miocene-Pliocene and **b**. Pliocene-Quaternary faults (adapted from Marrett and Emerman, 1992). Since ~10 Ma the direction of minimum compressive stress has changed from vertical to horizontal

This younger phase of deformation is easily seen in the northern region of the Puna Plateau where deformation is accommodated by five orogen parallel right-lateral strike-slip faults (Cladouhos et al., 1994) and in southern Bolivia-northwest Argentina where numerous shoshonitic flows are aligned with the NW-SE trending lineaments of Calama-Olcapato-El Toro and Archibara (Fig. 2.7 c) which are inferred to have accommodated 20 km of left lateral strike slip (Schreiber and Schwab, 2001).

This change in fault kinematics resulted in a change in the direction of the minimum compressive stress from vertical to horizontal. If magmatism during the Miocene occurred in the Central Andean back arc region it is likely the magma ascent through the crust to the surface was prevented by the horizontal nonlithostatic compression state of the crust. At this time, ascending mantle-derived melts may have stalled in the (lower) crust forming intrusions/intracrustal sill complexes thus promoting thermal weakening of the crust and initiating crustal anatexis, the processes and results of which have been well documented (e.g. production of voluminous ignimbrites; de Silva, 1989) and which will be discussed later in this thesis. A change in the stress

conditions towards the end of the Pliocene to a state of horizontal nonlithostatic tension within the crust would support vertical intrusion of mantle-derived magma and drive surface eruption i.e. changing the crustal stress pattern beneath the Altiplano-Puna Plateau may have promoted ascent of mantle-derived magma to the surface during activity of strike slip faulting during the Pliocene-Quaternary but not through thrust faulting during the Miocene-Pliocene. Subvertical discontinuities within the crust require the lowest magmatic pressure by ascending melts for penetration hence are potential pathways for ascending material.

These broad regions of strike slip activity in the Central Andes (Fig, 2.7 c) have also been associated with caldera collapses in the northern Puna Plateau of Argentina e.g. the Culampaja fault zone which crosses into northern Argentina from Chile. Riller et al., (2001) have similarly suggested that ignimbritic volcanism resulting from caldera collapses was related to activity on these NW-SE trending strike slip faults. The caldera collapses have been dated at ~10 Ma and younger which coincides with the change from a dominantly vertical thickening regime through thrust faulting to an orogen parallel stretching regime where strike slip tectonics dominated (as discussed above).

The spatial and temporal relationship between regional strike-slip faulting (and associated deformation) and mafic monogenetic volcanism since ~ 10 Ma throughout the Central Andean Plateau can be explained by a change in the direction of the least principal compression from vertical to horizontal. This change in fault kinematics in the Late Miocene is therefore attributed to the mechanical evolution of the plateau and not to changes in the subduction regime (Cladouhos et al., 1994, Riller et al., 2001).

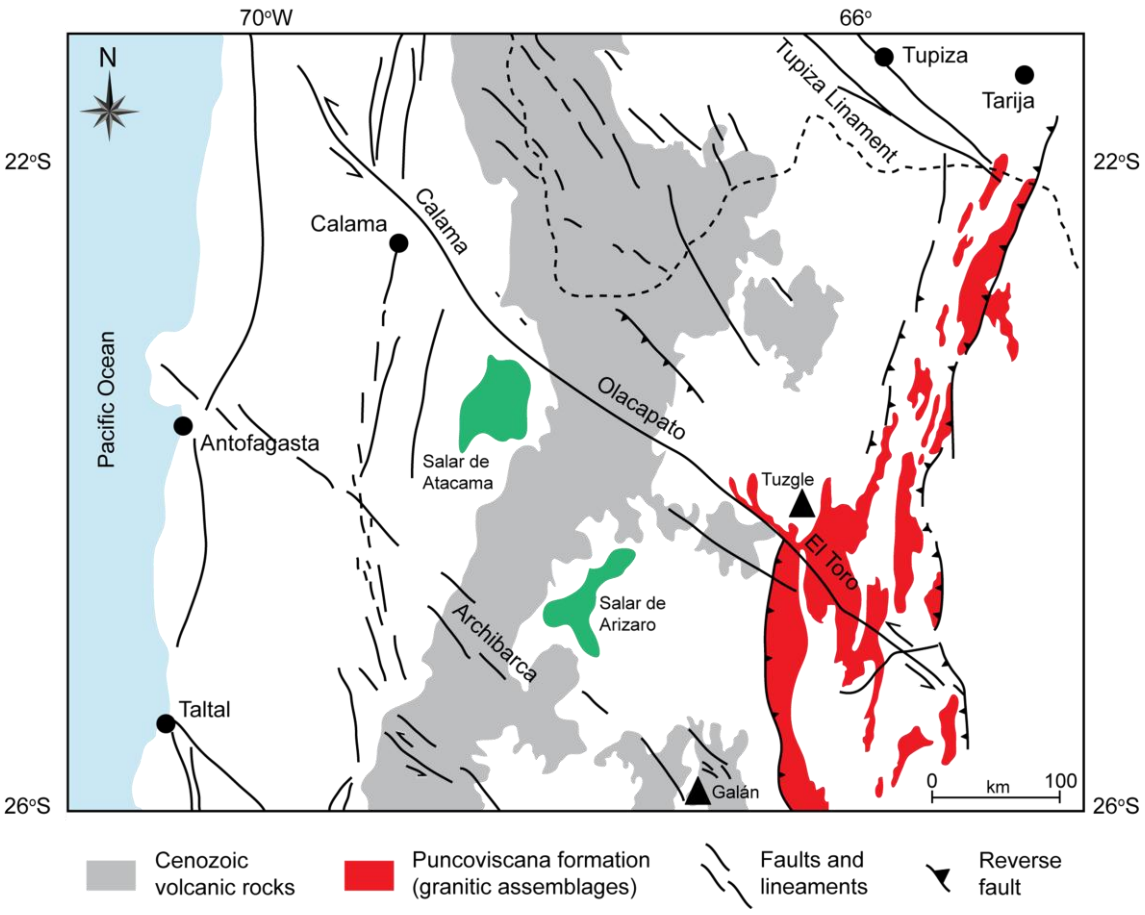

Fig. 2.7 c. Map showing the predominance of NW-SE trending lineaments in the CVZ from ~21°S to 26°S (modified from Schreiber and Schwab, 1991).

2.6 The Continental Crust of the Central Andes

The continental crust of the Central Andes is abnormally thick, reaching up to 80 km (Zandt et al., 1994). This is thicker than at any other subduction zone on Earth today (Wörner et al., 1992). This extreme thickness is attributed to shortening of the crust during the Tertiary and not to juvenile magmatic addition to the base of the crust (see discussions previously), thus implying a major contribution from pre-Tertiary material. Due to extensive sedimentary cover there are very few exposures of the metamorphic basement (Tosdal, 1996; Wörner et al., 2000) hence the nature of the continental crust in the Central Andes is very poorly constrained. It has been argued (e.g. Isacks, 1988; Lamb et al., 1997) that the Central Brazilian Shield has been underthrust beneath the Eastern Cordillera (see Fig. 2.2 at present day). Litherland et al., (1989) mapped

~220,000 km^2 of Proterozoic metamorphic basement in eastern Bolivia (approximately 16^{o}S, 62^{o}W) and found extensive exposures of granulites, gneisses and schists however the western extent of the Shield remains unknown.

The Rio de la Plata Craton outcrops in northwest Argentina (Coira et al., 1982; Allmendinger et al., 1983) where slates, phyllites and schists of greenschist facies outcrop and pass into medium high-grade rocks southwards. The craton's northern extent is unconstrained and no exposures in Bolivia have been reported. It is thought the majority of the Bolivian Altiplano is underlain by the Arequipa-Antofalla craton which is comprised of three domains that young to the south (Loewy et al., 2004, Fig. 2.8). A single surface exposure of the Bolivian metamorphic basement can be found at Cerro Uyarani on the western Altiplano (18^{o}30'S, 68^{o}40'W) where granulites, charnockites and rare amphibolites with early Proterozoic protoliths outcrop (Wörner et al., 2000). Other crystalline basement rocks are recorded in a San Andreas drilling hole (Lehmann, 1978) where the Precambrian basement (hornblende meta-granite and biotite meta-granite) is ~3 km below the surface and Palaeozoic strata are absent.

2.7 Geochemical signatures in Andean volcanic rocks

The aim of this section is to present a framework for discussions presented later in this thesis on the petrogenesis of Central Andean magmas. No attempt is made to 1) provide a detailed account of geochemical variability observed along and across the arc and back arc regions throughout the Andean Cordillera or 2) present a detailed discussion on the origin and subsequent evolution of Andean volcanic rocks. For this the reader is referred to Chapter 4 and (in particular) the articles of James, (1981); Hawkesworth et al., (1982); James, (1982); Harmon et al., (1984); Notsu et al., (1987); Kay et al., (1994); Bourdon et al., (2002); Bryant et al., (2006); Sørensen and Holm, (2008); Kay et al., (2010); Mamani et al., (2010).

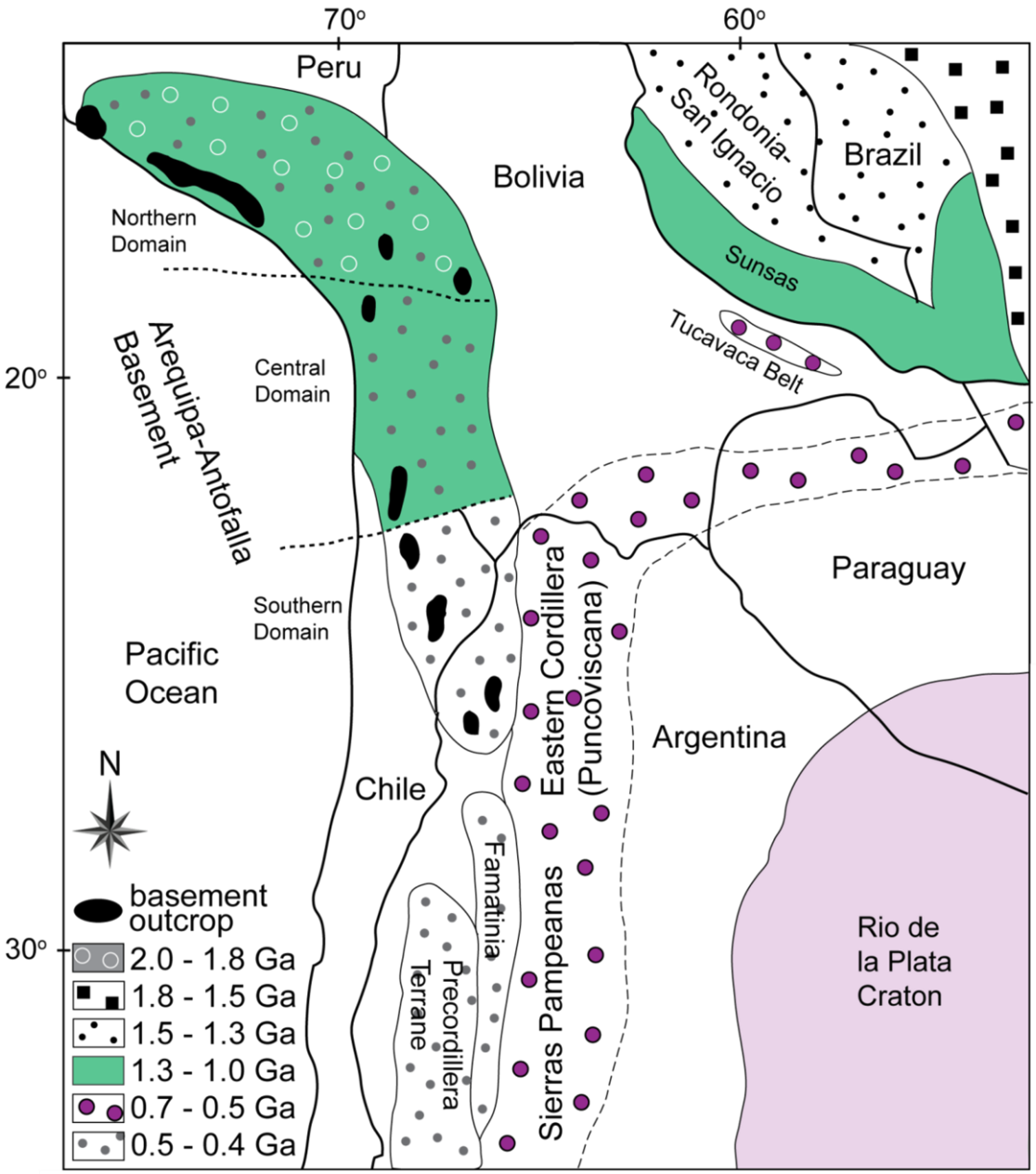

Fig. 2.8. Map showing the three cratonic regions (Brazilian Craton in northeast Bolivia; Rio de la Plata Craton in northern Argentina and the Arequipa-Antofalla Basement in Peru, Bolivia and Chile). Which are inferred to underlie the Central Andes. Map is modified after Loewy et al., (2004).

Investigations into the geochemical variability of volcanic rocks erupted at active arcs pose questions regarding the relative contributions from lithospheric and/or asthenospheric mantle, the subducted oceanic slab, subducting sediment on the downgoing plate and lower and upper crustal reservoirs. The degree to which mantle and crustal reservoirs influence the geochemical compositions of volcanic rocks from

the (Central) Andes has been a hotly debated research topic for decades. The volcanic rocks of three main volcanic zones of the Andean Cordillera (N-, C- and SVZ) can also be distinguished by their radiogenic isotopic compositions, particularly Sr and Pb (Fig. 2.9). The CVZ exhibits higher $^{87}Sr/^{86}Sr$ and $^{208}Pb/^{204}Pb$ than the northern and southern zones which are shown to be less radiogenic by comparison.

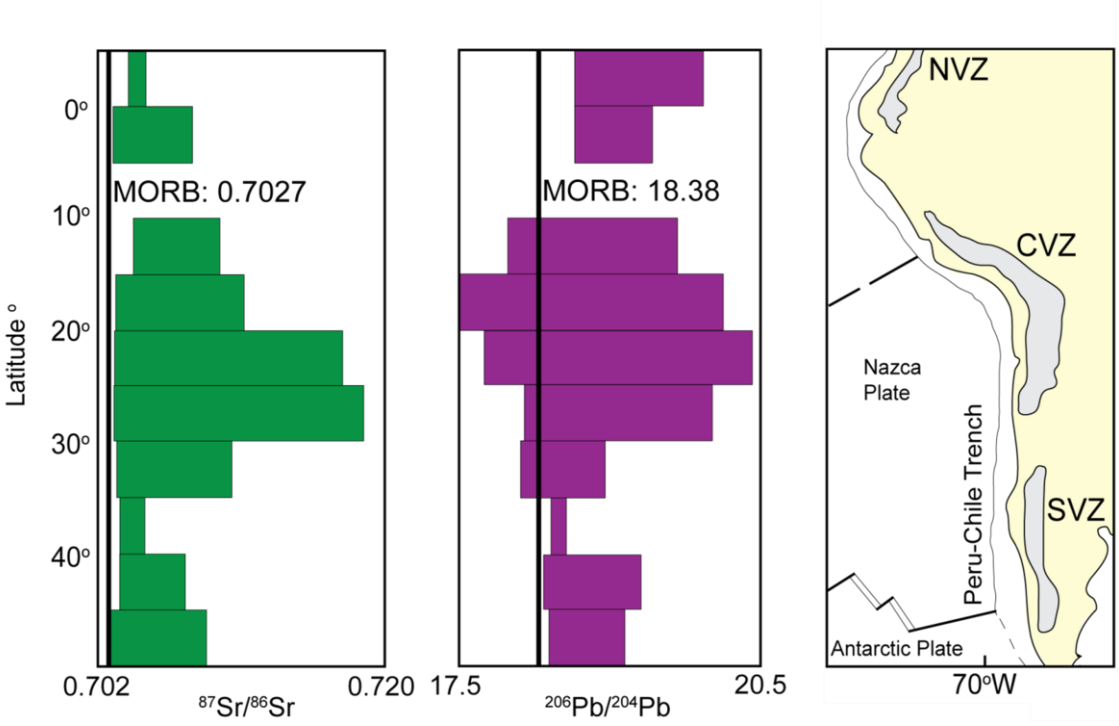

Fig. 2.9. Variation of $^{87}Sr/^{86}Sr$ and $^{206}Pb/^{204}Pb$ between Cenozoic (< 60 Ma) volcanic rocks of the NVZ, CVZ and SVZ (in 5° bins). Data were compiled from GEOROC, Map is modified from de Silva, 1989. Values for MORB after Kelemen et al., (2004)

The variable geochemical signatures observed in magmatic rocks throughout the Andean Cordillera have been attributed to a number of processes: 1) subduction erosion whereby the continental crust is removed from the downgoing slab and incorporated into the arc-mantle wedge (Stern, 1991). This process has been inferred to control the elevated $^{87}Sr/^{86}Sr$ of mafic magmas in the southern Central Andes and SVZ although this inference has been questioned on the basis of $\delta^{18}O$ data (Davidson, 1991); 2) sediment contamination which involves incorporation of sediment (or at least sediment derived fluids) from the downgoing slab into the arc-mantle wedge which is subsequently melted (Kilian and Behrmann, 2003). Sigmarsson et al., (1990) used the

positive correlation between $^{10}Be/^{9}Be$ and $^{238}U/^{230}Th$ in volcanic rocks from the SVZ as evidence for the role of subducted sediments and fluids derived therefrom in magma genesis. Kilian and Behrmann, (2003) sampled downgoing trench sediments off southern Chile and invoked the role of a 3-5% terrigenous sediment melt during arc magma petrogenesis between 41 and 47°S; 3) crustal contamination i.e. the process of contamination of mantle-derived melts by the continental crust (Bryant et al., 2006). In the Northern Andes, the crust is Cretaceous and older reaching up to 70 km in thickness and in part comprised of an accreted oceanic plateau (e.g. Feininger and Seguin, 1983; Kerr et al., 1996) and in the Southern Andes the crustal basement is Mesozoic and younger reaching a maximum of *c*. 40 km thickness. The Central Andes however is underlain by up to 80 km of crust (Zandt et al., 1994) which is cratonic and Precambrian in part at depth. This regional variation is inferred to lead to the greater geochemical variability in volcanic rocks as observed in Pb and Sr isotopic signatures in the CVZ (Fig. 2.9). Extensive intracrustal melting, where by large volumes of anatectic melts derived from the continental crust have mixed with mantle-derived magmas prior to eruption (e.g. de Silva, 1989), has traditionally been associated with large volume ignimbrite eruptions in the CVZ and SVZ. More recently Kay et al., (2010) inferred 50-50 mixes of enriched mantle-wedge derived melts and isotopically variable crustal melts on the basis of $^{87}Sr/^{86}Sr$ and $\delta^{18}O$ data for the genesis of late Miocene to recent ignimbrites on the Altiplano-Puna plateau; 4) slab melting (Gutscher et al., 1999). The concept that volcanic rocks erupted in the NVZ were the products of slab melting was suggested by Gutscher et al., (1999; 2000) on the basis of slab geometry and trace element geochemistry. These slab melts (referred to as adakites after Kay, 1978) characteristically exhibit high Sr/Y values (Sr > 400ppm, Y < 19ppm) however the idea that volcanic rocks in the NVZ are produced from metamorphosed basalt has recently been refuted on the basis of Sr/Y and SiO_2 geochemistry of 14 volcanoes along the arc in this region. Instead, melting of the arc-mantle wedge

followed by fractionation in, and assimilation of, the NVZ continental crust is inferred to generate the so-called "adakitic" signatures (Garrison and Davidson, 2003); 5) melting of enriched subcontinental lithospheric mantle (Drew et al., 2009). The origin of Cenozoic volcanic rocks erupted on the Puna Plateau in the SVZ has been attributed to the presence of mantle lithosphere that has been isolated from mantle convection for ~500 Ma. This interpretation was based on the striking similarity between Sr-Nd-Pb isotopic compositions of Ordovician igneous rocks and the more recent eruptives. Additionally in this region, Drew et al, (2009) also reported no evidence for the involvement of asthenospheric mantle during magma genesis; 6) melting of depleted continental lithosphere (Kay and Gordillo, 1994). In the flat slab region between the CVZ and SVZ (~32^{o}S) Kay and Gordillo, (1994) proposed that geochemical signatures in late Miocene volcanic rocks were indicative of melting of a depleted mantle source and the involvement of the lower crust. The suggestion that blocks from the base of the continental lithosphere could be removed and transported eastward into the mantle wedge was proposed in order to explain the relatively non radiogenic Sr (0.7034-0.7047) at εNd of 0 to +2 and low concentrations of U and Th observed; 7) cryptic metasomatism by carbonatitic melts (Gorring and Kay, 2001). It has been suggested variable carbonatitic metasomatism of the back arc continental lithosphere in the AVZ based on the high Zr/Hf, Nb/La and Ca/Al with low Ti/Eu of sampled Cr-diopside, spinel bearing peridotite xenoliths from Patagonia. This process of metasomatism was also invoked by Bjerg et al., (2009) to explain the low Ti/Nb and high Zr/Hf observed in sampled mantle derived, spinel bearing peridotites from the SVZ and AVZ; 8) Melting of the asthenospheric mantle (Kay and Gorring, 2001). This has been proposed to occur on the gap between the SVZ and AVZ where OIB-like geochemical characteristics were observed in Neogene lavas (e.g. low La/Ta (<20) and non-radiogenic $^{87}Sr/^{86}Sr$: 0.7038-0.7046.

Characterising the continental basement of the Central Andes: constraints from Bolivian crustal xenoliths

3

This chapter will be submitted as a paper to GSA Bulletin.

ABSTRACT

The composition of the continental crust has a significant influence on the petrogenesis of magmas at continental arcs. Investigating the evolution of continental arc magmas is, however, hampered by our limited knowledge of, and poor constraints on, the nature of the underlying crustal basement. This chapter reports results from a whole rock geochemical and *in-situ* geochronological study of a suite of crustal xenoliths from the Bolivian Altiplano, Central Andes. Sampled xenoliths are hosted in Plio-Pleistocene trachyandesitic/dacitic lavas which erupted from monogenetic volcanic centres during an episode of recent mafic volcanic activity in the Andean back-arc region. Samples are diverse with both igneous and metamorphic lithologies including diorites, microgranites, gneisses and garnet-mica schists. The isotopic heterogeneity exhibited by the xenolith suite is extreme with $^{87}Sr/^{86}Sr$ values extending to 0.7368 which is significantly more radiogenic than any Sr-isotopic signature exhibited by the recent (< 60 Ma) volcanic record. Pb isotopic signatures (particularly $^{206}Pb/^{204}Pb$) reflect the crustal domains previously constrained from scattered exposures of crustal basement rocks throughout the region. *In-situ* U-Pb dating of cores and rims from zircon separates from two of the sampled xenoliths reveal predominant Early Phanerozoic age peaks (*c*. 500 Ma; population 1), Late Mesoproterozoic (1.0-1.2 Ga; population 2) and Palaeoproterozoic (1.7-1.9 Ga; population 3). Populations 1 and 2 are well documented throughout the Andes and correspond to periods of supercontinent formation and break-up. Population 3 is, however, poorly represented in the zircon record of the Andes but may record geological events inherent to the construction of the Archean-Palaeoproterozoic Amazonian craton. The sampled crustal xenolith suite invites comparison with current bulk estimates of the composition of the continental crust. The majority of xenoliths exhibit Eu/Eu* < 1, characteristic of the upper (and middle) continental crust. However, they show little consistency in their geochemical affinity when other geochemical signatures are considered and consistently overlap (and extend beyond) compositional ranges for the lower, middle and upper crust.

3.1 Introduction

The continental basement at continental arcs deserves study for two principal reasons; 1) its compositions and structure dictate the potential effects on continental arc magmas as they ascend through, and differentiate within, the crust, and 2) the

composition, ages and structures are key to determining the geological and plate tectonic development of an active continental margin.

Constraining the nature of the continental crust in the Central Volcanic Zone (CVZ) of the Andean Cordillera, South America is of particular importance to palaeo-plate reconstruction models (e.g. Dalziel, 1997; Loewy et al., 2004) and geochemical studies (e.g. Sørensen and Holm, 2008; Mamani et al., 2010). Current models for the Neoproterozoic and early Palaeozoic history of the western margin of the South American continent have proposed a collision between the eastern Laurentian craton and western margin of Gondwana, of which modern-day South America was a part (e.g. Cordani et al., 2005). Fundamental to these models and associated basement terrane maps are samples and *in-situ* exposures of the crustal basement. Many geochemical studies of volcanic rocks throughout the Central Andes have invoked the variable role of the continental crust in the petrogenesis of magmatic rocks across the region in order to account for the geochemical differences observed within and between magmas erupted/emplaced along and across strike of the active arc (e.g. Wörner et al., 1992; Aitcheson et al., 1995; Davidson and de Silva, 1995; Caffe et al., 2002; see also Chapter 4). However, known compositions of potential crustal lithologies with which ascending arc magmas have interacted are scarce due to limited tectonics across the Altiplano region and the extensive Tertiary sedimentary sequences which blanket the region today.

The objective of this study is fourfold; (1) to provide long sought after constraints on the composition of crustal components for the modelling of open magmatic systems in the (Central) Andes; (2) to validate existing basement terrane models for this region of the Andes which are derived from scattered exposures of basement rocks across the Central Andes (e.g. Loewy et al., 2004); (3) to offer geochronological constraints on the

evolution of the western margin of the South American continent in order to explore the roles of crustal recycling in construction of the modern day Central Andean basement and (4) to compare the compositions of the sampled xenolith suite to bulk compositional estimates of the continental crust (e.g. Rudnick and Gao, 2003).

3.2 Geologic Setting

This study focuses on a suite of entrained crustal xenoliths hosted in Plio-Pleistocene lavas which have erupted from two monogenetic centres at Pampas Aullagas (PA; 19°S, 67°W) and Quillacas (QL; 19°S, 66°W, comprised of two small hills) on the Bolivian Altiplano (see Fig. 4.2 a, b, Chapter 4). Both centres consist of several lava flows which have erupted along NW-SE trending faults and form part of a lineament of minor volcanic centres which runs subparallel to the volcanic front (Fig. 1b of Davidson and de Silva, 1995; Fig. 4.1 of Chapter 4).

Surface exposure in Bolivia is constrained to a single outcrop at Cerro Uyarani on the Western Altiplano (18°30'S, 68°40'W, Fig. 3.1) where granulites, charnockites and rare amphibolites with early Proterozoic protoliths have been identified (Wörner et al., 2000). Across the Central Andes, at least ten surface exposures of the continental basement have been identified (Fig. 3.1). It is currently understood that the majority of the Bolivian Altiplano is underlain by the Arequipa-Antofalla basement block which is comprised of three domains that young to the south and which are exposed intermittently along the Arica embayment. This allochthonous domain is hypothesised to have accreted to the Amazonian margin as a single block during the Grenville-Sunsás Orogeny *c.* 1.0 Ga (Loewy et al., 2004), was not derived from Amazonia and was not emplaced as a parautochthonous block to the Amazonian margin along transcurrent faults (Tosdal, 1996). Western Bolivia and southern Peru are underlain by the Northern Domain which is comprised of Palaeoproterozoic (2.02-1.79 Ga)

intrusions that were later metamorphosed between 1.82 and 1.79 Ga (Loewy et al., 2004). The oldest rocks in the Central Domain are constrained to Mesoproterozoic in age with crystallisation of migmatites and orthogneisses at ~1254 Ma and ~1213 Ma respectively.

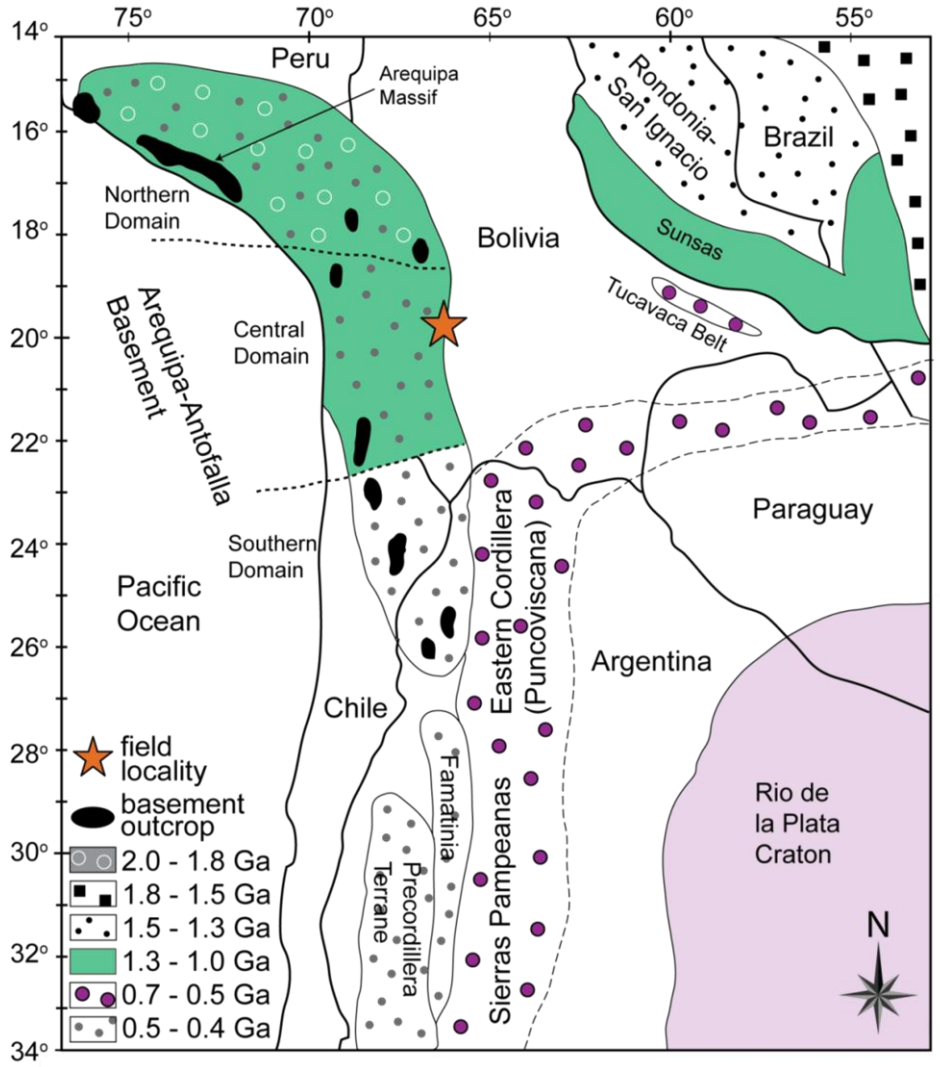

Fig. 3.1 Map showing the three domains of the Arequipa-Antofalla basement block of the Central Andes. Field locality at Pampas Aullagas and Quillacas is located at the eastern extent of the Central Domain. Map is modified from Loewy et al., (2004).

The Central and Northern Domains subsequently underwent metamorphism between 1.20 and 0.94 Ga, whereas the Southern Domain in northern Chile and north-western Argentina is composed of Ordovician rocks and experienced metamorphism at 440 Ma (Loewy et al., 2004). Evernden et al., (1977) reported clasts of red gneiss (K-Ar age of 647 Ma) and granite within the Azurita conglomerate ~200 km south of La Paz which

are inferred to have been derived from western Bolivia. These clasts, in addition to those found in the Mauri formation near Berenguela, western Bolivia, were found to be Precambrian (middle Proterozoic) in age and characteristic of the northern part of the Arequipa-Antofalla basement block (Loewy et al., 2004).

3.3 Analytical Techniques

Rock powders were produced from rock chips free of weathered material. Major element abundances were determined by XRF at the University of Edinburgh using the Panalytical PW2404 wavelength-dispersive sequential X-ray spectrometer. Trace element and REE concentrations were measured at NCIET (Northern Centre of Isotopic and Elemental Tracing) at Durham University, UK by inductivley coupled plasma mass spectrometry (ICP-MS) on a Perkin Elmer-Sciex Elan 6000. Sr-Nd isotopic analyses were determined on a multicollector VG mass spectrometer at the University of Califorrnia, Los Angeles (UCLA, see Davidson and de Silva, 1995). Additional Sr, Nd and also Pb isotopic compostions were measured on a plasma ionization multicollector mass spectrometer (PIMMS) using the ThermoElectron Neptune instrument at the Arthur Holmes Isotope Geology Laboratory (AHIGL), part of NCIET, at Durham University, UK. Electron microprobe analyses of biotites and garnets were undertaken at the School of Geosciences, University of Edinburgh using the CAMECA SX100 instrument. SIMS analyses for U-Pb ages in zircons were performed at the Department of Earth and Space Sciences, UCLA. Sample preparation for each of the analytical techniques and details of standards run are provided in Appendix E.

3.4 Samples

3.4.1 Sample collection

The sample suite constitutes 74 xenoliths which were collected during two field seasons. The first suite (denoted by prefix BC93-) was collected by Jon Davidson and

Shan de Silva in 1993 as part of a study which investigated the petrogenesis of a suite of minor, monogenetic volcanic centres across the Altiplano region (see Chapter 4; Davidson and de Silva, 1995). The second suite (denoted by prefix BC10-) was collected during a field season dedicated to work presented in this thesis in October 2010. Sample collection concentrated on recently excavated quarries on the south-western slopes of the Pampas Aullagas and Quillacas volcanic centres. Samples were also collected from the western slopes and summit of Pampas Aullagas.

3.4.2 Sample petrography

The xenolith suite comprises eight lithologies. Average modal mineralogical abundances are presented in Fig. 3.2, photomicrographs in Fig 3.3 and key characteristics here. Sampled diorites are characterised by abundant hornblende, plagioclase and biotite with biotite displaying alteration to orthopyroxene, consistent with biotite breakdown (plus melt). The measured wt. % MgO of sampled biotite ranges between 9.3 and 12.9, consistent with an igneous origin as metamorphic biotite is typically ≤ 8 wt. % (Deer et al., 1992). Gneisses and Garnet-mica schists are characterised by regular alternating layers of biotite-sillimanite ± garnet melanosomes and quartzofeldspathic leucosomes. Sampled garnets in the mica-schists are of almandine composition ($Py_{15}Alm_{70}Gr_5Sp_{10}$-$Py_{16}Alm_{76}Gr_4Sp_4$) as would be expected of garnet produced during regional metamorphism of argillaceous sediments (i.e. a pelitic protolith, Deer et al., 1992). Several of the sampled granulites and gneisses show evidence for partial melting in the form of quenched glass in which very fine grained (<200 μm) acicular crystals of anatase (TiO_2) are present (see Chapter 5).

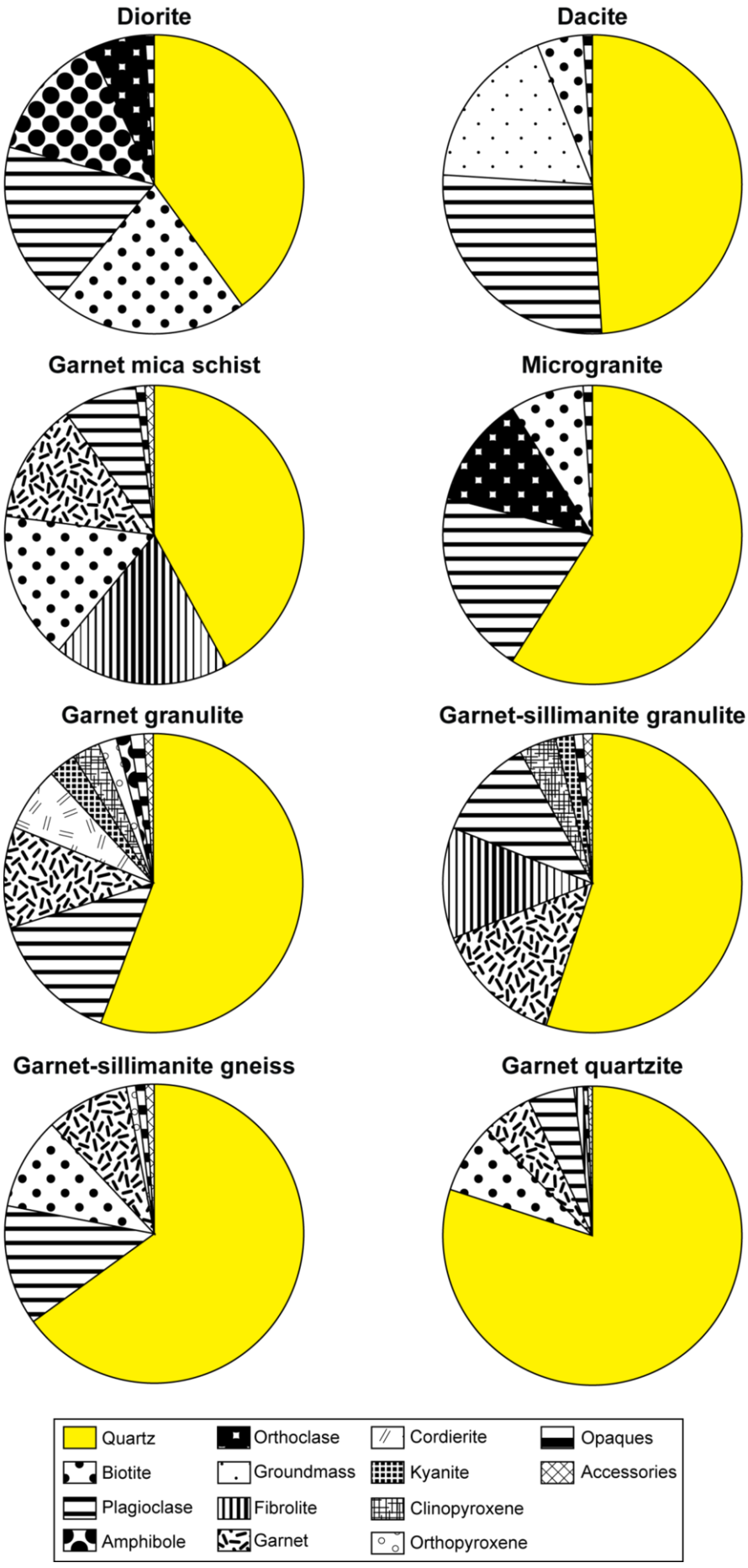

Fig. 3.2 a-h. Mineralogy of the eight sampled xenolith lithologies.

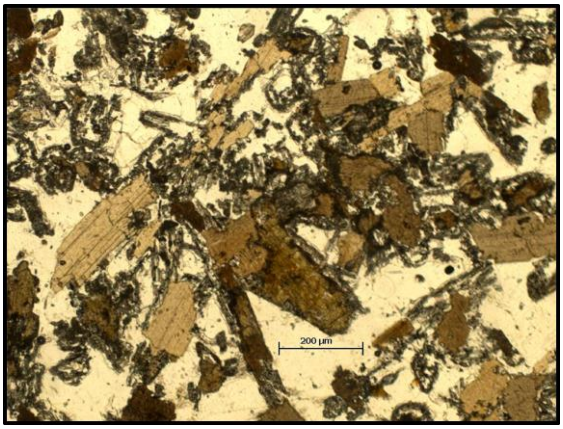

Fig. 3.3 a. Diorite.

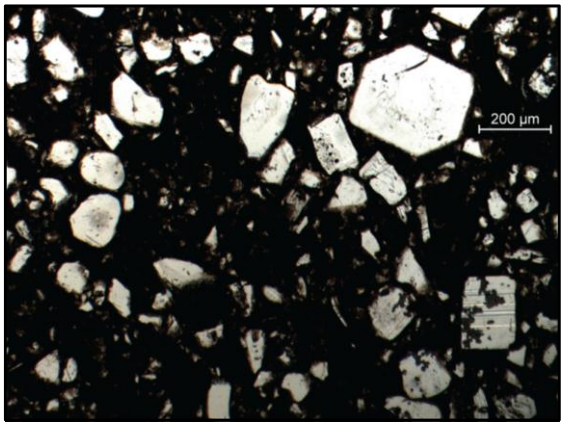

Fig. 3.3 b. Dacite.

Fig. 3.3 c. Garnet-mica schist.

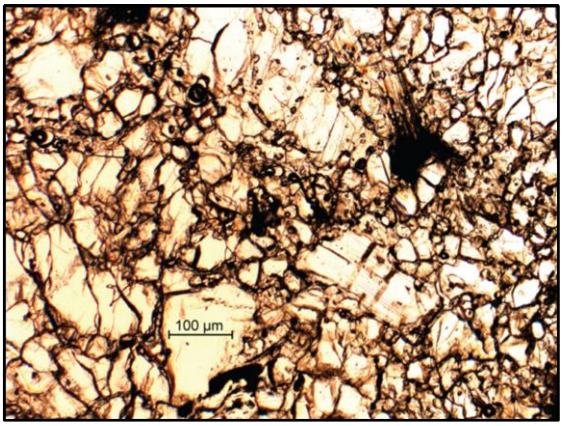

Fig. 3.3 d. Microgranite.

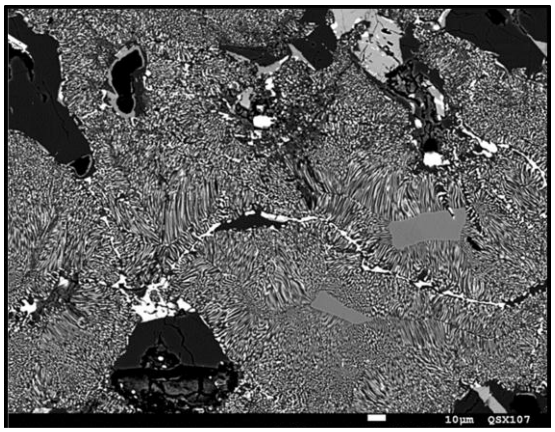

Fig. 3.3 e. Amphibole symplectite in Garnet granulite.

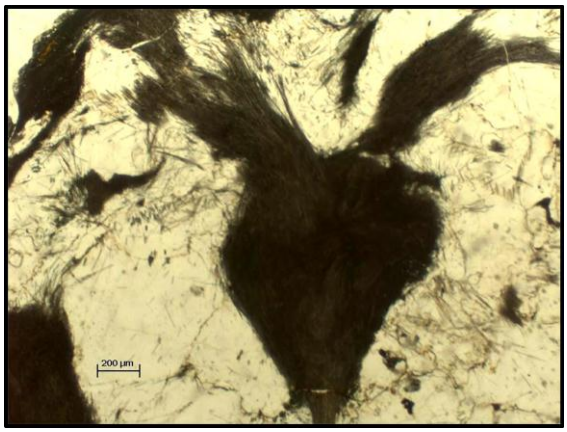

Fig. 3.3 f. Garnet-sillimanite granulite.

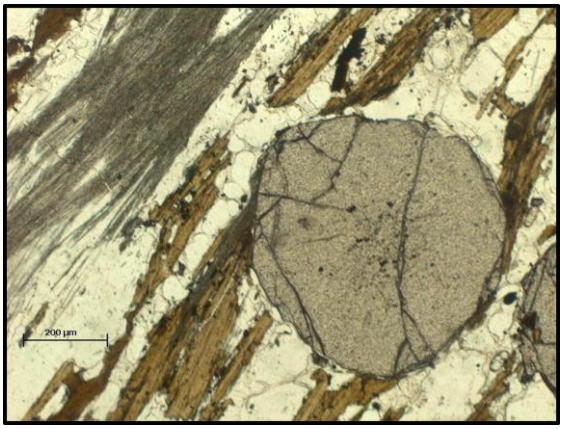

Fig. 3.3 g**.** Garnet-sillimanite gneiss.

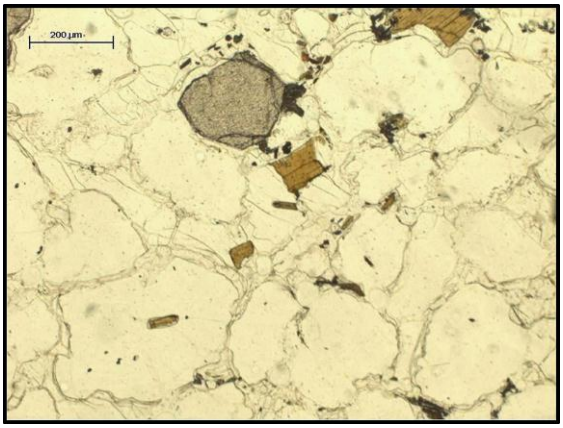

Fig. 3.3 h. Garnet quartzite.

3.5 Results

3.5.1 Geochemistry

3.5.1.1 Major elements

29 samples were chosen for whole rock major element analysis. Selected wt. % oxides are plotted against wt. % SiO_2 in Fig 3.4 a-g. Dioritic xenoliths are the most mafic of the sampled suite ranging from 52.7 to 57.7 SiO_2 at higher MgO (2.8-5.7); Fe_2O_3 (7.2-8.4) and K_2O (2.6-6.9) than the majority of the other xenoliths. These samples also exhibit some of the highest Cr and Ni abundances (Table 2, 4, Appendix B). Microgranitic and dacitic samples consistently display very similar major element chemical signatures over a restricted range of SiO_2 (66.7 to 69.3) and high $Na_2O + K_2O$ at ~8 wt. %. The remaining xenoliths show high Al_2O_3 contents which, coupled with the high abundance of aluminous minerals (garnet, sillimanite, biotite) indicate the aluminous nature of potential pelitic protoliths.

3.5.1.2 Trace elements

Fig. 3.5 a-h show primitive-mantle normalised trace element diagrams for the eight lithologies within the crustal xenolith suite. Diorites, dacites and microgranites display LILE enrichment (e.g. Rb, Ba) and exhibit broadly similar enrichment signatures from Ba through to Sm. There are notable peaks at U, K and Pb and troughs at Nb-Ta and Sr. Fig 3.6 a, b shows selected trace element abundances plotted in an attempt to characterise each lithology and illustrate any geochemical consistency within the suite. Fig. 3.6 a shows Sr (ppm) vs. Pb (ppm) which best separates the lithologies in terms of trace element composition with garnet granulites, diorites, garnet mica schists, garnet-sillimanite gneisses and granulites at low Pb (typically < 15ppm) at variable Sr each plotting in distinct Sr-Pb compositional space. The majority of xenoliths form a linear trend with respect to Sm and Nd (Fig. 3.6 b) at Sm/Nd of 0.2 which is broadly consistent with the upper and middle continental crust.

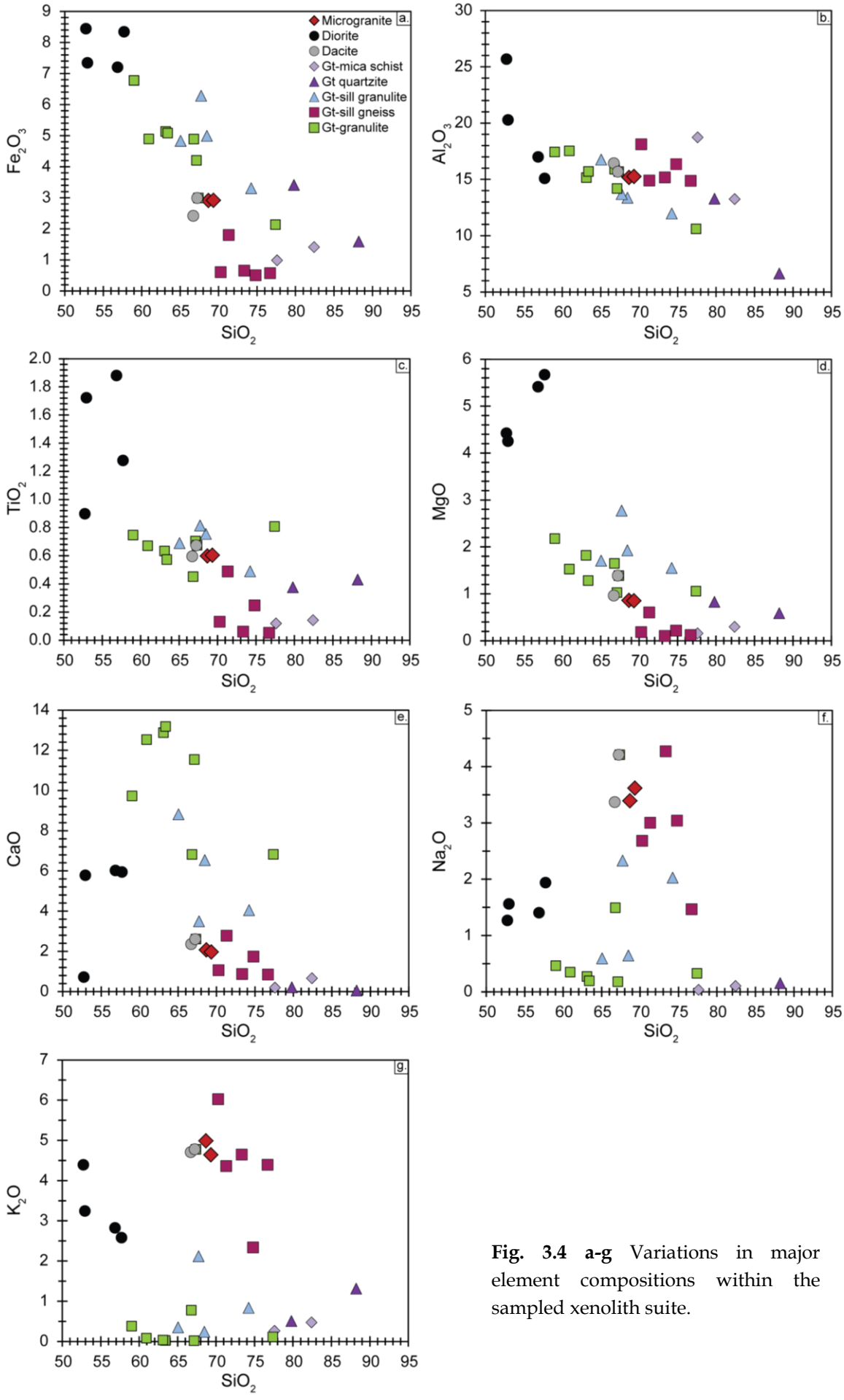

Fig. 3.4 a-g Variations in major element compositions within the sampled xenolith suite.

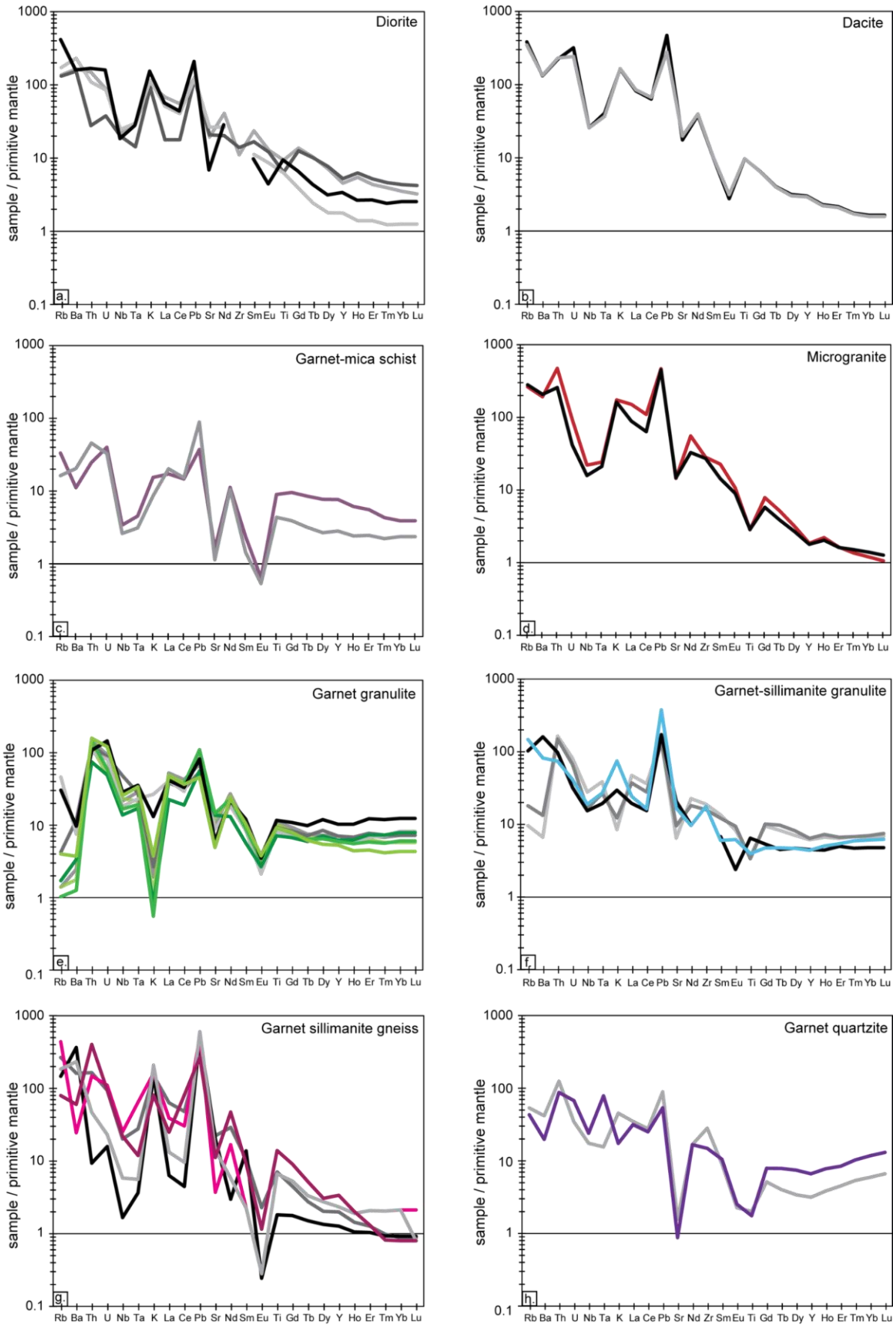

Fig. 3.5 a-h Primitive-mantle normalised trace element multi element diagrams for the eight sampled xenolith lithologies. Normalising values of McDonough et al., (1991).

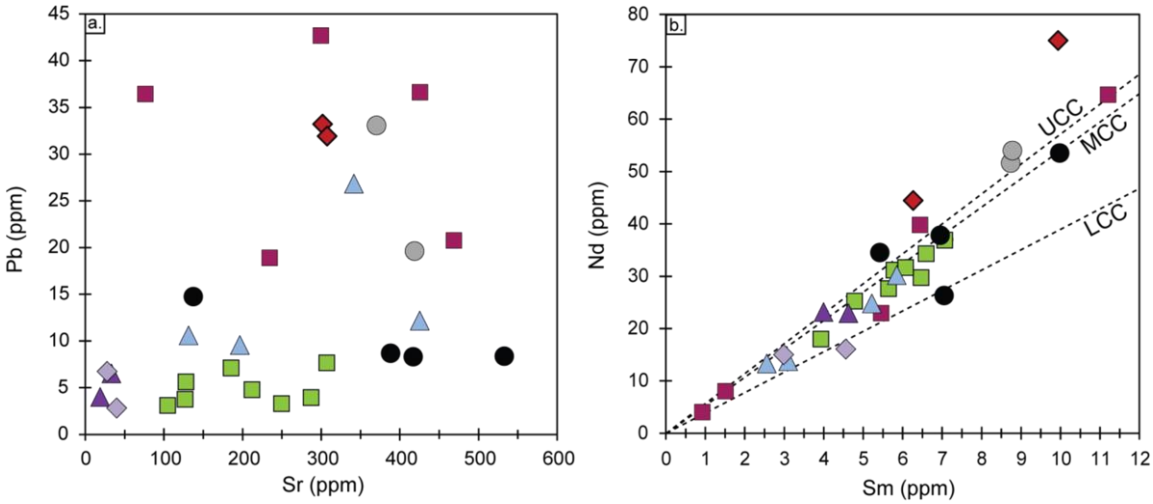

Fig. 3.6 a. Sr-Pb characteristics of the sampled xenolith suite. **b**. Sm-Nd signatures showing broad geochemical affinity to upper and middle crustal reservoirs. UCC, MCC and LCC: upper, middle and lower crust respectively (values from Rudnick and Gao, 2003). Symbols as in Fig. 3.4.

Fig 3.7 a-h show chondrite-normalised REE patterns. The majority of samples, to a greater or lesser degree, exhibit a negative Eu anomaly which is akin to REE patterns of the upper (and middle) continental crust (Rudnick and Fountain, 1995; Rudnick and Gao, 2003). The microgranite is LREE enriched, HREE depleted and exhibits the steepest profile with a high La_N/Yb_N at 125. The dacites and diorites are similarly enriched and depleted but to lesser degrees with La_N/Yb_N values between 45.8-48.6 and 19-42 respectively (one notably low diorite at 4). The relatively flat MREE to HREE profiles of the remaining xenolith suite (Dy_N/Yb_N 0.7 to 1.8) can be attributed to the presence of garnet which concentrates the HREE.

3.5.1.3 Sr-Nd-Pb isotopes

20 xenoliths were chosen for Sr-Nd-Pb isotopic analysis (Table 2, 4; Appendix B). Fig. 3.8 shows the sampled xenoliths and the Sr-Nd isotope compositional fields for sampled crustal basement rocks in neighbouring Chile and Argentina. Sampled xenoliths overlap compositions from previous basement studies, exhibit slightly higher

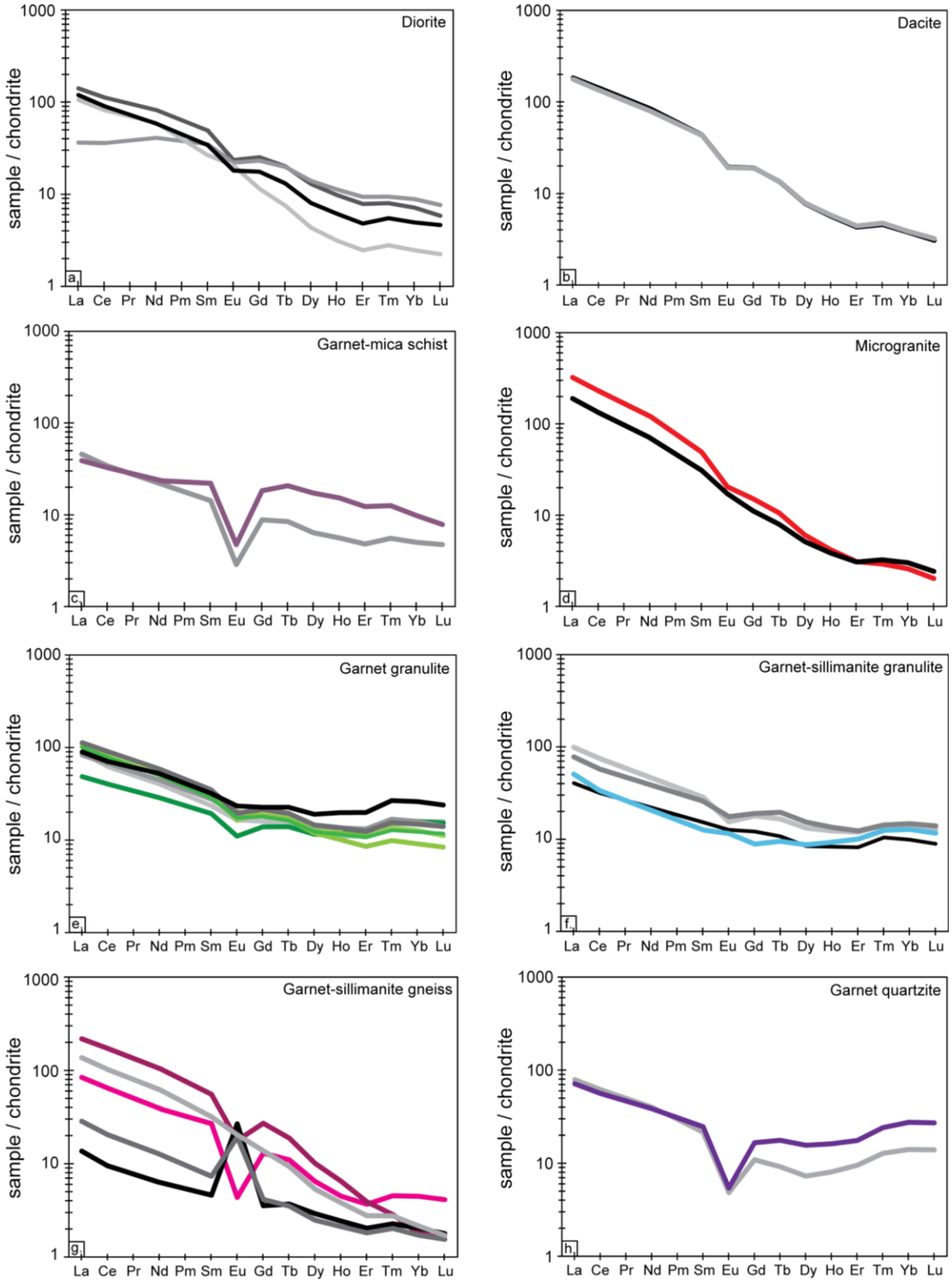

Fig. 3.7 a-h. Chondrite-normalised REE patterns for the eight sampled xenolith lithologies. Normalising values of Nakamura (1974).

$^{87}Sr/^{86}Sr$ at lower $^{143}Nd/^{144}Nd$ but do not extend to the extreme $^{87}Sr/^{86}Sr$ values of Palaeozoic Argentinian gneisses.

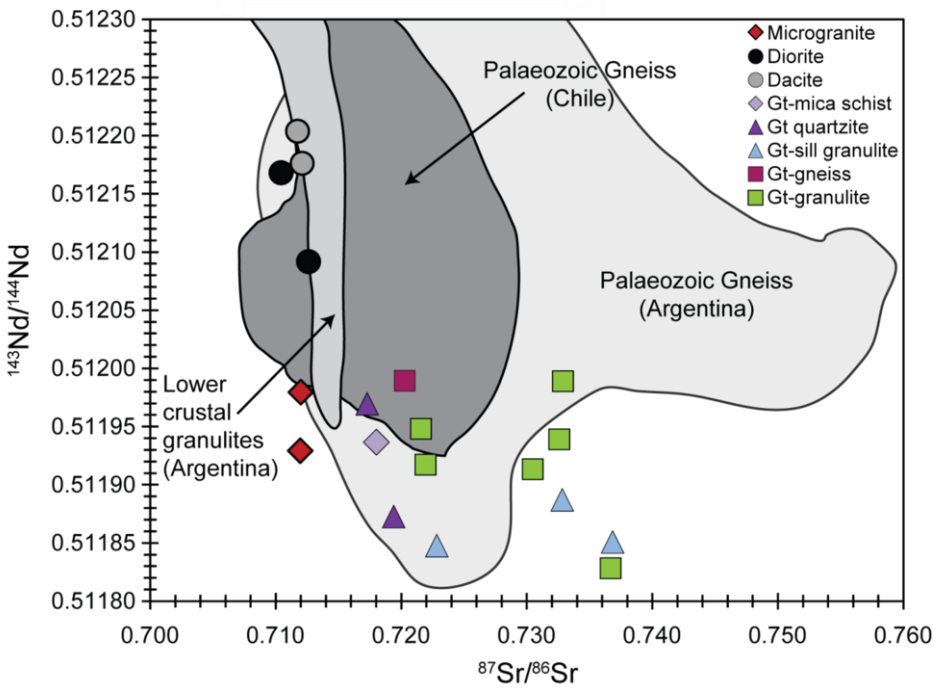

Fig. 3.8. Sr-Nd isotopic compositions of sampled Bolivian xenoliths. Compositional fields for previously studied outcrops of crustal basement throughout the central Andes are also shown. Data sources: James, (1982); Lucassen et al., (1999); Lucassen et al., (2001). The Precambrian Charcani Gneiss of Peru plots outwith the compositional field shown at significantly lower $^{143}Nd/^{144}Nd$ (0.5115) and $^{87}Sr/^{86}Sr$ of 0.740.

With respect to Pb isotopes sampled microgranites are relatively unradiogenic with characteristically low Pb isotopic signatures at <17.77 $^{206}Pb/^{204}Pb$; <15.61; $^{207}Pb/^{204}Pb$ and <38.49 $^{208}Pb/^{204}Pb$ (Fig. 3.9 a, b). The remaining xenoliths range from 18.17 to 18.93 ($^{206}Pb/^{204}Pb$), 15.64 to 15.69 ($^{207}Pb/^{204}Pb$) and 38.66-39.46 ($^{208}Pb/^{204}Pb$) and are broadly comparable to upper crustal evolution trends.

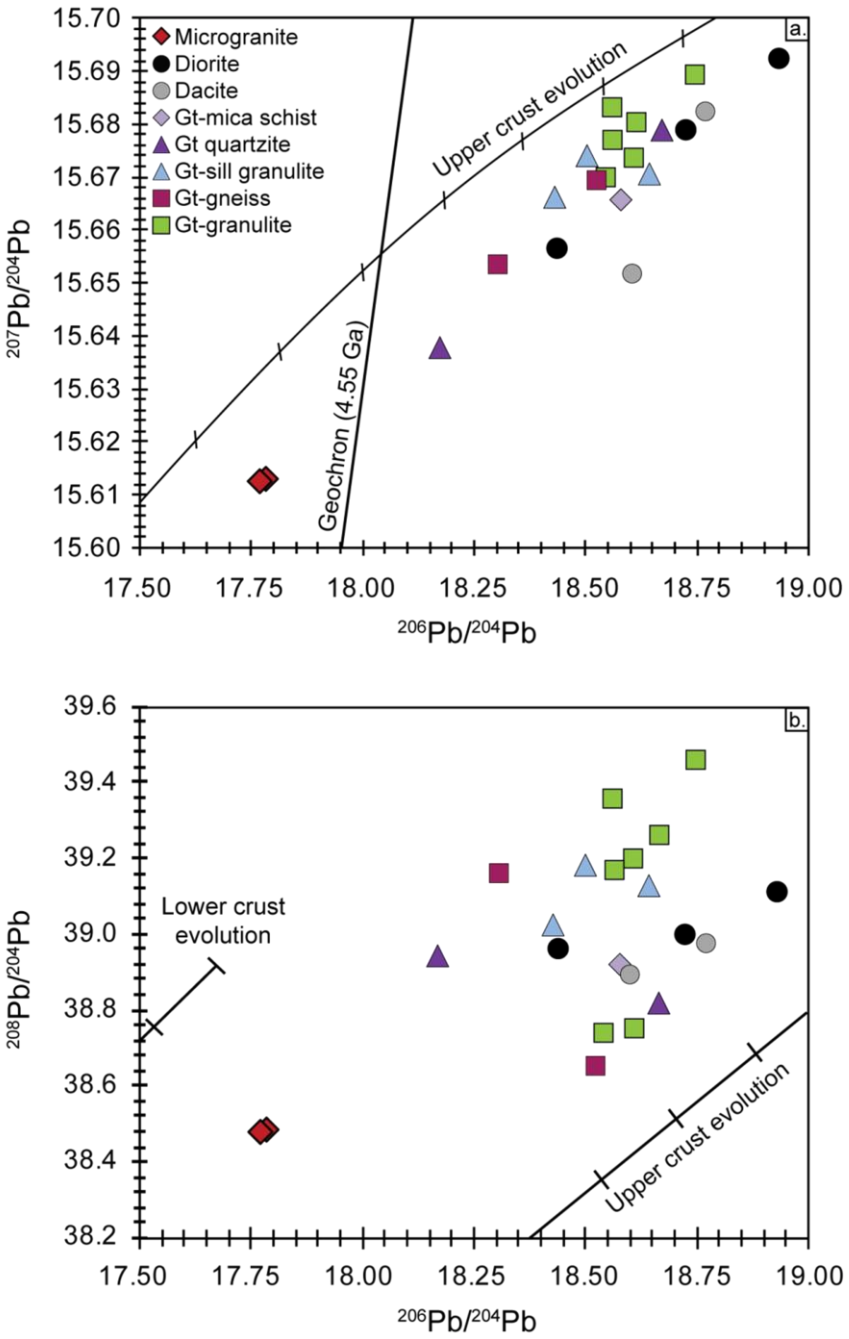

Fig. 3.9 a. $^{206}Pb/^{204}Pb$ vs. $^{207}Pb/^{204}Pb$ for sampled crustal xenoliths. **b**. $^{206}Pb/^{204}Pb$ vs. $^{208}Pb/^{204}Pb$ for sampled crustal xenoliths. Geochron and upper crustal evolution lines (each tick at 100 Ma intervals) after Zartman and Haines, (1988); Rollinson (1993).

3.5.2 Geochronology: U-Pb in zircons

Zircon is present as an accessory phase in the majority of sampled xenoliths (Fig. 3.10 a-c).

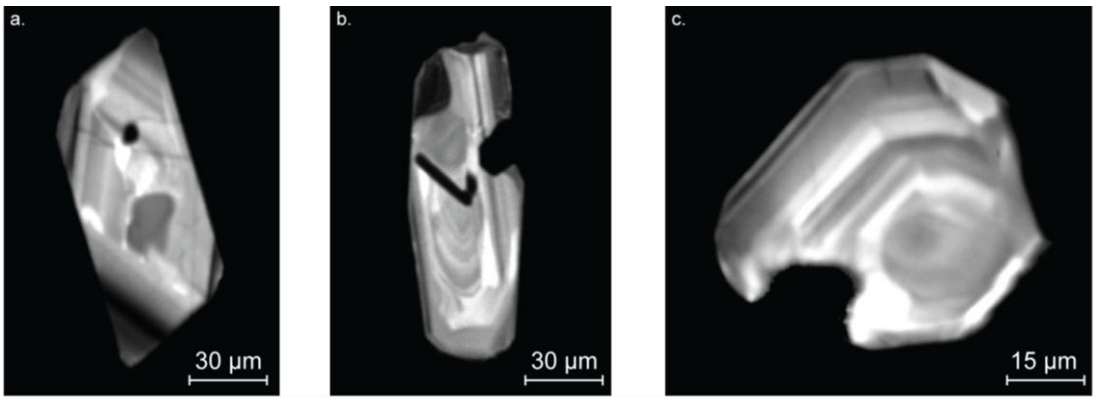

Fig. 3.10 a-c. CL images of zircons in the sampled xenolith suite. Note: these grains were not sampled for their U-Pb ages (see Figs. 3.11 a, b).

Zircon is a useful mineral to apply U-Pb geochronology to as it has a high closure temperature (~900^{o}C) and is physically and chemically robust, incorporating U and Th but little (if any) common Pb. Fig. 3.11 a, b and Fig. 3.12 a, b present $^{207}Pb/^{235}U$ and $^{206}Pb/^{238}U$ ion microprobe data on U-Pb concordia plots for 64 core and rim analyses from 31 zircon crystals derived from two sampled xenoliths of this study, analysed by SIMS (Table 5, Appendix B).

Zircon ages from sample BC93PAX14 (garnet-sillimanite granulite) are predominantly concordant with the oldest ages at 1857 ± 17 Ma and the youngest at 380 ± 14 Ma (Fig. 3.12 a). Sampled zircons exhibit a prominent age population between ~1.0 and ~1.2 Ga and a smaller peak from ~1.7 to ~1.9 Ga with one age at 1611 ± 21 Ma. A significant population of Silurian ages (eleven) is present between 439 ± 13 Ma and 487 ± 14 Ma (see inset graph). Additionally, two analyses yielded upper Devonian ages of 385 ± 11 Ma and 380 ± 14 Ma ($^{206}Pb/^{238}U$).

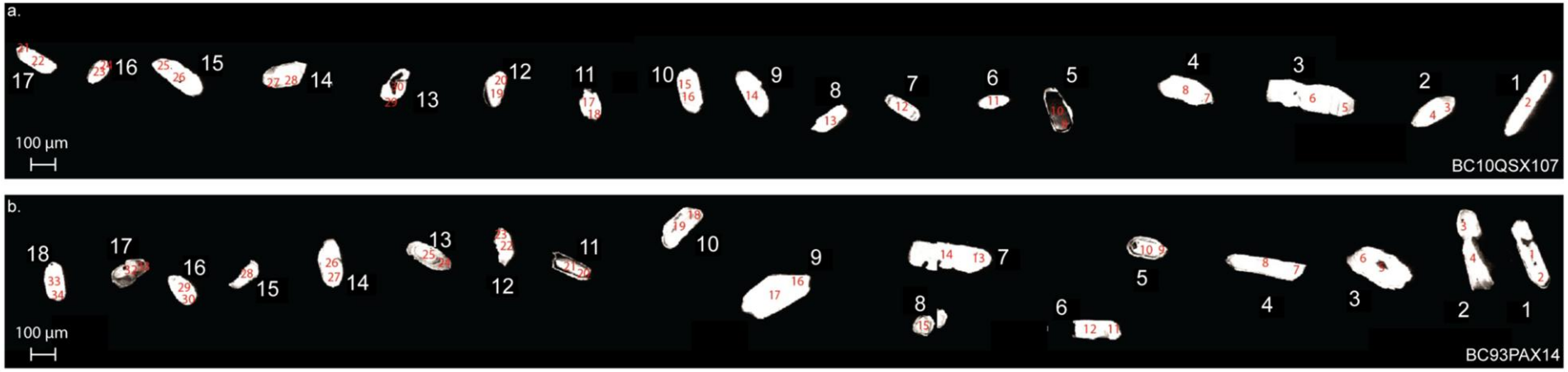

a. BC10QSX107 (R: rim; C: core)

Grain #	1	1	2	2	3	3	4	4	5	5	6	7	8	9	10	10	11	11	12	12	13	13	14	14	15	15	16	16	17	17
Spot #	1	2	3	4	5	6	7	8	9	10	11	12	13	14	15	16	17	18	19	20	29	30	27	18	25	26	23	24	21	22
Location	R	C	R	C	R	C	R	C	R	C	C	C	C	C	R	C	R	R	C	R	R	C	R	C	R	C	C	R	R	C

b. BC93PAX14 (R: rim; C: core)

Grain #	1	1	2	2	3	3	4	4	5	5	6	6	7	7	8	9	9	10	10	11	11	12	12	13	13	14	14	15	16	16	17	17	18	18
Spot #	1	2	3	4	5	6	7	8	9	10	11	12	13	14	15	16	17	18	19	20	21	22	23	24	25	26	27	28	29	30	31	32	33	34
Location	C	R	R	C	C	R	R	C	R	C	R	C	R	C	C	R	C	R	C	R	C	C	R	R	C	C	R	C	C	R	R	C	C	R

Fig. 3.11 a, b. Maps showing separated zircon grains and location of spot analyses. Images courtesy of Shan de Silva.

The zircons analysed from sample BC10QSX107 (garnet granulite, Fig. 3.12 b) yield predominantly concordant ages with significant age peaks from approximately 1.7 to 1.9 Ga and 1.0 to 1.2 Ga (see inset graph). A third clustering of ages is present between 417 ± 17 Ma and 495 ± 17 Ma. Five ages fall outside these populations with three showing late Neoproterozoic ages (average 653 ± 56 Ma) and two (off concordia) exhibiting early Palaeoproterozoic ages (2178 ± 7 Ma and 2503 ± 10 Ma).

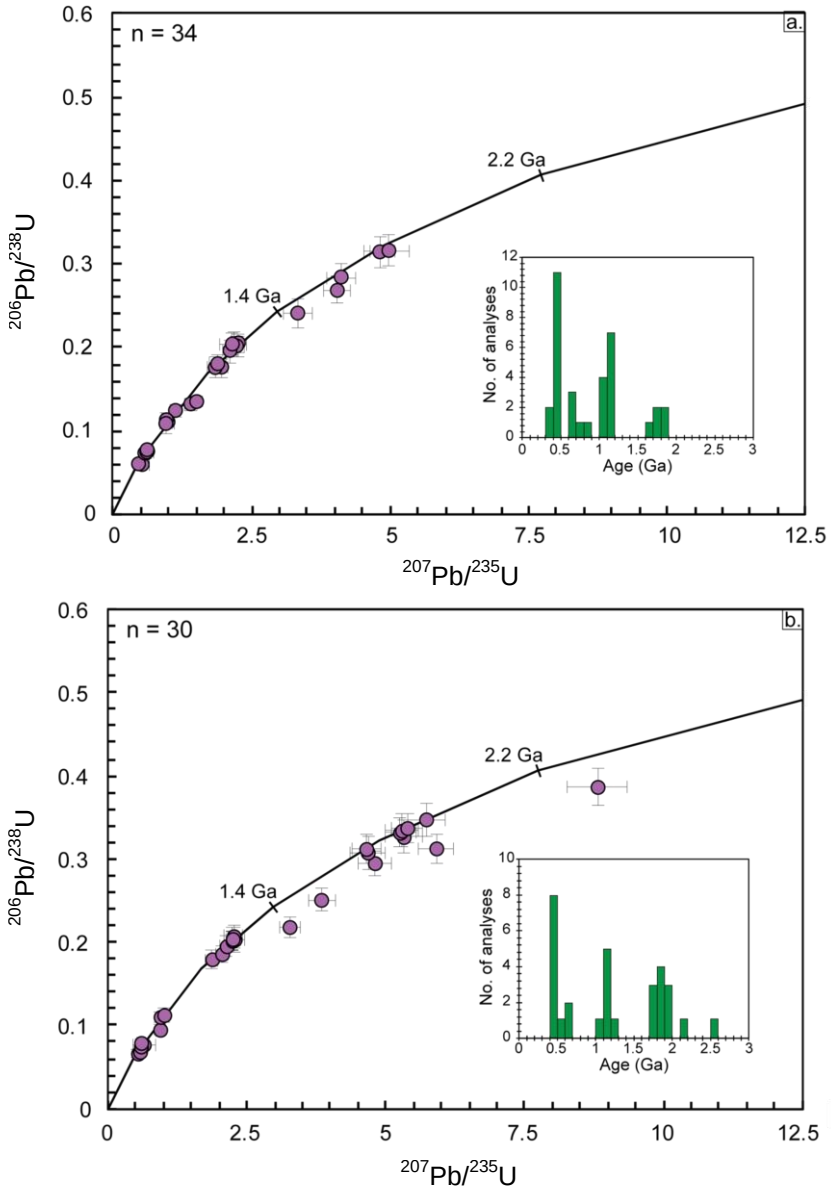

Fig. 3.12. U-Pb concordia plots for sampled cores and rims of zircons within **a**. BC93PAX14 and **b**. BC10QSX107.

Of the 64 ages yielded, 59 are concordant from which three age peaks at c. 500 (population 1), 1.0-1.2 (population 2) and 1.7-1.9 Ga (population 3) can be identified.

Arguably, population 1 could be split into 2 populations at ~300-500 Ma and ~500-800 Ma. This will be discussed later.

3.5.3 P-T estimates: initial work

Initial work on constraining the P-T, and therefore depth, at which sampled xenoliths are derived, was undertaken using the THERMOCALC model of Holland and Powell (1988). P-T pseudosections for the bulk composition of two xenoliths (BC93PAX14 and BC93QSX04) are shown in Fig. 3.13 a, b. These were calculated in the system NCKFMASH (Na_2O–CaO–K_2O–FeO–MgO–Al_2O_3–SiO_2–H_2O) with Ti taken up in ilmenite and H estimated from LOI values (Table 2, 4, Appendix B). Phase relations were modelled using the dataset of Holland and Powell (1998; updated 14 May 2001) and THERMOCALC v. 3.1 (Powell and Holland, 1988).

For BC93PAX14, P-T is constrained at ~7 kb and ~800^{o}C which is unsurprising given the lack of cordierite in the sample (Simon Harley, pers. comm). These conditions are consistent with a depth of ~23 km. In contrast, the microgranitic composition was shown to be stable over a large P-T field: between 700 and 875^{o}C and (at least) 5-9 kb. The yielded depth of ~23 km is interesting as beneath the Altiplano-Puna Plateau, a low seismic velocity zone has been identified at ~20 km (e.g. Zandt et al., 2003) and a recent study of the equilibrium P-T conditions of phenocryst crystallisation within the Aucanquilcha Volcanic Cluster in northern Chile also yielded depths of ~23 km (Walker et al., 2011). It is therefore tentatively suggested that this depth is significant regarding depth of magma storage and a significant depth of magma-crust interaction beneath Central Andean volcanic centres.

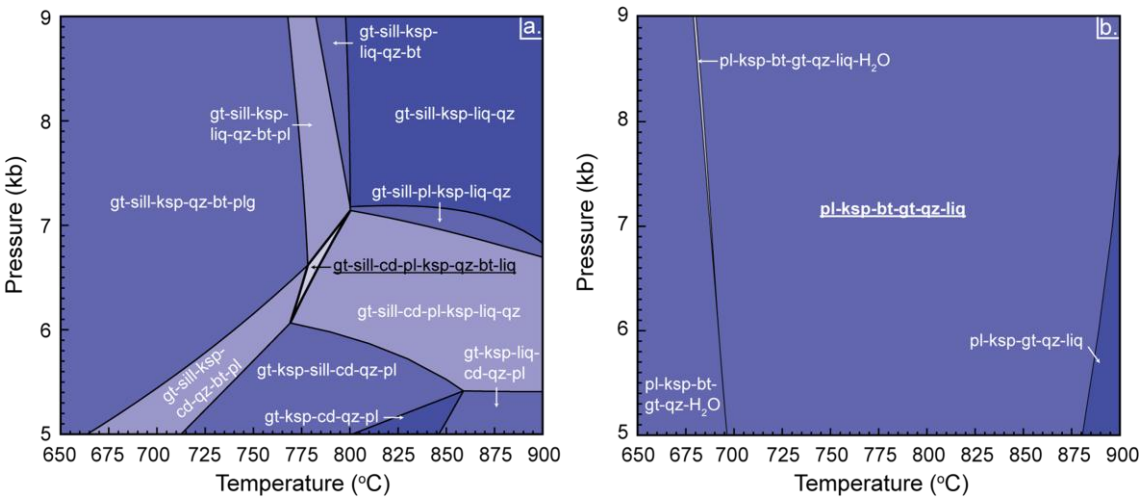

Fig. 3.13 a, b. Calculated P-T pseudosections for xenoliths BC93PAX14 (a.) and BC93QSX04 (b). Mineral assemblages of each sample are stated in bold and underlined (plus liquid, liq).

3.6 Discussion

3.6.1 Basement terrains

Figs. 3.14 a, b show the Pb-isotopic compositions of sampled xenoliths plotted alongside three previously identified crustal domains in the Arequipa-Antofalla basement block of the Central Andes by Loewy et al., (2004). The majority of sampled xenoliths plot in the Central Domain of the Arequipa-Antofalla basement which stretches from ~18°S to ~22°S consistent with the location of xenoliths sampled at Pampas Aullagas and Quillacas (see map in Fig. 3.1). Several samples display $^{208}Pb/^{204}Pb$ signatures akin to those of the Northern Domain which is present north of ~18°S to ~14°S and which incorporates the Precambrian Arequipa Massif. This may reflect local compositional heterogeneity with respect to $^{208}Pb/^{204}Pb$ within the Central Domain. Alternatively, this relatively radiogenic signature may be derived from crustal basement to the east of the Arequipa-Antofalla basement where the continental crust is uncharacterised, or may suggest that the domain boundary between the Northern and Central Domain is inclined and hence both may be sampled by a vertical conduit. In terms of $^{206}Pb/^{204}Pb$ vs. $^{207}Pb/^{204}Pb$ all samples are distinct from the Southern Domain which is present south of ~22°S in Chile and Argentina. Fig. 3.14 c shows Pb isotopic

data from this study combined with data from previous Central Andean studies on basement rocks (Tosdal, 1996; Wörner et al., 2000; Loewy et al., 2004). All sampled xenoliths follow the Arequipa-Brazilian Shield trend, above the Stacey and Kramers (1975) crustal evolution curve and just above the Pb isotopic evolution curve at μ=10. All sampled crustal rocks from this region of the Central Andes fall distinctly outwith the Pb isotopic signatures of Laurentian crust. This therefore excludes the role of any Laurentian crust (either as reworked crustal material or as protoliths) in the genesis of the Central Andean continental crust in this region.

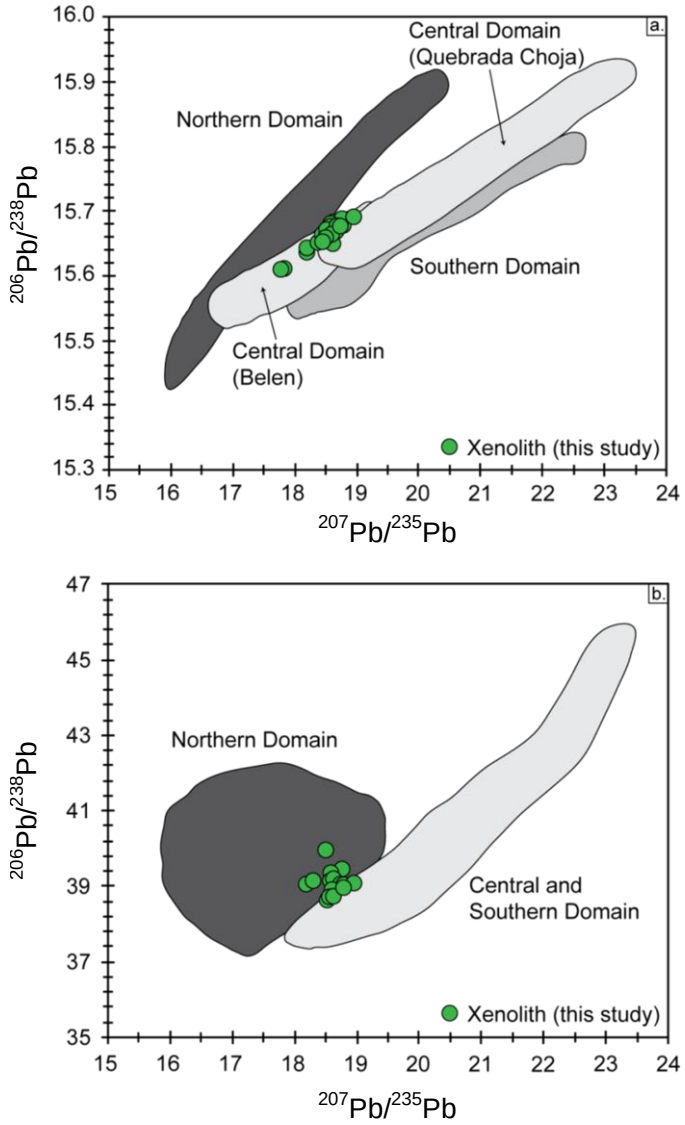

Fig. 3.14 a, b. Pb isotopic composition of sampled xenoliths plotted alongside the Northern, Central and Southern crustal domains of the Arequipa-Antofalla basement block. Domains are redrawn from Loewy et al., (2004).

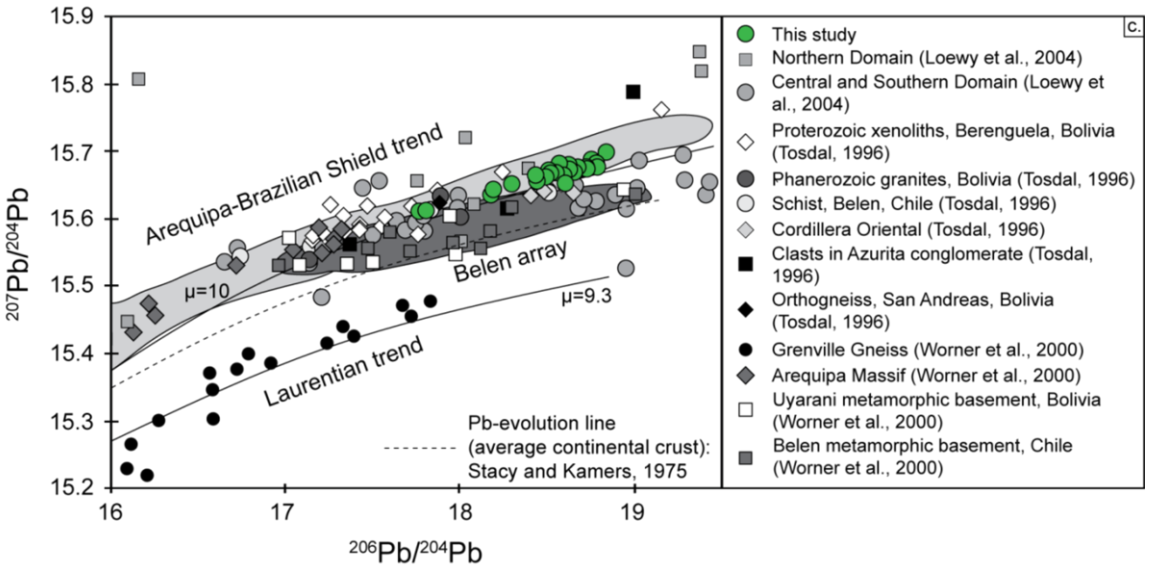

Fig. 3.14 c. $^{206}Pb/^{204}Pb$ vs. $^{207}Pb/^{204}Pb$ for crustal xenoliths of this study and from previous studies of continental basement rocks in the Central Andes. All samples are distinct from the Laurentian crustal trend at μ of ~9.3. Fields redrawn from Wörner et al., (2000).

3.6.2 Nd model ages

The calculation of an Nd model age is commonly used to calculate a "crust formation age" i.e. to calculate a time at which samples of the continental crust differentiated from their source (depleted mantle) and shared a common εNd value. The following equations were used in the calculations of εNd and T_{DM} (depleted mantle model age):

$$\varepsilon Nd = \left[\frac{(^{143}Nd/^{144}Nd)_{sample} - (^{143}Nd/^{144}Nd)_{CHUR}}{(^{143}Nd/^{144}Nd)_{CHUR}} \right] \times 10000 \quad (1)$$

$$T_{DM} = \frac{1}{\lambda} \ln \left[\frac{(^{143}Nd/^{144}Nd)_{sample} - (^{143}Nd/^{144}Nd)_{DM}}{(^{147}Sm/^{144}Nd)_{sample} - (^{147}Sm/^{144}Nd)_{DM}} + 1 \right] \quad (2)$$

$$(^{147}Sm/^{144}Nd)_{sample} = \left[(Sm/Nd)_{sample} \times (0.142556 \times (^{143}Nd/^{144}Nd)_{sample} + 0.531628) \right] \quad (3)$$

where $(^{143}Nd/^{144}Nd)_{CHUR} = 0.51315$ and $(^{147}Sm/^{144}Nd)_{DM} = 0.2137$

The Sm-Nd isotopic system is appropriate for this as crust evolves differently from the mantle due to the relative incompatibility of Nd (see inset graph on Fig. 3.15) such that crustal rocks have lower Sm/Nd values (50% lower than the depleted mantle, Arndt and Goldstein, 1987). Calculated xenolith εNd values range from -7.5 to -15.8. Calculated T_{DM} ages for the sampled xenolith suite form a continuous range from 2.6 to 1.0 Ga, with the exception of one diorite at ca. 2.9 Ga and the garnet mica schist which is anomalously high at ca. 4.0 Ga and (Fig. 3.15).

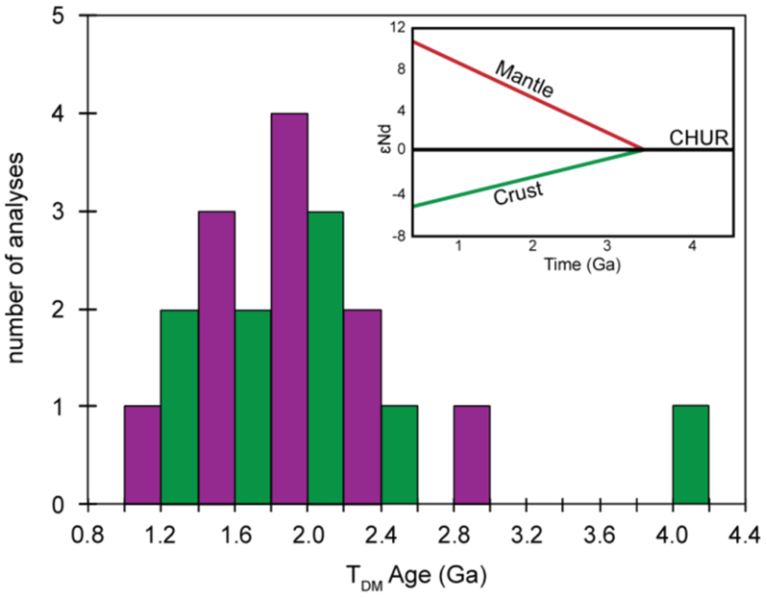

Fig. 3.15. Calculated T_{DM} ages of sampled xenoliths.

T_{DM} ages are broadly comparable to T_{DM} ages of the Northern and Central Domains of the Arequipa-Antofalla basement which range from 2.3 to 1.9 Ga and 2.2 to 1.3 Ga respectively (Loewy et al., 2004). T_{DM} ages in the younger Southern Domain range widely from 1.9 to 0.5 Ga. The attribution of model Nd ages to specific events, namely crust-formation, assumes the following are true: (1) the Sm-Nd evolution of the mantle source is known; (2) the Sm/Nd systematics of the sampled crust have not been disturbed since differentiation and (3) the crustal sample contains material derived from the mantle source during a single melting event. The first point is constrained from the composition of sampled mid ocean ridge basalt which is inferred to represent depleted upper mantle. The remaining two points are, however, more challenging to

corroborate and require additional, independent evidence (e.g. U-Pb zircon ages). Sample BC93PAX14 (garnet-sillimanite granulite) has a T_{DM} age of 2.34 Ga however; multiple analyses for the U-Pb ages in its zircons reveal events at *c.* 1.8, 1.0 and 0.5 Ga. The crystallisation age of zircons range from the Late Palaeoproterozoic to Early Devonian and clearly demonstrate the role of extensive crustal reworking. It is with caution therefore that calculated T_{DM} ages from the xenolith suite are inferred to be crustal formation ages. The calculated age of 4.0 Ga for the garnet mica schist is clearly false and the likely result of one or more of the above mentioned processes. Given that the (proto) Andean margin has been an active site of orogenesis and magmatism since (at least) the mid Proterozoic (see discussion below) calculated T_{DM} ages are likely an average age derived from both crustal and mantle sources and thus highlight the role of crustal recycling during growth of the modern Cordillera.

3.6.3 Age and Evolution of the proto-Andean margin

Constraining the early history of the proto-Andean margin is challenging due to 1) the numerous allochthonous tectonic blocks that are understood to have collided with the proto-Andean margin, 2) the fact that each of these blocks has a unique geological history and 3) each will have experienced multiple orogenic events throughout the Phanerozoic. Perhaps more importantly than these however, is the lack of exposure of Precambrian age basement rocks throughout the modern Central Andean Cordillera. As shown previously, the sampled zircons of this study exhibit three prominent age populations at the late Palaeoproterozoic (population 3), late Mesoproterozoic (population 2) and early Phanerozoic (population 1, see Fig. 3.16 a). Fig. 3.16 b, c shows concordant U-Pb zircon ages from provenance and basement studies across the Central Andes and throughout the Andean Cordillera where prominent age peaks are identified at *c.* 500 Ma (population 1 of this study) and *c.* 1.1 Ga (population 2) and a scattering of ages exists throughout the Palaeoproterozoic and into the Archean.

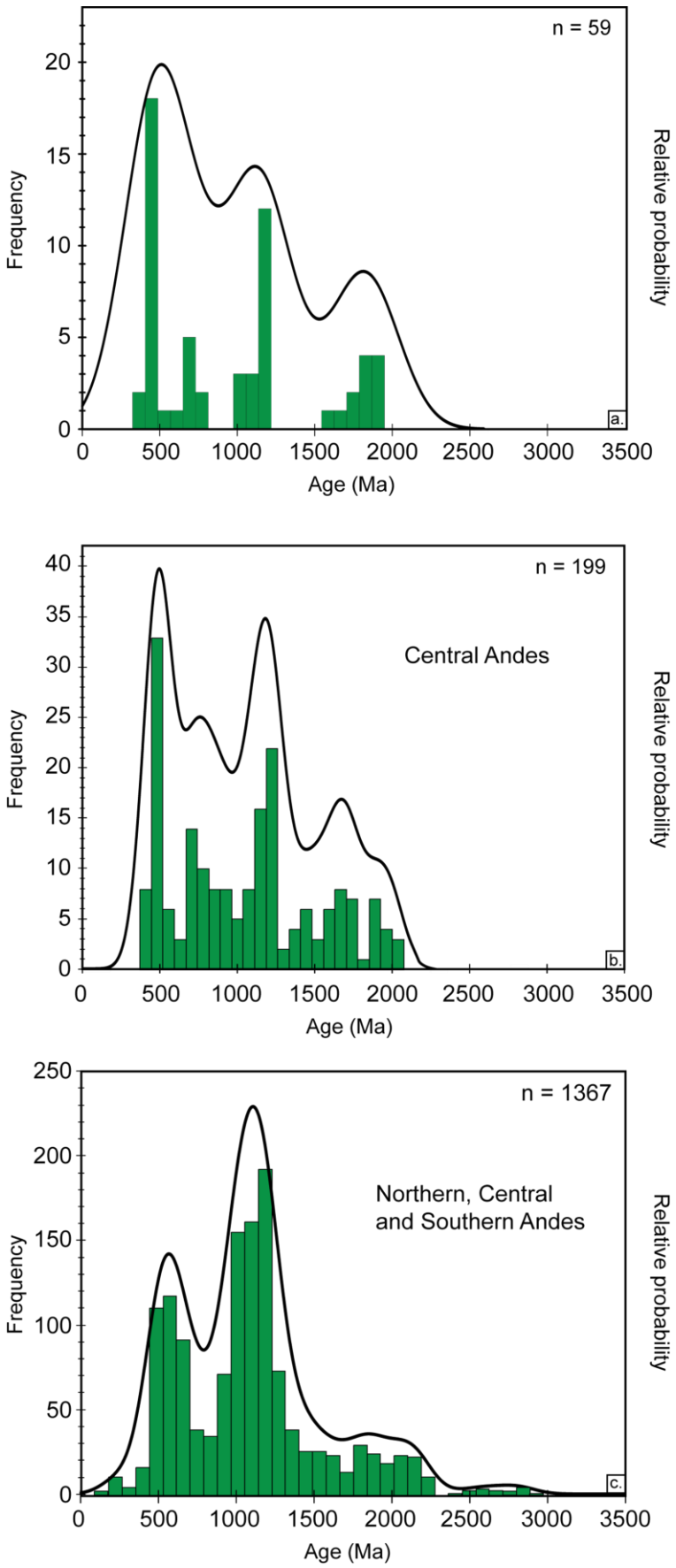

Fig. 3.16 a-c. U-Pb ages from *in-situ* analyses of zircon grains across the Andean Cordillera. For data sources see end of chapter.

3.6.3.1 Palaeoproterozoic ages (2.5-1.6 Ga)

A significant contribution form material > ~1.8 Ga is typically lacking from Central Andean U-Pb zircon data sets which has led to the suggestion that the Grenville-Sunsás orogen (1.0-1.3 Ga) acted as topographic barrier preventing the supply of material from the Archean-Palaeoproterozoic core of the Amazonian craton (Chew et al., 2007; 2011; Fig. 3.17 a, b).

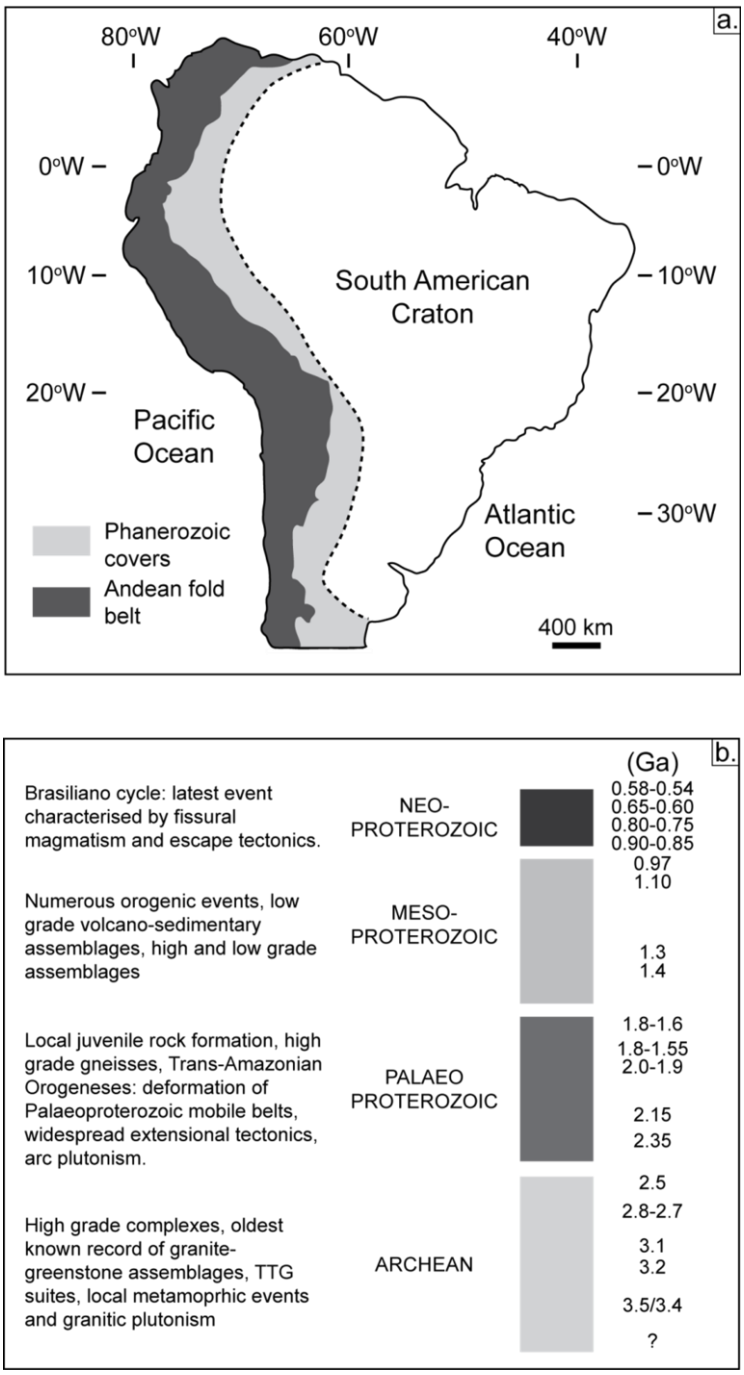

Fig. 3.17 a Map showing the cratonic interior of the South America continent and its extent relative to the modern day Andean fold belt. **b**. Geological history of the South American Craton. Map and timescale are modified from de Almeida et al., (2000).

A similar scenario has been invoked for the evolution of Newfoundland and the Appalachian mountain chains (e.g. Cawood et al., 2007). Palaeoproterozoic ages from this study range predominately from 1.9 to 1.7 Ga with late to mid Mesoproterozoic data (1.7-1.2 Ga) almost completely absent however, zircons with these earlier ages have been identified elsewhere throughout the Andean Cordillera (e.g. Peru, Loewy et al., 2004; Chew et al., 2008). During the mid Palaeoproterozoic (Rhyacian and Orosirian periods) the Trans-Amazonian Belt developed from northern Amazonia to Argentina as a tectonic collage and is understood to have been established by ~1.8 Ga. Following this, a series of tectonic events dominated by post-orogenic granitic plutonism, explosive and extrusive volcanism, crustal-scale shearing and rifting associated with the formation of volcano-sedimentary basins occurred from 1.8 to 1.6 Ga (de Almeida et al., 2000). These events could account for the ages observed throughout the Palaeoproterozoic but more importantly, the presence of ages >1600 Ma (Fig. 3.16) implies pre-Mesoproterozoic material was available to strata forming during the development of the proto-Andean margin.

3.6.3.2 Mesoproterozoic ages (1.6-1.0 Ga)

Approximately 1 Ga a single supercontinental mass, Rodinia, is hypothesised to have existed on Earth (McMenamin and McMenamin, 1990). The use of Grenvillian aged belts produced during the Mesoproterozoic and hence prior to supercontinent formation exist as scattered fragments across the continents on Earth today and have been used to reconstruct the paleogeography of Rodinia (e.g. Hoffman, 1991; Fig. 3.18). This reconstruction, alongside more recent efforts (e.g. Dalziel, 1997), present the Amazonian cratons western margin (Palaeoproterozoic to Archean in age) against Laurentia's eastern (Appalachian) margin. The Arequipa-Antofalla basement block of the Central Andes (after Loewy et al., 2004) is considered to represent a fragment of a Mesoproterozoic, Grenvillian-aged, orogenic belt which is allochthonous to Amazonia

(e.g. Ramos, 1988; Dalziel, 1994; Fuck et al., 2008). Its accretion to the proto-Andean margin has been proposed at 1000-1300 Ma during the Grenville-Sunsás orogenic episode and the building of the Rodinian supercontinent (Loewy et al., 2004) implying a major crustal domain boundary separates the two (Wörner et al., 2000).

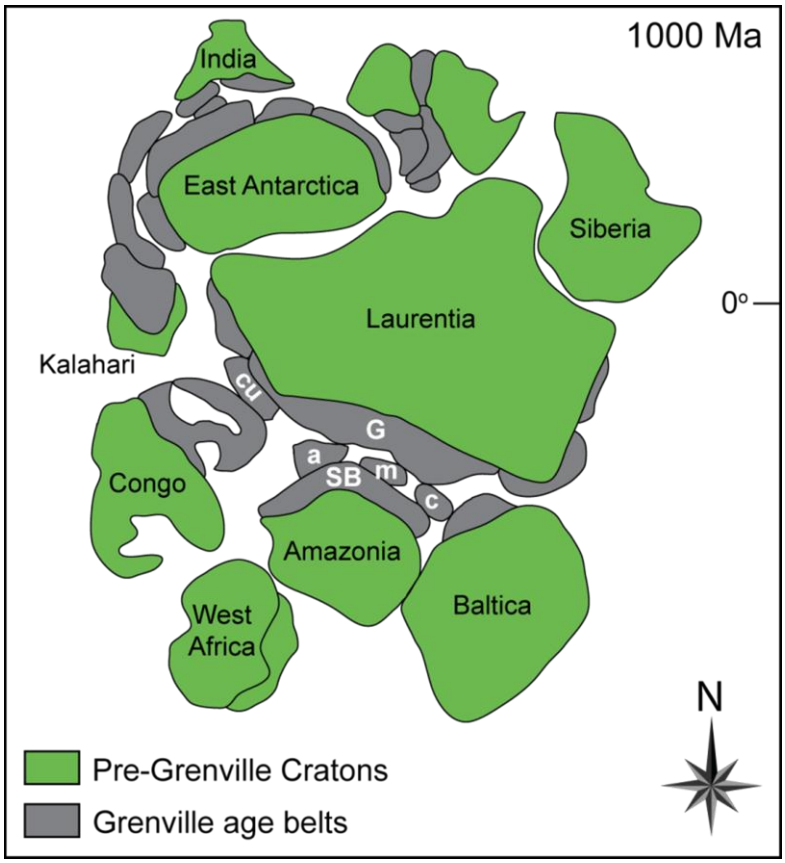

Fig. 3.18. Map showing reconstruction of the Rodinian supercontinent. The Grenvillian-aged belts (c. 1 Ga) are highlighted. The Andean inliers are also shown; SB: Sunsas belt; G: Grenville belt; c: Colombian Massifs; m: Mexican Massifs; a: Arequipa-Antofalla basement; cu: Cuyania terrane. Map is modified from Cordani et al., (2005).

The prominent age peak between 1 and 1.2 Ga is therefore attributable to a Grenville-Sunsás orogenic source associated with the construction of Rodinia (Fig. 3.18). This peak correlates extremely well with age peaks derived from numerous other U-Pb zircon studies aimed at reconstructing Rodinia e.g. California, Arizona and Sonara (Stewart, 2001); Mongolia (LaiCheng et al., 2007); the Mojave province, north-western Mexico (Farmer et al., 2005); Scotland, Newfoundland and the Appalachians (Cawood

et al., 2007). This peak can further be divided into two sub-populations: 1.13-1.21 Ga and 1.02-1.06 Ga which can be reconciled with discrete orogenic events associated with the proto-Andean margin; the Ottawan episode and the Elzevirian cycle after Cordani et al., (2005).

3.6.3.3 Neoproterozoic ages (1.0 Ga-0.54 Ga)

Rifting of the Rodinian supercontinent is understood to have been multi-staged and may have occurred as early as ~850 Ma (Torsvik, 2008) with the eventual formation of the Iapetus Ocean as Laurentia separated from western Gondwana (Fig. 3.19). Evidence for the link between the proto-Andean margin and the Iapetus Ocean is characterised by paleontological evidence from brachiopods in Argentina, Bolivia and Peru (Benedetto, 1998). Remnant basement blocks from the Sierra Pampeanas, Argentina, indicate active arc magmatism between 650 and 530 Ma on the western margin of Gondwana during Iapetus times, which is considerably earlier than that recorded on Laurentia (~500 Ma and younger, Chew et al., 2008). Neoproterozoic U-Pb ages throughout the (Central) Andean zircon record are attributable to the Pampean-Brasiliano orogenic cycle during which a magmatic arc developed on the proto-Andean margin (0.5-0.7 Ga, Loewy et al., 2004; Chew et al., 2008; Wotzlaw et al., 2011). This orogenic belt is understood to have developed during the assembly of western Gondwana as allochthonous terranes converged on the Amazonian craton (Fig. 3.19). However, the present day expression of this orogeny in Bolivia (the Tucavaca belt at ~16^{o}S, 65^{o}W, see Fig. 3.1) is composed of deformed sedimentary sequences and not oceanic lithosphere (Pimentel et al., 1999). A potential source for these Neoproterozoic ages therefore may be the Brasília Belt which lies to the northeast of the Tucavaca belt where syn-collisional and arc-related (granitoid) magmatism has been dated between 0.9 to 0.63 Ga (Chew et al., 2008).

3.6.3.4 Early Phanerozoic ages (<0.54 Ga)

At the onset of the Phanerozoic, the western margin of Gondwana was active (Fig. 3.19) but the number and associated ages of orogenic events throughout the Palaeozoic is poorly constrained (Chew et al., 2007).

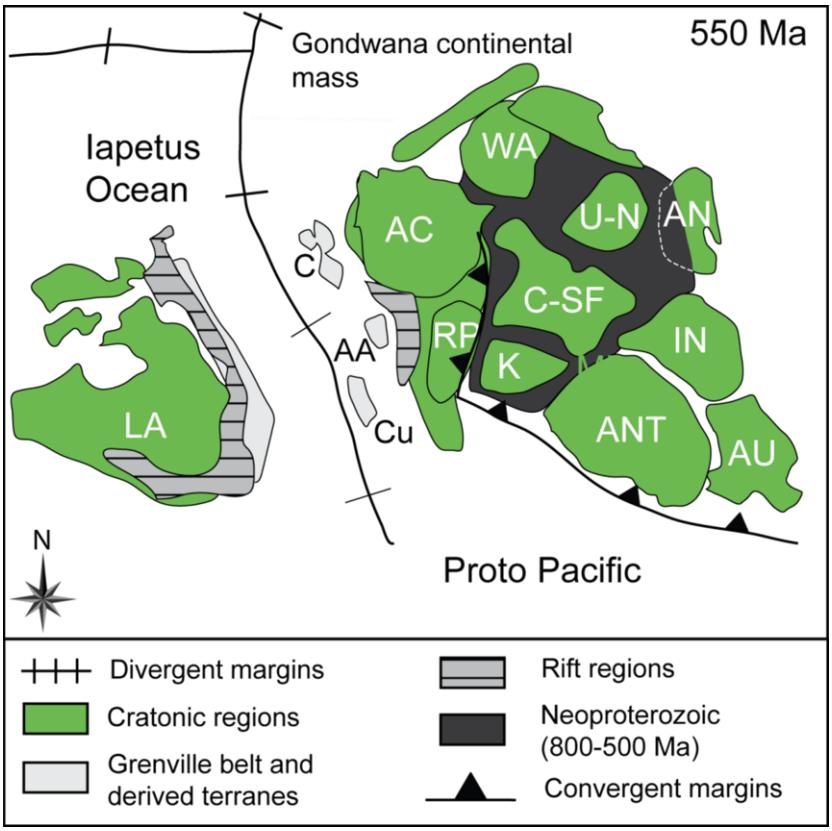

Fig. 3.19. Map showing the separation of Laurentia and Gondwana by the Iapetus Ocean at 550 Ma. AA: Arequipa-Antofalla; AC: Amazonian Craton; AN: Arabian-Nubian Shield; ANT: Antarctica; AU: Australia; AV: Avalonia; C-SF: Congo-San-Francisco; C: Colombian basement; Cu: Cuyania; IN: India; K: Kalahari; LA: Laurentia; MB: Mozambique belt; RP: Rio de la Plata (see Fig. 3.1); U-N: Uweinat-Nile; WA: Western Africa. (Map modified from Cordani et al., 2005).

A subduction regime is thought to have been established along the western Gondwana margin during the Cambrian which defined a convergent tectonic regime between the margins of eastern Laurentia and western Gondwana. This culminated in the closure of the Iapetus Ocean during the Famatinian orogeny *c.* 480 Ma (Caledonian orogeny of northern Europe; Salda et al., 1992).

Subsequent to ocean closure, granitic plutons were emplaced during the Devonian and Silurian (~440-370 Ma, e.g. Damm and Pichowiak, 1981) and this continent-continent collisional event has frequently been invoked by many authors to account for the early Palaeozoic age of granitoid basement rocks which outcrop on the western margin of South America (e.g. Allmendinger et al., 1982; Ramos, 1988). The peak and scatter of U-Pb ages at *c*. 500 Ma (Fig, 3.16 a-c) can therefore be attributed to a collisional tectonic regime during, and subsequent to, closure of the Iapetus Ocean.

Data from this study and throughout the Andean Cordillera indicates the presence of Grenville-aged crustal basement in the Central Andes and the existence of Grenville and Famatinian age peaks in the analysed zircon populations implies the availability of these orogenic belts to supply material to Palaeozoic strata. Today these belts may form, at least part of, the crust on which the modern day Andean mountain chain is built and may have been buried as recently as the Eocene-Oligocene (Chew et al., 2008). The U-Pb zircon record of the (Central) Andes therefore demonstrates consistently the development of the Andean margin from pre-Grenville times to the establishment of the modern-day tectonic regime through a sequence of supercontinent construction, subsequent break up, the docking of allochthonous crustal terrane blocks and the important role of crustal recycling. On a separate note, the prominent age peaks of zircon population 2 and 3 found in this study and throughout the Andean Cordillera can also be attributed to significant periods of continental crustal growth at 1.9 and 1.2 Ga (Condie, 1997).

3.6.4 Comparisons to "bulk" compositions of the continental crust

The Earth's continental crust can be divided into three principal layers; the lower, middle and upper (Rudnick and Fountain, 1995; Rudnick and Gao, 2003). The upper crust is the most geologically accessible region of Earth and many studies have aimed

to constrain its geochemical characteristics and elemental budgets (e.g. Taylor and McLennan, 1985; Gao et al., 1998; Rudnick and Gao, 2003). There are two common approaches to investigating the composition of the upper continental crust, 1) determining the average composition of rocks sampled at the surface (e.g. Clarke, 1889) and those brought up as xenoliths in volcanic (and plutonic) rocks and 2) determining the average concentrations of the insoluble elements found in clastic sediments, loess and glacial moraine (e.g. Goldschmidt, 1933). Given the decades of research into the nature of the continental crust, there are certainly broad geochemical characteristics that are well established and considered robust:

1) the bulk composition of the continental crust is andesitic with all bulk averages falling between 57.1 and 64.5 wt. % SiO_2 (e.g. Clarke, 1889, 1924; Taylor and McLennan, 1985; Rudnick and Fountain, 1995; Wedepohl, 1995; Rudnick and Gao, 2003);
2) the (incompatible) trace element enriched nature of the continental crust compliments the depleted mantle from which the crust was extracted;
3) whilst comprising only ~0.57 % by mass of the mantle, the crust is an important geochemical reservoir for incompatible elements e.g. Rb, Ba, Pb;
4) the upper and middle crust exhibits $Eu/Eu^* < 1$, the lower crust $Eu/Eu^* > 1$;
5) the upper crust exhibits high Rb/Sr (high $^{87}Sr/^{86}Sr$), low Sm/Nd (low $^{143}Nd/^{144}Nd$) and high U/Pb (high Pb isotopic ratios) whereas the lower crust is characterised by low Rb/Sr (low $^{87}Sr/^{86}Sr$) and U and Th depletion (low Pb isotopic ratios).

The crustal xenoliths erupted at the volcanic centres at Pampas Aullagas and Quillacas offer direct constraints of composition of the Central Andean continental crust. Given the clear lithological and geochemical heterogeneity that exists within the crust, the use of "bulk" elemental compositions to characterise the composition of the continental crust in this region may be a significant oversimplification, particularly when

evaluating potential crustal contaminants to ascending magmas. This is evaluated by comparing each of the sampled xenoliths to published data sets for the compositions of the upper, middle, lower and bulk continental crust (Fig. 3.20). Xenoliths which contain evidence for partial melting in the form of quenched anatectic melt, and have therefore potentially lost melt, are excluded.

With respect to all major oxides, sampled xenoliths overlap, and extend significantly beyond, the compositional range of numerous estimates for bulk crustal geochemical reservoirs, particularly SiO_2 (59-78 wt. %) and CaO (0.7-13 wt. %).

Fig. 3.21 shows Eu-anomalies vs. wt. % SiO_2 for sampled xenoliths plotted alongside upper, middle and lower crustal signatures. Consistently, the upper and middle crust, and the majority of sampled xenoliths, exhibit negative Eu anomalies. As similarly demonstrated by Fig. 3.20 however, significant heterogeneity exists at given SiO_2. The observed compositional variability within the xenolith suite warrants caution when assigning crustal affinity to a sampled xenolith suite (such as in this study) or a suite of magmatic rocks which have traversed through the crust based on typical "upper, middle or lower" crustal geochemical characteristics. As shown, sampled xenoliths from the Bolivian Altiplano extend beyond the range of bulk compositions for the crustal reservoirs indicating significant geochemical heterogeneity exists at depth. This heterogeneity is particularly crucial when evaluating the degree of crustal contamination in suite of magmatic rocks (e.g. Sørensen and Holm, 2008; Mamani et al., 2010).

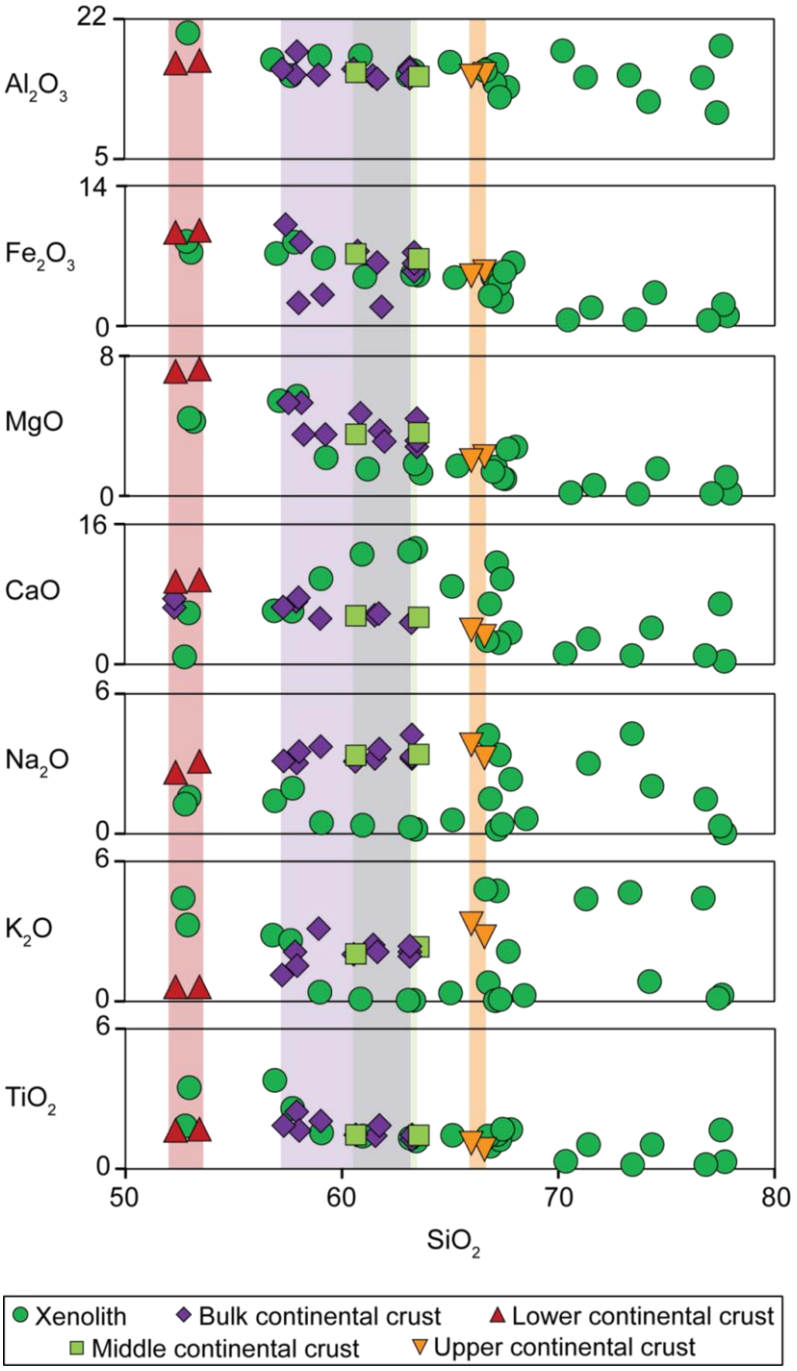

Fig. 3.20. Plot of SiO_2 vs. major oxides for all xenoliths of this study plotted alongside estimates for the lower, middle, upper and bulk continental crust (Data sources: Clarke, 1924; Pakiser and Robinson, 1966; Taylor and McLennan 1981; Weaver and Tarney, 1984; Taylor and McLennan, 1985; Shaw et al., 1986; Christensen and Mooney, 1995; Rudnick and Fountain, 1995; Wedepohl, 1995; Rudnick and Gao, 2003).

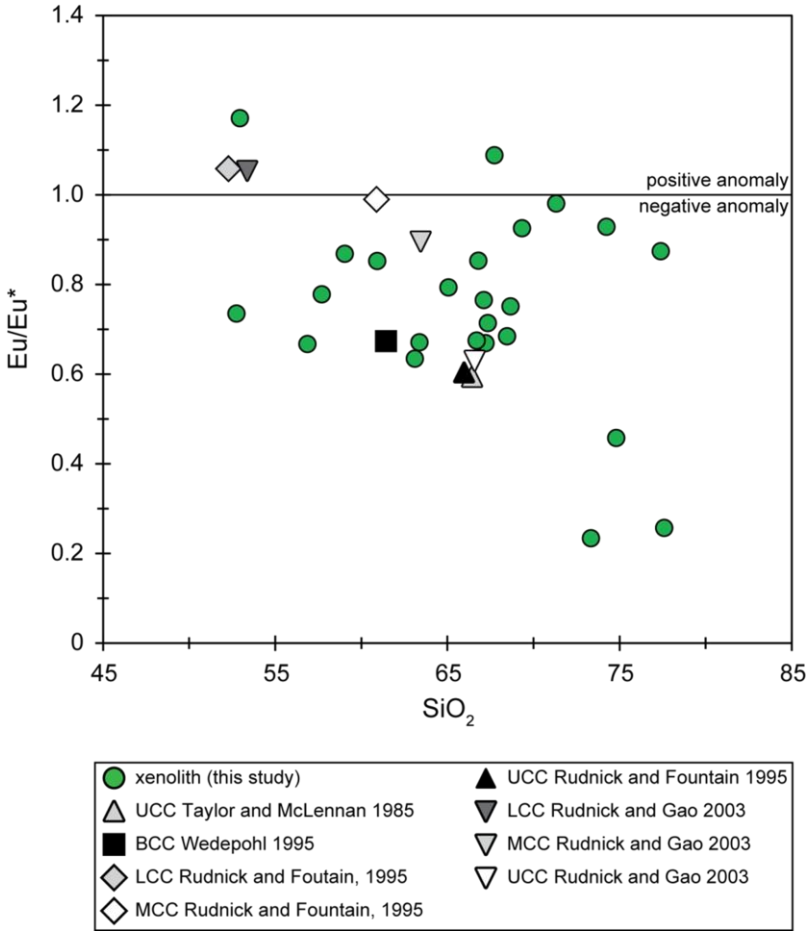

Fig. 3.21. SiO_2 vs. Eu anomalies for crustal reservoirs and sampled xenoliths.

This is illustrated in Fig. 3.22 where the lavas erupted at Pampas Aullagas and Quillacas are modelled through assimilation- fractional crystallisation (AFC) processes constrained by Central Andean crustal compositions from the sampled xenolith suite (see also Chapter 4).

The observed heterogeneity within the crustal xenolith suite emphasises the importance of identifying potential crustal assimilants as 1) bulk crustal estimates are averages of crust, more often than not, of data obtained from regions which lack a geological connection to the area of study e.g. the estimates of Taylor and McLennan, (1985) and Wedepohl, (1995) which are derived from the Canadian Shield and 2) more than one assimilant may be involved during contamination (Chapter 4, 5).

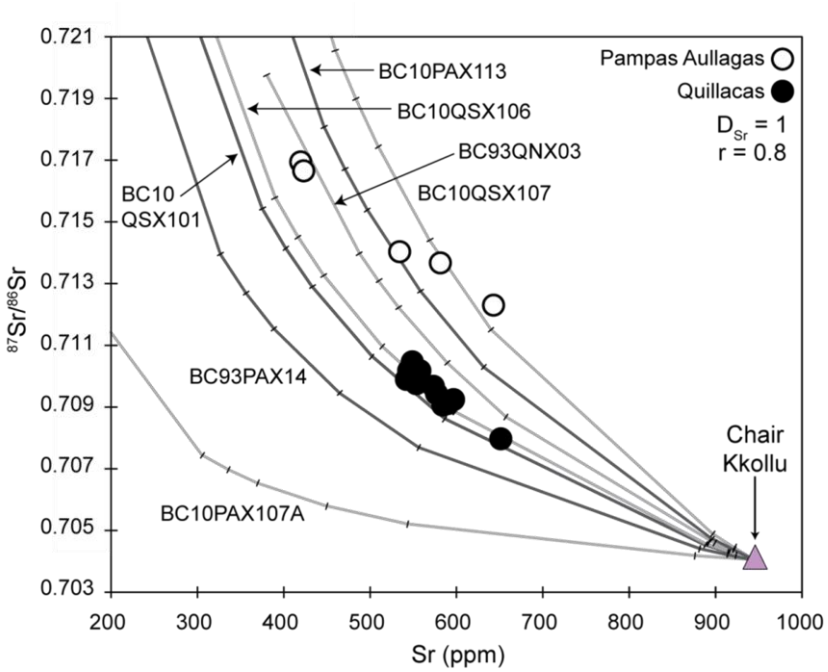

Fig. 3.22. AFC modelling of lavas at Pampas Aullagas and Quillacas. The most primitive volcanic rock in the Central Andes (the Chiar Kkollu basalt, Davidson and de Silva, 1992; 1995) is used as the mantle end-member. Tick marks represent 10% intervals.

Investigations which aim to constrain the crustal contamination history of a suite of magmatic rocks should therefore be encouraged to avoid bulk crustal estimates and where possible integrate known local and/or regional basement compositions whilst acknowledging the variability that will exist throughout a crustal column.

As noted, sampled Bolivian continental crust exhibits little geochemical consistency with characteristic upper, middle and lower crustal reservoirs with compositions ranging beyond published estimates (Fig. 3.20). However, the majority of xenoliths do exhibit broad, relative signatures, akin to those of the upper crust, and to a smaller degree the middle crust (e.g. LILE and LREE enrichment, negative Eu-anomalies; Fig. 3.5; 3.7; 3.21), Given a (preliminary) depth estimates of *c*. 20 km from three independent approaches aiming to constrain crustal source reservoirs in the Central Andes, the question of why does the crust at a depth typically associated with lower crustal reservoirs broadly resemble upper (and middle) crust? Fig. 3.23 a shows a cross section through the Central Andean continental crust at 21°S assuming ~320 km

shortening since the Cretaceous (see Fig. 2.2 in Chapter 2; Schmitz, 1994; Lamb et al., 2007). The detection of high velocity material beneath the Eastern Cordillera to the east of the study area has been inferred to represent detached material from the base of the crust which was subsequently overthrust. This subsequently led to crustal doubling in the back arc region (Schmitz, 1994). Hence, and as shown in Fig. 3.23 b, this process could be invoked as causing interleaving and vertical stacking of numerous upper, middle and lower crustal units within a crustal column. It should be noted however, that the continental crust beneath the plateau region is anomalously thick (~ 70 km, possibly up to 80 km, Zandt et al., 1994; Yuan et al., 2000) hence it is perhaps difficult to reconcile the depth and thickness divisions for typical upper-middle-lower crust associated to "normal" thickness crust of ~40 km (Mooney et al., 1998) with that beneath the Central Andes.

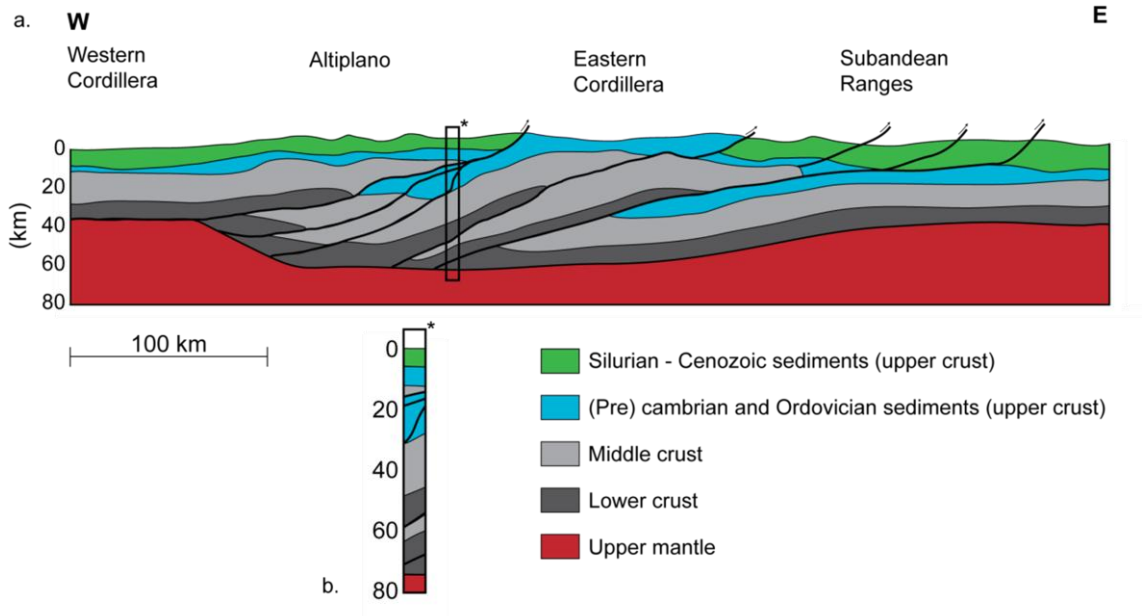

Fig. 3.23 a. Cross section at 21°S across the Central Andes. Modified from Schmitz, (1994). **b**. hypothetical vertical section through stacked crustal units.

3.7 Conclusions

This chapter presents geochemical and geochronological constraints on the composition and evolution of the Central Andean continental basement and (proto) Andean margin. Sampled crustal xenoliths from the back-arc region of the modern-day active Andean margin reveal significant lithological heterogeneity exists at depth. $^{87}Sr/^{86}Sr$ signatures of these crustal rocks vary significantly and extend beyond the range of Sr-isotopic signatures of recent volcanic rocks (< 60 Ma). The compositions of the variable lithologies provide an absolute geochemical dataset for potential crustal contaminants in studies of crustal contamination inherent to Central Andean magma genesis (e.g. Sørensen and Holm, 2008; Mamani et al., 2010).

The Pb isotope signatures have provided confirmation of the nature of the crustal basement beneath this region of the Bolivian Altiplano, and the geochronological results have strengthened the idea that Grenville-aged orogenic belts were available to source younger detritus but also that older, Palaeoproterozoic material may play a role in building the continental crust of the Central Andes throughout the Phanerozoic. Pb isotopic ratios also rule out the influence or contribution from Laurentian crust in the formation of continental basement in the Central Andes.

In-situ U-Pb age analyses at *c.* 1.8 Ga, *c.* 1.1 Ga and *c.* 0.5 Ga demonstrate the role of crustal recycling during the growth of the Andean margin. The age peaks observed correspond to episodes of continental collision and subsequent break-up e.g. the formation of Rodinia at *c.* 1.0 Ga. The broad lithological and geochemical heterogeneity exhibited by the sampled xenolith suite demonstrates the extreme variability of the continental crust beneath the Central Andes. When compared to bulk crustal compositional estimates for the lower, middle, upper and bulk continental (e.g. Rudnick and Fountain, 1995; Rudnick and Gao, 2003) the xenoliths typically exhibit

Eu/Eu* at < 1, consistent with upper (and middle) continental crust signatures. However, the significant geochemical variability that exists within the sampled suite demonstrates the need for careful consideration of potential crustal contaminants, not just in studies of (Central) Andean magma petrogenesis, but at active sites of volcanism across the continents where a continental crustal component is involved.

Data sources for Fig. 3.16 b, c

Tosdal, R. M. (1996) Tectonics, v. 15; p. 827–842;
Goldstein, S. L., (1997) Chemical Geology, v. 139; p. 271-286;
Restrepo-Pace, P. A., et al., (1997) Earth and Planetary Science Letters, v. 150; p. 427-441;
Rapela, C. W., et al., (1998). In: Pankhurst, R. J. and Rapela, C. W. (eds) The Proto-Andean Margin of Gondwana. Geological Society of London Special Publications, 142; p. 181-217;
Wörner, G., et al., (2000) Journal of South American Earth Science 13, 717–737;
Cordani, U. G., et al., (2005). Geological Society of London, Special Publications, v. 246; p. 329-346.
Rapela, C. W., et al., (2007) Earth Science Reviews, 83; p. 49-82;
Chew, D. M., et al., (2008) Precambrian Research, v. 167; p. 186-200;
Collo, G., et al., (2009) Journal of the Geological Society of London, 166; p. 303-319;
Folkes, C. B., et al., (2011) Journal of Volcanology and Geothermal Research, v. 206; p. 136-147.

Investigating crustal contamination and magma genesis beneath the Bolivian Altiplano, Central Andes

4

This chapter will be submitted as a paper to Journal of Petrology

ABSTRACT

Lavas erupted from Plio-Pleistocene monogenetic volcanic centres at Pampas Aullagas (PA) and Quillacas (QL) on the eastern Bolivian Altiplano (~180 km from the active Andean arc) are host to a suite of crustal xenoliths. Given the rare exposure of the Central Andean continental basement these xenoliths offer a unique opportunity to study, *in-situ*, the crustal contribution to Central Andean lavas. Sampled lavas are porphyritic, andesitic to dacitic in nature and display the typical geochemical signatures associated with continental arc magmas e.g. LILE enrichment. $^{87}Sr/^{86}Sr$ values at PA and QL range from 0.7080 to 0.7169 and record the highest Sr-isotopic compositions for recent (< 60 Ma) Central Andean volcanic rocks. The role of crustal contamination during the petrogenesis of these lavas is clear both petrographically (presence of xenocrysts) and geochemically with indices of differentiation (e.g. wt. % SiO_2) correlating with $^{87}Sr/^{86}Sr$. These contamination trends can be modelled through bulk mixing, AFC and EC-AFC but consistently require a high proportion of crustal material (up to 90%) to explain observed signatures. Given the extreme variability observed within lavas at one centre, the incorporation of numerous crustal lithologies during magmatic differentiation, rather than simple two component crust-magma interaction, is inferred. From La/Yb vs. Dy/Yb and REE inversion modelling, mantle melting beneath this region of the Central Andes in inferred to have occurred in the garnet stability field. Monogenetic volcanic centres of similar age exist to the west of PA and QL and offer an opportunity to assess across-arc changes (70 to 66°W) in the petrogenesis of magmas at ~18-21°S. From the K-h relationship and CaO vs. MgO it is inferred magmas behind the arc front and on the Central Altiplano experienced minimal upper crustal interaction ($^{87}Sr/^{86}Sr$ from 0.7047 to 0.7068, higher Sr/Y at >40) and erupted beneath thinner crust than the magmas beneath PA and QL. This is in agreement with recent geophysical observations.

4.1 Introduction

The Andes of South America are the type locality for the rock type andesite (Thorpe and Francis, 1979). They are differentiated, grey porphyritic volcanic rocks which are hypersthene-normative and often characterised by plagioclase, pyroxene, ± amphibole, ± biotite ± alkali feldspar (Gill, 1981). At continental arcs, andesites often exhibit geochemical characteristics akin to the continental crust e.g. LILE enrichment, HFSE

depletion (Fig. 4.1) and Sr-Pb isotopic compositions similar to those of the (upper) crust and/or subducted sediment.

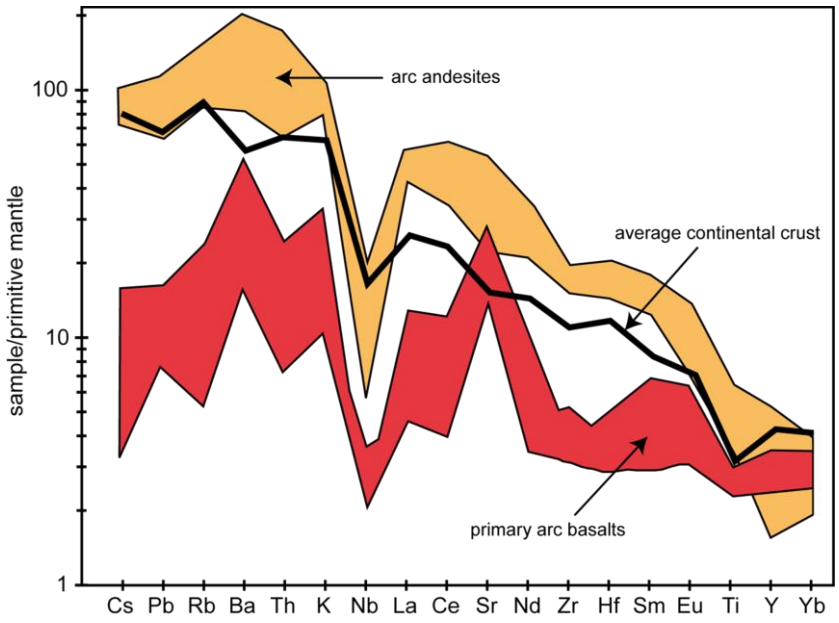

Fig. 4.1. Trace element similarity between arc andesites and (bulk) continental crust (Central Andes data, adapted from Davidson et al., 2005).

Assessing the degree to which a crustal component has played a role during magmatic differentiation is often challenging, as too is determining the nature of any potential crustal contaminant(s). This is particularly difficult to constrain in the Central Andes where no true basalts have erupted in the region at least during the Cenozoic, and exposures of crustal basement rocks are rare (Chapter 3).

The Central Andean continental crust is anomalously thick extending to depths of up to 80 km (Zandt et al., 1994) hence interaction between mantle-derived melts and surrounding crustal lithologies is highly likely. Magmas ascending beneath the composite volcanoes of the active arc undergo shallow level differentiation in upper crustal storage zones where processes occurring at depth and throughout the mantle-crustal column are masked by late-stage processing (Fig. 1.1, Chapter 1). Plio-Pleistocene lavas erupted from monogenetic volcanic centres at Pampas Aullagas (PA) and Quillacas (QL) on the Eastern Altiplano (Fig. 4.2 a) are hosts to a suite of crustal

xenoliths (Chapter 3). Given the poor constraints on the composition of any potential crustal contaminants to Central Andean magmas, these lavas and xenoliths present a unique opportunity to investigate, *in-situ*, the contribution of the continental crust to these Central Andean lavas. Additionally, a suite of lavas from monogenetic volcanic centres of comparable age (Hoke and Lamb, 2007) exists for ~180 km across the Altiplano from behind the arc at Ollagüe and Sajama, throughout the Central Altiplano north of Salar de Uyuni and on the Eastern Altiplano (Fig. 4.2 a). These have previously been characterised by Davidson and de Silva, (1992; 1995).

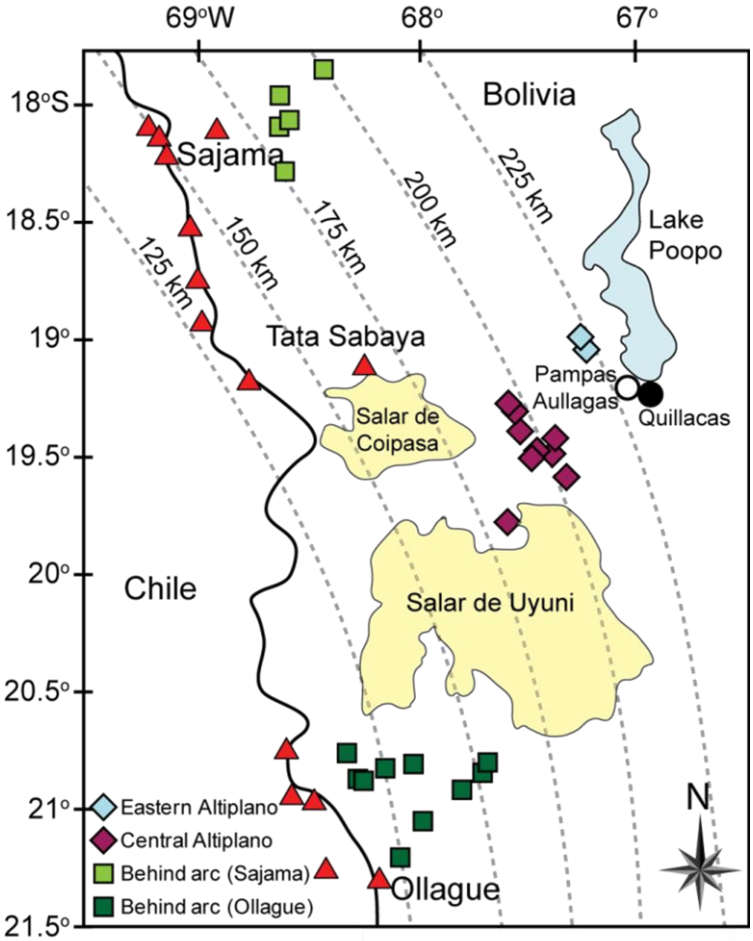

Fig. 4.2 a. Map showing the location of Pampas Aullagas and Quillacas minor monogenetic volcanic centres. Other Bolivian minor centres also shown. Dashed lines are depth contours to the Benioff zone (after Isacks, 1988) and red triangles are active arc volcanoes. Map is modified from Davidson and de Silva, (1995).

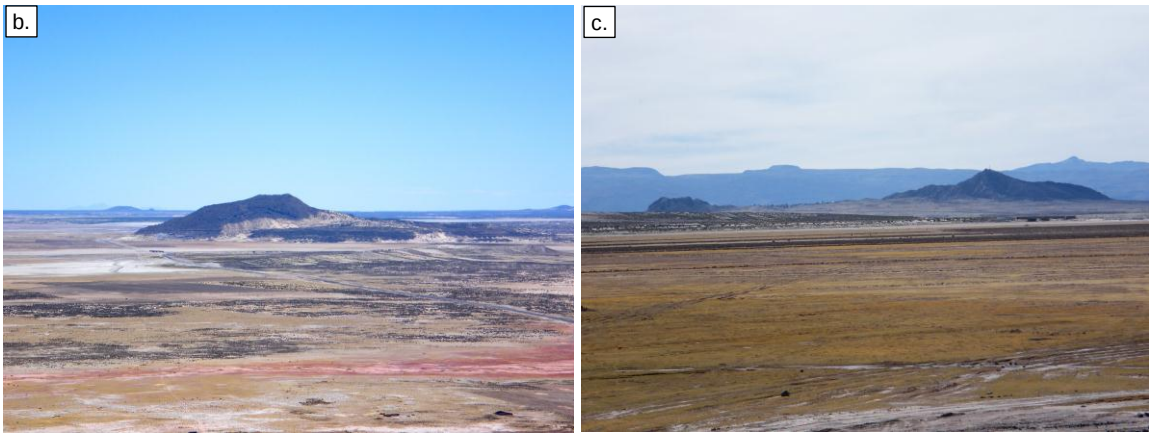

Fig. 4.2 b Monogenetic volcanic centre at Pampas Aullagas, 196 m high. **Fig. 4.2 c** Monogenetic volcanic centre at Quillacas. Southern hill (right hand side of image) is 126 m high.

Lavas erupted from these centres and those at PA and QL (Fig. 4.2 b, c) offer an opportunity to:

1) constrain the nature of mantle and crustal sources across the strike of the arc;
2) assess changes in the relative contribution from mantle and crustal sources with distance to the arc and;
3) investigate the extent to which shallow and deep level processes can be constrained beneath this region of the Central Andes.

4.2 Field area and previous work

At these latitudes, the descending Nazca plate subducts at 80 mm/yr in an ENE direction forming a Benioff zone which dips at ~30^{o} and shallows to the north and south (DeMets et al., 1994). It is currently understood that beneath the Central Andes from ~17^{o}S to ~ 22^{o}S a zone of active mantle melting is present at shallow depths (~80 km) where the lithosphere is relatively thin (<100 km, Hoke and Lamb, 2007). The eruption of the minor centres across the Altiplano is understood to have been controlled by activity on NW-SE trending strike-slip faults during the Miocene-Pliocene and Pliocene-Quaternary (see section 2.1.5, Chapter 2). Broadly, the monogenetic volcanic centres at Sajama and Ollagüe, on the Central Altiplano and on

the Eastern Altiplano, define trends sub-parallel to the arc front (Fig. 4.2 a; Fig. 1 b of Davidson and de Silva, 1995). All lavas erupted onto, and through, the local Miocene-Pliocene ignimbritic basement.

Results from rare earth element (REE) inversion modelling on recent (<25 Ma) lavas from several of the monogenetic centres across the Bolivian Altiplano by Hoke and Lamb, (2007) were interpreted as representing melting at <100 km in the spinel and spinel-garnet peridotite stability fields with two distinct melt sources; 1) depleted MORB between 75 and 110 km for centres <75 km behind the arc and 2) enriched MORB between 65 and 90 km depth for centres >100 km behind the arc. However, intrinsic to REE inversion calculations is the use of lava compositions which are unaffected by crustal inputs, either by the slab, via subduction erosion, by the continental crust or through variable contributions from all three. The study of Davidson and de Silva, (1995) inferred the mantle source to Bolivian Altiplano lavas as asthenospheric in nature and invoked a decreasing input from slab-derived fluids coupled with multi-staged crustal contamination by isotopically variable contaminants as an explanation for changes observed in the lavas geochemical signatures from west to east across the Altiplano.

The contribution of a subducted sediment component to the mantle source of (monogenetic) volcanism in this region of the Central Andes is understood to be negligible, if a contribution exists at all, as the Peru-Chile Trench is sediment free at these latitudes (Thornburg and Kulm, 1987).

Sampling of the lavas at PA and QL was undertaken by Jon Davidson and Shan de Silva during fieldwork in 1993. The volcanic centres can be accessed from route 603 which was in the process of being built during the October 2010 fieldwork which

focussed on sampling of the crustal xenoliths (see Chapter 3). From La Paz, route 1 provides access to the town of Oruro which lies at the northern extent of Lake Poopo (Fig. 4.2 a). From Oruro, route 602 extends south along the eastern shore of Lake Poopo from which route 603 is accessed. The Altiplano Plateau in this region is at ~3710 m above sea level.

4.2.1 Pampas Aullagas (PA)

The volcanic centre at Pampas Aullagas forms a 2 km, circular hill which rises ~196 m above the Altiplano surface ~6 km from the southern edge of Lake Poopo, an ephemeral lake which was once connected to Lake Titicaca (Fig. 4.2 a; 2.1 b, Chapter 2). Lavas erupted at 1.89±0.01 Ma (Davidson and de Silva, 1995) from a vent on the summit and produced an estimated ~0.61 km^3 of material based on current surface exposure (Fig, 4.2 b). From the summit, the western extent of the ~8500 km^2 Los Frailes ignimbrite complex (16 Ma-recent) can be viewed to the southeast and to the west, the peak of Tata Sabaya (the only volcano of the Andean arc in Bolivia) is visible on the horizon. In the late 1990s the edifice at Pampas Aullagas was hypothesised to be the remnants of Plato's Atlantis with the semi-circular depressions on the lower flanks interpreted as former water channels fed by the "sea" of Lake Poopo (Allen, 1998).

4.2.2 Quillacas (QL)

The monogenetic centre at Quillacas forms two small hills ~11 km southeast of Pampas Aullagas and ~9 km from the southern shore of Lake Poopo (Fig. 4.2 a, c). Lavas erupted 1.42±0.15 Ma (Davidson and de Silva, 1995). The town of Quillacas is nestled between hills to the north and south which rise ~80 m and ~120 m above the Altiplano Plateau respectively. The cumulative erupted volume of material is significantly less compared to Pampas Aullagas at ~0.18 km^3 based on current exposure. Bedded phreatomagmatic deposits ~30 m above the elevation of the Altiplano can be found on

the southeastern slope of the southern hill and lake terraces are present on the northern hill indicating eruption occurred during times of higher lake levels (Davidson and de Silva, 1995).

4.3 Analytical Techniques

Rock powders were produced from sampled lavas by initially removing weathered surfaces and xenocrystic material from the lavas before crushing in an agate ball mill. Major and selected trace element concentrations were measured on a Philips PW2404 XRF instrument at the School of Geosciences, University of Edinburgh. Precision on all elements was better than 1% and results from 4 USGS standards run throughout the course of two analytical sessions are presented in Appendix E. Additional trace element concentrations were measured in solution by ICPMS on the X-Series 2 and ELAN 6000 instruments in the Northern Centre of Elemental and Isotopic tracing (NCIET), Department of Earth Sciences, Durham University. Precision on all elements was better than 1% and results from 5 USGS standards run throughout the course of two analytical sessions are presented in Appendix E. Initial Sr-Nd-Pb isotopic analyses were carried out on a VG Sector 54-30 TIMS instrument at UCLA during which 15 analyses of the NBS987 standard yielded $^{87}Sr/^{86}Sr$ of 0.71022±13 (2σ) and analysis of the La Jolla standard yielded $^{143}Nd/^{144}Nd$ of 0.511840±11 (n=4, 2σ). Further analyses were made on the Neptune PIMMS instrument at NCIET. Sr-Nd-Pb isotopic analysis for sample suite prefix BC93 was carried out during one analytical session for each isotope, similarly for sample suite BC10. NBS987 yielded $^{87}Sr/^{86}Sr$ averages of 0.710254±11 (n=9, 2σ) and 0.710257±12 (n=13, 2σ). An in-house J&M standard (undoped and doped) collectively yielded $^{143}Nd/^{144}Nd$ of 0.511115±13 (n=8, 2σ) and $^{143}Nd/^{144}Nd$ of 0.511122±13 (n=8, 2σ). NBS981 yielded $^{206}Pb/^{204}Pb$, $^{207}Pb/^{204}Pb$ and $^{208}Pb/^{204}Pb$ of 16.9405±0.0001, 15.4977±0.0010, 36.7166±0.0035 (n=13, 2σ) and 16.9406±0.0001, 15.4980±0.0010, 36.7181±0.0035 (n=17, 2σ) respectively. Details of

preparation methods, chemical separation techniques and instrument running conditions are presented in Appendix E.

4.4 Sample Petrography

4.4.1 Lavas

Samples of the erupted lavas at PA and QL (Fig. 4.3 a) are fine grained and display seriate to porphyritic textures containing up to 40 vol% phenocrysts. They display similar characteristics to lavas erupted from several other mafic volcanic centres on the Bolivian Altiplano (Davidson and de Silva, 1995). The term 'phenocryst' throughout this study refers to relatively large crystals which crystallised from a magma (although a proportion of these may strictly be antecrysts), the term 'microphenocryst' refers to crystals ranging between 100 and 300 μm, the term 'microlite' describes crystals <100 μm and the term 'xenocryst' refers to crystals derived from the crustal basement.

The QL phenocryst assemblage is dominated by plagioclase + hornblende + biotite + Fe-Ti oxides, with rare orthopyroxene, augite, olivine and minor apatite. The groundmass is composed of plagioclase microlites + microphenocrysts of hornblende + orthopyroxene + Fe-Ti oxides + glass. Plagioclase occurs as individual phenocrysts or as clusters. Crystals exhibit sieve textures and oscillatory zoning. At QL, 35-40% of the population exhibit subrounded sieve-textured cores with overgrowth rims (up to 150 μm) and 10-15% display one or more sieve textured 'zones' from core to rim. Hornblende phenocrysts are euhedral, elongate (>0.3–1.2 mm) and occasionally exhibit oscillatory zoning. Rims are replaced by oxides to variable degrees (Fig. 4.3 b) perhaps as a result of dehydration related to pressure release upon eruption. This is also observed on hornblende microphenocrysts. Biotite phenocrysts are euhedral, contain subhedral inclusions of plagioclase and are heavily oxidised. Magnetite and ilmenite are present as (micro)phenocrysts throughout the sampled lava suite but are not

ubiquitous. Rare disseminated olivine phenocrysts are characterised by irregular fractures in-filled by iddingsite and alteration rims where olivine has been replaced by microphenocrysts of radiating serpentine. Augite phenocrysts also exhibit alteration to serpentine at their rims. Trachytic textures, defined by feldspar microlites, are observed in several of the QL samples. The sieve textures observed in the plagioclase from QL lavas indicate magma mixing may have occurred. Crustal xenocrysts constitute <5 vol. %. In PA lavas, olivine and hornblende are absent and augite is rare. Samples are characterised by a fine grained groundmass dominated by plagioclase phenocrysts and microlites (Fig. 4.3 c) and up to 10% xenocrysts with <10% phenocrystic biotite, and 5-10% oxide minerals.

Fig. 4.3 a. Lava outcrop at Quillacas. One Boliviano coin 2.7 cm width.

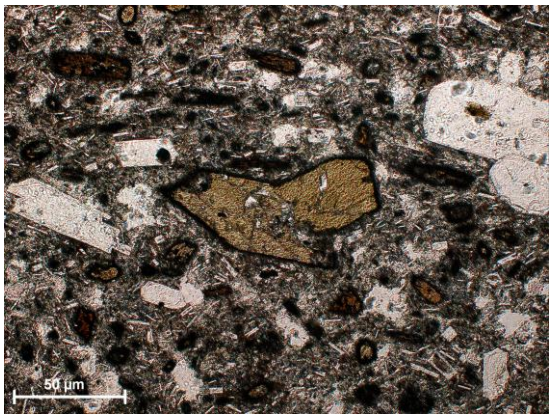

Fig. 4.3 b. Photomicrograph of QL lava.

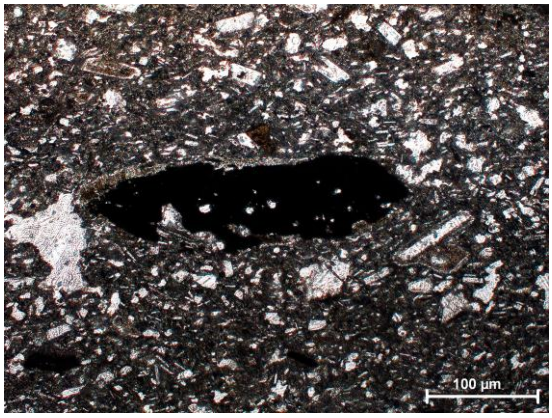

Fig. 4.3 c. Photomicrograph of PA lava.

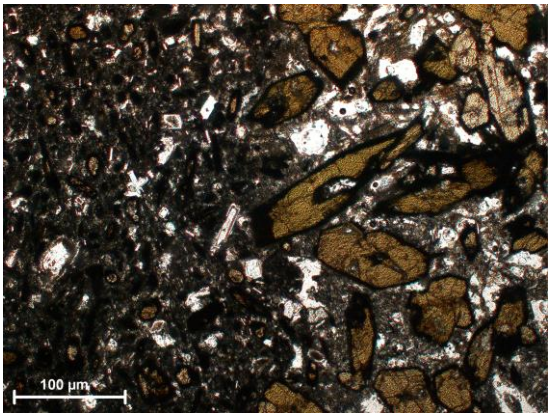

Fig. 4.3 d. Photomicrograph of mafic enclave at QL.

4.4.2 Mafic inclusions

Medium to coarse grained vesiculated mafic enclaves within QL lavas contain euhedral to acicular hornblende which is rimmed by magnetite in a groundmass of feldspar microphenocrysts and microlites (Fig. 4.3 d). Sieve textured plagioclase and oxide minerals are also present within the enclave. These enclaves are typical of magmatic inclusions found in Andean arc lavas (e.g. Selles et al., 2004) and suggest magma mingling occurred within the volcanic conduit prior to eruption. The hornblende phenocrysts within the QL lavas are not derived from these magmatic inclusions as they are smaller and disaggregation of hornblende from the magmatic inclusions into the surrounding lava has not extensively occurred (Fig. 4.3 d).

4.4.3 Xenocrysts

Xenocrysts derived from the underlying metamorphic basement are found throughout the majority of samples, particularly within PA lavas. Quartz grains are typically embayed by groundmass material or resorbed and rimmed by clinopyroxene. Biotite xenocrysts are often partially resorbed and garnets have broken down to form symplectites of plagioclase + orthopyroxene + clinopyroxene + oxides. Fibrolite (fine-grained, acicular high-temperature variety of the Al_2SiO_5 polymorph sillimanite) is commonly rimmed by plagioclase microphenocrysts and contains rare inclusions of cubic hercynitic spinel (up to 90 μm).

4.5 Geochemistry

Four lava samples from PA and eleven from QL were analysed for their major and trace element compositions. Results reported also include (data permitting) an additional four lavas sampled by Davidson and de Silva (1992, 1995); one from PA and three from QL. Samples from each centre are considered cogenetic.

4.5.1 Major elements

Fig. 4.4 a-h show major oxides plotted against wt. % SiO_2 (used as a differentiation index). The cogenetic suites from each centre consistently form two distinct arrays. Wt. % MgO, CaO, Na_2O and Fe_2O_3 exhibit well defined negative trends (r^2 values > 0.9) which likely reflect the fractionation of olivine, plagioclase and pyroxene during early magmatic differentiation. The trends observed with respect to TiO_2 and P_2O_5 are attributable to variable oxide (ilmenite) and apatite fractionation. The PA and QL lavas are hypersthene-quartz normative and are of a peraluminous natures with an alumina saturation index (ASI) of 1.4 and 1.6 respectively. Sampled mafic inclusions are nepheline normative and have a metaluminous nature: ASI of 0.98 (n=4).

The PA and QL lavas are dacitic and andesitic in nature respectively and can be classed as high-K, calc-alkaline (Fig. 4.5 a, b). This is in contrast to the majority of other mafic volcanic rocks from recent (<25 Ma) monogenetic eruptions across the Central Andes which display higher total alkali contents ranging from trachy-basaltic to trachytic compositions and include Hawaiites, Mugearites and Benmoreites (Delacour et al., 2007; Hoke and Lamb, 2007; Sørensen and Holm, 2008). This trend is governed by the relative "excess" of sodium as the majority of other lavas from monogenetic centres exhibit lower wt. % K_2O than the PA and QL lavas and include medium to high-K calc alkaline lavas (Fig. 4.5 b).

4.5.2 Trace elements

Fig. 4.6 a shows a primitive mantle-normalised spidergram for PA and QL lavas, two samples of the Los Frailes ignimbrite and a mafic enclave. Lavas display high degrees of LILE enrichment (e.g. Ba and Rb), prominent peaks at U and Th and HFSE depletion in Nb, Ta and Ti.

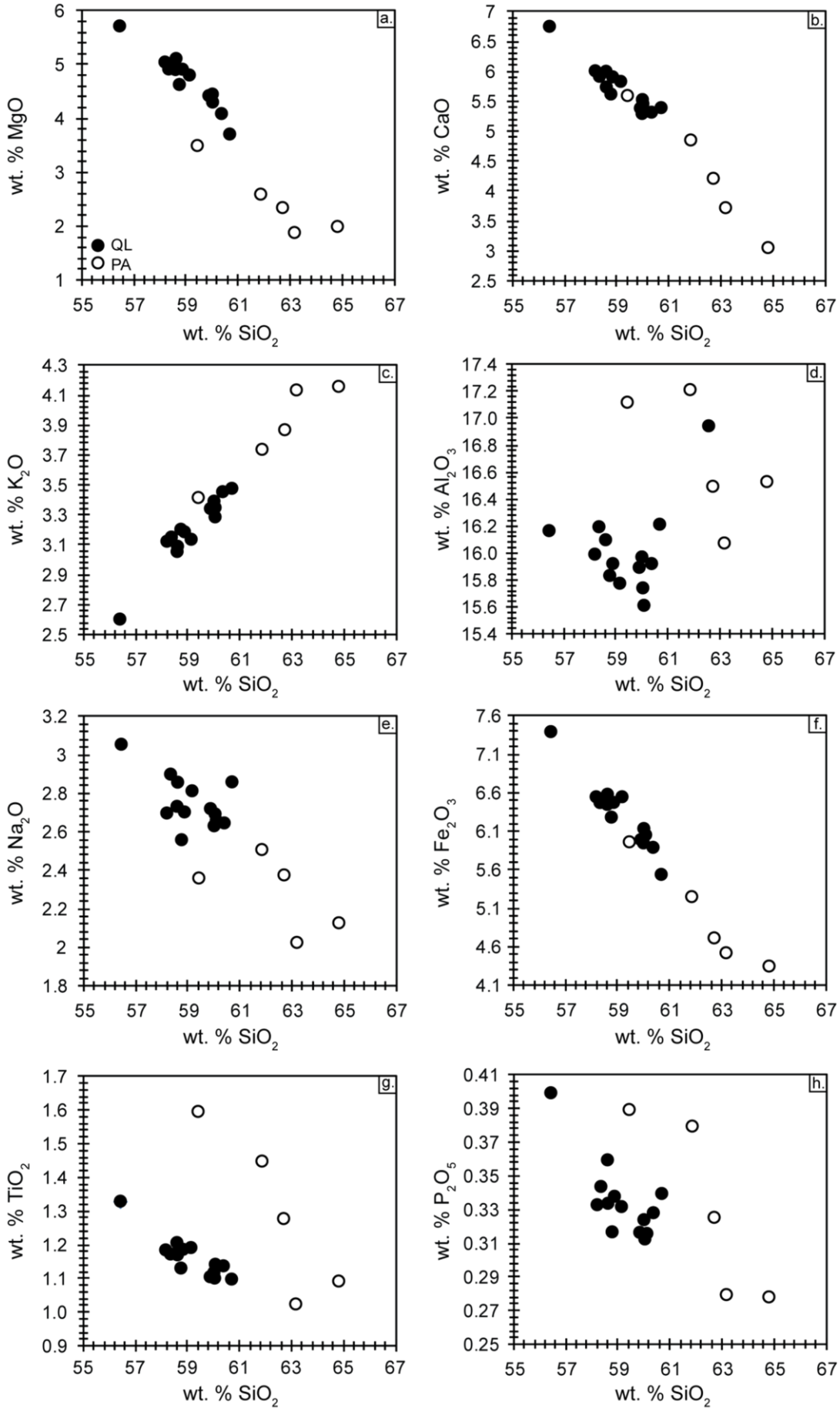

Fig. 4.4 a-h. Major oxide variations within PA and QL lavas.

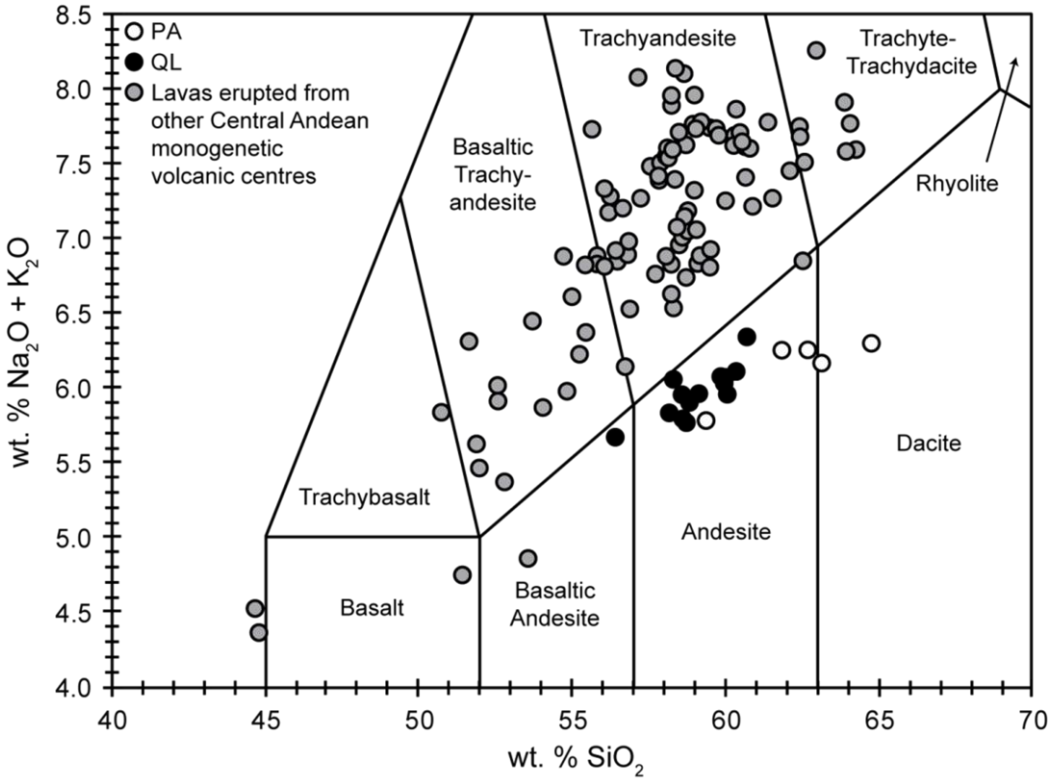

Fig. 4.5 a. TAS plot showing compositions of sampled lavas from monogenetic eruptions (<25 Ma) across the Central Andes.

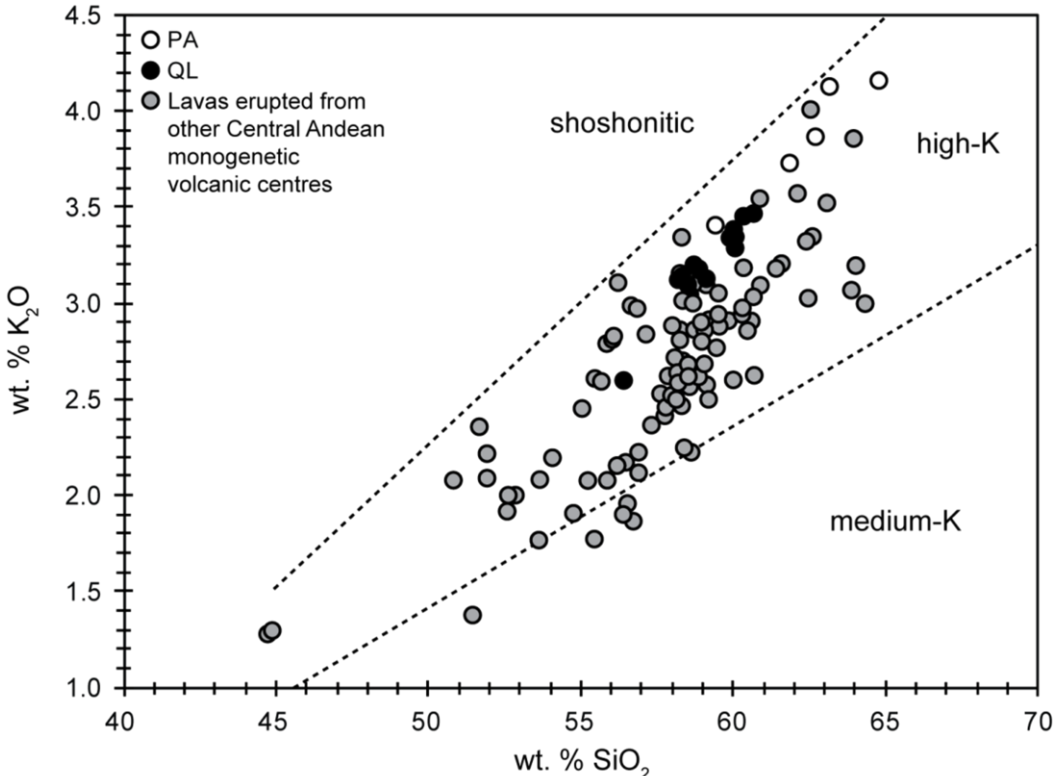

Fig. 4.5 b. Relatively high-K nature of PA and QL lavas

These characteristics are typical of arc magmas (Fig. 4.1) and similar to those observed in lavas from other minor centres across the Altiplano region (Davidson and de Silva, 1995). The trough at Sr is the likely result of plagioclase fractionation at low pressures in the upper crust. The Ba trough in the Los Frailes ignimbrite may indicate loss of Ba to fractionation of alkali feldspar, specifically sanidine.

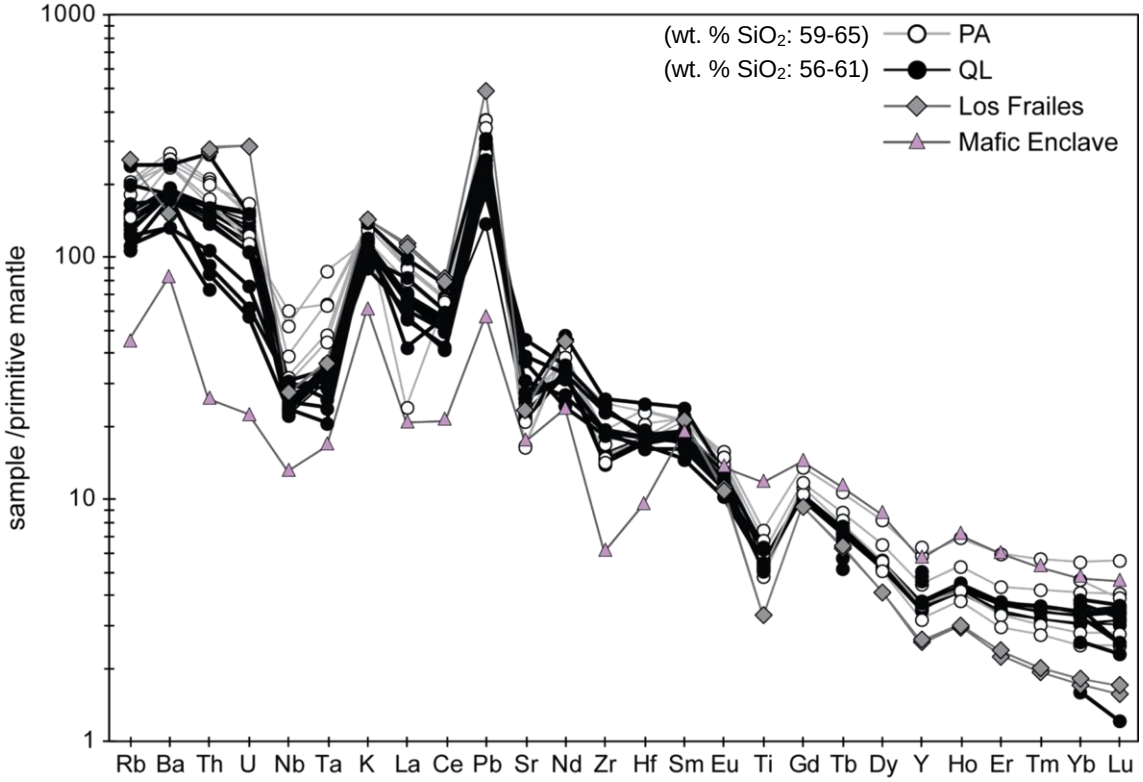

Fig. 4.6 a. Primitive mantle normalised spidergram. Normalising values of McDonough et al., (1991).

Fig. 4.6 b shows Th/U plotted against SiO_2 for the PA and QL lavas of this study. In a closed system, i.e. if fractional crystallisation was the only process operating, the ratio between two incompatible trace elements should remain (more or less) constant. This is clearly not the case and indicates an open magmatic system during differentiation. It should be noted that each lava sample from Davidson and de Silva, (1995) is from one centre and the lavas in each group (e.g. "Ollagüe") cannot be considered cogenetic.

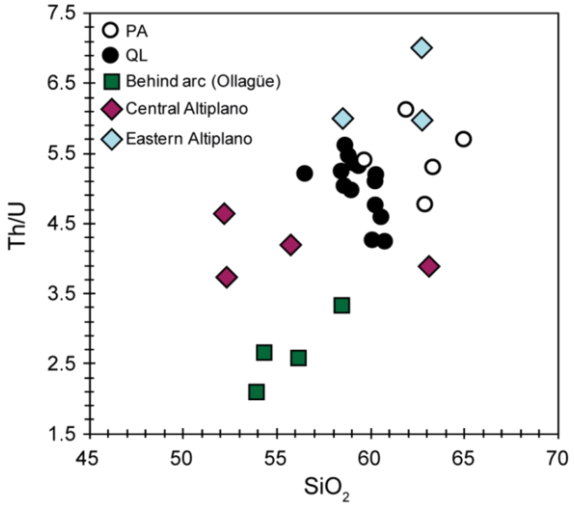

Fig. 4.6 b. Open system processing beneath centres at PA and QL.

PA and QL lavas exhibit higher Rb, Pb peaks and deeper Sr troughs than other Bolivian minor centres (Fig. 4.7 a, b).

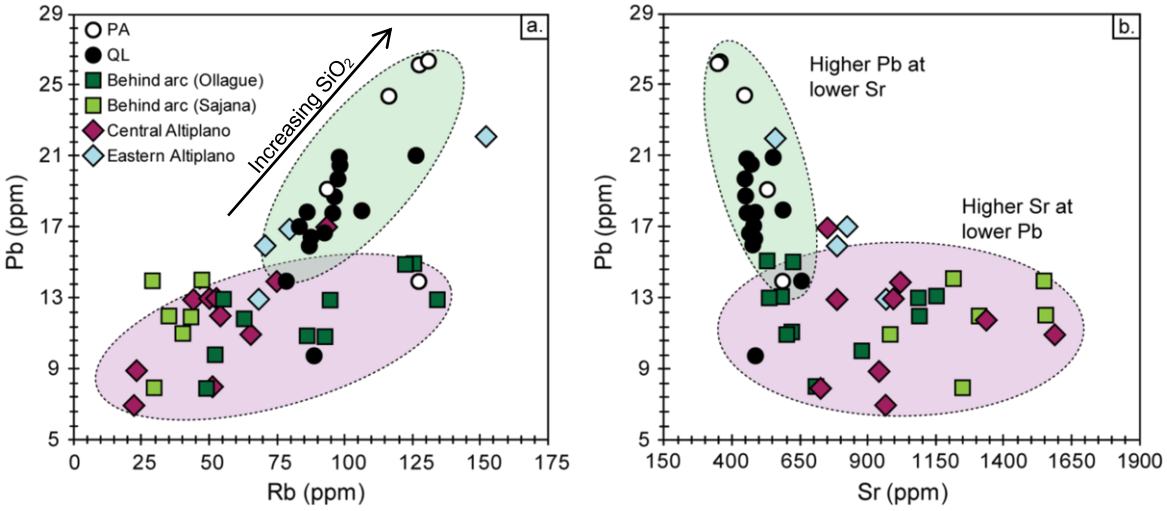

Fig. 4.7 a, b. Trace element characteristics of lavas from Bolivian minor centres.

PA and QL lavas also exhibit higher Ba/Nb values (at averages of 6.3 and 7.5) than the other centres closer to the arc (4.6, 4.9 and 2.2) indicating higher degrees of LILE enrichment (or greater degrees of Nb depletion). This signature is also observed the Eastern Altiplano lavas of Davidson and de Silva, (1995, up to 8.2).

PA and QL lavas exhibit prominent troughs at Nb-Ta. This signature is a common characteristic of subduction zone magmas (e.g. Fig. 4.1). The relative depletion of these elements in arc magmas is often attributed to their insolubility in aqueous, slab-derived, fluids and the stability of rutile in the downgoing slab (e.g. Brenan et al., 1994). Experimentally, rutile has been shown capable of producing the observed negative Nb-Ta anomaly in arc-derived magmas (K_ds of 96 and 195 respectively; Klemme et al., 2005). Rutile's presence, however, is not a prerequisite for establishing this geochemical signature as a similar anomaly can result from the presence of aluminous clinopyroxene in equilibrium with a fluid which contains proportionally few dissolved silicates e.g. in subducting (or arc mantle) eclogites (Baier et al., 2008). The observed depletion in Ti, Y and Yb is likely due to the occurrence of phases at depth that fractionate these elements e.g. garnet and/or amphibole.

Chondrite-normalised REE plots for the QL and PA lavas are shown in Fig. 4.8 with QL lavas displaying a (relatively) strikingly consistent internal data set. All samples exhibit strong LREE enrichment with (La_N/Yb_N) ratios between 18.9 and 22.4 at QL and between 14.3 and 35.8 at PA. HREE depletion is characterised by (Sm_N/Yb_N) values of ~5.2 at QL and a range from 8.4 to 3.9 at PA. This signature indicates HREE compatibility in high pressure minerals which readily partition these elements during fractionation (e.g. garnet) in a granulitic/eclogitic fractionate at depth. The lack of a "concave upwards" REE pattern argues against a control by amphibole (hornblende) fractionation. The sampled Los Frailes ignimbrite exhibits a significantly steeper REE pattern than those of the minor centres (La_N/Yb_N of 60.2). In contrast, the sampled mafic enclaves exhibit relative flat REE patterns (La_N/Yb_N at 4.3).

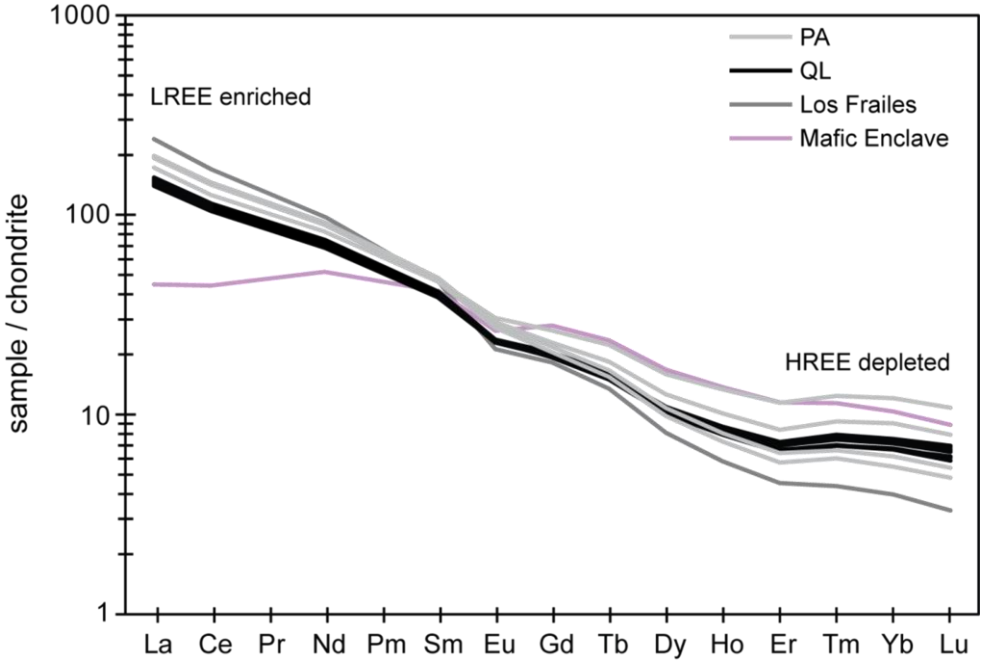

Fig. 4.8. REE patterns for sampled lavas, a mafic enclave and the Los Frailes ignimbrite.

The ratio of an MREE (e.g. Dy) to a HREE (e.g. Yb) can be used to differentiate between garnet and amphibole fractionation given that garnet will more readily incorporate the HREEs and amphibole the MREEs. This approach was similarly applied by Davidson et al., (2007) to a suite of data from five volcanic arcs (four oceanic and one data set from Cotopaxi in Ecuador, NVZ) in order to establish the role (or not) of amphibole during magmatic differentiation. Fig. 4.9 a, b show La/Yb and Dy/Yb plotted against wt. % SiO_2 for the sampled QL and PA lavas. The general trend of increasing Dy/Yb with differentiation indicates the stability of garnet.

Arguably more compelling is the trend of La/Yb vs. Dy/Yb (Fig. 4.9 c, r^2 of 0.95) where a clear positive relationship exists. The ratio of La to Yb will increase during both amphibole and garnet fractionation however, the concurrent increase in Dy/Yb indicates garnet control. The scatter observed when these ratios are plotted against a differentiation index may indicate overprinting of geochemical signatures obtained at depth has occurred. Such a process may have occurred at shallower levels where

different, low pressure phases, are stable e.g. plagioclase. The effect of garnet on La/Yb vs. Dy/Yb systematics indicates deep level fractionation has occurred. However, this signature raises the question of the origin of the amphibole crystals in the QL lavas. It is therefore likely these are antecrystic in nature and originated from a different magma batch to that which erupted at QL. Amphibole was clearly fractionating in some part of the magmatic system as indicated by the sampled mafic enclaves.

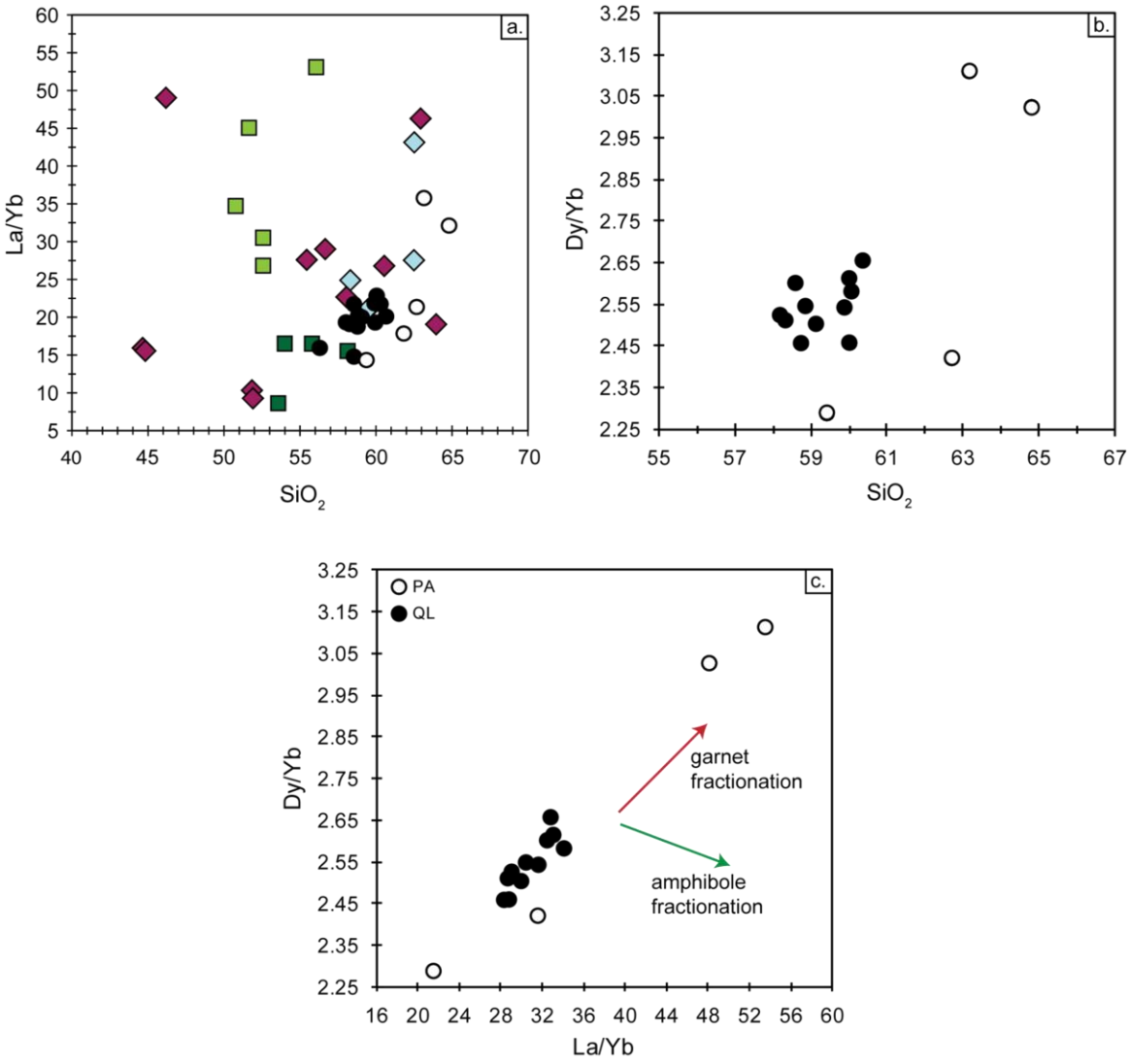

Fig. 4.9 a, b. La/Yb and Dy/Yb plotted for sampled lavas at PA and QL and the minor centres of Davidson and de Silva (1995, Yb data not given, symbols as in Fig. 4.7). **c**. Correlation between La/Yb and Dy/Yb indicative of garnet fractionation at depth.

Fig. 4.10 shows a broadly negative correlation between wt. % SiO_2 and Sr content for the PA and QL lavas, indicating Sr compatibility during differentiation and fractionation of plagioclase feldspar.

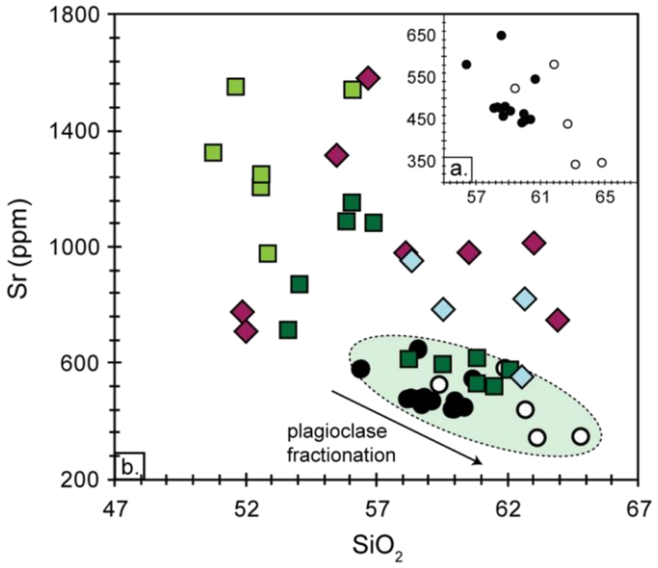

Fig. 4.10 a. SiO_2 vs. Sr for PA and QL lavas. **b**. PA and QL data plotted alongside lavas of Davidson and de Silva (1995). Symbols as in Fig. 4.7.

Calculated Eu anomalies are indicative of plagioclase feldspar fractionation. At QL values range from 0.81 to 0.85 and are slightly higher at PA (0.87-0.88, Fig. 4.11). The Los Frailes ignimbrite has a more prominent negative anomaly at 0.73, as too does the mafic enclave (0.77). Fig. 4.11 shows Eu/Eu* plotted against Sm/Yb.

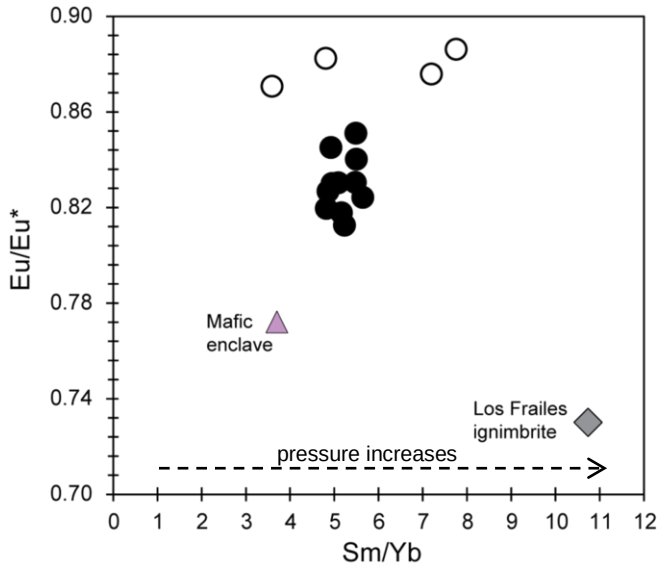

Fig. 4.11. Sm/Yb vs. calculated Eu anomaly. Symbols as in Fig. 4.6.

Higher Sm/Yb ratios (typically > 4) can be attributed to magmatic differentiation at deep crustal levels within the garnet stability field (Kay et al., 2010). As indicated by La/Yb vs. Dy/Yb, PA and QL lavas indicate fractionation occurred at deep levels in the presence of garnet however, there is a notable absence of a systematic correlation between Sm/Yb and Eu/Eu* as would be expected given the instability of plagioclase (i.e. high Eu/Eu* values) at depths where garnet fractionates. This may indicate the overprinting of signatures derived from depth by shallow level, upper crustal processes.

4.5.3 Isotopes

4.5.3.1 Sr-Nd

Fig. 4.12 a shows PA and QL lavas plotted alongside lavas from the suite of monogenetic centres studied by Davidson and de Silva, (1995). The $^{87}Sr/^{86}Sr$ isotopic variability in the Bolivian Eastern Altiplano lavas is significantly greater than the range exhibited by the other Bolivian lavas. Furthermore, the lavas erupted at PA and QL exhibit the highest Sr-isotope signatures in recent volcanic rocks across the CVZ, NVZ and SVZ. (Fig. 4.12 b; see also Fig. 2.9, Chapter 2, all data <60 Ma). These regional differences can be attributed to 1) the thickness of the underlying continental crust, and 2) its composition. The crust underlying the NVZ can reach up to 70 km (Guillier et al., 2001) and is understood to be young and composed predominantly of accreted oceanic terranes, the compositions of which are unlikely to exert significant leverage on the Sr-Nd isotopic signatures of ascending mantle-derived magmas. The lower ratios can therefore be attributed to magmas being predominantly derived from the mantle wedge with little crustal assimilation and/or interaction with relatively unradiogenic ($^{87}Sr/^{86}Sr$: 0.704-0.705) crust as indicated by sampled xenoliths (Weber et al., 2001). The crust beneath the SVZ is older, Palaeozoic in age, but is significantly thinner at ~40 km (Thorpe and Francis, 1979; Harmon et al., 1984).

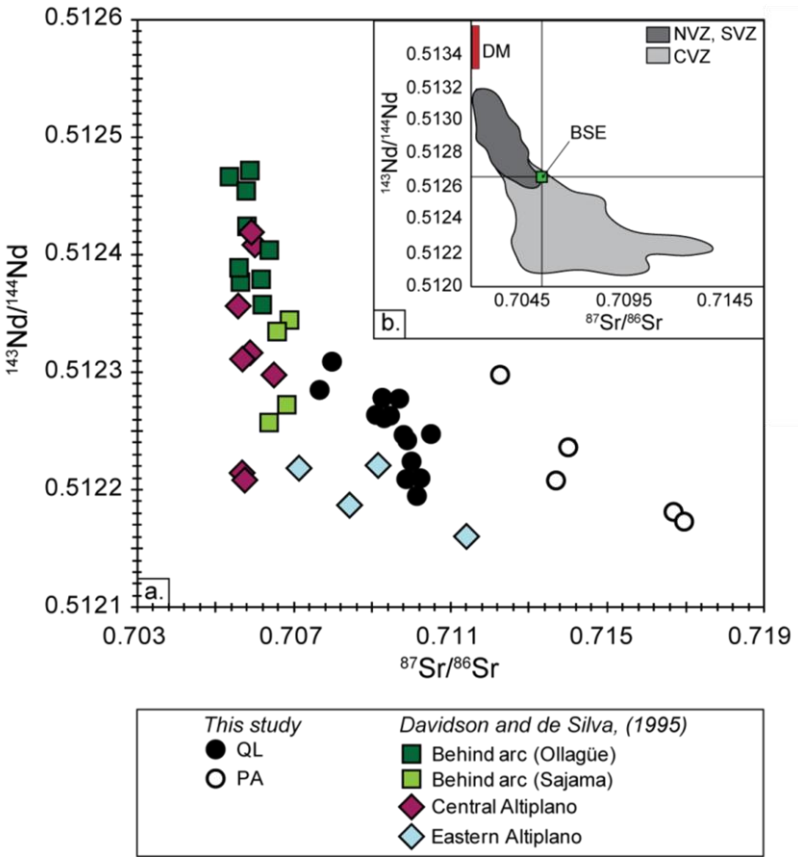

Fig. 4.12 a. Sr-Nd isotopic compositions of sampled PA and QL lavas. Signatures are significantly enriched relative to $^{87}Sr/^{86}Sr$ of lavas erupted from recent monogenetic volcanic centres in the Central Andes. **b**. Inset graph showing the elevated $^{87}Sr/^{86}Sr$ exhibited by Central Andean volcanic rocks and the relatively depleted nature of volcanic rocks from the NVZ and SVZ. DM: Depleted Mantle, BSE: Bulk Silicate Earth. Fields for Andean volcanic rocks are derived from GEOROC data (http://georoc.mpch-mainz.gwdg.de) for volcanic rocks aged 60 Ma or younger (database accessed 07.11.11).

It can be hypothesised therefore that magmas erupted in SVZ do not extend to crust-like isotopic signatures due to the thinner nature of the continental crust which would promote a smaller degree of interaction between mantle and crustal reservoirs during magmatic differentiation. The continental crust beneath the CVZ is both thick and old with Proterozoic crust understood to underlie Palaeozoic crust at depth (Wörner et al., 1992). The elevated $^{87}Sr/^{86}Sr$ signatures which characterise the volcanic rocks of the CVZ can therefore be attributed to relatively extensive interaction between mantle and crustal reservoirs.

The compositions of PA and QL lavas are far from representative of primary mantle melts and are more isotopically enriched than 1) the sampled mafic enclaves ($^{87}Sr/^{86}Sr$: 0.7073, see Table 1, Appendix B), and 2) the Chiar Kkollu sill ($^{87}Sr/^{86}Sr$: 0.7041), a 25 Ma basaltic sill (45.8 wt. % SiO_2, 9.2 wt. % MgO) which represents the most primitive volcanic rock currently known in the Central Andean region and outcrops ~20 km WNW of the PA (Davidson and de Silva, 1992; 1995). More recent basalts (< 3 Ma) however have been sampled on the Puna plateau in the southern Andes (47.5 wt. % SiO_2, 10.3 wt. % MgO; $^{87}Sr/^{86}Sr$: 0.7055; Drew et al., 2009).

The degree of isotopic heterogeneity exhibited by lavas erupted from the same volcanic centre at PA and QL is not easily reconciled through heterogeneity in the mantle source region. Instead, the enriched signatures are the likely result of interaction with, and contamination by (a number of), geochemically heterogeneous continental crustal lithologies at depth during differentiation (Fig. 4.12 c, see section 4.6.2 later).

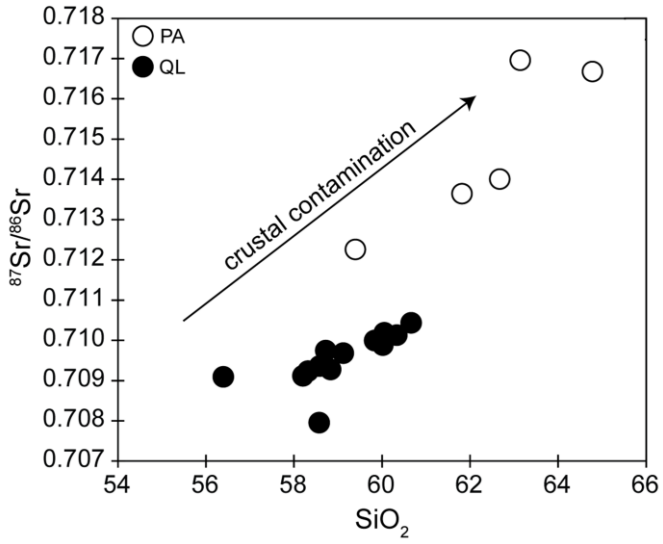

Fig. 4.12 c. Crustal contamination during magmatic differentiation beneath the PA and QL lavas.

4.5.3.2 Pb

Fig. 4.13 a shows $^{206}Pb/^{204}Pb$ plotted against $^{207}Pb/^{204}Pb$ for sampled lavas at PA and QL and the lavas of Davidson and de Silva, (1995, for which data is available). Lavas at PA and QL exhibit signatures akin to both upper (the local ignimbritic basement) and lower crustal domains, are generally distinct from a mantle source and show a range of compositions similar to that of the Los Frailes ignimbrite.

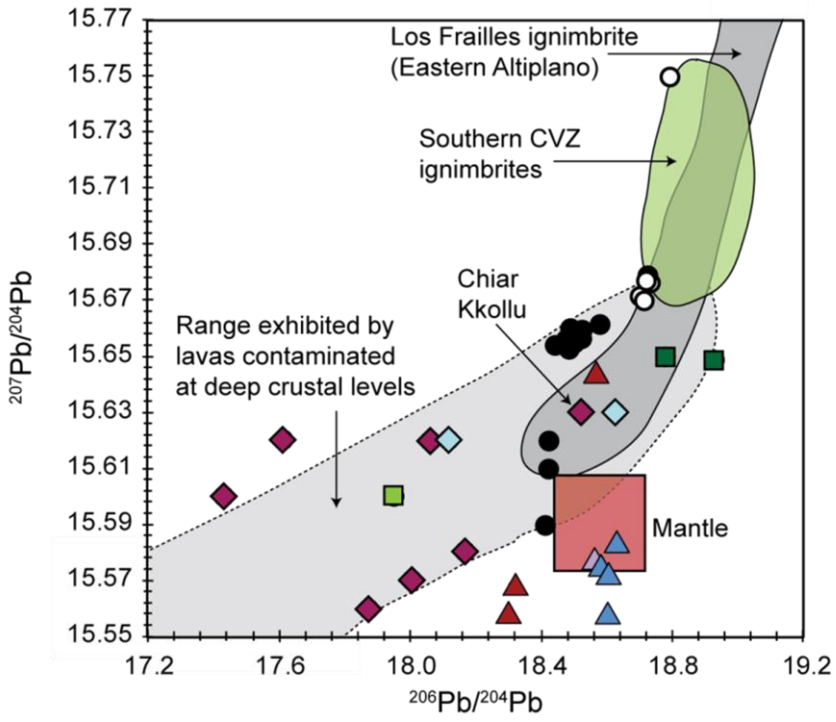

Fig. 4.13 a. $^{206}Pb/^{204}Pb$ vs. $^{207}Pb/^{204}Pb$ for Bolivian lavas. Fields re-drawn from Davidson and de Silva, (1995). Symbols as in Fig. 4.12 a.

A study by Aitcheson et al., (1995) in the Central Andes indicated four crustal basement domains may exist beneath the Altiplano region. This was based on sampling of over 400 ore and volcanic rocks samples (Fig. 4.13 b, c). The lavas of PA and QL plot in the Eastern Cordillera domain which is inferred to lie several kilometres west of PA and beneath QL. Consistent with their location (see map in Fig. 4.2 a), monogenetic centres at Sajama and on the Central Altiplano centres plot in the compositional field for the Northern Altiplano domain and Ollagüe centres plot in the Southern Altiplano domain.

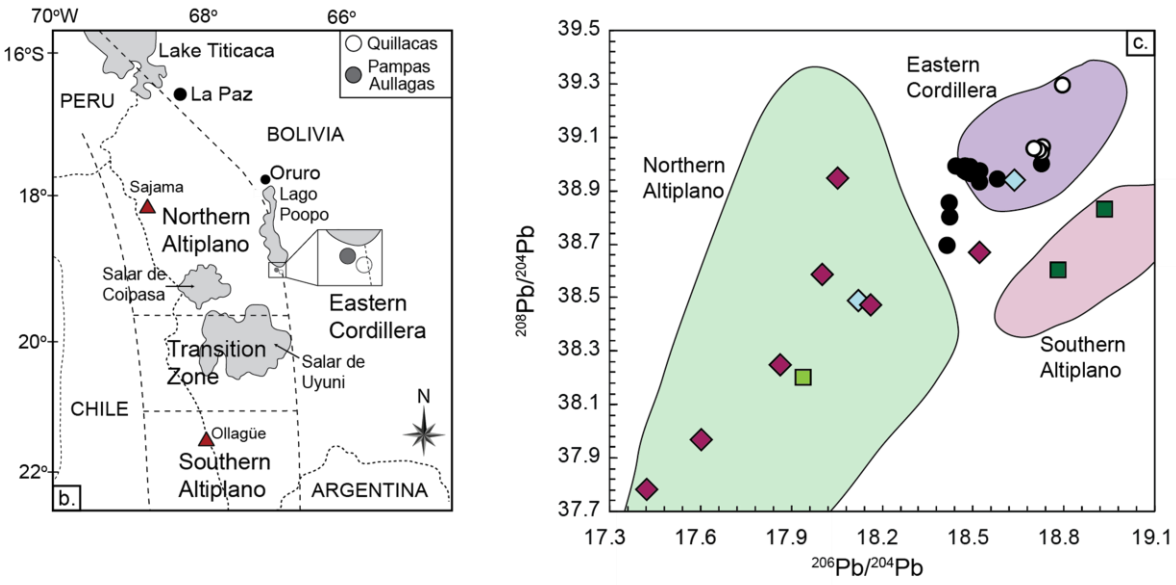

Fig. 4.13 b. Pb isotope domain showing the location of the PA and QL centres relative to the boundaries of inferred crustal provinces. Map modified from Aitcheson et al. (1995). **c**. Pb isotopic signatures in sampled volcanic rocks from minor centres on the Bolivian Altiplano. Symbols as in Fig. 4.12 a.

4.6 Discussion

4.6.1 Mantle source

The contaminated nature of lavas erupted at PA and QL means that direct investigation for their primary composition(s) is difficult. Instead, an attempt to characterise the parental nature of the Chiar Kkollu magma, through rare earth element inversion modelling was carried out (McKenzie and O'Nions, 1991). It should be noted that contamination (by the shallow or deep crust, or by a slab-derived component, see discussion later) cannot unequivocally be ruled out. The Chiar Kkollu basalt is simply the most primitive volcanic rock in this region of the Central Andes. Furthermore, many of the major element trends observed at PA and QL back-project towards a Chiar Kkollu-type composition (Fig. 4.14 a-c). REEs are a suitable suite of elements to implement in geochemical modelling as their properties vary systematically, making them strongly incompatible to moderately compatible in mantle phases. As discussed in McKenzie and O'Nions, (1991), and recognised by Hoffman and Feigenson, (1983), REE concentrations combined with inverse theory can

be used as a "powerful tool" in the examination of mantle melt generation as it can model the melt required to produce the observed REE concentration in sampled rocks i.e. data can be inverted in order to investigate the effects of removing melt from the mantle (assuming fractional, adiabatic melting).

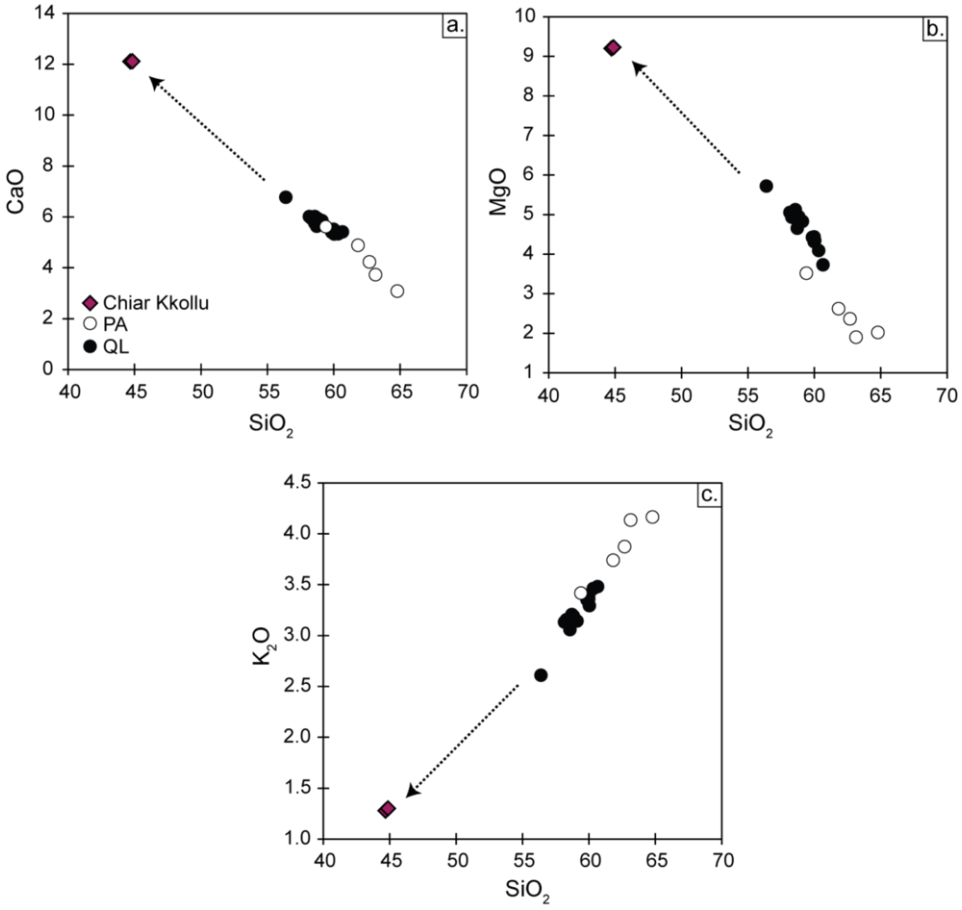

Fig. 4.14 a-c. Major element trends at PA and QL projecting back to Chiar Kkollu.

REE concentrations are used, as opposed to other trace elements, because they exist at low concentrations hence their activity in the residue and melt should be proportional to concentration. The distribution of the REEs can therefore be described using a partition coefficient and Henry's Law which essentially relates compatibility to pressure (McKenzie and O'Nions, 1991). An assumption in this approach is that the REE concentrations in a melt are primarily controlled by the stability of garnet, spinel and plagioclase which in turn is controlled by pressure (depth). Fractional crystallisation is ignored.

REE bulk distribution coefficients (D) in mantle phases (e.g. La) for garnet peridotite (olivine, orthopyroxene, clinopyroxene and garnet) and spinel peridotite (olivine, orthopyroxene, clinopyroxene and spinel) were calculated by:

$$\overline{D}^{La} = D_{ol}^{La}.x_{ol} + D_{opx}^{La}.x_{opx} + D_{cpx}^{La}.x_{cpx} + D_{gt}^{La}.x_{gt}$$

where the distribution coefficients (D) for La in each mineral phase are summed and weighted according to the mass fraction (x) of the phase in the mantle (values from Hanson, 1980 and McKenzie and O'Nions, 1991; 1995) and references therein; Appendix D). The distribution coefficients weighted according to their concentration in the melt (p) were calculated by:

$$\overline{P}^{La} = D_{ol}^{La}.p_{ol} + D_{opx}^{La}.p_{opx} + D_{cpx}^{La}.p_{cpx} + D_{gt}^{La}.p_{gt}$$

The concentration of a given element in the magma was thus calculated by:

$$C_L / C_0 = 1/(\overline{D} + F - \overline{P}F)$$

where C_L represents the concentration in the magma

C_0 the concentration in the source i.e. primitive mantle.

F represents the melt fraction with 0.05 implying 5% melting, 0.1 implying 10% melting etc.

REE abundances in basalt produced from melting garnet peridotite and spinel peridotite at F values of 0.005, 0.01, 0.05 and 0.1 were calculated using the above relationship and results are shown in Fig. 4.15 a, b.

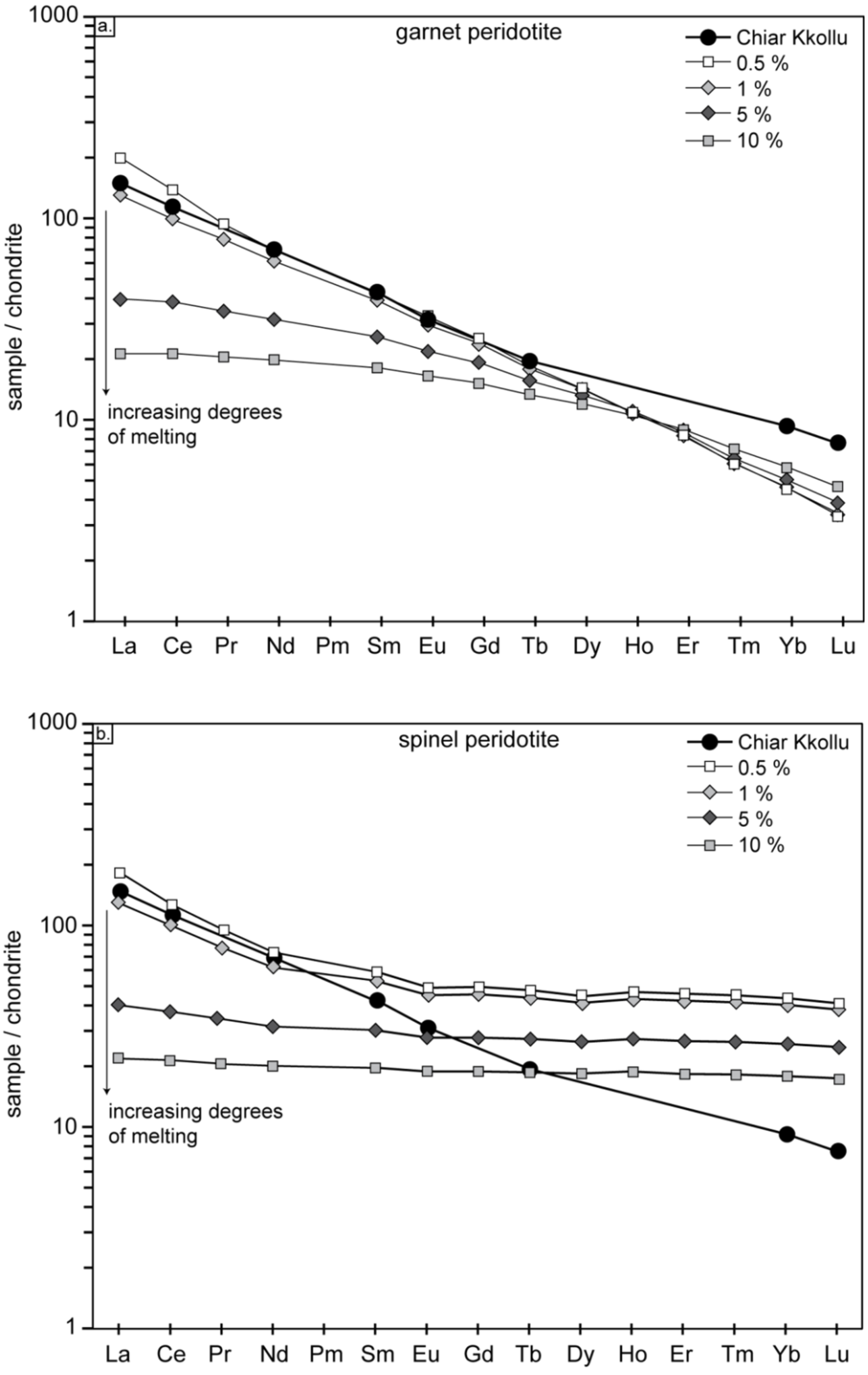

Fig. 4.15. REE abundances produced from melting **a**. garnet peridotite and **b**. spinel peridotite at F values of 0.005, 0.01, 0.05 and 0.1.

The REE nature of the Chiar Kkollu lava can be reconciled with melting in the garnet peridotite stability field as opposed to shallower depths of melting in the spinel stability field (<60km). LREE-MREE patterns are consistent with small degrees of partial melting between 0.5 and 1% melting however HREE depletion is over estimated at these conditions. This is likely to be due to the over estimation of Lu and Yb partition coefficients.

A study by Hoke and Lamb, (2007) inferred variable degrees of partial melting (from REE inversion modelling) of two different MORB sources at different depths in the spinel and spinel-garnet stability fields for the suite of minor centres across this region of the Central Andes (several of the centres were sampled by Davidson and de Silva, 1995). Their models ruled out the melting of garnet peridotite and invoked re-enrichment of a MORB source through the addition of variable degrees of partial melt from depth e.g. the addition of a 6% melt fraction from the melting of a MORB source within the garnet stability field at 0.4% to a shallower MORB source in the spinel stability field (i.e. a two-stage melting model).

Simply taking the isotopic ratio of the Chiar Kkollu basalt (0.7041) and the inference it is (at least relatively) uncontaminated, a MORB-type source is unlikely. Fig. 4.16 shows $^{87}Sr/^{86}Sr$ vs. $^{206}Pb/^{204}Pb$ for sampled lavas of this study and those of Davidson and de Silva, (1995). Pb isotopes were not reported by Hoke and Lamb (2007). From Hoke and Lamb, (2007) the centres behind the arc were inferred to sample a depleted MORB source whereas centres >100 km from the arc were inferred to tap an enriched MORB source. The minor centres behind the arc front, and those on the Central Altiplano, exhibit relatively consistent $^{87}Sr/^{86}Sr$ at significantly variable $^{206}Pb/^{208}Pb$ which is difficult to reconcile with melting of the same mantle source within each suite.

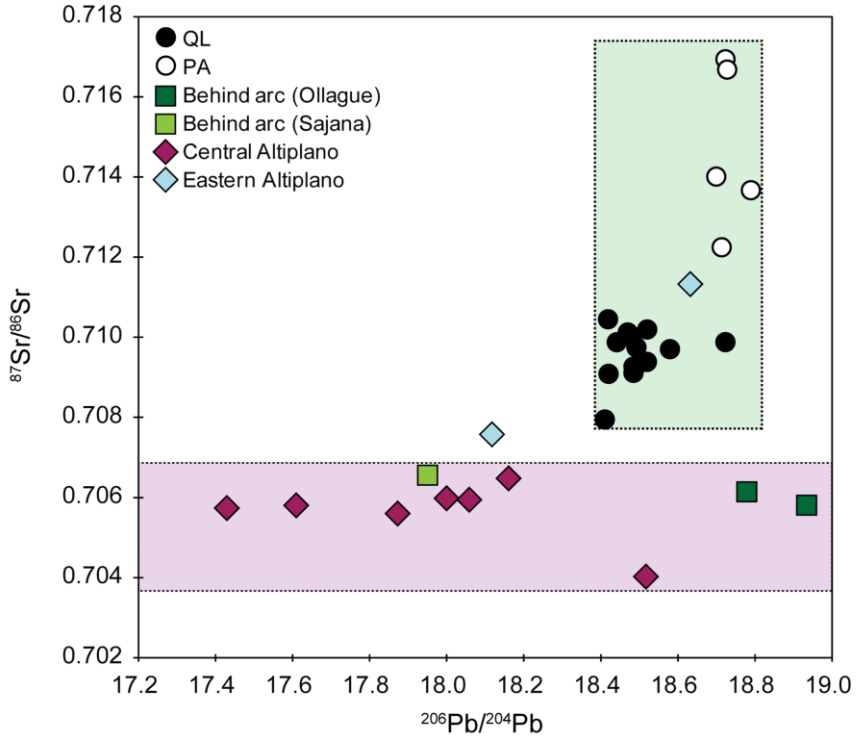

Fig. 4.16. Distinct Sr-Pb isotopic signatures in lavas sampled at PA and QL.

The lower range of $^{206}Pb/^{204}Pb$ values could be envisaged as a result of mantle melting e.g. the EM I and EM II domains however, the higher values (up to 18.93) are less easy to reconcile, especially if they are inferred to originate from the same MORB-type source (as in Hoke and Lamb, 2007). Unfortunately, the current data set does not allow for justifiable characterisation of the mantle sources to these Central Andean lavas beyond the conclusion that melting is likely to have originated at a depth where garnet is stable as previously suggested by La/Yb vs. Dy/Yb (Fig, 4.9 c).

4.6.2 Crustal contamination

From their petrographic and geochemical nature it is clear the magmas beneath PA and QL have experienced contamination by the continental crust during petrogenesis. Fig. 4.17 shows the results of simple bulk mixing between a Chiar Kkollu-type magma and the suite of sampled crustal xenoliths (Chapter 3) each of which represents a crustal lithology ascending magmas may have interacted with. The sampled xenoliths which

showed evidence of partial melting were not included in any contamination modelling throughout this work.

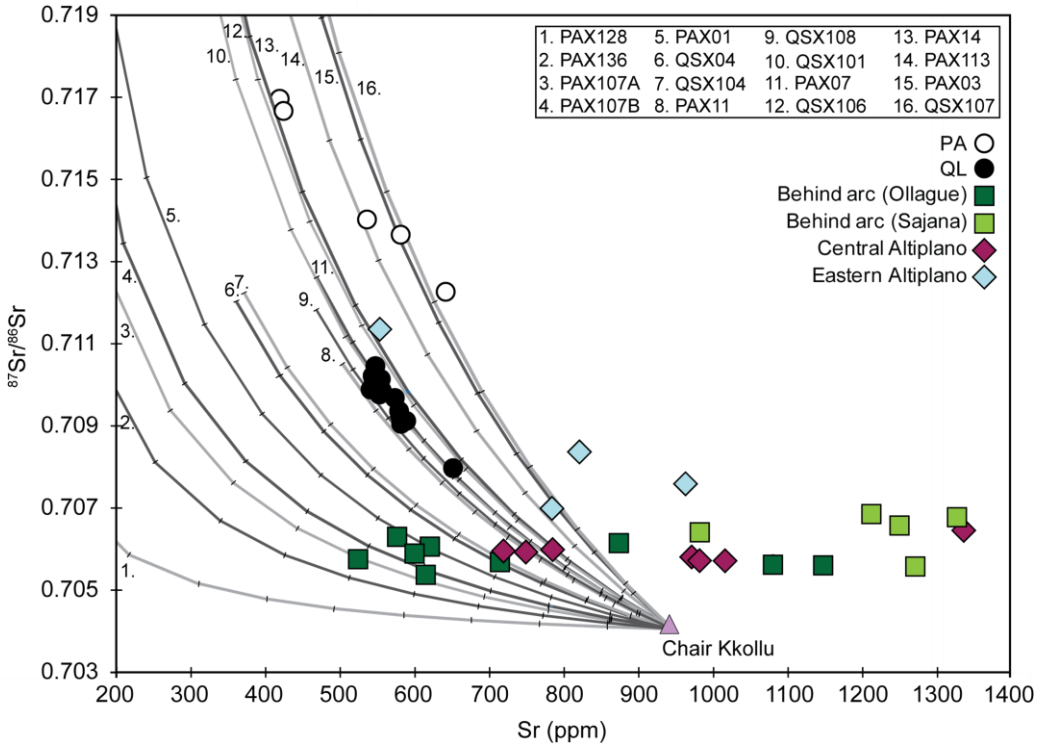

Fig. 4.17. Bulk mixing between Chiar Kkollu and sampled crustal xenoliths. Tick marks represent 10% intervals.

From this simple first order approach, the compositions of PA and QL lavas can be reproduced by incorporating between 40 and 90% of crustal material. Consistently, mixing with a single crustal lithology fails to reproduce the range observed in the PA lavas (e.g. mixing curve 15) whereas QL lavas can be modelled by mixing the a Chiar kkollu-type lava with several crustal compositions although the proportion of each end member varies considerably (e.g. mixing curves 9, 10 , 11).

In order to further assess the role of the continental crust, AFC modelling was carried out using the following approach of De Paolo, (1981):

$$C_i = C_{iA}f_i + r / (r - 1 + D_i)C_{iB}(1 - f_i)$$

$$\varepsilon_i = \varepsilon_{iA} + (\varepsilon_{iB}-\varepsilon_{iA})(1-((C_{iA}/C_i) \times f_i))$$

where C is the concentration

ε is the isotopic ratio

i is the element of interest (e.g. Sr)

A is the mantle-derived magma

B is the crustal assimilant

F is the proportion of magma

r is the rate of assimilation to fractional crystallisation

D is the bulk distribution coefficient of the element of interest

f_i is calculated from: $F - (r - 1 + D_i) / (r - 1)$

Results are shown in Fig. 4.18 a-f for scenarios in which Sr is both incompatible and compatible (i.e. variable D values) and for different values of r. Modelling was a carried out using sampled crustal xenoliths as crustal end members. These offer the best constraints to the nature of the crustal contaminant as at some point during their ascent, the sampled lavas came into contact with these lithologies. Simply, the trends defined by the PA and QL lavas can be reproduced through AFC modelling but require a high rate of assimilation to fractional crystallisation (between 0.5 and 0.8). These results indicate a significant contribution from the continental crust during magma petrogenesis, far greater than has previously been suggested for Central Andean magmas at between 10 and 20 % (Aitcheson et al., 1995; Davidson and de Silva, 1995).

The more recent EC-AFC (energy constrained-assimilation fractional crystallisation) model of Spera and Bohrson (2001) aims to characterise the physical and chemical dynamics of magma-crust interaction.

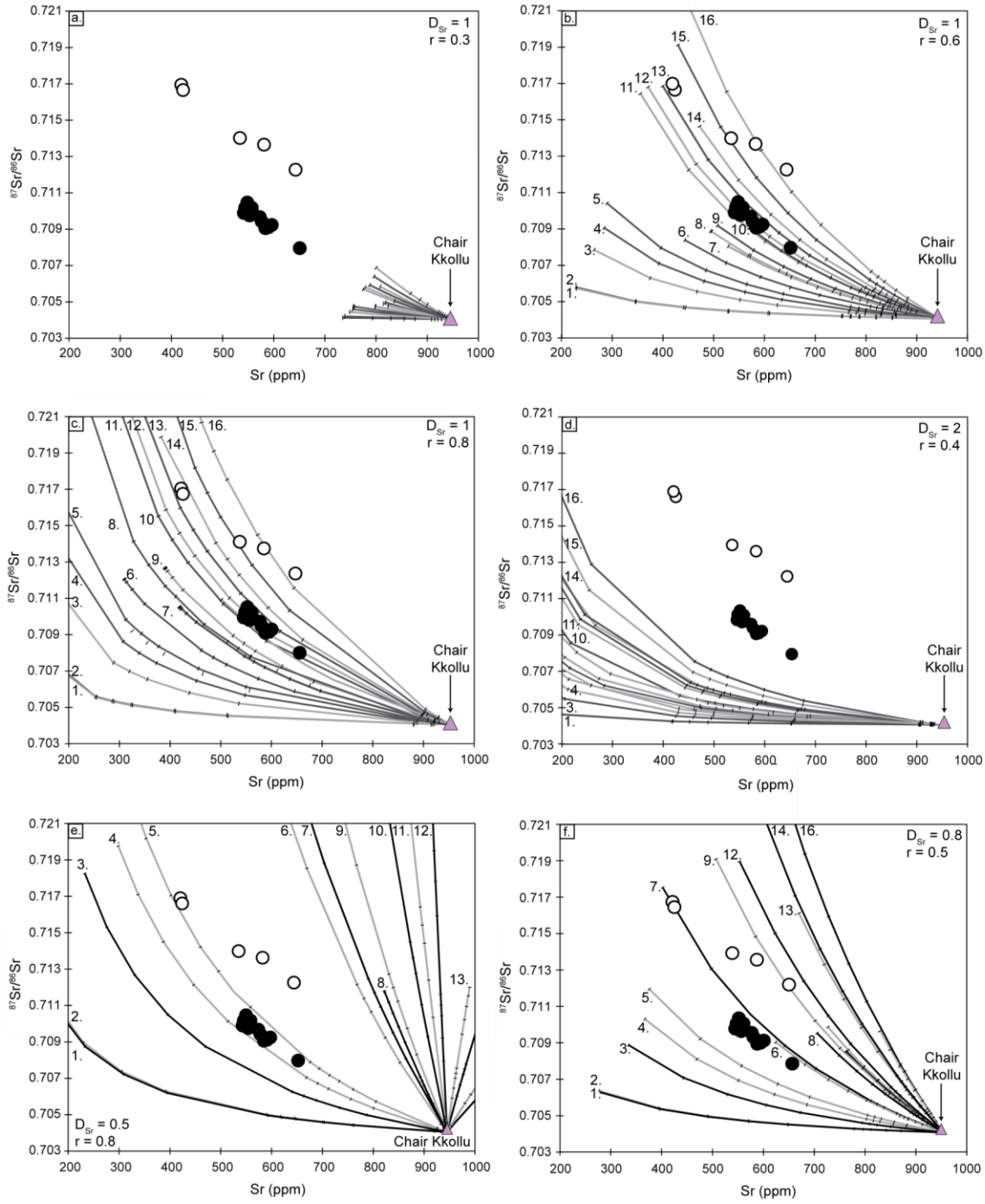

Fig. 4.18 a-f. Graphs showing the effects of AFC (equations of De Paolo, 1981) on $^{87}Sr/^{86}Sr$ vs. Sr (ppm) between a Chiar Kkollu-type magma and the sampled crustal xenoliths (Chapter 3). AFC parameters given in each figure. Each tick on the AFC curves represents melt left after assimilation (in 10% increments). Numbers correspond to xenoliths in Fig. 4.17. Where appropriate, numbers were omitted for clarity.

The model is based on the equations of De Paolo, (1981) but takes a far more sophisticated approach to quantifying the results of contamination of an ascending

magma by surrounding wall rock. It is designed to conserve mass and energy whilst adhering to compositional constraints and the parameters which require definition in the model are presented in Table 1. Results from EC-AFC modelling of the PA and QL lavas are shown in Fig. 4.19. The thermal parameters of Table 1 were used throughout however; the compositional parameters were changed in accordance with measured values from the sampled crustal xenolith suite (see Appendix D).

Thermal parameters	
Liquidus temperature of magma (T_{lm})	1280 ^{o}C
Initial temperature of magma (T_m^{o})	1280 ^{o}C
Liquidus temperature of assimilant (T_{la})	1000 ^{o}C
Initial temperature of assimilant (T_a^{o})	300 ^{o}C
Solidus (T_s)	900 ^{o}C
Equilibration temperature (T_{eq})	980 ^{o}C
Enthalpy of crystallisation (Δh_{cry})	396000 J/kg
Isobaric specific heat of magma (C_{pm})	1484 J/kg per K
Fusion enthalpy (Δh_{fus})	270000 J/kg
Isobaric specific heat of assimilant (C_{ps})	1370 J/kg per K

Compositional parameters	**Sr**
Initial concentration in magma (C_m^{o})	700 ppm
Isotopic ratio of magma (ε_m)	0.7035 ($^{87}Sr/^{86}Sr$)
Trace element distribution coefficient of magma (D_m)	1.5
Initial concentration in assimilant (C_a^{o})	350 ppm
Isotopic ratio of assimilant (ε_m)	0.7220 ($^{87}Sr/^{86}Sr$)
Trace element distribution coefficient of assimilant (D_a)	1.5

Table 1: Suggested parameter inputs for EC-AFC models (after Spera and Bohrson, 2001). Compositional inputs used in this study are presented in Appendix D.

The initial section of several of the model curves are horizontal and represent the time taken for the wallrock to reach its solidus temperature. As shown, and as similarly concluded from the bulk mixing and AFC approaches, the lava compositions at PA and QL can be reproduced by variable degrees of crust-magma interaction involving different crustal compositions.

Consistently throughout these calculations high proportions of crustal material are involved and whilst the geochemical signatures at QL can be reproduced, the lavas at PA cannot, at least by a unique contamination trend involving the crustal lithologies sampled.

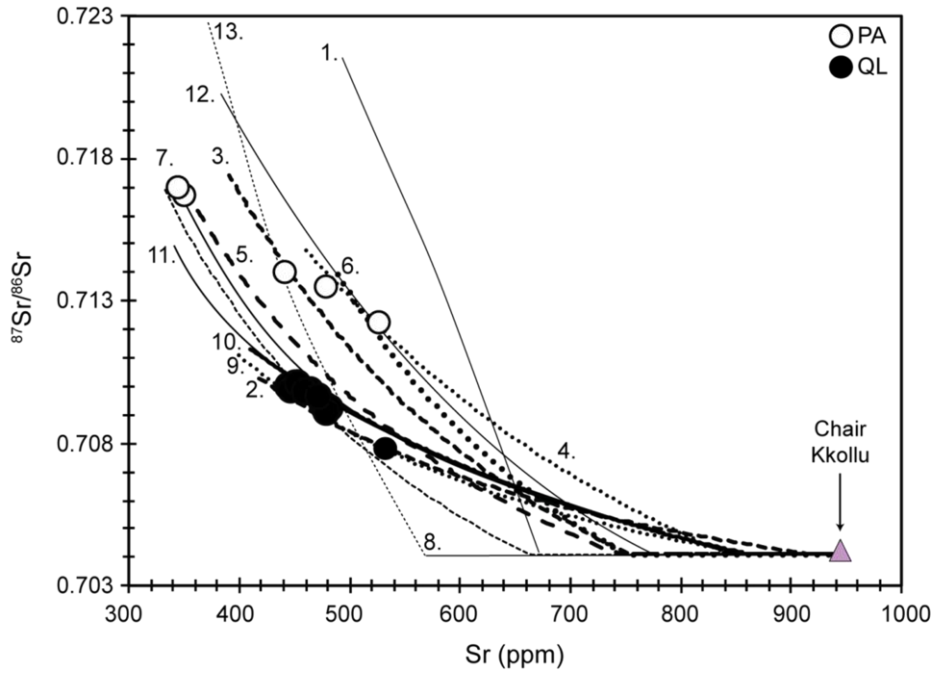

Fig. 4.19. Modelled EC-AFC curves for PA and QL lavas. Models shown are those which best fitted the data. Numbers correspond to model parameters presented in Appendix D.

Given the significant Sr-isotopic heterogeneity exhibited by sampled lava from the monogenetic eruptions at PA and QL it is unlikely that a single mixing, or (EC)AFC, model will realistically quantify the geochemical variation observed. The positive trend between $^{87}Sr/^{86}Sr$ and SiO_2 (Fig. 4.12 c) could simply be interpreted as representing incorporation of variable amounts of a single contaminant. However, ascending magmas have clearly interacted with more than one crustal lithology (as shown by the lithological diversity within the xenolith suite, Chapter 3). The variability in the lavas could also be explained by the incorporation of different contaminants from different lithologies into the ascending magmas. Within the models, values of D and r are assumed to be constant and in reality these may change (e.g. Roberts and Clemens,

1995). Additionally, the role of disequilibrium melting cannot be ruled out (e.g. Philpotts and Asher, 1993) whereby phases with high Rb/Sr (and hence high $^{87}Sr/^{86}Sr$) e.g. biotite preferentially melt out before lower Rb/Sr phases e.g. feldspars (see Chapter 5, 6).

4.6.3 Across arc geochemical differences

The correlation of Sr-isotopes with indices of differentiation e.g. SiO_2 is indicative of the role of crustal contamination during the petrogenesis of PA and QL lavas. These signatures are distinct from those exhibited by lavas from minor centres across the Central Andes sampled by Davidson and de Silva, (1995; Fig. 4.20 a). The Sr/Y ratio in lavas can be used as a proxy for the plagioclase to garnet ratio in a crystalline residue hence it can be an indicator of the depth of differentiation e.g. Bachmann et al., (2005). High Sr/Y values (>40) typically indicate the stability of garnet during magma production (either through differentiation or partial melting) at depth although other phases e.g. amphibole, sphene, and to some extent zircon, may also result in Y (and HREE) depletion. Low Sr/Y ratios (<40) will reflect differentiation at low pressure in the upper crust (≤ ~30 km, e.g. Sen et al., 2003). The plot of Sr/Y vs. $^{87}Sr/^{86}Sr$ (Fig. 4.20 b) indicates that crustal assimilation may have occurred at shallow crustal levels beneath the PA and QL centres. This is in contrast to the lavas sampled by Davidson and de Silva (1995) to the west of PA and QL and those of Delacour et al., (2007) and Sørensen and Holm, (2008) which consistently display lower $^{87}Sr/^{86}Sr$ ratios at higher Sr/Y. This may indicate the role of high pressure magma differentiation in the garnet stability field and relatively little (later) upper crustal contamination.

The relative lack of variation in Sr isotopic ratios at Sr/Y > 40 may suggest little $^{87}Sr/^{86}Sr$ variability exists in the lower continental crust and/or interaction with crustal lithologies was minimal. The upwelling of hot asthenospheric material to the base of

the crust may have enhanced heating and partial melting of the lower crust. This may have occurred in response to convective removal of an overthickened lithospheric root which was produced during significant crustal shortening in the Tertiary. A similar scenario has been suggested beneath the Puna Plateau in Argentina (e.g. Kay et al., 2010). This could have led to partial melting at high pressure at depth in MASH zones (Hildreth and Moorbath, 1988) leaving a garnet-bearing granulitic residue.

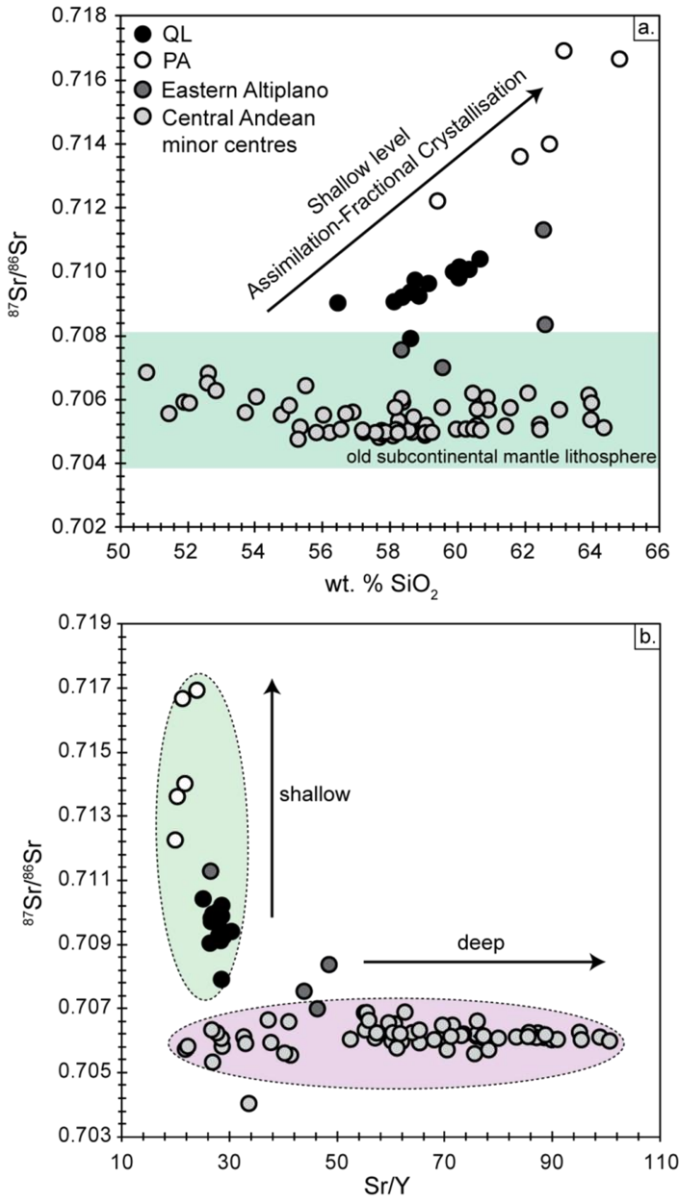

Fig. 4.20 a. Contaminated nature of PA and QL lavas. **b**. Deep vs. shallow level differentiation. Lavas of Hoke and Lamb, (2007) also included.

Early magma differentiation at depths where garnet is stable (as previously indicated by La/Yb vs. Dy/Yb systematics and REE inversion modelling) and assimilation at lower crustal levels may have occurred beneath the PA and QL centres. However, these signatures are likely to have been overprinted by shallow level processes in the upper crust as previously suggested by Eu-anomalies vs. Sm/Yb and SiO_2 vs. Sr.

The asymmetry of the subduction zone can be shown to exert a control on the geochemical composition of arc volcanism. The relative compatibilities of incompatible Ba, Nb and Zr during partial melting can, in theory, be used to track the release of slab-derived fluids with distance from the arc (as in Davidson and de Silva, 1995). The incompatibility of Ba is greater than Nb which is greater than Zr during partial melting and/or fractional crystallisation hence Zr/Nb vs. Ba/Nb produces a negative correlation (Fig. 4.21 a).

Fig. 4.21 b shows Zr/Nb plotted against estimated depths to the Benioff Zone and shows an overall decrease eastward as expected. This relationship holds true until the minor centres of the Eastern Cordillera are considered where ratios increase again. This can be inferred to indicate the involvement of the continental crust and the lack/absence of any influence from slab derived fluids in the mantle source region.

Fig. 4.21 c shows the inferred depth to the Benioff zone plotted against $^{87}Sr/^{86}Sr$. As previously shown in Fig. 4.20 a, the $^{87}Sr/^{86}Sr$ compositions of the western minor centres are relatively constant, even between centres, whereas at QL and PA, Sr-isotopic signatures are heterogeneous both between and within the centres.

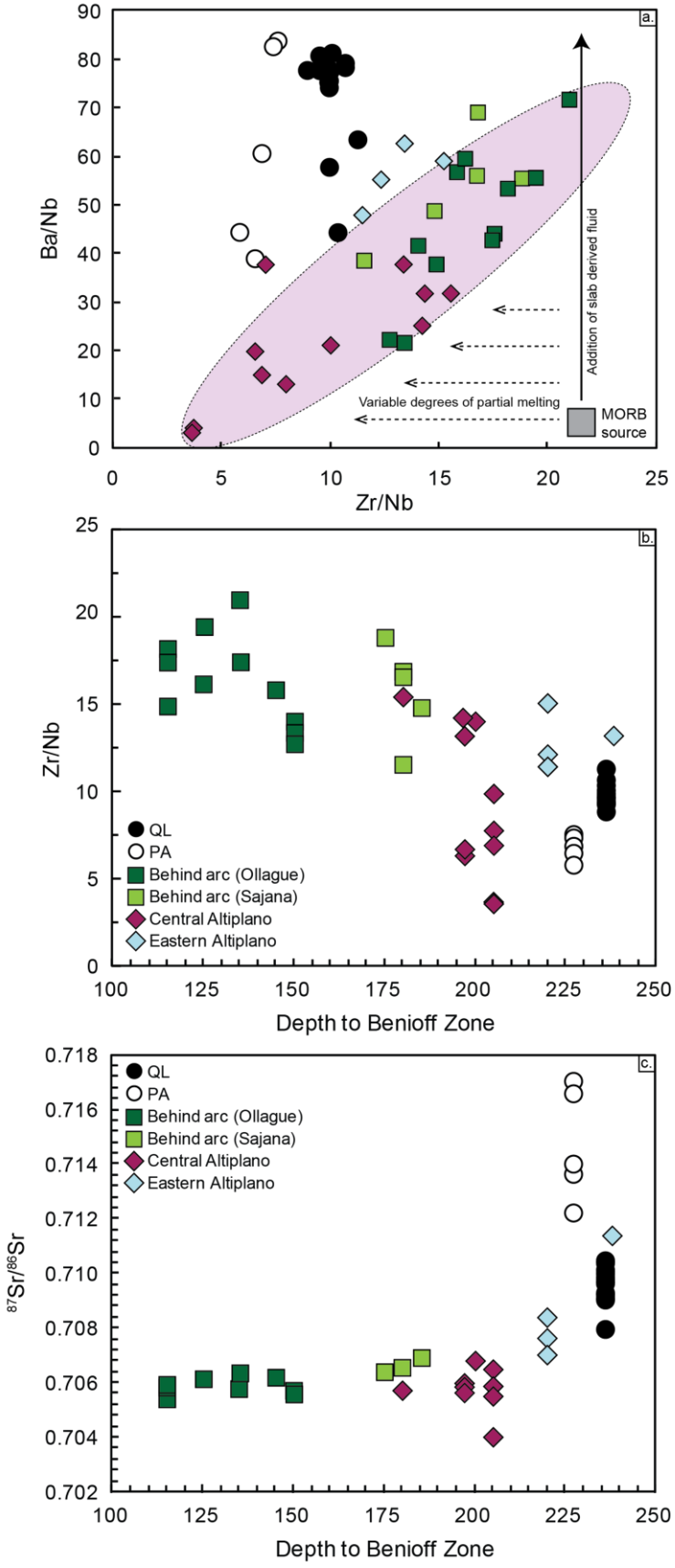

Fig. 4.21 a-c. Geochemical changes in lava geochemistry from west (behind arc) to the east (PA, QL and the Eastern Altiplano). For discussion see text.

By examining the major element signatures in the lavas, inferences on the underlying crustal structure can be made. This is in spite of the obvious influence of the continental crust during magmatic differentiation as major element systematics are predominantly controlled by fractional crystallisation alone (Davidson and de Silva, 1995).

It has been proposed that with increasing distance from the arc front, the K_2O content of erupted lavas will increase. This "K-h" relationship is understood to be controlled by the depth to the Benioff zone with relatively more alkalic magmas being generated at deeper mantle depths (Dickinson, 1975). It has also been suggested that K_2O contents will increase linearly with crustal thickness (Condie and Potts, 1969).

Lavas exhibiting high wt. % K_2O will equilibrate at greater depths relative to those with lower wt. % K_2O due to the depth-K_2O relationship being controlled by sanidine as the $KAlSi_3O_8$ component in the downgoing slab (Marsh and Carmichael, 1974) i.e. higher K_2O contents at higher pressures. Fig. 4.22 a shows a plot of the SiO_2-K_2O for the Bolivian Altiplano lavas with minor centres on the Eastern Altiplano (including PA and QL) plotting at higher K_2O contents. Primary magmas may therefore have originated at greater depths than those beneath monogenetic centres to the west although the role crustal contamination cannot unequivocally be ruled out. To examine the crustal structure further, the relationship between CaO, Na_2O and MgO contents can be assessed. Plank and Langmuir, (1988) identified a strong correlation of CaO, at a given wt. % MgO, with crustal thickness (higher CaO contents in lavas erupted through thinner crust, Fig. 4.22 b).

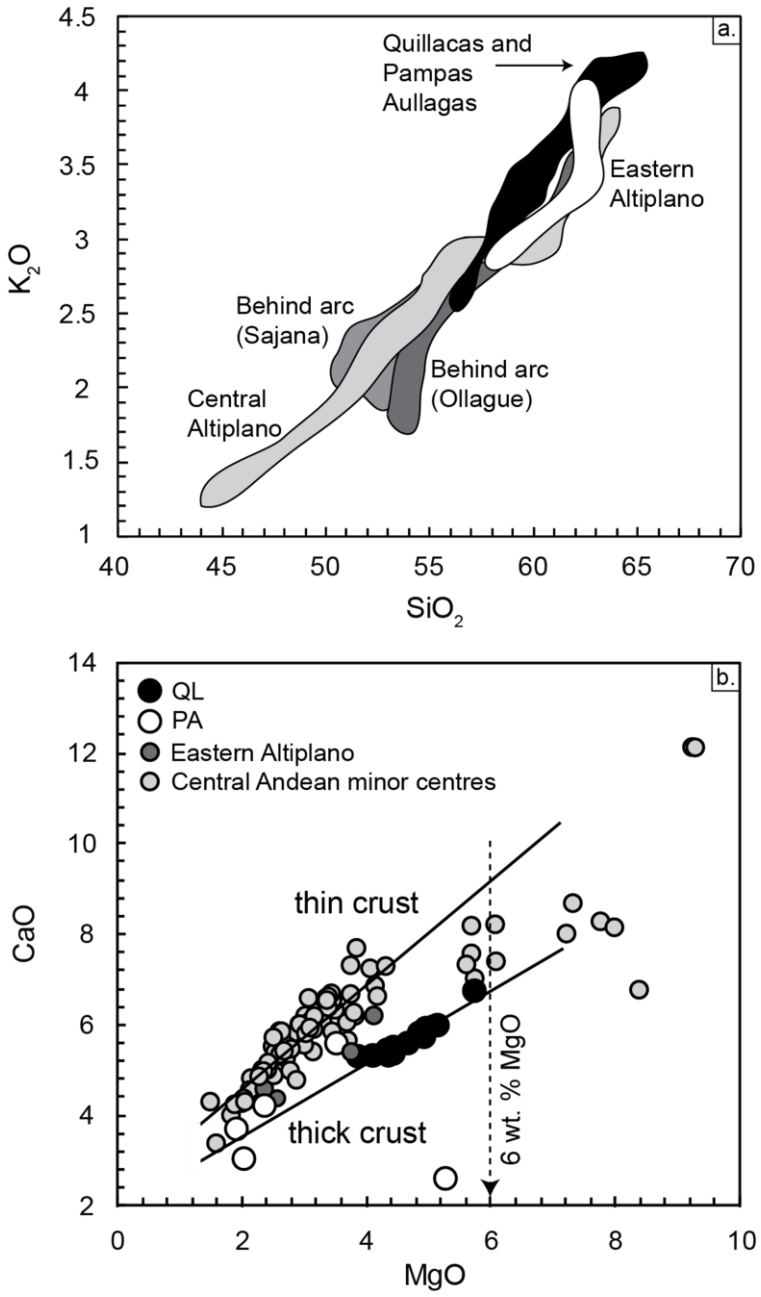

Fig. 4.22 a. K-h relationship highlighting higher K_2O contents in Eastern Altiplano (including PA and QL) lavas. **b**. Inference of thin and thick crust based on CaO at 6 wt. % MgO. See text for discussion.

At any arc, lithospheric thickness will control the length of the mantle column that can melt during arc-magma genesis. A thicker lithosphere will establish a shorter melt column, leading to smaller degrees of partial melting and thus produces lower CaO contents in the initial melt as less of the clinopyroxene component is released. Alternatively, if differentiation occurs at lower pressures in regions of thinner crust

(shallower depths), relatively less clinopyroxene would fractionate and thus be less effective in lowering the CaO of the melt. The lavas sampled by this study, particularly those at QL, clearly exhibit lower CaO at a given wt. % MgO in comparison to other minor centres e.g. 5.33 compared to ~ 6.24 at 4 wt. % MgO and 3.08 compared to ~4.45 at 2 wt. % MgO.

These signatures may therefore indicate a greater lithospheric thickness beneath the Eastern Altiplano than the Central Altiplano and the back arc regions of the Central Andes. Combined with inferences from the observed K-h relationship (Fig. 4.22 a) mantle melting beneath minor centres at Ollagüe, Sajama and on the Central Altiplano may have occurred beneath thinner crust than beneath minor centres on the Eastern Altiplano although as previously discussed, mantle melting beneath this entire region is likely to have occurred within the garnet stability field.

The inference that the role of the continental crust is more important during petrogenesis of magmas beneath the Eastern Altiplano than beneath centres to the west, i.e. furthest from the arc, and is thicker, is supported by helium isotopic analyses (Hoke et al, 1994, Lamb et al, 1997, Hoke and Lamb, 2007) and recent seismic survey results (Heit et al., 2008). A summary cartoon depicting the inferred across-arc changes is shown in Fig. 4.23 a.

Relatively high degrees of mantle degassing have been inferred beneath the behind-arc and Central Altiplano regions from helium isotopic analysis of geothermal springs, mineral water springs and olivine-hosted fluid inclusions (Hoke and Lamb, 2007). This is in contrast to the crustal-dominated Helium isotopic signatures measured at the arc and in the east (Fig. 4.23 a).

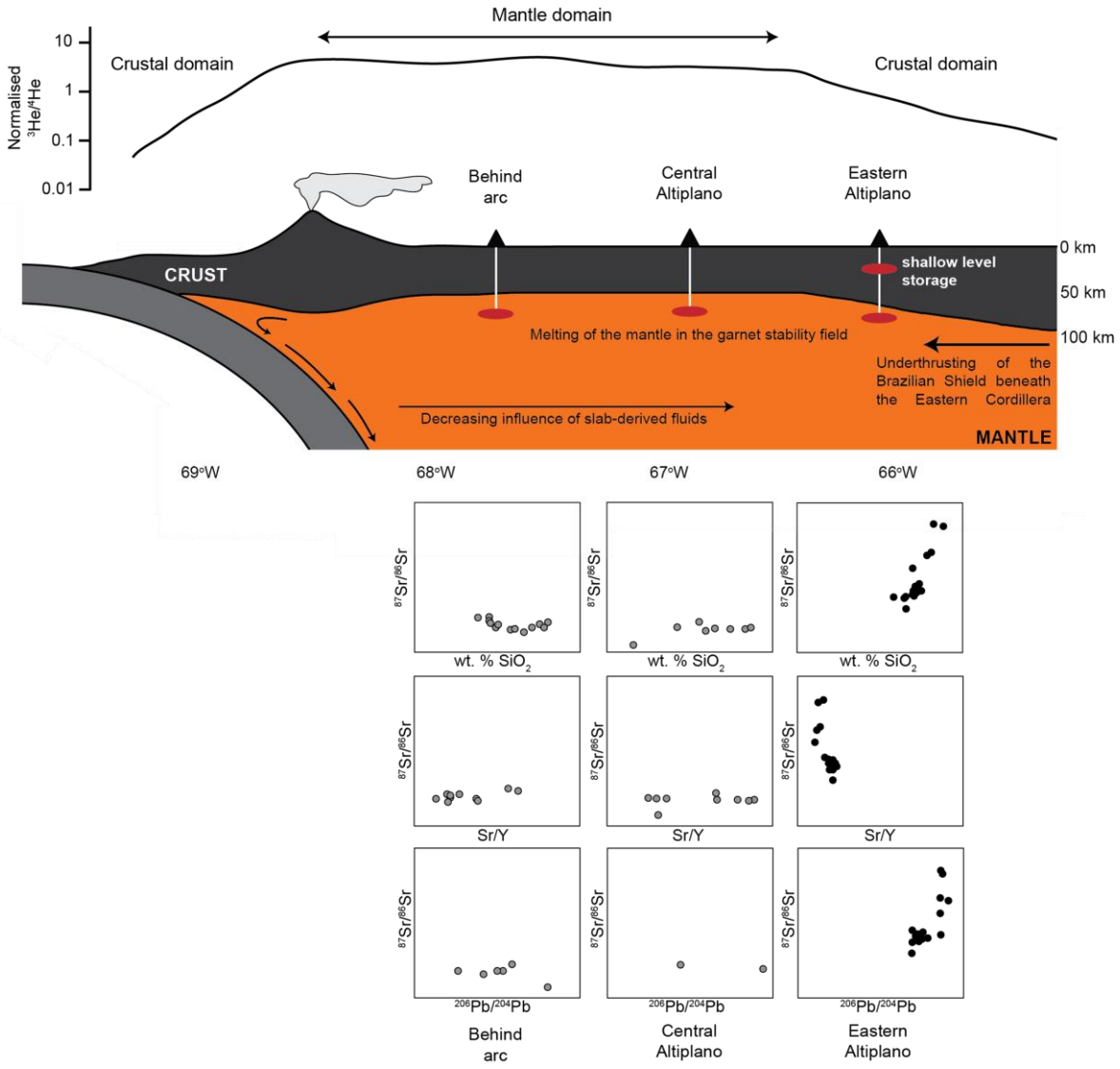

Fig. 4.23 a. Summary cartoon of observed across arc changes from the active Andean arc to the Eastern Altiplano at ~18-21°S. Grey and black circles represent lavas analysed throughout each region of the back arc.

Helium, as a volatile, incompatible element readily partitions into a melt. Mantle derived helium exhibits relatively enriched $^3He/^4He$ signature at between 6 and 8 R_A, which is similar to a MORB-type source at 8 ±1 R_A (Hilton et al. 1993, where R_A is atmospheric $^3He/^4He$). Crustal derived helium is produced from the decay of U and Th to ^4He and hence has a relatively low $^3He/^4He$ signature at 0.01 R_A (Hoke and Lamb, 2007). The observed change from crust-like Helium isotopic signatures on the Eastern Altiplano and at the arc to mantle-like compositions across the Central Altiplano is similar to the change in

R_A values observed across the Puna Plateau, Chile by Hilton et al. (1993). Mantle-like compositions were observed east of the arc in the back arc region (up to 6.72) and decreased arcwards to crust-like compositions e.g. 0.66. Beneath this region of the Puna, shallow mantle melting is inferred to have occurred as a result of delamination of the mantle lithosphere and the subsequent return flow of mantle asthenosphere (Hilton et al. 1993; Kay and Kay, 1994).

Results from a recently deployed seismic line transect at 21°S (from 2002 to 2004) support the presence of a low velocity zone beneath the Altiplano which may indicate the presence of melt at depth (Heit et al., 2008).

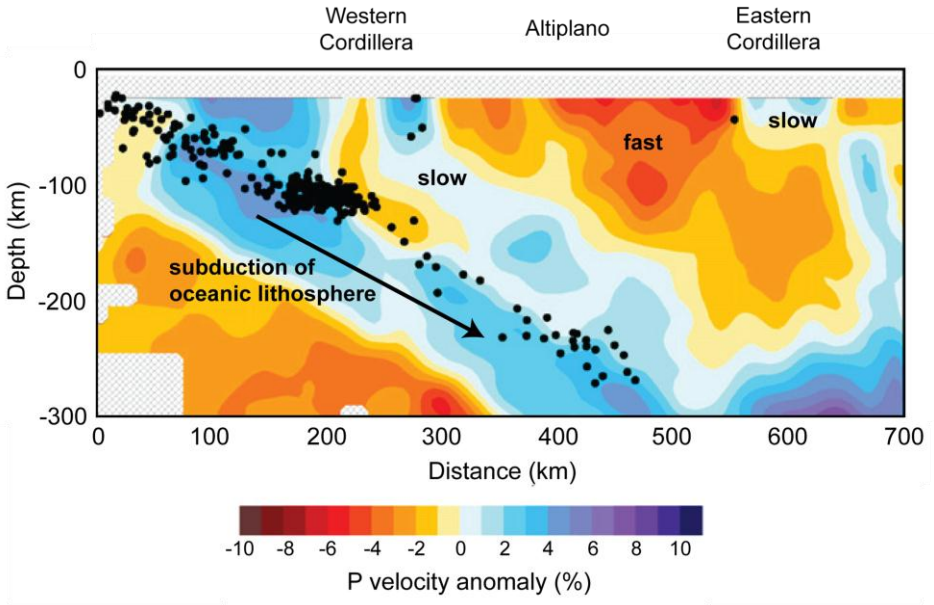

Fig. 4.23 b. Seismic profile constructed from P-wave residuals at 21°S. Earthquake hypocentres are represented by black circles. Profile is adapted from Heit et al., (2008).

Further east, a prominent high velocity is observed beneath the Eastern Cordillera and this has been attributed to the underthrusting of the cold, old, Brazilian Shield and hence, lithospheric thickening (Fig. 4.23 a-c, see also: Lamb et al., 1997; Beck and Zandt, 2002; Heit et al., 2008). This underthrusting has been shown not to extend beneath the

entire Altiplano. Furthermore, Beck and Zandt, (2002) inferred from P-wave velocity anomalies that the subcrustal lithosphere between 18°S and 21°S is currently being removed but only beneath the Central Altiplano has it been removed completely. This may therefore imply the presence of asthenospheric mantle at the base of the crust.

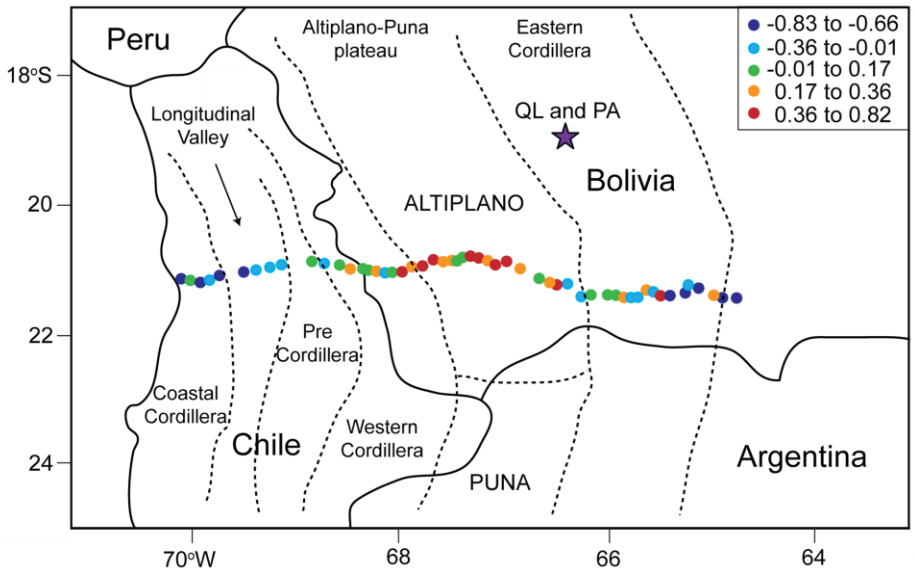

Fig. 4.23 c. Average residual seismic velocities (after correction for topography and the Moho discontinuity) across a ~600 km transect from Chile through to central southern Bolivia at 21°S. Areas recording fast seismic velocities are shown in blue, areas of slow seismic velocities are in red. Map is modified from Heit et al., (2008).

4.7 Conclusions

The lavas erupted in the Central Andes from monogenetic centres at PA and QL exhibit the highest $^{87}Sr/^{86}Sr$ values of any recent (< 60 Ma) volcanic rock on the Altiplano and indicate the role of the continental crust during their petrogenesis, as shown by $^{87}Sr/^{86}Sr$ correlating with indices of differentiation (e.g. SiO_2). These signatures (0.7080-07101 at QL; 0.7123-0.7169 at PA) can be reproduced through bulk mixing, AFC and EC-AFC modelling using as a parental end-member, the basalt at Chiar Kkollu (the most primitive volcanic rock in the Central Andes) and sampled crustal lithologies which were brought up as xenoliths in the PA and QL lavas.

However, the extreme geochemical variability observed in the lava from monogenetic eruptions requires a higher degree of complexity than simple two component crust-magma interaction between two distinct end members. Instead, the incorporation of different contaminants is inferred to account for the heterogeneity observed at a single centre.

The lavas are interpreted to originate from mantle depths at which garnet was stable as shown by La/Yb vs. Dy/Yb systematics, HREE depleted chondrite normalised patterns and REE inversion modelling of an inferred parental magma (Chiar Kkollu). Shallow level processing in the upper crust is also inferred from SiO_2 vs. Sr, Eu/Eu* vs. Sm/Yb and Sr/Y vs. $^{87}Sr/^{86}Sr$.

Monogenetic centres behind the arc at Ollagüe and Sajama and across the Central Altiplano define an across arc transect of ~180 km from the Western Cordillera (active arc) towards the Eastern Cordillera (fold and thrust belt) where PA and QL outcrop. The role of the continental crust during petrogenesis of these western lavas is less apparent with $^{87}Sr/^{86}Sr$ ratios consistently <0.7078. Instead, fractionation in high pressure MASH zones at lower crustal depths may be more important to their petrogenesis. A slab-derived component is understood to be present within this suite and inferred to decrease with distance from the arc as shown through Ba/Nb vs. Zr/Nb systematics. This slab-derived component is masked by crustal contamination, or is absent, from lavas at PA and QL. CaO vs. MgO signatures, (which can be used as a proxy for crustal thickness, see Plank and Langmuir, 1988) suggest that lavas at PA and QL may have erupted through thicker crust than centres to the west. This is in accordance with geophysical evidence for thinner crust beneath the immediate behind arc and Central Altiplano region and thicker crust towards the Eastern Cordillera. These observations are reconciled through lithospheric removal beneath the Central

Altiplano and lithospheric thickening beneath the Eastern Altiplano due to the underthrusting of the Brazilian Craton from the east.

Geochemical heterogeneity in natural anatectic melts: insights from partially melted Central Andean xenoliths.

5

This chapter forms the basis of a paper published in Geology. A copy of the accepted manuscript (and all the supplementary material) is included at the end of this chapter.

ABSTRACT

Contamination of ascending mantle-derived magmas by the continental crust was investigated and modelled for a suite of volcanic rocks and entrained crustal xenoliths from the Bolivian Altiplano, Central Andes, using bulk geochemical compositions for mantle-derived and crustal end-members as dictated by traditional approaches. The assumption that the crustal contaminant in these open magmatic systems is a single composition was assessed through *in-situ* analysis of quenched anatectic melt trapped within the xenolith. Our results show significant chemical and Sr-isotopic disequilibrium between melt and source over sub-millimetre length scales in a natural system. Sampled glass is rhyolitic and peraluminous in nature and enriched in LILE e.g. Ba, Rb and depleted in HREE. Analysis of the quenched anatectic melt (glass) for its $^{87}Sr/^{86}Sr$ composition revealed isotopic heterogeneity ranging from 0.7166 to 0.7281 over ~1.3 mm. The isotopic disequilibrium between melt and source is understood to reflect the melting of aged minerals with different Rb/Sr (and therefore $^{87}Sr/^{86}Sr$) more quickly than the isotopic composition can diffusively equilibrate between melt and minerals. Our results suggest that the mechanism of crustal anatexis produces melts which are geochemically heterogeneous both spatially and temporally. Furthermore, timescales of strontium diffusion and anatectic melt segregation can be shown to promote the preservation of isotopic disequilibrium at the micro (sub-mm) and macro (outcrop) scale. This highlights the need for detailed microscopic investigations coupled with petrogenetic modelling in order to develop a more robust characterisation and well-constrained quantification of crustal contamination in open magmatic systems.

5.1 Introduction

The formation and subsequent extraction of melts produced during crustal anatexis is fundamental to the differentiation, growth and evolution of the continental crust. Production of these melts can occur in a number of settings:

1) when the solidus is lowered by the addition of water;
2) when the crustal temperature is elevated above its solidus by intrusion and/or underplating by hotter material from depth;
3) when the geotherm is elevated as a result of decompression during rapid exhumation of deep crustal rocks (Zeng et al., 2005 and references therein).

4) shear heating/frictional melting of the (metapelitic) crust (e.g. Le Fort et al., 1987; Harrison et al., 1999).

Constraining the geochemical relationship between melts and their protoliths is however challenging as melts have risen, segregated (wholly or in part) at depth, differentiated, and been emplaced at shallower crustal levels where they are later sampled.

At "normal" mantle temperatures, *c*. 1280^{o}C (±20^{o}C, McKenzie and Bickle, 1988), it is generally accepted that diffusive geochemical equilibrium is capable of "keeping up" with the melting process. Indeed, much of our understanding of isotopically defined mantle reservoirs is predicated on this premise (Hofmann and Hart, 1978). Application of this assumption to shallower level processes occurring within the continental crust has received significant attention over the past several decades where it has been suggested that the geochemical characteristics of partial melts generated during crustal anatexis is controlled by the stoichiometry of the melting reactions i.e. melt compositions are dictated by the phase assemblages of the crustal lithologies and not the bulk composition (Deniel et al., 1987; Hammouda et al., 1994; Barbero et al., 1995; Knesel and Davidson, 1996; Tommasini and Davies, 1997; Knesel and Davidson, 1999; Zeng et al., 2005; Macera et al., 2011; Farina and Stevens, 2011).

During ascent towards the Earth's surface, primary basaltic magma has the potential to interact with overlying crustal rocks. This has been recognised since Bowen (1928) argued that assimilation of foreign material into a magma body should be treated as an inevitable consequence of fractional crystallisation, with a positive feedback loop between the extraction of heat due to assimilation and the generation of latent heat of crystallisation as crystallisation is promoted by heat extraction and cooling (e.g. Kuritani et al., 2005). In volcanic settings where the continental crust is in invoked to

have significantly contributed to the geochemical signatures measured in rocks sampled at the surface, e.g. in the Central Andes, and where the degree of this contribution has been extensively modelled through assimilation-fractional crystallisation (AFC: Chapter 4; Taylor, 1980; Spera and Bohrson, 2001; Sørensen and Holm, 2008; Mamani et al., 2010) the nature of crustal melts is crucial to assessing the degree of magma-crust interaction. However, very few constraints on the nature of the crustal basement exist (Chapter 3), let alone the compositions of any melts that may be derived therefrom.

The objective of this study is two fold, (1) to constrain the composition of naturally occurring anatectic melts (now quenched to glass) trapped within their protolith from partially melted crustal xenoliths erupted in Plio-Pleistocene lavas on the Bolivian Altiplano, Central Andes; (2) to assess the mechanisms of crustal anatexis and discuss to what extent the geochemical nature of micro-scale sampled melts can be used to infer processes at the macro-scale (i.e. hand specimen and plutonism).

5.2 Samples

Sampled crustal xenoliths preserve rare anatectic melts, solidified to glass, and it is the composition of this glass that offers a unique insight into the behaviour of the crust in open magmatic systems and which challenges our understanding of crustal anatexis and subsequent contamination of mantle-derived magmas.

Samples are hosted in trachyandesite/dacite lavas which erupted from monogenetic volcanic centres at Pampas Aullagas (PA; 1.89 Ma) and Quillacas (QL; 1.42 Ma) in the Central Andes (Chapter 4, for location see Fig. 4.1). On route to the surface, these magmas passed through ~70 km of continental crust. The entrained xenolith lithologies

vary from granulites to garnet mica schists with gneisses and several igneous lithologies including diorites and microgranites (Chapter 3).

Anatectic melt is present as glass in ~10% of the crustal xenolith suite (of samples which were sectioned, Fig. 5.1 a, b). The interstitial glass is not bound by crystal faces therefore implying it is not residual from crystallisation. Glasses are typically a murky-brown colour which can be vesiculated by up to 15% (termed "brown glass", Fig. 5.1 a) or transparent and isotropic (termed "clear glass", Fig. 5.1 b).

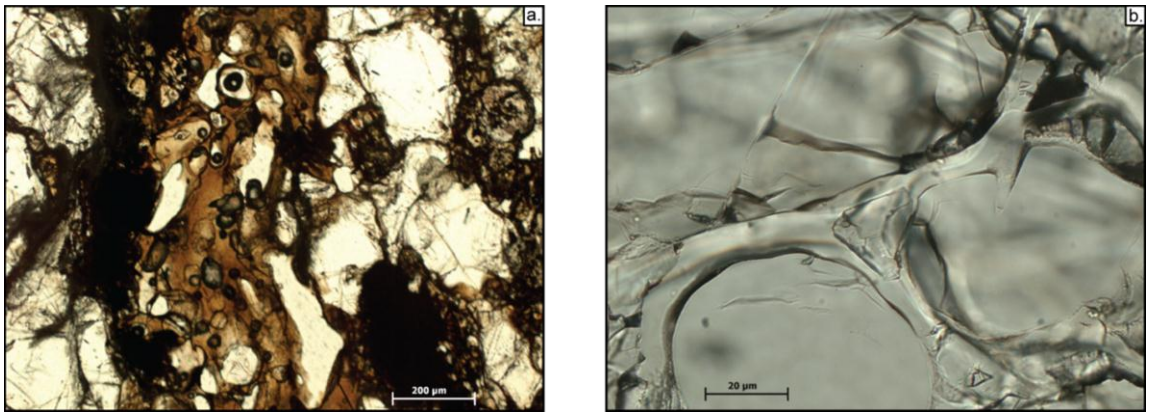

Fig. 5.1 a, b. Quenched anatectic melts in sampled Bolivian crustal xenoliths.

Glass is present at ≤ 2%, based on thick sections made. Brown glass forms abundant pools and channels whereas felsic glass is notably less abundant and typically forms thin channels (< 20 µm) throughout the crystalline restite.

Whole rock analyses of sampled host lavas clearly indicate the role of the continental crust during magma petrogenesis. This is demonstrated by their extreme Sr-isotopic diversity and with $^{87}Sr/^{86}Sr$ correlating with indices of differentiation such as SiO_2 (Fig. 5.2 a, b). All sample compositions are provided Appendix B, Table 1.

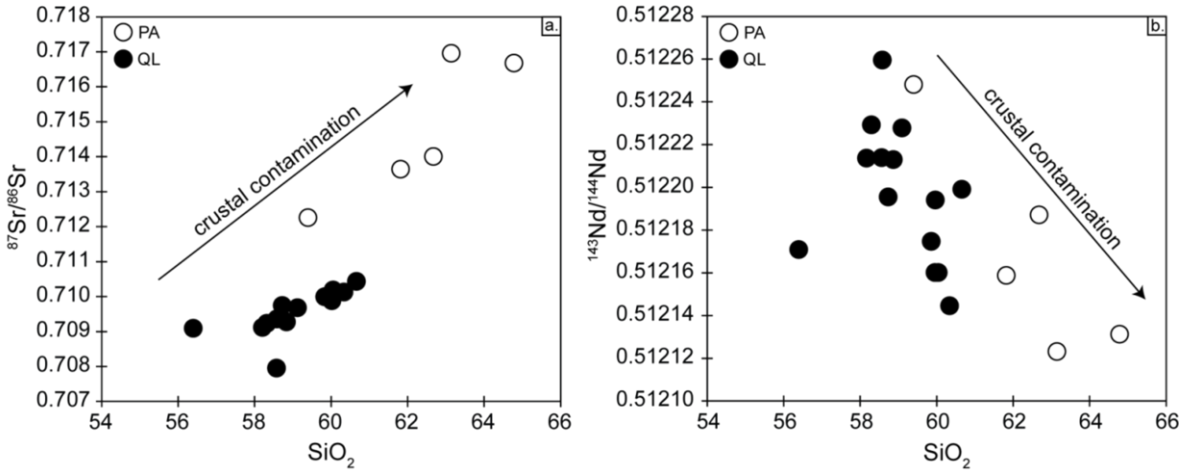

Fig. 5.2 a, b. Crustal contamination in lavas at Pampas Aullagas (PA) and Quillacas (QL).

5.3 Modelling crustal contamination

Numerous formulations aimed at evaluating and constraining the geochemical evolution in open magmatic systems have been developed over the past few decades (e.g. Taylor, 1980; De Paolo, 1981; Spera and Bohrson, 2001). The objective of these models is to meet the necessity for material mass balance whilst accounting for observed geochemical trends. Although a powerful petrogenetic tool, use of these models is only justifiable if the end member compositions are known i.e. those of the parental mantle-melt and those of the crustal assimilant, and in many studies at least one of those is unknown. Additionally, rates of assimilation to fractional crystallisation (r) and partition coefficients (e.g. D_{Sr}) need to be well constrained. The contaminated nature of the PA and QL lavas were investigated using the EC(AFC) model of Spera and Bohrson, (2001, see also Chapter 4). All sampled xenoliths are potential crustal lithologies with which ascending magmas may have interacted. Choosing a suitable parental magma composition is challenging as no true basalts have erupted recently in the Central Andes. Modelling was therefore carried out using an older Andean primitive magma represented by a Miocene sill (Chiar Kkollu) from 20 km WNW of the field area (see Chapter 4). The $^{87}Sr/^{86}Sr$ of the Chiar Kkollu basalt (0.7041) indicates relatively little assimilation of, and contamination by, the continental crust and its composition may be the closest representative of a parental melt that is currently

known for the region (Chapter 4; Davidson and de Silva, 1992). The results are presented in Fig. 5.3 but offer only a number of possible solutions that model the observed geochemical trends. Large values of r (>0.6) were required to model the lavas (see Appendix D for model input parameters).

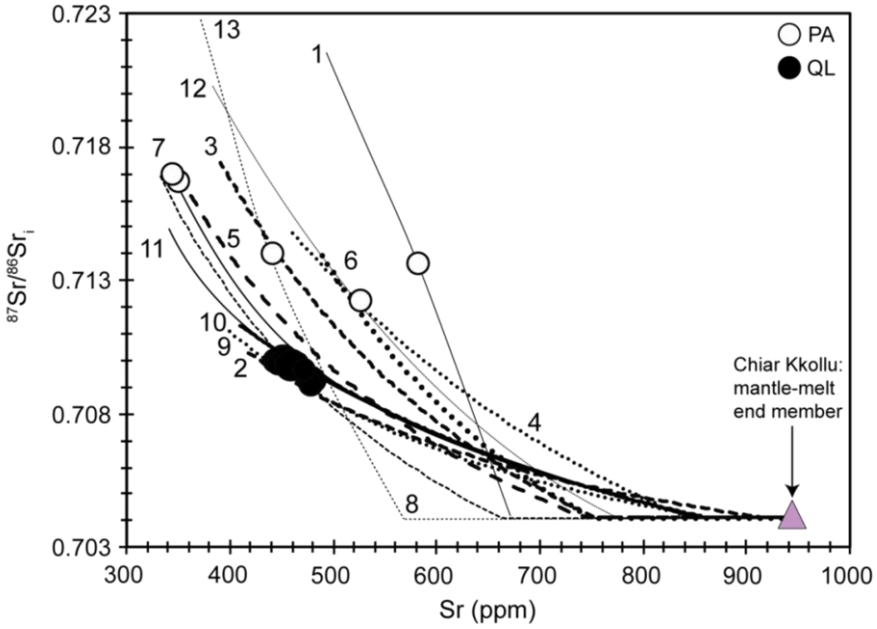

Fig. 5.3 EC-AFC modelling of PA and QL lavas. Numbers correspond to different EC-AFC models run, details are given in Appendix D.

5.4 Melt Geochemistry

The natural occurrence of preserved anatectic melt within sampled xenoliths offers a rare insight into the primary compositions of potential crustal contaminants as well as constraints on the initial composition of crustal melts produced during orogenesis. Quenched anatectic melt (brown) within one sample (BC93PAX12) was chosen for an in-depth geochemical study (major and trace elements, Sr-isotopes through micro-drilling). Clear melts within four samples (BC93 –QNX02, -QNX03. –PAX08, BC10PAX138) were analysed for their major element concentrations but were unfortunately not significantly spatially abundant to permit sampling through microdrilling for trace elements and Sr-isotopes. Data is presented in Appendix B, Table 6. Details of analytical methods used and standards run throughout the course of

this study are given in supplementary material to the accepted manuscript. These are provided at the end of this chapter and in Appendix E.

5.4.1 Major elements

All sampled glasses are rhyolitic in nature with brown glasses at lower $Na_2O + K_2O$ (< 6.8 wt. %), clear glasses at > 7.2 wt. % (Fig. 5.4).

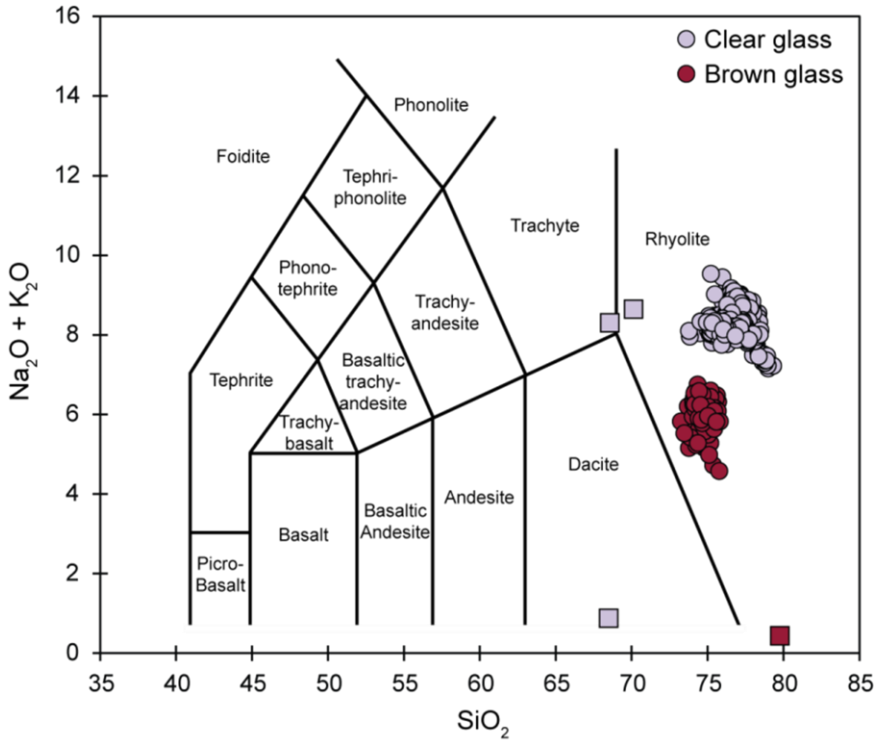

Fig. 5.4. TAS plot for sampled anatectic melts. Source xenoliths are also shown (squares); BC93PAX12 at 79.8 wt. % SiO_2, QNX02 at 68.47 wt. %, QNX03 at 68.67 wt. %, BC10PAX138 at 70.27 wt. %. BC93PAX08 was not analysed for its major element composition. For the full suite of xenolith major element compositions see Tables 2, 4 in Appendix B.

Sampled brown and clear glasses consistently plot within two distinct compositional fields with respect to major oxides (Fig. 5.5 a-h). Brown glasses range from 73 to 76 wt. % SiO_2 and clear glasses typically range from 75 to 79 wt. % SiO_2. Brown glasses exhibit higher total wt. % Fe_2O_3 + MgO at 1.2-3.8 compared to 0.7-1.9 for clear glasses and higher wt. % Al_2O_3, TiO_2 and MnO. All glasses can be considered peraluminous ($Al_2O_3/CaO+K_2O+Na_2O$ > 1) with brown glasses at higher values from 1.8 to 2.4 compared to 1.2-1.7 for clear glasses.

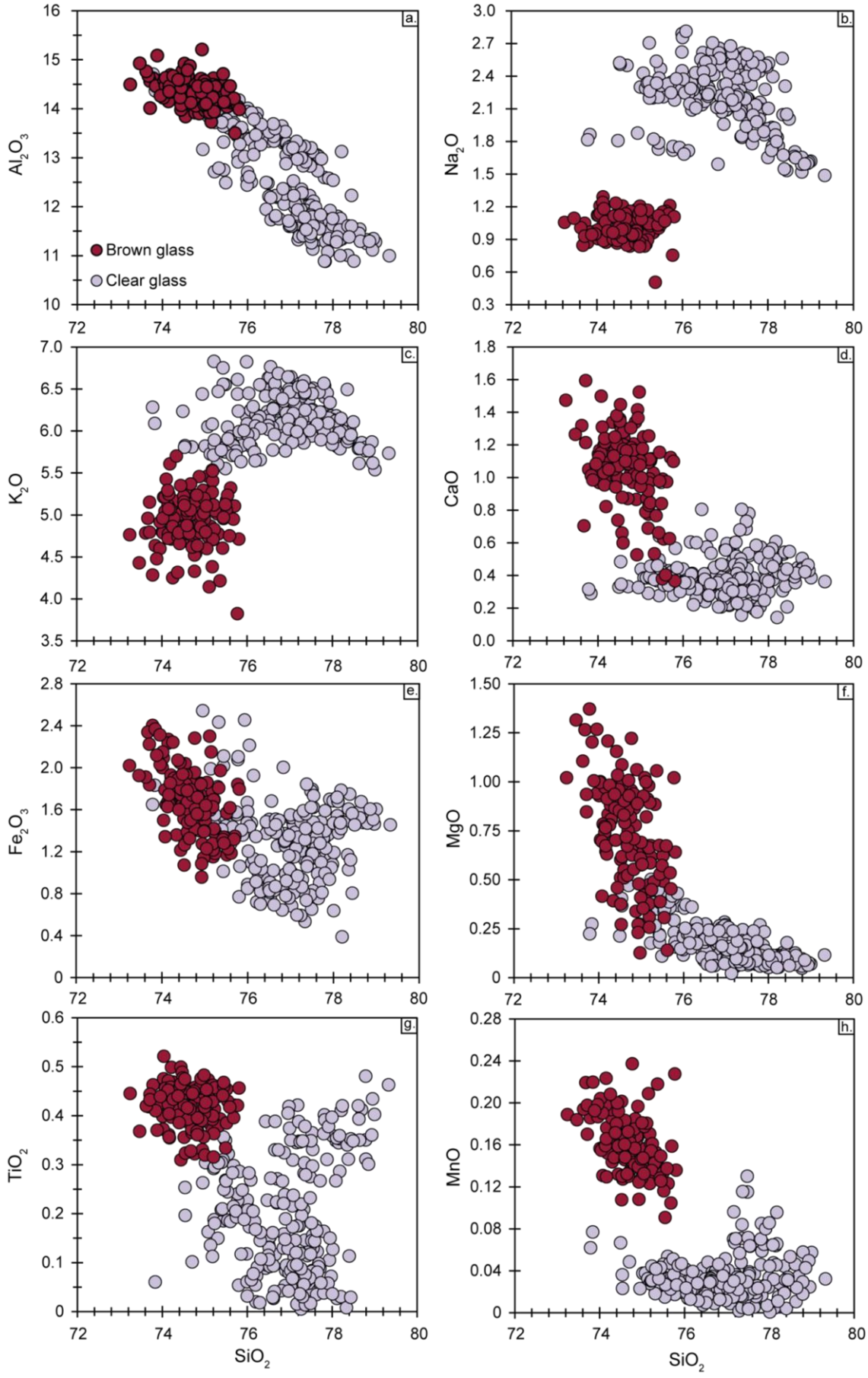

Fig. 5.5 a-h. Distinct geochemical nature of anatectic glasses with respect to major oxides.

From major element data alone, it could be hypothesised that the brown glass, relatively enriched in MgO+FeO may indicate the breakdown of biotite whereas the clear glass, which is slightly more silicic and exhibits higher Na_2O+K_2O, may indicate feldspar breakdown (e.g. Knesel and Davidson, 1996; 2002). Significant geochemical heterogeneity exists within sampled glasses (Fig. 5.6 a-c) with variations of up to 1.2 wt. % SiO_2 on the sub-millimetre scale.

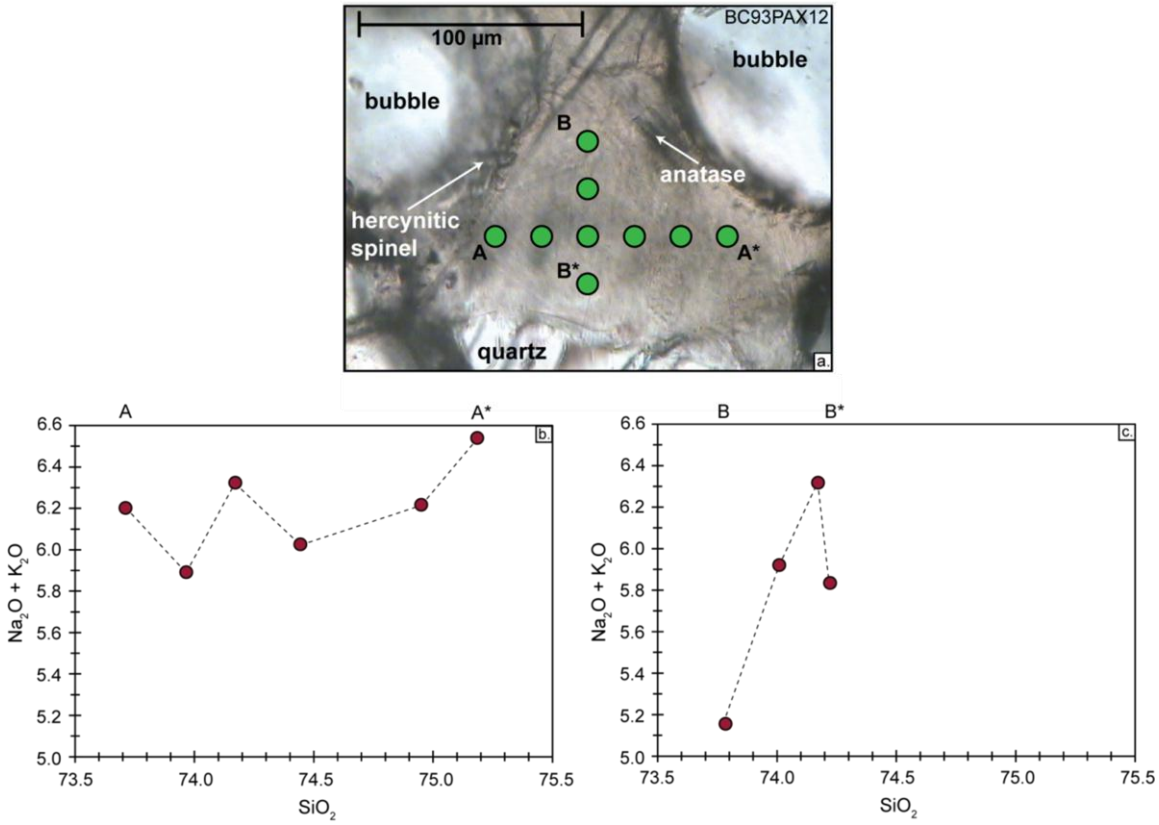

Fig. 5.6 a-c. Geochemical heterogeneity at the micro-scale within sampled brown glass.

5.4.2 Trace elements

Analysed brown glass from sample BC93PAX12 was sampled from two thick sections. This xenolith is a garnet-sillimanite gneiss and is characterised by biotite, sillimanite, garnet, plagioclase, quartz, minor anatase and opaque phases, accessory monazite and ~2% anatectic melt. Six samples were derived from within a large melt pool in section BC93PAX12_a and eight from within a melt channel in section BC93PAX12_b. Sample locations are shown in Fig. 5.7 a, b and results in Fig. 5.8 a, b.

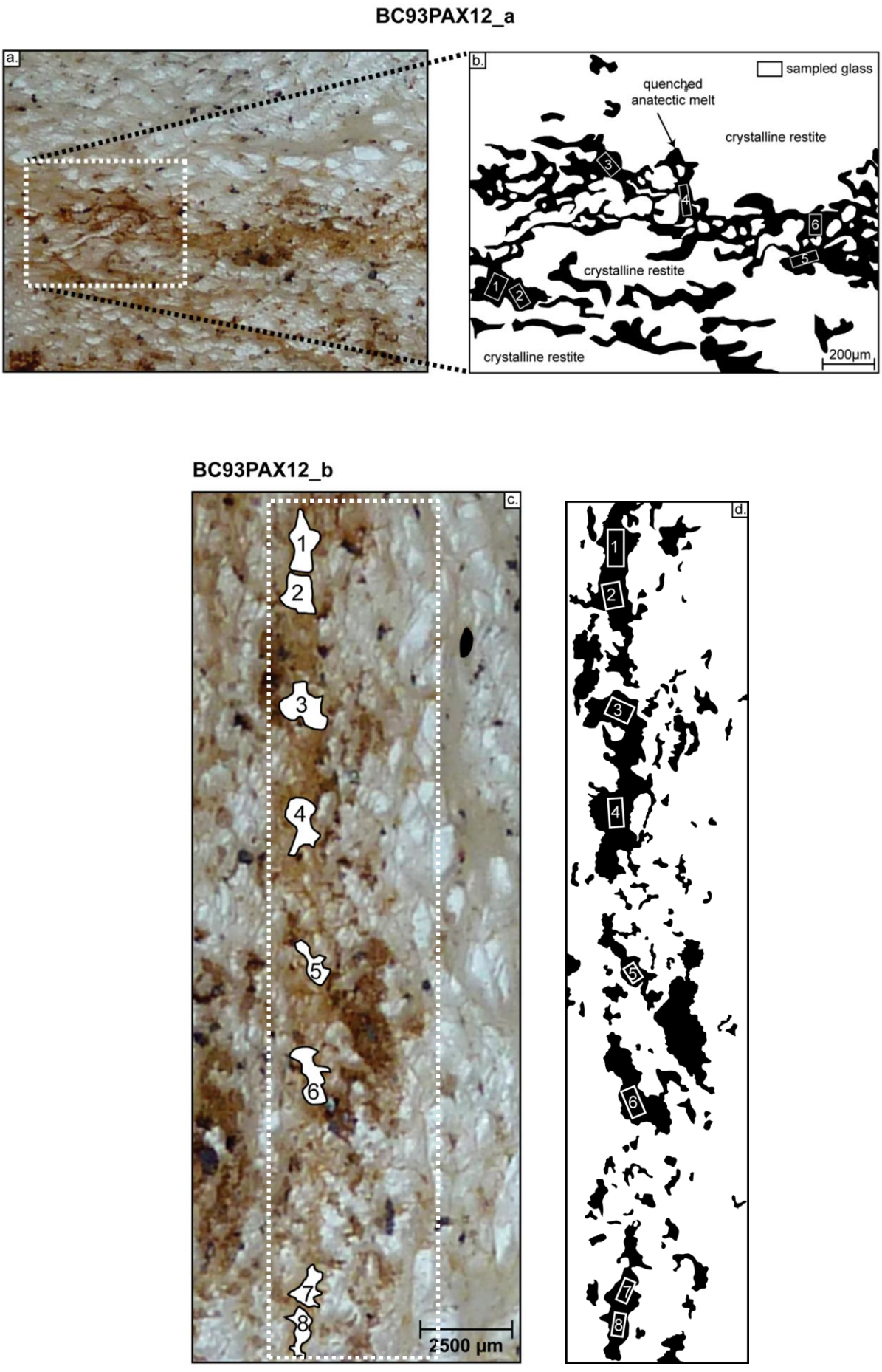

Fig. 5.7 a-d. Location maps of drill sites in two thick (100 µm) sections of xenolith BC93PAX12.

Euhedral hercynitic spinel (<100 μm) is present within the melt pools. This phase has previously been shown to be a common product of the incongruent breakdown of biotite (e.g. Cesare, 2000) and great care was taken during microsampling to avoid it.

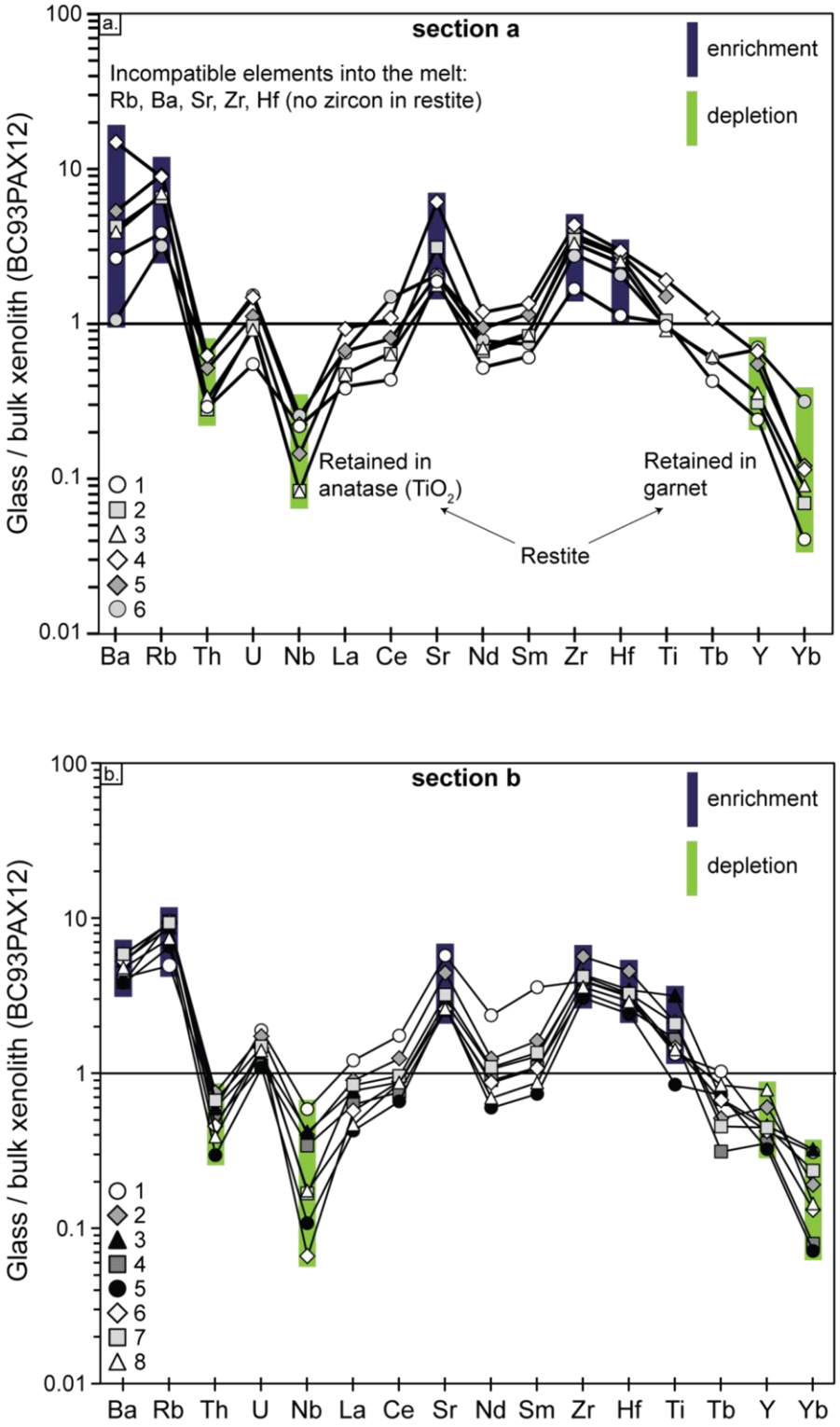

Fig. 5.8 a, b. Enrichment and depletion of sampled mafic anatectic melts relative to their source xenolith (BC93PAX12).

Sampled glass shows enrichment in LILE (Ba, Rb) and depletion in the HREE that is retained in residual garnet. The significant Nb depletion recorded in the glass is inferred to represent the stability of anatase, the metastable TiO_2 polymorph which is present as acicular crystals (<200 μm). The occurrence of anatase (as opposed to rutile, the more common form of TiO_2) is consistent with the experimental observation that anatase forms under rapid cooling conditions (i.e. quenching), whereas rutile will crystallise under near-equilibrium solidification conditions (Li and Ishigaki, 2002).

5.4.3. Sr-isotopes

Analysis for the Sr-isotopic composition of the quenched anatectic melt reveals extreme variability over sub-millimetre length scales and significant isotopic disequilibrium between the melt and its source (Fig. 5.9 a, b). Glass samples 5 and 6 (in section_a for example) bracket the range at 0.7281 to 0.7166 respectively but are within 200 μm of each other (Fig. 5.7 a).

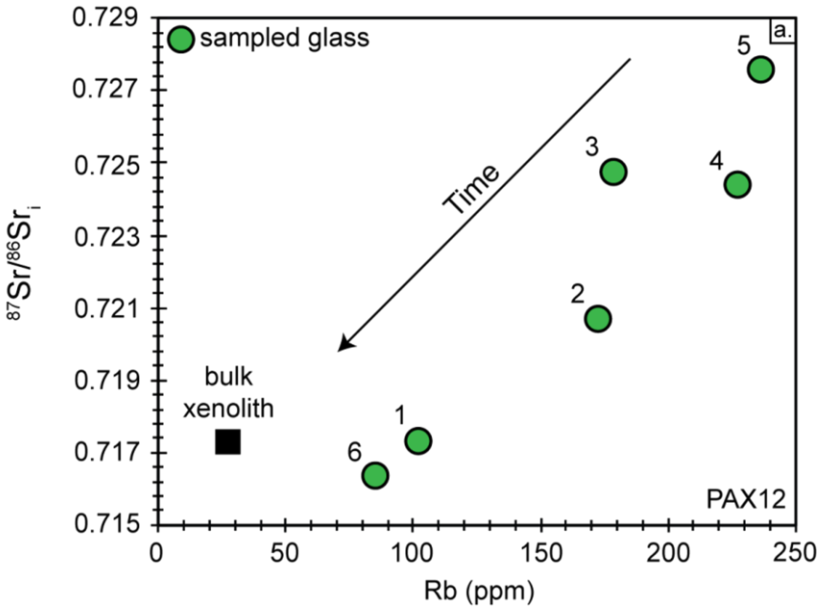

Fig. 5.9 a. Rb vs. $^{87}Sr/^{86}Sr_i$ for sampled mafic anatectic glasses, section BC93PAX12_a (Fig. 5.7 a, b). Compositions are age corrected for the Pliocene age of lava eruption (1.89 Ma). Time arrow infers the decreasing contribution from high Rb/Sr phases to the melt, for discussion see text.

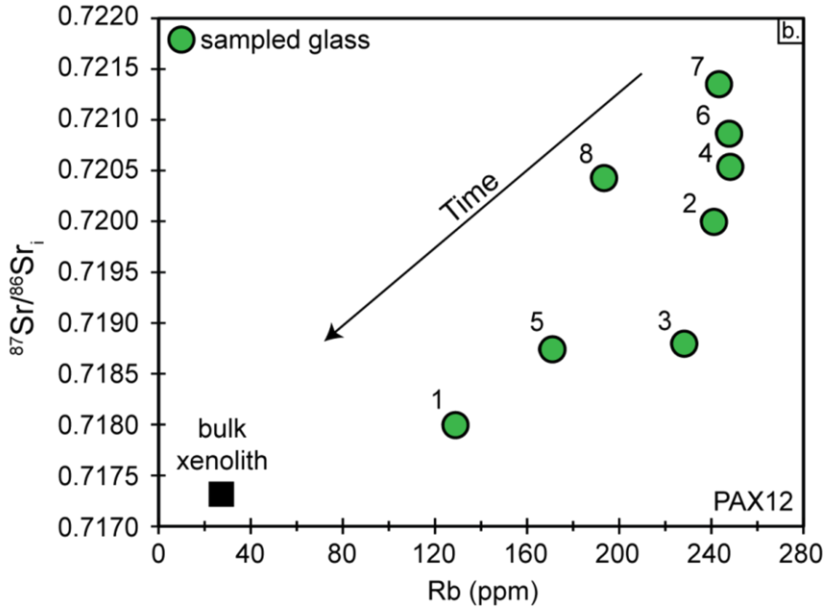

Fig. 5.9 b. Rb vs. $^{87}Sr/^{86}Sr_i$ for sampled mafic anatectic glasses, section BC93PAX12_b (Fig. 5.7 c, d). Compositions are age corrected for the Pliocene age of lava eruption (1.89 Ma). Time arrow infers the decreasing contribution from high Rb/Sr phases to the melt, for discussion see text.

All of the sampled glasses exhibit $^{87}Sr/^{86}Sr$ signatures which are more radiogenic than the host lavas (or of any volcanic rock across the Central Andes, < 60 Ma, see Fig. 2.9, Chapter 2; Chapter 4) indicating that the crustal signature inferred from the Sr-isotopic composition of volcanic rocks at the surface may provide little (if any) information about (1) how it got there and (2) constraints on the nature of the contaminant at depth. As shown through multiple analyses of lava groundmass glass for $^{87}Sr/^{86}Sr$ (Fig. 5.9 c), the sampled brown glass in the xenolith does not represent infiltrated host magma.

5.5 Disequilibrium melting and melt assimilation

The dominant mechanism of anatectic melt formation in the continental crust is the (fluid-absent) incongruent melting of hydrous silicates, e.g. the dehydration melting reaction of biotite; Biot + Plag + Qtz forms Opx + Melt (see Fig. 5.10) which leaves behind a less hydrous restitic assemblage.

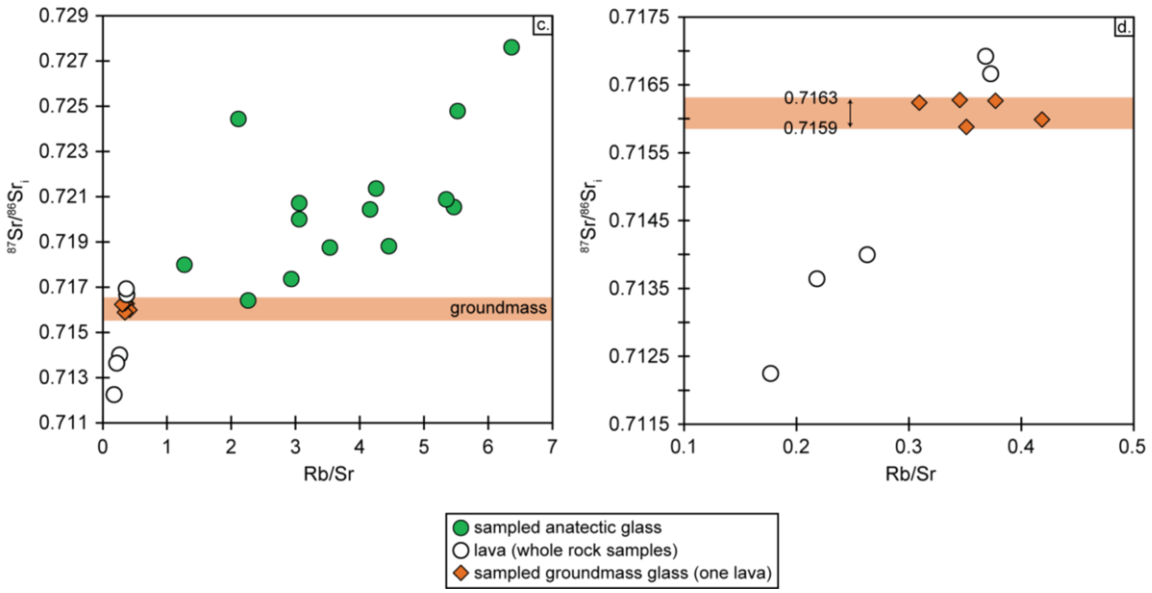

Fig. 5.9 c, d. Rb/Sr vs. $^{87}Sr/^{86}Sr_i$ for sampled mafic anatectic glasses, groundmass glass from within the same thick section and five whole rock analyses. All compositions are age corrected.

Additional experimental studies have determined the following melting reactions, and the Mg-number of biotite, as being crucial to melt production during anatexis of metapelites and metabasites (see also Fig. 5.10).

(1) Musc + Qtz + Plag → Sillm + Kspr + Melt (Dehydration melting)

(Clemens and Vielzeuf, 1987; Vielzeuf and Holloway, 1988);

(2) Musc + Plag + Qtz → Melt + Kspar + Sillm + Biot (Dehydration melting)

(Patiño-Douce and Harris, 1998);

(3) Musc + Plag + Qtz + H_2O →Melt (H_2O fluxed)

(Patiño-Douce and Harris, 1998);

(4) Biot + Sillm + Plag + Qtz→ Grt + Kspr + Melt (Dehydration melting)

(Clemens and Vielzeuf, 1987; Vielzeuf and Holloway, 1988);

(5) Biot + Plg (at ~An_{40}) + Qtz → ((Hbln + Plag (at <An_{40}) + titan)) / solids) + ((Plag (at <An_{40}) + Kspar) / Melt.

(Lappin and Hollister 1980; Kenah and Hollister, 1983).

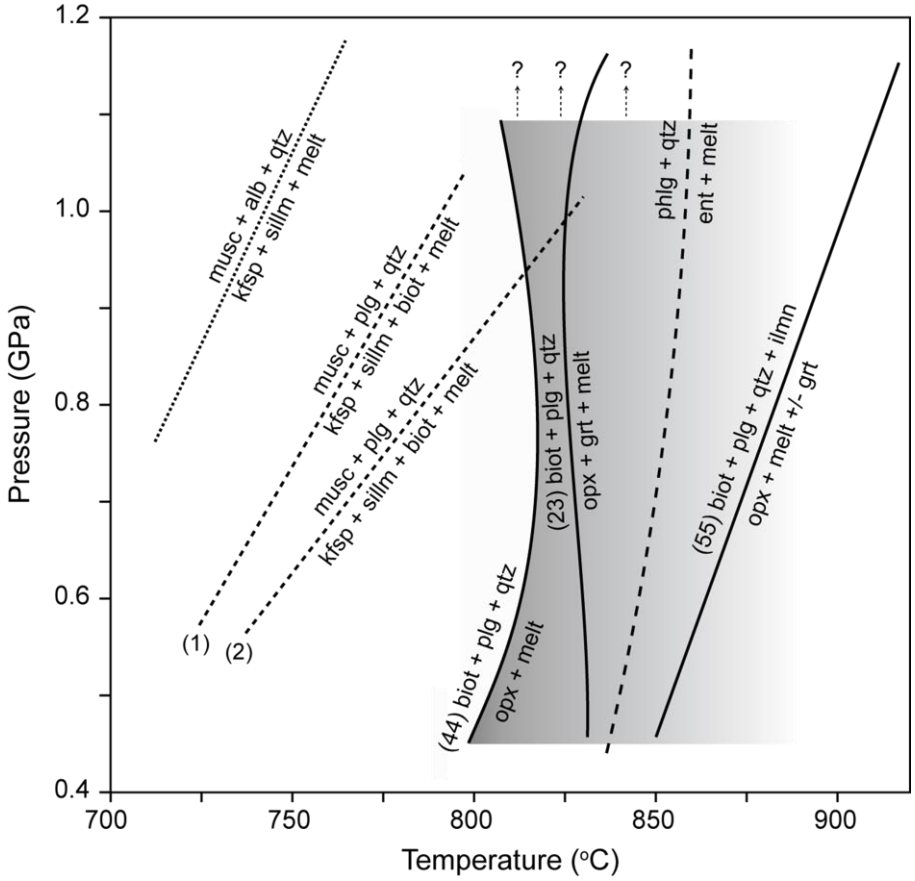

Fig. 5.10. Phase diagram for muscovite and biotite dehydration solidi. Adapted from Farina and Stevens, (2011). Shaded region represents potential temperature-pressure field for xenolith BC93PAX12. Dotted line: dehydration melting solidus from Peto (1976); dashed line (1): muscovite-schist solidus (Patiño-Douce and Harris, 1998); dashed line (2) muscovite schist dehydration solidus (Patiño-Douce and Harris, 1998); solid black lines: biotite dehydration at different biotite Mg# (in brackets) in the absence of muscovite (Vielzeuf and Montel, 1994; Patiño-Douce and Beard, 1995, 1996); dashed line: phlogopite-quartz solidus (Vielzeuf and Clemens, 1992).

Following these experimental approaches, partial melting during crustal anatexis can be described as being either fluid-absent or fluid-present with the breakdown of hydrous phases being the important control (Zeng et al., 2005). Alkali feldspar is generally not considered a significant component in pre-melting, meta-pelitic assemblages, nor is it an important reactant during mica consumption (see equations).

At equilibrium, partial melting redistributes trace elements as a function of their partition coefficients. Isotope ratios however are unaffected by this process and have therefore been implemented as tracers of geochemical reservoirs throughout the Earth.

Isotope ratios, are generally taken to reflect those of the source rock, because it is understood that diffusive equilibrium at the high temperatures of melting is capable of "keeping up" with the melting process. However, if diffusion cannot keep pace with melting then isotopic compositions will vary with the contributions of Sr from the individual phases present within the source i.e. disequilibrium melting (e.g. Knesel and Davidson, 2002; Rushmer and Knesel, 2010).

The Rb-Sr system in crustal rocks is predominantly controlled by key minerals i.e. feldspars and micas. Numerous cases of disequilibrium melting with respect to Sr-isotopes have been documented from laboratory experiments (e.g. Hammouda et al., 1996; Knesel and Davidson, 1996; 1999) and inferred in combined field and geochemical studies (e.g. Deniel et al., 1987; Barbero et al., 1995; Duffield and Ruiz, 1998).

Melting will typically begin with preferential breakdown of high Rb/Sr hydrous phases (see equations) producing an initial melt with a higher $^{87}Sr/^{86}Sr$ than the bulk source. If melting progresses relatively rapidly so that diffusive equilibration of $^{87}Sr/^{86}Sr$ does not occur, additional phases contribute Sr with different $^{87}Sr/^{86}Sr$ and the composition of the melt will change as shown schematically in Fig. 5.11 a. Feldspar, for instance, has a lower Rb/Sr and will consequently contribute less radiogenic Sr than biotite.

As analysis of natural anatectic melts shows, significant Sr-isotopic disequilibrium exists between product and protolith on the sub-mm scale (Fig. 5.9 a, b). Melting is likely to be non modal and the degree of variation is likely to be heterogeneous throughout the melt both spatially and temporally as the $^{87}Sr/^{86}Sr$ compositions will be

controlled by the relative proportions of the Rb/Sr phases at any given site and the rate at which these melt.

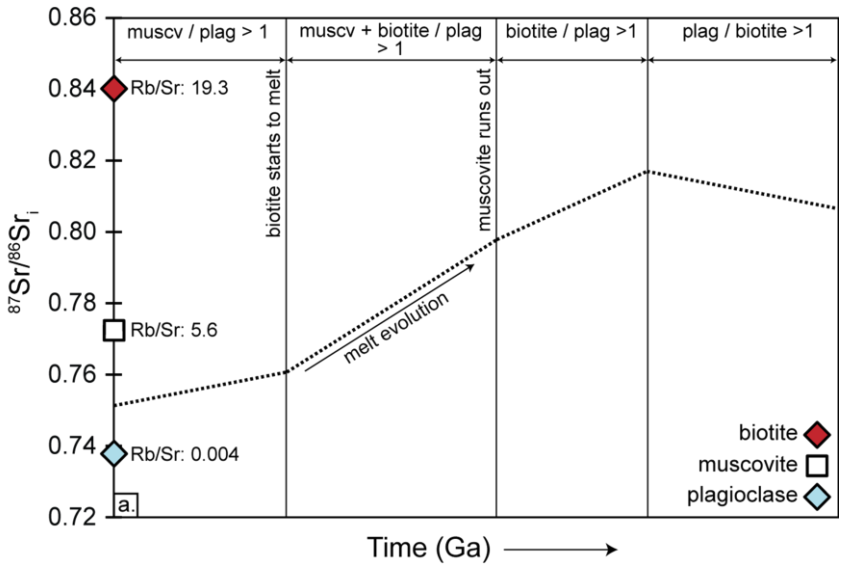

Fig. 5.11 a. Hypothetical melt evolution with respect to $^{87}Sr/^{86}Sr$ as a variable Rb/Sr phases breakdown during anatexis (compositions from Zeng et al., 2005).

Initially high $^{87}Sr/^{86}Sr$-bearing melts produced by biotite dehydration, will be diluted if melting continues and the less radiogenic phases breakdown e.g. feldspar. As anatexis proceeds, the $^{87}Sr/^{86}Sr$ of the contaminant will be lowered hence it is ultimately the relative rates at which the different Rb/Sr phases contribute to the melt that governs its compositional evolution (Fig. 5.11 a; e.g. Duffield and Ruiz, 1998).

The potential implications this process has for crustal contamination in open magmatic systems and the geochemical fingerprint this may leave in volcanic rocks is illustrated in Fig. 5.11 b for the Bolivian lava samples (Fig. 5.2 a, b). Note that there is no way of knowing the time at which melts were produced. However, Rb concentration can be used as a proxy, in that early melts may be dominated by biotite (high Rb) while later melts contain a greater contribution from feldspar (low Rb). Thus on Fig. 5.9 a, glass sample 5 is the earliest produced while 6 is the last.

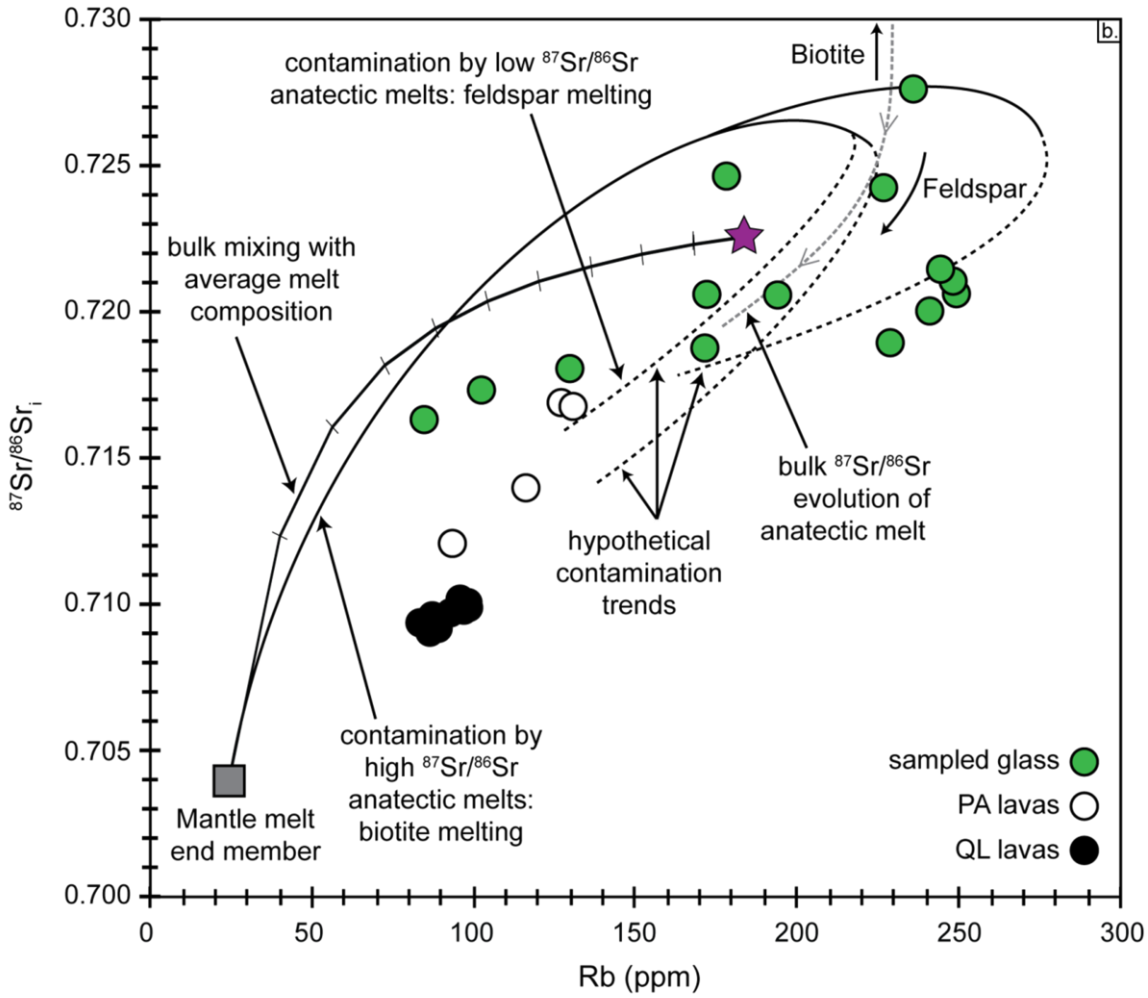

Fig. 5.11 b. Schematic control of isotope systematics by disequilibrium melting. Initially, high Rb/Sr phases may contribute more radiogenic Sr to the melt (e.g. biotite). As anatexis proceeds, the breakdown of lower Rb/Sr phases may dominate (e.g. plagioclase feldspar, see also, Fig. 5.11 a). The bulk mixing line (shown at 10% intervals) indicates bulk mixing between the Chiar Kkollu lava and the average composition of sampled anatectic glasses. Realistically however, the composition of the contaminant may change (see text for discussion). The solid black, and associated dashed black, trends illustrate the potential contamination pathways ascending mantle-derived magmas assimilating compositionally variable anatectic melts may have in terms of their Rb versus $^{87}Sr/^{86}Sr_i$ (based on bulk melt composition with Rb content used as a proxy for time, see Fig. 5.9). All compositions age corrected to eruption age (1.42 Ma for QL).

Fig. 5.12 shows Ba vs. Rb/Sr, the trends of which are controlled by the relative proportion of mica breaking down i.e. muscovite or biotite. Sampled glasses generally trend towards higher Ba content at higher Rb/Sr values indicating the role of biotite dehydration melting during anatexis. On the same diagram, the compositions of melts and their inferred protoliths from the Himalayan region are shown.

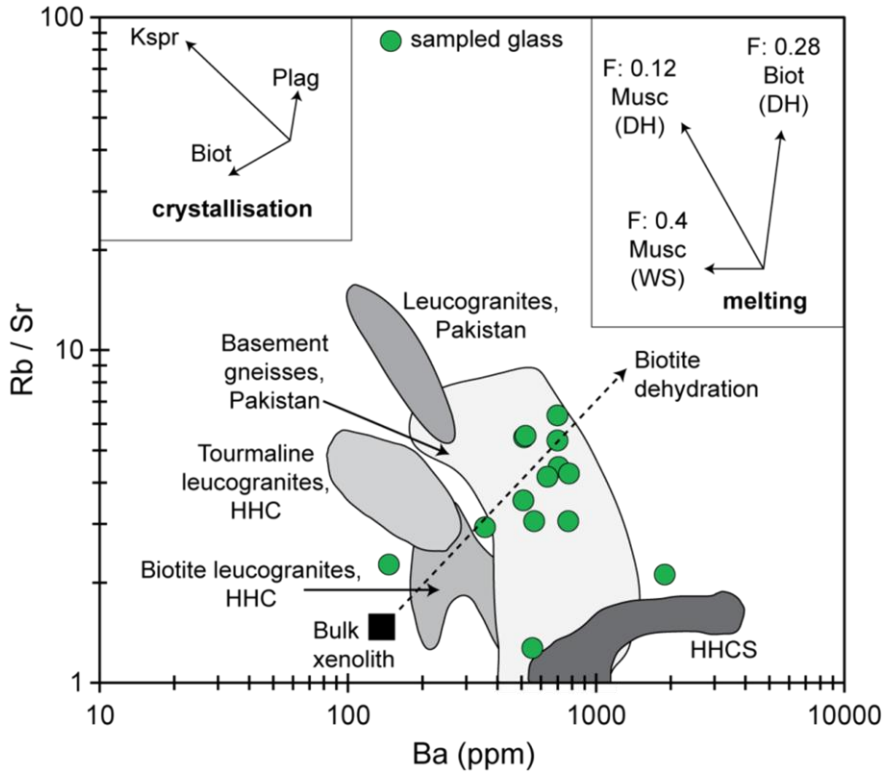

Fig. 5.12. The effects of crustal melting in Ba vs. Rb/Sr compositional space. Adapted from Whittington and Treloar, (2002). DH: dehydration, WS: water-saturated, HH(C): High Himalayan (Crystalline Series). Vectors show 10% change due to crystallisation of corresponding phase; F: melt volume fraction. For a detailed explanation on the controls governing melting and crystallisation see Whittington and Treloar, (2002).

These rocks have been subject to intense study over the past few decades regarding melt origin, timescales of melt segregation and whether or not disequilibrium melting has occurred during anatexis (Guillot and Le Fort, 1995; Harris et al., 1995; Patiño-Douce and Harris, 1998; Harris and Ayres, 1998; Whittington et al., 1999; Knesel and Davidson, 2002; Whittington and Treloar, 2002). In the Himalayan region, muscovite dehydration melting during leucogranite production is constrained to be more important than biotite dehydration melting, if the latter exists at all.

In short, the $^{87}Sr/^{86}Sr$ and Sr contents of bulk contaminants may be inappropriate input choices for modelling open system processes. Instead, the following points need to be considered and accounted for (1) the stoichiometry of melting reactions which control

the changing proportions of phases entering the melt; (2) the rate of melting with respect to Sr diffusivity in the melt, which defines the balance between melt production and the capacity to equilibrate diffusively; (3) the composition of phases consumed, which dictates, in conjunction with (1), the mass balance of Sr in the melt at any given time; (4) the grain size of phases which constrains the length scales of diffusive equilibration in the solid phases; and (5) the timescales of melt segregation (controlled by the permeability of the (molten) source rock and thus grain-scale distribution of the melts, Laporte, 1994). The majority of these processes are left unaccounted for in the current petrogenetic models (e.g. Fig. 5.3).

5.6 Implications for natural systems

The observation of Sr-isotopic disequilibrium in anatectic melts supports interpretations from experimental work which has previously aimed to evaluate the process of crustal anatexis e.g. Hammouda et al., (1996); Knesel and Davidson, (1996); Knesel and Davidson, (2002). These studies emphasise the importance of crustal source mineralogy on governing anatectic melt composition and relative Sr diffusion timescales. Ultimately, diffusion will work to eradicate compositional gradients and achieve isotopic equilibration, provided the melt remains in contact with the residuum through an interconnected grain boundary network which will act as a diffusion pathway. Therefore, in order for disequilibrium to be preserved, crustal melts must segregate on timescales shorter than those required for diffusive equilibration (e.g. Sawyer, 1991). Segregation of small degree, anatectic partial melts (e.g. Philpotts and Asher, 1993) from their protoliths has been shown to occur on rapid time scales (10^2-10^4 years, Sawyer, 1994). These timescales are significantly faster than those required for diffusion to erase Sr compositional gradients e.g. diffusion in feldspars (0.1-1 cm) at typical temperatures of anatexis (800-1000^{o}C) ranges between a few million years and 10s of millions of years (Tommasini and Davies, 1997). This in turn implies

disequilibrium melting may be an important process in governing the composition of crustal-scale melts (up to 40% melting, Barbero et al., 1995).

The micro-scale observations detailed in Fig. 5.9 a, b invite speculation on the potential significance of larger scale Sr-isotopic disequilibrium in the production of anatectic melts which may play a fundamental role in crustal differentiation (e.g. Sawyer, 1994). In order for Sr-isotopic disequilibrium melting to be preserved on a crustal scale, the timescale for melt segregation has to be (in comparison to orogenesis) instantaneous (Barbero et al., 1995). Evidence for the preservation of disequilibrium melting during regional metamorphism can be found in anatectic granitoids from Toledo, Spain where sampled leucogranites are out of isotopic equilibrium with their granulitic restite. Partial melting did not produce isotopically homogenous melts and Sr-isotope disequilibrium is observed on the mineral scale. In accordance with this study, Barbero et al., (1995) modelled and invoked the non-modal breakdown of variable Rb/Sr phases (biotite and plagioclase) along with restricted Sr-diffusion in order to account for the observed isotopic disequilibrium. Similarly, Tommasini and Davies, (1997) observed Sr-isotopic disequilibrium melting during contact metamorphism in the Sierra Nevada, California where trachyandesites intrude a granitic batholith. Sampled glasses were out of equilibrium at the outcrop and hand specimen scale (10s of m and cm respectively).

Small degrees of partial melt do not reach their critical mass fraction (CMF) needed to migrate due to buoyancy alone (~30%, Arzi, 1978). However, experimental studies have suggested that low melt fractions (1-5%) can develop interconnected networks between grain boundaries which, in turn, form a permeable matrix from which melt is extractable e.g. through non coaxial deformation during melting (Sawyer, 1991; 5-10%: Petford et al., 2000; Brown, 2007). This process has similarly been shown to occur on a

crustal scale during pluton emplacement (e.g. Guglielmo, 1993). In Fig. 5.7 b the melt fraction is estimated at 18% and clearly not interconnected hence opportunities for mixing and diffusive equilibration must rely on either a 3-D network not fully apparent in the 2-D section, or on tiny, unseen, films along grain boundaries. The ability of a melt to segregate is also a function of its viscosity as lower viscosity melts (mafic melts: $\eta = 10^2$-10^3 Pa s^{-1}) will segregate from their protolith more readily than felsic melts ($\eta = 10^4$-10^5 Pa s^{-1}) which are polymerised to a higher degree (Knesel and Davidson, 1996). It is therefore feasible that non modal, anatectic melts which exhibit heterogeneity with respect to Sr isotopes can (1) be produced in the crust on the micro- and macroscale and (2) segregate on timescales which will preserve melt-source disequilibrium.

The mechanisms through which crustal melts segregate from their source are poorly constrained. One of the primary controls on segregation (and the rate of) will be the permeability of the partially molten source (e.g. Laporte, 1994). In a system at equilibrium where temperature and pressure are fixed, the system will texturally evolve towards an equilibrated configuration. This will see the melt dispersed throughout the crystalline material in such a way that the interfacial energy is isotropic (Jurewicz and Watson, 1985). The equilibrated configuration will be controlled by (1) a constant dihedral (wetting) angle which is the angle at the contact between a melt and two crystals and (2) a constant mean curvature of the crystal-melt interface which, if not achieved, will produce gradients and promote mass transfer (Laporte and Watson, 1995). Melts will form interconnected networks along grain boundaries if the wetting angle (or dihedral angle, θ) is less than 60 but will exist as isolated pockets if $\theta \geq 60$ (Fig. 5.13 a, b). Textural equilibrium in cumulate rocks has been widely documented (e.g. O'Driscoll, 2005; Holness et al., 2006; Tollan et al., 2012) however, the attainment of a unique wetting angle and fixed grain curvature in systems where hydrous silicic

melts are in contact with refractory phases (e.g. biotite) has previously been shown not to occur (Laporte and Watson, 1989).

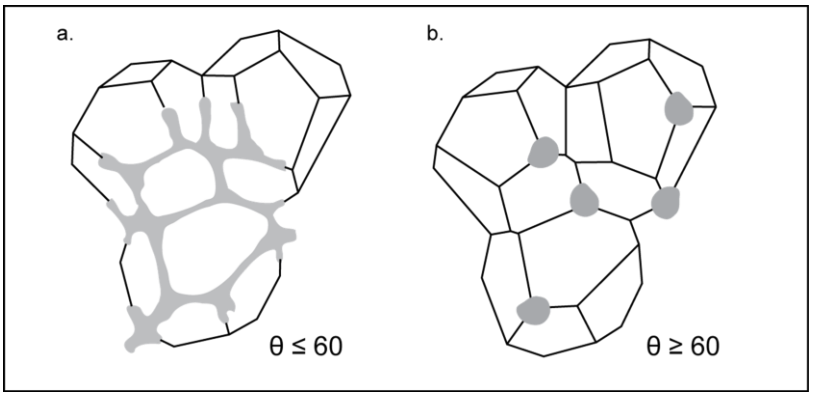

Fig. 5.13 a. Dihedral angle ≤ 60 forming an interconnected melt network. **b**. Dihedral angle ≥ 60 producing isolated melt pockets. Adapted from Laporte, (1994).

As noted earlier, the brown melt in BC93PAX12 is clearly not interconnected, at least in the 2-D section. At low degrees of partial melting, or conversely, in a crystal rich magma where small volumes of melt are present it could be hypothesised that the melt fraction is not interconnected throughout the system. The consequences of this scenario (schematically shown in Fig. 5.13 c) are that each melt fraction will evolve towards equilibration with the local environment.

In a silicic system, such as those which feed large rhyolitic eruptions e.g. the Taylor Creek Rhyolite and the Bishop Tuff, and in which variable Rb/Sr phases will have crystallised (e.g. micas and feldspars) geochemical gradients can be hypothesised to exist between inter-crystal melt and surrounding phases. The composition of the melt from which these phases are crystallising is therefore changing and spatially different. It could be further theorised that this scenario may account for the Sr-isotopic disequilibrium observed in sampled phases and glass from these erupted silicic flows e.g. Halliday et al., (1984); Duffield and Ruiz, (1998); Knesel et al., (1999). Upon

eruption, the spatial relationship between phases and the local environment in which they were crystallising is lost.

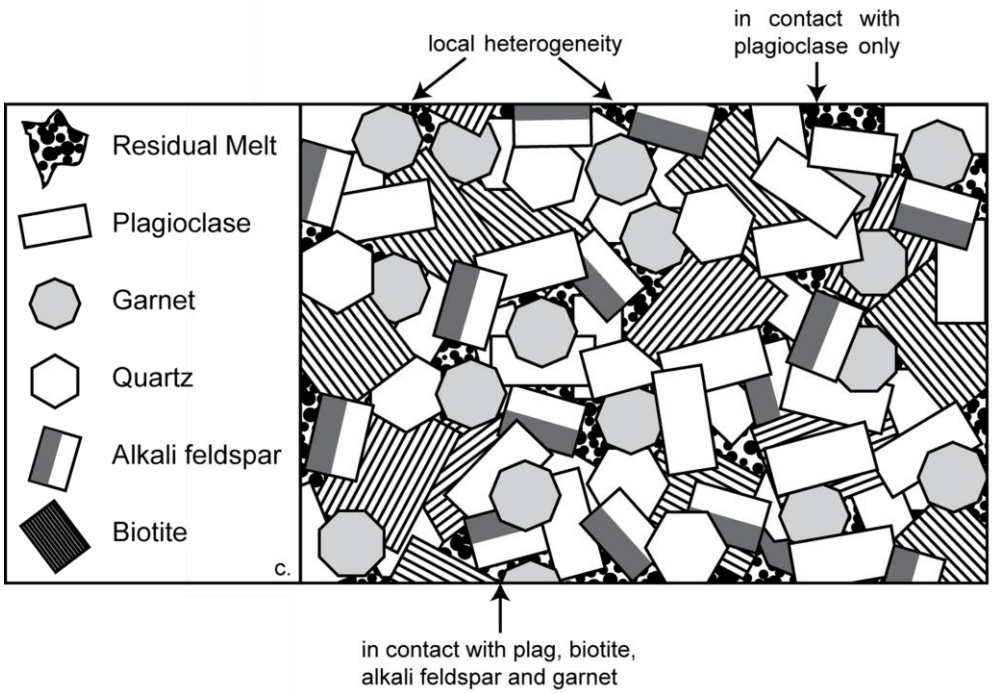

Fig. 5.13 c. Schematic illustrating how geochemical heterogeneity may arise in residual melt trapped within a crystal mush.

The coalescence of numerous crustal melts from compositionally distinct protoliths, each out of Sr-isotopic equilibrium (to variable degrees) has the potential to produce geochemically complex crustal magmas (Acosta-Vigil et al., 2010 and Deniel et al., 1987 respectively). The incorporation of multiple isotopically distinct melts into ascending magmas and/or the compositional evolution of disequilibrium anatectic melts as discussed throughout this paper is one mechanism through which the highly variable $^{87}Sr/^{86}Sr$ signatures in the lavas erupted from monogenetic centres at Pampas Aullagas and Quillacas may be attained (Fig. 5.2 a, see also Chapter 4). This process has also been applied to granitoid rocks where numerous melt pulses are inferred to construct Central Andean batholith bodies at depth (4-8 km). These reservoirs are understood to feed the recent ignimbritic activity (10- 1 Ma) across the Altiplano-Puna Plateau and it

has been suggested geochemical variability observed at the surface is (in part) controlled by variability within the source at depth (de Silva and Gosnold, 2007).

Similarly, the production of disequilibrium crustal melts has important implications for so-called "isotope basement mapping" whereby the Sr isotopic signatures in surface exposures of (predominantly) magmatic rocks are inferred to represent the composition of the crust through which they passed en route to the surface (e.g. Wörner et al., 1992). Thus, a relatively high initial $^{87}Sr/^{86}Sr$ signature may be interpreted as indicating the presence of old, Precambrian crust at depth (Blakes and Argles, 2003) whereas the high $^{87}Sr/^{86}Sr_i$ may equally be derived from relatively young crust in which the high Rb/Sr-bearing phases (and higher $^{87}Sr/^{86}Sr$) are melting out preferentially.

Whilst the Rb-Sr system during crustal anatexis will be primarily controlled by key rock forming minerals (as discussed), it is worth considering the Sm-Nd isotopic system which is also widely used to assess crust and mantle reservoir evolution and interaction. Considerably less experimental work has been carried out to assess and constrain the overriding control on the geochemical mass budgets of this system during crustal anatexis. It has been established however, that unlike the Rb-Sr system, where major constituent minerals i.e. micas and feldspars are crucial components, it is the accessory minerals, particularly apatite and monazite, which lever control on the Sm-Nd systematics (Zeng et al., 2005). Furthermore, it has been observed from field based studies of migmatites in Sierra Nevada, California that this isotopic system can preserve higher degrees of disequilibrium between melt and source than the Rb-Sr. This has been attributed to accessory phase control (Zeng et al., 2005).

It should be noted that results presented and references discussed here are intended not to;

1) imply that geochemical equilibrium is never attained during anatexis;
2) that equilibrium is not attained following a prograde heating event;
3) that current models of crustal contamination are invalid.

If timescales of melt extraction are sluggish relative to the timescales required for geochemical equilibrium through diffusion between melt and the restitic mineral assemblage then equilibrium will be promoted. Similarly, initial isotopic heterogeneities within a protolith may be eradicated by heating during orogenesis (Harris and Ayres, 1998). Simplistically, the process of crustal contamination can be viewed as a binary mixing process whereby a new composition is generated as a result of the interaction of two geochemically distinct end members. In reality though, the geochemical consequences of crustal anatexis are complex, the process of crustal anatexis is progressive and anatectic melts are not simple equilibrium partial melts.

5.7 Conclusions

AFC models are undoubtedly useful petrogenetic tools for investigating crustal contributions to mantle-derived magmas and this work does not intend to invalidate their use. However, the observations presented in this chapter suggest that such approaches should be used with caution and with a thorough understanding of their limitations. Additionally, the need for small-scale, microscopic studies has been documented if our understanding of the interaction and transfer between Earth's geochemical reservoirs is to advance.

In-situ analysis of anatectic melts associated with their crustal source reveals significant Sr-isotopic disequilibrium can exist between melt and protolith at the sub-mm scale.

This approach highlights the need for a greater appreciation of the complexities inherent to crustal anatexis and the geochemical consequences for modelling the contamination of volcanic rock suites. Hence existing models investigating the petrogenesis of open magmatic systems, combined with microanalysis of potential contaminants will lead to improved quantitative characterisation of crustal contamination.

Geology

Disequilibrium melting during crustal anatexis and implications for modeling open magmatic systems

Claire L. McLeod, Jon P. Davidson, Geoff M. Nowell and Shanaka L. de Silva

Geology 2012;40;435-438
doi: 10.1130/G33000.1

Notes

Disequilibrium melting during crustal anatexis and implications for modeling open magmatic systems

Claire L. McLeod[1], Jon P. Davidson[1], Geoff M. Nowell[1], and Shanaka L. de Silva[2]
[1]Northern Centre for Isotopic and Elemental Tracing (NCIET), Department of Earth Sciences, Durham University, South Road, Durham DH1 3LE, UK
[2]Oregon State University, Department of Geosciences, 104 Wilkinson Hall, Corvallis, Oregon 97331-5506, USA

ABSTRACT

Contamination of ascending mantle-derived magmas by the continental crust was investigated and modeled for a suite of volcanic rocks and entrained crustal xenoliths from the Central Andes using bulk geochemical compositions for mantle-derived and crustal end-members as dictated by traditional approaches. The assumption that the crustal contaminant in these open magmatic systems is a single composition was assessed through in situ analysis of quenched anatectic melt trapped within its crustal xenolith. Our results show for the first time significant chemical and Sr-isotopic disequilibrium between melt and source over submillimeter-length scales in a natural system. Sampled glass is rhyolitic in nature, enriched in large ion lithophile elements (LILE) and depleted in heavy rare earth elements (HREE). Analysis of the melt for its $^{87}Sr/^{86}Sr$ composition revealed isotopic heterogeneity ranging from 0.7164 to 0.7276. The isotopic disequilibrium between melt and source is understood to reflect the melting of minerals with different Rb/Sr (and therefore $^{87}Sr/^{86}Sr$) more quickly than the isotopic composition can diffusively equilibrate between melt and minerals. Our results suggest that the mechanism of crustal anatexis produces contaminating melts which are geochemically heterogeneous both spatially and temporally. Furthermore, time scales of Sr diffusion and anatectic melt segregation promote the preservation of isotopic disequilibrium at the micro (submillimeter) and macro (crustal) scale. This highlights the need for detailed microscopic investigations coupled with petrogenetic modeling in order to develop more robust characterization and quantification of contamination in open magmatic systems.

INTRODUCTION

During ascent toward the Earth's surface, primary basaltic magma has the potential to interact with overlying crustal rocks. This has been recognized since Bowen (1928) argued that assimilation of foreign material into a magma body should be treated as an inevitable consequence of fractional crystallization, with a positive feedback loop between the extraction of heat due to assimilation and the generation of latent heat of crystallization as crystallization is promoted by heat extraction and cooling. The degree to which mantle and crustal reservoirs have contributed to the geochemical signatures of volcanic rocks at continental arcs is frequently assessed through combined assimilation and fractional crystallization models (e.g., Spera and Bohrson, 2001). However the intricacies inherent to crustal anatexis, and thus the nature of contaminating crustal melts, are left unconsidered.

In order to investigate in detail the geochemical consequences of crustal anatexis and the subsequent implications for modeling contamination processes, the compositions of crustal xenoliths and their host lavas were investigated. The xenoliths preserve rare anatectic melts, solidified to glass, in their protoliths. It is the composition of this glass that offers a unique insight into the behavior of the crust in open magmatic systems and which challenges our understanding of crustal anatexis and subsequent contamination of mantle-derived magmas.

SAMPLES

Crustal xenolith samples are hosted in trachyandesite/dacite lavas that erupted from monogenetic volcanic centers at Pampas Aullagas (1.89 Ma) and Quillacas (1.42 Ma) on the Bolivian Altiplano, Central Andes. Prior to eruption, these magmas passed through ~70 km of continental crust (for locations, see Davidson and de Silva, 1992). Entrained xenolith lithologies vary from quartzite to granulites, with garnet mica schists, rarer gneisses, and several igneous lithologies including diorites and microgranites. Whole rock analyses of sampled lavas clearly indicate crustal contamination has occurred during petrogenesis. This is demonstrated by their extreme strontium (Sr)-isotopic diversity (Fig. 1A) and with $^{87}Sr/^{86}Sr$ correlating with indices of differentiation such as SiO_2 (Fig. 1B). All sample compositions are provided in the GSA Data Repository[1].

[1]GSA Data Repository item 2012114, analytical methods, major element data, and model parameters, is available online at www.geosociety.org/pubs/ft2012.htm, or on request from editing@geosociety.org or Documents Secretary, GSA, P.O. Box 9140, Boulder, CO 80301, USA.

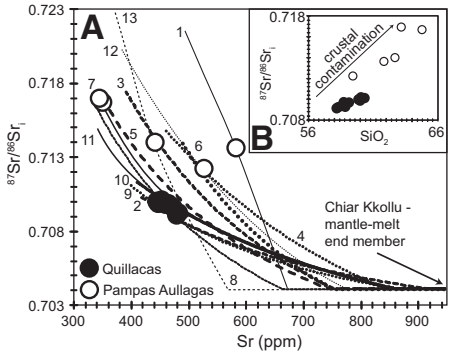

Figure 1. A: Sr-isotopic diversity exhibited by sampled lavas. Energy-constrained assimilation–fractional crystallization [(EC) AFC] curves use sampled bulk rock crustal xenoliths to contaminate a mantle-derived Andean basalt (Chiar Kkollu). Solutions shown are those that best modeled the data. Compositions of end members and model parameters for each numbered curve (1–13) are provided in the Data Repository (see footnote 1). B: Graph showing the increase of $^{87}Sr/^{86}Sr$ with increasing SiO_2 as evidence for AFC during the petrogenesis of sampled lavas (symbols as in A).

MODELING CRUSTAL CONTAMINATION

Numerous formulations aimed at evaluating geochemical evolution in open magmatic systems have been developed over the past few decades (e.g., Taylor, 1980; DePaolo, 1981). The objective of these models is to meet the necessity for material mass balance, while accounting for observed geochemical trends. Although a powerful petrogenetic tool, use of these models is only justifiable if the end member compositions are known; i.e., those of the parental mantle-melt and those of the crustal assimilant, and in many studies at least one of those is unknown. Additionally, rates of assimilation to fractional crystallization (r) and partition coefficients (e.g., D_{Sr}) need to be well constrained. The contaminated nature of the sampled lavas was investigated using the Energy-Constrained Assimilation–Fractional Crystallization [(EC) AFC] model of Spera and Bohrson, (2001). All sampled xenoliths are potential crustal lithologies with which ascending magmas may have interacted. Choosing a suitable parental magma composition is challenging, as no true basalts have erupted recently in the Central Andes. Modeling was therefore carried out using an

older Andean primitive magma represented by a Miocene sill (Chiar Kkollu) from 60 km WNW of the field area. The $^{87}Sr/^{86}Sr$ of the Chiar Kkollu basalt (0.7041) indicates relatively little assimilation of, and contamination by, the continental crust, and its composition may be the closest representative of a parental melt that is currently known for the region (Davidson and de Silva, 1992). Results are presented in Figure 1A, but offer only a number of possible solutions that model observed geochemical trends (see the Data Repository for model input parameters and detailed petrographic descriptions of xenolith lithologies).

TABLE 1. TRACE ELEMENT AND Sr-ISOTOPE DATA FOR THE BULK XENOLITH (BC93PAX12) AND THE SAMPLED GLASS (VALUES REPORTED IN PPM UNLESS STATED OTHERWISE)*

	Whole rock	Glass						
	BC93PAX12	1	2	3	4	5	6	Bulk
Ba	138.4	357.1	563.6	520.5	1893	699.2	146.5	696.7
Rb	27.3	101.8	172.2	178.4	226.6	236.1	84.3	166.7
Th	7.3	2.2	2.2	2.5	4.7	3.8	4.6	3.3
U	1.4	0.8	1.4	1.3	2	1.6	2.2	1.5
Nb	17.1	4	1.5	1.5	4	2.6	4.6	3
La	22.4	9	10.8	10.7	21	15	14.9	13.6
Ce	46	20.7	30.4	29.9	49.6	37.4	66.8	39.1
Sr	18.5	34.7	56.3	32.3	107.2	37.1	37.2	50.8
Nd	22.8	12.2	15.4	16.3	26.9	21.4	18	18.4
Sm	4.7	2.9	3.9	4	6.2	5.3	3.5	4.3
Zr	32.8	54.9	112.1	103.8	135.2	119.1	89.7	102.5
Hf	1.1	1.2	2.9	2.6	3.2	2.9	2.2	2.5
Ti (wt%)	0.3	0.3	0.3	0.3	0.5	0.4	0.3	0.3
Tb	0.8	0.4	-	0.5	0.9	-	0.5	0.6
Y	30.2	7.6	9.8	11	19.6	16.7	21	14.3
Yb	5.7	0.3	0.4	0.5	0.7	0.7	1.8	0.7
$^{87}Sr/^{86}Sr$	0.7173	0.7176	0.7209	0.7252	0.7246	0.7281	0.7166	-
$^{87}Sr/^{86}Sr_i$	-	0.7174	0.7207	0.7248	0.7244	0.7276	0.7164	0.7223

*Also shown is a calculated bulk composition for the anatectic melt.

CRUSTAL ANATEXIS

The process of crustal anatexis is fundamental to continental crust differentiation yet is difficult to evaluate due to anatectic melts having segregated from their protolith and been subsequently emplaced at shallower crustal levels. The dominant mechanism of anatectic melt formation in the continental crust is the (fluid-absent) incongruent melting of hydrous silicates; e.g., the dehydration melting reaction of biotite: Bt + Pl + Qz + Alms forms Grt (±Cor) ± Ksp + Melt (Patiño Douce et al., 1990), which leaves behind a less hydrous restitic assemblage. At equilibrium, partial melting redistributes trace elements as a function of their partition coefficients. Isotope ratios, however, are unaffected by this process and have therefore been implemented as tracers of geochemical reservoirs throughout Earth.

The natural occurrence of preserved anatectic melt offers a rare insight into the primary compositions of potential crustal contaminants to mantle-derived magmas and constraints on the nature of crustal melts produced during orogenesis. Quenched anatectic melt within one sample (BC93PAX12) was chosen for an in-depth geochemical study. Trace element and Sr-isotopic data are presented in Table. 1. (Major element data, analytical methods, and standards run throughout the course of this study are detailed in the Data Repository). The sample is a garnet-sillimanite gneiss and is characterized by biotite, sillimanite, garnet, plagioclase, quartz, minor anatase and opaque phases, accessory monazite and ~2% anatectic melt. Euhedral hercynitic spinel (<100 µm) is present within the melt pools. This phase has previously been shown to be a common product of the incongruent breakdown of biotite (e.g., Cesare, 2000). All analyzed glass is rhyolitic in nature (average wt% Na_2O + wt% K_2O of 5.82 ± 1; 2σ; average wt% SiO_2 of 73.19% ± 1.75; 2σ, n = 124). Analyzed glass shows enrichment in LILE (Ba, Rb; Fig. 2) and depletion in the HREE that are retained in residual garnet (Fig. 2). The Nb depletion recorded in the glass is inferred to represent the stability of anatase, the metastable TiO_2 polymorph that is present as acicular crystals (<200 µm). The occurrence of anatase (as opposed to rutile, the more common form of TiO_2) is consistent with the experimental observation that anatase forms under rapid cooling conditions (i.e., quenching), whereas rutile will crystallize under near-equilibrium solidification conditions (Li and Ishigaki, 2002). Analysis (by microdrill) for the Sr-isotopic composition of the quenched anatectic melt (Fig. 3A) reveals extreme variability over submillimeter-length scales, and significant isotopic disequilibrium between the melt and its source (Fig. 3B). Glass samples 5 and 6 bracket the range at 0.7276–0.7164 ($^{87}Sr/^{86}Sr_i$), respectively, but are within 200 µm of each other. The sampled anatectic glass is more radiogenic than the host lavas (or of any Pliocene–Pleistocene volcanic rock in the Central Andes), indicating that the crustal signature inferred from the Sr-isotopic composition of volcanic rocks at the surface may provide little (if any) information about (1) how it got there, and (2) the nature of the contaminant at depth.

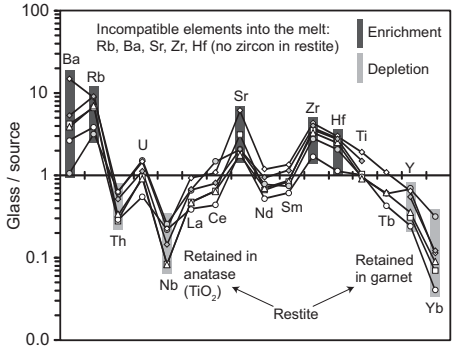

Figure 2. Trace-element composition of sampled glass normalized to bulk host xenolith (data in Table 1).

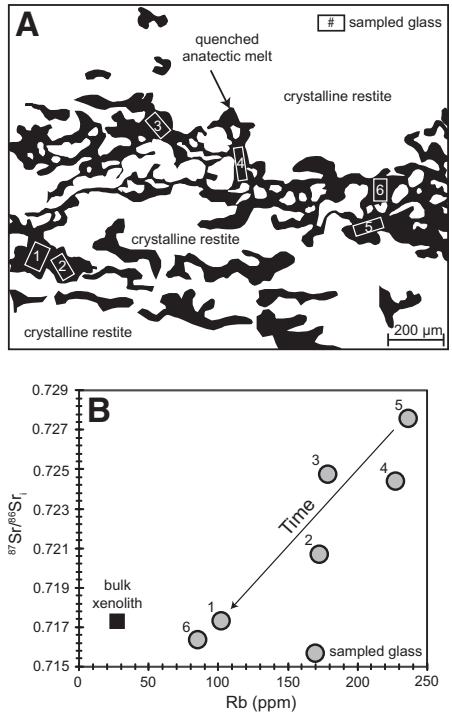

Figure 3. A: Sketch depicting quenched glass (black) and unmelted crystalline restite (white) of sample BC93PAX12. Sampled areas are outlined, and correspond to the sample numbers in Table 1. B: Sr-isotopic disequilibrium between anatectic melt and bulk source. Glass compositions are age corrected for the Pliocene age of lava eruption.

DISEQUILIBRIUM MELTING AND MELT ASSIMILATION

It is generally accepted that major and trace element abundances of melts from silicate rocks change as melting progresses. Isotope ratios, however, are generally taken to reflect those of the source rock, because diffusive equilibrium at the high temperatures of melting is capable of "keeping up" with the melting process. Indeed, much of our understanding of isotopically defined mantle reservoirs is predicated on this premise (Hofmann and Hart, 1978). However, if diffusion cannot keep pace with melting, then isotopic compositions will vary with the contributions of Sr from the individual phases present within the source (e.g., Rushmer and Knesel, 2010). Melting will typically begin with preferential breakdown of high Rb/Sr hydrous phases, producing an initial melt with a higher $^{87}Sr/^{86}Sr$ than the bulk source. If melting progresses relatively rapidly, so that diffusive equilibration of $^{87}Sr/^{86}Sr$ does not occur, additional phases contribute Sr with different $^{87}Sr/^{86}Sr$, and the composition of the melt will change as shown schematically in Figure 4A. Feldspar, for instance, has a lower Rb/Sr and will consequently contribute less radiogenic Sr than biotite.

Analysis of anatectic melts shows significant Sr-isotopic disequilibrium can exist between product and protolith at the submillimeter scale (Fig. 3B). Melting is likely to be non-modal and the degree of disequilibrium is likely to be heterogeneous throughout the melt, both spatially and temporally, as the $^{87}Sr/^{86}Sr$ compositions will be controlled by the relative proportions of the Rb/Sr phases melting at any given site (Fig. 4A). Initially high $^{87}Sr/^{86}Sr$-bearing melts produced by biotite dehydration will be diluted if melting continues and the less radiogenic phases breakdown; e.g., feldspar. As anatexis proceeds, the $^{87}Sr/^{86}Sr$ of the contaminant will be lowered, hence it is ultimately the relative rates at which the different Rb/Sr phases contribute to the melt that governs its compositional evolution (Duffield and Ruiz, 1998). The potential implications this process has for crustal contamination in open magmatic systems, and the geochemical fingerprint this may leave in volcanic rocks, is illustrated in Figure 4B for our Bolivian lava samples. Note that we do not have any way of knowing the time at which melts are produced, as shown schematically in Figure 4A. However, we can use Rb as a proxy, in that early melts will be dominated by biotite (high Rb) while later melts contain a greater contribution from feldspar (low Rb). Thus, in Figure 3B (and Fig. 4B), glass sample 5 is the earliest produced, while 6 is the last.

In short, the $^{87}Sr/^{86}Sr$ and Sr contents of bulk contaminants may be inappropriate input choices for modeling open system processes. Instead, we need to try and account for (1) the stoichiometry of melting reactions which control the changing proportions of phases entering the melt; (2) the rate of melting with respect to Sr diffusivity in the melt, which defines the balance between melt production and the capacity to equilibrate diffusively; (3) the composition of phases consumed, which dictates, in conjunction with 1, the mass balance of Sr in the melt at any given time; (4) the grain size of phases, which constrains the length scales of diffusive equilibration in the solid phases; and (5) the time scales of melt segregation. The majority of these processes are left unaccounted for in the current petrogenetic models.

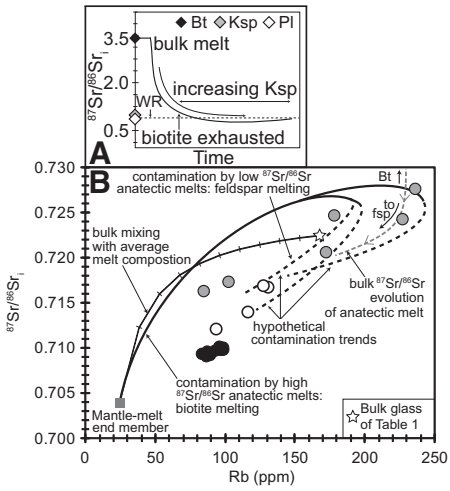

Figure 4. A: Hypothetical evolution of the Sr-isotopic composition of an anatectic melt. Starting compositions of mineral phases are from Knesel and Davidson, 2002. Initially, biotite (high Rb/Sr) is the only phase breaking down. As melting continues, other Rb/Sr bearing phases begin to melt; e.g., plagioclase (Pl) and alkali feldspar (Ksp). B: Solid gray-filled circles represent the compositions of sampled melt compositions. Remaining symbols as in Figure 1. The bulk mixing line (shown at 10% intervals) indicates bulk mixing between the Chiar Kkollu lava and the average composition of sampled anatectic glasses (Table 1). Realistically, however, the composition of the contaminant changes (see text for discussion). The solid black, and associated dashed black, trends illustrate the potential contamination pathways ascending mantle-derived magmas assimilating compositionally variable anatectic melts will have in terms of their Rb versus $^{87}Sr/^{86}Sr$ (based on bulk melt composition with Rb content used as a proxy for time).

IMPLICATIONS FOR NATURAL SYSTEMS

The observation of Sr-isotopic disequilibrium in anatectic melts supports interpretations from experimental work that has previously aimed to evaluate the process of crustal anatexis (e.g., Knesel and Davidson, 1996). These studies emphasize the importance of crustal source mineralogy on governing anatectic melt composition and relative Sr diffusion time scales. Ultimately, diffusion will work to eradicate compositional gradients and achieve isotopic equilibration, provided the melt remains in contact with the residuum through an interconnected grain boundary network which will act as a diffusion pathway. Therefore, in order for disequilibrium to be preserved, crustal melts must segregate on time scales shorter than those required for diffusive equilibration (e.g., Sawyer, 1991). Segregation of small-degree, anatectic partial melts (e.g., Philpotts and Asher, 1993, and those sampled by this study) from their protoliths has been shown to occur on rapid time scales (10^2–10^4 yr; Sawyer, 1994). These time scales are significantly faster than those required for diffusion to erase Sr compositional gradients; e.g., diffusion in feldspars (0.1–1 cm) at typical temperatures of anatexis (800–1000 °C) ranges between a few million years and tens of millions of years (Tommasini and Davies, 1997). This in turn implies disequilibrium melting may be an important process in governing the composition of crustal-scale melts (up to 40% melting, Barbero et al., 1995).

The micro-scale observations detailed in Figures 3A and 3B invite speculation on the potential significance of larger-scale Sr-isotopic disequilibrium in the production of anatectic melts, which may play a fundamental role in crustal differentiation (e.g., Sawyer, 1994). In order for Sr-isotopic disequilibrium melting to be preserved on a crustal scale, the time scale for melt segregation has to be (in comparison to orogenesis) instantaneous (Barbero et al., 1995). Evidence for the preservation of disequilibrium melting during regional metamorphism can be found in anatectic granitoids from Toledo, Spain, where sampled leucogranites are out of isotopic equilibrium with their granulitic restite. Partial melting did not produce isotopically homogenous melts, and Sr-isotope disequilibrium is observed on the mineral scale. In accordance with this study, Barbero et al. (1995) invoked the non-modal breakdown of variable Rb/Sr phases (biotite and plagioclase) along with restricted Sr-diffusion in order to account for the observed disequilibrium. Similarly, Tommasini and Davies (1997) observed Sr-isotopic disequilibrium melting during contact metamorphism in the Sierra Nevada, California, where trachyandesites intrude a granitic batholith. Sampled glasses were out of equilibrium at the outcrop and hand-specimen scale (tens of meters and centimeters, respectively).

Small degrees of partial melt, such as those sampled by this study, do not reach their critical mass fraction (CMF) needed to migrate due to buoyancy alone (~30%; Arzi, 1978). However, experimental studies have shown that low melt fractions (1%–5%) can develop interconnected

networks between grain boundaries which, in turn, form a permeable matrix from which melt is extractable; e.g., through non-coaxial deformation during melting (Sawyer, 1991). This process has similarly been shown to occur on a crustal scale during pluton emplacement (Guglielmo, 1993). It can therefore be demonstrated that non-modal, anatectic melts that exhibit heterogeneity with respect to Sr isotopes can (1) be produced in the crust on the micro- and macro scale, and (2) segregate on time scales that will preserve melt-source disequilibrium. In Figure 3A, the melt fraction is estimated at 18% and clearly not interconnected, hence opportunities for mixing and diffusive equilibration must rely on either a three-dimensional network not fully apparent in the two-dimensional section, or on tiny, unseen, films along grain boundaries.

The coalescence of numerous crustal melts from compositionally distinct protoliths, each out of Sr-isotopic equilibrium (to variable degrees), has the potential to produce geochemically complex crustal magmas (Acosta-Vigil et al., 2010). The incorporation of multiple isotopically distinct melts into ascending magmas and/or the compositional evolution of disequilibrium anatectic melts as discussed throughout this paper, can be envisaged as contributing to the highly variable $^{87}Sr/^{86}Sr$ signatures in the lavas erupted at Pampas Aullagas and Quillacas (Figs. 1A, 1B, and 4B). Similarly, the production of disequilibrium crustal melts has important implications for so-called "isotope basement mapping" whereby the Sr-isotopic signatures in surface exposures of (predominantly) magmatic rocks are inferred to represent the composition of the crust through which they passed en route to the surface (e.g., Wörner et al., 1992). Thus, a relatively high initial $^{87}Sr/^{86}Sr$ signature may be interpreted as indicating the presence of old, Precambrian crust at depth. Alternatively, this high $^{87}Sr/^{86}Sr_i$ may be derived from relatively young crust in which the high Rb/Sr-bearing phases are melting out preferentially.

Simplistically, the process of crustal contamination can be viewed as a binary mixing process whereby a new composition is generated as a result of the interaction of two geochemically distinct end members. In reality, the geochemical consequences of crustal anatexis are complex, the process of crustal anatexis is progressive, and anatectic melts are not simple equilibrium partial melts of a source.

CONCLUSIONS

Undoubtedly [(EC)AFC] models are useful petrogenetic tools for investigating crustal contributions to mantle-derived magmas, and we do not intend to invalidate their use; however, our observations suggest that such approaches should be used with caution and with a thorough understanding of their limitations. We have demonstrated the need for small-scale, microscopic studies if our understanding of the interaction and transfer between Earth's geochemical reservoirs is to advance. In situ analysis of anatectic melts reveals for the first time the scale at which Sr-isotopic disequilibrium within potential contaminating melts can occur. Our approach highlights the need for a greater appreciation of the complexities inherent to crustal anatexis and the subsequent geochemical consequences for modeling contamination. The use of existing models in conjunction with microanalysis of potential contaminants will therefore lead to an improved, quantitative characterization of crustal contamination.

ACKNOWLEDGMENTS

Financial support was provided to McLeod by Natural Environment Research Council studentship NE/G524036/1. Davidson and de Silva acknowledge U.S. National Science Foundation (grants EAR 8916496, EAR 0838536, and EAR 0908324) support for past and current work in the Central Andes. Additional thanks are extended to the Bolivian Geological Survey (GEOBOL), which provided assistance with the original fieldwork. We thank Christina Hansen, University of California–Los Angeles, for preliminary data collection; Chris Ottley, Durham University, for guidance during use of the ICPMS; and Sarah Collins and Kathy Mather who provided useful comments on early manuscript drafts. Further thanks are owed to Antonio Acosta-Vigil and two anonymous reviewers who provided detailed and constructive reviews that helped improve this manuscript.

REFERENCES CITED

Acosta-Vigil, A., Buick, I., Hermann, J., Cesare, B., Rubatto, D., London, D., and Morgan, G.B., VI, 2010, Mechanisms of crustal anatexis: A geochemical study of partially melted metapelitic enclaves and host dacite, SE Spain: Journal of Petrology, v. 51, p. 785–821, doi:10.1093/petrology/egp095.

Arzi, A.A., 1978, Critical phenomena in the rheology of partially melted rocks: Tectonophysics, v. 44, p. 173–184, doi:10.1016/0040-1951(78)90069-0.

Barbero, L., Villaseca, C., Rogers, G., and Brown, P.E., 1995, Geochemical and isotopic disequilibrium in crustal melting: An insight from the anatectic granitoids from Toledo, Spain: Journal of Geophysical Research, v. 100, p. 15745–15765, doi:10.1029/95JB00036.

Bowen, N.L., 1928, The Evolution of the Igneous Rocks: New York, Dover Publications.

Cesare, B., 2000, Incongruent melting of biotite to spinel in a quartz-free restite at El Joyazo (SE Spain): Textures and reaction characterisation: Contributions to Mineralogy and Petrology, v. 139, p. 273–284, doi:10.1007/s004100000137.

Davidson, J.P., and de Silva, S.L., 1992, Volcanic rocks from the Bolivian Altiplano: Insights into crustal structure, contamination and magma genesis in the Central Andes: Geology, v. 20, p. 1127–1130, doi:10.1130/0091-7613(1992)020<1127:VRFTBA>2.3.CO;2.

DePaolo, D.J., 1981, Trace element and isotopic effects of combined wallrock assimilation and fractional crystallization: Earth and Planetary Science Letters, v. 53, p. 189–202, doi:10.1016/0012-821X(81)90153-9.

Duffield, W.A., and Ruiz, J., 1998, A model that helps explain Sr-isotope disequilibrium between feldspar phenocrysts and melt in large-volume silicic magma systems: Journal of Volcanology and Geothermal Research, v. 87, p. 7–13, doi:10.1016/S0377-0273(98)00071-7.

Guglielmo, G., Jr., 1993, Interference between pluton expansion and non-coaxial tectonic deformation: Three-dimensional computer model and field implications: Journal of Structural Geology, v. 15, p. 593–608, doi:10.1016/0191-8141(93)90150-9.

Hofmann, A.W., and Hart, S.R., 1978, An assessment of local and regional isotopic equilibrium in the mantle: Earth and Planetary Science Letters, v. 38, p. 44–62, doi:10.1016/0012-821X(78)90125-5.

Knesel, K., and Davidson, J.P., 1996, Isotopic disequilibrium during melting of granite and implications for crustal contamination of magmas: Geology, v. 24, p. 243–246, doi:10.1130/0091-7613(1996)024<0243:IDDMOG>2.3.CO;2.

Li, Y., and Ishigaki, T., 2002, Thermodynamic analysis of nucleation of anatase and rutile from TiO_2 melt: Journal of Crystal Growth, v. 242, p. 511–516, doi:10.1016/S0022-0248(02)01438-0.

Patiño Douce, A.E., Humphreys, E.D., and Johnston, A.D., 1990, Anatexis and metamorphism in tectonically thickened continental crust exemplified by the Sevier hinterland, western North America: Earth and Planetary Science Letters, v. 97, p. 290–315, doi:10.1016/0012-821X(90)90048-3.

Philpotts, A.R., and Asher, P.M., 1993, Wallrock melting and reaction effects along the Higganum diabase dike in Connecticut: contamination of a continental flood basalt feeder: Journal of Petrology, v. 34, p. 1029–1058.

Rushmer, T., and Knesel, K., 2010, Defining Geochemical signatures and timescales of melting processes in the crust: An experimental tale of melt segregation, migration and emplacement, *in* Dosseto, A., Turner, S.P. and Van Orman, J.A., eds., Timescales of Magmatic Processes from Core to Atmosphere: Wiley-Blackwell.

Sawyer, E.W., 1991, Disequilibrium melting and the rate of melt-residuum separation during migmatization of mafic rocks from the Grenville Front, Quebec: Journal of Petrology, v. 32, p. 701–738.

Sawyer, E.W., 1994, Melt segregation in the continental crust: Geology, v. 22, p. 1019–1022, doi:10.1130/0091-7613(1994)022<1019:MSITCC>2.3.CO;2.

Spera, F.J., and Bohrson, W.A., 2001, Energy-constrained open-system magmatic processes I: General model and energy-constrained assimilation and fractional crystallization (EC-AFC) formulation: Journal of Petrology, v. 42, p. 999–1018, doi:10.1093/petrology/42.5.999.

Taylor, H.P., 1980, The effects of assimilation of country rocks by magmas on $^{18}O/^{16}O$ and $^{87}Sr/^{86}Sr$ systematic in igneous rock: Earth and Planetary Science Letters, v. 47, p. 243–254, doi:10.1016/0012-821X(80)90040-0.

Tommasini, S., and Davies, G.R., 1997, Isotope disequilibrium during anatexis: A case study of contact melting, Sierra Nevada, California: Earth and Planetary Science Letters, v. 148, p. 273–285, doi:10.1016/S0012-821X(97)00031-9.

Wörner, G., Moorbath, S., and Harmon, R.S., 1992, Andean Cenozoic centres reflect basement domains: Geology, v. 20, p. 1103–1106, doi:10.1130/0091-7613(1992)020<1103:ACVCRB>2.3.CO;2.

Manuscript received 7 November 2011
Manuscript accepted 16 December 2011

Printed in USA

Publisher: GSA
Journal: GEOL: Geology
Article ID: G33000

Disequilibrium melting during crustal anatexis and implications for modeling open magmatic systems

Claire L. McLeod[1], Jon P. Davidson[1], Geoff M. Nowell[1], and Shanaka L. de Silva[2]

[1]Northern Centre for Isotopic and Elemental Tracing (NCIET), Department of Earth Sciences, Durham University, South Road, Durham DH1 3LE, UK

[2]Oregon State University, Department of Geosciences, 104 Wilkinson Hall, Corvallis, Oregon 97331-5506, USA

ABSTRACT

Contamination of ascending mantle-derived magmas by the continental crust was investigated and modeled for a suite of volcanic rocks and entrained crustal xenoliths from the Central Andes using bulk geochemical compositions for mantle-derived and crustal end-members as dictated by traditional approaches. The assumption that the crustal contaminant in these open magmatic systems is a single composition was assessed through in situ analysis of quenched anatectic melt trapped within its crustal xenolith. Our results show for the first time significant chemical and Sr-isotopic disequilibrium between melt and source over submillimeter-length scales in a natural system. Sampled glass is rhyolitic in nature, enriched in large ion lithophile elements (LILE) and depleted in heavy rare earth elements (HREE). Analysis of the melt for its $^{87}Sr/^{86}Sr$ composition revealed isotopic heterogeneity ranging from 0.7164 to 0.7276. The isotopic disequilibrium between melt and source is understood to reflect the melting of minerals with different Rb/Sr (and therefore $^{87}Sr/^{86}Sr$) more quickly than the isotopic composition can diffusively equilibrate between melt and minerals. Our results suggest that the mechanism of crustal anatexis

produces contaminating melts which are geochemically heterogeneous both spatially and temporally. Furthermore, time scales of Sr diffusion and anatectic melt segregation promote the preservation of isotopic disequilibrium at the micro (submillimeter) and macro (crustal) scale. This highlights the need for detailed microscopic investigations coupled with petrogenetic modeling in order to develop more robust characterization and quantification of contamination in open magmatic systems.

INTRODUCTION

During ascent toward the Earth's surface, primary basaltic magma has the potential to interact with overlying crustal rocks. This has been recognized since Bowen (1928) argued that assimilation of foreign material into a magma body should be treated as an inevitable consequence of fractional crystallization, with a positive feedback loop between the extraction of heat due to assimilation and the generation of latent heat of crystallization as crystallization is promoted by heat extraction and cooling. The degree to which mantle and crustal reservoirs have contributed to the geochemical signatures of volcanic rocks at continental arcs is frequently assessed through combined assimilation and fractional crystallization models (e.g., Spera and Bohrson, 2001). However the intricacies inherent to crustal anatexis, and thus the nature of contaminating crustal melts, are left unconsidered.

In order to investigate in detail the geochemical consequences of crustal anatexis and the subsequent implications for modeling contamination processes, the compositions of crustal xenoliths and their host lavas were investigated. The xenoliths preserve rare anatectic melts, solidified to glass, in their protoliths. It is the composition of this glass that offers a unique insight into the behavior of the crust in open magmatic systems and which

challenges our understanding of crustal anatexis and subsequent contamination of mantle-derived magmas.

SAMPLES

Crustal xenolith samples are hosted in trachyandesite/dacite lavas that erupted from monogenetic volcanic centers at Pampas Aullagas (1.89 Ma) and Quillacas (1.42 Ma) on the Bolivian Altiplano, Central Andes. Prior to eruption, these magmas passed through ~70 km of continental crust (for locations, see Davidson and de Silva, 1992). Entrained xenolith lithologies vary from quartzite to granulites, with garnet mica schists, rarer gneisses, and several igneous lithologies including diorites and microgranites. Whole rock analyses of sampled lavas clearly indicate crustal contamination has occurred during petrogenesis. This is demonstrated by their extreme strontium (Sr)-isotopic diversity (Fig. 1A) and with $^{87}Sr/^{86}Sr$ correlating with indices of differentiation such as SiO_2 (Fig. 1B). All sample compositions are provided in the GSA Data Repository[1].

MODELING CRUSTAL CONTAMINATION

Numerous formulations aimed at evaluating geochemical evolution in open magmatic systems have been developed over the past few decades (e.g., Taylor, 1980; DePaolo, 1981). The objective of these models is to meet the necessity for material mass balance, while accounting for observed geochemical trends. Although a powerful petrogenetic tool, use of these models is only justifiable if the end member compositions are known; i.e., those of the parental mantle-melt and those of the crustal assimilant, and in many studies at least one of those is unknown. Additionally, rates of assimilation to fractional crystallization (r) and partition coefficients (e.g., D_{Sr}) need to be well

constrained. The contaminated nature of the sampled lavas were investigated using the Energy-Constrained Assimilation–Fractional Crystallization [(EC)AFC] model of Spera and Bohrson, (2001). All sampled xenoliths are potential crustal lithologies with which ascending magmas may have interacted. Choosing a suitable parental magma composition is challenging, as no true basalts have erupted recently in the Central Andes. Modeling was therefore carried out using an older Andean primitive magma represented by a Miocene sill (Chiar Kkollu) from 60 km WNW of the field area. The $^{87}Sr/^{86}Sr$ of the Chiar Kkollu basalt (0.7041) indicates relatively little assimilation of, and contamination by, the continental crust, and its composition may be the closest representative of a parental melt that is currently known for the region (Davidson and de Silva, 1992). Results are presented in Figure 1A, but offer only a number of possible solutions that model observed geochemical trends (see the Data Repository for model input parameters and detailed petrographic descriptions of xenolith lithologies).

CRUSTAL ANATEXIS

The process of crustal anatexis is fundamental to continental crust differentiation yet is difficult to evaluate due to anatectic melts having segregated from their protolith and been subsequently emplaced at shallower crustal levels. The dominant mechanism of anatectic melt formation in the continental crust is the (fluid-absent) incongruent melting of hydrous silicates; e.g., the dehydration melting reaction of biotite: Bt + Pl + Qz + Alms forms Grt (± Cor) ± Ksp + Melt (Patiño Douce et al., 1990), which leaves behind a less hydrous restitic assemblage. At equilibrium, partial melting redistributes trace elements as a function of their partition coefficients. Isotope ratios, however, are unaffected by this

process and have therefore been implemented as tracers of geochemical reservoirs throughout Earth.

The natural occurrence of preserved anatectic melt offers a rare insight into the primary compositions of potential crustal contaminants to mantle-derived magmas and constraints on the nature of crustal melts produced during orogenesis. Quenched anatectic melt within one sample (BC93PAX12) was chosen for an in-depth geochemical study. Trace element and Sr-isotopic data are presented in Table. 1. (Major element data, analytical methods, and standards run throughout the course of this study are detailed in the Data Repository). The sample is garnet-sillimanite gneiss and is characterized by biotite, sillimanite, garnet, plagioclase, quartz, minor anatase and opaque phases, accessory monazite and zircon and ~2% anatectic melt. Euhedral hercynitic spinel (<100 μm) is present within the melt pools. This phase has previously been shown to be a common product of the incongruent breakdown of biotite (e.g., Cesare, 2000). All analyzed glass is rhyolitic in nature (average wt% Na_2O + wt% K_2O of 5.82 ± 1; 2σ; average wt% SiO_2 of 73.19% ± 1.75; 2σ, n = 124). Analyzed glass shows enrichment in LILE (Ba, Rb; Fig. 2) and depletion in the HREEthat are retained in residual garnet (Fig. 2). The Nb depletion recorded in the glass is inferred to represent the stability of anatase, the metastable TiO_2 polymorph that is present as acicular crystals (<200 μm). The occurrence of anatase (as opposed to rutile, the more common form of TiO_2) is consistent with the experimental observation that anatase forms under rapid cooling conditions (i.e., quenching), whereas rutile will crystallize under near-equilibrium solidification conditions (Li and Ishigaki, 2002). Analysis (by microdrill) for the Sr-isotopic composition of the quenched anatectic melt (Fig. 3A) reveals extreme variability over submillimeter-length scales, and significant isotopic disequilibrium between the melt and its source (Fig. 3B). Glass samples 5 and 6

bracket the range at 0.7276–0.7164 ($^{87}Sr/^{86}Sr_i$), respectively, but are within 200 µm of each other. The sampled anatectic glass is more radiogenic than the host lavas (or of any Pliocene–Pleistocene volcanic rock in the Central Andes), indicating that the crustal signature inferred from the Sr-isotopic composition of volcanic rocks at the surface may provide little (if any) information about (1) how it got there, and (2) the nature of the contaminant at depth.

DISEQUILIBRIUM MELTING AND MELT ASSIMILATION

It is generally accepted that major and trace element abundances of melts from silicate rocks change as melting progresses. Isotope ratios, however, are generally taken to reflect those of the source rock, because diffusive equilibrium at the high temperatures of melting is capable of "keeping up" with the melting process. Indeed, much of our understanding of isotopically defined mantle reservoirs is predicated on this premise (Hofmann and Hart, 1978). However, if diffusion cannot keep pace with melting, then isotopic compositions will vary with the contributions of Sr from the individual phases present within the source (e.g., Rushmer and Knesel, 2010). Melting will typically begin with preferential breakdown of high Rb/Sr hydrous phases, producing an initial melt with a higher $^{87}Sr/^{86}Sr$ than the bulk source. If melting progresses relatively rapidly, so that diffusive equilibration of $^{87}Sr/^{86}Sr$ does not occur, additional phases contribute Sr with different $^{87}Sr/^{86}Sr$, and the composition of the melt will change as shown schematically in Figure 4A. Feldspar, for instance, has a lower Rb/Sr and will consequently contribute less radiogenic Sr than biotite.

Analysis of anatectic melts shows significant Sr-isotopic disequilibrium can exist between product and protolith at the submillimeter scale (Fig. 3B). Melting is likely to be

non-modal and the degree of disequilibrium is likely to be heterogeneous throughout the melt, both spatially and temporally, as the $^{87}Sr/^{86}Sr$ compositions will be controlled by the relative proportions of the Rb/Sr phases melting at any given site (Fig. 4A). Initially high $^{87}Sr/^{86}Sr$-bearing melts produced by biotite dehydration will be diluted if melting continues and the less radiogenic phases breakdown; e.g., feldspar. As anatexis proceeds, the $^{87}Sr/^{86}Sr$ of the contaminant will be lowered, hence it is ultimately the relative rates at which the different Rb/Sr phases contribute to the melt that governs its compositional evolution (Duffield and Ruiz, 1998). The potential implications this process has for crustal contamination in open magmatic systems, and the geochemical fingerprint this may leave in volcanic rocks, is illustrated in Figure 4B for our Bolivian lava samples. Note that we do not have any way of knowing the time at which melts are produced, as shown schematically in Figure 4A. However, we can use Rb as a proxy, in that early melts will be dominated by biotite (high Rb) while later melts contain a greater contribution from feldspar (low Rb). Thus, in Figure 3B (and Fig. 4B), glass sample 5 is the earliest produced, while 6 is the last.

In short, the $^{87}Sr/^{86}Sr$ and Sr contents of bulk contaminants may be inappropriate input choices for modeling open system processes. Instead, we need to try and account for (1) the stoichiometry of melting reactions which control the changing proportions of phases entering the melt; (2) the rate of melting with respect to Sr diffusivity in the melt, which defines the balance between melt production and the capacity to equilibrate diffusively; (3) the composition of phases consumed, which dictates, in conjunction with 1, the mass balance of Sr in the melt at any given time; (4) the grain size of phases, which constrains the length scales of diffusive equilibration in the solid phases; and (5) the time scales of melt segregation. The majority of these processes are left unaccounted for in the current petrogenetic models.

IMPLICATIONS FOR NATURAL SYSTEMS

The observation of Sr-isotopic disequilibrium in anatectic melts supports interpretations from experimental work that has previously aimed to evaluate the process of crustal anatexis (e.g., Knesel and Davidson, 1996). These studies emphasize the importance of crustal source mineralogy on governing anatectic melt composition and relative Sr diffusion time scales. Ultimately, diffusion will work to eradicate compositional gradients and achieve isotopic equilibration, provided the melt remains in contact with the residuum through an interconnected grain boundary network which will act as a diffusion pathway. Therefore, in order for disequilibrium to be preserved, crustal melts must segregate on time scales shorter than those required for diffusive equilibration (e.g., Sawyer, 1991). Segregation of small-degree, anatectic partial melts (e.g., Philpotts and Asher, 1993, and those sampled by this study) from their protoliths has been shown to occur on rapid time scales (10^2–10^4 yr; Sawyer, 1994). These time scales are significantly faster than those required for diffusion to erase Sr compositional gradients; e.g., diffusion in feldspars (0.1–1 cm) at typical temperatures of anatexis (800–1000 °C) ranges between a few million years and tens of millions of years (Tommasini and Davies, 1997). This in turn implies disequilibrium melting may be an important process in governing the composition of crustal-scale melts (up to 40% melting, Barbero et al., 1995).

The micro-scale observations detailed in Figures 3A and 3B invite speculation on the potential significance of larger-scale Sr-isotopic disequilibrium in the production of anatectic melts, which may play a fundamental role in crustal differentiation (e.g., Sawyer, 1994). In order for Sr-isotopic disequilibrium melting to be preserved on a crustal scale, the time scale for melt segregation has to be (in comparison to orogenesis) instantaneous

(Barbero et al., 1995). Evidence for the preservation of disequilibrium melting during regional metamorphism can be found in anatectic granitoids from Toledo, Spain, where sampled leucogranites are out of isotopic equilibrium with their granulitic restite. Partial melting did not produce isotopically homogenous melts, and Sr-isotope disequilibrium is observed on the mineral scale. In accordance with this study, Barbero et al. (1995) invoked the non-modal breakdown of variable Rb/Sr phases (biotite and plagioclase) along with restricted Sr-diffusion in order to account for the observed disequilibrium. Similarly, Tommasini and Davies (1997) observed Sr-isotopic disequilibrium melting during contact metamorphism in the Sierra Nevada, California, where trachyandesites intrude a granitic batholith. Sampled glasses were out of equilibrium at the outcrop and hand-specimen scale (tens of meters and centimeters, respectively).

Small degrees of partial melt, such as those sampled by this study, do not reach their critical mass fraction (CMF) needed to migrate due to buoyancy alone (~30%; Arzi, 1978). However, experimental studies have shown that low melt fractions (1–5%) can develop interconnected networks between grain boundaries which, in turn, form a permeable matrix from which melt is extractable; e.g., through non-coaxial deformation during melting (Sawyer, 1991). This process has similarly been shown to occur on a crustal scale during pluton emplacement (Guglielmo, 1993). It can therefore be demonstrated that non-modal, anatectic melts that exhibit heterogeneity with respect to Sr isotopes can (1) be produced in the crust on the micro- and macro scale, and (2) segregate on time scales that will preserve melt-source disequilibrium. In Figure 3A, the melt fraction is estimated at 18% and clearly not interconnected, hence opportunities for mixing and diffusive equilibration must rely on either a three-dimensional network not fully apparent in the two-dimensional section, or on tiny, unseen, films along grain boundaries.

The coalescence of numerous crustal melts from compositionally distinct protoliths, each out of Sr-isotopic equilibrium (to variable degrees), has the potential to produce geochemically complex crustal magmas (Acosta-Vigil et al., 2010). The incorporation of multiple isotopically distinct melts into ascending magmas and/or the compositional evolution of disequilibrium anatectic melts as discussed throughout this paper, can be envisaged as contributing to the highly variable $^{87}Sr/^{86}Sr$ signatures in the lavas erupted at Pampas Aullagas and Quillacas (Figs. 1A, 1B, and 4B). Similarly, the production of disequilibrium crustal melts has important implications for so-called "isotope basement mapping" whereby the Sr-isotopic signatures in surface exposures of (predominantly) magmatic rocks are inferred to represent the composition of the crust through which they passed en route to the surface (e.g., Wörner et al., 1992). Thus, a relatively high initial $^{87}Sr/^{86}Sr$ signature may be interpreted as indicating the presence of old, Precambrian crust at depth. Alternatively, this high $^{87}Sr/^{86}Sr_i$ may be derived from relatively young crust in which the high Rb/Sr-bearing phases are melting out preferentially.

Simplistically, the process of crustal contamination can be viewed as a binary mixing process whereby a new composition is generated as a result of the interaction of two geochemically distinct end members. In reality, the geochemical consequences of crustal anatexis are complex, the process of crustal anatexis is progressive, and anatectic melts are not simple equilibrium partial melts of a source.

CONCLUSIONS

Undoubtedly [(EC)AFC]models are useful petrogenetic tools for investigating crustal contributions to mantle-derived magmas, and we do not intend to invalidate their use; however, our observations suggest that such approaches should be used with caution

and with a thorough understanding of their limitations. We have demonstrated the need for small-scale, microscopic studies if our understanding of the interaction and transfer between Earth's geochemical reservoirs is to advance. In-situ analysis of anatectic melts reveals for the first time the scale at which Sr-isotopic disequilibrium within potential contaminating melts can occur. Our approach highlights the need for a greater appreciation of the complexities inherent to crustal anatexis and the subsequent geochemical consequences for modeling contamination. The use of existing models in conjunction with microanalysis of potential contaminants will therefore lead to an improved, quantitative characterization of crustal contamination.

ACKNOWLEDGMENTS

Financial support was provided to McLeod by Natural Environment Research Council studentship NE/G524036/1. Davidson and de Silva acknowledge U.S. National Science Foundation (grants EAR 8916496, EAR 0838536, and EAR 0908324) support for past and current work in the Central Andes. Additional thanks are extended to the Bolivian Geological Survey (GEOBOL), which provided assistance with the original fieldwork. We thank Christina Hansen, University of California–Los Angeles, for preliminary data collection; Chris Ottley, Durham University, for guidance during use of the ICPMS; and Sarah Collins and Kathy Mather who provided useful comments on early manuscript drafts. Further thanks are owed to Antonio Acosta-Vigil and two anonymous reviewers who provided detailed and constructive reviews that helped improve this manuscript.

REFERENCES CITED

Acosta-Vigil, A., Buick, I., Hermann, J., Cesare, B., Rubatto, D., London, D., and Morgan, G.B., VI, 2010, Mechanisms of crustal anatexis: A geochemical study of partially melted metapelitic enclaves and host dacite, SE Spain: Journal of Petrology, v. 51, p. 785–821, doi:10.1093/petrology/egp095.

Arzi, A.A., 1978, Critical phenomena in the rheology of partially melted rocks: Tectonophysics, v. 44, p. 173–184, doi:10.1016/0040-1951(78)90069-0.

Barbero, L., Villaseca, C., Rogers, G., and Brown, P.E., 1995, Geochemical and isotopic disequilibrium in crustal melting: An insight from the anatectic granitoids from Toledo, Spain: Journal of Geophysical Research, v. 100, p. 15745–15765, doi:10.1029/95JB00036.

Bowen, N.L., 1928, The Evolution of the Igneous Rocks: New York, Dover Publications.

Cesare, B., 2000, Incongruent melting of biotite to spinel in a quartz-free restite at El Joyazo (SE Spain): Textures and reaction characterisation: Contributions to Mineralogy and Petrology, v. 139, p. 273–284, doi:10.1007/s004100000137.

Davidson, J.P., and de Silva, S.L., 1992, Volcanic rocks from the Bolivian Altiplano: Insights into crustal structure, contamination and magma genesis in the Central Andes: Geology, v. 20, p. 1127–1130, doi:10.1130/0091-7613(1992)020<1127:VRFTBA>2.3.CO;2.

DePaolo, D.J., 1981, Trace element and isotopic effects of combined wallrock assimilation and fractional crystallization: Earth and Planetary Science Letters, v. 53, p. 189–202, doi:10.1016/0012-821X(81)90153-9.

Duffield, W.A., and Ruiz, J., 1998, A model that helps explain Sr-isotope disequilibrium between feldspar phenocrysts and melt in large-volume silicic magma systems: Journal

of Volcanology and Geothermal Research, v. 87, p. 7–13, doi:10.1016/S0377-0273(98)00071-7.

Guglielmo, G., Jr., 1993, Interference between pluton expansion and non-coaxial tectonic deformation: Three-dimensional computer model and field implications: Journal of Structural Geology, v. 15, p. 593–608, doi:10.1016/0191-8141(93)90150-9.

Hofmann, A.W., and Hart, S.R., 1978, An assessment of local and regional isotopic equilibrium in the mantle: Earth and Planetary Science Letters, v. 38, p. 44–62, doi:10.1016/0012-821X(78)90125-5.

Knesel, K., and Davidson, J.P., 1996, Isotopic disequilibrium during melting of granite and implications for crustal contamination of magmas: Geology, v. 24, p. 243–246, doi:10.1130/0091-7613(1996)024<0243:IDDMOG>2.3.CO;2.

Li, Y., and Ishigaki, T., 2002, Thermodynamic analysis of nucleation of anatase and rutile from TiO_2 melt: Journal of Crystal Growth, v. 242, p. 511–516, doi:10.1016/S0022-0248(02)01438-0.

Patiño Douce, A.E., Humphreys, E.D., and Johnston, A.D., 1990, Anatexis and metamorphism in tectonically thickened continental crust exemplified by the Sevier hinterland, western North America: Earth and Planetary Science Letters, v. 97, p. 290–315, doi:10.1016/0012-821X(90)90048-3.

Philpotts, A.R., and Asher, P.M., 1993, Wallrock melting and reaction effects along the Higganum diabase dike in Connecticut: contamination of a continental flood basalt feeder: Journal of Petrology, v. 34, p. 1029–1058.

Rushmer, T., and Knesel, K., 2010, Defining Geochemical signatures and timescales of melting processes in the crust: An experimental tale of melt segregation, migration and

emplacement, *in* Dosseto, A., Turner, S.P. and Van Orman, J.A., eds., Timescales of Magmatic Processes from Core to Atmosphere: Wiley-Blackwell.

Sawyer, E.W., 1991, Disequilibrium melting and the rate of melt-residuum separation during migmatization of mafic rocks from the Grenville Front, Quebec: Journal of Petrology, v. 32, p. 701–738.

Sawyer, E.W., 1994, Melt segregation in the continental crust: Geology, v. 22, p. 1019–1022, doi:10.1130/0091-7613(1994)022<1019:MSITCC>2.3.CO;2.

Spera, F.J., and Bohrson, W.A., 2001, Energy-constrained open-system magmatic processes I: General model and energy-constrained assimilation and fractional crystallization (EC-AFC) formulation: Journal of Petrology, v. 42, p. 999–1018, doi:10.1093/petrology/42.5.999.

Taylor, H.P., 1980, The effects of assimilation of country rocks by magmas on $^{18}O/^{16}O$ and $^{87}Sr/^{86}Sr$ systematic in igneous rock: Earth and Planetary Science Letters, v. 47, p. 243–254, doi:10.1016/0012-821X(80)90040-0.

Tommasini, S., and Davies, G.R., 1997, Isotope disequilibrium during anatexis: A case study of contact melting, Sierra Nevada, California: Earth and Planetary Science Letters, v. 148, p. 273–285, doi:10.1016/S0012-821X(97)00031-9.

Wörner, G., Moorbath, S., and Harmon, R.S., 1992, Andean Cenozoic centres reflect basement domains: Geology, v. 20, p. 1103–1106, doi:10.1130/0091-7613(1992)020<1103:ACVCRB>2.3.CO;2.

FIGURE CAPTIONS

Figure 1. A: Sr-isotopic diversity exhibited by sampled lavas. [(EC)AFC] curves use sampled bulk rock crustal xenoliths to contaminate a mantle-derived Andean basalt (Chiar

Kkollu). Solutions shown are those that best modeled the data. Compositions of end members and model parameters for each numbered curve (1–13) are provided in the Data Repository (see footnote 1). B: Graph showing the increase of $^{87}Sr/^{86}Sr$ with increasing SiO_2 as evidence for (AFC) during the petrogenesis of sampled lavas (symbols as in A).

Figure 2. Trace-element composition of sampled glass normalized to bulk host xenolith (data in Table 1).

Figure 3. A: Sketch depicting quenched glass (black) and unmelted crystalline restite (white) of sample BC93PAX12. Sampled areas are outlined, and correspond to the sample numbers in

Table 1. B: Sr-isotopic disequilibrium between anatectic melt and bulk source. Glass compositions are age corrected for the Pliocene age of lava eruption.

Figure 4. A: Hypothetical evolution of the Sr-isotopic composition of an anatectic melt. Starting compositions of mineral phases are from Knesel and Davidson, 2002. Initially, biotite (high Rb/Sr) is the only phase breaking down. As melting continues, other Rb/Sr bearing phases begin to melt; e.g., plagioclase (Pl) and alkali feldspar (Ksp). B: Solid gray-filled circles represent the compositions of sampled melt compositions. Remaining symbols as in Figure 1. The bulk mixing line (shown at 10% intervals) indicates bulk mixing between the Chiar Kkollu lava and the average composition of sampled anatectic glasses (Table 1). Realistically, however, the composition of the contaminant changes (see text for discussion). The solid black, and associated dashed black, trends illustrate the potential

contamination pathways ascending mantle-derived magmas assimilating compositionally variable anatectic melts will have in terms of their Rb versus $^{87}Sr/^{86}Sr$ (based on bulk melt composition with Rb content used as a proxy for time).

[1]GSA Data Repository item 2012xxx, xxxxxxxx, is available online at www.geosociety.org/pubs/ft2012.htm, or on request from editing@geosociety.org or Documents Secretary, GSA, P.O. Box 9140, Boulder, CO 80301, USA.

TABLE 1. TRACE ELEMENT AND Sr-ISOTOPE DATA FOR THE BULK XENOLITH (BC93PAX12) AND THE SAMPLED GLASS (values reported in ppm unless stated otherwise)*

	Whole rock	Glass						
	BC93PAX12	**1**	**2**	**3**	**4**	**5**	**6**	**Bulk**
Ba	138.4	357.1	563.6	520.5	1893	699.2	146.5	696.7
Rb	27.3	101.8	172.2	178.4	226.6	236.1	84.3	166.7
Th	7.3	2.2	2.2	2.5	4.7	3.8	4.6	3.3
U	1.4	0.8	1.4	1.3	2	1.6	2.2	1.5
Nb	17.1	4	1.5	1.5	4	2.6	4.6	3
La	22.4	9	10.8	10.7	21	15	14.9	13.6
Ce	46	20.7	30.4	29.9	49.6	37.4	66.8	39.1
Sr	18.5	34.7	56.3	32.3	107.2	37.1	37.2	50.8
Nd	22.8	12.2	15.4	16.3	26.9	21.4	18	18.4
Sm	4.7	2.9	3.9	4	6.2	5.3	3.5	4.3
Zr	32.8	54.9	112.1	103.8	135.2	119.1	89.7	102.5
Hf	1.1	1.2	2.9	2.6	3.2	2.9	2.2	2.5
Ti	0.3 (wt%)	0.3	0.3	0.3	0.5	0.4	0.3	0.3
Tb	0.8	0.4	-	0.5	0.9	-	0.5	0.6
Y	30.2	7.6	9.8	11	19.6	16.7	21	14.3
Yb	5.7	0.3	0.4	0.5	0.7	0.7	1.8	0.7
$^{87}Sr/^{86}Sr$	0.7173	0.7176	0.7209	0.7252	0.7246	0.7281	0.7166	-
$^{87}Sr/^{86}Sr_i$	-	0.7174	0.7207	0.7248	0.7244	0.7276	0.7164	0.7223

*Also shown is a calculated bulk composition for the anatectic melt.

Fig. 1
Width: 6.5161cm
Height: 11.7837cm

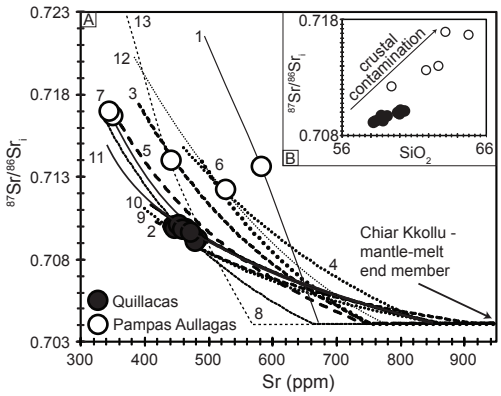

Fig. 2
Width: 6.3796cm
Height: 4.9200cm

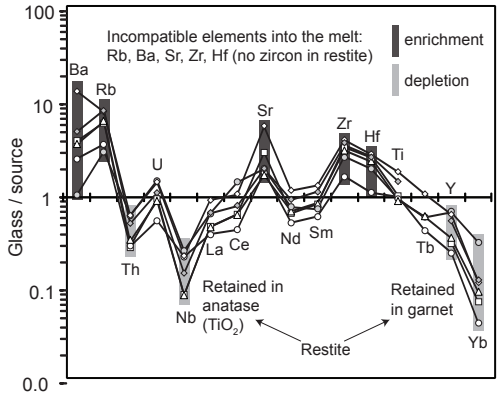

Fig. 3
Width: 6.3975cm
Height: 10.3717cm

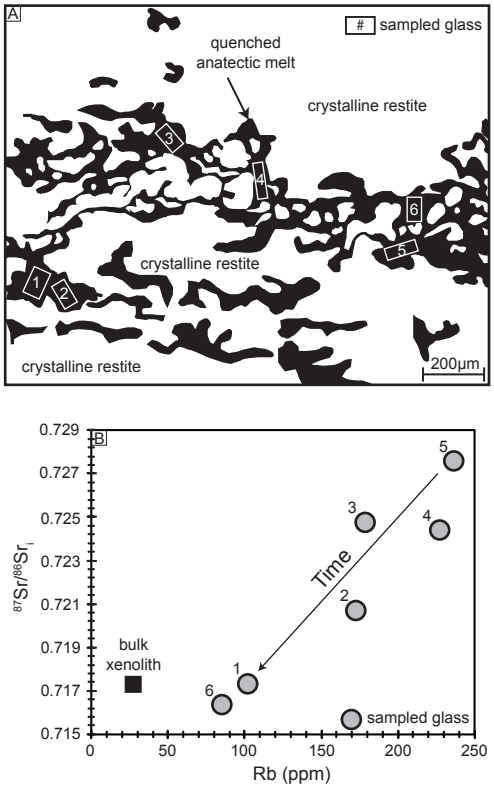

Fig. 4
Width: 6.3975cm
Height: 7.4923cm

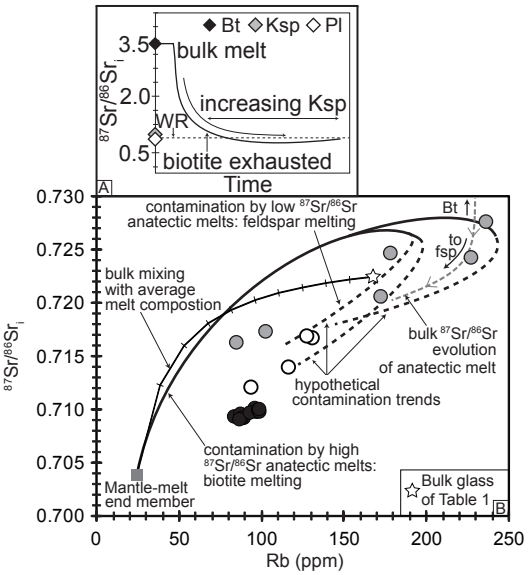

Partially-melted crustal xenoliths from the Wudalianchi volcanic field, northeast China: Insights into the compositions of anatectic melts.

6

This chapter forms the basis of a paper to be submitted to Contributions to Mineralogy and Petrology, first author Lucy McGee, (University of Auckland).

Abstract

A suite of partially-melted crustal xenoliths entrained within recent (1719-1721 AD) potassic lavas erupted in the Wudalianchi volcanic field in the Heilongjiang province of NE China are hosts to anatectic melts now quenched to glass. Associated with these lavas are samples of basement granite from the region which may offer an insight into a potential progenitor to the xenoliths that have experienced partial melting to variable degrees. The high bulk wt. % SiO_2 contents (up to 82.87) and relatively depleted LILE and LREE signatures of sampled anatectic melts may indicate loss of an earlier melt from the system. The glasses display significant Sr-isotopic disequilibrium with their source xenolith and the unmelted granite (and its constituent Rb/Sr bearing phases) ranging from a relatively non radiogenic $^{87}Sr/^{86}Sr$ value of 0.7148 to an extreme 0.9087. This compositional diversity is outwith the range expected if the sampled granite was indeed the progenitor lithology. The geochemical variability of the anatectic melts is indicative of Sr-isotopic disequilibrium melting involving a high Rb/Sr phase (e.g. muscovite) and precludes a direct relationship between the sampled xenoliths and the sampled basement granite. This comparative study supports the results presented and inferences made in Chapter 5 which concluded that melts produced during crustal anatexis are spatially and temporally geochemically heterogeneous, the compositions of which are controlled by the Rb/Sr-bearing phases breaking down.

6.1 Introduction

The contamination of mantle-derived magmas by the surrounding continental crust has been recognised as an important petrogenetic process since Bowen (1928) highlighted the likelihood for wallrock assimilation by an ascending magma through the latent heat of fractional crystallisation. As previously discussed, the process of crustal contamination has been investigated and modelled extensively over the past few decades (e.g. Taylor, 1980; DePaolo, 1981; Spera and Bohrson, 2001; see also Chapter 4). Quantification of the crustal component in open magmatic systems is often lacking as many of the parameters required for modelling are unknown and/or poorly constrained e.g. mineral-melt partition coefficients and the geochemical nature of the contaminant. Additional complication is introduced by the process through which the

crust melts in these complex systems. Previous studies, and work presented in this thesis, has demonstrated that potential contaminating melts can be out of equilibrium with their source to varying degrees both spatially and temporally during crustal anatexis (e.g. Knesel and Davidson, 2002; McLeod et al., 2012; Chapter 5).

The study presented in this chapter investigates the nature of quenched anatectic melts in a suite of partially-melted crustal xenoliths from the Wudalianchi volcanic field in the Heilongjiang Province, NE China which are enclosed in recent (1719-1721) alkali basaltic lavas. These samples are therefore suitable for a comparative study to the suite of partially-melted xenoliths from the Bolivian Altiplano, Central Andes from which the geochemical consequences of crustal contamination and anatexis was investigated (Chapter 4, 5). Analysis of the host lava and xenoliths and their constituent phases aims to constrain elemental and Sr-isotopic budgets during crustal anatexis and ultimately aims to support and reassert the concepts and implications of isotopic disequilibrium melting during crustal anatexis previously presented in Chapter 5. Sampled lava will establish whether or not crustal contamination is an important process during petrogenesis of these recent volcanic rocks; sampled, variably partially melted, xenoliths and their associated quenched glass will allow for the assessment and characterisation of the nature of crustal melts; and samples of a basement granite (unmelted) allows for the possible establishment of a genetic relationship among the xenoliths, crustal melts and their progenitor.

6.2 Field Area and previous work

The Wudalianchi volcanic field (48.72^{o}N, 126.12^{o}E) is one of three Cenozoic potassic volcanic fields which post date late Mesozoic calc-alkaline volcanism in the western Heilongjiang Province of NE China (Fig. 6.1).

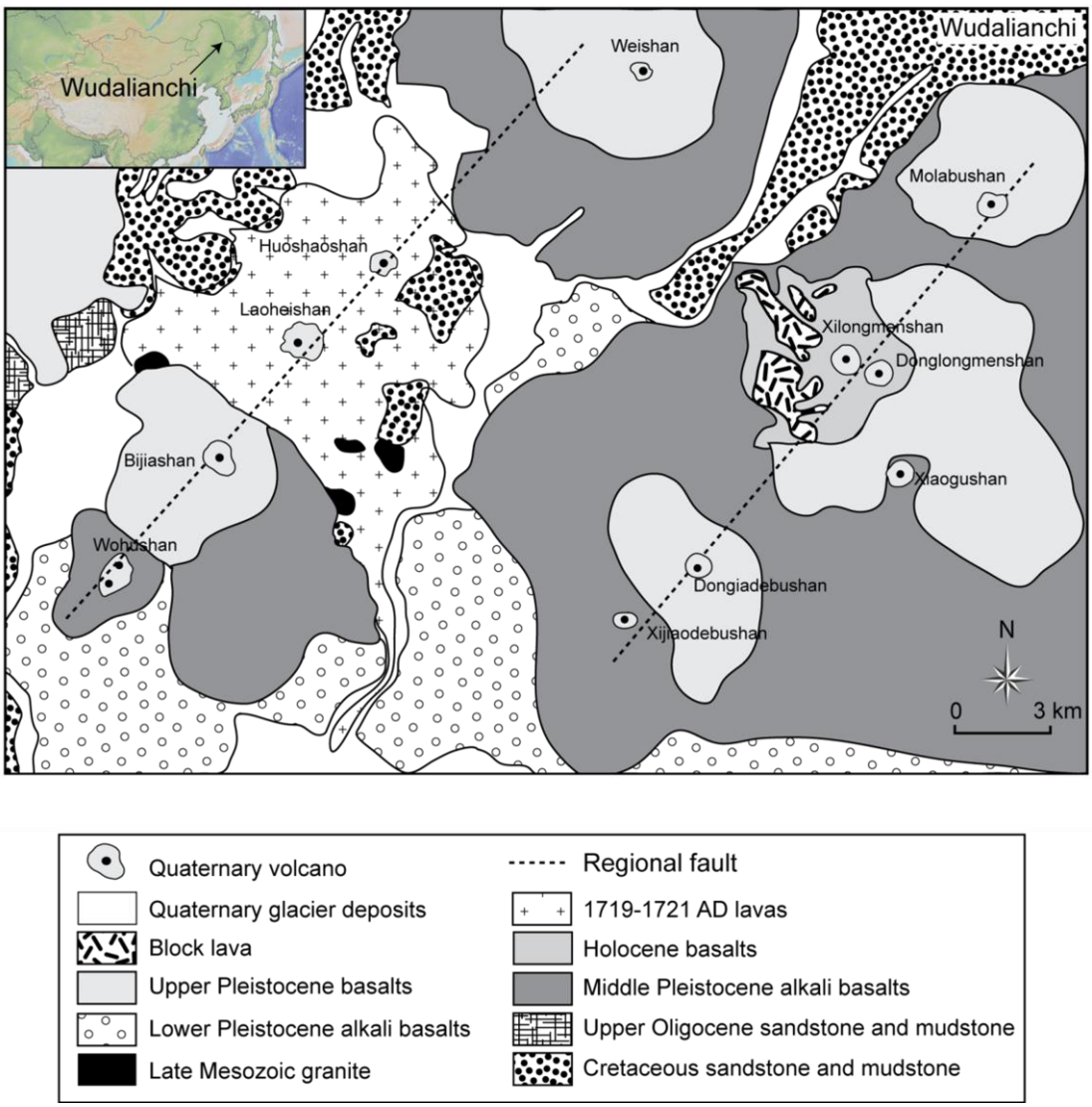

Fig. 6.1. Geological map of the Wudalianchi region (modified from Xiao and Wang, 2009).

The Wudalianchi field covers an area of ~800 km^2 and consists of fourteen Quaternary volcanoes (Hsu and Chen, 1998; Zou et al., 2003). It derives its name from the damming of the Bei river by several lava flows to form five lakes with Wudalianchi translating as "five big connected pools" and has recently been used as a terrestrial analogue for volcanism on Mars (Xiao and Wang, 2009). The underlying continental basement of the Wudalianchi volcanic field is Phanerozoic and consists of pre-Permian metasedimentary rocks, granites and sandstones and mudstones. The granites (Fig. 6.1) are typically biotite (and occasionally muscovite) bearing and were emplaced during orogenesis in the late Palaeozoic through to the Jurassic (Zhang et al., 1995). Overlying the granites is a 120 m thick Cretaceous sedimentary sequence which consists of

interbedded muds, shales and sands of a lucustrine origin (Feng and Whitford-Stark, 1986). Upper Tertiary sediments are 125 m thick and are composed of poorly-consolidated muds, sands and conglomerates. Only the upper 25 m is exposed at Wudalianchi (Feng and Whitford-Stark, 1986).

The origin of this intraplate volcanism in NE China is poorly constrained and currently under debate. Present theories include the existence of a mantle plume/hotspot (e.g. Deng et al., 1996); and lithospheric thinning/delamination from ~200 km in the Palaeozoic to the present day ~80 km (e.g. Wilde et al., 2003). It is generally accepted that the Wudalianchi magmas have an origin in the subcontinental lithospheric mantle, similar to the mantle reservoir of EM I (e.g. Zhang et al., 1991; Zou et al., 2003). Phlogopite-bearing garnet peridotites have been inferred as the dominant source rocks with the primary magma being generated by small degrees of partial melting at ~80-120 km depth (*c.* 20-45 kbar; Zhang et al., 1995; Zou et al., 2003) at temperatures of ~1068-1100^{o}C (Qui et al., 1991; Gong, 1997; cited in Wang and Chen, 2005). The two most recent eruptions in the Wudalianchi volcanic field occurred at Laoheishan (old black hill) and Huoshaoshan (fire burning hill, see Fig. 6.1) which are considered the best-preserved volcanoes in China (Xiao and Wang, 2009).

Seven samples of partially melted crustal xenoliths entrained within these recent lavas, lava from Huoshaoshan, and two samples of unmelted (basement) granite form the basis of this study.

6.3 Sample Petrography

Modal mineralogy of the basement granite is presented in Fig. 6.2 and the lava and xenoliths in Fig. 6.3. It should be noted that the xenoliths, particularly those with a significant proportion of quenched anatectic melt are petrographically heterogeneous

i.e. different modal abundances are yielded from different sections of the same sample. Every effort has been made to fully characterise each sample and provide a representative account of phase abundance.

6.3.1 Granite

The sampled granite displays no evidence of having undergone partial melting. Crystals are inequigranular ranging between 0.5 and 6 mm. Quartz, microcline, biotite (often altered to chlorite) and plagioclase dominate the mineralogical assemblage (~95%) in addition to rarer orthoclase (<5%) and sphene (<2%, Fig. 6.2 a, b) and minor apatite (<1%). Microperthitic textures are often displayed in the alkali feldspar. The mineralogy suggests this is an I type granite, and the presence of myrmekite and microcline feldspar indicates cooling of a subsolvus granite (Shelley, 1993).

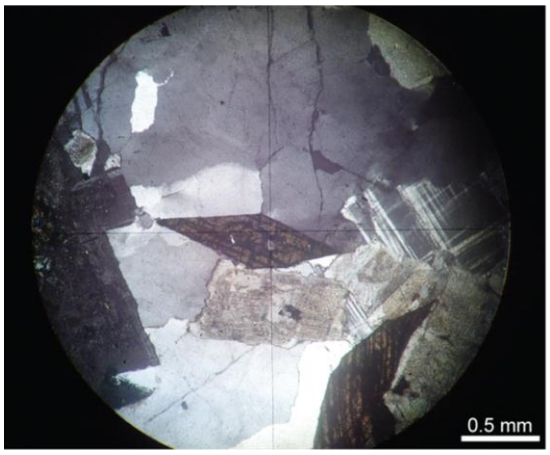

Fig. 6.2 a. Sphene in sampled basement granite.

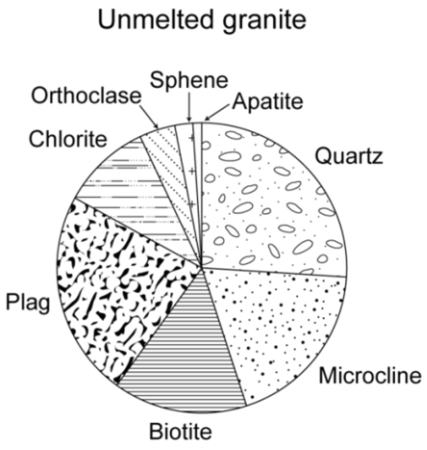

Fig. 6.2 b. Granite modal mineralogy.

6.3.2 Lava

The sampled lava consists predominantly of a glassy and fine grained pyroxene-feldspathic groundmass. Olivine and rare augite are the only phenocrystic phases present (<10%). Previous studies on the earlier potassic phases of volcanism in the area have reported the presence of leucite, olivine, clinopyroxene, nepheline, sodalite,

phlogopite, sodalite and minor rutile and apatite (Feng and Whitford-Stark, 1986; Zhang et al., 1995; Hsu and Chen, 1998).

6.3.3 Xenoliths

The xenoliths were sampled from the summit of Huoshaoshan (3a and 3b), a rootless cone (4a) from which the granite was also sampled and the recent 1719-1721 lava flows and associated tephra deposits (5a, b, d). The xenoliths are characterised by the ubiquitous occurrence of quenched felsic melt, now glass. They display a pumice-like texture (friable) due to the ubiquitous occurrence of vesicles which range from 0.4 to 3.2 mm. Vesicles appear rounded to sub rounded and occasionally show evidence of preferential orientation, perhaps indicative of the local stress fields in the felsic melt during xenolith entrainment i.e. elongate in the direction of magma flow in the volcanic conduit at the time of quenching. There is a suggestion that the different xenolith groups could correspond to different conditions of entrainment and heating (resulting in different degrees of melting) with melting being caused by contact heat from the enclosing basalt and potentially rapid decompression during ascent (Bayhan et al., 2006).

6.3.3.1 Xenoliths 3a, b

These xenoliths are hosted in lava which exhibits an a ‘a like texture. Xenolith 3a is dominated by vesicles which comprise almost 40% of the sample. The remaining portion of the sample consists of felsic and mafic glass (~10%) which can be seen mingling (Fig. 6.4), polycrystalline and strained quartz, microcline, opaque phases, plagioclase feldspar, sphene, hercynitic spinel which is intrinsically associated with the felsic glass, and rare accessory zircon. The production of hercynitic spinel during crustal anatexis has previously been attributed to biotite breakdown (Cesare, 2000).

Xenolith 3b is dominated by felsic glass (~15%) and vesicles (~40%) which are on average larger than those in 3a. The remaining crystalline assemblage is composed of polycrystalline and strained quartz which is often embayed, altered microcline, rare opaque phases and hercynitic spinel which again is associated with the felsic glass.

6.3.3.2 Xenolith 4a

Xenolith 4a is hosted in a'a lava, is vesiculated by ~60% and comprises ~15% felsic glass, <5% mafic glass. Rare sphene is present (~2%, Fig. 6.5) and is variably breaking down. The crystals range from distinctive diamond shaped lathes to equant anhedral shapes; the edges of crystals are ragged and lava has infiltrated parts leaving a murky texture.

6.3.3.3 Xenoliths 5a, b, d (Fig. 6.6)

These xenoliths are hosted in pahoehoe-textured lava. They contain up to 80% felsic glass and <5% mafic glass. Small-scale mingling between melts from the xenoliths and the basanite host is clearly seen in the complex mixing zone at the lava-xenolith contact of sample 5b and an olivine crystal appears to have been incorporated into the surrounding vesicles and silicic melt and become "stranded" (Fig. 6.7). Hercynitic spinel is again associated with the occurrence of felsic glass. Minor opaque phases are present (<2%) alongside polycrystalline and strained quartz (~20%).

Different degrees of partial melting are suggested for the different xenolith groups, based on melt volume, residual mineral abundance and type. Xenolith 4a contains vesicles, broken down sphene and a relatively small percentage of melt indicating it may be in the preliminary stages of melting. Xenoliths 3a-b contain similar abundances of vesicles and melt with plagioclase and biotite as residual minerals. Xenoliths 5a-d contain a greater abundance of vesicles and melt and have quartz as a residual phase.

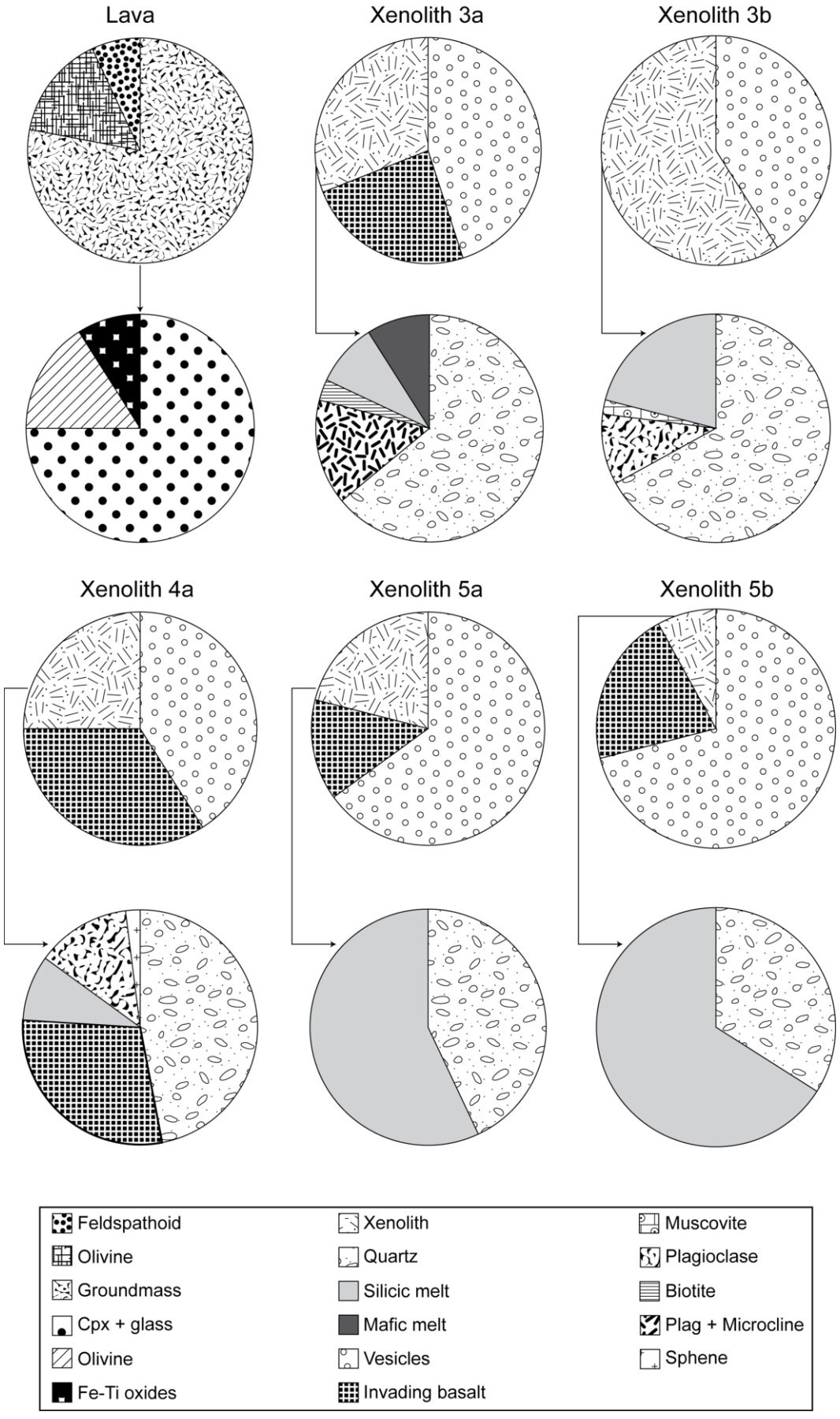

Fig. 6.3. Modal mineralogy of sampled lava and xenoliths.

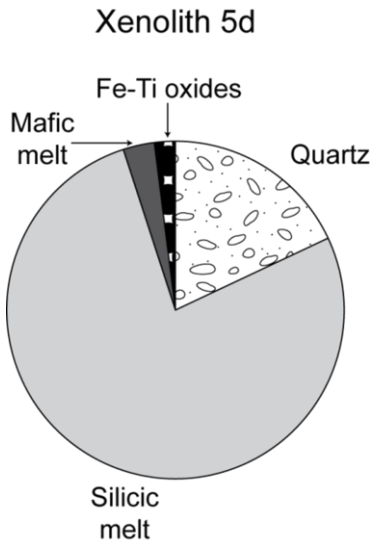

Fig. 6.3 cont. Representative modal mineralogy of Xenolith 5d.

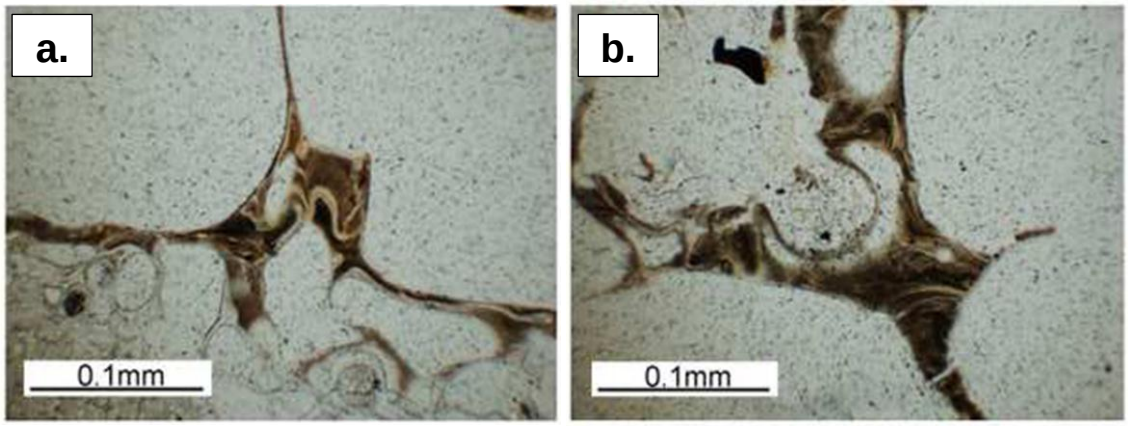

Fig. 6.4 a, b. Melt mixing within a lava pocket of partially melted granitic xenolith 3a. Photos courtesy of Lucy McGee.

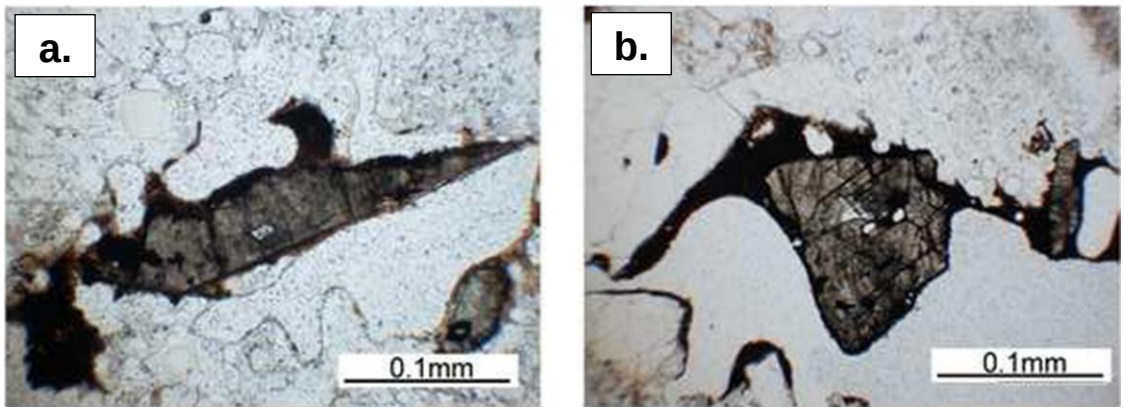

Fig. 6.5 a, b. Partially-melted sphene in xenolith 4a

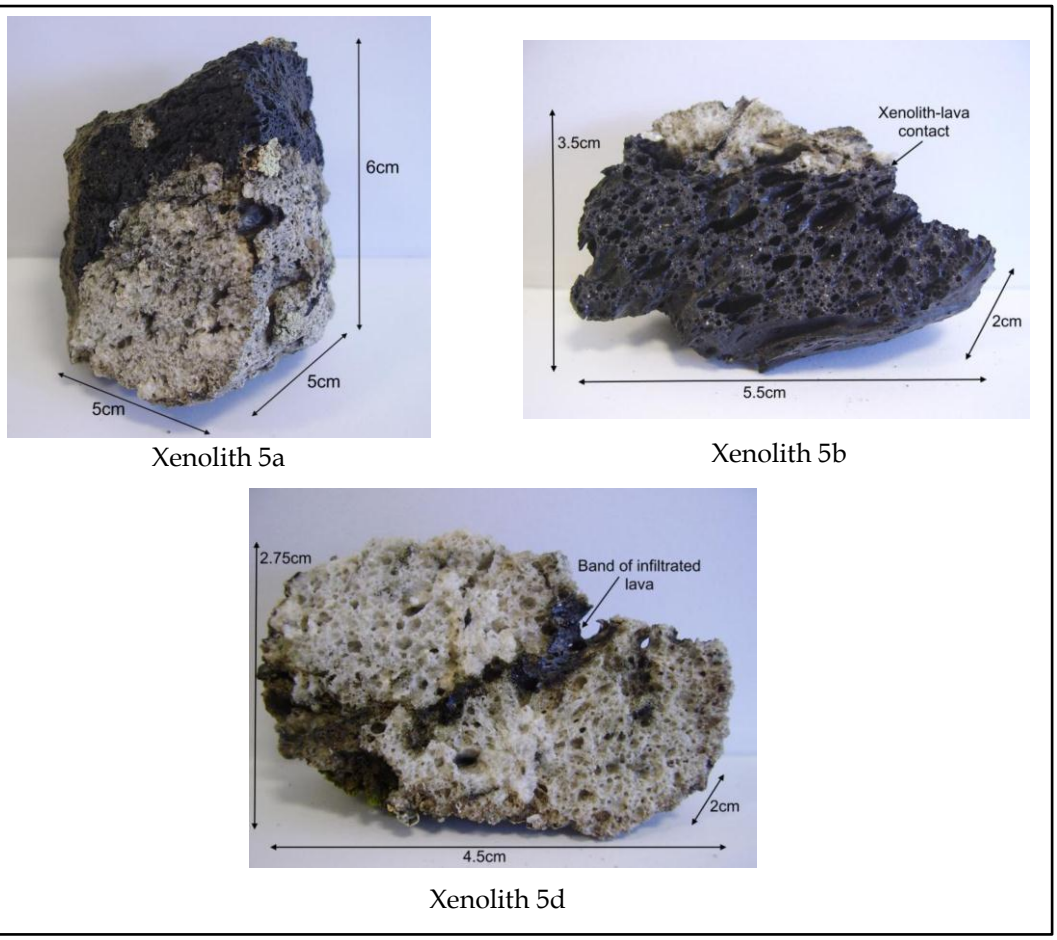

Fig. 6.6. Sampled partially melted crustal xenoliths (Suite 5). Photos courtesy of Lucy McGee.

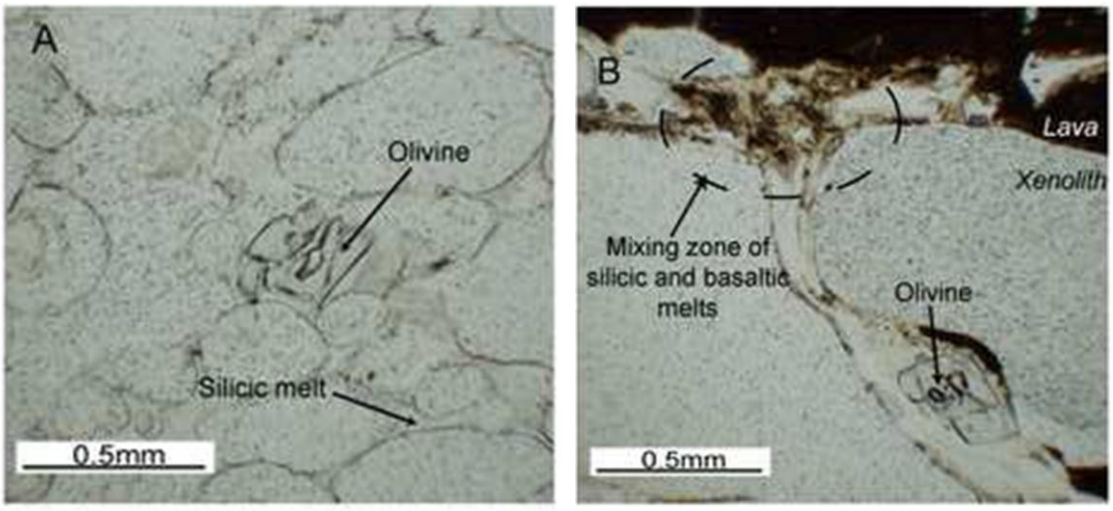

Fig. 6.7. **a**. 'Stranded' olivine crystal within silicic melt pockets and vesicles of partially melted granitic xenolith 5b. Olivine crystal is assumed to have been transferred from the enclosing basaltic magma to the xenolith when the two materials were partially molten and in contact, showing small-scale interaction**. b.** Lava-xenolith contact in sample 5b showing complex mixing zone between the silicic (colourless) and basaltic melts. Photos courtesy of Lucy McGee.

6.4 Analytical methods

Samples of the xenoliths were crushed and any pieces of lava removed so as to ensure only the bulk xenolith was prepared for analysis. Rock powders, mineral separates and glass from the lava, granite and sampled xenoliths were dissolved in HF and HNO_3 using standard dissolution procedures detailed in Appendix E. Whole rock major elements were measured by XRF at the School of Geosciences, University of Edinburgh and errors were <5%. Trace elements were analysed on the X-Series2 ICPMS at the Northern Centre for Isotopic and Elemental Tracing, Durham University following the procedures detailed in Ottley et al., (2002). The errors on reported trace element data range between 1 and 6% with some of the HREE displaying errors up to 10% due to low concentrations (≤1ppm). Repeat analyses of international standards were within <<5%. Repeat analyses of samples were variable and interpreted as real due to the heterogeneity of the samples. Isotope ratios for Sr and Nd on whole rock powders were determined using a plasma ionisation multicollector mass spectrometer (PIMMS) ThermoElectron Neptune instrument at the Arthur Holmes Isotope Geology Laboratory (AHIGL), Durham University. Instrument running conditions and data correction procedures are given in Nowell and Parrish (2002) and Nowell et al, (2003). Reproducibility on the acquired Sr data was tested by measuring the NBS987 standard which yielded an average $^{87}Sr/^{86}Sr$ of 0.710255 ± 0.000008 (2σ) (n = 10) and two USGS standards; BHVO-1 and BIR-1 which yielded averages of 0.703495 ± 0.000010 (2σ) (n = 3) and 0.703118 ± 0.000010 (2σ) (n = 3) respectively. Reproducibility on the acquired Nd data was tested by measuring the J&S standard, a Sm-doped J&S standard and two USGS standards; BHVO-1 and BIR-1. During analysis of the sampled xenoliths average $^{143}Nd/^{144}Nd$ values for the standards were 0.511116 ± 0.000006 (2σ) (n = 8), 0.511121 ± 0.000006 (2σ) (n = 6), 0.512991 ± 0.000010 (2σ) (n = 3) and 0.513098 ± 0.000007 (2σ) (n = 3) respectively.

Glass and mineral separates were analysed for Sr isotopes by TIMS at Durham University. Running conditions of the Thermo-Finnigan Triton TIMS system (and data corrections) are given in Font et al., (2008). Picked glass and mineral separates were dissolved in ultra-pure acids (HNO_3 and HF) and the Sr fraction was then separated using the micro-Sr column procedure given in Appendix E and Charlier et al., (2006). During this study, 24 analyses for the $^{87}Sr/^{86}Sr$ composition of the international standard NBS 987 yielded an average $^{87}Sr/^{86}Sr$ of 0.710269 ± 0.000010 (2σ) which is in excellent agreement with values reported by Thirwall, (1991) of 0.710248 ± 0.000023 (2σ) (n = 247). All sample data is presented in Table 7, 8 in Appendix B.

6.5 Whole rock geochemistry

6.5.1 Major elements

The sampled lava contains 51.8% SiO_2 and 6.8% K_2O which is consistent with the well established potassic nature of the Wudalianchi volcanic rocks (e.g. Zhang et al., 1995). The sampled basement granite contains ~69% SiO_2 (technically classifying it as an Si-rich granodiorite) and ~15 % Al_2O_3 with an ASI (alumina saturation index) value of 1.51 characterising it as peraluminous. Sampled xenoliths range from ~70 to ~ 83% SiO_2. The higher end of this range (if not the lower end too), and the abundance of residual quartz observed in thin section may indicate significant melt loss has occurred. SiO_2 correlates negatively with both K_2O (Fig. 6.8) and Al_2O_3. This may reflect increasing degrees of melt loss due to the predominantly potassic and aluminous nature of anatectic melts (see Chapter 5) and hence would account for the increasing wt. % SiO_2 as residual quartz dominates. Those with lower K_2O and Al_2O_3 and higher SiO_2 could thus be interpreted as having experienced the highest degree of melt loss. These negative correlations may therefore represent the preferential melting out of feldspar as shown by the decrease in modal abundance of plagioclase and alkali feldspar from xenolith 3a (both plagioclase and microcline), through 3b (plagioclase) to

5d (no visible feldspar). An attempt to correlate absolute mineral modal abundances within the xenoliths and bulk rock geochemical signatures failed e.g. SiO_2/K_2O vs. % quartz. This is understood to be due to the heterogeneous nature of the xenolith suite and the limited grains available in thin section for statistically valid point counting.

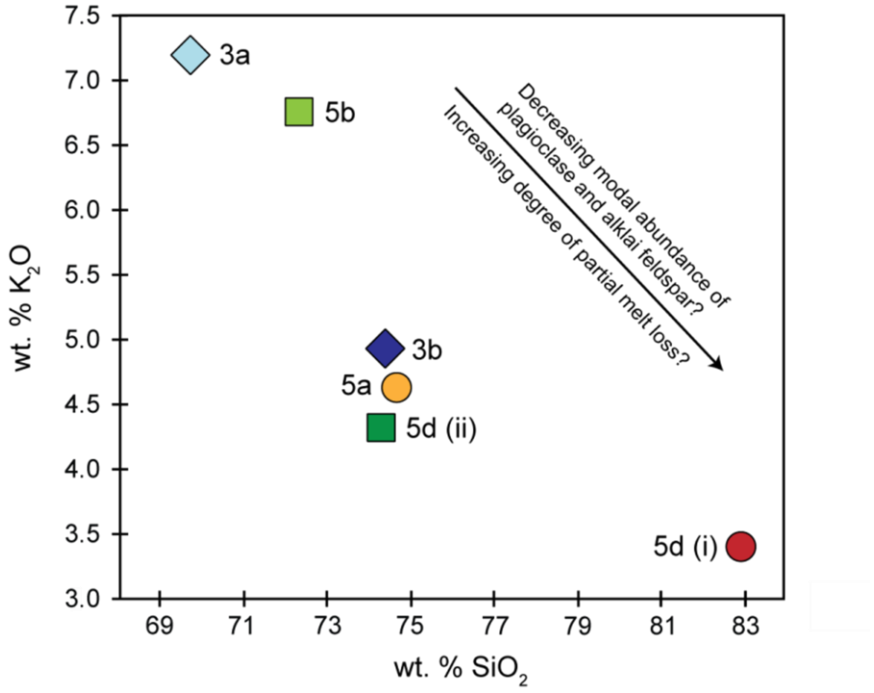

Fig. 6.8. SiO_2 vs. K_2O for sampled xenoliths.

6.5.2 Trace elements

While all samples were analysed for a full suite of trace elements (see Appendix B, Table 7) the relationships among the xenoliths are arguably best illustrated and considered using the REE (Fig. 6.9), which will behave in a more consistent way which is more amenable for discussion of inter-REE changes in comparison to trace elements with largely unconstrained distribution coefficients – at least in silicic systems such as this. Several features come out of the comparison of REE patterns of the different components of the system at Wudalianchi:

(1) The lava is more enriched than the granite by roughly one order of magnitude, and is particularly enriched in LREE;

(2) The partially melted xenoliths (with the exception of xenolith 5a, 5d (ii)) are less enriched in the LREE than the granite, and 5a-d are more enriched in HREE than the granite;

(3) Xenoliths 3a-b are the most depleted relative to the granite, and group together as do 5a-d;

(4) Xenoliths 5a-d are more enriched than 3a-b, and show HREE more enriched than the lava, but not LREE;

(5) La_N/Yb_N ratios reflect the relative flat nature of the REE profiles: 5.1-1.2 for 3b-5d (ii), slightly higher for xenolith 3a at 10.1.This may indicate variable loss of an early, LREE enriched melt.

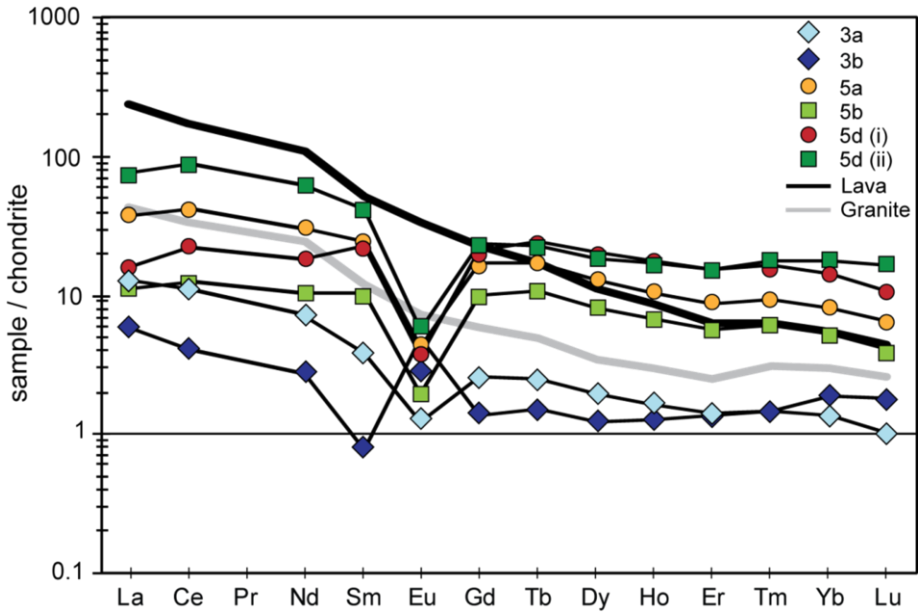

Fig. 6.9. Chondrite normalised REE pattern for sampled lava, xenoliths and basement granite.

The process of melt extraction following partial melting of assimilated material has been observed in other settings (e.g. Cesare et al., 1997), and from the above observations, the Wudalianchi xenoliths clearly do not indicate a simple closed system.

6.5.3 Sr-Nd isotopes

The lava exhibits a Sr-Nd isotopic signature similar to those of the lavas previously studied in the Wudalianchi region (Fig. 6.10, see Basu et al., 1991; Zhang et al., 1991). The Nd isotopic compositions of the granite and xenoliths are comparable which suggests that any (granitic) progenitors to the xenoliths may at least have similar ages.

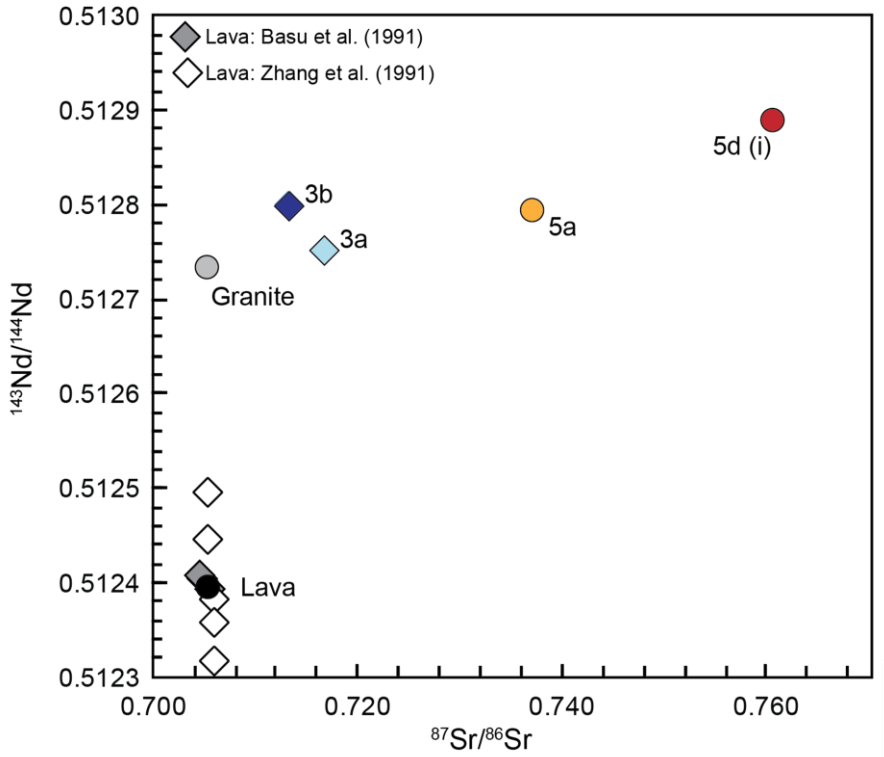

Fig. 6.10. Sr-Nd isotopic compositions of sampled lava, granite and xenoliths. Note: Error on 5d (i) is ± 0.000010.

6.6 Mineral and glass separates

6.6.1 Trace elements

Biotite, plagioclase feldspar and sphene mineral separates from the unmelted granite, plagioclase feldspar from xenoliths 3a and 3b and glass separates from xenoliths 3a, 3b and 5a were analysed for their trace element compositions. Fig. 6.11 a shows the relative proportion of selected trace elements in minerals from the granite, relative to the bulk composition of the granite with sphene clearly levering control on the Y, Nb, Nd, Th and U elemental budget and plagioclase feldspar on the Sr and Pb budget.

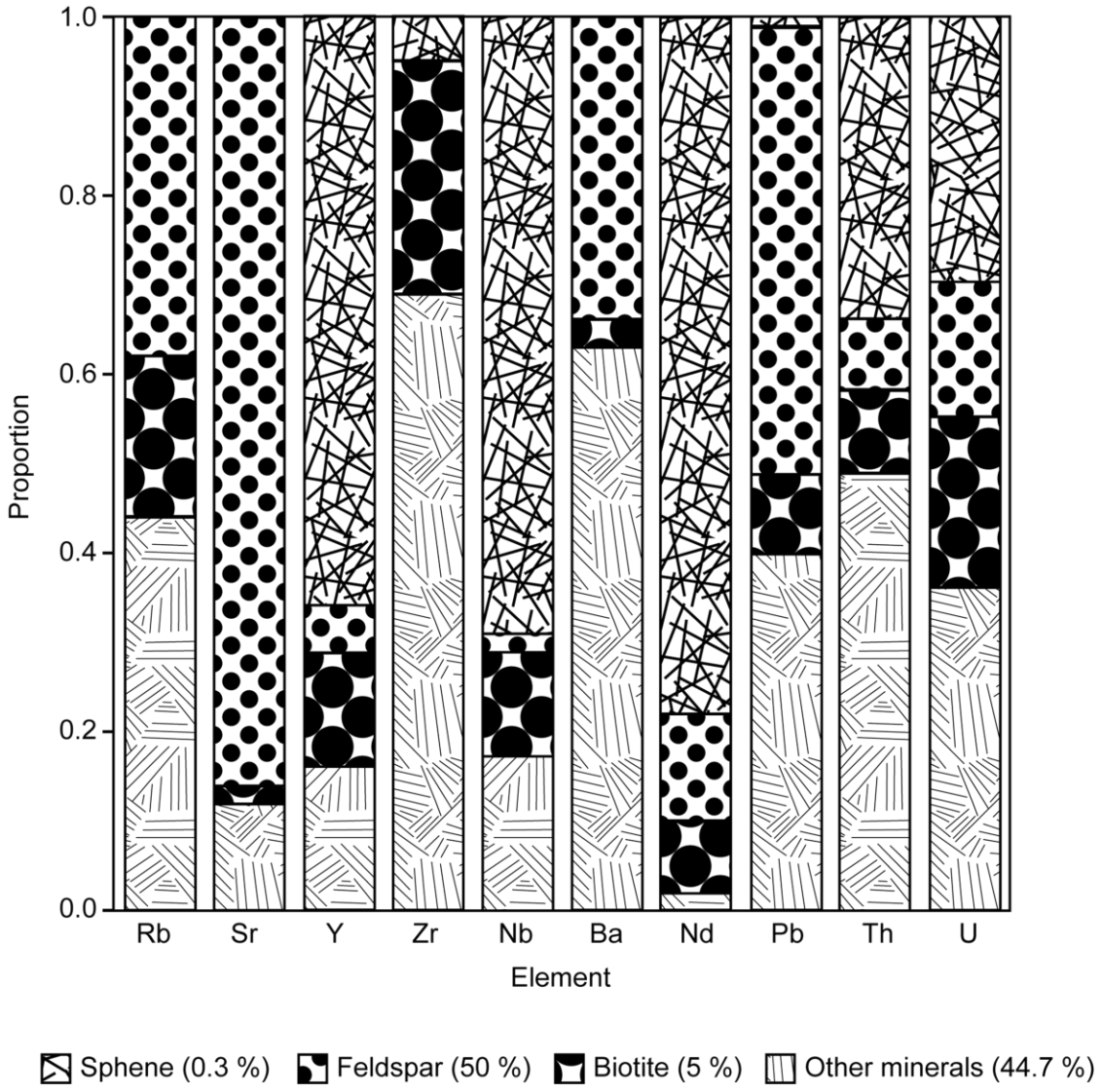

Fig. 6.11 a. Elemental budgets of sampled minerals in the basement granite.

Fig. 6.11 b illustrates the relative abundance of selected trace elements for sampled glasses and plagioclase mineral separates from the xenolith suite. As shown, between 85 and 95% of the trace element budget of the glasses is controlled by Rb, Sr and Ba.

Fig. 6.11 c-e shows the sampled glasses normalised to the bulk composition of the xenolith in which they are hosted. Glasses 3a and 5a are significantly more depleted that their bulk host whereas glasses 3b (i) and (ii) are relatively depleted but exhibit slight enrichment in Ba, Rb and Sm. The overall depleted nature of the glasses may indicate that an initial melt, enriched in incompatible elements, has been lost.

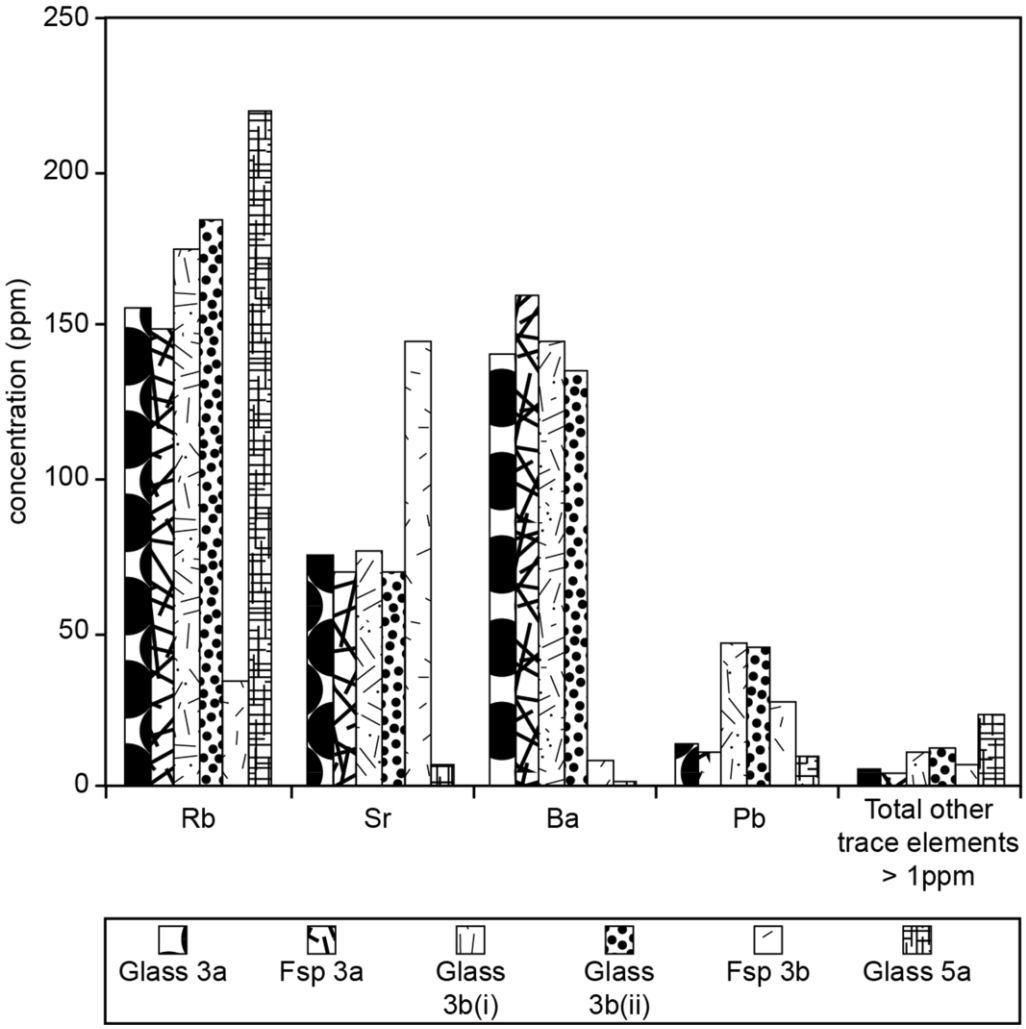

Fig. 6.11 b. Trace element characteristics of sampled glass and feldspars.

Fig 6.11 f shows a chondrite normalised plot of the sampled glasses and basement granite. Compared to sampled glass phases, the granite is enriched in LREE and depleted in HREE. Relative to the granite, sampled glasses are LREE depleted and with the exception of 3a, exhibit flat REE profiles. This signature may indicate the loss of LREE's to an earlier melt fraction as the glass and remaining minerals do not replicate the bulk composition of the presumed granite protolith.

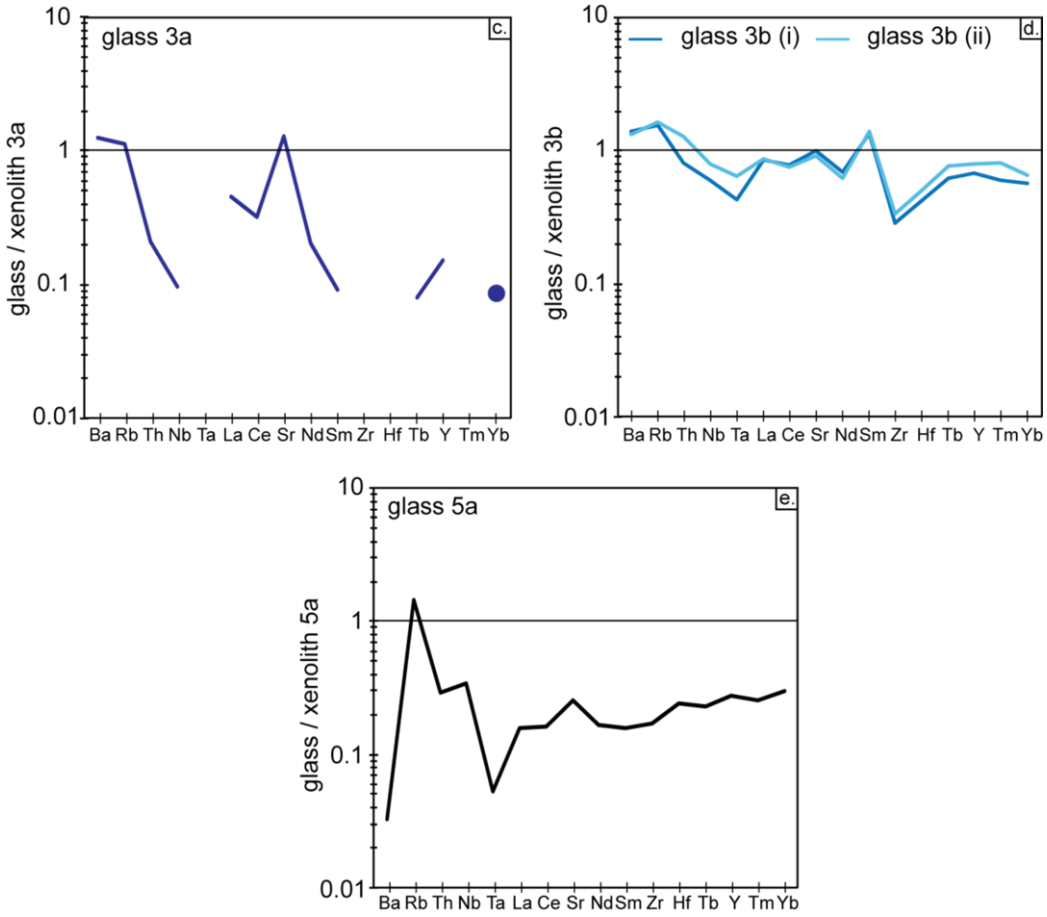

Fig. 6.11 c-e. Multi-element patterns for sampled glasses normalised to their host xenolith bulk composition.

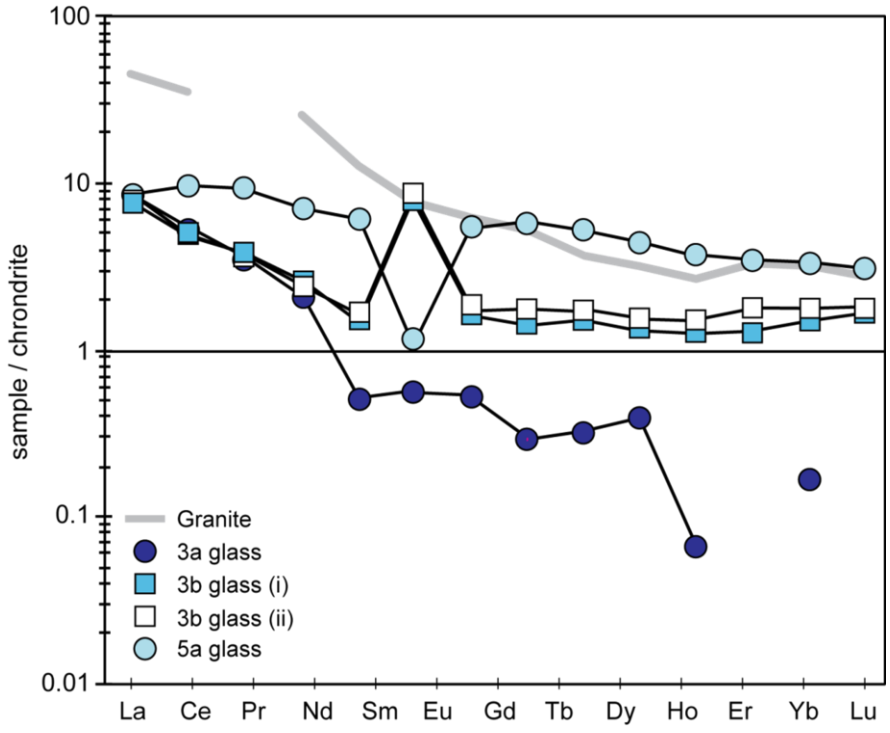

Fig. 6.11 f. Chondrite normalised REE patterns for sampled glasses and the basement granite. Normalising values of Nakamura (1974).

6.6.2 Sr-isotopes

Biotite and plagioclase separates from the basement granite and plagioclase from xenolith 3a were analysed for their $^{87}Sr/^{86}Sr$ composition (Fig. 6.12).

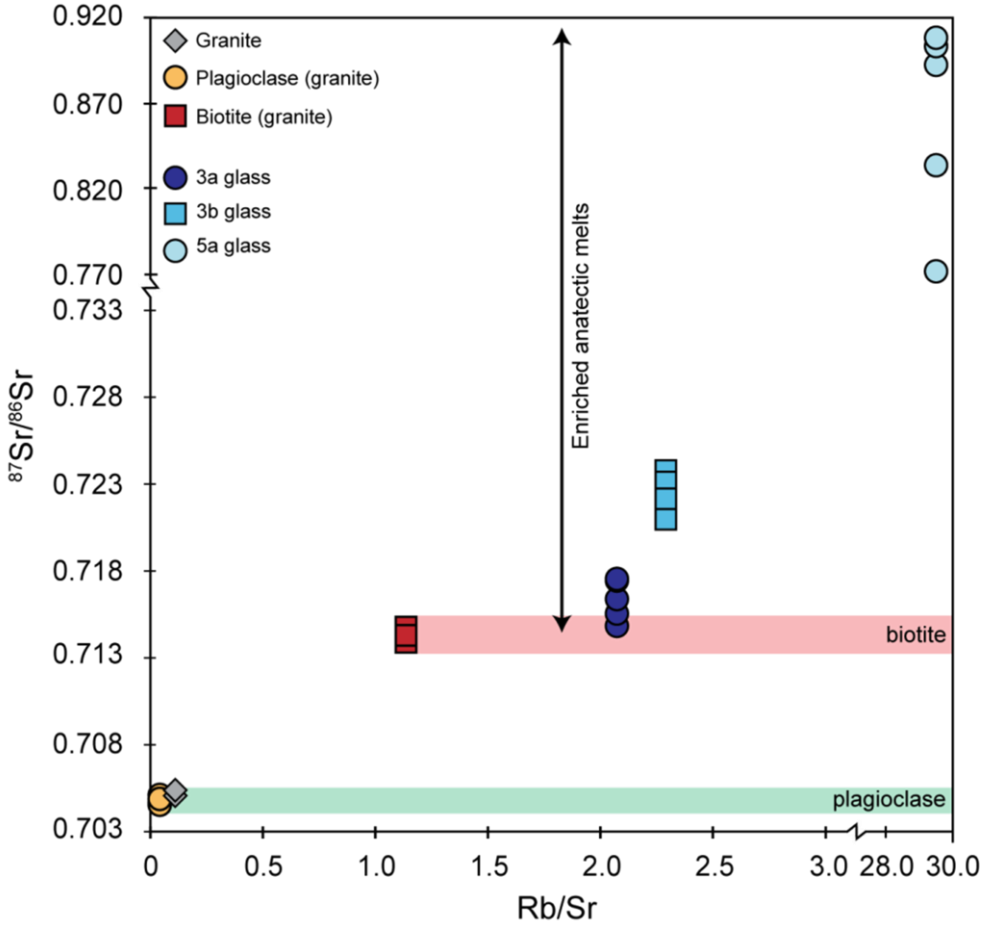

Fig. 6.12. $^{87}Sr/^{86}Sr$ compositions of the basement granite, its constituent minerals and sampled glasses. Note: Trace element concentrations were determined on one glass separate only.

In comparison to the whole rock granite (0.7052-0.7054), the granite plagioclase separates are non radiogenic at 0.7045-0.7050. The biotite, as would be expected from its higher Rb/Sr ratios (1.14 compared to 0.048 of the plagioclase, see Table 8; Appendix B), are significantly more radiogenic at 0.7138-0.7147. The glasses exhibit significant heterogeneity with overall $^{87}Sr/^{86}Sr$ ratios ranging from 0.7148 to 0.9087 (Fig. 6.12). The compositions of these glasses are significantly more radiogenic than the bulk granite (0.7052, 0.7054) with glass from 3b and 5a significantly enriched relative to the most radiogenic phase sampled in the granite (biotite at 0.7138-0.7147). These

results are in accordance with the Rb/Sr ratios displayed by the glasses with 3a and 3b exhibiting relatively low ratios (2.08-2.68) compared to the high Rb/Sr ratio exhibited by 5a of 29.4.

The granite, biotite and plagioclase feldspar plot on an Rb-Sr isochron which yields an age of 218 Ma (Fig. 6.13). This is consistent with the production of granites in the region during Palaeozoic through to Jurassic orogenesis (Zhang et al., 1995).

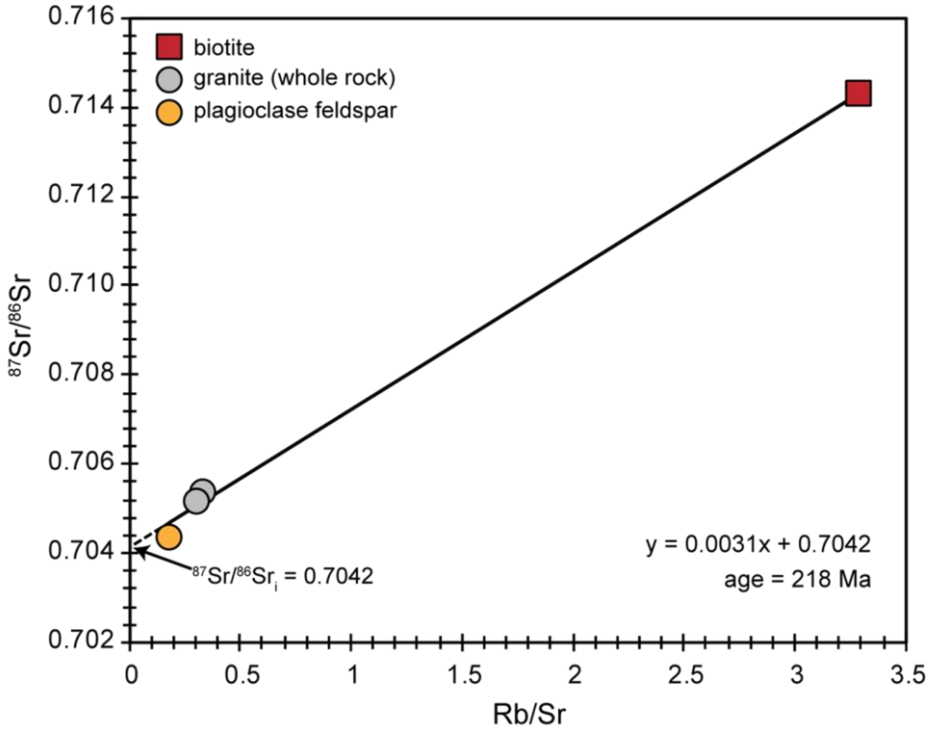

Fig. 6.13. Rb-Sr whole rock isochron for sample basement granite.

6.7 Discussion

Given the comprehensive geochemical dataset that exists for whole rock, mineral and glass separates in this complex volcanic system, an attempt is made to comprehensively address the following questions:

1) Does the sampled basement granite represent a progenitor to the suite of variably partially-melted crustal xenoliths?

2) To what extent can the glass compositions be used to identify the role of mineral phases which are breaking down during anatexis?
3) To what degree has contamination of the host lava by these (or similar) anatectic melts occurred?

6.7.1 Evaluating a granite progenitor and Sr-isotopic disequilibrium melting

The vesicular texture, presence of silicic melt and broken down minerals (such as the sphene, Fig. 6.5) and high proportions of quartz observed in the xenoliths allows them to be characterised them as 'partially melted' and the minerals which they contain 'residual'. Different degrees of partial melting can be suggested for the different xenolith groups, based on melt and vesicle volume, residual mineral abundance and type. As seen from Fig. 6.8, these xenoliths appear to form a melting spectrum from samples which contain two feldspars, quartz and a little biotite (xenolith 3a) to samples which contain only quartz (xenolith 5d); there is increasing volume of silicic melt through this series too.

The inference that the sampled basement granite represents the progenitor of the partially melted xenoliths is derived from two lines of evidence: (1) the observed and well-documented occurrence of granite as one of two basement rocks in the area (e.g. Feng and Whitford-Stark 1986) and (2) the presence of partially broken-down sphene in xenolith 4a which compares well with the pristine sphene seen in the granite samples. The purpose of the Sr-isotopic measurements was to evaluate the relationship between the assumed progenitor, the granite, and the partially melted xenoliths, and hence asses whether disequilibrium melting during crustal anatexis occurred.

There are a number of possibilities regarding the xenoliths relationship to the basement granite and the processes through which their unusual geochemistry could be produced:

(1) The xenoliths are related to the granite and display variations in geochemistry due to variable degrees of partial melting; a melt has been lost from some of these xenoliths into the host lava;

(2) As in (1), but a melt has not been lost to the lava, although it has been lost elsewhere in the system – such as to the wallrock;

(3) The xenoliths are not related to the sampled basement granite;

(4) No melt has necessarily been lost from the partially-melted xenoliths and the variable geochemical signatures within the sampled glasses are simply a reflection of the progenitor mineralogy;

(5) From (4), the xenoliths do not share a common progenitor.

If the xenoliths are simply the result of partially melting the granite then they should exhibit the same isotopic ratios, since partial melting will not affect the isotopic compositions. The Nd isotope ratios of the granite and partially melted xenoliths are comparable, thus suggesting that any granitic progenitors of the xenoliths at least have a similar age, but the Sr isotope ratios are notably different. This observation leads to the question of whether or not disequilibrium melting has occurred. From this, radiogenic disequilibrium melts, derived predominantly from high Rb/Sr i.e. micaceous phases, and/or non-radiogenic melts derived largely from low Rb/Sr phases i.e. feldspars could be produced. Examples of such relationships have been reported by Knesel and Davidson (1996, 1999); McLeod et al., (2012) and are presented in Chapter 5. The data shown in Fig. 6.12 indicate that although the biotite and feldspar from the unmelted granite do have high and low $^{87}Sr/^{86}Sr$ respectively, the range of $^{87}Sr/^{86}Sr$ observed among the xenoliths is far greater. Glass compositions are even more extreme (up to 0.9087), and feldspar separates from 3a are more radiogenic than

the granite biotites. This precludes a direct relationship between the granite and the sampled xenolith suite.

The Sr-isotopic compositions of sampled glasses are distinct from that of their bulk source (Fig. 6.14) and indicate that disequilibrium melting has occurred during crustal anatexis. The loss of an earlier melt from the xenoliths however cannot unequivocally be ruled out hence the measured composition of each xenolith sample may not be truly representative of the progenitor's original bulk $^{87}Sr/^{86}Sr$ composition.

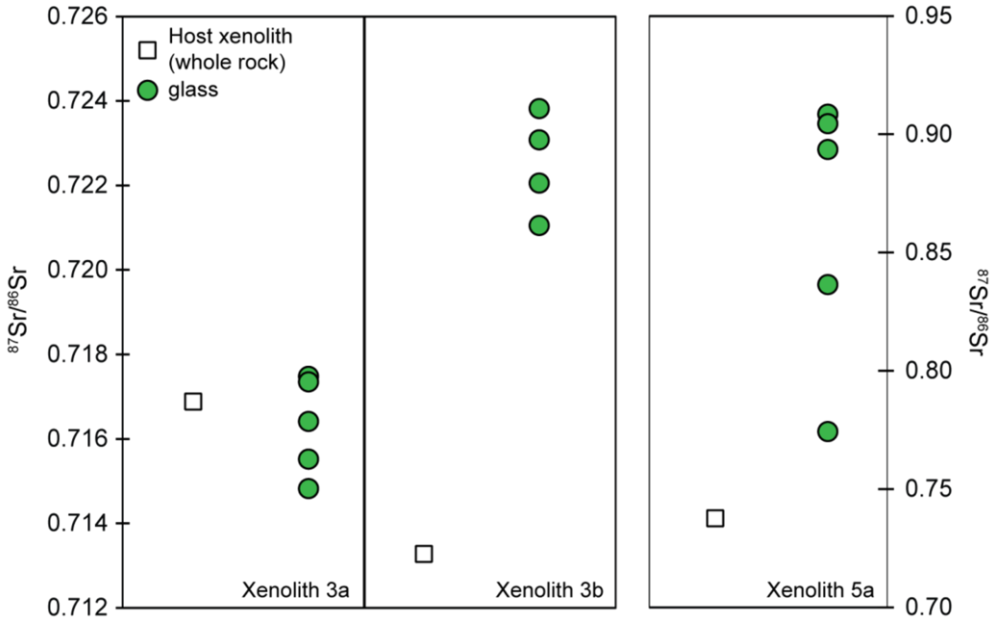

Fig. 6.14. Disequilibrium between source and melt.

From this, the question of what the Rb/Sr nature of the minerals which have contributed to the composition of the anatectic melts arises. As previously noted, the Rb/Sr composition of glass 5a is significantly higher at 29.4 than the other glasses and the sampled biotite and plagioclase feldspar which collectively range from 2.68 to 0.033. This may reflect the contribution from a high Rb/Sr mineral phase which has been exhausted during crustal anatexis. Ruling out biotite (at least that of similar composition to the granites), muscovite is a viable phase that could produce melts with a high Rb/Sr and elevated $^{87}Sr/^{86}Sr$ signatures. Glass 5a also exhibits the highest

concentration of Mn, Cs and Rb (Table 8, Appendix B) which all have Kds in mica of >2 (Adam and Green, 2006). The breakdown of muscovite has been shown to occur at low temperatures and pressures akin to upper amphibolite conditions and before biotite breakdown (Fig. 6.15).

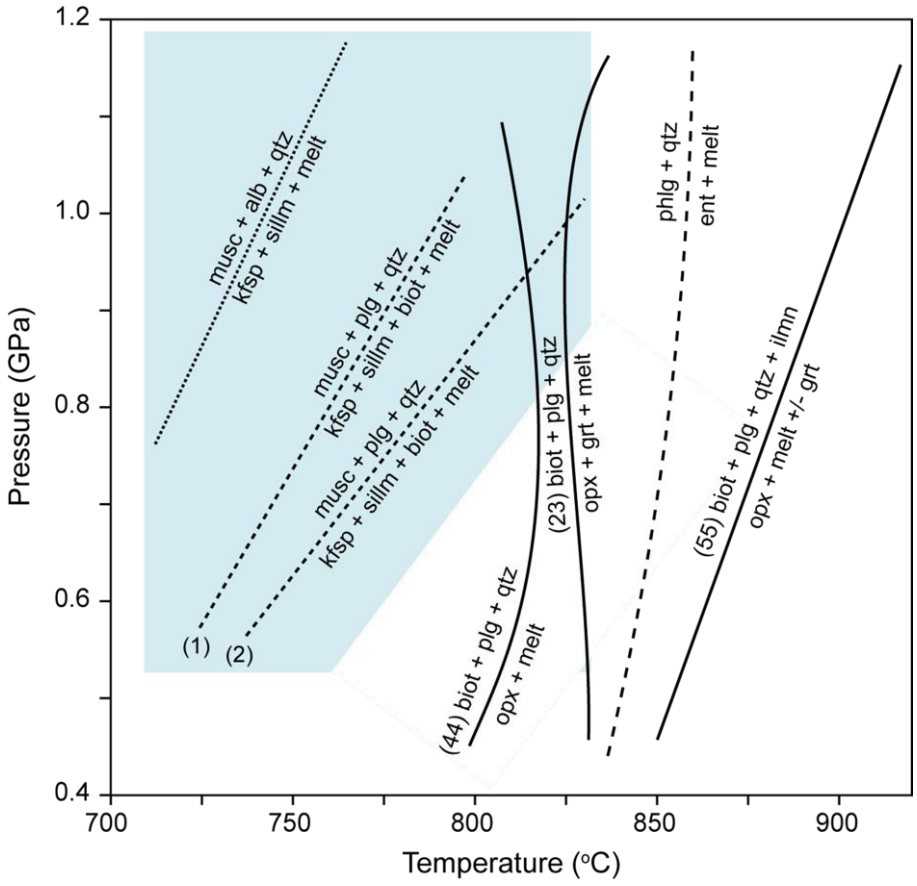

Fig. 6.15. Phase diagram for muscovite and biotite dehydration solidi. Adapted from Farina and Stevens, (2011). Muscovite dehydration field is highlighted in blue.

A progenitor basement lithology to these partially-melted xenoliths may therefore have contained a significant proportion of muscovite. Xenolith 4a may offer an insight into the nature of this lithology as it contains a small proportion (<2%) of muscovite and Zhang et al., (1995) previously reported the out cropping of muscovite-bearing granites in the region.

The extreme geochemical variability exhibited by these glasses (more so than observed in the glasses sampled from Bolivian partially melted xenoliths) supports and re-

affirms the conclusions made in Chapter 5 regarding the caution that should be taken when (1) modelling crustal contamination in open magmatic systems and (2) constraining the behaviour of the crust during anatexis.

6.7.2 Crustal contamination

It was first proposed by Gorai, (1940) that the lavas at Wudalianchi had been contaminated by the surrounding continental crust, through selective resorption of granitic rock leading to the formation of potassic, leucite-rich basalts. There are several analogous instances where ascending magma has assimilated wallrock resulting in anomalous geochemistry that could be compared to the situation at Wudalianchi. Textural similarities to the Wudalianchi xenoliths are seen within alkali-olivine basalts from the Northern Cordillera, British Columbia (Russell and Hauksdottir, 2000), the Mojave Desert of southern California (Knesel and Davidson, 1999) and in the Eifel field, Germany (Shaw, 2009). The former contains felsic xenoliths which are partially fused and either have reacted with or contain invasions of the host magma; they contain 60-90% glass, relict quartz and feldspar and are highly vesicular. Other similarities include streaky, colourless glass thought to be due to local mixing of basaltic and felsic melts (comparable to textures seen in xenolith 3b, Fig. 6.4), and negative Eu anomalies in the xenoliths which are not present in the host (Fig. 6.9). The emplacement of a basalt-andesitic plug into granite country rock in Eastern California was investigated by Al-Rawi and Carmichael, (1967), and it was found that the nearer to the contact, the more glass and less feldspar appeared in the intruding rock. This was inferred to be due to preferential melting of feldspar. This may indicate that the xenoliths from Wudalianchi in which feldspar is absent (5a, b, d) have experienced higher degrees of melting, perhaps due to a longer period of immersion in the hotter, host basanitic magma.

Given the constraints on the components of the crust-magma system provided by this study, the potential for crustal contamination of the 1719-1721 lavas should be evaluated. Fig. 6.16 shows the Sr-isotopic compositions of sampled lavas plotted against wt. % SiO_2 from previous studies for which data is available.

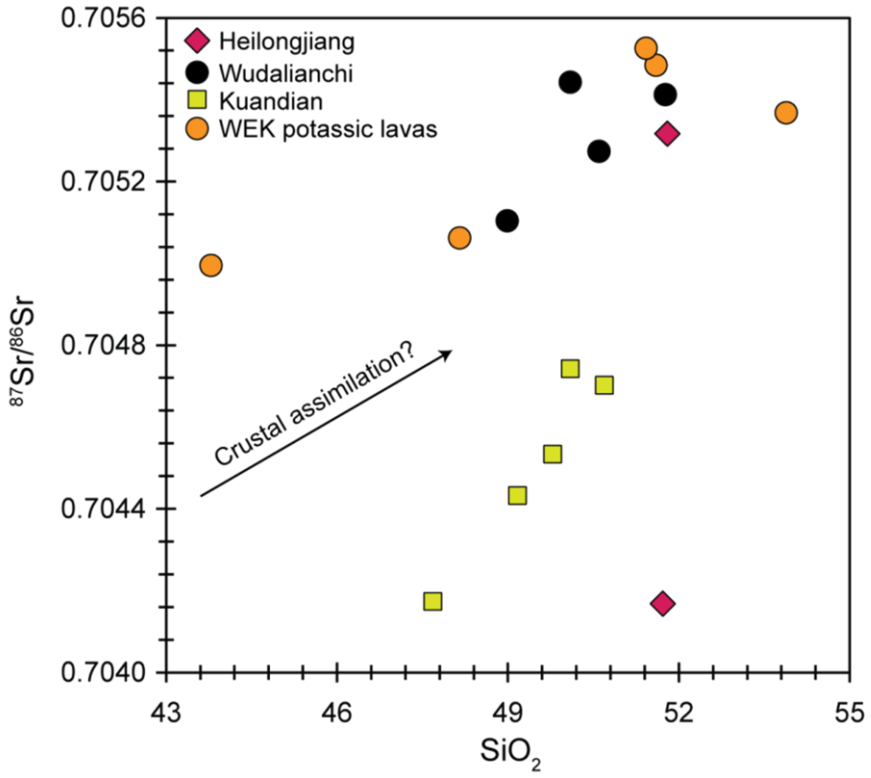

Fig. 6.16. Graph showing SiO_2 plotted against $^{87}Sr/^{86}Sr$ for lavas in NE China. Wudalianchi data from this study and Basu et al., (1991); Kuandian data from Basu et al., (1991), WEK (Wudalianchi-Erkeshan-Keluo) data from Zhang et al., (1991); Heilongjiang from Peng et al., (1986, no location given).

From Fig. 6.16, the lavas at Wudalianchi and the "WEK potassic lavas" were not derived from the same eruptions and no details are given regarding exact field location of the sampling site hence a genetic relationship cannot be verified. The Kuandian samples are from the same volcanic field which covers an area of 35 km by 15 km (Basu et al., 1991) but are derived from five different lava flows and therefore cannot be considered comagmatic.

The positive correlation between an index of differentiation and $^{87}Sr/^{86}Sr$ for sampled lavas in the NE China area is attributable to crustal contamination however, the lack of consistent sampling of comagmatic lava suites limits the degree of interpretation that can be made regarding the role of crustal contamination during magma petrogenesis in this region.

With respect to $^{87}Sr/^{86}Sr$ signatures, the isotopically enriched nature of the glasses precludes incorporation of crustal derived melts, at least those sampled by this study, by ascending mantle-derived melts beneath the Wudalianchi volcanic field. It could be postulated that the trace element signature of the sampled lava could be modelled through mixing between a mantle source and the sampled crustal melts (Fig. 6.17).

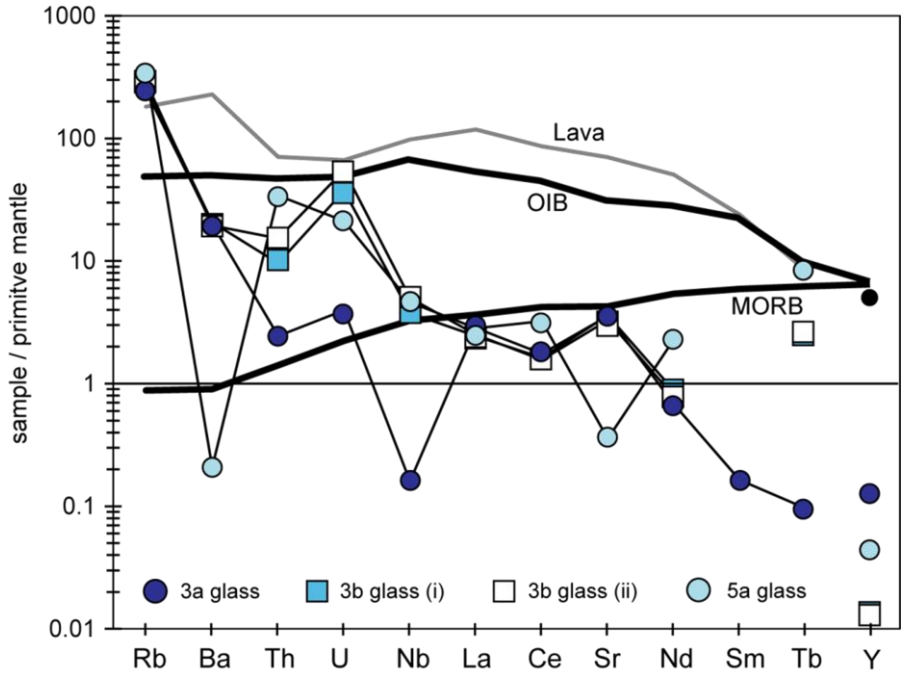

Fig. 6.17. Interaction between an OIB-type source and the sampled melts would fail to reproduce the slightly enriched nature of the lava. OIB, MORB and primitive mantle values from Sun and McDonough, (1989).

As shown in Fig. 6.17, this approach would be unsuccessful given the relatively depleted nature of the glasses. The sampled lava is similar to that of a potential OIB-mantle source with slightly elevated Ba, Rb, and La-Nd. If indeed a melt from the

partially melted xenoliths has been lost, all be it at variable degrees from each xenolith, initial melts may have contributed to this enriched nature. Alternatively, it is possible that initial anatectic melts were removed from the xenoliths prior to quenching during entrainment and have been lost to part of the volcanic system which is unable to be sampled e.g. the surrounding wallrock of the volcanic conduit and the sampled glasses represent a melt composition spatially and temporally unique to each xenolith.

6.8 Conclusions

This study has found that the crustal xenoliths found in recent Wudalianchi lavas are partially melted to different degrees, as seen from textures and mineralogy, melt volume, and type and abundance of residual minerals. Bulk xenolith geochemistry may indicate the loss of an enriched melt from the xenoliths in varying amounts, as seen from relatively LREE-depleted nature of sampled glasses. The Sr-isotopic composition of xenolith mineral phases and glass are significantly different from phases in a sample of unmelted basement granite. This weakens the claim that the sampled granite is the progenitor lithology to the xenoliths, although whole rock Nd isotopes for the granite and xenoliths are similar.

The variations in geochemistry observed throughout the xenolith suite may indicate different degrees of melting and the potential variable loss/extraction of melt. The incorporation of such a melt into the lava is not necessarily reflected in the composition of the host basanite, however transfers of material obviously do occur – as petrographic observation shows that melt interaction occurs on a micro-scale in this system. The Sr-isotopic compositions of sampled anatectic melt are distinct from their source and hence demonstrate that disequilibrium melting has occurred during crustal anatexis.

Despite the initial, apparently simple, relationship between the components of this system, further complexity is clearly required in order to explain all of the observed geochemical signatures. This study has highlighted the importance of a combined petrographical and geochemical approach when investigating complex magmatic systems and demonstrated the extreme Sr-isotopic variability that can exist in potential crustal contaminants.

The Sr-isotopic composition of natural anatectic melts in partially melted xenoliths from El Joyazo, southeast Spain.

7

The data presented in this chapter are the result of a pilot study of the xenoliths at El Joyazo. No manuscript is currently being prepared.

Abstract

The natural occurrence of quenched anatectic melts within partially melted crustal xenoliths erupted within a high-K, dacitic lava from the El Joyazo volcanic centre in southeastern Spain offers an opportunity to assess the Sr-isotopic composition of melts produced during crustal anatexis. Sampled glass is isotopically heterogeneous with respect to $^{87}Sr/^{86}Sr$ signatures ranging from 0.718002 to 0.720216 on the millimetre scale. Sampled plagioclase and biotite exhibit relatively radiogenic and non-radiogenic Sr-isotopic signatures which bracket the range observed in the glass: 0.708479-0.709369 and 0.723402-0.723370 respectively. The initially intuitive relationship between these sampled phases i.e. that the glass represents the variable contribution from the high Rb/Sr mica and low Rb/Sr feldspar phases may not hold true when the isotopic signatures are considered in conjunction with recently published trace element data from the same rock suite (Acosta-Vigil et al., 2010). Instead, the sampled glass may represent muscovite breakdown during early anatexis of the crustal protolith. Chemical disequilibrium is shown to occur between host dacite and enclosed xenoliths, melts quenched within the dacite and xenolith, minerals within the xenolith and within the sampled melt phase. This further documents the inefficiency of Sr-(self)diffusion to establish equilibrium on timescales during which open magmatic systems operate as previously discussed in Chapters 5 and 6.

7.1 Introduction

The high-K dacite erupted from the El Joyazo (Cerro del Hoyazo) volcanic centre in the Neogene Volcanic Province (NVP) of south-eastern Spain has been the focus of intense study since Zeck (1968, 1970) first interpreted the lavas as an erupted crustal-derived melt. Of particular interest at this locality is the abundance of crustal rocks (20-25 vol. %) within the sampled lavas represented by variably partially melted garnet-biotite-sillimanite (Grt-Bt-Sill), spinel-cordierite (Spn-Crd) and quartz-cordierite (Qtz-Crd) xenoliths. These have widely been inferred to have experienced significant partial melt loss (30-55 vol. %, Cesare et al., 1997), a melt which may (Zeck, 1970; Cesare et al., 1997; Perini et al., 2009) or may not (Acosta-Vigil et al., 2010) be represented by the host dacite.

The partially melted xenoliths contain quenched anatectic melt and provide a natural system in which to assess the behaviour of Sr-isotopes during crustal anatexis. This study area offers an ideal opportunity to undertake a comparative study to those presented and discussed in Chapters 5 and 6.

7.2 Geological Setting

The Alborán domain of the western Mediterranean forms part of the Betic-Rif orogen (Fig. 7.1, 7.2 a), a mountain belt produced as a result of subduction during the Cretaceous to Oligocene (de Jong, 1993; Benito et al., 1999) due to the convergent motion between Africa and Eurasia.

Fig. 7.1. Annotated Google Earth image showing the location of the El Joyazo volcanic centre relative to nearby major Spanish cities and neighbouring countries.

The region is characterised by high heat flow, seismic wave attenuation and high, positive, Bouguer gravity anomalies (Torne et al., 2000). This implies that the asthenospheric mantle and/or significant bodies of mantle-derived magmas exist at shallow depths. Results from ODP leg 161 (Comas et al., 1999) indicate that the

continental crust thickens from the floor of the Alborán Sea towards the Betic domain. Similarly, the depth to the Moho has been shown to increase to ~35 km in the heart of the Betic Cordilleras from <12 km in the Alborán domain (Torne et al., 2000).

In the late Miocene, orogenic extension produced a basin which resulted in the thinning of the continental crust, subsequent partial melting and the production of post-collisional Neogene igneous rocks on the European and African Mediterranean margin. Existing models explaining the cause of volcanism in this region include; mantle diapirism (Weijermars, 1985); subduction of oceanic lithosphere beneath the European continental margin accompanied by slab roll back and subsequent detachment (de Jong, 1991); convective removal of a dense lithospheric root (Platt and Vissers, 1989) and delamination of the subcontinental lithosphere (Garcia-Dueñas et al., 1992; Seber et al., 1996).

The NVP of SE Spain trends for ~250 km along the Mediterranean coast from Cabo de Gata in the south west to Mar Menor in the north east (Fig. 7.2 b) and is built on a suite of Palaeozoic metamorphic basement rocks which are overlain by Miocene sediments (Perini et al., 2009). Volcanism is understood to have started at ~15 Ma with the eruption of a calc-alkaline suite at Cabo de Gata. This was followed by high-K calc-alkaline rocks inland at El Joyazo, Mazarrón and Mar Menor and shoshonitic rocks at Vera, Mazarrón and Cartagena (Cesare et al., 2003). Ultrapotassic rocks were emplaced at Vera, Mazarrón and in the northern area of the province before volcanism ceased ~2.7 Ma at Cartagena with the eruption of alkali basalts (Benito et al., 1999). Different models have been proposed to account for the geochemical variability observed between the rock suites, all of which stem from either (1) the melting of different mantle reservoirs or (2) the variable interaction between mantle-derived and crustal-derived melts (e.g. Benito et al., 1999; Turner et al., 1999; Duggen et al., 2005).

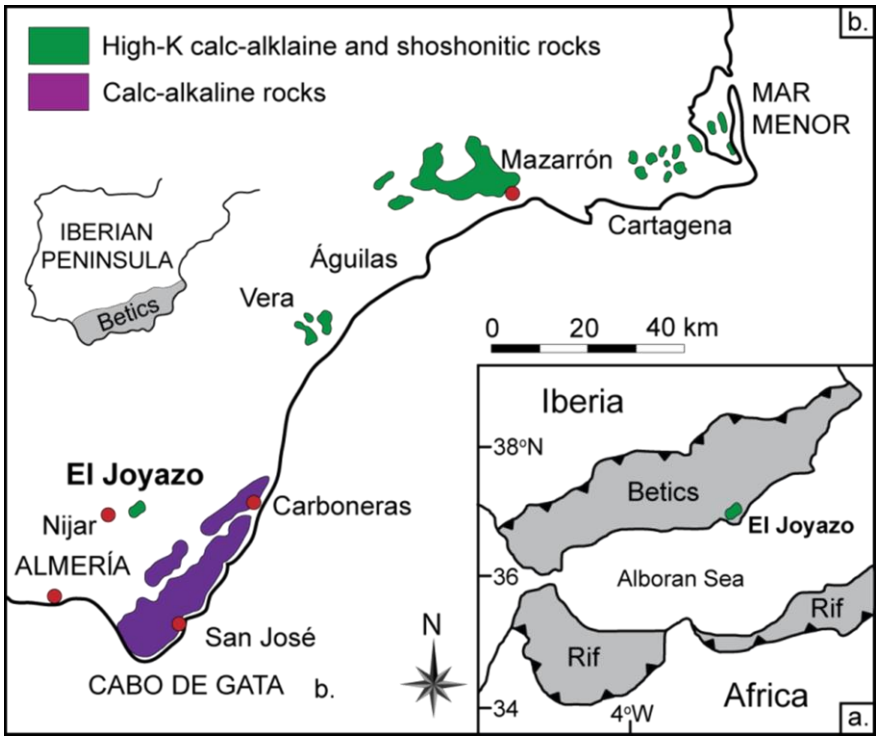

Fig. 7.2 a. Map showing location of the Betic cordillera orogen in south-eastern Spain and conjugate Rif orogen in north-western Africa (map is modified from Cesare et al., 2003). **b**. Map showing distribution of volcanic rocks throughout the Neogene Volcanic Province. Outcrop localities define a NE-SW trend from Almeria to Mar Menor (map is modified from Benito et al., 1999).

One of the most intensely studied volcanic centres in the province is that of El Joyazo, otherwise known as the "garnet volcano" due to the abundance of garnets which are scattered throughout the locality. Their abundance has led this to be the only economic deposit of garnets in Spain (Muñoz-Espadas et al., 2000). The presence of a low velocity zone at 24 ± 1 km depth beneath the volcanic centre and associated high Vp/Vs ratios suggests a high melt content associated with that zone (Julià et al., 2005). El Joyazo has been the focus for numerous geochemical studies over the past three decades due to the relative abundance of partially melted, meta-pelitic, crustal enclaves in the erupted lavas (Zeck, 1970; Bellon et al., 1983; Munksgaard, 1984; Venturelli, 1984; Nelson, 1986; Zeck, 1992; Cesare et al., 1997; Zeck et al., 1998; Cesare and Maineri, 1999; Cesare, 2000; Cesare and Gómez-Pugnaire, 2001; Zeck and Williams, 2002; Cesare et al., 2003a; Cesare et al., 2003b; Perini et al., 2009; Ventura et al., 2009; Álvarez-Valero and Waters,

2010; Acosta-Vigil et al., 2010). An anatectic event beneath the El Joyazo centre is inferred to have occurred at 9.74 ± 0.21 Ma (from monazite, Cesare et al., 2003). This date agrees with the zircon U-Pb age from a growth rim on recycled, basement-derived zircon (Zeck and Williams, 2002; 9.63 ± 0.26 Ma). Dacitic lavas were erupted *c.* 3.4 Ma later at ~6.3 Ma (e.g. Cesare and Gómez-Pugnaire, 2001) but the genetic relationship, if one exists at all, between the two events is not well constrained.

7.3 The El Joyazo centre

This study concentrates on the crustal-derived rocks enclosed within the dacite lavas at El Joyazo which is located 3 km east of Nijar on the southern slope of the Sierra Alhamilla (Fig. 7.3).

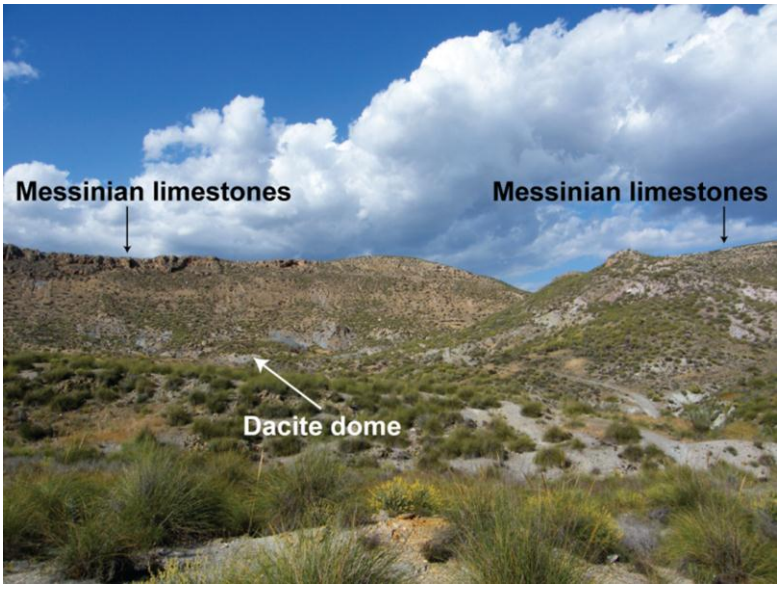

Fig. 7.3. Field photograph of the El Joyazo volcanic centre composed of three dacitic domes set in a circular depression rimmed by Messinian limestones. Photo taken looking north-north-east.

It forms a *c.* 1 km^2 circular valley surrounded by Messinian reef limestones which were deposited on the remnants of the volcanic centre (Fig. 7.3). The location of this volcanism is inferred to be controlled by the Carboneras and Palomares faults, an active strike-slip system which developed as a result of the existing compressional

tectonic regime (Gracia et al., 2006). The volcanic rocks erupted at El Joyazo are cordierite-bearing dacites which are strongly peraluminous and contain ~20-25 vol. % anatectic metapelitic xenoliths and < 10 vol. % of mafic material (enclaves). The metapelitic rocks can be classified into three groups based on their petrography: Grt-Bt-Sill (which are volumetrically the most abundant), Spn-Crd and Qtz-Crd (Zeck, 1970). This study focusses on samples of the Grt-Bt-Sill xenoliths as they contain the highest modal abundance of quenched anatectic melt. The metapelitic xenoliths exhibit evidence for partial melting and subsequent melt extraction in the form of quenched anatectic melt, now glass, as inclusions in the majority of minerals, as intergranular films around constituent phases and as intergrowths with fibrous sillimanite (fibrolite, termed "mix" by Cesare, 2000).

This glass has been shown to be the result of incongruent melting of the metasedimentary protoliths and not a result of melt infiltration from the host dacitic magma (Cesare et al., 2003). The restitic xenoliths are understood to represent crustal residues from 30-55% rhyolitic melt extraction (Cesare et al., 1997) from graphitic metapelitic source rocks, proposed by Cesare and Gómez-Pugnaire, (2001) as the Bt-Grt bearing phyllites of the Alpujárride basement. From the intensive study of the Grt-Bt-Sill xenoliths (Cesare, 2000; Cesare and Gómez-Pugnaire, 2001; Álvarez-Valero et al., 2005; 2007; Acosta-Vigil et al., 2010) two melting events have been identified 1) an early, regional melting event at ~9.6 Ma which led to syn-deformation of the partially melted crustal fragments at 5-7 kbar and 850 ± 50°C. These conditions correlate to a depth of ~25 km which approximates the depth to the Moho in this region indicating that melting occurred close to the crust-mantle boundary, and 2) a less extensive melting event occurring at higher temperatures and lower pressures (900-950°C at 5 kbar, ~6.3 Ma at El Joyazo) which has been attributed to partial melting of the

previously partially-melted xenoliths within the dacitic host magma during residence, ascent and eruption.

A range of petrogenetic models have been put forward for the El Joyazo dacites: anatexis of pelitic metamorphic rocks (Zeck, 1970; Munksgaard, 1984); anatexis of crustal rocks of different lithologies and ages (Zeck et al., 1999); mixing of anatectic and mantle-derived magmas (Zeck, 1992); assimilation of pelitic material into magmas similar to calc-alkaline rocks (Bello et al., 1983); partial melting of a subduction enriched mantle source that has lost a magmatic component prior to a metasomatic event (Venturelli et al., 1984); partial melting of a mantle source metasommatised by fluids derived from a subducting plate ± interaction with crustal liquids (Benito et al., 1999). Despite these different models, many early studies agreed that the metapelitic enclaves and the host dacitic lava were genetically related, with the enclosing dacite representing the anatectic product generated from the melting of, and extraction from, a crustal protolith represented by (or similar to) that represented by the metasedimentary enclaves (e.g. Zeck, 1970; Munskgaard, 1984; Cesare et al., 1997). The erupted dacite was therefore considered the product of crustal anatexis of the metapelites in part contaminated by a mafic magma derived from the mantle as indicated by the presence of rarer mafic enclaves. Alternatively, Cesare and Gómez-Pugnaire, (2001) argued against a cogenetic relationship between the El Joyazo dacite and the enclosed xenoliths and proposed the extracted rhyolitic melt crystallised to form unsampled, plutonic bodies at depth beneath the Alborán domain. This interpretation was recently supported by an in-depth study by Acosta-Vigil et al., (2010) of the trace element composition of the interstitial glass and melt inclusions from the Grt-Bt-Sil xenoliths as well as from the groundmass of the host dacitic lava. The xenolith and dacite-hosted glasses were shown to be compositionally distinct with the

glass in the dacite host representing a higher temperature melt in comparison to the glass within the xenoliths.

The *in-situ* work of this study aims to contribute to the debate regarding the origin of the anatectic melt quenched within the Grt-Bt-Sill xenoliths in addition to examining the Sr-isotopic composition of anatectic melts during crustal melting as previously discussed and presented in Chapters 5 and 6.

7.4 Samples

7.4.1 Host Lavas

The host lava to the suite of partially melted xenoliths is a calc-alkaline, porphyritic dacite (Fig. 7.4 a, b). It consists predominantly of a glassy, rhyolitic groundmass (~50 vol. %) and a crystal assemblage dominated by biotite, cordierite and plagioclase which may constitute the only truly phenocrystic phases present. Antecrystic phases include garnet, biotite, cordierite, graphite, fibrolite (fibrous form of sillimanite), quartz (clearly resorbed), rare orthopyroxene, hornblende, chalcopyrite and hercynitic spinel and accessory apatite, monazite and zircon.

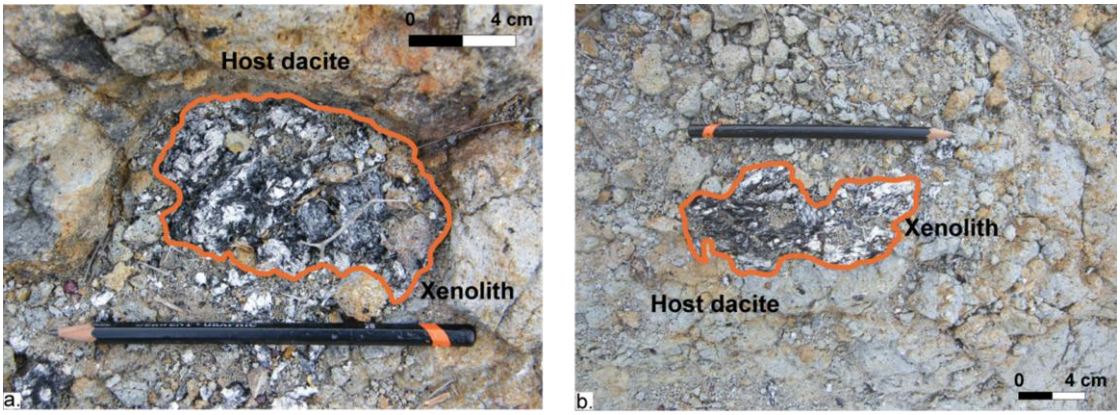

Fig. 7.4. a, b. Field photographs of Grt-Bt-Sill partially melted crustal xenoliths hosted in dacite.

The antecrystic cordierite is compositionally and microstructurally distinct from the phenocrystic cordierite (Buick et al., unpub. data, cited in Acosta-Vigil et al., 2010)

whereas the antecrystic garnet exhibits major and trace element zoning patterns comparable to those observed in garnets within the Grt-Bt-Sill xenoliths (e.g. Munksgaard, 1984). Antecrystic orthopyroxene and hornblende may be derived from the small number (< 10 vol. %) of basic igneous enclaves (aphyric basaltoid rocks after Zeck, 1970) which are scattered throughout the dacites.

7.4.2 Xenoliths

~10-15 vol. % of entrained xenoliths are examples of the Grt-Bt-Sill suite. These occur as subrounded inclusions which range from <2 cm to 15 cm across. Foliation is defined by alternating lenses of biotite and sillimanite which mantles coarse grained almandine-garnet porphyroblasts (0.1-0.9 mm, $Alm_{74-82}Pyp_{10-14}Sps_{1-7}Grs_3$, Cesare et al., 2003) and is clearly visible in hand specimen (Fig. 7.5 a).

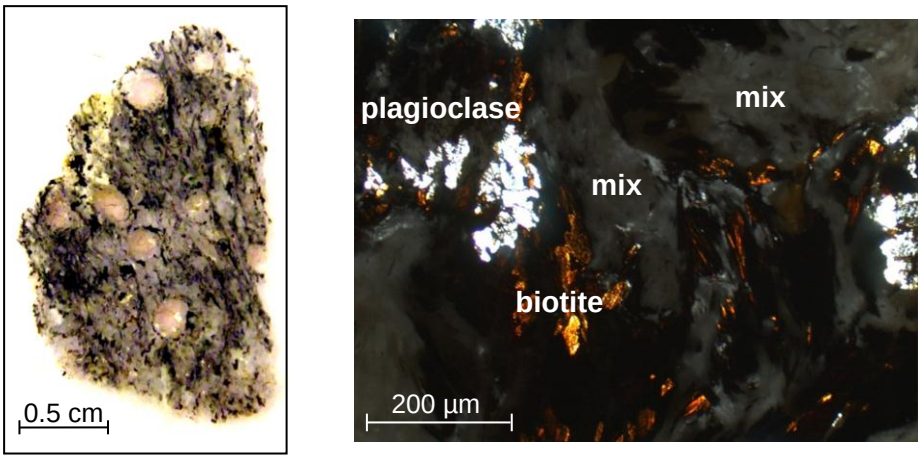

Fig. 7.5 a. Thick section (100 µm) of a Grt-Bt-Sill xenolith containing characteristic garnet porphyroblasts (found as xenocrysts within the dacite host. **b**. intergrown needles of sillimanite and quenched anatectic melt ("mix").

The mineralogical assemblage is further characterised by plagioclase (An_{30-35}, Cesare and Gómez-Pugnaire, 2001), cordierite, graphite, glass, hercynitic spinel, rarer apatite and accessory zircon and monazite which are present as inclusions in garnet. An intricate study of the graphite within these xenoliths by Cesare and Mainer, (1999) revealed peak metamorphic conditions recorded by the Grt-Bt-Sill xenoliths in the

granulite-facies. Glass is present as melt inclusions within garnet and plagioclase indicating these phases grew in the presence of a melt phase. Glass is present between grain boundaries and is intergrown with sillimanite (referred to as "mix" from now on, Fig. 7.5 b) and quartz is present at <1 % or not at all.

7.5 Whole rock Geochemistry (previous work)

Previous studies have characterised the El Joyazo lavas as high-K dacites. They are compositionally similar to volcanic rocks which erupted throughout the NVP which collectively show geochemical signatures akin to active margins e.g. > 13 wt. % Al_2O_3, high Ba/La, La/Nb, Ba/Nb and Zr/Nb (Benito et al., 1999 and references therein). The erupted dacite at El Joyazo exhibits variable $^{87}Sr/^{86}Sr$ signatures ranging from 0.7110 to 0.7143 (Fig. 7.6).

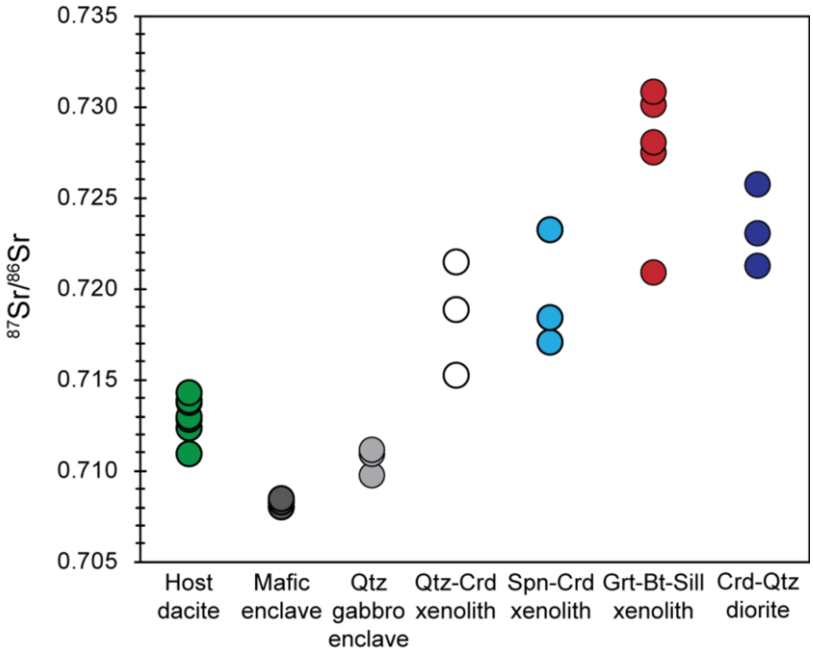

Fig. 7.6. Graph showing Sr-isotopic variability between the different rock types sampled at El Joyazo (whole rock data sourced from Munksgaard, 1984; Benito et al., 1999; Turner et al., 1999; Perini et al., 2009).

These radiogenic values attest to the involvement of continental crust during their petrogenesis. Sampled mafic enclaves within the dacite exhibit lower $^{87}Sr/^{86}Sr$ values and have been hypothesised to represent a mantle-derived influx from depth which ultimately triggered eruption. The Qtz-Crd and Spn-Crd xenolith suites exhibit lower $^{87}Sr/^{86}Sr$ signatures than the Grt-Bt-Sill suite with values ranging from 0.7211 to 0.7310 in the latter compared to a range between 0.7153 and 0.7234 in the former (Fig. 7.6).

7.6 Analytical Methods (microsampling)

The glass phase targeted in this study is the "mix" since matrix glass and melt inclusions were unfortunately too small to sample. The contribution of Sr from sillimanite was assumed to be insignificant (if a contribution existed at all) given the incompatibility of Sr in aluminosilicate phases (Zeng et al., 2005). This assumption was tested by sampling three individual fibrolite grains within the same section as the targeted "mix", each of which failed to produce a signal during analysis on the mass spectrometer. Contribution to the measured $^{87}Sr/^{86}Sr$ from this phase during analysis of the "mix" is therefore ruled out. Details of the microdrilling technique used to sample the "mix" can be found in Appendix E and in Charlier et al., (2006). Details of the procedure used to load small (ng) Sr samples, TIMS running conditions and data correction are given Appendix E and Font et al., (2008). The average $^{87}Sr/^{86}Sr$ for international standard NBS987 during analysis of these samples was 0.710263 ± 0.000011 (2σ, n=18) which agrees extremely well with the accepted NBS987 $^{87}Sr/^{86}Sr$ reported by Thirlwall, (1991) of 0.710248 ± 0.000023 (2σ) (n=427).

7.7 Results

Sampled anatectic melt exhibits variability in its Sr-isotopic composition. Measured $^{87}Sr/^{86}Sr$ values range from 0.718002 to 0.720216 (Fig. 7.7) within the mix over

millimetre length scales. Two sampled biotite crystals are isotopically enriched relative to the sampled glasses at 0.723402 ± 0.000032 and 0.723370 ± 0.000009 whereas sampled plagioclase is less radiogenic at 0.708479 ± 0.000018 and 0.709369 ± 0.000037. Fig. 7.7 also compares the observed variability in the phases analysed during this study to a previous study which analysed mineral $^{87}Sr/^{86}Sr$ compositions within a Grt-Bt-Sill xenolith (Perini et al., 2009). Whole rock analyses of the Grt-Bt-Sill xenolith suite revealed significant Sr-isotopic heterogeneity between individual xenoliths and disequilibrium between constituent biotite, garnet and plagioclase.

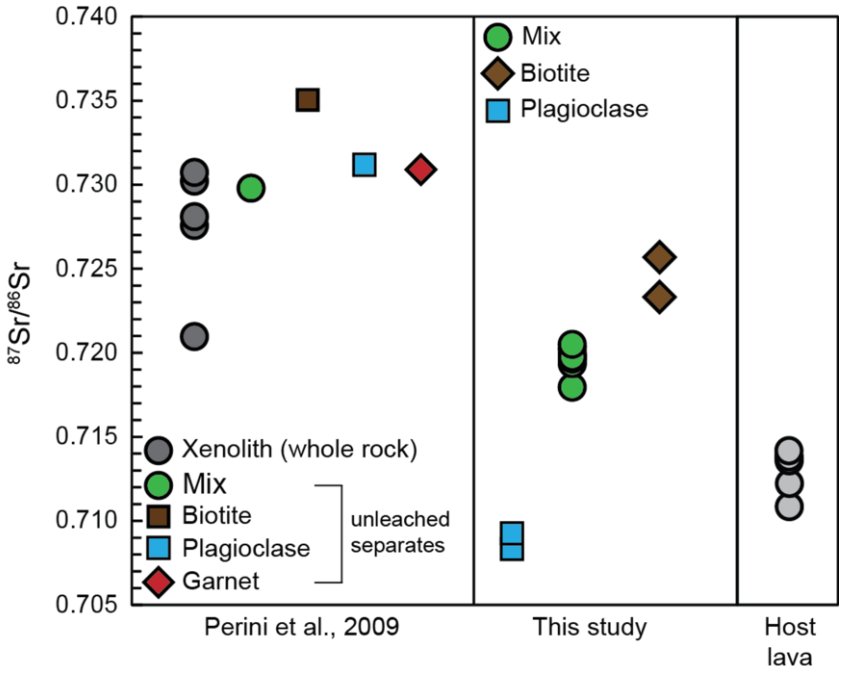

Fig. 7.7. Variable $^{87}Sr/^{86}Sr$ signatures recorded in sampled "mix" (aggregate of sillimanite needles and quenched melt). Also shown is the relatively radiogenic nature of sampled biotite and un-radiogenic nature of plagioclase. Data is compared to $^{87}Sr/^{86}Sr$ values obtained by this study to those of Perini et al., (2009) on mix and mineral separates from the Grt-Bt-Sill xenolith suite. Whole rock values for Grt-Bt-Sill xenoliths from Munksgaard, (1984) and Perini et al., (2009).

7.8 Discussion

The variability observed in $^{87}Sr/^{86}Sr$ within the sampled crustal melts of this study could be interpreted as reflecting variable contributions from different phases breaking

down during anatexis. It could therefore be inferred that the sampled glass is a product of either the dehydration-melting of biotite (e.g. Bt + Pl + Qtz → Melt + Opx) or muscovite (e.g Musc + Plag + Qtz → Melt + Kspar + Sillm + Biot) as discussed in previous chapters (Fig. 5.10, Chapter 5; Fig. 6.14, Chapter 6; Farina and Stevens, 2011).

The high modal abundances of biotite and sillimanite within the Grt-Bt-Sill xenolith suite may indicate their presence in the low-grade, metasedimentary protolith. Alternatively, these phases could be the products of the rapid dehydration of muscovite and chlorite (± garnet, staurolite and quartz, Yardley, 1989). From Acosta-Vigil et al., (2010), the trace element compositions of melt inclusions quenched within garnet, plagioclase and matrix glass within a Grt-Bt-Sill xenolith and the matrix glass within the host dacitic lava were shown to be distinct. This observation questioned the genetic relationship between the host dacite and the partially melted xenoliths i.e. does the dacite magma represent a melt extracted from the xenoliths?

Given the existence of compositionally distinct xenolith suites (Grt-Bt-Sill, Spn-Crd and Qtz-Crd) within the dacite it is easy to envisage that the host lava originated from a number of different crustal protoliths (not necessarily those sampled) and may represent a suite of amalgamated melts with a variable mantle input. This scenario could explain the Sr-isotopic variability observed in the dacite host (whole rock analyses) with $^{87}Sr/^{86}Sr$ ranging from 0.7110 to 0.7143.

Sr-isotopic disequilibrium exists between the host dacite (0.7110 to 0.7143) and the Grt-Bt-Sill xenoliths (0.7211 to 0.7310), between the constituent Rb/Sr phases within a single xenolith (this study; 0.7094-0.7234) and within the melt phase itself (this study; 0.7180-0.7204, Fig. 7.7). The significant $^{87}Sr/^{86}Sr$ heterogeneity within the Grt-Bt-Sill xenolith suite could be attributed to significant differences in the modal abundances of

variable Rb/Sr bearing phases. Alternatively, these signatures may represent variable degrees of anatectic melt removal. The fact that melt is present as primary inclusions within mineral phases, as matrix glass and is intergrown with sillimanite indicates that a melt phase was present throughout the melting history of these xenoliths but does not preclude removal of a fraction of it.

An attempt here is made to put the results from this pilot study for the Sr-isotopic compositions of the anatectic glasses in the xenoliths into the context of El Joyazos history. The significant differences in reported $^{87}Sr/^{86}Sr$ values for the Rb/Sr bearing phases within the Grt-Bt-Sill suite by Perini et al., (2009) and this study warrant evaluation (Fig. 7.7). Measured $^{87}Sr/^{86}Sr$ of biotite in this study is significantly less radiogenic than previously measured: 0.7234 (n=2) compared to 0.7351. This is also true for sampled plagioclase: 0.7085 and 0.7094 compared to 0.7314 of Perini et al., (2009). The values obtained in this study were obtained through microdrilling. This allowed for precise sampling within a phase to take place hence melt and/or mineral inclusions within the grain of interest were avoided. Perini et al., (2009) measured $^{87}Sr/^{86}Sr$ on bulk separates and also reported values for leached (in HCl) garnet separates. In addition, they reported $^{87}Sr/^{86}Sr$ values for numerous unleached and leached mineral separates from xenoliths erupted at Mazarrón volcanic centre ~100 km northeast of El Joyazo (for location see map in Fig. 7.2 b). Consistently, leached samples recorded significantly lower $^{87}Sr/^{86}Sr$ values e.g. 0.7133 ± 0.0006 (2σ, n=2) compared to 0.7309 for garnet at El Joyazo and 0.7113 compared to 0.7233 for biotite at Mazarrón. The significant differences may be the result of phosphate inclusions (apatite ± monazite ± xenotime) present within garnet and biotite which did not attain Sr-isotopic equilibrium with their host (Perini et al., 2009). In the crystal lattices of biotite and garnet, Sr is incompatible: K_ds of between 0.7 (Villemant et al., 1981) and 0.01 (Bea et al., 1994) and between 0.12 (Shimizu, 1980) and 0.0005 (Keleman and Dunn, 1992)

respectively. The host minerals could therefore have acted as chemical barriers to Sr-diffusion. The contribution of phosphate inclusions, or high Rb/Sr melt inclusions (up to 7.5, Acosta-Vigil et al., 2010), to the measured $^{87}Sr/^{86}Sr$ values for the mix and plagioclase separates of Perini et al., (2009) cannot be unequivocally ruled out as no comparative leached samples for these phases are reported.

The minerals involved at the initial anatexis stage of the low grade protolith to the Grt-Bt-Sill xenoliths have been constrained to muscovite, plagioclase and quartz ± biotite ± potassium feldspar on the basis of melt and mineral trace element chemistry (Acosta-Vigil et al., 2010). This may correspond to the anatectic event at *c*. 9.74 Ma identified by Cesare et al., (2003). The intrinsic textural relationship between melt and needles of sillimanite ("mix") can be attributed to a peritectic melting reaction involving muscovite, plagioclase and quartz with the intergrown aluminosilicate phase and melt phase a reaction product:

e.g. Musc + Plg + Qtz → Kfsp + Sillm + Biot + Melt (see Fig. 6.15, Chapter 6)

Acosta-Vigil et al., (2010) suggested a second melting event occurred, possibly associated with the eruption of the dacite *c*. 6.3 Ma, Cesare and Gómez-Pugnaire, (2001), based on the significant difference in compositions between the melt inclusions in phases within the Grt-Bt-Sill xenoliths and matrix glasses within the dacite. The latter exhibited lower LILE concentrations and higher REE and was inferred to indicate the breakdown of biotite:

e.g. Biot + Plg + Qtz → Opx + Grt + Melt (see Fig. 6.15, Chapter 6)

The variable $^{87}Sr/^{86}Sr$ composition of the sampled glass by this study may therefore not to be genetically related to the biotite sampled in the same thick section even though compositions fall between those of the sampled biotite and plagioclase. Instead, the intergrown glass and fibrolite may have crystallised from a melt which formed during the initial stages of crustal anatexis and involved muscovite and plagioclase (± potassium feldspar).

Within the Grt-Bt-Sill xenoliths, two populations of plagioclase and biotite exist, one remnant from the protolith and one a product of partial crystallisation from anatectic melts (Cesare, pers. comm). Texturally, the sampled, microdrilled crystals were euhedral, tabular, displayed no evidence of crystal dissolution and exhibited well-defined edges. Remnant crystals from the protolith, which have experienced numerous melting events might, as a result, be expected to exhibit evidence for dissolution e.g. resorbed and embayed edges. Sampled biotite and plagioclase in this study may therefore represent a secondary stage of crystallisation of these phases.

At El Joyazo, it has been shown that Sr-isotopic heterogeneity exists between; (1) the host dacite and entrained Grt-Bt-Sill xenoliths; (2) the minerals which constitute the sampled xenolith; (3) the glass phases and sampled minerals and (4) within the glass phase itself.

In order to constrain further the melting history of the crustal xenoliths sampled at El Joyazo, detailed microsampling of glass and mineral phases within numerous partially melted xenoliths needs to be undertaken, including the Spn-Crd and Qtz-Crd suites. Only then will it be established if a genetic link between the crustal xenoliths within the erupted dacite exists or not and the degree to which Sr-isotopic disequilibrium

during crustal anatexis has occurred throughout the melting history. This work is, unfortunately, outwith the scope of this thesis.

7.9 Conclusions

At El Joyazo, sampled anatectic melt is compositionally heterogeneous with respect to Sr-isotopes ($^{87}Sr/^{86}Sr$) with measured values ranging from 0.718002 to 0.720216. This range is distinct from the compositions of sampled biotite and plagioclase in the host xenolith demonstrating that Sr-isotopic disequilibrium exists at the mineral scale. As previously documented, melts produced during crustal anatexis can be heterogeneous with respect to Sr-isotopes. The range of $^{87}Sr/^{86}Sr$ compositions observed within the quenched melt at El Joyazo can be attributed to the dehydration melting of muscovite (now exhausted) and feldspar. Subsequent crystallisation of sillimanite and quenching of the melt phase sampled by this study, is inferred to have occurred. This initial study of the El Joyazo xenoliths highlights the need for thorough petrographic and textural characterisation of phases which contribute to the composition of potential contaminating melts produced during anatexis. Importantly, it has been demonstrated that the geological history and context of the protolith needs to be well-constrained in order to comprehensively assess the geochemical evolution of, and evaluate the elemental and isotopic budgets within, an open magmatic system.

Conclusions and Future Work 8

8.1 Introduction

This thesis investigated the nature of the Central Andean continental basement, sampled as crustal xenoliths. From these, rare insights were provided into the lithological and geochemical nature of the crust in this region and constraints on the evolution of the Central Andean margin at ~19^{o}S attained. Evaluation of the crustal contribution to the lavas in which they were hosted was undertaken and the relative crust-mantle contributions to recent (< 25 Ma) monogenetic volcanism across the Bolivian Altiplano investigated. The geochemical characteristics of potential crustal contaminants to ascending mantle-derived magmas were constrained by *in-situ* analyses of quenched anatectic melts and analyses of picked glass and mineral separates from partially melted crustal xenoliths from Bolivia, China and southeast Spain.

The following chapter aims to:

1) succinctly synthesise the conclusions of the previous five chapters in order to address the aims presented in Chapter 1 and;
2) provide suggested directions for future work.

8.2 Conclusions

8.2.1 The Central Andean continental basement

The sampled crustal xenolith suite entrained within lavas at the monogenetic centres of Pampas Aullagas and Quillacas on the Bolivian Altiplano is diverse with lithologies including diorite, microgranite, gneiss and garnet-mica schist. Due to the limited *in-situ* exposure of the continental basement across the region, these xenoliths offer a rare insight into the lithological and geochemical diversity that exists at depth within the crust and provide compositional constraints to investigations of crust-magma

interaction (see 8.2.2). The isotopic heterogeneity exhibited by the xenolith suite is extreme with $^{87}Sr/^{86}Sr$ values extending to 0.7368 which is significantly more radiogenic than any Sr-isotopic signature exhibited by the recent (< 60 Ma) volcanic record. Pb isotopic signatures (particularly $^{206}Pb/^{204}Pb$) reflect the crustal domains previously constrained from scattered exposures of crustal basement rocks throughout the region. Results from *in-situ* U-Pb dating of zircon separates reveal three age populations at *c.* 500 Ma, 1.0-1.2 Ga; and 1.7-1.9 Ga. These age peaks can be correlated to periods of supercontinent formation and break-up and terrane accretion to the proto-Andean margin. The compositional heterogeneity observed within the xenolith suite consistently extends beyond the ranges estimated for the average bulk, lower, middle and upper continental crust demonstrating the need for careful consideration of potential crustal contaminants in open magmatic systems and the need for caution when characterising crustal domains.

8.2.2 Crustal signatures in Central Andean magmas

Lavas erupted from the Plio-Pleistocene monogenetic centres at Pampas Aullagas and Quillacas ~180 km east of the active Andean arc exhibit the highest $^{87}Sr/^{86}Sr$ values of any recent (< 60 Ma) volcanic rock on the Bolivian Altiplano analysed to date. The role of the continental crust during their petrogenesis is clear from petrographical study (presence of xenocrysts) and geochemical characteristics (with $^{87}Sr/^{86}Sr$ correlating with indices of differentiation e.g. SiO_2). The enriched signatures can be modelled through bulk mixing, AFC and EC-AFC modelling using the relatively primitive Chiar Kkollu basalt (44. 7 wt. % SiO_2; 9.25 wt. % MgO) and sampled crustal lithologies as end members. Simple two-component interaction is, however, ruled out and the incorporation of different crustal contaminants is inferred to account for the Sr-isotopic heterogeneity observed within lavas from a single centre. The lavas are interpreted to originate from mantle depths at which garnet was stable but this deep signature has

been overprinted by shallow level processing in the upper crust. The contribution from the continental crust during petrogenesis of lavas erupted from monogenetic volcanic centres towards the arc front is less apparent. Instead, the role of a slab-derived fluid, the contribution of which decreases with distance from the arc, is identified. From major element systematics (e.g. MgO vs. CaO), crustal thickness is inferred to be less beneath the centres behind the arc and on the Central Altiplano and thicker eastward beneath Pampas Aullagas and Quillacas. This is in accordance with recent geophysical evidence which identifies lithospheric thickening due to underthrusting of the Brazilian Craton in the east and lithospheric removal beneath the Central Altiplano to the west.

8.2.3 Geochemical characteristics of anatectic melts

Analysis of quenched crustal melts (glass) for their elemental and Sr-isotopic compositions reveals significant chemical and Sr-isotopic disequilibrium between melt and source existing over sub-millimetre length scales in a natural system. This observed heterogeneity demands that a more robust characterisation of the crustal component (which goes beyond the traditional whole rock approach) be obtained in geochemical investigations of open magmatic systems. The chemical variability, with particular reference to Sr-isotopes, observed in sampled glasses is reconciled with variable contributions from the different Rb/Sr bearing phases in the protolith i.e. micas and feldspar, which will contribute radiogenic and non-radiogenic Sr respectively. Considering melt segregation and Sr diffusion timescales, the process by which heterogeneities observed at the micro-scale are produced can be scaled up i.e. the variability can be shown to account for the geochemical disequilibrium observed at the hand specimen and outcrop scale.

8.3 Future Work

8.3.1 Crustal Anatexis

In-situ analysis of quenched anatectic melts for their elemental and Sr-isotopic characteristics from this work has provided an exciting insight into 1) how the continental crust melts, and 2) the implications that complexities inherent to this process have for modelling open magmatic systems. Further constraints could be yielded from the Pb-isotopic compositions of these melts as the Pb-isotope system is widely used as a "crustal basement mapping" tool. Isotopically distinct crustal domains at depth have been inferred to exist by the signature they leave in the volcanic rocks which have erupted through them (see Chapter 4, Wörner et al., 1992; Aitcheson et al., 1995) yet the process through which Pb-isotopic signature is inherited remains unconstrained.

Additional insights could be yielded from the Sm-Nd isotopic system. Unlike the Rb-Sr system which is controlled by key rock forming minerals (micas and feldspars), results from recent experimental work, and modelling derived therefrom (Zeng et al., 2005), has demonstrated the control of Sm/Nd ratios and Nd-isotopic signatures in anatectic melts by the dissolution of accessory phases such as apatite and monazite. This system should not however be considered in isolation as the occurrence (or not) of the dehydration reactions involving muscovite and biotite, which play a key role in assessing the Rb-Sr systematics of crustal melts, have been shown to influence the rate at which apatite and monazite relatively dissolve (Zeng et al., 2005). Further constraints on the generation of crustal melts and intra crustal differentiation could be yielded by combining the micro-analytical approach with 1) investigations of the physical conditions such as pressure, temperature, water content ± the presence of

fluids in partially-melted systems through multi-component experiments; 2) timescales of diffusion and; 3) melt segregation i.e. from source to surface.

8.3.2 The Central Andes

The U-Pb ages yielded from *in-situ* analyses of cores and rims in metamorphic zircons from crustal xenoliths derived from the Bolivian continental basement provided a rare insight into the evolution of the Central Andean continental margin. The U-Pb work carried out on the xenolith suite (presented in Chapter 3) was a pilot study carried out on a suite of zircon separates from only two of the sampled xenoliths. Additional insights into the evolution of the Central Andean margin could be yielded from zircon separates from many of the remaining 72 xenoliths. By comparing results from the crustal xenolith study with those derived from zircons in the Miocene to recent ignimbrites of the Altiplano-Puna Volcanic Complex (APVC, Kaiser et al., 2011; Kern et al., 2011; Iriarte et al., 2011) an interesting evaluation of the role of crustal recycling in the genesis of one of the largest ignimbrite plateaus on Earth would be provided. Initial results are encouraging and indicate the presence of antecrystic, crustal derived zircons in the erupted units (*c*. 1.4 Ga; Jamie Kern and Shan de Silva, pers. comm).

The lavas at Pampas Aullagas (PA), Quillacas (QL) and numerous other monogenetic centres across the Altiplano at ~19^{o}S have been used to evaluate the relative importance of crust and mantle contributions during the petrogenesis of magmas with distance from the active Andean arc. Whilst a comprehensive data set for the centres at PA and QL exists, each of the other centres is characterised by one sample only. Multiple analyses of lavas from the monogenetic centres of PA and QL revealed significant geochemical heterogeneity, particularly in Sr-isotopic signatures. In order to 1) improve characterisation of mantle and crustal sources and 2) to further

understanding of how these contributions change with distance from an arc (i.e. subduction zone geometry) further sampling of the suite of monogenetic centres across the Bolivian Altiplano is suggested. Identification of potential mantle sources in this region of anomalously thick crust would improve petrogenetic modelling of crust-mantle interaction i.e. sampling of mantle xenoliths. However, mantle xenoliths have not yet been identified in this region of the Central Andes.

8.3.3 The Andean Cordillera

8.3.3.1 U-Series disequilibria

The short lived disequilibria between the nuclides produced from U and Th decay (Fig. 8.1) has been used to track magmatic processes at subduction zones e.g. time scales of magma differentiation and sediment fluxes from the downgoing slab (Turner et al., 2000; Handley et al., 2011; Turner et al., 2012). The following characteristics for mantle derived U-series disequilibria have been identified:

1) The fluid mobile elements U and Ra (^{226}Ra having decayed from ^{238}U) have been shown to correlate with Ba/Th ratios (as indicators of fluid metasomatism) and are interpreted as recording recent fluid addition to the sub arc mantle wedge (e.g. Turner and Hawkesworth, 1997);
2) correlations between ^{230}Th/^{232}Th and ^{238}U/^{232}Th have been used as an indicator of the time between addition of fluid to the mantle wedge and eruption at the arc (Turner et al., 2001: 20 – 150 kyr);
3) ^{226}Ra excesses suggests as few as several hundred years for the transport described in 2) (Turner et al., 2001);
4) Excess ^{231}Pa (^{231}Pa/^{235}U) is understood to represent the overprinting of partial melting processes i.e. decompression melting, on slab-fluid signatures (e.g. Thomas et al., 2002; Turner et al., 2006).

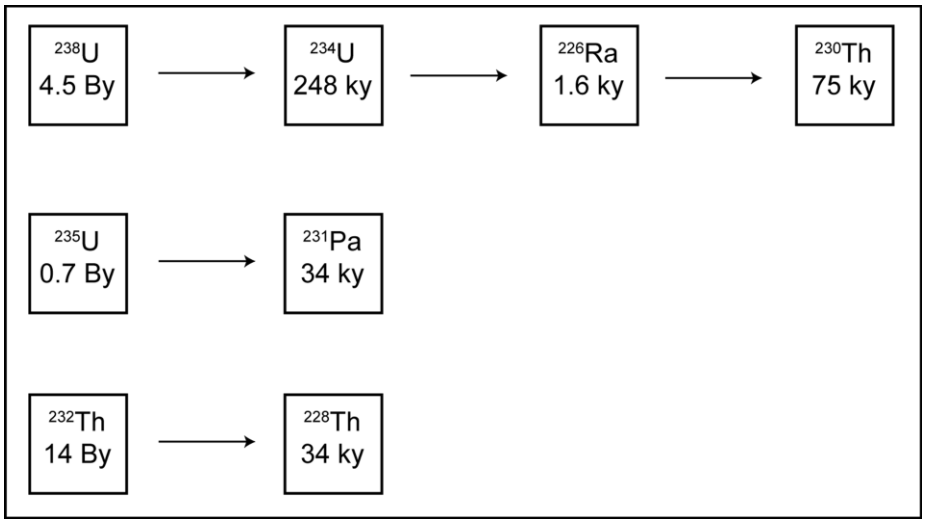

Fig. 8.1. U-Th decay scheme for isotopes (and half lives) used during U-series disequilibria studies in arc rocks. Note: not all decay products are shown.

Few studies on individual volcanic centres exist but often reveal significant changes in the geochemical characteristics of erupted units over time. These variations could be the result of variable interaction over short time scales with the overlying continental crust (e.g. Price et al., 2007; Handley et al., 2008).

Recent U-series work in the Andes has focused on Cotopaxi Volcano in Ecuador, Garrison et al., (2006), Volcan Llaima in Chile, Reubi et al., (2011) and Volcan Quizapu in Central Chile (Ruprecht and Cooper, 2012). Results from the former two studies emphasised the importance of considering the role of the continental crust during magma petrogenesis with fractionation of apatite and allanite in rhyolites (i.e. highly differentiated magmas) identified as a possible source of observed ^{238}U excess (Garrison et al., 2006). Further to this, Reubi et al., (2011) cautioned the use of compositional arrays defined by incompatible trace elements ratios (see 1) above) and U-series data on the basis that these trends could also represent bulk assimilation of plutonic crustal lithologies and variable degrees of magma mingling. Ruprecht and Cooper, (2012) integrated crystal residence ages from the ^{226}Ra-^{230}Th system with

elemental diffusion timescales on plagioclase populations within dacitic magmas to show that mixing of different magma batches at depth occurred in the order of days to weeks prior to eruption.

A dedicated U-series study of recent lavas erupted along the Andean arc would aim to;

1) provide a more robust characterisation of the role of the continental crust in the U-series signatures; to what extent is the crustal contribution quantifiable?;
2) identify along-arc changes both in the crust and mantle contribution and
3) highlight a potential relationship between U-series and crustal thickness as discussed in Garrison et al., (2006) and reveal any along-arc differences.

8.3.3.2 Thermobarometry

The Andes form the longest active mountain chain on Earth and the volcanic rocks erupted at each volcano on the arc, from Nevado del Ruiz in Colombia to Fueguino in the Tierra del Fuego archipelago (Chile/Argentina), provide a unique record of each edifices evolution. The crystal cargo within the andesites (and basalts, trachy-andesites etc.) can be used to offer an insight into the conditions of crystallisation beneath the surface. It has long been recognised that the crystal population entrained within lavas at arcs has 1) not crystallised from the magma it is observed in and 2) may contribute to a significant antecrystic population. The different crystal populations within these lavas therefore provide a record of differentiation at an unconstrained crustal level in the conduit system beneath the volcano. Thermobarometric constraints from crystal populations have the potential to provide insights into the magma storage system at various crustal levels beneath arc volcanos e.g. the thermobarometers of Yang et al., (1996) and Putirka, (2008) for glass and coexisting equilibrium minerals e.g. clinopyroxene-melt and plagioclase-melt. These have recently been applied to tephras

from the 2010 Eyjafjalljökull eruption in Iceland **(**Keiding and Sigmarsson, *in press* in JGR-Solid Earth). The hornblende-plagioclase thermobarometer (e.g. Schmidt, 1992; Holland and Blundy, 1994; Ridolfi, 2011) can similarly be used to identify different crystal cargos and magma mingling such as been done for the andesites-dacites at Mt Hood in the Cascades, western USA (Koleszar et al., 2011).

Relatively little work aimed at investigating the depth at which magmas crystallise beneath Andean arc volcanoes has been carried out. An interesting potential project could therefore be to pick apart crystal populations from previously-studied, well - characterised volcanoes along the arc and to carry out detailed thermobarometric work on the different crystal cargos in order to establish along arc changes in the magma plumbing system.

From this, the effect (or not) of crustal thickness and its nature on the storage system could be evaluated as the northern Andes are underlain by thick, young and mafic crust, the central Andes by thick, old and felsic crust and the southern Andes by thin, young crust.

References

Acosta-Vigil, A., Buick, I., Hermann, J., Cesare, B., Rubatto, D., London, D., and Morgan VI, G. B. (2010). Mechanisms of Crustal Anatexis: a Geochemical Study of Partially Melted Metapelitic Enclaves and Host Dacite, SE Spain: Journal of Petrology, v. 51; p. 785-821.

Adam, J., and Green, T. (2006). Trace element partitioning between mica- and amphibole-bearing garnet lherzolite and hydrous basanitic melt: 1. Experimental results and the investigation of controls on partitioning behaviour: Contributions to Mineralogy and Petrology, v. 152; p. 1-17.

Aitcheson, S. J., Harmon, R. S., Moorbath, S., Schneider, A., Soler, P., Soria, E. E., Steele, G., Swainbank, I., and Wörner, G. (1995). Pb isotopes define basement domains of the Altiplano, Central Andes: Geology, v. 23; p. 555–558.

Allen, J. M. (1998). Atlantis: The Andes Solution: The Discovery of south America as the Legendary Continent of Atlantis: The Theory and the Evidence, W & N Publishers; 184p.

Allmendinger, R. W., Jordan, T. E Palma, M and Ramos, V. A. (1982). Perfil estructural en la Puna Catamarqueña Quinto Congreso Latinoamericano de Geologia, Buenos Aires, Argentina, Actas 1; p. 499–518.

Allmendinger R. W., Ramos, V. A., Jordan, T. E., Palma, M., and Isacks, B. L., (1983). Paleogeography and Andean structural geometry, northwest Argentina: Tectonics, v.2; p. 1–16.

Allmendinger, R. W., and Gubbels, T. (1996). Pure and simple shear plateau uplift, Altiplano-Puna, Argentina and Bolivia: Tectonophysics, v. 259; p. 1-13.

Allmendinger, R. W., Jordan, T. E., Kay, S. M., and Isacks, B. L. (1997). The evolution of the Altiplano- Puna plateau of the Central Andes: Annual Review of Earth and Planetary Sciences, v. 25; p. 139–174.

Al-Rawi, Y., and Carmichael, I. S. E. (1967). A note on the natural fusion of granite: The American Mineralogist, v. 52; p. 1806-1814.

Álvarez-Valero, A. M., Cesare, B., Kriegsman, L. M. (2005). Formation of elliptical garnets in a metapelitic enclave by melt-assisted dissolution and reprecipitation: Journal of Metamorphic Geology, v. 23; p. 65-74.

Álvarez-Valero, A. M., Cesare, B., Kriegsman, L. M. (2007). Formation of melt-bearing spinel–cordierite–feldspars coronas after garnet in metapelitic xenoliths. Reaction modelling and geodynamic implication: Journal of Metamorphic Geology, v. 25; p. 305-320.

Álvarez-Valero, A. M and Waters, D. J. (2010). Partially Melted Crustal Xenoltihs as a Window into Sub-Volcanic Processes: Evidence from the Neogene Magmatic Province of the Betic Cordillera, SE Spain: Journal of Petrology, v. 51; p. 973-991.

Aspden, J. A., McCourt, W. J., and Brook, M. (1987). Geometrical control of subduction-related magmatism: the Mesozoic and Cenozoic plutonic history of Western Colombia: Journal of the Geological Society of London, v. 144; p. 893-905.

Arndt, N. T., and Goldstein, S. L. (1987). Use and abuse of crust-formation ages: Geology, v. 15; p. 893-895.

Arzi, A. A. (1978). Critical phenomena in the rheology of partially melted rocks: Tectonophysics, v. 44; p. 173-184.

Babeyko, A. Y., and Sobolev, S. V. (2005). Quantifying different models of the late Cenozoic shortening in the central Andes: Geology, v. 33; p. 621–624.

Bachmann, O., Dungan, M. A., and Bussy, F. (2005). Insights into shallow magmatic processes in large silicic magma bodies: the trace element record in the Fish Canyon magma body, Colorado: Contributions to Mineralogy and Petrology, v. 149; p. 338-349.

Baier, J., Audétat, A., and Keppler, H. (2008). The origin of the negative niobium tantalum anomaly in subduction zone magmas: Earth and Planetary Science Letters, v. 267; p. 290-300.

Barbero, L., Villaseca, C., Rogers, G., and Brown, P. E. (1995). Geochemical and isotopic disequilibrium in crustal melting: An insight from the anatectic granitoids from Toledo, Spain: Journal of Geophysical Research, v. 100; p. 15745-15765.

Bard, J.-P., Botello, R., Martinez, C., and Subieta, T. (1974) Relations entre tectonique, métamorphisme et mise en place d'un granite éohercynien á deux micas dans la Cordillére Real de Bolivie (massif de Zongo-Yani): Serie Geologie, v. 6; p.3-18.

Barnes, J. B., Ehlers, T. A., McQuarrie, N., O'Sullivan, P. B., and Tawackoli, S. (2008). Thermochronometer record of central Andean Plateau growth: Tectonics, v. 27; TC3003.

Barnes, J. B., and Ehlers, T. A. (2009). End member models for Andean Plateau uplift: Earth Science Reviews, v. 97; p.105–132.

Basu, A. R., Junwen, W., Wankang, H., Guanghong, X., and Tatsumoto, M. (1991). Major element, REE, and Pb, Nd and Sr isotopic geochemistry of Cenozoic volcanic rocks of eastern China: implications for their origin from suboceanic-type mantle reservoirs: Earth and Planetary Science Letters, v. 105; p. 149-169.

Bayhan, H., Aydar, E., Erdal, S. and Gourgaud, A. (2006). Melting of crustal xenoliths within ascending basalt: Example from the Kula volcanic field, western Anatolia, Turkey: Comptes Rendus Geoscience, v. 338; p. 237-243.

Bea, F., Pereira, M. D., and Stroh, A. (1994). Mineral/leucosome trace-element partitioning in a peraluminous migmatite (a laser ablation-ICP-MS study): Chemical Geology, v. 117; p. 291-312.

Beck, M. E. (1988). Analysis of Late Jurassic-Recent paleomagnetic data from active plate margins of South America: Journal of South American Earth Sciences, v. 1; p. 39-52.

Beck, S. L., Zandt, G., Myers, S. C., Wallace, T. C., Silver, P. G., and Drake, L. (1996). Crustal-thickness variations in the central Andes: Geology, v. 24; p. 407–410.

Beck, S., and Zandt, G., (2002). The nature of orogenic crust in the central Andes: Journal of Geophysical Research, v. 107; p. ESE 7-1.

Bellon, H., Bordet, P., and Montenat, C. (1983). Le magmatisme néogène des Cordillères Bétiques (Espagne): chronologie et principaux caractères géochimiques: Bulletin de la Societe Geologique de France, v. 25; p. 205-218.

Benito, R., López-Ruiz, J., Cebriá, J. M., Hertogen, J., Doblas, M., Oyarzun, R. and Demaiffe, D. (1999). Sr and O isotope constraints on source and crustal contamination in the high-K calc-alkaline and shoshonitic Neogene volcanic rocks of SE Spain: Lithos, v. 46; p. 773-802.

Burchfield, B. C., and Davis, G. A. (1975). Structural Framework and Evolution of the Southern Part of the Cordilleran Orogen, Western United States: American Journal of Science, v. 272; p. 97-118.

Bjerg, E. A., Ntaflos, T., Thöni, M., Aliani, P., and Labudia, C. H. (2009). Heterogenous Lithospheric Mantle beneath Northern Patagonia: Evidence from Prahuaniyeu Garnet- and Spinel-Peridotites: Journal of Petrology, v. 50; p. 1267-1298.

Bourdon, E., Eissen, J. P., Gutscher, M. A., Monzier, M., Samaniego, P., Robin, C., Bollinger, C., and Cotten, J. (2002). Slab melting and slab melt metasommatism in the northern Andean volcanic zone: Adakites and high-Mg andesites from Pichincha volcano (Ecuador): Bulletin de la Societe Geologique de France, v. 173; p. 195–206.

Bowen, N. L. (1928). The Evolution of the Igneous Rocks, Dover Publications, New York.

Brenan J. M., Shaw H. F., Phinney D. L., and Ryerson F. J. (1994). Rutile-aqueous fluid partitioning of Nb, Ta, Hf, Zr, U and Th: Implications for high field strength element depletions in island-arc basalts: Earth and Planetary Science Letters, v. 128; p. 327–339.

Brown, M., and Rushmer, T. (2006). Evolution and Differentiation of the Continental Crust. Cambridge University Press.

Brown, M. (2007). Crustal melting and melt extraction, ascent and emplacement in orogens: mechanisms and consequences: Journal of the Geological Society of London, v. 164; p. 709–730.

Bryant, J. A., Yogodzinski, G. M., Hall, M. L., Lewicki, J. L., and Bailey, D. G. (2006). Geochemical Constraints on the Origin of Volcanic Rocks from the Andean Northern Volcanic Zone, Ecuador: Journal of Petrology, v. 47; p. 1147-1175.

Caffe, P. L., Trumbull, R. B., Coira, B. L., and Romer, R. L. (2002). Petrogenesis of Early Neogene Magmatism in the Northern Puna; Implications for Magma Genesis and Crustal Processes in the Central Andean Plateau: Journal of Petrology, v. 43; p. 907-942.

Carlier, G., Grandin, G., Laubacher, G., Marocco, R., and Mégard, F. (1982). Present Knowledge of the Magmatic Evolution of the Eastern Cordillera of Peru: Earth Science Reviews, v. 18; p. 253-283.

Casquet, C., Pankhurst, R. J., Rapela, C. W., Galindo, C., Fanning, C. M., Chiaradia, M., Balso, E., González-Casado, J. M., and Dahlquist, J. A. (2008). The Mesoproterozoic Maz terrane in the Western Sierras Pampeanas Argentina, equivalent to the Arequipa-Antofalla block of Southern Peru? Implications for West Gondwana margin evolution: Gondwana Research, v. 13; p. 163-175.

Cawood, P. A., Nemchin, A . A., Strachan, R. (2007). Provenance record of Laurentian passive-margin strata in the northern Caledonides: Implications for paleodrainage and paleogeography: Geological Society of America Bulletin, v. 119; p. 993-1003.

Cesare, B., and Maineri, C. (1999). Fluid-present anatexis of metapelites at El Joyazo (SE Spain): constraints from Raman spectroscopy of graphite: Contributions to Mineralogy and Petrology, v. 135; p. 41-52.

Cesare, B., Salvioli-Mariani, E., and Venturelli, G. (1997). Crustal anatexis and melt extraction during deformation in the restitic xenoliths at El Joyazo (SE Spain): Mineralogical Magazine, v. 61; p. 15-27.

Cesare, B. (2000). Incongruent melting of biotite to spinel in a quartz-free restite at El Joyazo (SE Spain): Textures and reaction characterization: Contributions to Mineralogy and Petrology, v. 139; p. 273-284.

Cesare, B., and Gómez-Pugnaire, M. T. (2001). Crustal melting in the Alborán Domain: Constraints from Xenoliths of the Neogene Volcanic Province: Physics and Chemistry of the Earth (A); p. 255-260.

Cesare, B., Gómez-Pugnaire, M. T., and Rubatto, D. (2003a). Residence time of S-type anatectic magmas beneath the Neogene Volcanic Province of SE Spain: a zircon and monazite SHRIMP study: Contributions to Mineralogy and Petrology, v. 146; v. 28-43.

Cesare, B., Meli, S., Nodari, L., and Russo, U. (2003b). Hydrogen deficiency in Ti-rich biotite from anatectic metapelites (El Joyazo – SE Spain): crystal-chemical aspects and implications for high-temperature petrogenesis: American Mineralogist, v. 88; p. 583-595.

Charlier, B. L. A., Ginibre, C., Morgan, D., Nowell, G. M., Pearson, D. G., Davidson, J. P. and Ottley, C. J. (2006). Methods for microsampling and high-precision analysis of strontium and rubidium isotopes at single crystal scale for petrological and geochronological applications: Chemical Geology, v. 232; p. 114-133.

Chew, D. M., Kirkland, C. L., Schaltegger, U., and Goodhue, R. (2007). Neoproterozoic glaciation in the Proto-Andes: Tectonic implications and global correlation: Geology, v. 35; p. 1095–1099.

Chew, D. M., Magna, T., Kirkland, C. L., Miskovic, A., Cardona, A., Spikings, R., and Schaltegger, U. (2008). Detrital zircon fingerprint of the Proto-Andes: Evidence for a Neoproterozoic active margin?: Precambrian Research, v. 167; p. 186–200.

Chew, D. M., Cardona, A., and Miškovi□, A. (2011). Tectonic evolution of western Amazonia from the assembly of Rodinia to its break-up: International Geology Review, v. 53; p. 1280-1296.

Christensen. N. I., and Mooney, W. D. (1995). Seismic velocity structure and composition of the continental crust: A global view: Journal of Geophysical Research, v. 100; p. 9761-9788.

Cladouhos, T. T., Allmendinger, R. W., Coira, B., and Farrar, E. (1994). Late Cenozoic deformation in the Central Andes: fault kinematics from the northern Puna, northwest Argentina and southwestern Bolivia: Journal of South American Earth Sciences, vol. 7; p. 209-228.

Clarke F. W. (1889). The relative abundance of the chemical elements: Philosophical Society of Washington Bulletin v. 11; p. 131–142.

Clarke F. W. and Washington H. S. (1924). The composition of the Earth's crust. USGS Professional Paper, v. 127; 117p.

Clemens J. D., and Vielzeuf, D. (1987). Constraints on melting and magma production in the crust: Earth and Planetary Science Letters, v. 86; p. 287-306.

Coira, B., Davidson. J., Mpodozis. C., and Ramos. V. A. (1982). Tectonic and magmatic evolution of the Andes of northern Argentina and Chile: Earth Science Reviews, v. 18; p. 303–332.

Collo, G., Astini, R. A., Cawood, P. A., Buchan, C., and Pimental, M. (2009). U-Pb detrital zircon ages and Sm-Nd isotopic features in low-grade metasedimentary rocks of the Famatina belt: implications for late Neoproterozoic-early Palaeozoic evolution of the proto-Andean margin of Gondwana: Journal of the Geological Society of London, v. 166; p. 303-319.

Comas, M. C., Platt, J. P., Soto, J. I., and Watts, A. B. (1999). The origin and tectonic history of the Alboran Basin: insights from Leg 161. In: Zahn, R., Comas, M.C., Klaus, A. (Eds.), Proceedings ODP: Scientific Results, v. 161, p. 555–579.

Condie, K. C., and Potts, M. J. (1969). Calk-alkaline volcanism and the thickness of the early Precambrian crust in North America: Canadian Journal of Earth Sciences, v. 6; p. 1179-1184.

Condie, K. C. (1993). Chemical composition and evolution of the upper continental crust: contrasting results from surface samples and shales. Chemical Geology, 104; p. 1-37.

Condie, K. C. (1998). Episodic continental growth and supercontinents: a mantle avalanche connection? Earth and Planetary Science Letters, v. 163; p. 97-108.

Cordani, U. G., Cardona, A., Jimenez, D. M., Liu, D., and Nutman, A. P. (2005). Geochronology of Proterozoic basement inliers in the Colombian Andes: tectonic history or remnants of a fragmented Grenville belt From*:* Vaughan, A. R. M., Leat, P. T., Pankhurst, R. J. (eds) 2005. Terrane Processes at the Margins of Gondwana: Geological Society of London Special Publications, v. 246; p. 329-346.

Dalziel, I. W. D. (1994). Precambrian Scotland as a Laurentia-Gondwana link: Origin and significance of cratonic promontories: Geology, v. 22; p. 589–592.

Dalziel, I. (1997). Neoproterozoic-Palaeozoic geography and tectonics: Review, hypothesis, environmental speculation: Geological Society of American Bulletin, v. 109; p. 16-42.

Damm, K. W., and Pichowiak, S. (1981). Geodynamik und Magmengenese in der Kiistenkordillere Nordchiles zwischen Taltal und Chafiaral: Geotekt. Forsch, v. 61, 166p.

Davidson, J. P (1991). Comment and Reply on "Role of subduction erosion in the generation of Andean magmas": Geology p.1054-1055.

Davidson, J.P., and de Silva, S.L. (1992). Volcanic rocks from the Bolivian Altiplano: insights into crustal structure, contamination and magma genesis in the Central Andes: Geology, v. 20; p. 1127–1130.

Davidson, J. P. and de Silva, S. L. (1995). Late Cenozoic magmatism of the Bolivian Altiplano: Contributions to Mineralogy and Petrology, v. 119, 387–408.

Davidson. J. P., Hora, J. M., Garrison, J. M., and Dungan, M. A. (2005). Crustal forensics in arc magmas: Journal of Volcanology and Geothermal Research, v. 140; p. 157-170.

Davidson, J. P., Turner, S., Handley, H., Macpherson, C., and Dosseto, A., (2007). Amphibole "sponge" in arc crust?: Geology, v. 35; p. 787-790.

de Almeida, F. F. M., de Brito Neves, B. B., and Careneiro, C. D. R. (2000). The origin and evolution of the South American Platform: Earth Science Reviews, v. 50; p. 77-111.

Deer, W. A., Howie, R. A., and Zussman, J. (1992). The Rock Forming Minerals. 2nd Edition, Prentice Hall.

de Jong, K. (1991). Tectono-metamorphic studies and radiometric dating in the Betic Cordilleras (SE Spain) — with implications for the dynamics of extension and compression in the western Mediterranean area: Ph.D. thesis, Vrije Universiteit Amsterdam; 204p.

de Jong, K. (1993). The tectono-metamorphic evolution and chronologic development of the Betic Zone (SE Spain) with implications for the geodynamic evolution of the western Mediterranean area: Proceedings Koninkliijke Nederlandse Akademie van Wetenschappen, v. 96; p. 295-333.

DeMets, C., Gordon, R. G., Argus, D. F., and Stein, S. (1994). Effect of recent revisions to the geomagnetic reversal timescale on estimates of current plate motions: Geophysical Research Letters, v. 21; p. 2191-2194.

de Silva S. L., (1989). The Altiplano-Puna Volcanic Complex of the Central Andes: Geology, v. 17; p. 1102– 1106.

de Silva, S.L., and Francis, P. W. (1991). Volcanoes of the Central Andes, Springer-Berlin, pp. 1-216. Heidelberg, New York.

de Silva S. L., and Gosnold W. A. (2007). Episodic construction of batholiths: Insights from the spatiotemporal development of an ignimbrite flare-up: Journal of Volcanology and Geothermal Research, v. 167; p. 320– 335.

Delacour, A., Gerbe, M. C., Thouret, J. C., Wörner, G., and Paquereau-Lebti, P. (2007). Magma evolution of Quaternary minor volcanic centres in Southern Peru, Central Andes: Bulletin of Volcanology, v. 69; p. 581–606.

Deng, Q. C., Shefa, S., Fangnin, Z., Shilong, W., Yipeng, Z., Weigi, J., Decheng, B., Burchfiel, C., Molnar, P., Royden, L., and Peizhen, Z. (1986). Variations in the geometry and amount of slip on the Haiyuan (Nanxihaushan) fault zone, China, and the surface rupture of the 1920 Haiyuan earthquake. In Earthquake Source Mechanics, Geophysical Monograph Series, v. 37; pp. 169– 182.

Deniel, C., Vidal, P., Fernandez, A., Le Fort, P., and Pencat, J-J. (1987). Isotopic study of the Manaslu granite (Himalaya, Nepal): inferences on the age and source of Himalayan leucogranites: Contributions to Mineralogy and Petrology, v. 96; p. 78-92.

De Paolo, D. J. (1981). Trace element and isotopic effects of combined wallrock assimilation and fractional crystallization: Earth and Planetary Science Letters, v. 53; p. 189–202.

de Silva, S. L. (1989). Altiplano-Puna volcanic complex of the central Andes: Geology, v. 17; p. 1102-1106.

Dickinson, W. R., (1975). Potash-Depth (K-h) Relations in Continental Margin and Intra-Oceanic Magmatic Arcs: Geology, v. 3; p. 53-56.

Drew, S. T., Ducea, M. N., and Schoenbohm, L. M. (2009). Mafic volcanism on the Puna Plateau, NW Argentina: Implications for lithospheric composition and evolution with an emphasis on lithospheric foundering: Lithosphere, v. 1; p. 305-318.

Duffield, W.A., and Ruiz, J. (1998). A model that helps explain Sr-isotope disequilibrium between feldspar phenocrysts and melt in large-volume silicic magma systems: Journal of Volcanology and Geothermal Research, v. 87; p. 7-13.

Duggen, S., Hoernle, K., Van Den Bogaard, P. and Garbe-Schönberg, D. (2005). Post-collisional Transition from Subduction- to Intraplate-type Magmatism in the Westernmost Mediterranean: Evidence for Continental-Edge delamination of Subcontinental Lithosphere: Journal of Petrology, v. 46; p. 1155-1201.

Eng;and, P. C., and Houseman, G. A. (1988). The mechanics of the Tibetan Plateau: Royal Society of London Philosophical Transactions, v. 326; p. 301-319.

Evernden J. F., Kriz S. J., and Cherroni M. C. (1977). Potassium-argon ages of some Bolivian rocks: Economic Geology, v. 72; p. 1042–1061.

Farina, F., and Stevens, G. (2011). Source controlled $^{87}Sr/^{86}Sr$ isotope variability in granitic magmas: The inevitable consequence of mineral-scale isotopic disequilibrium in the protolith: Lithos, v. 122; p. 189-200.

Farmer, G. L., Bowring, S. A., Matzel, J., Maldonado, G. E., Fedo, C., and Wooden, J. (2005). Paleoproterozoic Mojave province in northwestern Mexico? Isotopic and U-Pb zircon geochronologic studies of Precambrian and Cambrian crystalline and sedimentary rocks, Caborca, Sonora: Geological Society of America Special Papers, v. 393; p. 183-198.

Feininger, T., and Seguin, M. K. (1983). Simple Bouguer gravity anomaly field and the inferred crustal structure of continental Ecuador: Geology, v. 11; p. 40-44.

Feng, M., and Whitford-Stark, J. L. (1986). The 1719-1721 eruptions of potassium-rich lavas at Wudalianchi, China: Journal of Volcanology and Geothermal Research, v. 30; p. 131-148.

Fitton, J. G., Saunders, A. D., Larsen, L. M., Hardarson, B. S., and Norry, M. J. (1998). Volcanic rocks from the southeast Greenland margin at 63^{o}N: composition, petrogenesis and mantle sources. In: Sounders, A. D., Larsen, H. C. and Wise, S. W. Jr (eds) Proceedings of the Ocean Drilling Program, Scientific Results, 152. College station, TX: Ocean Drilling Program; p. 331-350.

Folkes, C. B., de Silva, S. L., Schmitt, A. K., and Cas, R. A. F. (2011). A reconnaissance of U-Pb zircon ages in the Cerro Galán system, NW Argentina: Prolonged magma residence, crystal recycling, and crustal assimilation: Journal of Volcanology and Geothermal Research, v. 206; p. 136-147.

Font, L., Nowell, G. M., Pearson, D. G., Ottley, C. and Willis, S. G. (2007). Sr isotope analysis of bird feathers by TIMS: a tool to trace bird migration paths and breeding sites: Journal of Analytical Atomic Spectrometry, v. 22; p. 513-522.

Font, L., Davidson, J. P., Pearson, D. G., Nowell, G. M., Jerram, D. A, and Ottley, C. J. (2008). Sr and Pb Isotope Micro-analysis of Plagioclase Crystals from Skye Lavas: an insight into Open-system processes in a flood basalt province: Journal of Petrology, v. 49; p. 1449-1471.

Fuck, R. A., Neves, B. B. B., and Schobbenhaus, C. (2008). Rodinia descendants in South America: Precambrian Research, v. 160; p. 108-126.

Gao, S., Luo, T. C., Zhang, B. R., Zhang, H. F., Han, Y, W., Hu, Y. K., and Zhao, Z. D. (1998). Chemical composition of the continental crust as revealed by studies in east China: Geochimica et Cosmochimica Acta, v. 62; p. 1959-1975.

Galer, S. J. G. (1997). Optimal triple spiking for high precision lead isotope ratio determination: Terra Nova, v. 9; p. 441.

García-Dueñas V., Balanyá J. C., and Martínez-Martínez J. M. (1992). Miocene extensional detachments in the outcropping basement of the Northern Alboran Basin (Betics) and their Tectonic Implications: Geo-Marine Letters, v. 12; p. 88-95.

Garrison, J. M., and Davidson, J. P. (2003). Dubious case for slab melting in the Northern volcanic zone of the Andes: Geology, v. 31; p. 565-568.

Garrison, J., Davidson, J., Reid, M., Turner, S. (2006). Source versus differentiation controls on U-series disequilibria: insights from Cotopaxi volcano Ecuador: Earth and Planetary Science Letters, v. 244; p. 548–565.

Garzione, C. N., Molnar, P., Libarkin, J. C., MacFadden, B. J. (2006). Rapid late Miocene rise of the Bolivian Altiplano: Evidence for removal of mantle lithosphere: Earth and Planetary Science Letters, v. 241; p. 543-556.

Ghosh, P., Garzione, C. N., and Eiler, J. M. (2006). Revealed Through ^{13}C-^{18}O Bonds in Paleosol Carbonates: Science, v. 311; p. 511-515.

Gill, J. B. (1981). Orogenic Andesites and Plate Tectonics: Springer-Verlag, 390 pp.

Goldschmidt, V., M. (1933). Grundlagen der quantitative Geochemie. Fortschr. Mienral: Kirst. Petrogr, v. 17; p. 112.

Goldstein, S. L., Arndt, N. T., and Stallard, R. F. (1997). The history of a continent from U-Pb ages of zircons from Orinoco river sand and Sm-Nd isotopes in the Orinoco basin river sediments. Chemical Geology, 139; p. 271-286.

Gorai, M. (1940). A consideration of the genesis of alkali basalts from Wu-ta-lien-chih volcano, North Manchuria: Journal of the Geological Society of Japan v. 47; p. 456-498 (in Japanese with English abstract).

Gorring, M. L., and Kay, S. M. (2000). Carbonatite metasomatized peridotite xenoliths from southern Patagonia: implications for lithospheric processes and Neogene plateau magmatism: Contributions to Mineralogy and Petrology, v. 140; p. 55-72.

Govindaraju, K. (1994). 1994 compilation of working values and sample description for 383 Geostandards; Geostandards newsletter, v. 18; p. 1-158.

Gracia, E., Pallas, R., Soto, J. I., Comas, M., Moreno, X., Masan, E., Santanach, P., Diez, S., García. and Danobeitia, J. (2006). Active fautling offshore SE Spain (Alboran Sea): Implications for earthquake hazard assessment in the Southen Iberian Margin: Earth and Planetary Science Letters, v. 241; p. 734-749.

Gregory-Wodzicki, K. M., McIntosh, W. C., Velasquez, K., and McIntosh., W.C. (1998). Paleoclimate and paleoelevation of the late Miocene Jakokkota flora, Bolivian Altiplano: Journal of South American Earth Sciences, v. 11, p. 533–560.

Gregory- Wodzicki, K. M. (2000). Uplift history of the Central and Northern Andes: A review: Geological Society of American Bulletin, v. 112; p. 1091-1105.

Guglielmo, Jr, G. (1993). Interference between pluton expansion and non-coaxial tectonic deformation: three-dimensional computer model and field implications: Journal of Structural Geology, v. 15; p. 593-608.

Guillier, B., Chatelain, J.-L., Jaillard, É., Yepes, H., Poupinet, G., and Fels, J.-F. (2001). Seismological evidence on the geometry of the orogenic system in central-northern Ecuador (South America): Geophysical Research Letters, v. 28; p. 3729-3752.

Guillot, S., and LeFort, P. (1995). Geochemical constraints on the bimodal origin of High Himalayan leucogranites: Lithos v. 35; p. 221–34.

Gutscher, M.-A., Olivet, J.-L., Aslanian, D., Maury, R., and Eissen, J.-P. (1999). The "lost Inca Plateau": Cause of flat subduction beneath Peru?: Earth and Planetary Science Letters, v. 171; p. 335-341.

Gutscher, M.-A., Maury, R., Eissen, J-P., Bourdon, E. (2000). Can slab melting be caused by flat subduction?: Geology, v. 28; p. 535-538.

Halliday, A.N., Fallick, A.E., Hutchinson, J. and Hildreth, W. (1984). A Nd, Sr and O isotopic investigation into the causes of chemical and isotopic zonation in the Bishop Tuff; California: Earth and Planetary Science Letters, v. 68; p. 379-391.

Hammouda, T., Pichavant, M., Chaussidon, M. (1994). Mechansims of isotope equlibrtaion during partial melting: an experimental test of the behaviour of Sr: Mineralogical Magazine, v. 58A; Goldschmidt Conference Abstracts.

Hammouda, T., Pichavant, M., and Chaussidon, M. (1996). Isotopic equilibration during partial melting: an experimental test of the behaviour of Sr: Earth and Planetary Science Letters, v. 144; p. 109-121.

Handley, H. K., Turner, S. P., Smith, I. E. M., Stewart, R. B., Cronin, S. J. (2008). Rapid timescales of differentiation and evidence for crustal contamination at intraoceanic arcs: geochemical and U-Th–Ra–Sr–Nd isotopic constraints from Lopevi Volcano, Vanuatu SW Pacific: Earth and Planetary Science Letters, v. 273; p. 184–194.

Handley, H. K., Turner, S., Berlo, K., Beier, C., Saal, A. (2011). Insights into the Galápagos plume from Uranium-series isotopes of recently erupted basalts: Geochemistry Geophysics Geosystems, v. 12, Q0AC14.

Harmon, R. S., Barreiro, B. A., Moorbath, S., Hoefs, J., Francis, P. W., Thorpe, R. S., Deruelle, B., McHugh, J., and Viglino, J. A. (1984). Regional O-, Sr-, and Pb-isotope relationships in Late Cenozoic calc-alkaline lavas of the Andean cordillera: Journal of the Geological Society of London v. 141; p. 803–22.

Harris, N., Ayers, M., and Massey, J. (1995). Geochemistry of granitic melts produced during the incongruent melting of muscovite: Implications for the extraction of Himalayan leucogranite magmas: Journal of Geophysical Research, v. 100; p. 15767–15777.

Harris, N., Ayres, M., (1998). The implications of Sr-isotope disequilibrium for rates of prograde metamorphism and melt extraction in anatectic terrains. In: Treloar, P.J., O'Brien, P.J. (Eds.), What Drives Metamorphism and Metamorphic Reactions?: Geological Society of London Special Publications, v. 138; p. 171–182.

Harrison, T. M., Grove, M., McKeegan, K., Coath, C. D., Lovera, O. M. and Le Fort, P. (1999). Origin and episodic emplacement of the Manaslu Intrusive Complex, Central Himalaya: Journal of Petrology, v. 40; p. 3–19.

Hawkesworth, C.J., Hammil, M., Gledhill, A.R., van Calsteren, P., and Rogers, G. (1982). Isotope and trace element evidence for late-stage intra-crustal melting in the High Andes: Earth and Planetary Science Letters, v. 58; p. 240–254.

Heaman, L., and Parrish, P. (1991). U-Pb geochronology of accessory minerals. In: Short Course Handbook on Applications of radiogenic isotope systems to problems in Geology, Mineralogical Society of Canada; Heaman, L., and Ludden, J. N (Eds), Toronto. 498p.

Heit, B., Koulakov, I., Asch, G., Yuan, X., Kind, R., Alcocer-Rodriguez, I., Tawackoli, S., and Wilke, H. (2008). More constraints to determine the seismic structure beneath the Central Andes at 21°S using teleseismic tomography analysis: Journal of South American Earth Sciences, v. 25; p. 22-36.

Hildreth, W., and Moorbath S. (1988). Crustal contributions to arc magmatism in the Andes of Central Chile: Contributions to Mineralogy and Petrology, v. 98; p. 455–489.

Hilton, D. R., Hammerschmidt, K., Teufel, S., and Friedrichsen. (1993). Helium isotope characteristics of Andean geothermal fluids and lavas: Earth and Planetary Science Letters, v. 120; p. 265-282.

Hofmann, A. W., and Hart, S. R. (1978). An assessment of local and regional isotopic equilibrium in the mantle: Earth and Planetary Science Letters, v. 38; p. 44-62.

Hofmann, A. W., and Feigenson, M. D. (1983). Case studies on the origin of basalt. I. Theory and reassessment of Grenada basalts: Contributions to Mineralogy and Petrology, v. 84; p. 382–389.

Hoke, L., Hilton, D. R., Lamb, S. H., Hammerschmidt, K. and Friedrichsen, H. (1994). ^{3}He evidence for a wide zone of active mantle melting beneath the Central Andes: Earth and Planetary Science Letters, v. 128; p. 341–355.

Hoke, L., and Lamb, S. (2007). Cenozoic behind-arc volcanism in the Bolivian Andes, South America: implications for mantle melt generation and lithospheric structure: Journal of the Geological Society of London, v. 164; p. 795–814.

Holland, T. J. B. and Powell, R. (1998). An internally consistent thermodynamic data set for phases of petrological interest: Journal of Metamorphic Geology, v. 16; p. 309-343.

Holland, T., and Blundy, J. (1994). Non-ideal interactions in calcic amphiboles and their bearing on amphibole-plagioclase thermometry: Contributions to Mineralogy and Petrology, v. 116; p. 433-447.

Holland, T., and Powell, R. (2001). Calculation of phase relations involving haplogranitic melts using an internally consistent thermodynamic dataset: Journal of Petrology, v. 42; p. 673-683.

Holness, M. B., Nielsen,T. F. D., and Tegner, C. (2006). Textural maturity of cumulates: a record of chamber filling, liquidus assemblage, cooling rate and large-scale convection in layered intrusions: Journal of Petrology, v. 46; p. 141-157.

Hoorn, C., Wesselingh, F. P., ter Steege, H., Bermudez, M. A., Mora, A., Sevink, J., Sanmartín, I., Sanchez-Meseguer, A., Anderson, C. L., Figueiredo, J. P., Jaramillo, C., Riff, D., Negri, F. R., Hooghiemstra, H., Lundberg, J., Stadler, T., Särkinen, T and Antonelli, A. (2010). Amazonia Through Time: Andean Uplift, Climate Change, Landscape Evolution and Biodiversity: Science, v. 330; p.927-931.

Hsu, C.-N., and Chen, J. (1998). Geochemistry of late Cenozoic basalts from Wudaluanchi and Jingpohu areas, Heilongjiang Province, northeast China: Journal of Asian Earth Sciences, v. 16; p. 385-405.

Husson, L. and Sempere, T. (2003). Thickening the Altiplano crust by gravity-driven crustal channel flow: Geophysical Research Letters, v. 30; p.1243-1247.

Iaffaldano, G., Giuseppe, E. d., Cordi, F., Funiciello, F., Faccenna, C., and Bunge, H. –P. (2012). Varying mechanical coupling along the Andean margin: Implications for trench curvature, shortening and topography: Tectonophysics, v. 526-529; p. 16-23.

Iriarte, R., de Silva, S. L., Jimenez, N., Ort, M. H. (2011). The Cerro Guacha Caldera complex: An Upper Miocene-Pliocene polycyclic volcano-tectonic structure in the Altiplano Puna Volcanic Complex of the Central Andes of Bolivia: AGU Fall Meeting Abstracts, 2011.

Isacks., B. L. (1988). Uplift of the Central Andean Plateau and bending of the Bolivian Orocline: Journal of Geophysical Research, v. 93; p. 3211–3231.

James, D. E. (1981). The combined use of oxygen and radiogenic isotopes as indicators of crustal contamination: Annual Review of Earth and Planetary Sciences, v. 9; p. 311-344.

James, D. E. (1982). A combined O, Sr, Nd and Pb isotopic and trace element study of crustal contamination in the central Andean lavas, I. Local geochemical variations: Earth and Planetary Science Letters, v. 57; p. 47–62.

Jiménez, N., and López-Velásquez, S. (2008). Magmatism in the Huarina fold and thrust belt, Bolivia, and its geotectonic implications: Tectonophysics, v. 459, 85–106.

Jordan, T. E., Isacks, B. L., Allmendinger, R. W., Brewer, J. A., Ramos,V. A., and Ando, C. J. (1983). Andean tectonics related to geometry of subducted Nazca plate: Geological Society of America Bulletin, v. 94; p. 341–361.

Julià, J., Mancilla, F., and Marales, J. (2005). Seismic signature of intracrustal magmatic intrusions in the Eastern Betics (Internal Zone), SE Iberia: Geophysical Research Letters, v. 32; L16304.

Jurewicz, S. R., and Watson, E. B. (1985). The distribution of partial melt in a granitic system: The application of liquid-phase sintering theory: Geochimica et Cosmochimica Acta, v. 49; p. 1109-1122

Kaiser, J. F., de Silva, S. L., Ort, M. H., Sunagua, M. (2011). The Pastos Grandes Caldera Complex of SW Bolivia: The building of a composite upper crustal batholith: AGU Fall Meeting Abstracts, 2011.

Kay, R. W. (1978). Aleutian magnesian andesites: Melts from subducted Pacific Ocean crust: Journal of Volcanology and Geothermal Research, v. 4; p. 117-132.

Kay, R. W., and Kay, S. M. (1993). Delamination and delamination magmatism: Tectonophysics, v. 219; p. 177–189.

Kay, S. M., and Gordillo, C. E. (1994). Pocho volcanic rocks and the melting of depleted continental lithosphere above a shallowly dipping subduction zone in the central Andes: Contributions to Mineralogy and Petrology, v. 117; p. 25-44.

Kay, S. M., Coira, B., and Viramonte, J. (1994). Young mafic back arc volcanic rocks as indicators of continental lithospheric delamination beneath the Argentine Puna plateau, Central Andes: Journal of Geophysical Research, v. 99; p. 24323–24339.

Kay, S. M., and Gorring, M. L. (2001). Mantle Processes and Sources of Neogene Slab Window Magmas from Southern Patagonia, Argentina: Journal of Petrology, v. 42; p. 1067-1094.

Kay, S. M., Coira, B., Caffe, P. J., and Chen, C.-H. (2010). Regional chemical diversity, crustal and mantle sources and evolution of central Andean Puna Plateau Ignimbrites: Journal of Volcanology and Geothermal Research, v. 198; p. 81–111.

Keating, J. (2009). Bolivia's Lithium-Powered Future. Foreign Policy, October Issue.

Keiding, J. K., and Sigmarsson, O. (2012). Geothermobarometry of the 2010 Eyjafjalljökull eruption - New constraints on Icelandic magma plumbing systems: Journal of Geophysical Research, in press (doi:10.1029/2011JB008829).

Keleman, P. B., and Dunn, J. T. (1992). Depletion of Nb relative to other highly incompatible elements by melt/rock reaction in the upper mantle: EOS, Transactions of the American Geophysical Union, v. 73; p. 656-657.

Kelemen, P. B., Hanghoj, K., and Greene, A. R. (2004). One View of the Geochemistry of Subduction-related Magmatic Arcs, with an Emphasis on Primitive Andesite and Lower Crust. In: Treatise on Geochemistry. Holland, H. D. and Turekian, K. K. (Eds), Elsevier, Amsterdam; p. 593-659.

Kenah, C., and Hollister, L.S. (1983). Anatexis in the Central Gneiss Complex, British Columbia. In Atherton, M. P., and Gribble, C. D. (Eds). Migmatites, melting and metamorphisrn, p. 142-162. Shiva Publishing Co.

Kern, J., de Silva, S. L., and Schmitt, A. K. (2011). Investigating sources of ignimbrites in the Altiplano-Puna Volcanic Complex using U-Pb dating of zircons: AGU Fall Meeting Abstracts, 2011.

Kerr, A. C., Marriner, G. F., Arndt, N. T., Tarney, J., Nivia, A., Saunders, A. D., Duncan, R. A. (1996). The petrogenesis of Gorgona komatiites, picrites and basalts: new field, petrographic and geochemical constraints: Lithos v. 37; p. 245-260.

Kilian, R., and Behrmann, J. H. (2003). Geochemical constraints on the sources of continent-related deep sea sediments and their recycling in arc magmas of the Southern Andes: Journal of the Geological Society of London, v. 160; p. 57-70.

Klemme, S., Prowatke, S., and Hametner, K. (2005). The partitioning of trace elements between rutile and silicate melts: Implications for subduction zones: Geochimica et Cosmochimica Acta, v. 6; p. 2361-2371.

Kley, J and Monaldi, C. R. (1998). Tectonic shortening and crustal thickness in the Central Andes: How good is the correlation?: Geology, v. 26; p.723-726.

Knesel, K., and Davidson, J. P. (1996). Isotopic disequilibrium during melting of granite and implications for crustal contamination of magmas: Geology, v. 24; p. 243-246.

Knesel, K. M., and Davidson, J. P. (1999). Sr isotope systematics during melt generation by intrusion of basalt into continental crust: Contributions to Mineralogy and Petrology, v. 136; p. 285-295.

Knesel, K. M., Davidson, J. P., Duffield, W. A. (1999). Open system evolution of silicic magma by assimilation followed by recharge: evidence from Sr isotopes in sanidine phenocrysts, Taylor Creek Rhyolite, NM: Journal of Petrology, v. 40; p. 773–786.

Knesel, K. M., and Davidson, J. P. (2002). Insights into Collisional Magmatism from Isotopic Fingerprints of Melting Reactions: Science, v. 296; p. 2206-2208.

Koleszar, A. M. and Kent, A. J. (2011). Compositional diversity and plumbing systems: Evidence from amphiboles from Mount Hood, Oregon: AGU Fall Meeting Abstracts, 2011.

Kuritani, T., Kitagawa, H., and Nakamura, E., (2005). Assimilation and Fractional Crystallisation Controlled by Transport Process of Crustal Melt: Implications from an Alkali Basalt-Dacite Suite from Rishiri Volcano, Japan: Journal of Petrology, v. 46; p.1421-1442.

LaiCheng, M., Liu, D., Zhang, F., Fan, W., Shi, Y., and Xie, H. (2007). Zircon SHRIMP U-Pb ages of the "Xinghuadukou Group" in Hanjiayuanzi and Xinlin areas and the "Zhalantun Group" in Inner Mongolia, Da Hinggan Mountains: Chinese Science Bulletin, v. 52; p. 1112-1124.

Lamb, S., Hoke, L., Kennan, L., and Dewey, J. (1997). Cenozoic evolution of the Central Andes in Bolivia and Northern Chile: Geological Society of London Special Publication, v. 121; p.237-264.

Lappin, A. R., and Hollister, L. S. (1980). Partial melting in the Central Gneiss Complex near Prince Rupert, British Columbia: American Journal of Science, v. 280; p. 518-545.

Laporte, D., and Watson, E. B. (1989). Wetting behaviour of H_2O-CO_2-NaCl fluids in quartzites under crustal conditions: (abs.) Eos, v. 70; p. 1406.

Laporte, D. (1994). Wetting behaviour of partial melts during crustal anatexis: the distribution of hydrous silicic melts in polycrystalline aggregates of quartz: Contributions to Mineralogy and Petrology, v. 116; p. 486–499

Laporte, D., and Watson, E. B. (1995). Experimental and theoretical constraints on melt distribution in crustal sources: The effect of crystalline anisotropy on melt interconnectivity: Chemical Geology, v. 124; p. 161-184.

Laubacher, G., and Mégard, F. (1985). The Hercynian basement: a review. In Pitcher, W. S., Atherton, M. P., Cobbing, E. J., and Beckinsale, R. D (eds) Magmatism at a Plate Edge *in* The Peruvian Andes. p. 29-37. John Wiley and Sons, New York.

Le Fort, P., Cuney, M., Deniel, C., France-Lanord, C., Sheppard, S. M. F., Upreto, B. N., and Vidal, P. (1987). Crustal generation of the Himalayan leucogranites: Tectonophysics, v. 134; p. 39-57.

Lehmann, B. (1978). A Precambrian core sample from the Altiplano/Bolivia: Geologische Rundschau, v. 67; p. 270–278.

Li, Y., and Ishigaki, T. (2002). Thermodynamic analysis of nucleation of anatase and rutile from TiO_2 melt: Journal of Crystal Growth, v. 242, p. 511-516.

Litherland, M., Annells, R. N., Darbyshire, D. P. F., Fletcher, C. J. N., Hawkins, M. P., Klinck, B. A., Mitchell, W. I., O'Connor, E. A., Pitfield, P. E. J., Power, G., and Webb, B.C. (1989). The Proterozoic of eastern Bolivia and its relationship to the Andean mobile belt: Precambrian Research, v. 43; p. 157–174.

Loewy, S. L., Connelly, J. N., and Dalziel, Q. W. D. (2004). An orphaned basement block: The Arequipa-Antofalla basement of the central Andean margin of South America. Geological Society of America Bulletin, v. 116; p. 171–187.

Lonsdale, P. (2005). Creation of the Cocos and Nazca plates by fission of the Farallon plate: Tectonophysics, v.404; p. 237–264.

Lucassen, F., Franz, G., and Laber, A. (1999). Permian high pressure rocks—the basement of the Sierra de Limón Verde in Northern Chile**:** Journal of South American Earth Sciences, v. 12; p. 183–199.

Lucassen, F., Becchio, R., Wilke, H. G., Franz, G., Thirlwall, M. F., Viramonte, J., and Wemmer, K. (2000). Proterozoic-Paleozoic development of the basement of the Central Andes (18-26 degrees S) - a mobile belt of the South American craton: Journal of South American Earth Sciences v. 13; p. 697-715.

Lucassen, F., Becchio, R., Harmon, R., Kasemann, S., Franz, G., Trumbull, R., Wilke, Hans-G., Romer, R. L., and Dulski, P. (2001). Composition and density model of the continental crust at an active continental margin – the Central Andes between 21^{o}S and 27^{o}S: Tectonophysics, v. 341; p. 195-223.

Macera, P., Di Pisa, A., and Gasperini, D. (2011). Geochemical and Sr-Nd isotope disequilibria during multi-stage anatexis in a metasedimentary Hercynian crust: European Journal of Mineralogy, v. 23; p. 207-222.

Marrett, R and Emerman, S. H. (1992). The relations between faulting and mafic magmatism in the Altiplano-Puna plateau (central Andes): Earth and Planetary Science Letters, v. 112; p. 53-59.

Mamani, M., Wörner, G., and Sempere, T. (2010). Geochemical variations in igneous rocks of the Central Andean Orocline (13^{o}S to 18^{o}S): Tracing crustal thickening and magma generation through time: Geological Society of America Bulletin, v. 122; p. 162-182.

Marsh, B. D., and Carmichael, I. S. E., (1974). Benioff Zone Magmatism: Journal of Geophysical Research, v. 79; p. 1196-1206.

McDonough, W. F., Sun, S., Ringwood, A. E., Jagoutz, E. and Hofmann, A. W. (1991). K, Rb and Cs in the earth and moon and the evolution of the earth's mantle: Geochimica et Cosmochimica Acta, Ross Taylor Symposium volume; p. 93-101.

Mégard, F. (1984). The Andean orogenic period and its major structures in central and northern Peru: Journal of the Geological Society of London, v. 141; p. 893-900.

McDonough, W. F., Sun, S. –S., Ringwood, A. E., Jagoutz, E., and Hofmann, A. W. (1992). Potassium, rubidium and cesium in the Earth and Moon and the evolution of the mantle of the Earth: Geochimica et Cosmochimica Acta, v. 56; p. 1001-1012.

McKenzie, D., and Bickle, M. J. (1988). The volume and composition of melt generated by extension of lithosphere: Journal of Petrology, v. 29; p. 625– 679.

McKenzie, D., and O'Nions, R. K. (1991). Partial Melt Distributions from Inversion of Rare Earth Element Concentration's: Journal of Petrology, v. 32; p. 1021-1091.

McKenzie, D., and O'Nions, R. K. (1995). The Source Regions of Ocean Island Basalts: Journal of Petrology, v. 36; p. 133-159.

McLeod, C. L., Davidson, J. P., Nowell, G. N., de Silva, S. L. (2012). Disequilibrium melting during crustal anatexis and implications for modelling open magmatic systems: Geology; in press.

McMenamin, A. S., and McMenamin, D. S. (1990). The Emergence of Animals: The Cambrian Breakthrough. Columbia University Press.

McNutt, R. H., Crocket, J. H., Clark, A. H., Caelles, J. C., Farrar, E., Haynes, S. J., and Zentilli, M. (1975). Initial $^{87}Sr/^{86}Sr$ ratios of plutonic and volcanic rocks of the central Andes between latitudes 26° and 29° south: Earth and Planetary Science Letters, v. 27; p. 305–313.

McQuarrie, N. (2002). The kinematic history of the central Andean fold-thrust belt, Bolivia: Implications for building a high plateau: Geological Society of America Bulletin, v. 114; p. 950-963.

McQuarrie, N., Horton, B. K., Zandt, G., Beck, S., and DeCelles, P. G. (2005). Lithospheric evolution of the Andean fold-thrust belt, Bolivia, and the origin of the central Andean plateau: Tectonophysics, v. 399; p. 15–37.

Mooney, W. D., Laske, G., and Masters, G. T. (1998). CRUST 5.1; a global crustal model at 5 degrees X 5 degrees: Journal of Geophysical Research, v. 103; p. 727-747.

Munksgaard, N. C. (1984). High $\delta^{18}O$ and possible pre-eruptional Rb-Sr isochrones in cordierite-bearing volcanics from SE Spain: Contributions to Mineralogy and Petrology, v. 87; p. 351-358.

Muñoz-Espadas, M. J., Lunar, R., and Martínez-Frías, J. (2000). The garnet placer deposit from SE Spain: industrial recovery and geochemical features: Episodes, v. 23; p. 266–269.

Myers, S. C., Beck, S., Zandt, G., and Wallace, T. (1988). Lithospheric-scale structure across the Bolivian Andes from tomographic images of velocity and attenuation for P and S waves: Journal of Geophysical Research; v.103, p. 21233–21252.

Nakamura, N. (1974). Determination of REE, Ba, Fe, Mg, Na, and K in carbonaceous and ordinary chondrites: Geochimica et Cosmochimica Acta, v. 38; p. 757-775.

Nelson, D. R., McCulloch, M. T. and Sun, S. S. (1986). The origin of ultrapotassic rocks as inferred from Sr, Nd and Pb isotopes: Geochemica et Cosmochemica Acta, v. 50; p. 231-245.

Noble, D. C., and Mégard, F. (1979). Early Tertiary "Incaic" tectonism, uplift and volcanic activity, Andes of central Peru: Geological Society of America Bulletin, v. 90; part 1; p. 903-907.

Notsu, K.., Lopez-Escobar, L., and Onuma, N. (1987). Along-arc variation of Sr-isotope composition in volcanic rocks from the Southern Andes (33^oS-55^oS): Geochemical Journal, v. 21; p. 307-313.

Nowell, G. M. and Parrish, R. R. (2002). Simultaneous acquisition of isotope compositions and parent/daughter ratios by non-isotope dilution solution-mode Plasma ionisation Multi-

collector Mass Spectrometry (PIMMS): Plasma Source Mass Spectrometry The New Millenium p. 298-310.

Nowell, G. M., Pearson, D. G., Ottley, C. J., Schweiters, J. and Dowall, D. (2003). Long-term performance characteristics of a plasma ionisation multi-collector mass spectrometer (PIMMS): the ThermoFinnigan Neptune. In: Holland, J. G. and Tanner, S. D. (eds) Plasma Source Mass Spectrometry: Applications and Emerging Technologies. Cambridge: Royal Society of Chemistry, pp. 307-320.

Nye, C. J., and Reid, M. R. (1986). Geochemistry of primary and least fractionated lavas from Okmok Volcano, central Aleutians – implications for arc magma genesis: Journal of Geophysical Research, v. 91; p. 10271–10287.

O'Driscoll, B. (2005). Textural equilibrium in magmatic layers of the Lough Fee ultramafic intrusion, NW Connemara: implications for adcumulus mineral growth: Irish Journal of Earth Sciences, v. 23; p. 39–45

Oncken, O., Hindle, D., Kley, J., Elger, K., Victor, P., and Schemmann., K. (2006). Deformation of the central Andean upper plate system – facts, fiction, and constraints for plateau models. In: Oncken, O., Chong, G., Franz, G., Giese, P., Götze, H-J., Ramos, V. A., Strecker, M. R., Wigger, P., (eds) The Andes – active subduction orogeny. Frontiers in Earth Science Series, Vol 1; pp 3–28. Springer-Verlag, Berlin Heidelberg New York.

Paces, J. B., and Miller, J.D. (1993). Precise U-Pb ages of Duluth Complex and related mafic intrusions, northeastern Minnesota; geochronological insights to physical, petrogenetic, paleomagnetic, and tectonomagmatic processes associated with the 1.1 Ga Midcontinent Rift System: Journal of Geophysical Research, v. 98; 13997–14013.

Pakiser, L. C. and Robinson, R. (1966). Composition and evolution of the continental crust as suggested by seismic observations: Tectonophysics, v. 3; p. 547-557.

Patiño Douce, A. E., Humphreys, E. D., and Johnston, A. D. (1990). Anatexis and metamorphism in tectonically thickened continental crust exemplified by the Sevier hinterland, western North America: Earth and Planetary Science Letters, v. 97; p. 290-315.

Patiño Douce, A.E., and Beard, J. S. 1995. Dehydration-melting of biotite gneiss and quartz amphibolite from 3 to 15 kbar: Journal of Petrology, v. 36; p. 707–738.

Patiño Douce, A. E., and Beard, J. S. (1996). Effect of P, f(O2) and Mg/Fe ratio on dehydration melting of model metagreywackes: Journal of Petrology, v. 37; p. 999–1024.

Patiño Douce, A. E., and Harris, N. (1998). Experimental constraints on Himalayan anatexis: Journal of Petrology, v. 39; p. 689–710.

Pearson, D. G., and Nowell, G. M. (2005). Accuracy and precision in plasma ionisation multi-collector mass spectrometry: constraints from neodymium and hafnium isotope measurements: Plasma Source Mass Spectrometry, Current Trends and Future Developments, Special Publication of the Royal Society of Chemistry; Holland, G and Bandura, D. R (Eds); p. 284-314.

Petford, N., Cruden, A.R., McCaffrey, K. J. W., Vigneresse, J.-L. (2000). Granite magma formation, transport and emplacement in the Earth's crust: Nature, v. 408; p. 669–673.

Peto, P. (1976). An experimental investigation of melting relations involving muscovite and paragonite in the silica-saturated portion of the system K_2O–Na_2O–Al_2O_3–SiO_2–H_2O to 15 kb total pressure: Progress in Experimental Petrology v. 3; p. 41–5.

Perini, G., Cesare, B., Gómez-Pugnaire, M. T., Ghezzi, L., and Tommasini, S. (2009). Armouring effect on Sr-Nd isotopes during disequilibrium crustal melting: the case study of frozen migmatites from El Hoyazo and Mazarrón, SE Spain: European Journal of Mineralogy, v. 21; p. 117-131.

Philpotts, A. R., and Asher, P. M. (1993). Wallrock melting and reaction effects along the Higganum diabase dike in Connecticut: contamination of a continental flood basalt feeder: Journal of Petrology, v. 34; p. 1029-1058.

Picard, D., Sempere, T., and Plantard, O. (2008). Direction and timing of uplift propagation in the Peruvian Andes deduced from molecular phylogenetics of highland biotaxa: Earth and Planetary Science Letters, v. 271; p. 326–336.

Pimentel, M. M., Fuck, R. A., Botelho, N. F. (1999). Granites and the geodynamic history of the neoproterozoic Brasília belt, Central Brazil: a review: Lithos, v. 46; p. 463–483.

Plank, T., and Langmuir, C. H. (1988). An evaluation of the global variations in the major element chemistry of arc basalts: Earth and Planetary Science Letters, v. 90; p. 349-370.

Platt, J. P., Vissers, R. L M. (1989). Extensional collapse of thickened continental lithosphere: a working hypothesis for the Alborán Sea and Gibraltar arc: Geology, v. 17; p. 540–543.

Pouchou, J-L., and Pichoir, F. (1988). A simplified version of the "PAP" model for matrix corrections in epma, in Newbury, D. E (ed): Microbeam Analysis, p. 315-318.

Powell, R., and Holland, T. J. B. (1988). An internally consistent thermodynamic dataset with uncertainties and correlations. III. Application methods, worked examples and a computer program: Journal of Metamorphic Geology, v. 6; p. 173-204.

Price, R. C., George, R., Gamble, J. A., Turner, S., Smith, I. E. M., Cook, C., Hobden, B., Dosseto, A. (2007). U–Th–Ra fractionation during crustal-level andesite formation at Ruapehu volcano, New Zealand: Chemical Geology, v. 244; p. 437–451.

Putirka, K. D. (2008). Thermometers and barometers for volcanic systems. In, Putirka, K. D., and Tepley, F. (eds): Reviews in Mineralogy and Petrology, v. 69; p 61-120.

Ramos, V.A. (19**88**). Late Proterozoic-early Paleozoic of South America; a collosional history: Episodes, v. 11; p. 168-174.

Rapela, C. W., Pankhurst, R. J., Casquet, C., Baldo, E., Saavedra, J., Galindo, C., and Fanning, C. M. (1998). The Pampean Orogeny of the southern proto-Andes: Cambrian continental collision in the Sierras de Córdoba. In*:* Pankhurst, R. J. and Rapela, C. W. (eds) The Proto-Andean Margin of Gondwana: Geological Society of London Special Publications, 142; p. 181-217.

Rapela, C. W., Pankhurst, R. J., Casquet, C., Fanning, C. M., Baldo, E. G., González-Casado, J. M., Galindo, C., and Dahlquist, J. (2007). The Rio de la Plata craton and the assembly of SW Gondwana: Earth Science Reviews, v. 83; p. 49-82.

Rech, J.A., Currie, B.S., Michalski, G., and Cowan, A.M. (2006). Neogene climate change and uplift in the Atacama Desert, Chile: Geology, v. 34; p. 761–764.

Reubi, O., Bourdon, B., Dungan, M. A., Koornneef. J. M., Sellés, D., Langmuir, C. H., and Aciego, S. (2011). Assimilation of the plutonic roots of the Andean arc controls variations in U-series disequilibria at Volcan Llaima, Chile: Earth and Planetary Science Letters, v. 303; p. 37-47.

Ridolfi, F., and Renzulli, A. (2011). Calcic amphiboles in calc-alkaline and alkaline magmas: thermobarometric and chemometric empirical equations valid up to 1,130oC and 2.2 GPa: Contributions to Mineralogy and Petrology; Online First: DOI 10.1007/s00410-011-0704-6.

Riller, U., Petrinovic, I., Ramelow, J., Strecker, M., and Oncken, O. (2001). Late Cenozoic tectonism, collapse caldera and plateau formation in the Central Andes: Earth and Planetary Science Letters, v. 188; p. 299-311.

Roberts M. P., and Clemens, J. D. (1995). Feasibility of AFC models for the petrogenesis of calc-alkaline magma series: Contributions to Mineralogy and Petrology, v. 121; p. 139-147.

Rollinson, H. R. (1993). Using Geochemical Data: Evaluation, Presentation, Interpretation, Prentice Hall; 384pp.

Romanyuk, T. V., Götze, H. J., and Halvorson, P. F. (1999). A density model of the Andean subduction zone: The Leading Edge, v.**18**; p.264–268.

Ronov, A. B., and Yaroshevsky, A. A. (1967). Chemical structure of the Earth's crust.: Geokhimiya, v. 11; p. 1285-1309.

Rudnick, R., and Fountain, D. M. (1995). Nature and Composition of the Continental Crust: A Lower Crustal Perspective: Reviews of Geophysics, v. 33; p. 267-309.

Rudnick, R., and Gao, S. (2003). Composition of the Continental Crust. Treatise on Geochemistry, v. 3; p. 1-64.

Ruprecht, P., and Cooper, K. M. (2012). Integrating the Uranium-Series and elemental Diffusion Geochronometers in Mixed Magamas from Volcan Quizapu, Central Chile: Journal of Petrology, Advance Access: doi:10.1093/petrology/egs001.

Rushmer, T. and Knesel, K. (2010). Defining Geochemical signatures and timescales of melting processes in the crust: An experimental tale of melt segregation, migration and emplacement. In: Timescales of magmatic processes from core to atmosphere (eds) Dosseto, A., Turner, S. P. and Van Orman, J. A., Wiley-Blackwell.

Russell, J. K., and Hauksdottir, S. (2000). Estimates of crustal assimilation in Quaternary lavas from the Northern Cordillera, British Columbia: The Canadian Mineralogist, v. 39; p. 275-295.

Salda, L. D., Cingolani, C., and Varela, R. (1992). Early Paleozoic orogenic belt of the Andes in southwestern South America: Result of Laurentia-Gondwana collision?: Geology, v. 20; p. 617-620.

Sassi, R., Venturini, C., and Árkai, P. (2004). The boundary between the metamorphic and non-to anchi-metamorphic domains in the South alpine Basement s.l. of the eastern Southern Alps: A review. In: Castelli, D., and Cesare, B. (eds). Advances in Metamorphic Petrology: Browsing through Italian classic areas, case studies and approaches. Period Mineral Special Issue v. 2; p. 131–143.

Sawyer, E. W. (1991). Disequilibrium Melting and the Rae of Melt-Residuum Separation During Migmatization of Mafic Rocks from the Grenville Front, Quebec: Journal of Petrology, v. 32; p. 701-738.

Sawyer, E. W. (1994). Melt segregation in the continental crust: Geology, v. 22; p. 1019-1022.

Scanlan, P. M., and Turner, P. (1992). Structural constraints on palaeomagnetic rotations south of the Arica Bend, northern Chile: implications for the Bolivian Orocline: Tectonophysics, v. 205; p. 141-154.

Scheuber, E., and Giese, P. (1999). Architecture of the Central Andes: a compilation of geoscientific data along a transect at 21°S: Journal of South American Earth Sciences, v.12; p. 103–107.

Schmidt, M. W. (1992). Amphibole composition in tonalite as a function of pressure: An experimental calibration of the AI-in-hornblende barometer: Contributions to Mineralogy and Petrology, v. 110; p. 304-310.

Schmitz, M. (1994). A balanced model of the southern Central Andes: Tectonics, v. 13; p. 484–492.

Schmitz, M. D., Lessel, K., Giese, P., Wigger, P., Araneda, M., Bribach, J., Graeber, F., Grunewald, S., Haberland, C., Lüth, S., Röwer, P., Ryberg, T., and Schulze, A. (1999). The crustal structure beneath the Central Andean forearc and magmatic arc as derived from seismic studies – the PISCO 94 experiment in northern Chile (21°–23°S): Journal of South American Earth Sciences, v.12; p. 237–260.

Schmitz, M. D., Bowring, S. A., and Ireland, T. R. (2003). Evaluation of Duluth Complex anorthositic series (AS3) zircon as a U-Pb geochronological standard: New high-precision isotope dilution thermal ionization mass spectrometry result: Geochimica et Cosmochimica Acta, vol. 67; p. 3665-3672.

Schnetzler, C. C., and Philpotts, J. A. (1970). Partition coefficients of rare-earth elements between igneous matrix material and rock-forming mineral phenocrysts; II: Geochimica et Cosmochimica Acta, v. 34; p. 331-340.

Schreiber, U., and Schwab, K. (1991). Geochemistry of Quaternary shoshonitic lavas related to the Calama-Olacapato-El Toro Lineament, NW Argentina: Journal of South American Earth Sciences, v. 4; p. 73-85.

Seber, D., Barazangi, M., Ibenbrahim, A., and Demnati, A. (1996). Geophysical evidence for lithospheric delamination beneath the Alboran Sea and Rif-Betic mountains: Nature, v. 379; p. 785-790.

Sellés, D., Rodríguez, A.C., Dungan, M.A., Naranjo, J.A., Gardeweg, M. (2004). Geochemistry of Nevado de Longaví Volcano (36.2°S): a compositionally atypical arc volcano in the Southern Volcanic Zone of the Andes: Revista Geológica de Chile, v. 31; p. 293-315.

Sempere, T., Herail, G., Oller, J., and Bonhomme, M. G. (1990). Late Oligocene-early Miocene major tectonic crisis and related basins in Bolivia: Geology, v. 18; p. 946 – 949.

Sempere, T., Hartley, A., and Roperch, P. (2006). Comment on "Rapid Uplift of the Altiplano Revealed Through 13C-18O Bonds in Paleosol Carbonates": Science, v. 314; p. 760b.

Sébrier, M., Lavenu, A., Fornari, M., and Soulas, J. (1988). Tectonics and uplift in Central Andes (Peru, Bolivia and northern Chile) from Eocene to present: Géodynamique, v. 3; p. 85–106.

Sen, G., Yang, H-J., and Ducea, M. (2003). Anomalous isotopes and trace element zoning in plagioclase peridotite xenoliths of Oahu (Hawaii): implications for the Hawaiian plume: Earth and Planetary Science Letters, v. 207; p. 23-28.

Shaw, D. M., Cramer, J. J., Higgins, M. D. and Truscott, M. G. (1986). Composition of the Canadian Precambrian shield and the continental crust of the Earth. In: Geological Society Special Publications: The nature of the lower continental crust. Dawson, J. D., Carswell, D. A., Hall, J. and Wedepohl, K. H. (Eds), Geological Society of London, v. 24; 275-282.

Shaw, C. S. J. (2009). Caught in the act -- The first few hours of xenolith assimilation preserved in lavas of the Rockeskyllerkopf volcano, West Eifel, Germany: Lithos, v. 112; p. 511-523.

Shelley, D. (1993). Igneous and metamorphic rocks under the microscope: classification, textures, microstructures and mineral preferred orientations. Chapman and Hall, London, 445p.

Shimizu, H. (1980). Experimental study on rare-earth element partitioning in minerals formed at 20 and 30kb for basaltic systems: Geochemical Journal, v. 14; p. 185-202.

Sisson, T. W. and Bacon, C. R. (1992). Garnet High-Silica Rhyolite Trace-Element Partition-Coefficients Measured by Ion Microprobe. Geochimica et Cosmochimica Acta v. 56; p. 2133-2136.

Spera, F. J., and Bohrson, W, A. (2001). Energy-Constrained Open-System Magmatic Processes I: General Model and Energy-Constrained Assimilation and Fractional Crystallization (EC-AFC) Formulation: Journal of Petrology, v. 42; p. 999–1018.

Sørensen, E. V., and Holm, P. M. (2008). Petrological inferences on the evolution of magmas erupted in the Adagua Valley, Peru (Central Volcanic Zone): Journal of Volcanological and Geothermal Research, v. 177; p. 378–396.

Stacey, J. S., and Kramers, J. D. (1975). Approximation of Terrestrial Lead Isotope Evolution by a Two-Stage Model: Earth and Planetary Science Letters, v. 26; p. 207-221.

Steinmann, G. (1929). Geologie von Peru. Karl Winter, Heidelberg.

Stern, C. H., Amini, H., Charrier, R., Godoy, E., Hervé, F., and Varela, J. (1984). Petrochemistry and age of rhyolitic pyroclastic flows which occur along the drainage valleys of the río Maipo and río Cachapoal (Chile) and the río Yaucha and río Papagayos (Argentina): Revista Geológica de Chile, v. 23; p. 39–52.

Stern C. R. (1991). Role of subduction erosion in the generation of Andean magmas: Geology v. 19; p. 78–81.

Stewart, J. H., Gehrels, G. E, Barth, A. P., Link, P. K., Christie-Blick, N., and Wrucke, T. (2001). Detrital zircon provenance of Mesoproterozoic to Cambrian arenites in the western United States and northwestern Mexico: Geological Society of American Bulletin, v. 113; p. 1343-1356.

Strecker, M. R., Alonso, r., Bookhagen, B., Carrapa, B., Coutand, I., Hain, M. P., Hilley, E., Mortimer, E., Schoenbohm, L., and Sobel, E. R. (2009). Does the topographic distribution

of the central Andean Puna plateau result from climatic or geodynamic processes: Geology, v. 37; p. 643-646.

Sun S. S., and McDonough W. F. (1989). Chemical and isotopic systematics of oceanic basalts: Implications for mantle composition and processes Magmatism in the Oceanic Basins. (Edited by Saunders A. D. and Norry M. J.): Geological Society Special Publication, v. 42, p. 313-345.

Taylor, H. P. (1980). The effects of assimilation of country rocks by magmas on $^{18}O/^{16}O$ and $^{87}Sr/^{86}Sr$ systematic in igneous rock: Earth and Planetary Science Letters, v. 47; p. 243-254.

Taylor, S. R., and McLennan, S. M. (1981). The composition and evolution of the continental crust: rare earth element evidence from sedimentary rocks. Philosophical Transactions of the Royal Society A301, 381-399.

Taylor, S. R., and McLennan, S. M. (1985). The Continental Crust: Its Composition and Evolution. Blackwell, Oxford.

Taylor, S. R., and McLennan, S. M. (1995). The geochemical evolution of the continental crust: Reviews of Geophysics, v. 33; p. 241-265.

Thirlwall, M. F. (1991). Long-term reproducibility of multicollector Sr and Nd isotope ratio analysis: Chemical Geology, v. 94; p. 85-104.

Thomas, R. B., Hirschmann, M. M., Cheng, H., Reagan, M. K., Edwards, R.L. (2002). ($Pa-^{231}/U-^{235}$)–($Th-^{230}/U-^{238}$) of young mafic volcanic rocks from Nicaragua and Costa Rica and the influence of flux melting on U-series systematics of arc lavas: Geochimica et Cosmochimica Acta, v. 66; p. 4287–4309.

Thorpe, R. S., and Francis, P. W. (1979). Variations in Andean andesite compositions and their petrogenetic significance: Tectonophysics, v. 57; p. 53-70.

Thorpe R. S., Francis P. W., and Harmon R. S. (1981). Andean andesites and crustal growth: Philosophical Transactions of the Royal Society of London. Series A: Mathematical and Physical Sciences, v. 301; p. 305–320.

Tollan P. M. E., Bindeman, I., and Blundy, J. D. (2012). Cumulate xenoliths from St. Vincent, Lesser Antilles Island Arc: a window into upper crustal differentiation of mantle-derived basalts: Contributions to Mineralogy and Petrology, v. 163; p. 189-208.

Tommasini, S., and Davies, G. R. (1997). Isotope disequilibrium during anatexis: a case study of contact melting, Sierra Nevada, California: Earth and Planetary Science Letters, v. 148; p. 273-285.

Torné, M., Fernàndez, M., Comas, C., and Soto, J. I. (2000). Lithospheric structure beneath the Alborán Basin: Results from 3D gravity modeling and tectonic relevance: Journal of Geophysical Research, v. 105: p. 3209-3228.

Torsvik, T. H., Gaina, C., and Redfield, T. F. (2008). Antarctica and Global Paleogeography: From Rodinia, Through Gondwanaland and Pangea, to the Birth of the Southern Ocean and the Opening of Gateways in Cooper, A. K., Barrett, P. J., Stagg, H., Storey, B., Stump, E., and Wise, W., and the 10th ISAES editorial team, (eds); Antarctica: A Keystone in a

Changing World. Proceedings of the 10th International Symposium on Antarctic Earth Sciences. Washington, DC: The National Academies Press.

Tosdal, R. M. (1996). The Amazon-Laurentian connection as viewed from the middle proterozoic rocks in the central Andes, western Bolivia and northern Chile: Tectonics, v. 15; p. 827–842.

Trumbull, R., Riller, U., Oncken, O., Scheuber, E., Munier, K., and Hongn, F. (2006). The time-space distribution of Cenozoic volcanism in the south-central Andes: A new data compilation and some tectonic implications, in Chong, G., Franz, G., Giese, P., Götze, H-J., Ramos, V. A., Strecker, M. R., Wigger, P. (eds). The Andes: Active Subduction Orogeny: Berlin, Springer-Verlag, Frontiers in Earth Sciences; p. 29–43.

Turner, S. P., Platt, J. P., George, R. M .M., Kelley, S. P., Pearson, D. G., Nowell, G.M. (1999). Magmatism associated with orogenic collapse of the Betic–Alborán domain southeast Spain: Journal of Petrology, v. 40; p. 1011–1036.

Turner, S., and Hawkesworth, C. (1997). Constraints on flux rates and mantle dynamics beneath island arcs from Tonga-Kermadec lava geochemistry: Nature, v. 389; p; 568–573.

Turner, S., Bourdon, B., Hawkesworth, C., Evans, P. (2000). ^{226}Ra–^{230}Th evidence for multiple dehydration events, rapid melt ascent and the time scales of differentiation beneath the Tonga-Kermadec island arc: Earth and Planetary Science Letters, v. 179; p. 581–593.

Turner, S., Evans, P., Hawkesworth, C. (2001). Ultrafast source-to-surface movement of melt at island arcs from ^{226}Ra–^{230}Th systematics: Science, v. 292; p. 1363–1366.

Turner, S., Regelous, M., Hawkesworth, C., Rostami, K. (2006). Partial melting processes above subducting plates: constraints from ^{231}Pa–^{235}U disequilibria: Geochimica et Cosmochimica Acta, v. 70; p. 480–503.

Turner, S., Caulfield, J., Turner, M., van Keken, P., Maury, R., Sandiford, M., and Prouteau, G. (2012). Recent contribution of sediments and fluids to the mantle's volatile budget: Nature Geoscience, v. 3; p. 50-54.

Vielzeuf, D., Clemens, J. D. (1992). The fluid-absent melting of phlogopite+quartz: experiments and models. American Mineralogist, v. 77; p. 1206–1222.

Ventura, D., Bellatreccia, F. B., Harley, S., and Piccinini, M. (2009). FTIR microspectroscopy and SIMS study of water-poor cordierite from El Hoyazo, Spain: Application to mineral and melt devolatization: Lithos, v. 113; p. 498-506.

Venturelli, G., Capedri, S., Di Battistini, M., Crawford, A., Kogarko, L. N. and Celestini, S. (1984). The ultrapotassic rocks from southeastern Spain: Lithos, v. 17; p. 37-54.

Vielzeuf, D., Holloway, J. R. (1988). Experimental determination of the fluid-absent melting relations in the pelitic system, consequences for crustal differentiation: Contributions to Mineralogy and Petrology, v. 98; p. 257–276.

Vielzeuf, D., and Montel, J. M. (1994). Partial melting of metagreywackes, part I. Fluid absent experiments and phase relationships: Contributions to Mineralogy and Petrology, v. 117; p. 375–393.

Villemant, B., Jaffrezic, H., Joron, J. L. and Treuil, M. (1981). Distribution Coefficients of Major and Trace-Elements - Fractional Crystallization in the Alkali Basalt Series of Chaine-Des-Puys (Massif Central, France): Geochimica et Cosmochimica Acta, v. 45; p. 1997-2016.

Walker, B. A., Grunder, A., and Klemetti, E. W. (2011). Eleven million years of fractionation, magma mixing, and MASH zone expansion: geochemical constraints on the evolution of the Aucanquilcha magma system, northern Chile. AGU Fall Meeting Abstracts, 2011.

Wang, Y., and Chen, H. (2005). Tectonic controls on the Pleistocene-Holocene Wudalianchi volcanic field (northeastern China): Journal of Asian Earth Sciences, v. 24; p. 419-431.

Weaver, B. L. and Tarney, J. (1984). Empirical approach to estimating the composition of the continental crust.: Nature, v. 310; p. 575-577.

Wedepohl, H. (1995). The composition of the continental crust: Geochimica et Cosmochimica Acta, v. 59; p. 1217-1239.

Weber, M. B. I., Tarney, J., Kempton, P. D., and Kent, R. W. (2001). Crustal make-up of the northern Andes: evidence based on deep crustal xenolith, Mercedes, SW Colombia: Tectonophysics, v. 345; p. 49-82.

Weijermars, R. (1985). Uplift and subsidence history of the Alboran Basin and a profile of the Alboran Diapir (W. Mediterranean): Geologie en Mijnbouw, v. 64; p. 349-356.

White, W. M., McBirney, A. R., and Duncan, R. A. (1993). Petrology and geochemistry of the Galápagos Islands: Portrait of a pathological mantle plume: Journal of Geophysical Research, v. 98; p. 19533–19563.

Whitman, D., Isacks, B. L., and Kay, S. M. (1996). Lithospheric Structure and Along-Strike Segmentation of the Central Andean Plateau, 17-29°S: Second International Symposium on Andean Geodynamics (ISAG) Abstracts, Oxford, UK.

Whittington, A. G., Harris, N. B. W., and Butler, R. W. H. (1999). Contrasting anatectic styles at Nanga Parbat, northern Pakistan. In Macfarlane, A., Sorkhabi, R. B. and Quade, J. (eds) Himalaya and Tibet: Mountain Roots to Mountain Tops: Geological Society of America, Special Paper v. 328; p. 129–44.

Whittington, A. G., and Treloar, P. J. (2002). Crustal anatexis and its relation to the exhumation of collisional orogenic belts, with particular reference to the Himalaya: Mineralogical Magazine, v. 66; p. 53-91.

Wilde, S. A., Zhou, X. H., Nemchin, A. A., and Sun, M. (2003). Mesozoic crust-mantle beneath the North China craton: a consequence of the dispersal of Gondwanaland and accretion of Asia: Geology, v. 31; p. 817-820.

Wotzlaw, J. F., Decou, A., von Eynatten, H., Wörner, G., and Frei, D. (2011). Jurassic to Palaeogene tectono-magmatic evolution of northern Chile and adjacent Bolivia from detrital zircon U-Pb geochronology and heavy mineral provenance. Terra Nova, v. 23; p. 399-406.

Wörner, G., Moorbath, S., and Harmon, R. S. (1992). Andean Cenozoic volcanic centres reflect basement isotopic domains: Geology, v. 20; p. 1103-1106.

Wörner, G., Lezaun, J., Beck, J., Heber, V., Lucassen, F., Zinngrebe, E., Rößling, R., and Wilke, H-G. (2000). Precambrian and Early Paleozoic evolution of the Andean basement at Belen

(northern Chile) and Cerro Uyarani (western Bolivia Altiplano): Journal of South American Earth Science, v. 13; p. 717–737.

Xiao, L., and Wang, C. (2009). Geologic features of Wudalianchi volcanic field, northeastern China: Implications for Martian volcanology: Planetary and Space Science, v. 57; p. 685-698.

Yardley, B. D. (1989). An Introduction to Metamorphic Petrology. Harlow: Longman, 248 pp.

Yuan, X., Sobolev, S.V., and Kind, R. (2002). Moho topography in the central Andes and its geodynamic implications: Earth and Planetary Science Letters, v. 199; p. 389–402.

Yang, H.-J., Kinzler, R. J., and Grove, T. L. (1996). Experiments and models of anhydrous, basaltic olivine–plagioclase–augite saturated melts from 0·001 to 10 kbar: Contributions to Mineralogy and Petrology, v. 124; p. 1–18.

Zandt, G., Velasco, A. A., and Beck, S. L. (1994). Composition and thickness of southern Altiplano crust, Bolivia: Geology, v. 22; p. 1003–1006.

Zartman, R. E., and Haines, S. M. (1988). The plumbotectonic model for Pb isotopic systematics among major terrestrial reservoirs – A case for bi-directional transport: Geochimica et Cosmochimica Acta, v. 52; p. 1327-1339.

Zeck, H. P. (1968). PhD thesis: University of Amsterdam. Anatectic origin and further petrogenesis of almandine-bearing biotite cordierite–labradorite-dacite with many inclusions of restite and basaltoid material, Cerro del Hoyazo, SE Spain.

Zeck, H. P. (1970). An erupted migmatite from Cerro del Hoyazo, SE Spain: Contributions to Mineralogy and Petrology, v. 26; p. 225-246.

Zeck, H. P. (1992). Restite-melt and mafic-felsic magma mingling in an S-type dacite, Cerro del Hoyazo, southeastern Spain: Transactions of the Royal Society of Edinburgh: Earth Sciences, v. 83; p. 139-144.

Zeck, H. P., Kristensen, A. B., and Williams, I. S. (1998). Post-collisional volcanism in a sinking slab setting – crustal anatectic origin of pyroxene-andesite magma, Caldear Volcanic Group, Neogene Alborán volcanic Province, southeastern Spain: Lithos, v. 45; p. 499-522.

Zeck, H. P and Williams, I. S. (2002). Inherited and Magmatic Zircon from Neogene Hoyazo Cordierite Dacite, SE Spain – Anatectic Source Rock Provenance and Magmatic Evolution: Journal of Petrology, v. 43; p. 1089-1104.

Zeng, L., Asimow, P., Saleeby, J. B. (2005). Coupling of anatectic reactions and dissolution of accessory phases and the Sr and Nd isotope systematic of anatectic melts from a metasedimentary source: Geochimica et Cosmochimica Acta, v. 69; p. 3671–3682.

Zhang, M., Menzies, M. A., Suddaby, P., and Thirlwall, M. F. (1991). EM-I signature from within the post-Archean subcontinental lithospheric mantle. Isotopic evidence from the potassic volcanic rocks in NE China: Geochemical Journal, v. 25; p. 387-398.

Zhang, M., Suddaby, P., Thompson, R. N., Thirwall, M. F., and Menzies, M. A. (1995). Potassic Volcanic Rocks in NE China: Geochemical Constraints on Mantle source and Magma Genesis: Journal of Petrology, v. 36; p. 1275-1303.

Zheng, J. P., O'Reilly, S. Y., Griffin, W., Lu, F. X., Zhang, M., and Pearson, N. (2001). Relict refractory mantle beneath the eastern North China block: significance for lithosphere evolution: Lithos, v. 57; p. 43-66.

Zou, H., Reid, M. R., Liu, Y., Yao, Y., Xu, X., and Fan, Q. (2003). Constraints on the origin of historic potassic basalts from northeast China by U-Th disequilibrium data: Chemical Geology, v. 200; p. 189-201.

Appendix A: Sample ID

Table 1. List of Central Andean samples

Sample ID	Rock type	Lithology
BC93QNL01	Lava	Andesite
BC93QNL02	Lava	Andesite
BC93QSL01	Lava	Andesite
BC93QSL02	Lava	Andesite
BC93QSL03	Lava	Andesite
BC93QSL04	Lava	Andesite
BC93QSL05	Lava	Andesite
BC93QSL06	Lava	Andesite
BC93QSL07	Lava	Andesite
BC93QSL08	Lava	Andesite
BC93QSL09	Lava	Andesite
BC93PAL01	Lava	Dacite
BC93PAL02	Lava	Dacite
BC93PAL03	Lava	Dacite
BC93PAL04	Lava	Dacite
BC93QMI01	Mafic enclave	Basalt
BC93QMI02	Mafic enclave	Basalt
BC93QMI03	Mafic enclave	Basalt
BC93QMI04	Mafic enclave	Basalt
BC93FRIG01	Ignimbrite	Dacite
BC93FRIG02	Ignimbrite	Dacite
BC93FRIG03	Ignimbrite	Dacite
BC93FRIG04	Ignimbrite	Dacite
BC93QNX02	Crustal Xenolith	Garnet sillimanite granulite
BC93QNX03	Crustal Xenolith	Microgranite
BC93QSX04	Crustal Xenolith	Microgranite
BC93PAX01	Crustal Xenolith	Garnet sillimanite gneiss
BC93PAX03	Crustal Xenolith	Garnet sillimanite granulite
BC93PAX07	Crustal Xenolith	Diorite
BC93PAX11	Crustal Xenolith	Diorite
BC93PAX12	Crustal Xenolith	Garnet sillimanite gneiss
BC93PAX14	Crustal Xenolith	Garnet sillimanite granulite
BC10PAL101	Lava	Dacite
BC10PAL102	Lava	Dacite
BC10QMI103	Mafic enclave	Basaltic Andesite
BC10PMI106	Mafic enclave	Basalt
BC10QSX101	Crustal Xenolith	Garnet granulite
BC10QSX104	Crustal Xenolith	Dacite
BC10QSX106	Crustal Xenolith	Garnet granulite
BC10QSX107	Crustal Xenolith	Garnet granulite
BC10QSX108	Crustal Xenolith	Garnet quartzite
BC10QSX111	Crustal Xenolith	Dacite
BC10PAX102	Crustal Xenolith	Garnet mica schist
BC10PAX103	Crustal Xenolith	Diorite
BC10PAX107a	Crustal Xenolith	Garnet granulite
BC10PAX107b	Crustal Xenolith	Garnet granulite
BC10PAX110	Crustal Xenolith	Garnet granulite
BC10PAX112	Crustal Xenolith	Garnet granulite
BC10PAX113	Crustal Xenolith	Garnet granulite
BC10PAX127	Crustal Xenolith	Diorite
BC10PAX128	Crustal Xenolith	Garnet mica schist
BC10PAX131	Crustal Xenolith	Garnet quartzite
BC10PAX132	Crustal Xenolith	Garnet quartzite
BC10PAX134	Crustal Xenolith	Garnet sillimanite granulite
BC10PAX136	Crustal Xenolith	Garnet quartzite
BC10PAX138	Crustal Xenolith	Garnet quartzite

Appendix B: Data

Table 1: Whole rock composition of Pampas Aullagas and Quillacas lavas, Quillacas mafic enlcaves and the Los Frailles ignimbrite (prefix BC93-).

	QNL01	QNL02	QSL01	QSL02	QSL03	QSL04	QSL05	QSL06	QSL07
SiO_2	60.3	60.0	58.2	58.3	59.9	58.7	60.0	60.0	58.8
Al_2O_3	15.9	15.7	16.0	16.2	15.9	15.8	16.0	15.6	15.9
Fe_2O_3	5.9	6.0	6.6	6.5	6.0	6.3	6.1	6.1	6.5
MgO	4.1	4.3	5.1	4.9	4.4	4.7	4.4	4.3	4.9
CaO	5.3	5.5	6.0	5.9	5.4	5.6	5.5	5.3	5.9
Na_2O	2.6	2.6	2.7	2.9	2.7	2.6	2.7	2.7	2.7
K_2O	3.5	3.4	3.1	3.2	3.4	3.2	3.4	3.3	3.2
TiO_2	1.1	1.1	1.2	1.2	1.1	1.1	1.1	1.1	1.2
MnO	0.1	0.1	0.1	0.1	0.1	0.1	0.1	0.1	0.1
P_2O_5	0.3	0.3	0.3	0.3	0.3	0.3	0.3	0.3	0.3
LOI	0.3	0.8	0.0	0.3	0.3	0.3	0.3	0.6	0.2
Total	99.5	99.9	99.2	99.9	99.4	98.8	100.0	99.5	99.8
Sc	11.4	12.0	13.5	13.4	12.4	13.9	12.9	11.8	13.6
V	98.8	105.4	117.6	117.6	108.0	116.6	110.2	104.6	119.2
Cr	113.7	129.2	157.6	166.0	151.2	143.4	160.7	143.7	156.1
Mn	0.1	0.1	0.1	0.1	0.1	0.1	0.1	0.1	0.1
Co	12.0	13.0	14.7	14.4	12.9	13.6	12.8	12.9	13.9
Ni	37.9	34.9	36.1	42.0	34.7	33.5	39.0	28.7	31.9
Cu	16.8	16.5	33.8	18.3	16.3	26.7	16.5	15.8	18.4
Zn	73.5	76.4	81.5	77.3	74.2	74.2	71.2	74.2	74.5
Ga	18.3	18.7	18.3	18.5	18.6	18.5	18.4	18.6	18.5
Rb	97.9	98.1	86.1	87.5	97.3	92.4	96.5	95.5	88.5
Sr	450.6	464.9	478.2	479.4	443.2	459.0	445.9	452.7	482.0
Y	16.2	16.3	16.9	17.0	16.6	17.4	17.0	16.0	17.2
Zr	213.3	208.0	207.2	207.0	208.6	205.8	203.0	213.5	206.6
Nb	17.5	17.2	16.7	16.8	16.7	16.6	16.8	16.3	16.9
Cs	2.8	2.8	2.2	2.4	3.3	2.5	2.8	2.6	2.3
Ba	1357.1	1336.2	1257.2	1275.8	1338.0	1289.4	1313.4	1321.3	1306.5
La	48.0	48.8	46.0	46.1	49.8	46.8	47.0	50.7	49.4
Ce	94.2	95.2	90.5	91.2	97.3	91.7	91.9	99.0	97.5
Pr	11.5	11.6	11.0	11.2	11.9	11.2	11.2	12.0	11.8
Nd	45.0	46.2	44.2	44.5	46.8	44.4	44.4	47.8	47.1
Sm	8.0	8.1	7.8	8.0	8.2	8.0	8.0	8.4	8.4
Eu	2.0	2.0	2.0	2.0	2.0	2.0	2.0	2.0	2.1
Gd	6.1	5.9	6.0	6.1	6.2	6.1	6.0	6.0	6.3
Tb	0.8	0.8	0.8	0.8	0.8	0.8	0.8	0.8	0.8
Dy	3.9	3.9	4.0	4.0	4.0	4.1	4.0	3.8	4.2
Ho	0.7	0.7	0.7	0.7	0.7	0.7	0.7	0.7	0.7
Er	1.7	1.6	1.8	1.8	1.7	1.8	1.8	1.6	1.8
Tm	0.2	0.2	0.3	0.3	0.3	0.3	0.3	0.2	0.3
Yb	1.5	1.5	1.6	1.6	1.6	1.7	1.6	1.5	1.6
Lu	0.2	0.2	0.3	0.3	0.2	0.3	0.3	0.2	0.3
Hf	5.2	5.2	5.3	5.3	5.2	5.2	5.2	5.3	5.4
Ta	1.5	1.5	1.4	1.4	1.4	1.4	1.5	1.3	1.4
Pb	20.9	20.6	17.8	16.4	19.8	16.7	18.8	17.8	9.8
Th	13.6	13.9	12.3	12.3	14.0	12.9	13.5	13.7	13.4
U	3.0	2.7	2.3	2.4	3.3	2.6	2.8	2.6	2.5
$^{87}Sr/^{86}Sr$	0.710122	0.709885	0.709128	0.709255	0.710002	0.709751	0.709871	0.710182	0.709292
$^{143}Nd/^{144}Nd$	0.512145	0.512194	0.512214	0.512229	0.512175	0.512196	0.512160	0.512160	0.512213
$^{206}Pb/^{204}Pb$	18.47	18.72	18.48	18.48	18.48	18.49	18.44	18.52	18.49
$^{207}Pb/^{204}Pb$	15.66	15.68	15.65	15.65	15.66	15.66	15.65	15.66	15.66
$^{208}Pb/^{204}Pb$	38.99	39.00	38.96	38.96	38.98	38.99	39.00	38.98	38.98

Table 1 (cont).

	QSL08	QSL09	PAL01	PAL02	PAL03	PAL04	QMI01	QMI02	QMI03
SiO_2	59.1	58.6	64.8	63.1	62.7	59.4	44.2	44.1	43.6
Al_2O_3	15.8	15.6	16.5	16.1	16.5	17.1	13.9	13.8	13.8
Fe_2O_3	6.5	6.5	4.4	4.5	4.7	6.0	11.4	11.2	11.9
MgO	4.8	4.9	2.0	1.9	2.4	3.5	12.5	12.6	12.3
CaO	5.8	5.8	3.1	3.7	4.2	5.6	10.5	10.4	10.4
Na_2O	2.8	2.7	2.1	2.0	2.4	2.4	1.9	1.9	1.8
K_2O	3.1	3.1	4.2	4.1	3.9	3.4	1.8	1.8	1.8
TiO_2	1.2	1.2	1.1	1.0	1.3	1.6	2.5	2.5	2.5
MnO	0.1	0.1	0.1	0.1	0.1	0.1	0.1	0.1	0.1
P_2O_5	0.3	0.3	0.3	0.3	0.3	0.4	0.3	0.2	0.3
LOI	0.2	0.6	1.4	2.7	1.1	0.3	0.8	1.1	1.2
Total	99.9	99.3	99.9	99.6	99.5	99.8	100.0	99.6	99.6
Sc	13.6	12.5	8.3	7.5	10.4	17.6	52.7	-	-
V	119.2	114.3	77.0	72.5	92.3	135.6	412.4	-	-
Cr	165.8	164.8	31.9	31.3	21.9	41.1	52.0	-	-
Mn	0.1	0.1	0.0	0.0	0.1	0.1	0.1	-	-
Co	15.1	14.8	5.1	3.7	3.3	4.9	26.0	-	-
Ni	38.3	33.5	15.5	8.7	5.0	8.0	4.5	-	-
Cu	19.8	19.2	12.5	12.6	6.2	8.4	15.4	-	-
Zn	76.2	74.9	76.6	72.6	74.5	77.1	68.0	-	-
Ga	18.7	18.2	20.5	19.8	20.5	20.5	15.0	-	-
Rb	86.7	83.2	130.6	127.0	115.9	93.2	28.7	-	-
Sr	471.4	475.8	350.1	344.9	440.6	525.9	361.7	-	-
Y	17.1	15.8	16.7	14.5	20.3	26.7	26.0	-	-
Zr	216.8	214.1	248.6	241.7	258.9	273.1	80.5	-	-
Nb	16.3	15.8	22.8	21.3	28.0	37.2	9.3	-	-
Cs	2.5	2.0	4.5	4.0	3.2	3.1	2.8	-	-
Ba	1284.3	1234.6	1885.1	1786.2	1700.6	1647.5	582.4	-	-
La	48.7	47.7	65.2	64.4	63.5	56.8	14.8	-	-
Ce	95.8	93.8	126.0	124.1	122.7	108.9	38.3	-	-
Pr	11.7	11.5	15.0	14.8	14.7	13.2	6.2	-	-
Nd	47.0	45.8	58.2	56.8	56.8	52.4	32.3	-	-
Sm	8.2	8.0	9.8	9.3	9.6	9.5	8.4	-	-
Eu	2.1	2.0	2.5	2.4	2.5	2.7	2.3	-	-
Gd	6.2	5.9	6.7	6.3	7.0	8.1	8.6	-	-
Tb	0.8	0.8	0.9	0.8	1.0	1.2	1.2	-	-
Dy	4.1	3.8	4.1	3.7	4.8	6.1	6.4	-	-
Ho	0.7	0.7	0.7	0.6	0.9	1.1	1.2	-	-
Er	1.8	1.7	1.6	1.4	2.1	2.9	2.9	-	-
Tm	0.3	0.2	0.2	0.2	0.3	0.4	0.4	-	-
Yb	1.6	1.5	1.4	1.2	2.0	2.7	2.3	-	-
Lu	0.3	0.2	0.2	0.2	0.3	0.4	0.3	-	-
Hf	5.5	5.4	5.5	5.4	6.3	7.2	2.9	-	-
Ta	1.3	1.3	2.0	1.8	2.6	3.6	0.7	-	-
Pb	16.1	17.1	26.3	26.2	24.4	19.1	4.1	-	-
Th	12.6	12.1	17.8	17.2	16.8	14.0	2.2	-	-
U	2.4	2.2	3.1	3.2	3.5	2.6	0.5	-	-
$^{87}Sr/^{86}Sr$	0.709694	0.709372	0.716691	0.716947	0.714015	0.712261	0.707314	-	-
$^{143}Nd/^{144}Nd$	0.512228	0.512214	0.512131	0.512123	0.512187	0.512248	0.512316	-	-
$^{206}Pb/^{204}Pb$	18.58	18.52	18.73	18.72	18.70	18.71	-	-	-
$^{207}Pb/^{204}Pb$	15.66	15.66	15.68	15.68	15.67	15.67	-	-	-
$^{208}Pb/^{204}Pb$	38.95	38.94	39.07	39.05	39.06	39.05	-	-	-

Table 1 (cont).

	QMI04	FRIG01	FRIG02	FRIG03	FRIG04
SiO_2	44.0	68.1	68.3	68.0	67.7
Al_2O_3	13.9	15.5	15.5	15.9	15.8
Fe_2O_3	11.8	3.2	3.2	3.2	3.2
MgO	12.2	1.0	1.1	1.0	1.0
CaO	10.5	2.3	2.3	2.3	2.3
Na_2O	1.9	2.7	2.6	2.7	2.7
K_2O	1.8	4.1	4.2	4.2	4.1
TiO_2	2.5	0.7	0.7	0.7	0.7
MnO	0.1	0.0	0.0	0.0	0.0
P_2O_5	0.2	0.3	0.3	0.3	0.3
LOI	0.9	1.6	1.5	1.5	1.6
Total	99.9	99.5	99.6	99.9	99.5
Sc	-	4.4	-	-	-
V	-	43.6	-	-	-
Cr	-	11.4	-	-	-
Mn	-	0.0	-	-	-
Co	-	4.7	-	-	-
Ni	-	7.6	-	-	-
Cu	-	5.4	-	-	-
Zn	-	78.3	-	-	-
Ga	-	19.3	-	-	-
Rb	-	159.3	-	-	-
Sr	-	488.4	-	-	-
Y	-	11.8	-	-	-
Zr	-	221.3	-	-	-
Nb	-	19.6	-	-	-
Cs	-	26.7	-	-	-
Ba	-	1051.9	-	-	-
La	-	78.9	-	-	-
Ce	-	146.9	-	-	-
Pr	-	16.7	-	-	-
Nd	-	61.0	-	-	-
Sm	-	9.4	-	-	-
Eu	-	1.8	-	-	-
Gd	-	5.6	-	-	-
Tb	-	0.7	-	-	-
Dy	-	**3.1**	-	-	-
Ho	-	0.5	-	-	-
Er	-	1.1	-	-	-
Tm	-	0.1	-	-	-
Yb	-	0.9	-	-	-
Lu	-	0.1	-	-	-
Hf	-	1.0	-	-	-
Ta	-	1.5	-	-	-
Pb	-	34.8	-	-	-
Th	-	23.5	-	-	-
U	-	6.1	-	-	-
$^{87}Sr/^{86}Sr$	-	0.710514	0.710434	0.710541	0.710534
$^{143}Nd/^{144}Nd$	-	0.512263	0.512275	0.512257	0.512322
$^{206}Pb/^{204}Pb$	-	-	-	-	-
$^{207}Pb/^{204}Pb$	-	-	-	-	-
$^{208}Pb/^{204}Pb$	-	-	-	-	-

Table 2: Whole rock composition of Pampas Aullagas and Quillacas xenoliths (prefix BC93-).

	QNX02	QNX03	QSX04	PAX01	PAX03	PAX07	PAX11	PAX12	PAX14
SiO2	68.5	68.7	69.3	88.2	67.7	56.9	57.7	79.8	65.1
Al2O3	13.4	15.2	15.3	6.6	13.7	17.0	15.1	13.3	16.7
Fe2O3	0.2	5.0	4.6	1.3	2.1	2.8	2.6	0.5	0.3
MgO	1.9	0.9	0.8	0.6	2.8	5.4	5.7	0.8	1.7
CaO	6.5	2.1	2.0	0.0	3.5	6.0	5.9	0.2	8.8
Na2O	0.6	3.4	3.6	0.2	2.3	1.4	1.9	0.0	0.6
K2O	0.2	5.0	4.6	1.3	2.1	2.8	2.6	0.5	0.3
TiO2	0.8	0.6	0.6	0.4	0.8	1.9	1.3	0.4	0.7
MnO	0.2	0.0	0.0	0.1	0.1	0.1	0.2	0.3	0.2
P2O5	0.2	0.2	0.2	0.0	0.2	0.2	0.4	0.2	0.3
LOI	2.0	0.6	0.2	0.4	0.2	0.7	0.5	0.5	0.1
Total	99.3	99.5	99.6	99.4	99.7	99.6	99.6	99.3	99.3
Sc	11.2	3.1	2.8	7.7	12.3	13.6	24.7	8.5	13.2
V	84.8	35.7	34.4	19.9	77.8	175.4	124.9	27.9	82.5
Cr	58.3	11.3	7.3	14.7	46.1	51.7	199.7	22.6	43.1
Mn	0.2	0.0	0.0	0.1	0.1	0.1	0.1	0.2	0.2
Co	6.9	3.7	3.5	1.7	4.9	8.1	13.9	2.0	6.0
Ni	17.6	4.6	2.2	4.0	13.7	13.5	26.7	4.1	11.4
Cu	13.9	4.4	5.7	2.5	18.0	10.9	11.9	6.5	11.8
Zn	42.9	70.4	67.3	20.2	36.9	99.5	103.6	27.2	42.9
Ga	14.7	22.5	21.7	11.4	12.8	19.5	20.0	15.7	16.2
Rb	5.9	165.6	176.7	34.0	91.9	84.1	81.4	27.3	11.1
Sr	131.3	301.7	307.1	33.1	343.0	388.4	416.4	18.5	194.7
Y	26.9	8.3	8.0	14.3	19.2	19.3	22.2	30.2	28.2
Zr	206.3	313.2	301.8	314.4	191.0	117.2	147.6	166.9	172.9
Nb	19.3	15.5	11.2	12.4	13.0	14.5	13.5	17.1	11.4
Cs	1.3	1.8	1.6	0.5	6.4	1.5	1.0	1.5	0.5
Ba	44.6	1333.8	1440.8	291.4	561.3	1123.2	1043.8	138.4	89.8
La	32.7	106.2	62.4	24.7	16.7	46.5	11.9	22.4	25.7
Ce	64.8	199.8	115.4	50.6	29.1	97.3	31.1	46.0	49.7
Pr	7.7	21.6	12.7	5.9	3.3	12.7	5.1	5.6	6.0
Nd	30.1	75.1	44.3	22.9	12.7	53.5	26.3	22.8	24.0
Sm	5.8	10.0	6.3	4.0	2.6	10.0	7.1	4.7	5.2
Eu	1.3	1.8	1.5	0.4	1.0	2.0	1.9	0.4	1.5
Gd	5.5	4.6	3.4	3.1	2.7	7.7	7.1	4.7	5.8
Tb	0.9	0.6	0.4	0.4	0.5	1.0	1.0	0.8	1.0
Dy	5.0	2.3	1.9	2.5	3.3	4.9	5.3	5.5	5.8
Ho	1.0	0.4	0.3	0.6	0.8	0.8	1.0	1.3	1.1
Er	3.0	0.8	0.8	2.2	2.5	1.9	2.3	4.0	3.1
Tm	0.5	0.1	0.1	0.4	0.4	0.3	0.3	0.8	0.5
Yb	3.1	0.6	0.7	2.8	2.8	1.6	1.9	5.7	3.2
Lu	0.5	0.1	0.1	0.5	0.4	0.2	0.3	1.0	0.5
Hf	1.0	0.3	0.1	0.3	0.2	0.7	1.0	1.1	0.2
Ta	1.5	1.0	0.9	0.6	1.1	1.1	0.6	3.2	1.1
Pb	10.4	33.0	32.0	6.3	26.5	8.7	8.3	3.8	9.4
Th	13.6	39.4	21.5	10.5	6.1	12.2	2.2	7.3	12.3
U	1.7	2.0	0.9	0.7	0.8	1.8	0.8	1.4	1.4
$^{87}Sr/^{86}Sr$	0.736760	0.712017	0.712014	0.719380	0.722624	0.712595	0.710481	0.717314	0.732878
$^{143}Nd/^{144}Nd$	0.511850	0.511929	0.511980	0.511872	0.511846	0.512091	0.512168	0.511966	0.511885
$^{206}Pb/^{204}Pb$	18.65	17.77	17.79	18.17	18.43	18.72	18.44	18.67	18.50
$^{207}Pb/^{204}Pb$	15.67	15.61	15.61	15.64	15.67	15.68	15.66	15.68	15.67
$^{208}Pb/^{204}Pb$	39.13	38.47	38.49	38.95	39.02	39.00	38.96	38.82	39.17

Table 3: Whole rock composition of Pampas Aullagas and Quillacas lavas, from Davidson and de Silva, (1995)

	BC9022	BC9023	BC9024	BC9025
SiO2	58.6	56.4	60.7	61.8
Al2O3	16.1	16.2	16.2	17.2
Fe2O3	6.9	7.4	5.5	5.3
MgO	5.1	5.7	3.7	2.6
CaO	6.0	6.8	5.4	4.9
Na2O	2.9	3.1	2.9	2.5
K2O	3.1	2.6	3.5	3.7
TiO2	1.2	1.3	1.1	1.5
MnO	0.1	0.1	0.1	0.1
P2O5	0.4	0.4	0.3	0.4
LOI	0.0	0.0	0.6	0.0
Total	99.6	99.6	99.6	99.7
Sc	-	-	-	-
V	-	-	-	-
Cr	238.0	197.0	122.0	54.0
Mn	-	-	-	-
Co	-	-	-	-
Ni	40.0	43.0	30.0	17.0
Cu	-	-	-	-
Zn	-	-	-	-
Ga	22.0	23.0	24.0	27.0
Rb	78.0	106.0	126.0	127.0
Sr	651.0	582.0	547.0	582.0
Y	23.0	22.0	22.0	29.0
Zr	216.0	213.0	218.0	278.0
Nb	21.0	19.0	22.0	43.0
Cs	-	-	-	-
Ba	931.0	1214.0	1270.0	1681.0
La	40.0	44.0	49.4	59.9
Ce	76.2	91.7	103.5	120.3
Pr	-	-	-	-
Nd	36.7	43.4	42.5	48.7
Sm	7.1	7.7	8.2	9.4
Eu	1.9	1.9	1.9	2.5
Gd	-	-	-	-
Tb	0.8	0.8	0.8	0.9
Dy	-	-	-	-
Ho	-	-	-	-
Er	-	-	-	-
Tm	-	-	-	-
Yb	1.8	1.9	1.7	2.2
Lu	0.2	0.3	0.3	0.3
Hf	5.0	5.5	5.6	7.1
Ta	1.2	1.3	1.4	2.6
Pb	14.0	18.0	21.0	14.0
Th	9.0	11.6	13.5	14.7
U	1.6	2.2	3.2	2.4
$^{87}Sr/^{86}Sr$	0.707955	0.709084	0.710443	0.713657
$^{143}Nd/^{144}Nd$	0.512260	0.512171	0.512199	0.512159
$^{206}Pb/^{204}Pb$	18.41	18.42	18.42	18.79
$^{207}Pb/^{204}Pb$	15.59	15.61	15.62	15.75
$^{208}Pb/^{204}Pb$	38.70	38.81	38.86	39.30

Table 4: Whole rock composition of Pampas Aullagas and Quillacas xenoliths (prefix BC10-).

	QSX101	QSX104	QSX106	QSX107	QSX108	QSX111	PAX102	PAX103	PAX107a
SiO2	67.4	67.2	63.1	67.1	71.3	66.7	77.6	53.0	77.4
Al2O3	12.5	16.4	15.2	14.2	14.9	15.7	18.7	20.3	10.6
Fe2O3	0.1	4.7	0.03	0.02	4.4	4.8	0.3	3.2	0.1
MgO	2.7	1.0	1.8	1.0	0.6	1.4	0.2	4.3	1.1
CaO	9.7	2.4	12.9	11.5	2.8	2.6	0.2	5.8	6.8
Na2O	0.4	3.4	0.3	0.2	3.0	4.2	0.03	1.6	0.3
K2O	0.1	4.7	0.03	0.02	4.4	4.8	0.3	3.2	0.1
TiO2	0.8	0.6	0.6	0.7	0.5	0.7	0.1	1.7	0.8
MnO	0.3	0.02	0.3	0.2	0.02	0.04	0.02	0.1	0.1
P2O5	0.1	0.3	0.3	0.2	0.3	0.3	0.2	0.2	0.2
LOI	0.6	1.2	0.2	0.1	0.6	0.2	1.3	1.9	0.1
Total	94.5	101.8	94.7	95.2	102.6	101.4	98.7	95.2	97.7
Sc	12.1	5.3	11.0	11.2	3.8	5.3	3.3	10.8	8.4
V	84.3	40.9	85.6	109.2	28.9	47.8	38.6	187.7	45.9
Cr	15.9	6.5	17.2	14.8	26.8	27.9	6.8	68.2	95.8
Mn	0.2	0.0	0.2	0.2	0.0	0.0	0.0	0.1	0.1
Co	10.8	3.7	7.5	4.2	3.2	6.4	0.8	10.8	5.7
Ni	0.8	0.4	0.9	0.7	11.8	12.5	0.2	21.7	57.6
Cu	13.0	7.6	17.3	4.8	7.7	12.8	1.8	29.7	16.8
Zn	42.6	48.8	34.3	33.7	51.9	63.1	12.0	119.7	54.7
Ga	14.9	25.5	21.6	19.7	18.9	24.7	25.7	24.3	15.2
Rb	0.9	242.6	0.9	0.7	168.9	219.8	10.9	106.6	2.5
Sr	214.3	371.5	251.0	306.7	468.7	419.1	24.7	533.1	104.1
Y	32.9	14.4	30.5	29.5	9.3	13.9	12.6	7.5	24.8
Zr	21.6	14.3	52.6	35.2	6.9	17.5	9.5	10.7	42.5
Nb	15.4	18.4	16.6	11.9	14.4	18.3	1.9	16.7	18.3
Cs	0.1	12.7	0.1	0.1	3.5	7.1	0.8	2.1	0.2
Ba	17.3	919.1	12.4	8.8	1131.0	932.6	150.6	1583.0	26.1
La	37.2	58.1	34.8	32.9	44.9	60.2	15.1	34.8	33.7
Ce	78.0	116.4	70.8	67.5	88.3	122.5	29.4	71.1	66.9
Pr	9.4	13.9	8.6	8.0	10.6	14.4	3.9	8.9	8.2
Nd	37.0	52.1	34.3	31.1	39.7	54.3	14.9	34.5	31.8
Sm	7.1	8.8	6.6	5.8	6.4	8.8	2.9	5.4	6.1
Eu	1.7	1.7	1.4	1.5	1.8	1.7	0.3	1.8	1.8
Gd	6.6	5.8	6.2	5.5	4.2	5.8	2.7	3.5	5.5
Tb	1.0	0.7	0.9	0.8	0.5	0.7	0.4	0.4	0.9
Dy	5.5	3.0	4.9	4.7	2.0	3.0	2.4	1.7	4.6
Ho	1.2	0.5	1.0	1.0	0.3	0.5	0.5	0.3	0.9
Er	3.1	1.1	2.7	2.7	0.7	1.1	1.2	0.6	2.1
Tm	0.5	0.2	0.5	0.4	0.1	0.2	0.2	0.1	0.3
Yb	3.3	0.8	2.8	2.7	0.5	0.8	1.1	0.5	2.0
Lu	0.5	0.1	0.4	0.4	0.1	0.1	0.2	0.1	0.3
Hf	0.8	0.6	1.9	1.2	0.3	0.6	0.3	0.6	1.5
Ta	1.2	1.7	0.9	0.8	1.1	1.5	0.1	1.2	1.4
Pb	4.9	33.3	3.3	7.8	21.0	19.7	6.7	8.5	3.2
Th	12.2	18.7	9.9	12.1	13.8	19.3	4.1	8.9	13.3
U	2.0	6.7	1.1	1.3	2.0	5.1	0.7	1.7	2.5
$^{87}Sr/^{86}Sr$	-	0.712227	0.730022	0.736619	-	0.711805	-	-	0.721485
$^{143}Nd/^{144}Nd$	-	0.512179	0.511913	0.511829	-	0.512207	-	-	0.511917
$^{206}Pb/^{204}Pb$	-	18.60	18.75	18.61	-	18.77	-	-	18.61
$^{207}Pb/^{204}Pb$	-	15.65	15.69	15.68	-	15.68	-	-	15.67
$^{208}Pb/^{204}Pb$	-	38.91	39.46	39.20	-	38.99	-	-	38.76

Table 4 (cont).

	PAX107b	PAX110	PAX112	PAX113	PAX127	PAX128	PAX131	PAX132	PAX134
SiO2	59.0	60.9	66.8	63.4	52.8	82.4	74.8	76.7	74.2
Al2O3	17.4	17.5	15.9	15.7	25.7	13.2	16.3	14.9	12.0
Fe2O3	0.4	0.1	0.8	0.0	4.4	0.5	2.3	4.4	0.8
MgO	2.2	1.5	1.6	1.3	4.4	0.3	0.2	0.1	1.5
CaO	9.7	12.5	6.8	13.2	0.7	0.7	1.7	0.8	4.0
Na2O	0.5	0.4	1.5	0.2	1.3	0.1	3.0	1.5	2.0
K2O	0.4	0.1	0.8	0.0	4.4	0.5	2.3	4.4	0.8
TiO2	0.7	0.7	0.5	0.6	0.9	0.1	0.2	0.1	0.5
MnO	0.8	0.4	0.2	0.4	0.1	0.0	0.0	0.0	0.2
P2O5	0.3	0.3	0.6	0.2	0.1	0.5	0.1	0.1	0.3
LOI	1.6	0.6	0.1	0.0	0.9	0.2	0.3	0.3	0.4
Total	93.0	94.9	95.5	94.9	95.5	98.4	101.4	103.3	96.9
Sc	11.2	8.8	11.9	10.3	19.7	3.2	14.6	2.5	5.6
V	105.6	110.4	93.8	107.4	174.1	22.5	6.3	5.7	34.3
Cr	9.8	9.4	15.4	8.5	26.3	58.1	2.5	2.9	5.4
Mn	0.7	0.4	0.2	0.3	0.1	0.0	0.0	0.0	0.2
Co	5.8	8.0	4.3	7.0	6.0	5.0	0.8	0.7	2.5
Ni	0.2	0.4	7.1	0.7	14.8	68.4	0.2	0.9	0.3
Cu	3.5	4.7	8.2	2.8	17.8	28.8	1.7	2.6	7.6
Zn	41.5	33.5	49.6	24.3	136.4	138.5	10.8	8.6	25.4
Ga	24.6	46.1	16.9	22.9	27.9	17.4	27.0	10.3	10.4
Rb	19.3	2.7	29.3	1.1	264.0	22.4	50.6	93.0	63.8
Sr	127.6	127.3	186.8	288.8	138.2	35.1	235.8	426.6	425.3
Y	54.3	38.4	30.3	32.3	13.5	36.6	14.0	6.1	20.6
Zr	67.5	27.6	4.6	18.2	12.9	8.3	2.9	4.2	6.7
Nb	20.3	34.2	13.0	9.8	12.7	2.5	15.6	1.2	10.6
Cs	0.6	0.2	1.7	0.1	19.3	1.5	0.9	1.4	9.2
Ba	67.9	81.9	52.4	23.5	1105.0	81.6	420.6	2549.0	1102.0
La	29.5	27.2	28.9	16.0	39.3	12.8	17.7	4.5	13.3
Ce	60.9	57.9	53.6	34.8	78.3	28.2	148.5	8.2	27.4
Pr	7.5	6.9	6.4	4.4	9.7	3.7	16.8	1.0	3.3
Nd	29.8	27.6	25.2	17.9	37.8	16.1	64.5	4.1	13.1
Sm	6.5	5.6	4.8	3.9	7.0	4.5	11.2	0.9	3.1
Eu	2.0	1.7	1.4	1.0	1.6	0.4	1.5	2.3	1.1
Gd	6.9	5.6	4.9	4.2	5.4	5.6	8.3	1.1	3.7
Tb	1.2	0.9	0.8	0.7	0.7	1.1	1.0	0.2	0.6
Dy	7.2	5.3	4.4	4.4	3.1	6.6	3.8	1.1	3.2
Ho	1.7	1.2	0.9	1.0	0.5	1.3	0.6	0.2	0.7
Er	4.9	3.3	2.8	3.0	1.2	3.1	1.0	0.5	2.0
Tm	0.9	0.6	0.5	0.5	0.2	0.4	0.1	0.1	0.4
Yb	5.7	3.5	3.4	3.5	1.1	2.2	0.4	0.4	2.2
Lu	0.9	0.5	0.6	0.6	0.2	0.3	0.1	0.1	0.3
Hf	2.1	1.0	0.2	0.7	0.4	0.3	0.1	0.1	0.2
Ta	1.5	1.1	0.9	0.7	1.1	0.2	0.5	0.2	0.8
Pb	5.8	3.8	7.2	4.0	14.7	2.8	19.0	36.6	12.0
Th	9.1	10.4	8.5	6.3	14.0	2.2	33.9	0.8	8.0
U	3.1	1.9	1.7	1.0	3.3	0.9	2.0	0.3	0.7
$^{87}Sr/^{86}Sr$	0.721154	-	-	0.732611	-	0.718070	-	-	-
$^{143}Nd/^{144}Nd$	0.511948	-	-	0.511989	-	0.511937	-	-	-
$^{206}Pb/^{204}Pb$	18.54	-	-	18.56	18.93	18.58	-	18.51	-
$^{207}Pb/^{204}Pb$	15.67	-	-	15.68	15.69	15.67	-	15.67	-
$^{208}Pb/^{204}Pb$	38.74	-	-	39.36	39.11	38.92	-	38.66	-

Table 4 (cont).

	PAX136	PAX138
SiO2	73.3	70.3
Al2O3	15.2	18.1
Fe2O3	4.6	6.0
MgO	0.1	0.2
CaO	0.9	1.1
Na2O	4.3	2.7
K2O	4.6	6.0
TiO2	0.1	0.1
MnO	0.0	0.0
P2O5	0.1	0.0
LOI	0.5	0.6
Total	103.7	105.1
Sc	2.9	5.3
V	2.3	4.0
Cr	1.2	1.8
Mn	0.0	0.0
Co	0.4	0.9
Ni	0.1	0.1
Cu	3.3	3.3
Zn	24.7	11.7
Ga	23.6	21.5
Rb	278.5	117.3
Sr	78.7	299.1
Y	12.5	5.4
Zr	1.5	2.6
Nb	18.1	4.2
Cs	4.2	1.0
Ba	171.1	1629.0
La	27.6	9.4
Ce	55.8	17.7
Pr	6.6	2.1
Nd	23.0	7.9
Sm	5.4	1.5
Eu	0.4	1.7
Gd	4.0	1.3
Tb	0.6	0.2
Dy	2.5	0.9
Ho	0.4	0.2
Er	0.9	0.5
Tm	0.2	0.1
Yb	1.0	0.4
Lu	0.2	0.1
Hf	0.1	0.1
Ta	2.7	0.2
Pb	36.4	42.7
Th	12.4	3.9
U	2.3	0.5
$^{87}Sr/^{86}Sr$	0.720317	-
$^{143}Nd/^{144}Nd$	0.511990	-
$^{206}Pb/^{204}Pb$	18.29	-
$^{207}Pb/^{204}Pb$	15.65	-
$^{208}Pb/^{204}Pb$	39.18	-

Table 5: U-Pb zircon ages: BC10QSX107			$^{206}Pb^*/^{238}U$	$^{206}Pb^*/^{238}U$	$^{207}Pb^*/^{235}U$	$^{207}Pb^*/^{235}U$	$^{207}Pb^*/^{206}Pb^*$	$^{207}Pb^*/^{206}Pb^*$	$^{204}Pb/^{206}Pb$	$^{204}Pb/^{206}Pb$	**Age (Ma)** $^{206}Pb/^{238}U$	**Age (Ma)** $^{206}Pb/^{238}U$	**Age (Ma)** $^{207}Pb/^{235}U$	**Age (Ma)** $^{207}Pb/^{235}U$	**Age (Ma)** $^{207}Pb/^{206}Pb$	**Age (Ma)** $^{207}Pb/^{206}Pb$
grain	**spot**	**location**		**1 s.e.**		**1 s.e.**		**1 s.e.**		**1 s.e.**		**1 s.e.**		**1 s.e.**		**1 s.e.**
1	1	rim	0.2082	0.0066	2.2420	0.0791	0.0781	0.0012	0.00005	0.00003	1219	35	1194	25	1150	30
1	2	**core**	0.2038	0.0074	2.2590	0.0825	0.0804	0.0011	0.00007	0.00004	1196	40	1200	26	1207	27
2	3	rim	0.1802	0.0053	1.8560	0.0533	0.0747	0.0003	0.00002	0.00001	1068	29	1066	19	1060	8
2	4	**core**	0.3087	0.0097	4.6550	0.1611	0.1094	0.0011	0.00004	0.00002	1734	48	1759	29	1789	19
3	5	rim	0.1109	0.0033	0.9250	0.0312	0.0605	0.0011	0.00011	0.00005	678	19	665	16	621	41
3	6	**core**	0.1133	0.0038	0.9896	0.0375	0.0634	0.0008	n.d.	n.d.	692	22	699	19	721	28
4	7	rim	0.0956	0.0028	0.9197	0.0408	0.0698	0.0021	0.00077	0.00012	589	17	662	22	921	62
4	8	**core**	0.1868	0.0054	2.0330	0.0608	0.0789	0.0007	0.00002	0.00001	1104	29	1127	20	1170	17
5	9	rim	0.3384	0.0090	5.3680	0.1431	0.1151	0.0003	0.00001	0.00000	1879	43	1880	23	1881	5
5	10	**core**	0.3324	0.0087	5.2400	0.1354	0.1143	0.0002	0.00002	0.00001	1850	42	1859	22	1869	3
6	11	**core**	0.3128	0.0088	4.6290	0.1253	0.1073	0.0006	0.00001	0.00001	1755	43	1755	23	1754	11
7	12	**core**	0.0799	0.0029	0.5771	0.0335	0.0524	0.0022	0.00044	0.00013	495	17	463	22	303	97
8	13	**core**	0.2187	0.0058	3.2550	0.0897	0.1079	0.0010	0.00011	0.00004	1275	31	1470	21	1765	16
9	14	**core**	0.3348	0.0100	5.2700	0.1483	0.1141	0.0008	0.00001	0.00001	1862	49	1864	24	1866	12
10	15	rim	0.0756	0.0024	0.5707	0.0297	0.0547	0.0022	0.00047	0.00013	470	14	459	19	401	89
10	16	**core**	0.0776	0.0023	0.6239	0.0279	0.0583	0.0019	0.00012	0.00010	482	14	492	18	542	70
11	17	rim	0.3275	0.0097	5.2990	0.1667	0.1173	0.0007	0.00002	0.00001	1826	47	1869	27	1916	11
11	18	rim	0.3486	0.0101	5.7060	0.1696	0.1187	0.0005	n.d.	n.d.	1928	48	1932	26	1937	7
12	19	**core**	0.0690	0.0025	0.5604	0.0316	0.0589	0.0019	n.d.	n.d.	430	15	452	21	565	69
12	20	rim	0.0668	0.0027	0.5211	0.0281	0.0566	0.0022	0.00019	0.00012	417	17	426	19	475	84
17	21	**core**	0.0785	0.0026	0.6273	0.0965	0.0579	0.0082	0.00381	0.00032	487	15	494	60	528	310
17	22	rim	0.0777	0.0023	0.6104	0.0195	0.0570	0.0008	n.d.	n.d.	482	14	484	12	491	31
16	23	**core**	0.1961	0.0061	2.1170	0.0670	0.0783	0.0010	0.00006	0.00004	1154	33	1154	22	1154	24
16	24	rim	0.2049	0.0064	2.2260	0.0775	0.0788	0.0010	0.00012	0.00005	1201	35	1189	24	1168	25
15	25	rim	0.0776	0.0029	0.5917	0.0259	0.0553	0.0015	n.d.	n.d.	482	17	472	17	424	62
15	26	**core**	0.2960	0.0079	4.7830	0.1482	0.1172	0.0018	0.00133	0.00012	1672	39	1782	26	1914	28
14	27	rim	0.2031	0.0057	2.2250	0.0646	0.0795	0.0003	n.d.	n.d.	1192	30	1189	20	1183	8
14	28	**core**	0.2516	0.0068	3.8320	0.1163	0.1105	0.0012	0.00004	0.00002	1447	35	1600	24	1807	20
13	29	rim	0.3138	0.0089	5.8890	0.1622	0.1361	0.0005	0.00001	0.00001	1760	44	1960	24	2178	7
13	30	**core**	0.3875	0.0115	8.7930	0.2685	0.1646	0.0010	n.d.	n.d.	2111	53	2317	28	2503	10

Table 5: U-Pb zircon ages: BC93PAX14			$^{206}Pb^*/^{238}U$	$^{206}Pb^*/^{238}U$	$^{207}Pb^*/^{235}U$	$^{207}Pb^*/^{235}U$	$^{207}Pb^*/^{206}Pb^*$	$^{207}Pb^*/^{206}Pb^*$	$^{204}Pb/^{206}Pb$	$^{204}Pb/^{206}Pb$	Age (Ma) $^{206}Pb/^{238}U$	Age (Ma) $^{206}Pb/^{238}U$	Age (Ma) $^{207}Pb/^{235}U$	Age (Ma) $^{207}Pb/^{235}U$	Age (Ma) $^{207}Pb/^{206}Pb$	Age (Ma) $^{207}Pb/^{206}Pb$
grain	**spot**	**location**		**1 s.e.**		**1 s.e.**		**1 s.e.**		**1 s.e.**		**1 s.e.**		**1 s.e.**		**1 s.e.**
1	2	rim	0.0747	0.0027	0.5568	0.0293	0.0541	0.0023	0.00020	0.00011	464	16	450	19	375	96
2	3	rim	0.1145	0.0041	0.9468	0.0399	0.0600	0.0009	0.00007	0.00003	699	24	677	21	603	31
2	4	**core**	0.1100	0.0060	0.9374	0.0662	0.0618	0.0030	0.00026	0.00019	673	35	672	35	667	102
3	5	**core**	0.2423	0.0090	3.3170	0.1241	0.0993	0.0011	0.00002	0.00002	1398	47	1485	29	1611	21
3	6	rim	0.3172	0.0095	4.9650	0.1722	0.1135	0.0011	0.00009	0.00003	1776	47	1813	29	1857	17
4	7	rim	0.1767	0.0060	1.8210	0.0743	0.0747	0.0008	n.d.	n.d.	1049	33	1053	27	1061	23
4	8	**core**	0.1814	0.0057	1.8590	0.0678	0.0743	0.0010	0.00005	0.00003	1075	31	1067	24	1051	27
5	9	rim	0.2853	0.0084	4.1090	0.1308	0.1045	0.0008	0.00001	0.00001	1618	42	1656	26	1705	15
5	10	**core**	0.3154	0.0097	4.8010	0.1397	0.1104	0.0005	0.00001	0.00001	1767	47	1785	25	1806	9
6	11	rim	0.0767	0.0024	0.6076	0.0209	0.0575	0.0011	n.d.	n.d.	476	15	482	13	510	40
6	12	**core**	0.0744	0.0021	0.5743	0.0236	0.0560	0.0018	0.00007	0.00007	462	13	461	15	453	70
7	13	rim	0.0758	0.0027	0.5813	0.0300	0.0557	0.0021	0.00014	0.00010	471	16	465	19	439	83
7	14	**core**	0.0769	0.0023	0.5924	0.0227	0.0559	0.0016	0.00010	0.00007	478	14	472	14	446	66
8	15	**core**	0.2026	0.0058	2.2200	0.0627	0.0795	0.0007	0.00003	0.00002	1189	31	1187	20	1184	18
9	16	rim	0.0616	0.0018	0.4454	0.0238	0.0524	0.0020	0.00031	0.00011	385	11	374	17	304	85
9	17	**core**	0.0768	0.0027	0.6045	0.0450	0.0571	0.0035	0.00029	0.00021	477	17	480	29	495	134
10	18	rim	0.1963	0.0063	2.0970	0.0658	0.0775	0.0009	0.00019	0.00005	1155	34	1148	22	1133	23
10	19	**core**	0.2028	0.0061	2.2140	0.0734	0.0792	0.0007	n.d.	n.d.	1190	33	1185	23	1176	18
11	20	rim	0.1360	0.0034	1.4870	0.0386	0.0793	0.0004	0.00001	0.00001	822	19	925	16	1179	10
11	21	**core**	0.2703	0.0077	4.0070	0.1181	0.1075	0.0009	0.00004	0.00002	1542	39	1636	24	1757	16
12	22	**core**	0.0776	0.0026	0.6017	0.0215	0.0562	0.0009	0.00010	0.00004	482	16	478	14	461	34
12	23	rim	0.0784	0.0023	0.6007	0.0199	0.0556	0.0007	0.00003	0.00003	487	14	478	13	436	29
13	24	rim	0.1113	0.0032	0.9754	0.0320	0.0636	0.0008	0.00007	0.00004	680	19	691	17	727	28
13	25	**core**	0.1253	0.0036	1.1130	0.0374	0.0644	0.0010	0.00007	0.00004	761	21	760	18	755	32
14	26	**core**	0.2045	0.0078	2.1450	0.1175	0.0761	0.0029	0.00034	0.00017	1199	42	1163	38	1097	76
14	27	rim	0.1774	0.0055	1.9350	0.0613	0.0791	0.0008	0.00009	0.00004	1053	30	1093	21	1174	19
15	28	**core**	0.1334	0.0039	1.3870	0.0516	0.0754	0.0015	0.00078	0.00010	807	22	883	22	1079	41
16	29	**core**	0.2058	0.0058	2.2530	0.0643	0.0794	0.0006	0.00004	0.00002	1207	31	1198	20	1182	14
16	30	rim	0.0607	0.0023	0.5097	0.0657	0.0609	0.0068	0.00103	0.00041	380	14	418	44	637	239
17	31	rim	0.1792	0.0062	1.8100	0.0590	0.0732	0.0006	0.00002	0.00001	1063	34	1049	21	1021	17
17	32	**core**	0.1726	0.0048	1.7630	0.0495	0.0741	0.0004	n.d.	n.d.	1027	26	1032	18	1044	11
18	33	**core**	0.0708	0.0023	0.5254	0.0350	0.0538	0.0030	0.00040	0.00018	441	14	429	23	363	124
18	34	rim	0.0704	0.0022	0.5329	0.0332	0.0549	0.0029	0.00031	0.00018	439	13	434	22	408	119

Table 6: Major element compositions of sampled glasses

QNX02	Na_2O	Al_2O_3	SiO_2	K_2O	CaO	TiO_2	Fe_2O_3	MgO	P_2O_5	MnO
1	2.22	11.59	77.16	6.37	0.56	0.35	1.48	0.14	0.05	0.07
2	2.16	10.88	77.82	6.54	0.55	0.40	1.34	0.14	0.06	0.08
3	2.14	11.32	77.19	6.53	0.60	0.42	1.49	0.15	0.06	0.07
4	2.08	11.28	77.83	6.40	0.57	0.39	1.20	0.12	0.07	0.06
5	2.04	11.01	78.35	6.49	0.53	0.34	1.03	0.09	0.06	0.04
6	2.09	11.08	77.88	6.45	0.50	0.31	1.36	0.16	0.06	0.07
7	2.18	11.55	77.17	6.54	0.49	0.35	1.42	0.12	0.06	0.10
8	2.19	11.24	77.55	6.51	0.52	0.33	1.40	0.11	0.06	0.06
1	2.55	11.74	77.71	6.04	0.28	0.09	1.48	0.07	0.00	0.01
2	2.61	11.99	77.40	6.04	0.34	0.12	1.31	0.13	0.02	0.02
3	2.47	12.09	77.07	6.19	0.34	0.22	1.46	0.11	0.01	0.03
4	2.66	12.27	76.86	6.05	0.42	0.16	1.37	0.12	0.02	0.04
5	2.61	12.48	76.48	6.23	0.37	0.23	1.45	0.09	0.02	0.03
6	2.58	12.19	76.70	6.26	0.43	0.22	1.40	0.16	0.02	0.03
7	2.63	12.22	76.70	6.47	0.35	0.22	1.26	0.13	0.02	0.01
8	2.79	12.57	75.99	6.17	0.40	0.22	1.67	0.12	0.02	0.03
9	2.75	12.70	76.00	6.08	0.44	0.23	1.58	0.16	0.02	0.02
10	2.81	12.50	76.09	6.25	0.38	0.27	1.47	0.18	0.03	0.01
11	2.71	12.23	76.71	6.09	0.33	0.27	1.50	0.11	0.03	0.01
12	2.44	12.52	77.08	6.29	0.36	0.31	0.87	0.08	0.03	0.01
13	2.53	12.02	77.22	6.05	0.35	0.35	1.30	0.09	0.02	0.04
14	2.50	12.17	77.33	6.14	0.37	0.21	1.12	0.08	0.02	0.03
15	2.54	11.99	77.11	6.38	0.38	0.11	1.38	0.06	0.01	0.03
16	2.53	12.12	77.22	6.21	0.32	0.18	1.32	0.06	0.01	0.03
17	2.46	11.96	77.29	6.33	0.34	0.20	1.30	0.11	0.00	0.00
18	2.49	11.74	77.53	6.09	0.36	0.13	1.48	0.11	0.00	0.04
19	2.50	11.79	77.65	6.12	0.34	0.12	1.30	0.11	0.02	0.04
20	2.40	11.80	78.12	5.81	0.37	0.03	1.38	0.08	0.01	0.00
21	2.56	11.57	78.34	5.87	0.31	0.01	1.17	0.13	0.01	0.02
22	2.39	12.22	77.46	6.08	0.41	0.04	1.20	0.12	0.02	0.03
23	2.57	12.35	77.27	6.04	0.35	0.01	1.29	0.09	0.01	0.03
24	2.37	12.04	77.44	6.36	0.43	0.06	1.12	0.12	0.01	0.02
25	2.56	11.80	77.54	6.25	0.34	0.08	1.32	0.08	0.01	0.01
26	2.57	11.55	77.77	6.22	0.34	0.05	1.33	0.10	0.01	0.02
27	2.57	12.01	77.42	6.10	0.40	0.11	1.27	0.08	0.01	0.02
28	2.41	12.11	77.55	6.06	0.36	0.13	1.28	0.07	0.00	0.03
29	2.31	11.55	78.40	6.02	0.33	0.11	1.12	0.12	0.01	0.00
30	2.53	12.09	77.17	6.29	0.42	0.09	1.23	0.14	0.02	0.02
31	2.45	12.02	77.49	6.05	0.39	0.13	1.27	0.12	0.02	0.03
32	2.44	11.72	77.80	5.97	0.33	0.16	1.40	0.12	0.01	0.02
33	2.52	11.92	77.36	6.20	0.41	0.15	1.22	0.16	0.04	0.01
34	2.50	11.76	77.55	6.14	0.36	0.16	1.39	0.10	0.03	0.01
35	2.55	12.49	76.44	6.50	0.35	0.09	1.37	0.14	0.02	0.01
36	2.28	11.92	77.94	6.02	0.43	0.10	1.14	0.14	0.01	0.03
37	2.56	11.94	77.26	6.28	0.45	0.12	1.21	0.13	0.02	0.03
38	2.48	11.74	77.98	6.18	0.32	0.07	1.08	0.08	0.02	0.02
39	2.32	11.93	77.61	6.10	0.35	0.17	1.35	0.13	0.01	0.01
40	2.61	11.84	77.17	6.41	0.39	0.17	1.26	0.08	0.02	0.02
41	2.53	11.87	77.52	6.17	0.37	0.14	1.28	0.07	0.01	0.01

42	2.47	11.99	77.59	6.06	0.33	0.14	1.24	0.11	0.02	0.03
43	2.52	11.73	78.02	6.03	0.30	0.13	1.19	0.06	0.01	0.00
44	2.50	11.52	77.95	6.34	0.37	0.15	1.05	0.07	0.02	0.01
45	2.49	11.74	77.82	6.17	0.31	0.04	1.23	0.11	0.01	0.02
46	2.50	12.33	76.88	6.24	0.43	0.24	1.25	0.11	0.02	0.00
47	2.61	12.05	76.86	6.35	0.41	0.22	1.30	0.12	0.02	0.03
48	2.56	12.26	76.88	6.03	0.47	0.32	1.30	0.09	0.03	0.02
49	2.53	11.64	77.64	6.12	0.39	0.16	1.43	0.09	0.01	0.01
50	2.40	11.82	77.49	6.49	0.37	0.12	1.18	0.09	0.01	0.03
51	2.60	11.79	77.51	6.22	0.35	0.18	1.18	0.12	0.02	0.00
52	2.37	12.28	77.28	6.41	0.38	0.22	0.93	0.06	0.02	0.02
53	2.68	12.05	77.13	6.32	0.37	0.15	1.23	0.02	0.02	0.02
54	2.43	12.23	77.08	6.38	0.35	0.24	1.15	0.08	0.02	0.02
55	2.50	11.93	77.18	6.46	0.40	0.02	1.34	0.15	0.01	0.02
56	2.53	12.22	76.66	6.52	0.41	0.12	1.38	0.09	0.02	0.03
57	2.41	11.55	77.69	6.46	0.33	0.10	1.28	0.12	0.02	0.02
58	2.62	12.44	75.99	6.82	0.36	0.12	1.47	0.14	0.01	0.03
59	2.49	12.21	76.51	6.63	0.33	0.14	1.51	0.13	0.02	0.02
60	2.53	12.18	76.54	6.64	0.36	0.15	1.41	0.13	0.00	0.02
61	2.70	12.71	75.22	6.83	0.41	0.19	1.69	0.18	0.01	0.03

QNX03	Na_2O	Al_2O_3	SiO_2	K_2O	CaO	TiO_2	Fe_2O_3	MgO	P_2O_5	MnO
1	1.62	11.28	79.00	5.54	0.39	0.40	1.60	0.07	0.03	0.06
2	1.65	11.29	78.70	5.86	0.45	0.41	1.48	0.10	0.03	0.03
3	1.49	11.00	79.33	5.73	0.36	0.46	1.45	0.12	0.01	0.03
4	1.61	11.34	78.96	5.62	0.43	0.43	1.46	0.08	0.02	0.02
5	1.70	11.54	78.63	5.61	0.36	0.39	1.59	0.13	0.02	0.01
6	1.52	11.25	78.80	5.77	0.50	0.31	1.49	0.10	0.17	0.06
7	1.93	11.28	78.10	6.18	0.47	0.35	1.54	0.06	0.02	0.05
8	1.84	11.34	78.22	6.08	0.45	0.41	1.48	0.11	0.03	0.02
9	1.59	11.32	78.79	5.76	0.44	0.48	1.51	0.05	0.02	0.03
10	1.65	11.32	78.79	5.80	0.44	0.35	1.47	0.06	0.06	0.02
11	1.76	11.56	78.24	6.00	0.42	0.42	1.48	0.05	0.02	0.03
12	1.92	11.63	78.00	6.13	0.36	0.36	1.47	0.05	0.02	0.03
13	1.66	11.45	78.62	5.79	0.39	0.42	1.52	0.07	0.02	0.05
14	2.32	11.94	76.44	6.42	0.80	0.39	1.48	0.10	0.02	0.04
15	2.21	11.60	76.98	6.50	0.56	0.42	1.53	0.14	0.02	0.02
16	2.09	11.60	77.03	6.64	0.60	0.35	1.53	0.10	0.03	0.04
17	2.28	11.73	76.56	6.76	0.57	0.27	1.68	0.07	0.02	0.05
18	2.29	11.63	77.00	6.46	0.56	0.37	1.55	0.08	0.02	0.02
19	2.40	11.80	76.66	6.57	0.54	0.33	1.51	0.10	0.03	0.04
20	2.41	11.75	76.73	6.68	0.45	0.33	1.50	0.06	0.02	0.04
21	2.46	11.81	76.66	6.44	0.65	0.39	1.46	0.06	0.02	0.03
22	2.25	11.41	77.25	6.57	0.52	0.35	1.48	0.10	0.02	0.03
23	2.19	11.13	77.53	6.44	0.54	0.36	1.62	0.11	0.02	0.04
24	2.47	12.49	75.49	6.55	0.97	0.35	1.49	0.11	0.03	0.03
25	2.06	11.78	77.34	6.60	0.47	0.28	1.31	0.08	0.02	0.05
26	1.92	11.31	78.16	6.12	0.50	0.34	1.46	0.08	0.02	0.06
27	1.85	11.75	78.18	5.79	0.50	0.29	1.42	0.11	0.02	0.07
28	1.82	11.52	78.16	5.98	0.50	0.35	1.47	0.11	0.02	0.05
29	2.32	11.70	76.97	6.64	0.46	0.41	1.36	0.07	0.01	0.05
30	2.27	11.50	77.35	6.44	0.50	0.30	1.42	0.10	0.03	0.07

31	2.27	11.39	77.21	6.53	0.47	0.39	1.54	0.08	0.03	0.07
32	2.20	11.26	77.50	6.25	0.44	0.35	1.79	0.08	0.02	0.07
33	2.10	10.88	77.80	6.57	0.51	0.36	1.59	0.06	0.02	0.07
34	2.07	11.53	77.36	6.46	0.47	0.38	1.56	0.07	0.02	0.08
35	2.19	11.41	77.30	6.54	0.44	0.35	1.59	0.08	0.02	0.06
36	1.86	11.35	77.92	6.15	0.45	0.38	1.70	0.06	0.04	0.08
37	1.65	11.76	78.00	5.84	0.48	0.40	1.69	0.07	0.02	0.09
38	1.65	11.29	78.65	5.79	0.41	0.35	1.68	0.11	0.02	0.02
39	1.67	11.61	78.36	5.87	0.40	0.34	1.61	0.10	0.01	0.02
40	1.53	11.60	78.44	5.92	0.44	0.35	1.56	0.09	0.01	0.03
41	1.60	11.12	78.93	5.87	0.46	0.36	1.51	0.06	0.02	0.05
42	1.59	11.29	78.86	5.76	0.42	0.30	1.61	0.09	0.02	0.04
43	1.75	11.38	78.11	6.09	0.45	0.35	1.68	0.11	0.02	0.03
44	1.55	11.38	78.38	5.91	0.54	0.31	1.75	0.11	0.01	0.03

PAX08	Na_2O	Al_2O_3	SiO_2	K_2O	CaO	TiO_2	Fe_2O_3	MgO	P_2O_5	MnO
1	2.13	11.83	77.72	6.23	0.58	0.27	1.10	0.09	0.03	0.03
2	2.01	10.88	78.50	6.11	0.55	0.35	1.46	0.06	0.03	0.05
3	1.86	11.00	78.18	5.99	0.61	0.36	1.79	0.10	0.01	0.10
4	1.86	11.61	77.54	5.98	0.78	0.30	1.73	0.07	0.05	0.06
5	1.72	11.28	78.09	6.12	0.56	0.27	1.72	0.08	0.06	0.06
6	2.11	11.45	77.49	6.14	0.73	0.23	1.62	0.08	0.03	0.12
7	1.84	11.53	77.38	6.04	0.80	0.28	1.84	0.09	0.05	0.12
8	2.04	11.39	77.48	6.04	0.69	0.28	1.78	0.10	0.09	0.13
9	2.13	11.83	77.72	6.23	0.58	0.27	1.10	0.09	0.03	0.03
10	2.01	10.88	78.50	6.11	0.55	0.35	1.46	0.06	0.03	0.05
11	1.86	11.00	78.18	5.99	0.61	0.36	1.79	0.10	0.01	0.10
12	1.86	11.61	77.54	5.98	0.78	0.30	1.73	0.07	0.05	0.06
13	1.72	11.28	78.09	6.12	0.56	0.27	1.72	0.08	0.06	0.06
14	2.11	11.45	77.49	6.14	0.73	0.23	1.62	0.08	0.03	0.12
15	1.84	11.53	77.38	6.04	0.80	0.28	1.84	0.09	0.05	0.12
16	1.81	14.15	74.49	6.23	0.33	-0.02	1.69	0.21	1.00	0.07
17	1.86	14.36	73.84	6.09	0.29	0.06	1.83	0.27	1.30	0.08
18	1.81	14.70	73.79	6.28	0.32	-0.04	1.65	0.22	1.19	0.06
19	1.72	13.04	75.78	6.44	0.32	0.23	2.08	0.29	0.05	0.02
20	1.75	12.91	75.78	6.61	0.28	0.24	2.10	0.23	0.05	0.04
21	1.73	13.32	75.44	6.75	0.28	0.19	2.02	0.22	0.04	0.03
22	1.84	13.05	77.40	6.05	0.19	0.06	1.10	0.24	0.04	0.02
23	1.78	13.05	77.64	6.01	0.21	0.03	0.99	0.22	0.03	0.02
24	1.85	13.02	77.68	5.98	0.19	0.09	0.91	0.20	0.04	0.02
25	2.00	12.59	77.80	5.99	0.21	0.04	0.99	0.27	0.03	0.05
26	1.96	13.08	76.97	6.22	0.24	0.05	1.16	0.28	0.02	0.03
27	1.89	12.58	77.91	6.09	0.25	0.06	0.94	0.23	0.03	0.03
28	1.80	13.12	78.21	6.15	0.14	0.03	0.39	0.05	0.09	0.01
29	1.96	13.11	77.52	5.94	0.30	0.08	0.83	0.13	0.05	0.04
30	1.85	12.85	77.39	6.21	0.30	0.07	1.06	0.19	0.06	0.03
31	2.05	12.23	78.44	5.95	0.21	0.03	0.81	0.18	0.06	0.03
32	2.11	13.17	77.37	6.14	0.16	0.01	0.75	0.19	0.07	0.02
33	1.94	13.20	77.49	6.18	0.22	0.02	0.65	0.19	0.07	0.02
34	2.09	13.16	77.03	6.10	0.23	0.05	1.00	0.23	0.06	0.02
35	2.16	13.05	76.91	6.15	0.30	0.08	0.98	0.25	0.06	0.03
36	2.14	13.61	76.46	6.09	0.29	0.10	0.96	0.26	0.05	0.03

37	2.17	13.24	76.99	5.91	0.33	0.08	0.88	0.27	0.05	0.03
38	2.11	13.29	76.85	6.06	0.37	0.13	0.83	0.26	0.06	0.02
39	2.10	13.30	76.89	6.03	0.28	0.05	0.99	0.25	0.04	0.03
40	2.09	13.90	76.22	6.11	0.39	0.07	0.89	0.24	0.06	0.03
41	2.23	13.62	76.54	6.02	0.37	0.09	0.74	0.27	0.06	0.03
42	2.04	12.73	77.65	6.08	0.31	0.08	0.75	0.24	0.07	0.02
43	2.07	13.30	76.92	6.21	0.34	0.09	0.79	0.16	0.06	0.04
44	2.16	13.04	77.26	5.94	0.41	0.07	0.83	0.17	0.05	0.03
45	2.19	12.83	77.47	6.00	0.38	0.07	0.79	0.17	0.05	0.03
46	2.23	12.83	77.30	6.14	0.38	0.03	0.82	0.14	0.06	0.03
47	2.07	12.91	77.37	6.25	0.38	0.08	0.74	0.15	0.03	0.02
48	2.33	13.24	77.02	6.02	0.38	0.08	0.68	0.14	0.06	0.02
49	2.26	14.18	75.80	6.24	0.41	0.05	0.77	0.18	0.07	0.03
50	2.33	13.78	76.21	6.19	0.41	0.02	0.72	0.19	0.07	0.04
51	2.11	13.64	76.81	6.09	0.36	0.04	0.64	0.18	0.06	0.05
52	2.19	13.57	76.52	6.19	0.24	0.13	0.81	0.22	0.05	0.03
53	2.13	13.11	77.09	6.21	0.22	0.09	0.82	0.24	0.05	0.02
54	2.17	13.52	76.52	6.12	0.24	0.13	0.91	0.27	0.06	0.03
55	2.43	13.48	76.31	6.17	0.26	0.14	0.82	0.28	0.06	0.04
56	2.21	13.61	76.30	6.55	0.33	0.02	0.70	0.18	0.05	0.03
57	2.21	13.12	77.08	6.08	0.22	0.17	0.81	0.22	0.05	0.03
58	2.21	13.54	76.60	6.04	0.28	0.16	0.84	0.23	0.05	0.03
59	2.16	13.21	76.97	6.14	0.26	0.13	0.76	0.26	0.05	0.03
60	2.27	13.72	76.24	6.13	0.22	0.09	1.00	0.24	0.05	0.02
61	2.22	13.53	76.89	5.92	0.21	0.15	0.78	0.20	0.05	0.03
62	2.10	12.54	78.01	5.91	0.54	0.04	0.64	0.11	0.04	0.04
63	2.05	13.23	77.34	5.86	0.68	0.06	0.54	0.16	0.06	0.02

PAX138	**Na_2O**	**Al_2O_3**	**SiO_2**	**K_2O**	**CaO**	**TiO_2**	**Fe_2O_3**	**MgO**	**P_2O_5**	**MnO**
1	2.13	13.23	77.24	5.91	0.60	0.04	0.59	0.10	0.08	0.02
2	2.44	13.34	76.50	6.06	0.41	0.11	0.85	0.18	0.05	0.03
3	2.20	13.33	77.15	6.01	0.35	0.12	0.60	0.15	0.06	0.01
4	2.24	13.34	76.62	6.27	0.33	0.09	0.83	0.19	0.04	0.03
5	2.29	13.43	76.62	6.26	0.34	0.03	0.69	0.22	0.06	0.03
6	2.33	14.00	76.00	6.09	0.32	0.03	0.89	0.22	0.07	0.03
7	2.45	13.93	76.00	5.96	0.44	0.06	0.85	0.21	0.05	0.04
8	2.29	13.81	76.20	6.06	0.39	0.05	0.91	0.21	0.05	0.02
9	2.36	13.52	76.51	6.02	0.38	0.11	0.83	0.20	0.05	0.01
10	2.26	13.59	76.65	5.96	0.35	0.04	0.87	0.20	0.05	0.03
11	2.21	12.99	77.27	6.09	0.23	0.09	0.86	0.19	0.06	0.02
12	2.19	13.17	76.98	6.02	0.28	0.04	1.03	0.23	0.06	0.01
13	2.24	13.20	77.07	5.86	0.32	0.07	0.90	0.26	0.06	0.02
14	2.23	13.69	76.60	5.77	0.28	0.03	1.02	0.24	0.07	0.03
15	2.18	12.96	77.17	5.99	0.30	0.10	0.97	0.24	0.05	0.03
16	2.13	13.68	76.32	6.03	0.32	0.11	1.04	0.25	0.08	0.01
17	2.28	13.92	76.10	5.81	0.38	0.06	1.09	0.22	0.07	0.03
18	2.24	13.78	76.15	5.96	0.32	0.08	1.13	0.22	0.07	0.02
19	2.31	13.52	75.88	5.83	0.36	0.25	1.36	0.37	0.08	0.03
20	2.33	13.72	75.55	6.05	0.41	0.19	1.22	0.38	0.09	0.03
21	2.54	13.84	75.39	5.82	0.37	0.21	1.30	0.35	0.09	0.04
22	2.27	13.96	75.49	5.55	0.42	0.27	1.45	0.43	0.09	0.03
23	2.37	13.39	76.02	5.95	0.36	0.21	1.20	0.35	0.09	0.04

24	2.26	14.02	75.54	5.84	0.40	0.24	1.26	0.34	0.06	0.01
25	2.27	14.10	75.42	5.79	0.39	0.21	1.29	0.39	0.09	0.04
26	2.24	13.83	75.61	5.93	0.43	0.18	1.28	0.37	0.08	0.05
27	2.38	13.81	75.45	5.75	0.46	0.25	1.37	0.38	0.08	0.03
28	2.30	14.13	75.02	5.82	0.44	0.30	1.42	0.40	0.08	0.04
29	2.33	13.53	75.68	5.84	0.43	0.21	1.39	0.44	0.09	0.02
30	2.27	13.71	75.68	5.82	0.38	0.30	1.36	0.36	0.09	0.03
31	2.35	13.46	75.75	5.76	0.36	0.19	1.55	0.40	0.09	0.04
32	2.21	13.61	75.55	5.91	0.34	0.32	1.57	0.35	0.09	0.03
33	2.43	13.84	75.08	6.05	0.39	0.16	1.48	0.43	0.10	0.04
34	2.25	13.37	76.05	5.85	0.36	0.17	1.44	0.37	0.10	0.02
35	2.20	13.99	75.31	5.60	0.38	0.15	1.82	0.42	0.09	0.02
36	2.50	14.08	74.71	5.81	0.33	0.10	1.85	0.47	0.09	0.05
37	2.29	13.82	75.14	5.73	0.39	0.14	1.99	0.38	0.09	0.03
38	2.51	14.39	74.54	5.82	0.35	0.20	1.67	0.37	0.10	0.02
39	2.34	13.87	75.18	6.08	0.29	0.11	1.56	0.40	0.10	0.03
40	2.15	13.20	76.18	5.75	0.60	0.18	1.04	0.15	0.69	0.03
41	2.11	13.26	76.31	5.66	0.60	0.16	1.11	0.17	0.58	0.03
42	2.18	13.28	75.82	5.99	0.57	0.29	1.06	0.16	0.61	0.03
43	2.21	13.64	75.43	5.77	0.50	0.31	1.01	0.18	0.87	0.04
44	2.11	12.87	76.91	5.76	0.47	0.19	0.92	0.16	0.54	0.04
45	1.98	12.97	77.74	5.89	0.18	0.06	0.81	0.18	0.14	0.02
46	2.20	14.05	75.23	5.82	0.39	0.18	1.48	0.50	0.08	0.04
47	2.31	13.78	75.51	5.75	0.42	0.27	1.37	0.43	0.09	0.05
48	2.34	14.01	75.22	5.71	0.39	0.29	1.46	0.44	0.09	0.03
49	2.33	13.68	75.66	5.71	0.34	0.28	1.43	0.39	0.10	0.05
50	2.26	13.72	75.24	5.89	0.46	0.30	1.55	0.44	0.08	0.03
51	2.52	14.29	74.54	5.81	0.48	0.25	1.54	0.40	0.09	0.04
52	2.25	13.53	75.74	5.71	0.42	0.21	1.58	0.42	0.08	0.05
53	2.34	13.72	75.40	5.77	0.46	0.30	1.41	0.45	0.10	0.03
54	2.29	13.47	76.20	5.64	0.41	0.17	1.34	0.36	0.07	0.04
55	2.38	13.61	75.86	5.63	0.45	0.12	1.41	0.43	0.06	0.04

PAX12	Na_2O	Al_2O_3	SiO_2	K_2O	CaO	TiO_2	Fe_2O_3	MgO	P_2O_5	MnO
1	1.00	14.51	74.30	4.97	1.13	0.40	1.82	0.81	0.91	0.14
2	1.05	13.94	74.84	4.88	1.21	0.37	1.77	0.87	0.89	0.18
3	1.06	14.57	74.69	4.79	1.18	0.39	1.50	0.79	0.87	0.14
4	1.07	14.13	75.23	5.05	1.10	0.40	1.40	0.62	0.83	0.15
5	1.04	14.43	74.79	4.54	1.02	0.38	1.82	0.95	0.88	0.16
6	1.02	13.84	74.54	4.69	1.25	0.45	2.04	1.09	0.93	0.13
7	1.10	14.24	74.77	4.52	1.07	0.32	1.96	0.96	0.89	0.15
8	1.12	14.48	74.01	4.80	1.14	0.40	2.00	0.93	0.93	0.16
9	0.87	14.62	73.78	4.28	1.05	0.46	2.40	1.37	0.96	0.19
10	1.12	14.53	74.22	4.71	1.15	0.40	1.90	0.83	0.94	0.18
11	1.11	14.47	74.23	5.09	1.10	0.45	1.72	0.70	0.97	0.16
12	0.91	14.54	74.04	4.79	0.97	0.48	2.10	1.00	0.98	0.19
13	0.88	14.77	74.47	4.98	0.74	0.44	1.64	0.99	0.92	0.16
14	0.87	14.41	74.21	4.79	1.01	0.50	1.93	1.21	0.88	0.16
15	1.05	14.56	73.71	5.15	1.21	0.44	1.84	0.85	0.99	0.17
16	0.98	14.41	73.96	4.92	1.07	0.43	2.03	0.94	1.04	0.19
17	1.11	14.46	74.17	5.21	1.18	0.35	1.69	0.64	0.98	0.18
18	1.04	13.98	74.44	4.99	1.17	0.50	1.86	0.86	0.98	0.16

19	1.02	14.17	74.95	5.19	1.00	0.39	1.51	0.67	0.99	0.14
20	1.01	14.36	75.19	5.53	0.78	0.38	1.23	0.47	0.89	0.13
21	0.94	14.13	75.13	5.13	0.79	0.40	1.60	0.82	0.91	0.14
22	1.06	14.49	74.44	5.01	1.00	0.31	1.74	0.90	0.88	0.13
23	0.95	14.05	74.90	4.97	0.87	0.42	1.74	1.06	0.87	0.17
24	0.95	14.69	74.19	5.61	0.82	0.41	1.66	0.63	0.86	0.15
25	0.98	14.21	74.57	5.23	0.66	0.42	1.93	0.99	0.86	0.15
26	0.85	14.67	73.67	4.96	0.70	0.42	2.34	1.27	0.88	0.22
27	0.97	14.21	74.29	5.17	1.12	0.45	1.90	0.81	0.88	0.19
28	0.97	14.46	73.84	4.63	1.01	0.41	2.37	1.20	0.88	0.22
29	0.87	14.00	74.91	5.10	1.09	0.44	1.85	0.66	0.87	0.20
30	1.05	14.41	74.34	5.70	1.34	0.41	1.36	0.39	0.80	0.15
31	1.00	14.27	74.10	5.42	1.31	0.44	1.65	0.78	0.84	0.16
32	1.05	14.05	75.07	5.46	1.25	0.41	1.23	0.42	0.86	0.16
33	1.00	14.30	74.28	4.96	1.20	0.44	1.85	0.88	0.88	0.19
34	0.91	14.31	74.52	5.15	1.32	0.39	1.62	0.60	0.96	0.20
35	0.51	14.61	75.37	4.21	0.77	0.39	1.97	1.06	0.90	0.22
36	0.84	13.92	74.77	4.33	1.02	0.46	2.28	1.22	0.91	0.24
37	1.03	13.90	74.86	5.16	1.03	0.46	1.70	0.78	0.86	0.16
38	0.99	14.31	74.55	5.30	1.30	0.32	1.56	0.62	0.86	0.17
39	1.01	14.76	73.62	4.78	1.32	0.42	1.91	1.11	0.83	0.19
40	0.97	14.47	74.52	5.22	1.36	0.36	1.51	0.51	0.87	0.16
41	0.96	14.28	74.75	5.09	1.14	0.45	1.45	0.82	0.87	0.16
42	0.93	14.01	73.71	4.79	1.59	0.43	2.22	0.93	1.16	0.20
43	1.09	14.05	74.88	5.46	1.34	0.39	1.40	0.34	0.87	0.17
44	0.89	14.52	74.15	4.77	0.95	0.36	2.27	0.97	0.87	0.22
45	0.86	13.73	75.15	4.86	0.87	0.38	2.15	0.91	0.86	0.21
46	0.87	14.43	74.47	4.85	1.00	0.49	1.79	0.96	0.98	0.18
47	0.85	14.40	74.70	4.72	0.87	0.37	1.84	1.01	1.06	0.17
48	0.96	13.95	75.18	5.09	0.69	0.37	1.77	0.98	0.88	0.13
49	1.11	14.04	75.52	5.17	0.99	0.45	1.17	0.49	0.89	0.14
50	0.90	14.13	75.09	4.74	0.95	0.47	1.67	1.02	0.83	0.16
51	0.97	14.50	74.70	5.01	1.08	0.37	1.60	0.75	0.87	0.13
52	1.21	13.50	75.70	5.11	1.12	0.42	1.35	0.45	0.96	0.16
53	1.04	14.18	74.15	4.72	1.07	0.42	2.23	0.97	1.02	0.20
54	1.09	14.33	74.26	4.86	1.13	0.47	1.83	0.78	1.02	0.21
55	1.12	14.57	74.04	5.21	1.17	0.52	1.50	0.70	1.00	0.15
56	1.01	14.28	74.61	4.87	1.25	0.42	1.60	0.79	0.98	0.17
57	1.06	14.60	74.93	5.19	1.42	0.39	0.96	0.27	1.06	0.11
58	1.06	14.10	75.20	5.40	1.26	0.44	1.15	0.31	0.93	0.12
59	1.13	14.32	74.57	4.84	0.88	0.41	1.84	0.88	0.94	0.17
60	1.18	14.25	74.94	5.08	1.37	0.33	1.27	0.48	0.94	0.14
61	0.94	14.32	74.68	4.81	1.19	0.44	1.72	0.85	0.88	0.15
62	1.16	14.12	75.62	5.32	0.97	0.42	1.19	0.14	0.92	0.12
63	1.15	14.43	75.55	5.23	0.62	0.43	1.23	0.31	0.94	0.09
64	1.15	14.35	74.60	5.01	1.20	0.41	1.67	0.55	0.89	0.15
65	1.06	14.49	73.25	4.76	1.47	0.45	2.02	1.02	1.30	0.19
66	1.29	14.15	74.14	5.11	1.20	0.47	1.68	0.74	1.02	0.20
67	1.21	14.47	74.07	5.04	1.15	0.46	1.79	0.70	0.91	0.19
68	1.20	13.96	75.01	5.23	1.13	0.32	1.49	0.58	0.92	0.14
69	1.11	14.09	74.82	4.78	0.97	0.37	1.75	0.94	0.97	0.18
70	1.21	14.34	74.60	5.05	1.28	0.45	1.39	0.51	0.98	0.18

71	0.99	14.22	74.02	4.96	1.12	0.37	2.15	1.00	0.95	0.20
72	0.87	14.61	74.91	4.79	1.13	0.41	1.55	0.64	0.96	0.14
73	1.04	14.62	75.20	4.70	0.83	0.46	1.39	0.67	0.93	0.15
74	0.96	14.17	75.33	4.77	0.53	0.38	1.81	0.89	1.01	0.15
75	0.96	14.33	75.30	5.01	1.03	0.44	1.31	0.49	0.97	0.14
76	0.99	14.48	75.23	4.83	0.84	0.41	1.39	0.67	0.98	0.14
77	1.05	14.34	75.52	5.06	0.38	0.38	1.57	0.62	0.95	0.12
78	0.95	14.17	75.21	4.71	0.99	0.32	1.70	0.89	0.91	0.16
79	1.09	14.16	74.77	5.10	1.30	0.43	1.42	0.66	0.90	0.14
80	1.16	14.06	74.78	5.16	1.18	0.41	1.60	0.63	0.86	0.14
81	1.12	14.07	74.45	4.81	1.21	0.43	1.80	1.03	0.88	0.19
82	0.90	14.49	75.18	4.38	1.09	0.39	1.63	0.66	1.09	0.17
83	0.76	14.04	75.77	3.82	1.10	0.42	1.84	1.02	1.00	0.23
84	0.90	14.58	74.38	4.74	1.05	0.40	1.89	0.86	0.98	0.17
85	0.89	14.00	75.06	4.60	1.11	0.42	1.86	0.93	0.95	0.18
86	1.02	14.45	75.24	5.05	1.11	0.46	1.18	0.45	0.84	0.16
87	1.07	14.24	75.20	5.52	0.97	0.40	1.22	0.26	0.98	0.13
88	0.84	13.92	75.11	4.14	1.11	0.43	2.30	1.00	0.92	0.18
89	0.89	14.52	74.49	4.69	1.07	0.48	1.94	0.85	0.92	0.16
90	1.04	13.94	75.21	5.12	1.11	0.36	1.42	0.59	1.03	0.15
91	1.14	14.63	74.08	5.21	1.50	0.44	1.34	0.42	1.10	0.13
92	1.09	14.30	74.97	5.29	1.52	0.36	1.14	0.13	1.05	0.14
93	0.92	14.68	74.60	4.78	1.17	0.39	1.48	0.90	0.88	0.15
94	1.17	14.23	75.19	5.27	0.92	0.43	1.28	0.38	1.00	0.12
95	1.13	14.28	74.68	5.37	0.99	0.42	1.50	0.52	0.97	0.13
96	0.87	14.56	74.99	5.20	1.10	0.40	1.40	0.41	0.91	0.13
97	0.83	14.49	75.00	4.95	0.94	0.42	1.56	0.69	0.94	0.18
98	0.93	14.21	74.82	5.24	1.17	0.36	1.56	0.55	1.01	0.14
99	1.00	14.13	75.45	4.96	0.98	0.46	1.34	0.53	0.98	0.15
100	0.98	15.21	74.93	4.99	1.01	0.39	1.08	0.23	1.05	0.12
101	1.01	14.92	74.52	5.16	1.34	0.42	1.07	0.37	1.07	0.11
102	0.97	14.31	74.71	4.62	1.08	0.45	1.74	0.93	1.02	0.16
103	1.09	14.12	74.67	5.06	1.16	0.33	1.79	0.67	0.91	0.17
104	1.06	14.34	74.20	5.07	1.06	0.46	1.85	0.91	0.88	0.17
105	1.20	14.46	74.16	5.25	1.22	0.36	1.66	0.67	0.89	0.13
106	1.24	14.34	74.14	5.29	1.03	0.45	1.63	0.77	0.91	0.16
107	0.95	14.26	73.96	4.60	1.08	0.44	2.31	1.27	0.95	0.20
108	1.18	14.35	74.16	5.07	1.24	0.40	1.74	0.77	0.91	0.17
109	0.96	14.23	74.42	4.66	0.94	0.46	2.05	1.16	0.90	0.20
110	0.95	14.33	74.92	4.86	0.53	0.48	1.84	0.89	1.06	0.14
111	0.94	14.46	74.83	4.64	1.09	0.40	1.72	0.71	1.05	0.16
112	1.14	14.08	74.98	5.02	1.08	0.48	1.39	0.61	1.05	0.15
113	0.98	14.66	74.26	4.25	1.05	0.43	2.24	0.98	0.90	0.21
114	1.23	14.43	74.44	5.35	1.38	0.46	1.22	0.46	0.84	0.16
115	1.04	14.14	75.49	5.12	0.84	0.33	1.30	0.57	1.00	0.13
116	1.03	14.71	75.43	4.60	0.66	0.44	1.32	0.67	1.00	0.13
117	1.13	14.21	75.68	4.95	0.63	0.40	1.32	0.53	1.02	0.10
118	1.09	14.44	75.05	5.11	1.18	0.45	1.23	0.35	0.97	0.13
119	1.11	14.58	74.40	4.79	1.25	0.39	1.60	0.70	1.00	0.18
120	1.12	14.62	74.53	5.11	1.45	0.47	1.27	0.27	1.01	0.13
121	1.00	14.87	74.65	4.78	1.10	0.41	1.33	0.72	1.00	0.13
122	0.99	14.78	74.59	4.87	0.60	0.42	1.78	0.83	0.96	0.16

123	0.94	15.08	73.88	4.48	0.98	0.37	2.12	1.01	0.94	0.19
124	1.12	14.13	75.45	4.97	1.15	0.47	1.28	0.39	0.91	0.13
125	1.17	14.10	75.03	4.80	1.00	0.43	1.64	0.58	1.08	0.15
126	1.11	13.98	75.81	4.71	0.37	0.46	1.79	0.64	1.00	0.14
127	1.09	14.92	73.47	4.43	1.26	0.37	1.93	1.31	1.01	0.18
128	0.96	14.59	74.37	4.32	1.13	0.44	2.07	0.94	1.01	0.17
129	1.07	14.46	75.59	4.75	0.40	0.42	1.62	0.67	0.87	0.14

	BC93PAX12_a						BC93PAX12_b							
	1	**2**	**3**	**4**	**5**	**6**	**1**	**2**	**3**	**4**	**5**	**6**	**7**	**8**
Ba	357.07	563.58	520.53	1893.04	699.16	146.51	554.40	773.58	706.47	513.90	509.57	700.36	778.71	637.39
Rb	101.79	172.18	178.44	226.57	236.08	84.28	129.79	241.09	228.53	248.71	171.13	247.86	243.70	193.82
Th	2.16	2.18	2.48	4.69	3.84	4.65	4.28	5.37	4.28	3.52	2.13	3.25	4.76	2.79
U	0.80	1.35	1.31	2.04	1.57	2.16	2.57	2.35	1.71	1.53	1.48	1.97	2.02	1.91
Nb	3.96	1.55	1.51	3.99	2.63	4.57	9.79	6.70	7.02	5.73	1.82	1.12	2.84	2.94
La	9.02	10.83	10.74	21.00	14.98	14.88	26.34	19.65	16.87	13.76	9.36	12.56	18.32	10.21
Ce	20.72	30.43	29.91	49.64	37.39	66.76	77.91	55.61	39.31	33.95	29.59	39.72	43.03	39.09
Sr	34.69	56.34	32.31	107.17	37.10	37.18	102.03	78.85	51.31	45.49	48.40	46.37	57.24	46.59
Nd	12.24	15.35	16.26	26.90	21.43	18.04	52.10	27.48	23.63	19.99	13.34	19.32	24.30	15.44
Sm	2.92	3.91	4.01	6.21	5.32	3.49	16.25	7.38	5.87	5.00	3.37	4.92	6.19	3.99
Zr	54.95	112.12	103.83	135.17	119.14	89.66	124.11	178.08	136.32	105.38	96.79	125.14	132.77	113.59
Hf	1.21	2.87	2.63	3.16	2.94	2.20	3.30	4.81	3.67	2.75	2.56	3.39	3.45	3.08
Ti	0.28	0.28	0.25	0.51	0.40	0.26	0.39	0.62	0.91	0.48	0.25	0.42	0.61	0.41
Tb	0.38	-	0.53	0.92	-	0.51	0.81	0.25	0.23	0.16	0.11	0.16	0.24	0.13
Y	7.62	9.84	10.99	19.59	16.73	20.98	7.94	2.31	2.61	1.17	0.85	1.30	2.69	1.28
Yb	0.25	0.42	0.55	0.68	0.72	1.84	1.73	1.07	1.80	0.45	0.40	0.74	1.32	0.81
$^{87}Sr/^{86}Sr$	0.717582	0.720943	0.725214	0.724592	0.728091	0.716588	0.717989	0.720001	0.718801	0.720533	0.718742	0.720869	0.721358	0.720431

Table 6 cont. Trace element and Sr-isotopic compositions of microdrilled glass

Table 7: Whole rock compositions of sampled lava, granite and crustal xenoliths from the Wudalianchi volcanic field, NE China.

	Lava	Granite	Granite	xeno3a	xeno3b	xeno5a	xeno5b	xeno5di	xeno5dii
SiO_2	51.8	68.2	69.8	69.8	74.4	74.6	72.4	82.9	74.3
Al_2O_3	2.2	15.3	14.7	16.5	13.9	12.7	14.3	8.6	10.9
FeO	14.5	2.3	2.6	0.4	0.5	1.0	0.9	0.7	2.7
MgO	8.4	1.3	1.4	0.2	0.1	0.2	0.1	0.2	0.4
CaO	0.1	2.5	2.1	0.3	1.0	0.2	0.1	0.1	0.5
Na_2O	6.9	4.5	4.2	4.6	4.1	4.5	4.2	3.0	4.0
K_2O	6.8	3.2	3.4	7.2	5.0	4.6	6.8	3.4	4.3
TiO_2	3.9	0.4	0.5	0.0	0.1	0.1	0.1	0.1	0.4
MnO	5.1	0.0	0.0	0.0	0.0	0.1	0.0	0.1	0.3
P_2O_5	1.1	0.2	0.2	0.0	0.0	0.0	0.0	0.0	0.1
LOI	-	1.7	1.0	1.2	0.6	1.3	1.1	0.7	1.7
Total	100.8	99.5	99.9	100.2	99.6	99.5	100.0	99.7	99.4
Sc	13	5	5	2	2	3	3	3	8
V	119	42	51	2	3	5	2	2	6
Cr	186.96	37.27	39.84	1.72	2.24	4.12	2.95	2.35	6.07
Co	31	7	6	1	1	1	1	1	1
Ni	180	21	21	2.34	0.14	1.89	1.62	0.79	4.5
Cu	35.1	10	1.9	5.4	3.8	2.7	13.9	2.7	5.9
Zn	128	39	27	11	11	66	22	27	118
Ga	24	19	18	25	18	23	26	16	20
Rb	115	70	65	138	111	156	220	125	167
Sr	1480	659	564	58	75	30	21	12	46
Y	22	6	9	4	4	28	19	43	46
Zr	530	30	30	10	10	40	30	110	280
Nb	70	3.63	6.31	1.18	4.45	9.86	10	30	50
Cs	0.9	1.5	3.5	1.2	0.7	1.9	2.2	1.4	2
Ba	1600	700	760.16	112.5	101.87	45.59	25.48	15.04	55.91
La	81.16	13.05	16.08	4.35	1.97	12.59	3.68	5.4	25.76
Ce	152.82	25.17	33.49	9.74	3.66	36.23	11.01	19.05	76.24
Pr	18.52	3.07	5.15	1.29	0.45	5.02	1.61	2.75	10.41
Nd	68.64	11.21	19.99	4.56	1.72	19.1	6.6	11.82	39.04
Sm	10.6	1.63	3.25	0.79	0.16	4.98	2.16	4.74	8.7
Eu	2.94	0.56	0.74	0.11	0.44	0.38	0.17	0.33	0.5
Gd	7.14	1.25	2.36	0.81	0.43	5.23	3.09	6.68	7.3
Tb	0.9	0.19	0.33	0.13	0.08	0.89	0.56	1.28	1.21
Dy	4.39	0.96	1.73	0.75	0.48	5.03	3.17	7.79	7.15
Ho	0.74	0.18	0.33	0.14	0.11	0.91	0.59	1.54	1.46
Er	1.58	0.48	0.79	0.36	0.34	2.18	1.43	3.85	3.84
Tm	0.22	0.08	0.13	0.05	0.05	0.32	0.21	0.58	0.61
Yb	1.22	0.53	0.79	0.3	0.42	1.78	1.18	3.19	3.94
Lu	0.17	0.08	0.12	0.04	0.07	0.25	0.16	0.41	0.63
Hf	11.42	1.17	1.28	0.35	0.4	1.47	1.11	3.6	8.04
Ta	3.6	0.3	0.5	0.1	0.6	10.1	0.7	1.7	2.1
Pb	14	23	10	12	30	14	63	516	255
Th	6	4	10	1	1	10	12	18	26
U	1.4	1.2	1.3	0.3	1.5	2.4	1.9	5.9	4.9
$^{87}Sr/^{86}Sr$	0.705411	0.705200	0.705402	0.716864	0.713273	0.737135	-	0.760430	-
$^{144}Nd/^{143}Nd$	0.512395	0.512747	0.512724	0.512752	0.512800	0.512795	-	0.512891	-

Table 8: Compositions of glass separates and minerals from sampled granite and partially-melted crustal xenoliths, Wudalianchi volcanic field, NE China.

	glass3a	fsp3a	glass(i)3b	glass(ii)3b	fsp3b	glass5a
Sc	n.d	n.d	n.d	n.d	n.d	n.d
Ti	n.d	n.d	178.95	246.27	123.50	60.85
V	n.d	n.d	n.d	n.d	n.d	n.d
Cr	n.d	n.d	n.d	n.d	n.d	n.d
Mn	n.d	n.d	0.02	0.02	0.01	0.03
Co	n.d	n.d	n.d	n.d	n.d	n.d
Ni	n.d	n.d	n.d	n.d	n.d	n.d
Cu	0.50	0.39	0.58	0.85	0.70	2.11
Zn	n.d	n.d	n.d	n.d	n.d	n.d
Ga	30.23	30.72	18.84	19.52	28.76	31.82
Rb	156.12	148.49	174.53	184.18	34.92	220.62
Sr	75.17	70.08	76.26	69.31	145.38	7.50
Y	0.61	0.52	2.71	3.18	1.72	7.68
Zr	n.d	n.d	2.84	3.33	0.36	6.78
Nb	0.11	0.17	2.69	3.57	1.71	3.30
Cs	1.15	1.30	0.86	0.91	0.12	2.31
Ba	140.44	159.47	144.40	135.93	8.00	1.45
La	1.96	1.11	1.68	1.73	1.71	1.95
Ce	3.12	1.89	2.88	2.78	2.51	5.72
Pr	0.32	0.22	0.35	0.33	0.28	0.84
Nd	0.93	0.63	1.19	1.07	0.88	3.11
Sm	0.07	0.03	0.22	0.23	0.12	0.89
Eu	0.03	0.03	0.44	0.46	0.56	0.06
Gd	0.10	0.07	0.32	0.33	0.16	1.07
Tb	0.01	0.01	0.05	0.06	0.03	0.20
Dy	0.08	0.06	0.36	0.41	0.21	1.22
Ho	0.02	0.01	0.07	0.08	0.05	0.23
Er	0.01	0.01	0.19	0.23	0.11	0.56
Tm	n.d	n.d	0.03	0.04	0.02	0.08
Yb	0.03	0.03	0.24	0.28	0.16	0.52
Lu	n.d	n.d	0.04	0.04	0.02	0.07
Hf	n.d	n.d	0.17	0.20	0.05	0.35
Ta	n.d	n.d	0.26	0.39	0.15	0.53
Pb	14.04	10.84	46.09	44.64	26.89	9.88
Th	0.21	0.18	0.82	1.30	0.43	2.91
U	0.08	0.09	0.79	1.16	0.60	0.45

Table 8 cont.

	sphene	fsp_gran	fsp_gran	biotite_gran	fspxeno3a	fspxeno3b
Sc	1.88	n.d	n.d	20.64	n.d	n.d
Ti	32.12	0.01	0.02	2.09	0.00	123.50
V	811.64	n.d	n.d	320.56	n.d	n.d
Cr	170.78	n.d	n.d	304.94	n.d	n.d
Mn	0.12	0.01	0.02	0.24	0.00	0.01
Co	0.28	n.d	n.d	53.28	n.d	n.d
Ni	128.70	29.77	n.d	167.64	n.d	n.d
Cu	91.85	7.59	9.11	25.49	0.39	0.70
Zn	247.95	n.d	n.d	106.96	n.d	n.d
Ga	36.48	23.30	23.84	43.36	30.72	28.76
Rb	3.86	37.22	70.65	245.88	148.49	34.92
Sr	204.25	1133.00	1136.31	216.08	70.08	145.38
Y	1317.25	0.47	0.77	16.02	0.52	1.72
Zr	474.18	n.d	0.26	158.60	n.d	0.36
Nb	830.84	0.07	0.17	8.56	0.17	1.71
Cs	0.27	1.28	1.76	13.18	1.30	0.12
Ba	23.78	373.17	571.73	394.58	159.47	8.00
La	1696.86	8.02	8.68	34.09	1.11	1.71
Ce	4934.43	9.64	10.57	52.03	1.89	2.51
Pr	689.26	0.85	0.98	5.34	0.22	0.28
Nd	2892.26	2.44	2.97	18.50	0.63	0.88
Sm	490.67	0.25	0.32	3.18	0.03	0.12
Eu	96.51	0.53	0.48	1.04	0.03	0.56
Gd	370.83	0.16	0.23	3.09	0.07	0.16
Tb	48.03	0.01	0.02	0.44	0.01	0.03
Dy	248.38	0.07	0.13	2.48	0.06	0.21
Ho	45.84	0.01	0.02	0.50	0.01	0.05
Er	116.45	n.d	0.03	1.35	0.01	0.11
Tm	17.89	n.d	n.d	0.22	n.d	0.02
Yb	111.11	0.03	0.06	1.53	0.03	0.16
Lu	16.23	n.d	n.d	0.27	n.d	0.02
Hf	35.31	n.d	0.01	5.54	n.d	0.05
Ta	85.77	0.02	0.01	0.19	n.d	0.15
Pb	70.39	23.46	22.19	42.99	10.84	26.89
Th	453.39	0.60	0.67	7.10	0.18	0.43
U	120.18	0.32	0.41	4.45	0.09	0.60

Table 8 cont.

	glass3a	fsp3a	glass3b	fsp_gran	biot_gran	glass5a
$^{87}Sr/^{86}Sr$	0.715504	0.720383	0.723799	0.704984	0.713843	0.908683
$^{87}Sr/^{86}Sr$	0.716399	0.719389	0.721010	0.704565	0.714773	0.904507
$^{87}Sr/^{86}Sr$	0.714819		0.722060	0.704482	0.714356	0.893833
$^{87}Sr/^{86}Sr$	0.717460		0.723057	0.704721		0.836298
$^{87}Sr/^{86}Sr$	0.717385					0.773997

Table 9: Sr-isotopic compositions of microdrilled mix (glass + sillimanite) and minerals in Grt-Bt-Sill xenoliths, El Joyazo, southeast Spain.

	plagioclase	biotite	mix
$^{87}Sr/^{86}Sr$	0.708479	0.723402	0.718002
$^{87}Sr/^{86}Sr$	0.709369	0.723370	0.720443
$^{87}Sr/^{86}Sr$			0.719410
$^{87}Sr/^{86}Sr$			0.719767
$^{87}Sr/^{86}Sr$			0.719730
$^{87}Sr/^{86}Sr$			0.719512
$^{87}Sr/^{86}Sr$			0.719617
$^{87}Sr/^{86}Sr$			0.719426
$^{87}Sr/^{86}Sr$			0.720235
$^{87}Sr/^{86}Sr$			0.719605
$^{87}Sr/^{86}Sr$			0.719508
$^{87}Sr/^{86}Sr$			0.720216

Appendix C: Normalising Values

Table 1: Normalising values used througout this thesis: values of Nakamura, (1974); Thompson, (1982); Taylor and McLennan, (1985); McDonough et al., (1991).

Element	Primitive Mantle	Chondrite	MORB	OIB
K	240.0	120	830	9600
Ti	1280	620	8400	20000
Rb	0.635	0.35	1	22
Sr	21.10	11.8	136	800
Y	4.550	2	35	30
Zr	11.20	6.84	88	220
Nb	0.713	0.35	2.5	53
Ba	6.990	6.9	12	380
La	0.708	0.329	3	35
Ce	1.833	0.865	10	72
Nd	1.366	0.63	8	35
Sm	0.444	0.203	3.3	13
Eu	0.168	0.087	1.2	-
Gd	0.595	0.306	-	-
Tb	0.108	0.052	0.71	-
Dy	0.737	0.381	-	-
Ho	0.163	0.0851	-	-
Er	0.479	0.249	-	-
Tm	0.074	0.034	-	-
Yb	0.480	0.22	-	-
Lu	0.0737	0.0381	-	-
Hf	0.309	0.2	2.5	-
Ta	0.041	0.02	0.17	3
Pb	0.071	-	-	-
Th	0.084	0.042	0.2	3.4
U	0.021	-	0.1	1.1

Appendix D: Model parameters

EC-AFC model parameters

Model 1

Equilibration Parameters		**tlm**	1200	degC	**Element**	Sr
Teq Norm	0.752	**tm0**	1200	degC	**Magma: conc.**	945
Teq deg C	834.65632	**tla**	1150	degC	**bulk D0**	1.4
Mm	0.48986821	**ta0**	700	degC	**enthalpy**	0
Mao	4.07226141	**ts**	800	degC	**Assimilant: conc.**	131.3
Ma*	0.40322741	**cpm**	1484	J/kg K	**bulk D0**	0.2
Mc	0.9133592	**cpa**	1388	J/kg K	**enthalpy**	0
fa	0.09901806	**hcry**	396000	J/kg	**Isotope**	$^{87}Sr/^{86}Sr$
fm	0.0866408	**hfus**	354000	J/kg	**ratio magma**	0.7041
Mao/Mc	4.4585541				**ratio assimilant**	0.73676
Ma*/Mc	0.44147736					

Model 2

Equilibration Parameters		**tlm**	1200	degC	**Element**	Sr
Teq Norm	0.682	**tm0**	1200	degC	**Magma: conc.**	945
Teq deg C	731.53512	**tla**	1100	degC	**bulk D0**	1.027
Mm	0.46243923	**ta0**	600	degC	**enthalpy**	0
Mao	5.06570445	**ts**	700	degC	**Assimilant: conc.**	131.3
Ma*	0.39936899	**cpm**	1484	J/kg K	**bulk D0**	1.027
Mc	0.93692976	**cpa**	1388	J/kg K	**enthalpy**	0
fa	0.0788378	**hcry**	396000	J/kg	**Isotope**	$^{87}Sr/^{86}Sr$
fm	0.06307024	**hfus**	354000	J/kg	**ratio magma**	0.7041
Mao/Mc	5.40670674				**ratio assimilant**	0.73676
Ma*/Mc	0.42625286					

Model 3

Equilibration Parameters		**tlm**	1200	degC	**Element**	Sr
Teq Norm	0.715	**tm0**	1200	degC	**Magma: conc.**	945
Teq deg C	780.1494	**tla**	1100	degC	**bulk D0**	1.5
Mm	0.75682553	**ta0**	600	degC	**enthalpy**	0
Mao	2.97707395	**ts**	700	degC	**Assimilant: conc.**	194.7
Ma*	0.59652673	**cpm**	1484	J/kg K	**bulk D0**	0.5
Mc	0.8397012	**cpa**	1388	J/kg K	**enthalpy**	3
fa	0.2003735	**hcry**	396000	J/kg	**Isotope**	$^{87}Sr/^{86}Sr$
fm	0.1602988	**hfus**	354000	J/kg	**ratio magma**	0.7041
Mao/Mc	3.54539681				**ratio assimilant**	0.732878
Ma*/Mc	0.71040357					

Model 4

Equilibration Parameters		**tlm**	1200	degC	**Element**	Sr
Teq Norm	0.736	**tm0**	1200	degC	**Magma: conc.**	945
Teq deg C	811.08576	**tla**	1100	degC	**bulk D0**	1.35
Mm	0.85039903	**ta0**	600	degC	**enthalpy**	0
Mao	2.26213516	**ts**	700	degC	**Assimilant: conc.**	194.7
Ma*	0.62822751	**cpm**	1484	J/kg K	**bulk D0**	0.5
Mc	0.77782848	**cpa**	1388	J/kg K	**enthalpy**	0
fa	0.2777144	**hcry**	396000	J/kg	**Isotope**	$^{87}Sr/^{86}Sr$
fm	0.22217152	**hfus**	354000	J/kg	**ratio magma**	0.7041
Mao/Mc	2.9082699				**ratio assimilant**	0.732878
Ma*/Mc	0.80766843					

Model 5

Equilibration Parameters						
Teq Norm	0.695	**tlm**	1200	degC	**Element**	Sr
Teq deg C	750.6862	**tm0**	1200	degC	**Magma: conc.**	945
Mm	0.61152652	**tla**	1100	degC	**bulk D0**	1.35
Mao	4.02598042	**ta0**	600	degC	**enthalpy**	0
Ma*	0.51015412	**ts**	700	degC	**Assimilant: conc.**	131.3
Mc	0.8986276	**cpm**	1484	J/kg K	**bulk D0**	0.5
fa	0.1267155	**cpa**	1388	J/kg K	**enthalpy**	0
fm	0.1013724	**hcry**	396000	J/kg	**Isotope**	$^{87}Sr/^{86}Sr$
Mao/Mc	4.48014329	**hfus**	354000	J/kg	**ratio magma**	0.7041
Ma*/Mc	0.5677036				**ratio assimilant**	0.73676

Model 6

Equilibration Parameters						
Teq Norm	0.696	**tlm**	1200	degC	**Element**	Sr
Teq deg C	752.15936	**tm0**	1200	degC	**Magma: conc.**	945
Mm	0.62077073	**tla**	1100	degC	**bulk D0**	1.35
Mao	3.96057012	**ta0**	600	degC	**enthalpy**	0
Ma*	0.51645201	**ts**	700	degC	**Assimilant: conc.**	343
Mc	0.89568128	**cpm**	1484	J/kg K	**bulk D0**	0.7
fa	0.1303984	**cpa**	1388	J/kg K	**enthalpy**	3
fm	0.10431872	**hcry**	396000	J/kg	**Isotope**	$^{87}Sr/^{86}Sr$
Mao/Mc	4.42185207	**hfus**	354000	J/kg	**ratio magma**	0.7041
Ma*/Mc	0.57660243				**ratio assimilant**	0.722624

Model 7

Equilibration Parameters						
Teq Norm	0.684	**tlm**	1200	degC	**Element**	Sr
Teq deg C	734.48144	**tm0**	1200	degC	**Magma: conc.**	945
Mm	0.4895173	**tla**	1100	degC	**bulk D0**	1.35
Mao	4.87861787	**ta0**	600	degC	**enthalpy**	0
Ma*	0.42055442	**ts**	700	degC	**Assimilant: conc.**	194.7
Mc	0.93103712	**cpm**	1484	J/kg K	**bulk D0**	0.7
fa	0.0862036	**cpa**	1388	J/kg K	**enthalpy**	3
fm	0.06896288	**hcry**	396000	J/kg	**Isotope**	$^{87}Sr/^{86}Sr$
Mao/Mc	5.23998213	**hfus**	354000	J/kg	**ratio magma**	0.7041
Ma*/Mc	0.45170532				**ratio assimilant**	0.732878

Model 8

Equilibration Parameters						
Teq Norm	0.668	**tlm**	1200	degC	**Element**	Sr
Teq deg C	710.91088	**tm0**	1200	degC	**Magma: conc.**	945
Mm	0.20742075	**tla**	1100	degC	**bulk D0**	1.2
Mao	6.80418038	**ta0**	600	degC	**enthalpy**	0
Ma*	0.18559899	**ts**	700	degC	**Assimilant: conc.**	131.3
Mc	0.97817824	**cpm**	1484	J/kg K	**bulk D0**	0.6
fa	0.0272772	**cpa**	1388	J/kg K	**enthalpy**	3
fm	0.02182176	**hcry**	396000	J/kg	**Isotope**	$^{87}Sr/^{86}Sr$
Mao/Mc	6.95597193	**hfus**	354000	J/kg	**ratio magma**	0.7041
Ma*/Mc	0.18973944				**ratio assimilant**	0.73676

Model 9

Equilibration Parameters						
Teq Norm	0.744	**tlm**	1200	degC	**Element**	Sr
Teq deg C	822.87104	**tm0**	1200	degC	**Magma: conc.**	945
Mm	0.87638887	**tla**	1100	degC	**bulk D0**	1.3
Mao	2.05303639	**ta0**	600	degC	**enthalpy**	0
Ma*	0.63064679	**ts**	700	degC	**Assimilant: conc.**	131.1
Mc	0.75425792	**cpm**	1484	J/kg K	**bulk D0**	0.75
fa	0.3071776	**cpa**	1388	J/kg K	**enthalpy**	3
fm	0.24574208	**hcry**	396000	J/kg	**Isotope**	$^{87}Sr/^{86}Sr$
Mao/Mc	2.72192885	**hfus**	354000	J/kg	**ratio magma**	0.7041
Ma*/Mc	0.83611557				**ratio assimilant**	0.73676

Model 10

Equilibration Parameters						
Teq Norm	0.781	**tlm**	1200	degC	**Element**	Sr
Teq deg C	877.37796	**tm0**	1200	degC	**Magma: conc.**	945
Mm	0.9555458	**tla**	1100	degC	**bulk D0**	1.5
Mao	1.35482421	**ta0**	600	degC	**enthalpy**	0
Ma*	0.60078988	**ts**	700	degC	**Assimilant: conc.**	131.1
Mc	0.64524408	**cpm**	1484	J/kg K	**bulk D0**	0.5
fa	0.4434449	**cpa**	1388	J/kg K	**enthalpy**	3
fm	0.35475592	**hcry**	396000	J/kg	**Isotope**	$^{87}Sr/^{86}Sr$
Mao/Mc	2.09970808	**hfus**	354000	J/kg	**ratio magma**	0.7041
Ma*/Mc	0.93110484				**ratio assimilant**	0.73676

Model 11

Equilibration Parameters						
Teq Norm	0.746	**tlm**	1100	degC	**Element**	Sr
Teq deg C	751.21736	**tm0**	1100	degC	**Magma: conc.**	945
Mm	0.59093536	**tla**	1200	degC	**bulk D0**	1.5
Mao	4.51889716	**ta0**	650	degC	**enthalpy**	0
Ma*	0.46289196	**ts**	700	degC	**Assimilant: conc.**	131.1
Mc	0.8719566	**cpm**	1452	J/kg K	**bulk D0**	0.5
fa	0.10243472	**cpa**	1400	J/kg K	**enthalpy**	3
fm	0.1280434	**hcry**	350000	J/kg	**Isotope**	$^{87}Sr/^{86}Sr$
Mao/Mc	5.18247944	**hfus**	370000	J/kg	**ratio magma**	0.7041
Ma*/Mc	0.53086583				**ratio assimilant**	0.73676

Model 12

Equilibration Parameters						
Teq Norm	0.698	**tlm**	1200	degC	**Element**	Sr
Teq deg C	755.10568	**tm0**	1200	degC	**Magma: conc.**	945
Mm	0.77595287	**tla**	1100	degC	**bulk D0**	1.5
Mao	4.83247105	**ta0**	650	degC	**enthalpy**	0
Ma*	0.66574151	**ts**	700	degC	**Assimilant: conc.**	131.3
Mc	0.88978864	**cpm**	1452	J/kg K	**bulk D0**	0.3
fa	0.1377642	**cpa**	1400	J/kg K	**enthalpy**	3
fm	0.11021136	**hcry**	350000	J/kg	**Isotope**	$^{87}Sr/^{86}Sr$
Mao/Mc	5.43103253	**hfus**	370000	J/kg	**ratio magma**	0.7041
Ma*/Mc	0.74820185				**ratio assimilant**	0.73676

Model 13

Equilibration Parameters		**tlm**	1200	degC	**Element**	Sr
Teq Norm	0.671	**tm0**	1200	degC	**Magma: conc.**	945
Teq deg C	715.33036	**tla**	1100	degC	**bulk D0**	1.5
Mm	0.40905047	**ta0**	650	degC	**enthalpy**	0
Mao	9.87295141	**ts**	700	degC	**Assimilant: conc.**	131.3
Ma*	0.37838975	**cpm**	1452	J/kg K	**bulk D0**	0.3
Mc	0.96933928	**cpa**	1400	J/kg K	**enthalpy**	3
fa	0.0383259	**hcry**	350000	J/kg	**Isotope**	$^{87}Sr/^{86}Sr$
fm	0.03066072	**hfus**	370000	J/kg	**ratio magma**	0.7041
Mao/Mc	10.1852382				**ratio assimilant**	0.73676
Ma*/Mc	0.39035842					

"D" VALUES

	La (gt pd)	(x gt pd)	0.0059152
olivine	0.0004	0.598	
opx	0.002	0.211	
cpx	0.054	0.076	
gt	0.01	0.115	

	La (sp pd)	(x sp pd)	0.0075272
olivine	0.0004	0.578	
opx	0.002	0.27	
cpx	0.054	0.119	
sp	0.01	0.033	

	Ce (gt pd)		0.010795
olivine	0.0005	0.598	
opx	0.003	0.211	
cpx	0.098	0.076	
gt	0.021	0.115	

	Ce (sp pd)		0.013091
olivine	0.0005	0.578	
opx	0.003	0.27	
cpx	0.098	0.119	
sp	0.01	0.033	

	Pr (gt pd)		0.0191012
olivine	0.0008	0.598	
opx	0.0048	0.211	
cpx	0.15	0.076	
gt	0.054	0.115	

	Pr (sp pd)		0.5801019
olivine	0.0008	0.578	
opx	0.0048	0.27	
cpx	0.15	0.119	
sp	0.01	0.033	

	Nd (gt pd)		0.2199928
olivine	0.001	0.598	
opx	0.0068	0.211	
cpx	0.21	0.076	
gt	0.087	0.115	

	Nd (sp pd)		0.027734
olivine	0.001	0.578	
opx	0.0068	0.27	
cpx	0.21	0.119	
sp	0.01	0.033	

	Sm (gt pd)		0.0476024
olivine	0.0013	0.598	
opx	0.01	0.211	
cpx	0.26	0.076	
gt	0.217	0.115	

	Sm (sp pd)		0.0347214
olivine	0.0013	0.578	
opx	0.01	0.27	
cpx	0.26	0.119	
sp	0.01	0.033	

	Eu (gt pd)		0.0640598
olivine	0.0016	0.598	
opx	0.013	0.211	
cpx	0.31	0.076	
gt	0.32	0.115	

	Eu (sp pd)		0.0416548
olivine	0.0016	0.578	
opx	0.013	0.27	
cpx	0.31	0.119	
sp	0.01	0.033	

	Gd (gt pd)		0.084343
olivine	0.0015	0.598	
opx	0.016	0.211	
cpx	0.3	0.076	
gt	0.498	0.115	

	Gd (sp pd)		0.041217
olivine	0.0015	0.578	
opx	0.016	0.27	
cpx	0.3	0.119	
sp	0.01	0.033	

	Tb (gt pd)		0.114716
olivine	0.0015	0.598	
opx	0.019	0.211	
cpx	0.31	0.076	
gt	0.75	0.115	

	Tb (sp pd)		0.043217
olivine	0.0015	0.578	
opx	0.019	0.27	
cpx	0.31	0.119	
sp	0.01	0.033	

	Dy (gt lherz)		0.1526386
olivine	0.0017	0.598	
opx	0.022	0.211	
cpx	0.33	0.076	
gt	1.06	0.115	

	Dy (sp pd)		0.0465226
olivine	0.0017	0.578	
opx	0.022	0.27	
cpx	0.33	0.119	
sp	0.01	0.033	

"D" VALUES

	Ho (gt pd)		**0.2060126**
olivine	0.0017	0.598	
opx	0.026	0.211	
cpx	0.31	0.076	
gt	1.53	0.115	

	Ho (sp pd)		**0.0452226**
olivine	0.0017	0.578	
opx	0.026	0.27	
cpx	0.31	0.119	
sp	0.01	0.033	

	Er (gt pd)		**0.260027**
olivine	0.0015	0.598	
opx	0.03	0.211	
cpx	0.3	0.076	
gt	2	0.115	

	Er (sp pd)		**0.044997**
olivine	0.0015	0.578	
opx	0.03	0.27	
cpx	0.3	0.119	
sp	0.01	0.033	

	Tm (gt pd)		**0.376377**
olivine	0.0015	0.598	
opx	0.04	0.211	
cpx	0.29	0.076	
gt	3	0.115	

	Tm (sp pd)		**0.046507**
olivine	0.0015	0.578	
opx	0.04	0.27	
cpx	0.29	0.119	
sp	0.01	0.033	

	Yb (gt pd)		**0.495966**
olivine	0.0015	0.598	
opx	0.049	0.211	
cpx	0.28	0.076	
gt	4.03	0.115	

	Yb (sp pd)		**0.047747**
olivine	0.0015	0.578	
opx	0.049	0.27	
cpx	0.28	0.119	
sp	0.01	0.033	

	Lu (gt pd)		**0.667337**
olivine	0.0015	0.598	
opx	0.06	0.211	
cpx	0.28	0.076	
gt	5.5	0.115	

	Lu (sp pd)		**0.050717**
olivine	0.0015	0.578	
opx	0.06	0.27	
cpx	0.28	0.119	
sp	0.01	0.033	

"p" VALUES

	La (gt pd)	(p gt pd)	0.028832		La (sp pd)	(p sp pd)	0.03736
olivine	0.0004	0.03		olivine	0.0004	0.1	
opx	0.002	0.03		opx	0.002	0.2	
cpx	0.054	0.44		cpx	0.054	0.68	
gt	0.01	0.5		sp	0.01	0.02	

	Ce (gt pd)		0.053725		Ce (sp pd)		0.06749
olivine	0.0005	0.03		olivine	0.0005	0.1	
opx	0.003	0.03		opx	0.003	0.2	
cpx	0.098	0.44		cpx	0.098	0.68	
gt	0.021	0.5		sp	0.01	0.02	

	Pr (gt pd)		0.093168		Pr (sp pd)		0.1017804
olivine	0.0008	0.03		olivine	0.0008	0.1	
opx	0.0048	0.03		opx	0.0048	0.2	
cpx	0.15	0.44		cpx	0.15	0.68	
gt	0.054	0.5		sp	0.01	0.02	

	Nd (gt pd)		0.679634		Nd (sp pd)		0.14446
olivine	0.001	0.03		olivine	0.001	0.1	
opx	0.0068	0.03		opx	0.0068	0.2	
cpx	0.21	0.44		cpx	0.21	0.68	
gt	0.087	0.5		sp	0.01	0.02	

	Sm (gt pd)		0.223239		Sm (sppd)		0.17913
olivine	0.0013	0.03		olivine	0.0013	0.1	
opx	0.01	0.03		opx	0.01	0.2	
cpx	0.26	0.44		cpx	0.26	0.68	
gt	0.217	0.5		sp	0.01	0.02	

	Eu (gt pd)		0.296838		Eu (sp pd)		0.21376
olivine	0.0016	0.03		olivine	0.0016	0.1	
opx	0.013	0.03		opx	0.013	0.2	
cpx	0.31	0.44		cpx	0.31	0.68	
gt	0.32	0.5		sp	0.01	0.02	

	Gd (gt pd)		0.381525		Gd (sp pd)		0.20755
olivine	0.0015	0.03		olivine	0.0015	0.1	
opx	0.016	0.03		opx	0.016	0.2	
cpx	0.3	0.44		cpx	0.3	0.68	
gt	0.498	0.5		sp	0.01	0.02	

	Tb (gt pd)		0.512015		Tb (sp pd)		0.21495
olivine	0.0015	0.03		olivine	0.0015	0.1	
opx	0.019	0.03		opx	0.019	0.2	
cpx	0.31	0.44		cpx	0.31	0.68	
gt	0.75	0.5		sp	0.01	0.02	

	Dy (gt pd)		0.675911		Dy (sp pd)		0.22917
olivine	0.0017	0.03		olivine	0.0017	0.1	
opx	0.022	0.03		opx	0.022	0.2	
cpx	0.33	0.44		cpx	0.33	0.68	
gt	1.06	0.5		sp	0.01	0.02	

"p" VALUES

	Ho (gt pd)		**0.902231**		**Ho (sp pd)**		**0.21637**
olivine	0.0017	0.03		olivine	0.0017	0.1	
opx	0.026	0.03		opx	0.026	0.2	
cpx	0.31	0.44		cpx	0.31	0.68	
gt	1.53	0.5		sp	0.01	0.02	
	Er (gt pd)		**1.132945**		**Er (sp pd)**		**0.21035**
olivine	0.0015	0.03		olivine	0.0015	0.1	
opx	0.03	0.03		opx	0.03	0.2	
cpx	0.3	0.44		cpx	0.3	0.68	
gt	2	0.5		sp	0.01	0.02	
	Tm (gt pd)		**1.628845**		**Tm (sp pd)**		**0.20555**
olivine	0.0015	0.03		olivine	0.0015	0.1	
opx	0.04	0.03		opx	0.04	0.2	
cpx	0.29	0.44		cpx	0.29	0.68	
gt	3	0.5		sp	0.01	0.02	
	Yb (gt pd)		**2.139715**		**Yb (sp pd)**		**0.20055**
olivine	0.0015	0.03		olivine	0.0015	0.1	
opx	0.049	0.03		opx	0.049	0.2	
cpx	0.28	0.44		cpx	0.28	0.68	
gt	4.03	0.5		sp	0.01	0.02	
	Lu (gt pd)		**2.875045**		**Lu (sp pd)**		**0.20275**
olivine	0.0015	0.03		olivine	0.0015	0.1	
opx	0.06	0.03		opx	0.06	0.2	
cpx	0.28	0.44		cpx	0.28	0.68	
gt	5.5	0.5		sp	0.01	0.02	

Prim.Mant (C0)	D (gt perid)	P (gt perid)	F	(CL)	Chondrite	(CL/Chondrite)	Element
0.550	0.006	0.029	0.005	51.063	0.245	208.761	La
1.440	0.011	0.054	0.005	92.745	0.638	145.392	Ce
0.220	0.019	0.093	0.005	9.308	0.096	96.587	Pr
1.080	0.220	0.680	0.005	4.874	0.474	10.287	Nd
0.350	0.048	0.223	0.005	6.798	0.154	44.142	Sm
0.130	0.064	0.297	0.005	1.924	0.058	33.157	Eu
0.457	0.084	0.382	0.005	5.227	0.204	25.584	Gd
0.084	0.115	0.512	0.005	0.717	0.037	19.145	Tb
0.570	0.153	0.676	0.005	3.695	0.254	14.542	Dy
0.130	0.206	0.902	0.005	0.630	0.057	11.103	Ho
0.372	0.260	1.133	0.005	1.434	0.166	8.640	Er
0.058	0.376	1.629	0.005	0.155	0.026	6.068	Tm
0.372	0.496	2.140	0.005	0.759	0.165	4.596	Yb
0.057	0.667	2.875	0.005	0.087	0.025	3.412	Lu
0.550	0.006	0.029	0.010	35.196	0.245	143.891	La
1.440	0.011	0.054	0.010	71.084	0.638	111.434	Ce
0.220	0.019	0.093	0.010	7.810	0.096	81.040	Pr
1.080	0.220	0.680	0.010	4.839	0.474	10.213	Nd
0.350	0.048	0.223	0.010	6.321	0.154	41.046	Sm
0.130	0.064	0.297	0.010	1.829	0.058	31.517	Eu
0.457	0.084	0.382	0.010	5.048	0.204	24.710	Gd
0.084	0.115	0.512	0.010	0.702	0.037	18.755	Tb
0.570	0.153	0.676	0.010	3.657	0.254	14.391	Dy
0.130	0.206	0.902	0.010	0.628	0.057	11.077	Ho
0.372	0.260	1.133	0.010	1.438	0.166	8.662	Er
0.058	0.376	1.629	0.010	0.157	0.026	6.119	Tm
0.372	0.496	2.140	0.010	0.768	0.165	4.650	Yb
0.057	0.667	2.875	0.010	0.088	0.025	3.461	Lu
0.550	0.006	0.029	0.050	10.097	0.245	41.278	La
1.440	0.011	0.054	0.050	24.781	0.638	38.848	Ce
0.220	0.019	0.093	0.050	3.414	0.096	35.425	Pr
1.080	0.220	0.680	0.050	4.576	0.474	9.658	Nd
0.350	0.048	0.223	0.050	4.049	0.154	26.292	Sm
0.130	0.064	0.297	0.050	1.310	0.058	22.583	Eu
0.457	0.084	0.382	0.050	3.965	0.204	19.406	Gd
0.084	0.115	0.512	0.050	0.604	0.037	16.123	Tb
0.570	0.153	0.676	0.050	3.376	0.254	13.286	Dy
0.130	0.206	0.902	0.050	0.616	0.057	10.871	Ho
0.372	0.260	1.133	0.050	1.468	0.166	8.844	Er
0.058	0.376	1.629	0.050	0.168	0.026	6.566	Tm
0.372	0.496	2.140	0.050	0.847	0.165	5.133	Yb
0.057	0.667	2.875	0.050	0.099	0.025	3.914	Lu
0.550	0.006	0.029	0.100	5.338	0.245	21.824	La
1.440	0.011	0.054	0.100	13.659	0.638	21.413	Ce
0.220	0.019	0.093	0.100	2.004	0.096	20.794	Pr
1.080	0.220	0.680	0.100	4.285	0.474	9.044	Nd
0.350	0.048	0.223	0.100	2.794	0.154	18.141	Sm
0.130	0.064	0.297	0.100	0.967	0.058	16.674	Eu
0.457	0.084	0.382	0.100	3.126	0.204	15.301	Gd
0.084	0.115	0.512	0.100	0.514	0.037	13.717	Tb
0.570	0.153	0.676	0.100	3.080	0.254	12.122	Dy
0.130	0.206	0.902	0.100	0.602	0.057	10.625	Ho
0.372	0.260	1.133	0.100	1.508	0.166	9.083	Er
0.058	0.376	1.629	0.100	0.185	0.026	7.224	Tm
0.372	0.496	2.140	0.100	0.974	0.165	5.898	Yb
0.057	0.667	2.875	0.100	0.119	0.025	4.679	Lu

Prim.Mant (C0)	D (spn perid)	P (spn perid)	F	(CL)	Chondrite	(CL/Chondrite)	Element
0.550	0.008	0.037	0.005	44.569	0.245	182.212	La
1.440	0.013	0.067	0.005	81.111	0.638	127.152	Ce
0.220	0.580	0.102	0.005	0.376	0.096	3.905	Pr
1.080	0.028	0.144	0.005	33.738	0.474	71.207	Nd
0.350	0.035	0.179	0.005	9.015	0.154	58.537	Sm
0.130	0.042	0.214	0.005	2.852	0.058	49.151	Eu
0.457	0.041	0.208	0.005	10.115	0.204	49.512	Gd
0.084	0.043	0.215	0.005	1.782	0.037	47.579	Tb
0.570	0.047	0.229	0.005	11.315	0.254	44.529	Dy
0.130	0.045	0.216	0.005	2.645	0.057	46.657	Ho
0.372	0.045	0.210	0.005	7.600	0.166	45.785	Er
0.058	0.047	0.206	0.005	1.149	0.026	44.865	Tm
0.372	0.048	0.201	0.005	7.189	0.165	43.545	Yb
0.057	0.051	0.203	0.005	1.042	0.025	41.039	Lu
0.550	0.008	0.037	0.010	32.063	0.245	131.084	La
1.440	0.013	0.067	0.010	64.240	0.638	100.705	Ce
0.220	0.580	0.102	0.010	0.373	0.096	3.875	Pr
1.080	0.028	0.144	0.010	29.761	0.474	62.813	Nd
0.350	0.035	0.179	0.010	8.153	0.154	52.940	Sm
0.130	0.042	0.214	0.010	2.625	0.058	45.249	Eu
0.457	0.041	0.208	0.010	9.300	0.204	45.520	Gd
0.084	0.043	0.215	0.010	1.645	0.037	43.922	Tb
0.570	0.047	0.229	0.010	10.511	0.254	41.364	Dy
0.130	0.045	0.216	0.010	2.450	0.057	43.212	Ho
0.372	0.045	0.210	0.010	7.033	0.166	42.367	Er
0.058	0.047	0.206	0.010	1.065	0.026	41.592	Tm
0.372	0.048	0.201	0.010	6.674	0.165	40.422	Yb
0.057	0.051	0.203	0.010	0.971	0.025	38.252	Lu
0.550	0.008	0.037	0.050	9.882	0.245	40.399	La
1.440	0.013	0.067	0.050	24.114	0.638	37.802	Ce
0.220	0.580	0.102	0.050	0.352	0.096	3.653	Pr
1.080	0.028	0.144	0.050	15.317	0.474	32.327	Nd
0.350	0.035	0.179	0.050	4.620	0.154	29.997	Sm
0.130	0.042	0.214	0.050	1.606	0.058	27.673	Eu
0.457	0.041	0.208	0.050	5.653	0.204	27.671	Gd
0.084	0.043	0.215	0.050	1.019	0.037	27.198	Tb
0.570	0.047	0.229	0.050	6.701	0.254	26.371	Dy
0.130	0.045	0.216	0.050	1.540	0.057	27.164	Ho
0.372	0.045	0.210	0.050	4.403	0.166	26.527	Er
0.058	0.047	0.206	0.050	0.673	0.026	26.264	Tm
0.372	0.048	0.201	0.050	4.241	0.165	25.686	Yb
0.057	0.051	0.203	0.050	0.629	0.025	24.785	Lu
0.550	0.008	0.037	0.100	5.299	0.245	21.664	La
1.440	0.013	0.067	0.100	13.541	0.638	21.228	Ce
0.220	0.580	0.102	0.100	0.328	0.096	3.408	Pr
1.080	0.028	0.144	0.100	9.533	0.474	20.121	Nd
0.350	0.035	0.179	0.100	2.996	0.154	19.457	Sm
0.130	0.042	0.214	0.100	1.081	0.058	18.628	Eu
0.457	0.041	0.208	0.100	3.794	0.204	18.569	Gd
0.084	0.043	0.215	0.100	0.690	0.037	18.427	Tb
0.570	0.047	0.229	0.100	4.611	0.254	18.148	Dy
0.130	0.045	0.216	0.100	1.052	0.057	18.552	Ho
0.372	0.045	0.210	0.100	3.001	0.166	18.078	Er
0.058	0.047	0.206	0.100	0.460	0.026	17.981	Tm
0.372	0.048	0.201	0.100	2.913	0.165	17.645	Yb
0.057	0.051	0.203	0.100	0.437	0.025	17.211	Lu

Appendix E: Analytical Methods and standard data

E.1 Introduction

The following section details the sample preparation and analysis carried out at Durham University, The University of Edinburgh and The University of California, Los Angeles throughout the course of this work. Only samples free of altered and weathered material were chosen for whole rock, mineral and *in-situ* geochemical study.

E.2 General sample preparation

Samples collected in the field were made as fresh and unaltered as possible by chipping off weathered surfaces using a rock hammer. Each sample was then split in two using a jaw crush at Durham University. One part was kept for thin (30 μm) and thick (100 μm) sectioning and/or mineral picking. The remaining part was crushed in a fly-press to grains <2 cm^3. Any remaining, visibly altered material was removed at this point. The fly-press was cleaned using blue roll and water and subsequently dried using compressed air between each sample crush. The crushed sample splits were powdered in an agate ball mill for 30-40 minutes. 8 samples could be powdered in one run. Prior to and in-between powdering of samples, the agate-ball mill components were thoroughly washed and dried using water, blue roll and compressed air. Picking of minerals and glass shards was carried out by hand using a binocular microscope and tweezers. For zircon separation see section E.5.5.1

E.3 Imaging

Acquisition of sample images was undertaken using a variety of techniques at Durham University.

E.3.1 Photomicrographs

Images of thin and thick sections were taken using a Leica DM2500 laboratory binocular microscope.

E.3.2 SEM (Secondary Electron Microscopy)

Secondary electron (SE) images were acquired using the Hitachi TM-1000 Tabletop SEM which has a depth of focus of 0.5 mm, a spatial resolution of 30 nm and a 15kV accelerating voltage. Use of the attached Oxford Instruments SwiftED-TM EDX (energy-dispersive X-ray) system for chemical microanalysis was used when necessary although results were only ever taken as qualitative and never as quantitative.

E.3.2.1 CL (CathodoLuminescence)

CL images of zircons in thick sections were acquired using the Hitachi SU-70 FEG SEM which forms part of the Durham GJ Russell Microscopy Facility in the Department of Physics, Durham University. CL images of zircons in resin mounts for U-Pb analysis were taken using the

E.3.2.3 Image analysis

Sketching of the melt phase within BC93PAX12 was carried out using the ImageJ software which is a public domain Java based image processing program that can be run as an online applet or as a downloaded application (see Fig. 5.7, Chapter 5).

E.4 Whole rock geochemistry

E.4.1 XRF analysis (X-ray Fluorescence)

Analysis of whole rock sample splits for their major (samples with prefix BC93 and BC10) and trace element (samples with prefix BC93 only) concentrations collected during the 1993 and 2010 fieldwork seasons were carried out at the School of Geosciences, University of Edinburgh. Major element concentrations were determined on glass discs and trace element contents on pressed powder pellets. The two procedures are detailed in the following sections.

E.4.1.1 Glass disc preparation

Prior to glass disc preparation, 2 ± 0.1g of each rock powder was weighed out into 10 ml glass bottles and dried for 3 hours at 110°C in a Gallenkamp oven to eradicate any non-structural moisture. From this, 0.95 ± 0.05g was used to make each glass disc. Samples were prepared in batches of six or eight.

Note: For flux addition and loss on ignition (LOI) calculations see Table 1 and section 3.4.1.2.

0.95 ± 0.05g of each sample powder was weighed into lettered and/or numbered 95%Pt/5%Au crucibles and the required flux addition calculated. A 95%Pt/5%Au lid was placed on each crucible and all capsules were placed on a silica tray which was placed in a LTD (Letton Thermal Designs) furnace and fused at 1100°C for 20 minutes during which the target total weight was calculated. Once cooled, each crucible was reweighed and the loss on ignition (LOI) values calculated (Table E.1). The calculated flux weight (Johnson Matthey Spectroflux 105*) was added to each sample using a spatula so that the total weight was reached. The dried sample was gently lifted off the base of the capsule so that the sample was completely surrounded by the flux to aid dissolution. The crucibles (plus lids) were returned to furnace to fuse at 1100°C for 20 minutes. After the crucibles were removed from the furnace, the lids were removed and the melt gently swirled to ensure all the powder had dissolved. Once cooled, the crucibles were re-weighed and extra flux added to make up to the total weight value (± 0.00003g). The lids were replaced onto the crucibles and fused over a Bunsen burner for 3-4 minutes after which the melt was swirled to remove any bubbles, aid dissolution and ensure melt homogenisation. The crucible was replaced on the bunsen burner for a further 2-3 minutes. The melt was vigorously swirled again and then cast immediately by pouring it onto the centre of a pre-heated (~220°C) 37 mm diameter

graphite mould on a hot plate (~220°C). Whilst the melt was still yellow-red hot it was pressed with a plunger to a thickness of 1.5 mm and width of 37 mm. After 2-3 minutes the plunger was removed and a glass petri dish placed over the top of the graphite mould. This acted to cut off the air circulation and lowered the cooling rate thus reducing the chance of the glass disc cracking. This way the discs were also protected from dust. The used crucibles were instantly quenched in water and then transferred to a solution of 20% HCl on a hotplate for cleaning. Once the discs had cooled (up to 2 hours) excess glass was trimmed off using small pliers. The reverse side of the disc (side to the graphite mould) was labelled with a 20 mm diameter sticker and placed into a labelled self-sealing polythene bag which was then placed into a larger named polythene bag and stored in a desiccator prior to analysis.

* Based on an alkali metal borate lanthanum oxide as a heavy absorber to minimise inter-element effects. Lanthanum Oxide (La_2O_3) increases the basicity of the flux and assists in the formation of a glass.

E.4.1.2 Calculation of loss on ignition values (LOI)

LOI values take account of the volatile phases within the sample powders (predominantly chlorine, CO_2, fluorine, H_2O) which are lost throughout the fusion process and hence are undetectable by analysis by XRF. LOI values can be negative due to weight gain through iron oxidation (FeO to Fe_2O_3).

For samples with potentially high silica contents the LOI values were calculated slightly differently from the procedure detailed in Table E.1/section E.4.1.1 as the initial ignition step at 1100°C had the potential to cause the sample powder to resist subsequent dissolution with the flux. Each sample was instead weighed out twice into separate crucibles. One sample was weighed and placed into the furnace at 1100°C.

The sample was re-weighed and the LOI calculated. The calculated flux was added to the second weighed sample to bring total weight to value T and subsequently mixed thoroughly in order to homogenise the distribution of flux throughout the sample. This second sample was then used to produce the glass disc.

E.4.1.3 Pressed powder pellet preparation

Trace element concentrations were determined on pressed powder pellets. Glass discs were used for major element analysis as glass discs are 1 in 6 parts sample powder hence the trace element signature is diluted. Additionally, the emission depth for X-rays of particular trace elements can be in excess of the 1.5 mm disc depth.

Prior to formation of pressed pellets, the following components were washed in hot water and thoroughly dried:

- 40 mm internal diameter steel mould
- Stainless steel mould
- Stainless steel spatulas
- Perspex rod
- Glass beaker
- Glass rod

The lower and upper tungsten carbide discs were polished with acetone.

8 ± 0.1g of each sample was weighed into the cleaned glass beaker and using the glass rod, was mixed thoroughly with 8 drops of binding agent MOWIOL (2% aqueous solution of polyvinyl alcohol) until its distribution was even throughout the sample (~1 minute). Each drop formed a separate spot on the sample surface. The X-PRESS mould

was assembled and a 40 mm diameter aluminium cap placed on the lower tungsten carbide disc. A 38 mm internal diameter inner sleeve was inserted. The sample was fed into the aluminium cap using the inner sleeve as a guide in preventing the sample from overspilling the cap. The perspex rod was inserted into the inner sleeve and rotated in order to gently press the sample powder down and to spread the sample evenly. The perspex rod and steel sleeve were removed carefully and a spatula carefully used to remove any powder from the perimeter of the cap into the centre of the pellet. The upper tungsten carbide disc was inserted (polished side down) followed by the steel plunger. The mould assemblage was then firmly held together and placed in the centre of the X-PRESS hydraulic press and pressed to 8 tons (0.6tons/cm^2) for 2 minutes. During this time, the beaker, glass rod, steel sleeve and perspex rod were cleaned in hot water and dried thoroughly.

The pressure on the mould was released slowly and the assemblage removed. The mould was inverted and the steel base plate and lower tungsten carbide disc removed. The pressed powder pellet was removed from the upper tungsten carbide disc, labelled on the base (sample name, user, date) and placed in a self-sealing plastic bag to reduce vaporisation of halogens.

E.4.1.4 Measurement

Major and trace element concentrations of prepared samples were determined on a Philips PW2404 automatic X-ray fluorescence spectrometer equipped with a Rh-anode X-ray tube for sample irradiation. Instrument operating conditions are given in Table E.2. The matrix effects on major element intensities were corrected for using theoretical alpha coefficients which were calculated using the Philips software. Alpha coefficients were calculated to take account for the additional flux that replaced the volatile components in the sample in order for analytical totals to be 100% less the LOI values.

Corrections on the longer-wavelength trace element intensities (Ba only in this case) were made using alpha coefficients based on major element concentrations from measurement of the powdered samples. Matrix corrections for the other trace elements were applied by using the count rate from the RhKα Compton scatter line (internal standard). Line-overlap corrections were made using synthetic standards. Throughout the duration of analysis, four international standards were run (BCR, BEN, BHVO-1 and BIR-1) for their trace element compositions. Results are presented in Table E.3 and Fig. E.1 where they are compared to the accepted values (given in Govindaraju, 1994).

E.4.2 ICP-MS analysis (Inductively Coupled Plasma Mass Spectrometry)

Whole rock trace and rare earth element analyses were undertaken at the Northern Centre for Elemental and Isotopic Tracing (NCIET), Durham University. Reagents were used directly from the supplier and the water used (as a cleanser, diluent and reagent) was MilliQ (~18.3 MΩ m^{-1}).

E.4.2.1 Dissolution procedure

For typical whole rock trace and rare earth elemental analyses 0.1g ± 0.001 of sample was required. The reference standards used were USGS standards AGV-1 (andesite from Guano Valley, Oregon), BHVO-1 (Hawaiian basalt), BIR-1 (Icelandic basalt) and W-2 (Diabase from Centreville, Virginia) and NIST standard NBS 688 (basalt).

1. Weigh out sample and standards into a clean 15 ml Teflon beaker.
2. Add 1 ml Aristar HNO_3 and leave for 5 minutes to allow the acid to react with any reactive species.
3. Add 4 ml Aristar HF. Leave on hotplate for 48 hours at 130-150^{o}C.
4. Remove beakers from hotplate and allow to cool for ~30 minutes.

5. Dry down solution to a paste at 130-150°C (silica removed as SiF_4). Take care not allow all the acid to evaporate, a few µl should remain so that the sample does not oxidise.
6. Remove beakers from hotplate and allow to cool for ~30 minutes.
7. Add 1 ml of Aristar HNO_3, return beakers to the hotplate (130-150°C) and dry down to a moist residue.
8. Repeat steps 6 and 7.
9. Remove beakers from hotplate and allow to cool for ~30 minutes.
10. Add 2.5 ml of Aristar HNO_3. Add 10-15 ml of MQ, return beakers to hotplate (130-150°C) and leave overnight.
11. Remove beakers from hotplate and allow to cool for ~30 minutes.
12. Check for undissolved material, sample should not be used if particulate material is evident. Add 1 ml of internal standard to each sample (a 2 ppm Bi, Re and Rh solution).
13. Transfer solution to a precleaned 50 ml polypropylene volumetric flask. Rinse the beaker with MQ and transfer washings to the polypropylene flask. Make the flask up to 50 ml with MQ. The flask now contains the sample diluted to 50 ml in 3.5% HNO_3 with the internal standard at 50 ppb.
14. Add 1 ml of solution into a 60 ml vial precleaned with 5-10% HNO_3. Add 10 ml 3.5% HNO_3.

E.4.2.2 Measurement

Trace and rare earth element concentrations for samples denoted with the prefix BC93 were determined on the Perkin Elmer-Sciex Elan 6000 ICP-MS. Samples were analysed using an autosampler. Solutions were run for 38 elements and analysed against a calibration line derived from USGS standards AGV-1, BHVO-1, BIR-1 and W-2 and NIST standard reference material NBS 688. Analyses of standards (excluding W-2) took

place throughout the run sequence in order to monitor instrument drift. Full details are given in Table E.4 and a comparison with accepted values presented in Fig. E.2.

Trace and rare earth element concentrations for samples denoted with the prefix BC10 were determined on the ThermoScientific X-Series 2 ICP-MS. Samples were analysed using an autosampler. Solutions were run for 36 elements and analysed against a calibration line derived from USGS standards AGV-1, BHVO-1 and W-2. USGS standards run at the start and end of the analytical sequence also included BIR-1, BEN and NIST standard reference material NBS 688. W-2 was run intermittently throughout the sequence in order to monitor instrument drift. Full details are given in Table E.5 and a comparison with accepted values presented in Fig. E.3.

E.4.2.3 Beaker cleaning

Beakers for **whole rock digestions** were cleaned using the following procedure:

1. Dispense 2 ml of Analar HNO_3 (or equivalent grade) into each of the vials and hand tighten the lid.
2. Within a fume cupboard, space the vials out on a hot plate at 130-150^{o}C for 24 hours. The HNO_3 refluxes within the vial dissolving any metal species present. (Caution: Teflon softens at 200^{o}C and melts at 230^{o}C).
3. After 24 hours, turn off the hot plate and allow the vials to cool for 30 minutes.
4. Check the lid is still secure, tap the bottom of the vial on a hard surface. The condensed drops of acids will fall to the bottom of the vial. Remove the lid and pour the acid to waste diluting greatly with MQ H_2O.
5. Rinse the vial thoroughly with MQ H_2O. Fill the vial with MQ H_2O, replace the lid and shake. Repeat.
6. Place the lid back on the vial and the outside of the vial with tissue.
7. Teflon vials are now ready for sample addition.

E.4.3 PIMMS analysis (Plasma Ionisation Multicollector Mass Spectrometry)

Whole rock Sr-Nd-Pb isotopic analysis was undertaken at the Arthur Holmes Isotope Geology Laboratory (AHIGL), Durham University. Water used was MQ (~18.3 MΩ m^{-1}) for diluting acids and as a reagent. All dissolutions were undertaken in laminar flow fume hoods and in teflon beakers. The sample procedure is described below.

E.4.3.1 Dissolution procedure

For typical whole rock Sr-Nd-Pb analyses ~100mg of sample is required. The USGS reference standards used were BHVO-1 and BIR-1.

1. Weigh out sample and standards into a clean 7 ml Teflon beaker.
2. Add 3 ml 29N TD HF and 1 ml 16N TD HNO_3. Place on hotplate in a hotblock overnight at 100°C.
3. Dry down solution to a paste at 100°C.
4. Add 1 ml 16N TD HNO_3 to redissolve. Leave on hotplate overnight at 100°C.
5. Dry down solution to a paste at 100°C.
6. Add 1 ml 16N TD HNO_3 and dry down completely.
7. Add 400 µl 3N TD HNO_3 to redissolve and leave on hotplate at 100°C for ~2 hours.
8. Transfer solution to 1.5 ml microcentrifuge tubes pre-rinsed with 3N TD HNO_3. Centrifuge at 13000 rpm for 10 minutes. Any insoluble precipitates will form a solid mass at the base of the tube.

The next stage is the column chemistry procedure.

Note: Nd column chemistry was carried out separately using the waste collected during the Sr-Pb column procedure.

E.4.3.2 Sr-Pb column procedure

Note: Columns used were 1000 µl pipette tips

1. Rinse with 1 CV (column volume) of 6N TD HCl.
2. Rinse with 2 CV's of MQ H_2O.
3. Load 40 µl Sr-spec resin as a slurry in MQ H_2O. Ensure column is free of air bubbles in and around the frit.
4. Elute 1 CV 6N TD HCl.
5. Elute 2 CV's MQ H_2O.
6. Precondition resin with 2 x 100 µl 3N TD HNO_3.
7. Load sample in 400 µl 3N TD HNO_3 from 500 µl microcentrifuge tube using 2 x 200 µl pipette – **do not** disturb the solid precipitates. Collect to Nd sample beaker used in dilution.
8. Re-load sample and collect to Nd sample beaker.
9. Add 0.5 ml 6N TD HCl to sample beaker used during dilution and sweat on hotplate at 100°C.
10. Wash on 50 µl 3N TD HNO_3 (collect to Nd sample beaker).
11. Wash on 100 µl 3N TD HNO_3 (collect to Nd sample beaker).
12. Wash on 250+ µl 3N TD HNO_3 (collect to Nd sample beaker).
13. Recover beakers from hotplate and discard 6N HCl.
14. Elute 2 x 200 µl MQ H_2O and collect Sr fraction in recovered beaker.
15. Wash on 2 x 100 µl 2.5N TD HCl (collect to Nd sample beaker).
16. Elute 500 µl 8N TD HCl and collect Pb fraction in clean 7 ml Teflon beaker.
17. Dispose of column by wrapping it carefully in clingfilm so that the dry resin will not become airborne.
18. Dry Sr and Pb fractions down on hotplate at 80°C.

E.4.3.3 Nd pre-column procedure

1. Dry down collected Nd fraction on hotplate at 100°C.
2. Dissolve in 1 ml 1N TD HCl on hotplate at 50°C.
3. Transfer solution to 1.5 ml microcentrifuge tube pre-rinsed with MQ H_2O. Centrifuge at 13000 rpm for 10 minutes.

E.4.3.4 Nd cation column procedure

Note: unless stated, collect to waste beakers.

1. Wash Nd-Hf cation column tips with 6N HCl.
2. Rinse with 5 mls 29N TD HF.
3. Rinse with 10 mls MQ H_2O.
4. Rinse with 10 mls 6N TD HCl.
5. Rinse with 10 mls MQ H2O.
6. Rinse with 10 mls TD 1N HF – 1N HCl.
7. Load sample in 1 ml TD 1N HCl
8. Elute 3 mls TD 1N – 1N HCl
9. Elute 13 mls TD 1N – 1N HCl
10. Elute 14 mls 2.5N TD HCl.
11. Elute 10 mls 2N TD HNO_3.
12. Wash on 12 mls 6N TD HCl and collect Nd fraction to cleaned 14 ml Teflon beaker.

E.4.3.5 Column cleaning procedure

1. Wash column tips with 6N TD HCl.
2. Rinse with 5 mls 29N TD HF.

3. Rinse with 10 mls MQ H_2O.
4. Rinse with 10 mls 6N TD HCl.
5. Store in 6N HCl.

E.4.3.6 Preparation for isotope measurement

Sr

1. Add 1 ml 3% TD HNO_3 to dried down sample (500 µl to blanks). Place on hotplate at 70°C for 15-20 minutes.
2. Transfer solution to 1.5 ml microcentrifuge tube pre rinsed with 3% TD HNO_3. Centrifuge at 13000 rpm for 10 minutes. Any insoluble particles will form a solid mass at the base of the tube.
3. Transfer solution to 1.5 ml microcentrifuge tube pre-rinsed with 3% TD HNO_3.

Nd and Pb

1. Add 500 µl 3% TD HNO_3 to dried down sample. Place on hotplate at 70°C for 15-20 minutes.
2. Transfer solution to 500 µl microcentrifuge tube pre rinsed with 3% TD HNO_3. Centrifuge at 13000 rpm for 10 minutes. Any insoluble particles will form a solid mass at the base of the tube.
3. Transfer solution to 500 µl microcentrifuge tube pre-rinsed with 3% TD HNO_3.

E.4.3.7 Measurement

Isotope ratios for Sr, Nd and Pb were determined using a PIMMS ThermoElectron Neptune instrument at AHIGL, Durham University. The basic analytical method for both Pb and Sr on the Neptune comprises a static multi-collection routine of 1 block of 50 cycles with an integration time of 4 s per cycle; total analysis time is 3-5 minutes.

Sr whole-rock sample solutions were taken up in 1 ml of 3% TD HNO_3 and introduced into the Neptune using an ESI PFA50 nebulizer and a dual cyclonic-Scott Double Pass spray chamber. With this sample introduction setup, and the normal H skimmer cone, the sensitivity for Sr on the Neptune is typically ~60V total Sr ppm^{-1} at an uptake rate of 90 µl min^{-1}. Prior to analysis a small aliquot was first tested to establish the Sr concentration of each sample by monitoring the size of the ^{88}Sr beam from which a dilution factor was calculated to yield a beam of ~ 20V ^{88}Sr. Instrumental mass bias was corrected for using the $^{88}Sr/^{86}Sr$ ratio (the reciprocal of the $^{86}Sr/^{88}Sr$ ratio) and an exponential law. The average $^{87}Sr/^{86}Sr$ for the NBS 987 standard throughout the course of this study was 0.710256 ± 0.000011 (2σ, n = 23). All sample data throughout this work is reported to relative to a NBS987 standard value of 0.71024 (Thirlwall, 1991). Results are presented in Table E.5 and Fig. E.6.

Nd whole rock sample solutions were taken up in 500 µl of 3% TD HNO_3 and introduced into the Neptune using an ESI PFA50 nebulizer and a dual cyclonic-Scott Double Pass spray chamber. With this sample introduction setup, and the normal H skimmer cone, the sensitivity for Nd on the Neptune is typically ~60-80V total Nd ppm^{-1} at an uptake rate of 90 µl min^{-1}. Instrumental mass bias was corrected for by using a $^{146}Nd/^{145}Nd$ value of 2.079143 (equivalent to a $^{146}Nd/^{144}Nd$ value of 0.7219 which is more commonly used) and an exponential law). The $^{146}Nd/^{145}Nd$ value is used because the Nd isotopic compositions of samples are measured on a total REE-cut from the first stage of cation column chemistry and this ratio is the only Ce and Sm free stable Nd isotopic ratio. The use of the $^{146}Nd/^{145}Nd$ however requires a correction for isobaric interferences from Sm on ^{144}, ^{148} and ^{150}Nd. This correction is based on the method given in Nowell and Parrish, (2001). The average values of $^{143}Nd/^{144}Nd$ for the in-house J&M and Sm-doped J&M standard throughout the course of this study were 0.511111 ± 0.000014 (2σ, n = 22) and 0.511121 ± 0.000010 (2σ, n = 7) respectively. These

values are comparable to the values reported by Pearson and Nowell, (2005) for the long-term reproducibility of this standard. All sample data throughout this work is reported to relative to a J&M standard value of 0.5111110 which is equivalent to a La Jolla value of 0.511862. Results are presented in Table E.6 and Fig. E.6.

Pb whole-rock sample solutions were taken up in 500 µl of 3% TD HNO_3. Prior to analysis each sample was tested to determine its Pb concentration. This value was subsequently used to calculate the appropriate amount of Tl spike to add to the sample in order to obtain a Pb/Tl ratio of ~12, which simultaneously minimises the tails from ^{205}Tl onto ^{204}Pb and from ^{206}Pb onto ^{205}Tl. After spiking with Tl each sample was introduced into the Neptune using an ESI PFA50 nebulizer and a Cinnabar cyclonic spray chamber. With this setup, and the normal H skimmer cone, the sensitivity for Pb on the Neptune is typically ~100V total Pb ppm^{-1} at an uptake rate of 90 µl min^{-1}. Pb mass bias was externally corrected using the $^{205}Tl/^{203}Tl$ ratio and an exponential law. The $^{205}Tl/^{203}Tl$ used for correcting the Pb ratios was determined for each analytical session by minimising the difference in offset between the session average Pb ratios (all ratios for NBS987) and the Galer, (1997) triple spike Pb isotope values i.e. the Tl isotope ratio was calculated to give the best fit to all the Pb isotope ratios of Galer, (1997) simultaneously. The average $^{206}Pb/^{204}Pb$, $^{207}Pb/^{204}Pb$ and $^{208}Pb/^{204}Pb$ ratios for the NBS981 Pb standard throughout the course of this study were 16.94046 ± 0.00088, 15.49762 ± 0.00116, 36.71676 ± 0.00367 (all 2σ, n = 48). Results are presented in Table E.7 and Fig. E.6.

E.4.3.8 Beaker cleaning

Beakers for **whole rock digestions** were cleaned using the following procedure:

1. Remove any labels with ethanol.
2. Rinse beakers and lids with MQ H_2O.

3. Wipe inside of beaker with micropure wipe to dislodge any remnant material.
4. Fill beaker to a depth of 1 cm with ANALAR HCl. Rotate beaker to dispatch HCl around the beaker and discard.
5. Fill to a depth of 0.5 cm with 29N HF (used HF stock from step 14) and leave on hotplate at 90^{o}C for 24 hours.
6. Remove from hotplate and leave to cool for 30 minutes -1 hour.
7. Remove HF and rinse beaker with MQ H_2O.
8. Immerse beakers in 900 ml of 90% MQ H_2O – 10% 16N HNO_3 for 24 hours at 60-100^{o}C.
9. Remove beakers from acid and rinse twice with MQ H_2O.
10. Immerse beakers in 1 litre of MQ H_2O for 24 hours at 60-100^{o}C.
11. Remove beakers from MQ H_2O and rinse thoroughly with MQ H_2O.
12. Fill beakers to a depth of 0.5 cm, cap, and place on hotplate overnight at 100^{o}C.
13. Remove from hotplate and leave to cool for 30 minutes -1 hour.
14. Discard HF and rinse with MQ H_2O.
15. Leave beakers and lids to dry upside down on micropure wipe.
16. Beakers cleaned and ready for use.

E.5 In-situ geochemistry

E.5.1 EMP analysis (Electron Micro Probe)

Electron microprobe analyses were performed at the School of Geosciences, University of Edinburgh using the CAMECA SX100 microprobe. Samples were analysed with a 10 nA electron beam accelerated to 15 kV with a spot size between 5 and 10 μm depending on the phase being analysed.

E.5.2 Microdrilling

In-situ microsampling for trace and rare earth elements and Sr-isotopes was carried out at AHIGL, Durham University on the New Wave Micromill. Samples for microdrilling were mounted on thick sections (100 μm thick) prior to sampling. Initial study of samples in hand specimen and thin section (30 μm thick) was undertaken in order to choose suitable samples for further *in-situ* study.

E.5.2.1 Microdrill setup

The microdrill consists of a binocular microscope, an X-Y stage with movements that could be reproduced to ± 1 μm, a drill chuck into which tungsten carbide or diamond tipped drill bits can be inserted (diamond tipped bits were used throughout the course of this study) and a computer workstation from which the drill, stage and microscope could be controlled using custom designed software. Movement of the stage in the Z direction was determined by the movement of the microscope.

Before any microsampling using this technique was undertaken SEM images and EMP analyses were carried out as the microdrill method is destructive.

Prior to each sample being drilled, the thick section was placed in a teflon beaker containing MQ H_2O and the drill bit in a teflon beaker containing ethanol for cleaning. Both beakers were then placed in an ultrasonic bath for 3 minutes. The sample was then removed, dried and placed on the sample plate. Prior to selecting the sample site, the drill bit location, position of the sample surface and the offset between the optical axis of the microscope and the drill axis needed to be established. After these calibrations the sampling localities were chosen (either as a series of spots or as a line of spots) and the sampling parameters set: depth of milling, drill speed, spot size, number of passes. A warmed square of parafilm with a *c.* 2.5 mm diameter hole in its

centre was placed over the proposed sample area. A few drops of MQ were then placed over the exposed sample site, kept in place by the parafilm. Drilling is carried out in MQ which cools and lubricates the drill bit during sampling and collects the sample dust, aiding sample recovery. Throughout drilling, the drill tip was kept within the MQ drop. When sampling was complete, the suspended sample within the MQ droplet was pipetted into a *c.* 3 mm diameter gold boat which was weighed prior to pipetting. The water was then evaporated by placing the gold boat in the lid of a 3 ml teflon beaker and placing that on a hot plate within an ultra-clean fume hood. The gold boat was then reweighed and the sample mass calculated. The subsequent chemical procedure is described below.

Note: To avoid issues of sample heterogeneity, trace element and Sr-isotope compositions were determined on the same sample solution by removing a 10% aliquot of the solution. The remaining 90% was used to separate the Sr fractions for isotope analysis.

E.5.2.2 Dissolution

1. Add 150 µl UpA HF and 50 µl UpA HNO_3 to drilled sample (in gold boat) and leave in hotplate overnight at 100°C.
2. Remove gold boat and dry solution to paste,
3. Add 150 µl 6N UpA HCl and leave on hotplate overnight at 100°C.
4. Dry down solution to a paste – do not overbake.
5. Add 200 µl 3N UpA HNO_3 to solution and dissolve at 100°C.
6. Remove 20 µl aliquot to 1.5 ml microcentrifuge tube pre-leached with 6N UpA HCl.

E.5.2.3 Micro-Sr column procedure

1. Rinse columns with 2 CV's MQ H_2O.
2. Load 40 µl Eichrom Sr-spec resin as a slurry in MQ H_2O. Ensure column is free of air bubbles in and around the frit.
3. Elute 1 CV 6N UpA HCl.
4. Elute 2 CV's MQ H_2O.
5. Precondition resin with 2 x 100 µl 3N UpA HNO_3.
6. Load sample in 180 µl 3N UpA HNO_3, collect to sample beaker and reload.
7. Add 0.5 ml 6N UpA HCl to sample beaker used during dilution and sweat on hotplate at 100°C.
8. Wash on 50 µl 3N UpA HNO_3
9. Wash on 100 µl 3N UpA HNO_3
10. Wash on 250+ µl 3N UpA HNO_3.
11. Recover beakers from hotplate and discard 6N UpA HCl.
12. Elute 100 µl MQ H_2O.
13. Elute 2 x 200 µl MQ H_2O.
14. Dry down on hotplate at 80°C.

E.5.2.4 Micro-Sr beaker cleaning

Beakers for **microdrilled** samples were cleaned using the following procedure:

1. Remove any labels with ethanol
2. Rinse beakers and lids with MQ H_2O.
3. Wipe inside of beaker with micropure wipe to dislodge any remnant material.
4. Fill beaker to depth of 0.4 cm with 6N UpA HCl and leach on hotplate overnight at 80°C.
5. Empty beaker and rinse thoroughly with MQ H_2O.

6. Fill beaker to depth of 0.4 cm with 6N UpA HCl and leach on hotplate overnight at 80°C.
7. Empty beaker and rinse thoroughly with MQ H_2O.
8. Put closed beakers into large Teflon beaker (filled with MQ H_2O) and leave in hotplate overnight at 80°C.
9. Empty and rinse with MQ H_2O.
10. Open beakers and put in large Teflon beaker containing dilute (10%) UpA HNO_3. Leave on hotplate overnight at 80°C.
11. Empty and put in large Teflon beaker containing MQ H_2O. Leave on hotplate overnight at 80°C.
12. Empty and put in large Teflon beaker containing MQ H_2O. Leave on hotplate overnight at 80°C.
13. Rinse thoroughly with MQ H_2O.
14. Fill to a depth of 0.4 cm with 6N UpA HCl and leach on hotplate overnight at 100°C.
15. Empty and rinse with MQ H_2O.
16. Fill to a depth of 0.4 cm with MQ H_2O and leach on hotplate overnight at 80°C.
17. Empty and rinse with MQ H_2O.
18. Fill to a depth of 0.4 cm with 6N UpA HCl and leach on hotplate overnight at 100°C.
19. Empty and rinse with MQ H_2O.
20. Fill to a depth of 0.4 cm with MQ H_2O and leach on hotplate overnight at 80°C.
21. Empty and rinse with MQ H_2O.
22. Beakers cleaned and ready for use.

E.5.3 ICP-MS analysis (Inductively Coupled Plasma Mass Spectrometry)

Trace element and REE concentrations in microdrilled samples and picked minerals and glass shards was carried out by ICP-MS using a ThermoElectron Element II system at NCIET, Durham University. Prior to analysis, 480 µl 3N UpA HNO_3 was added to the 20 µl aliquot which was removed prior to running micro-Sr column chemistry. Solutions were run for 21 trace elements and analysed against a calibration line derived from USGS standards AGV-1, BHVO-1 and W-2. W-2 was subsequently diluted to match the concentration range within the samples. The calibration line was established prior to running any samples and the standard materials run as "unknowns" throughout the analysis time (on average, every six samples) in order to monitor drift and the accuracy and precision of the calibration line. A wash blank (3% UpA HNO_3) was run in-between each sample in order to monitor the instruments background. W-2 was run intermittently throughout each analytical run. Procedural blanks for Sr are presented in Table E.8. Standard results for W-2 are presented in Table E.9 and in Fig. E.7.

E.5.4 TIMS analysis (Thermal Ionisation Mass Spectrometry)

Isotope measurement for Sr was measured by TIMS using a ThermoElectron Triton system at AHIGL, Durham University. The Sr fractions were loaded onto Re filaments using a TaF_5 activator to enhance ionisation of small Sr samples or standards. Large Sr standards (~600 ng) used to monitor the performance of the system were loaded onto Ta filaments using 1 ml H_3PO_4. Samples were analysed at a pressure of $< 4 \times 10^{-9}$ mbar. The filaments were heated at 200 mA/minute until a Rb signal was observed (typically between 750 and 1200 mA). The current remained constant until the Rb signal decreased at which point the current was increase at a rate of 50-100 mA/minute to reduce the Rb. The current was increased until the ^{88}Sr signal was stable at 10 mV (typically between 1750 and 2300 mA). At this point the instrument performed a

baseline measurement (30 seconds). $^{87}Sr/^{86}Sr$ ratios were measured using a static multi-collection routine. An analysis consisted of 20 blocks of 10 cycles with an integration time of 4 seconds per cycle. $^{87}Sr/^{86}Sr$ and $^{84}Sr/^{86}Sr$ ratios were corrected for mass fractionation using an exponential law and a $^{86}Sr/^{88}Sr$ ratio of 0.1194. Throughout the period of study, 102 analyses of the international standard NBS 987 were taken averaging a $^{87}Sr/^{86}Sr$ of 0.710256 ± 0.000020 (2σ) which is in excellent agreement with the values reported by Thirlwall, (1991) of 0.710248 ± 0.000023 (2σ) (n = 247). Results are presented in Table E.10 and Fig. E.8.

E.5.5 SIMS analysis (Secondary Ionisation Mass Spectrometry)

In-situ U-Pb isotopic analysis of zircons was undertaken at the University of California, Los Angeles on the CAMECA ims-1270 ion probe which forms part of the NSF (National Science Foundation) Instrumentation and Facilities Program. Separation of zircons from their host rocks was undertaken at Oregon State University by Shan de Silva and his graduate students Jason Kaiser and Rodrigo Iriarte using the procedure detailed below.

E 5.5.1 Zircon separation

For a detailed account of the traditional accessory mineral separation methods see Heaman and Parrish, (1991).

Splits of samples BC93PAX14 and BC10QSX107 were crushed using a hydraulic press and a disk mill. Splits of samples BC93PAX14 and BC10QSX107 were crushed using a hydraulic press to reduce the size to ≤ 1 cm. The sample was subsequently crushed using a disc mill to produce a coarse grained powder. Powders were then sieved in order to separate grains <355 microns. A Rogers shaking table was used to separate out the heavy mineral fractions using the table vibrations and water. The collected heavy

mineral fraction was put into a funnel containing heavy liquid (density of 3.28-33) in which the heavy minerals collected at the bottom whilst the lighter grains floated at the top. The heavy fraction is then passed through a Frantz isodynamic separator which separates the magnetic and non-magnetic (zircon) fractions. From this fraction, zircon grains were handpicked and cleaned with acetone. These were subsequently mounted in epoxy resin and sectioned so that the grain surface was exposed. This surface was then polished with 1 μm of Al_2O_3.

E.5.5.2 Measurement

Prior to analysis on the ion probe, mounted zircon grains were imaged using cathodoluminescence (CL) to identify growth zonation patterns and any inclusions, the latter which would be avoided during analysis. Resin blocks were coated with 10 μm of gold and were analysed using a mass-filtered 10-20 nA $^{16}O^-$ beam which was focussed to a spot size diameter of 25-30 μm. The secondary ions were extracted at 10 kV at 50 eV. Surface Pb contamination was reduced by sputtering the target areas for 4 minutes prior to analysis. The sensitivity on U and Pb were constrained through analysis of zircon standard AS3. The $^{206}Pb/^{238}U$ age for AS3 is reproducible to within 1.6%, and its $^{207}Pb/^{206}U$ age is accurate to within 0.3% (see Table E.11 and Fig. E.9). Further details of the analytical protocol for the UCLA SIMS is given in Folkes et al., (2011). Details of reference zircon AS3 are given in Paces and Miller, (1993) and Schmitz et al., (2003).

Table E.1. Calculation of Loss on Ignition (LOI) values.

Sample No.	QNL01	QNL02	QSL01	QSL02	QSL03	QSL04	QSL05	QSL06	QSL07	QSL08	QSL09	PAL01	PAL02	PAL03
Crucible No.	UN	D	F	E	C	H	UN	B	F	E	C	H	UN	SB
Crucible (C)	17.92	17.93	17.35	17.93	17.66	17.49	17.92	17.88	17.35	17.93	17.66	17.49	18.04	15.63
Crucible + Sample (UNIG)	18.88	18.89	18.31	18.88	18.61	18.45	18.87	18.83	18.30	18.88	18.61	18.44	18.99	16.58
Crucible + Sample (IG)	18.88	18.88	18.31	18.87	18.60	18.45	18.87	18.82	18.30	18.88	18.60	18.43	18.97	16.57
Sample (UNIG-C)	0.96	0.96	0.96	0.95	0.95	0.95	0.95	0.95	0.95	0.95	0.95	0.95	0.96	0.95
Flux (S x 5)	4.78	4.78	4.78	4.73	4.74	4.78	4.75	4.76	4.77	4.75	4.73	4.74	4.78	4.75
Total (UNIG + F)	23.66	23.67	23.09	23.61	23.34	23.23	23.62	23.59	23.07	23.63	23.34	23.18	23.77	21.34
LOI (%) = 100(UNIG-IG)/S	0.25	0.83	0.01	0.23	0.29	0.31	0.32	0.56	0.15	0.22	0.59	1.38	2.73	1.09

Sample No.	PAL04	QLMI01	QLMI02	QLMI03	QLMI04	QNX02	QNX03	QSX04	PAX01	PAX03	PAX07	PAX11	PAX12	PAX14
Crucible No.	3.00	5.00	6.00	8.00	PT	UN	UN	B	E	F	G	H	8.00	PT
Crucible (C)	15.64	15.64	16.15	15.85	15.73	17.94	17.92	17.88	17.93	17.35	17.66	17.49	15.85	15.73
Crucible + Sample (UNIG)	16.60	16.59	17.10	16.81	16.68	18.89	18.88	18.83	18.88	18.31	18.62	18.45	16.80	16.69
Crucible + Sample (IG)	16.60	16.58	17.09	16.80	16.67	18.87	18.87	18.83	18.88	18.29	18.61	18.44	16.80	16.69
Sample (S = UNIG – C)	0.95	0.95	0.95	0.96	0.95	0.95	0.96	0.95	0.95	0.96	0.96	0.95	0.95	0.96
Flux (F = S x 5)	4.77	4.75	4.75	4.79	4.73	4.75	4.78	4.77	4.75	4.78	4.78	4.76	4.75	4.78
Total (T = UNIG + F)	21.37	21.34	21.85	21.60	21.42	23.64	23.66	23.60	23.63	23.08	23.40	23.21	21.56	21.47
LOI (%) = 100(UNIG-IG)/S	0.28	0.82	1.12	1.16	0.88	1.96	0.59	0.16	0.34	0.17	0.66	0.54	0.45	0.06

Sample No.	QSL02*	QSL03*	FRIG01	FRIG02	FRIG03	FRIG04	QSL02*	QSL03*	FRIG01	FRIG02	FRIG03	FRIG04
Crucible No.	3.00	5.00	6.00	SB	A	C	UN	B	C	E	F	H
Crucible (C)	15.64	15.64	16.15	15.63	18.04	17.94	17.92	17.88	17.66	17.93	17.35	17.49
Crucible + Sample (UNIG)	16.60	16.59	17.10	16.59	18.99	18.90	18.88	18.83	18.61	18.89	18.30	18.45
Crucible + Sample (IG)	-	-	-	-	-	-	18.87	18.82	18.59	18.87	18.29	18.44
Sample (S = UNIG – C)	0.95	0.95	0.95	0.96	0.95	0.96	0.95	0.95	0.95	0.96	0.95	0.96
Flux (F = S x 5)	4.78	4.75	4.75	4.78	4.75	4.78	-	-	-	-	-	-
Total (T = UNIG + F)	21.36	21.34	21.85	21.36	23.74	23.68	-	-	-	-	-	-
LOI (%) = 100(UNIG-IG)/S	-	-	-	-	-	-	0.32	0.40	1.63	1.48	1.52	1.57

* These samples did not dissolve 100% during the first run through of the procedure and were subsequently treated identically to those samples with potential high silica contents.

Table E.1. Calculation of Loss on Ignition (LOI) values.

Sample No.	QSMI103	PAMI106	PAL101.1	PAL101.2	QSX101	QSX104	QSX106	QSX107	QSX108	QSX110	QSX111	PAX102
Crucible No.	UN	A	B	D	E	F	G	H	SB	C	3	5
Crucible (C)	17.9098	18.0230	17.9297	17.9148	17.9160	17.3440	17.6422	17.4782	16.6228	17.8625	15.6368	15.6291
Crucible + Sample (UNIG)	18.8621	18.9659	18.8779	18.8681	18.8661	18.2953	18.5938	18.4295	16.5798	18.8135	16.5856	16.5733
Crucible + Sample (IG)	18.8516	18.9559	18.8685	18.8626	18.8607	18.2842	18.5921	18.4287	16.5745	18.8088	16.5837	16.5614
Sample (UNIG-C)	0.9523	0.9429	0.9482	0.9533	0.9501	0.9513	0.9516	0.9513	0.9570	0.9510	0.9488	0.9442
Flux (S x 5)	4.7615	4.7145	4.7410	4.7665	4.7505	4.7565	4.7580	4.7565	4.7850	4.7550	4.7440	4.7210
Total (UNIG + F)	23.6236	23.6804	23.6189	23.6346	23.6166	23.0518	23.3518	23.1860	21.3648	23.5685	21.3296	21.2943
LOI (%) = 100(UNIG-IG)/S	1.1026	1.0606	0.9914	0.5769	0.5684	1.1668	0.1845	0.0841	0.5538	0.4942	0.2003	1.2603

Sample No.	PAX103	PAX107A	PAX107B	PAX110	PAX112	PAX113	PAX127	PAX128	PAX131	PAX132	PAX134	PAX135
Crucible No.	6	7	UN	B	C	E	F	G	H	3	5	6
Crucible (C)	16.1441	15.7256	17.9102	15.9248	17.9294	17.9144	17.9156	17.3434	17.6409	17.4776	17.9097	18.0222
Crucible + Sample (UNIG)	17.0928	16.6711	18.8675	16.8724	18.8773	18.8643	18.8661	18.2997	18.5925	18.4269	18.8576	18.9746
Crucible + Sample (IG)	17.0748	16.6700	18.8527	16.8670	18.8701	18.8642	18.8578	18.2981	18.5901	18.4244	18.8535	18.9687
Sample (S = UNIG – C)	0.9487	0.9455	0.9573	0.9476	0.9479	0.9499	0.9505	0.9563	0.9516	0.9493	0.9479	0.9524
Flux (F = S x 5)	4.7435	4.7275	4.7865	4.7380	4.7393	4.7495	4.7525	4.7815	4.7580	4.7465	4.7395	4.7620
Total (T = UNIG + F)	21.8363	21.3986	23.6540	21.6104	23.6166	23.5838	2.3619	23.0812	23.3505	23.1734	23.5968	23.7366
LOI (%) = 100(UNIG-IG)/S	1.8973	0.1163	1.5460	0.5699	0.1266	0.0095	0.8732	0.1673	0.2522	0.2634	0.4325	0.6195

Sample No.	PAX136	PAX138
Crucible No.	7	8
Crucible (C)	17.9288	15.6291
Crucible + Sample (UNIG)	18.8779	16.5751
Crucible + Sample (IG)	18.8731	16.5698
Sample (S = UNIG – C)	0.9491	0.9460
Flux (F = S x 5)	4.7455	4.7300
Total (T = UNIG + F)	23.6234	21.3051
LOI (%) = 100(UNIG-IG)/S	0.5057	0.5603

Table E.2. Operating conditions of Philips PW2404 XRFinstrument, University of Edinburgh.

Element	Generator settings		mA	Primary collimator	Analysing crystal	Background offset (°2θ)	Detector	Line overlap	Peak and background count times (s)	Typical 1σ
	Line	kV								
Fe	Kα	50	50	Fine	LiF200	-2.5	Flow		10	0.03%
Mn	Kα	50	50	Fine	LiF200	2.5	Flow		10	0.007
Ti	Kα	50	50	Fine	LiF200	3.5	Flow		20	0.006
Ca	Kα	50	50	Fine	LiF200	-4	Flow		20	0.03
K	Kα	50	50	Fine	LiF200	-5	Flow		20	0.005
P	Kα	40	60	Coarse	Ge111	3	Flow		50	0.003
Si	Kα	40	60	Coarse	PE	4	Flow		50	0.1
Al	Kα	40	60	Coarse	PE	-6.5	Flow		50	0.05
Mg	Kα	40	60	Coarse	PX1	3.1	Flow		50	0.05
Na	Kα	40	60	Coarse	PX1	6.2	Flow		50	0.05
Nb	Kα	80	30	Fine	LiF200	±0.36	Scint.	$YK\beta_1$	500	0.1 ppm
Zr	Kα	80	30	Fine	LiF200	+0.66, -0.76	Fl.+scint.	$SrK\beta_1$	100	0.4
Y	Kα	80	30	Fine	LiF200	±0.60	Fl.+scint.	$RbK\beta_1$	100	0.4
Sr	Kα	80	30	Fine	LiF200	±0.76	Fl.+scint.		40	0.5
Rb	Kα	80	30	Fine	LiF200	+0.50, -0.34	Fl.+scint.		100	0.3
Th	$L\alpha_1$	80	30	Fine	LiF200	+0.22, -0.36	Scint.		500	0.4
Pb	$L\beta_1$	80	30	Fine	LiF200	±0.26	Scint.		500	0.4
La	$L\alpha_1$	50	50	Fine	LiF200	±0.66	Flow		500	1
Ce	$L\beta_1$	50	50	Fine	LiF200	+1.15, -0.64	Flow	CrKa†	500	1.5
Nd	$L\alpha_1$	50	50	Fine	LiF200	+0.64, -1.15	Flow	$CeL\beta_1$, CrKα†	500	1
Zn	Kα	50	50	Fine	LiF200	±0.66	Fl.+scint.		40	0.5
Cu	Kα	50	50	Fine	LiF200	+1.70, -0.70	Flow		40	0.5
Ni	Kα	50	50	Fine	LiF200	+1.30, -1.95	Flow		40	1
Co	Kα	50	50	Fine	LiF200	1.2	Flow	FeKβ	100	1
Cr	Kα	50	50	Fine	LiF200	+1.62, -0.88	Flow	VKβ	40	1
V	Kα	50	50	Fine	LiF220	+3.54, -1.30	Flow	TiKβ	40	2
Ba	$L\alpha_1$	50	50	Fine	Ge220	+1.60, -2.70	Flow	TiKα, ScKβ	200	5
Sc	Kα	50	50	Fine	LiF200	-2	Flow	CaKβ	100	0.5
Ga	Kα	50	50	Fine	LiF200	±0.60	Fl.+scint.		100	0.4

* = standard deviation: in wt% for Fe to Na, in ppm for Nb to Ga. † = overlap on background position.

Table E.3: Trace element data for international standards analysed by XRF at the School of Geosciences, University of Edinburgh during analysis of samples with prefix BC93. All

	This study (n = 3)				Govindaraju, (1994)			
	BCR	**BEN**	**BHVO-1**	**BIR**	**BCR**	**BEN**	**BHVO-1**	**BIR**
Nb	12.7	117.1	19.3	0.6	14	105	19	0.6
1σ	0.1	0.3	0.1	0				
Zr1	191.3	271.5	174.5	17.5	190	260	179	15.5
1σ	1.1	1	0.6	0.5				
Y	38.2	29.8	27.4	16.6	38	30	27.6	16
1σ	0.3	0.2	0.2	0.2				
Sr	333.2	1384.4	390.9	109	330	1370	403	108
1σ	2.9	4.7	0.8	0.3				
Rb	47.7	47.8	9.5	0.5	47.2	47	11	0.3
1σ	0.3	0.2	0.1	0.1				
Zn	125.5	126.5	103.8	67.2	129.5	120	105	71
1σ	0.4	0.5	0.5	0.3				
Cu	19.5	73.3	136.4	123.2	19	72	136	126
1σ	0.6	0.5	0.2	0.4				
Ni	12.2	272.8	116.4	150.9	13	267	121	166
1σ	0.1	0.6	0.3	0.7				
Cr	n.d	393.6	299.8	389.1	16	360	289	382
1σ	-	0.8	0.7	0.6				
V	402.1	250.5	319.7	306.7	407	235	317	313
1σ	0.9	2.3	1.9	1				
Ba	665.2	1011.5	126	12.4	681	1025	139	7
1σ	1.5	1.4	2.8	0.9				
Sc	34	21.6	33.6	41	32.6	22	31.8	44
1σ	0.2	0.5	0.5	0.2				
La	23.6	87.6	12.2	-0.6	24.9	82	15.8	0.6
1σ	0.6	0.7	0.5	0.3				
Ce	53.1	154.5	37.7	-1.3	53.7	152	39	2
1σ	0.2	0.8	0.7	0.5				
Nd	29.4	67.3	27.1	5	28.8	67	25.2	2.5
1σ	0.3	0.4	1.2	0.9				

Table E.4. Trace element data for international standards analysed by ICPMS (ELAN 6000) during analysis of samples with prefix BC93. All data is reported in ppm unless stated otherwise.

	This study					Accepted Values				
	W2 (n=6)	**AGV 1 (n=2)**	**BIR1 (n=2)**	**BHVO-1 (n=2)**	**NBS688 (n=2)**	**W2**	**AGV-1**	**BIR-1**	**BHVO-1**	**NBS688**
Sc	34.87	11.22	37.84	30.87	36.6	35.9	12.3	43	31	38.00
1σ	0.84	0.36	2.36	1.88		0.8	0.5	2	2	
TiO_2 (wt. %)	1.02	0.94	0.81	2.66	1.13	1.06	1.05	0.97	2.75	
1σ	0.02	0.05	0.05	0.16		0.01	0.05	0.03	0.04	
V	260.36	109.43	279.34	310.33	244.01	268	119	319	318	242
1σ	4.43	5.15	15.73	14.76		10	6	18	15	
Cr	90.83	10.12	349.17	283.8	320.87	93	9	391	287	332
1σ	1.25	0.42	17.51	11.33		6	1.2	15	15	
MnO (wt. %)	0.17	0.09	0.15	0.17	0.16	0.167	0.1	0.18	0.17	
1σ	0.003	0.003	0.007	0.01		0.004	0.01	0.01	0.01	
Ni	80.15	16.48	170.44	134.9	169.1	72	15.5	166	118	158
1σ	1.23	0.35	0.98	0.46		4	0.8	7	6	
Cu	103.91	55.36	105.5	140.75	86.91	105	58	119	137	96.00
1σ	0.65	0.2	0.78	0.36		3	2	8	9	
Zn	76.06	81.04	90.25	112.56	94.97	77	87	72	106	84.00
1σ	0.48	0.44	36.13	0.16		6	4	18	9	
Ga	0.00	19.01	13.45	21.33	16.41	18	20.2	15.3	21	17.00
1σ	0.00	0.05	0.27	0.72		1	0.5	0.8	2	
Rb	0.00	67.19	0.21	10.01	2.04	21	66.6	0.2	9.19	1.91
1σ	0.00	0.58	0.01	0.16		1	0.4	0.01	0.17	
Sr	200.93	647.17	98.75	414.67	172.61	196	660	109	396	169
1σ	0.81	4	1.07	7.04		5	6	2	1	
Y	22.43	19.08	14.48	27.95	20.95	22	19	15.6	26	17.00
1σ	0.12	0.01	0.1	0.45		1	1	0.9	2	
Zr	92.48	224.71	13.43	180.24	56.56	92	231	14	174	61.00
1σ	0.71	0.21	0.04	0.55		4	9	0.1	9	
Nb	7.75	14.06	0.53	19.89	4.33	7.5	14.6	0.55	18.6	5.00
1σ	0.05	0.09	0.02	0.14		0.6	1	0.05	1.8	
Cs	0.93	1.28	0.01	0.1	0.04	0.92	1.26	0.01	0.1	0.24
1σ	0.03	0.07	0.002	0.003		0.07	0.07	0.003	0.01	
Ba	178.88	1205.41	6.4	138.9	178.67	172	1200	7.14	133	200
1σ	1.70	19.76	0.4	3.35		7	8	n.d	1.00	
La	10.87	37.36	0.55	15.92	5.22	10.8	38.2	0.62	15.5	5.30
1σ	0.12	0.64	0.01	0.36		0.5	0.04	0.02	0.1	

Table E.4. Trace element data for international standards analysed by ICPMS (ELAN 6000) during analysis of samples with prefix BC93. All data is reported in ppm unless stated otherwise.

	This study					Accepted Values				
	W2 (n=6)	**AGV 1 (n=2)**	**BIR1 (n=2)**	**BHVO-1 (n=2)**	**NBS688 (n=2)**	**W2**	**AGV-1**	**BIR-1**	**BHVO-1**	**NBS688**
Ce	23.16	64.98	1.7	37.94	11.77	23.4	67.6	1.92	38.1	13.00
1σ	0.22	1.54	0.02	1.29		0.7	1.1	0.08	0.2	
Pr	3.07	8.08	0.34	5.47	1.74	3	8.3	0.37	5.42	2.40
1σ	0.03	0.27	0.01	0.24		0.1	0.5	0.02	0.19	
Nd	13.83	31.83	2.18	26.09	8.7	13	31.7	2.38	24.7	9.60
1σ	0.16	1.07	0.03	0.98		0.5	0.1	0.01	0.1	
Sm	3.37	5.52	0.97	6.25	2.39	3.3	5.72	1.12	6.12	2.50
1σ	0.07	0.2	0.03	0.28		0.08	0.03	0.02	0.03	
Eu	1.11	1.59	0.45	2.03	0.97	1.08	1.58	0.53	2.09	1.01
1σ	0.01	0.06	0.01	0.09		0.03	0.02	n.d	0.02	
Gd	3.94	4.5	1.79	6.55	3.16	3.66	4.7	1.87	6.33	3.20
1σ	0.09	0.15	0.03	0.21		0.12	0.05	0.04	0.06	
Tb	0.65	0.63	0.35	0.97	0.54	0.62	0.69	0.36	0.96	0.52
1σ	0.01	0.02	0.02	0.03		0.03	0.04	0.03	0.06	
Dy	3.87	3.31	2.28	5.27	3.37	3.79	3.55	2.51	5.31	3.40
1σ	0.03	0.06	0.04	0.22		0.09	0.03	n.d	0.03	
Er	2.14	1.64	1.43	2.38	2.03	2.22	1.82	1.66	2.55	2.10
1σ	0.03	0.04	0.03	0.1		0.1	0.02	n.d	0.02	
Tm	0.33	0.24	0.23	0.33	0.32	0.33	0.28	0.25	0.33	0.29
1σ	0.01	0.001	0.004	0.01		0.02	0.02	0.03	0.03	
Yb	2.08	1.58	1.47	2.02	2.09	2.05	1.63	1.65	2	2.05
1σ	0.02	0.03	0.01	0.06		0.04	0.02	n.d	0.03	
Lu	0.33	0.25	0.25	0.31	0.34	0.31	0.24	0.25	0.27	0.35
1σ	0.01	0.005	0.002	0.01		0.01	0.002	0.02	0.01	
Hf	2.45	4.9	0.52	4.49	1.53	2.45	5.1	0.58	4.46	1.55
1σ	0.03	0.09	0.01	0.12		0.18	0.2	0.004	0.17	
Ta	0.5	0.85	0.04	1.26	0.29	0.47	0.87	0.0357	1.21	0.31
1σ	0.01	0.02	0.003	0.03		0.04	0.05	0.0004	0.15	
Pb	8.05	36.13	4.73	2.5	4.08	7.7	37.4	3.1	2.4	3.30
1σ	0.07	0.23	2.32	0.06		0.6	2.9	0.3	0.9	
Th	2.31	6.43	0.03	1.32	0.34	2.17	6.4	0.03	1.23	0.33
1σ	0.03	0.05	0.01	0.05		0.09	0.3	0.004	0.07	
U	0.53	1.9	0.01	0.45	0.41	0.51	1.93	0.01	0.41	0.31
1σ	0.01	0.03	0	0.01		0.02	0.06	0.001	0.002	

Table E.5. Trace element data for international standards analysed by ICPMS (X-Series 2) during analysis of samples with prefix BC10. All data is reported in ppm unless stated otherwise.

	This study					Accepted values				
	W2 (n=5)	**AGV 1 (n=2)**	**BIR1 (n=2)**	**BHVO-1 (n=2)**	**NBS688 (n=2)**	**W2**	**AGV-1**	**BIR-1**	**BHVO-1**	**NBS688**
Sc	34.18	12.08	46.69	30.00	32.55	35.9	12.3	43	31	38.00
1σ	0.91	0.46	1.25	1.08	0.43	0.8	0.5	2	2	
TiO_2 (wt. %)	1.00	0.96	0.93	2.68		1.06	1.05	0.97	2.75	
1σ	0.01	0.00	0.00	0.03	0.01	0.01	0.05	0.03	0.04	
V	259.84	111.00	314.65	309.20	239.95	268	119	319	318	242
1σ	2.02	0.48	1.86	2.14	0.24	10	6	18	15	
Cr	258.16	59.76	118.13	102.26	68.49	93	9	391	287	332
1σ	1.87	0.34	0.62	0.76	0.32	6	1.2	15	15	
MnO (wt. %)	0.17	0.09	0.17	0.17		0.167	0.1	0.18	0.17	
1σ	0.00	0.00	2.00	0.00	0.00	0.004	0.01	0.01	0.01	
Ni	93.28	23.36	5.74	5.01	3.20	72	15.5	166	118	158
1σ	0.81	0.04	0.03	0.03	0.03	4	0.8	7	6	
Cu	111.98	54.45	107.95	126.30	76.54	105	58	119	137	96.00
1σ	1.27	0.67	0.59	0.95	0.98	3	2	8	9	
Zn	115.06	77.80	60.25	83.32	60.10	77	87	72	106	84.00
1σ	1.19	0.99	0.10	0.47	0.98	6	4	18	9	
Ga	17.39	19.67	14.62	20.93	15.40	18	20.2	15.3	21	17.00
1σ	0.14	0.08	0.04	0.38	0.06	1	0.5	0.8	2	
Rb	20.86	66.63	0.57	9.78	2.25	21	66.6	0.2	9.19	1.91
1σ	0.22	0.34	0.06	0.17	0.05	1	0.4	0.01	0.17	
Sr	209.24	660.20	110.50	410.70	170.70	196	660	109	396	169
1σ	2.98	2.10	0.57	2.75	2.28	5	6	2	1	
Y	22.77	19.51	16.19	27.63	20.71	22	19	15.6	26	17.00
1σ	0.26	0.13	0.13	0.15	0.20	1	1	0.9	2	
Zr	87.78	223.15	14.32	174.60	52.49	92	231	14	174	61.00
1σ	0.53	1.50	0.10	1.32	0.58	4	9	0.1	9	
Nb	7.66	14.16	0.63	19.42	4.25	7.5	14.6	0.55	18.6	5.00
1σ	0.06	0.10	0.01	0.13	0.02	0.6	1	0.05	1.8	
Cs	0.94	1.20	0.02	0.12	0.05	0.92	1.26	0.01	0.1	0.24
1σ	0.01	0.03	0.00	0.00	0.00	0.07	0.07	0.003	0.01	
Ba	170.90	1232.00	9.16	134.30	168.90	172	1200	7.14	133	200
1σ	1.57	8.57	0.02	1.10	2.20	7	8	n.d	1.00	
La	10.69	37.30	0.73	15.59	5.06	10.8	38.2	0.62	15.5	5.30
1σ	0.08	0.15	0.00	0.12	0.03	0.5	0.04	0.02	0.1	

Table E.5. Trace element data for international standards analysed by ICPMS (X-Series 2) during analysis of samples with prefix BC10. All data is reported in ppm unless stated otherwise.

	This study					Accepted Values				
	W2 (n=5)	**AGV 1 (n=2)**	**BIR1 (n=2)**	**BHVO-1 (n=2)**	**NBS688 (n=2)**	**W2**	**AGV-1**	**BIR-1**	**BHVO-1**	**NBS688**
Ce	22.77	65.70	1.91	37.57	11.31	23.4	67.6	1.92	38.1	13.00
1σ	0.18	0.38	0.01	0.38	0.17	0.7	1.1	0.08	0.2	
Pr	3.12	8.44	0.40	5.58	1.78	3	8.3	0.37	5.42	2.40
1σ	0.03	0.05	0.00	0.02	0.03	0.1	0.5	0.02	0.19	
Nd	13.79	32.87	2.58	26.33	8.89	13	31.7	2.38	24.7	9.60
1σ	0.12	0.22	0.01	0.06	0.14	0.5	0.1	0.01	0.1	
Sm	3.33	5.80	1.12	6.29	2.42	3.3	5.72	1.12	6.12	2.50
1σ	0.03	0.25	0.09	0.05	0.03	0.08	0.03	0.02	0.03	
Eu	1.10	1.67	0.52	2.11	1.01	1.08	1.58	0.53	2.09	1.01
1σ	0.01	0.02	0.00	0.01	0.00	0.03	0.02	n.d	0.02	
Gd	3.84	5.36	1.93	6.53	3.26	3.66	4.7	1.87	6.33	3.20
1σ	0.05	0.10	0.03	0.07	0.03	0.12	0.05	0.04	0.06	
Tb	0.63	0.69	0.37	0.98	0.54	0.62	0.69	0.36	0.96	0.52
1σ	0.02	0.01	0.00	0.01	0.00	0.03	0.04	0.03	0.06	
Dy	3.71	3.45	2.44	5.16	3.28	3.79	3.55	2.51	5.31	3.40
1σ	0.02	0.03	0.03	0.08	0.01	0.09	0.03	n.d	0.03	
Er	2.11	1.73	1.59	2.42	2.02	2.22	1.82	1.66	2.55	2.10
1σ	0.01	0.01	0.02	0.01	0.00	0.1	0.02	n.d	0.02	
Tm	0.35	0.27	0.27	0.36	0.34	0.33	0.28	0.25	0.33	0.29
1σ	0.00	0.00	0.00	0.00	0.00	0.02	0.02	0.03	0.03	
Yb	2.06	1.65	1.66	2.00	2.11	2.05	1.63	1.65	2	2.05
1σ	0.02	0.02	0.00	0.01	0.01	0.04	0.02	n.d	0.03	
Lu	0.33	0.26	0.27	0.31	0.31	0.31	0.24	0.25	0.27	0.35
1σ	0.00	0.00	0.00	0.00	0.00	0.01	0.002	0.02	0.01	
Hf	2.43	4.98	0.58	4.46	1.48	2.45	5.1	0.58	4.46	1.55
1σ	0.01	0.42	0.00	0.00	0.01	0.18	0.2	0.004	0.17	
Ta	0.51	0.90	0.05	1.27	0.30	0.47	0.87	0.0357	1.21	0.31
1σ	0.00	0.00	0.00	0.00	0.00	0.04	0.05	0.0004	0.15	
Pb	7.40	22.88	3.84	3.61	2.38	7.7	37.4	3.1	2.4	3.30
1σ	0.06	0.16	0.03	0.01	0.01	0.6	2.9	0.3	0.9	
Th	2.29	6.12	0.05	1.26	0.32	2.17	6.4	0.03	1.23	0.33
1σ	0.02	0.03	0.00	0.01	0.00	0.09	0.3	0.004	0.07	
U	0.54	1.84	0.00	0.42	0.29	0.51	1.93	0.01	0.41	0.31
1σ	0.00	0.02	0.00	0.00	0.00	0.02	0.06	0.001	0.002	

Table E.6. Details of all analyses of international standard NBS987 ($^{87}Sr/^{86}Sr$) and in-house standard J & M ($^{143}Nd/^{144}Nd$) run on the Neptune PIMMS instrument throughout the course of this work

	NBS 987		J & M		J & M doped	
	$^{87}Sr/^{86}Sr$	2 SE	$^{143}Nd/^{144}Nd$	2 SE	$^{143}Nd/^{144}Nd$	2 SE
	0.710247	0.000003	0.511111	0.000003	0.511112	0.000003
	0.710251	0.000004	0.511105	0.000003	0.511118	0.000003
	0.710252	0.000003	0.511107	0.000004	0.511119	0.000002
	0.710246	0.000004	0.511121	0.000004	0.511123	0.000003
	0.710260	0.000004	0.511124	0.000004	0.511126	0.000004
	0.710259	0.000004	0.511110	0.000003	0.511125	0.000003
	0.710261	0.000004	0.511123	0.000003	0.511121	0.000003
	0.710257	0.000004	0.511127	0.000003		
	0.710254	0.000004	0.511116	0.000003		
	0.710260	0.000004	0.511106	0.000003		
	0.710258	0.000004	0.511105	0.000003		
	0.710251	0.000004	0.511105	0.000004		
	0.710262	0.000005	0.511106	0.000004		
	0.710264	0.000007	0.511105	0.000004		
	0.710253	0.000008	0.511104	0.000003		
	0.710248	0.000007	0.511111	0.000003		
	0.710255	0.000006	0.511112	0.000003		
	0.710261	0.000008	0.511111	0.000003		
	0.710254	0.000007	0.511108	0.000004		
	0.710257	0.000006	0.511109	0.000004		
	0.710267	0.000006	0.511105	0.000003		
	0.710248	0.000006	0.511108	0.000003		
	0.710256	0.000012				
Average	**0.710256**		**0.511111**		**0.511121**	
2 * st.dev	**0.000011**		**0.000014**		**0.000010**	

Table E.7. Details of all analyses of international standard NBS981 run on the Neptune PIMMS instrument throughout the course of this work

Ratio $^{206}Pb/^{204}Pb$	2SE	Ratio $^{207}Pb/^{204}Pb$	2SE	Ratio $^{208}Pb/^{204}Pb$	2SE
16.94081	0.00085	15.49788	0.00108	36.71819	0.00261
16.94011	0.00067	15.49750	0.00075	36.71656	0.00187
16.93991	0.00083	15.49606	0.00094	36.71321	0.00271
16.94089	0.00076	15.49806	0.00081	36.71855	0.00257
16.94008	0.00105	15.49760	0.00146	36.71511	0.00330
16.94020	0.00081	15.49799	0.00103	36.72036	0.00224
16.94000	0.00074	15.49733	0.00084	36.71540	0.00267
16.94001	0.00080	15.49662	0.00098	36.71418	0.00269
16.94132	0.00071	15.49822	0.00081	36.71808	0.00217
16.94057	0.00070	15.49739	0.00090	36.71657	0.00237
16.94076	0.00080	15.49724	0.00101	36.71565	0.00230
16.94023	0.00070	15.49687	0.00084	36.71608	0.00217
16.94082	0.00085	15.49786	0.00102	36.71769	0.00249
16.94017	0.00070	15.49709	0.00116	36.71527	0.00156
16.94062	0.00069	15.49784	0.00094	36.71620	0.00213
16.94035	0.00050	15.49746	0.00069	36.71462	0.00174
16.94035	0.00068	15.49752	0.00088	36.71525	0.00201
16.94118	0.00067	15.49811	0.00096	36.71806	0.00185
16.94034	0.00054	15.49742	0.00083	36.71531	0.00140
16.94121	0.00068	15.49883	0.00086	36.71852	0.00239
16.94012	0.00080	15.49724	0.00073	36.71439	0.00218
16.94009	0.00058	15.49694	0.00073	36.71515	0.00209
16.93971	0.00050	15.49676	0.00061	36.71315	0.00166
16.94056	0.00073	15.49784	0.00088	36.71678	0.00245
16.94137	0.00075	15.49817	0.00087	36.71838	0.00240
16.94023	0.00060	15.49738	0.00058	36.71655	0.00178
16.94058	0.00059	15.49781	0.00075	36.71635	0.00238
16.94098	0.00080	15.49870	0.00084	36.71989	0.00235
16.94025	0.00071	15.49747	0.00082	36.71590	0.00237
16.94063	0.00082	15.49764	0.00094	36.71814	0.00238
16.94036	0.00065	15.49764	0.00079	36.71668	0.00207
16.94047	0.00072	15.49755	0.00077	36.71644	0.00231
16.94021	0.00062	15.49736	0.00076	36.71553	0.00236
16.94122	0.00071	15.49805	0.00085	36.71838	0.00240
16.94077	0.00055	15.49820	0.00071	36.71959	0.00190
16.94037	0.00065	15.49770	0.00076	36.71683	0.00219
16.94010	0.00085	15.49698	0.00099	36.71600	0.00256
16.94075	0.00071	15.49760	0.00088	36.71722	0.00223
16.94064	0.00064	15.49781	0.00076	36.71805	0.00201
16.93957	0.00071	15.49709	0.00077	36.71594	0.00209
16.94069	0.00074	15.49807	0.00091	36.71840	0.00248
16.93977	0.00071	15.49707	0.00091	36.71559	0.00202
16.94023	0.00093	15.49766	0.00122	36.71636	0.00289
16.93996	0.00078	15.49721	0.00081	36.71531	0.00232
16.94068	0.00090	15.49835	0.00093	36.71839	0.00287
16.93995	0.00081	15.49716	0.00098	36.71496	0.00280
16.94050	0.00080	15.49851	0.00092	36.71982	0.00239
16.94118	0.00071	15.49909	0.00082	36.72141	0.00248
16.94046		**15.49762**		**36.71676**	
0.00088		**0.00116**		**0.00367**	

Average
2 * st. dev

Table E.8. Sr blank (pg) for each batch of chemsitry run for Sr-isotope analysis. The range of Sr within the samples of that batch is shown as too is the average. The blank contribution shown is a percentage of this average.

Blank ID	Blank (pg)	Range in sample (ng)	Average	Blank contribution
M91-11	15.3	8.2-27.3	17.6	0.09
M91-12	14.2	8.2-27.3	17.6	0.08
M92-1	11.0	12.4-19.5	16.3	0.07
M99-1	13.9	5.6-17.5	19.2	0.07
M99-6	22.0	5.6-17.5	19.2	0.11
M99-11	1.7	5.6-17.5	19.2	0.01
M105-1	19.2	7.8-13.0	21.6	0.09
M105-6	21.3	7.8-13.0	21.6	0.10
M105-12	6.1	7.8-13.0	21.6	0.03
M115-1	8.2	2.3-25.6	13.7	0.06
M115-6	6.8	2.3-25.6	13.7	0.05
M115-12	0.5	2.3-25.6	13.7	0.00
M116-6	14.6	1.2-29.5	14.8	0.10
M116-12	16.7	1.2-29.5	14.8	0.11
M124-24	0.3	5.7-27.8	21.5	0.00
M124-25	0.7	5.7-27.8	21.5	0.00

Table E.9. Details of all analyses of USGS standard W-2 run throughout the course of this work on the Element II ICPMS. All values reported in ppm. 1-100 denotes diluton factor of 100; 1-100 a dilution factor of 1000. Standards are diluted so that concentrations are of comparable magnitude to those in microdrilled samples.

	Accepted values	W-2 (1-100)													W-2 (1-1000)							
	(dilution factor 100)	1	2	3	4	5	6	7	8	9	10	11	12	Av.	1	2	3	4	5	6	7	Av.
Rb	0.41	0.374	0.385	0.389	0.421	0.402	0.415	0.417	0.395	0.402	0.391	0.382	0.382	**0.396**	0.032	0.035	0.038	0.036	0.038	0.039	0.039	**0.037**
Sr	3.87	3.682	3.785	3.671	3.795	3.852	3.598	3.685	3.742	3.784	3.794	3.986	3.711	**3.757**	0.365	0.384	0.394	0.384	0.378	0.378	0.385	**0.381**
Y	0.43	0.421	0.413	0.445	0.412	0.435	0.429	0.425	0.438	0.412	0.419	0.421	0.451	**0.427**	0.032	0.035	0.036	0.038	0.040	0.039	0.037	**0.037**
Zr	1.86	1.784	1.581	1.682	1.671	1.751	1.956	1.845	1.625	1.627	1.654	1.684	1.637	**1.708**	0.174	0.175	0.154	0.168	0.187	0.148	0.157	**0.166**
Nb	0.16	0.148	0.138	0.141	0.165	0.124	0.154	0.129	0.125	0.131	0.134	0.127	0.125	**0.137**	0.012	0.012	0.013	0.014	0.012	0.013	0.015	**0.013**
Cs	0.02	0.028	0.029	0.031	0.031	0.035	0.031	0.029	0.032	0.034	0.036	0.031	0.031	**0.032**	0.002	0.002	0.002	0.002	0.001	0.001	0.002	**0.002**
Ba	3.34	3.152	3.120	3.031	3.689	3.197	3.156	3.160	3.175	3.490	3.875	3.450	3.654	**3.346**	0.342	0.323	0.312	0.319	0.398	0.341	0.387	**0.346**
La	0.21	0.197	0.228	0.221	0.213	0.185	0.187	0.165	0.178	0.189	0.191	0.184	0.182	**0.193**	0.015	0.016	0.018	0.017	0.019	0.018	0.016	**0.017**
Ce	0.46	0.428	0.389	0.394	0.412	0.471	0.481	0.450	0.405	0.389	0.391	0.385	0.373	**0.414**	0.037	0.035	0.039	0.031	0.032	0.034	0.032	**0.037**
Pr	0.06	0.057	0.085	0.081	0.074	0.052	0.078	0.071	0.069	0.075	0.071	0.056	0.052	**0.068**	0.004	0.004	0.004	0.004	0.005	0.004	0.003	**0.004**
Nd	0.26	0.241	0.284	0.286	0.297	0.291	0.293	0.293	0.302	0.309	0.312	0.309	0.314	**0.294**	0.021	0.023	0.024	0.023	0.023	0.021	0.025	**0.025**
Sm	0.07	0.061	0.082	0.087	0.075	0.079	0.070	0.068	0.084	0.083	0.094	0.084	0.083	**0.079**	0.006	0.007	0.007	0.007	0.007	0.007	0.007	**0.007**
Eu	0.02	0.016	0.019	0.018	0.018	0.014	0.015	0.013	0.015	0.016	0.018	0.019	0.018	**0.017**	0.002	0.001	0.002	0.002	0.002	0.002	0.002	**0.002**
Gd	0.07	0.067	0.084	0.086	0.079	0.086	0.087	0.091	0.084	0.089	0.098	0.096	0.091	**0.087**	0.008	0.008	0.008	0.007	0.007	0.007	0.007	**0.008**
Tb	0.01	0.013	0.014	0.016	0.014	0.021	0.019	0.018	0.017	0.021	0.020	0.023	0.019	**0.018**	0.001	0.001	0.001	0.001	0.001	0.005	0.001	**0.002**
Dy	0.07	0.072	0.078	0.076	0.085	0.087	0.082	0.086	0.089	0.087	0.082	0.080	0.092	**0.083**	0.008	0.007	0.007	0.008	0.008	0.007	0.007	**0.007**
Er	0.04	0.037	0.059	0.045	0.068	0.058	0.051	0.059	0.061	0.067	0.069	0.075	0.071	**0.060**	0.005	0.006	0.005	0.006	0.005	0.005	0.005	**0.005**
Tm	0.01	0.012	0.016	0.023	0.021	0.020	0.017	0.025	0.026	0.028	0.024	0.023	0.024	**0.022**	0.001	0.001	0.001	0.001	0.001	0.001	0.001	**0.001**
Yb	0.04	0.038	0.048	0.042	0.041	0.038	0.049	0.035	0.036	0.048	0.047	0.037	0.049	**0.042**	0.003	0.004	0.005	0.005	0.005	0.005	0.004	**0.004**
Lu	0.01	0.008	0.008	0.009	0.009	0.009	0.009	0.001	0.008	0.006	0.009	0.006	0.006	**0.007**	0.000	0.000	0.000	0.000	0.000	0.000	0.000	**0.000**
Hf	0.05	0.051	0.006	0.059	0.061	0.054	0.053	0.058	0.052	0.068	0.062	0.065	0.062	**0.054**	0.005	0.005	0.006	0.006	0.006	0.006	0.006	**0.006**
Ta	0.01	0.009	0.009	0.009	0.013	0.009	0.009	0.001	0.000	0.009	0.008	0.008	0.008	**0.008**	0.001	0.001	0.001	0.001	0.001	0.001	0.001	**0.001**
Pb	0.16	0.149	0.168	0.148	0.156	0.136	0.158	0.164	0.148	0.159	0.164	0.135	0.169	**0.155**	0.016	0.017	0.018	0.016	0.017	0.017	0.017	**0.017**
Th	0.04	0.038	0.042	0.049	0.051	0.053	0.051	0.057	0.054	0.052	0.048	0.045	0.041	**0.048**	0.005	0.006	0.006	0.006	0.005	0.006	0.007	**0.006**
U	0.01	0.011	0.013	0.015	0.013	0.013	0.018	0.012	0.012	0.017	0.018	0.014	0.012	**0.014**	0.001	0.001	0.001	0.001	0.001	0.001	0.001	**0.001**

Table E.10: Details of all analyses of international standard NBS987 run on the Triton TIMS instrument for different load sizes during this work.

Load size: 600 ng		Load size:12 ng		Load size: 6 ng		Load size: 3 ng		Load size: 1 ng	
$^{87}Sr/^{86}Sr$	2 SE	$^{87}Sr/^{86}Sr$	2 SE	$^{87}Sr/^{86}Sr$	2 SE	$^{87}Sr/^{86}Sr$	2 SE	$^{87}Sr/^{86}Sr$	2 SE
0.710240	0.000003	0.710261	0.000010	0.710273	0.000008	0.710280	0.000005	0.710258	0.000008
0.710239	0.000003	0.710275	0.000010	0.710262	0.000010	0.710270	0.000006	0.710265	0.000010
0.710244	0.000003	0.710267	0.000008	0.710267	0.000010	0.710277	0.000007	0.710252	0.000008
0.710248	0.000003	0.710251	0.000006	0.710261	0.000014	0.710256	0.000005	0.710252	0.000008
0.710249	0.000003	0.710265	0.000006	0.710269	0.000010	0.710267	0.000004	0.710252	0.000008
		0.710264	0.000010	0.710275	0.000010	0.710256	0.000007	0.710253	0.000012
		0.710269	0.000010	0.710274	0.000008	0.710260	0.000005	0.710246	0.000016
		0.710254	0.000010	0.710275	0.000010	0.710252	0.000005	0.710253	0.000010
		0.710261	0.000006	0.710262	0.000008	0.710258	0.000004	0.710271	0.000010
		0.710255	0.000006	0.710266	0.000016	0.710259	0.000004	0.710245	0.000010
		0.710253	0.000008	0.710263	0.000006	0.710245	0.000005	0.710268	0.000014
		0.710259	0.000006	0.710258	0.000014	0.710248	0.000005	0.710251	0.000010
		0.710248	0.000008	0.710266	0.000008	0.710258	0.000003	0.710258	0.000012
		0.710238	0.000012	0.710267	0.000008	0.710249	0.000005		
		0.710255	0.000012	0.710254	0.000008	0.710259	0.000005		
				0.710250	0.000008	0.710254	0.000004		
				0.710247	0.000006	0.710250	0.000004		
				0.710248	0.000008	0.710257	0.000004		
				0.710257	0.000010	0.710259	0.000004		
				0.710248	0.000008	0.710254	0.000004		
				0.710248	0.000008	0.710261	0.000004		
				0.710252	0.000008	0.710253	0.000004		
				0.710257	0.000010	0.710250	0.000005		
				0.710261	0.000006	0.710237	0.000006		
				0.710265	0.000008	0.710242	0.000006		
				0.710249	0.000008	0.710267	0.000005		
				0.710247	0.000010	0.710243	0.000005		
				0.710246	0.000010	0.710258	0.000008		
				0.710239	0.000012	0.710259	0.000006		
				0.710249	0.000012	0.710275	0.000005		
				0.710254	0.000012	0.710248	0.000005		
				0.710235	0.000008	0.710270	0.000005		
				0.710254	0.000012	0.710245	0.000004		
						0.710252	0.000003		
						0.710250	0.000006		
						0.710257	0.000005		

Table E.11. Composition and age (U-Pb) for zircon standard AS3 analysed during the course of this work at UCLA by SIMS.

	Isotopic ratios						Age (Ma)						Composition			
Analysis #	$^{206}Pb^*/^{238}U$	1 s.e.	$^{207}Pb^*/^{235}U$	1 s.e.	$^{207}Pb^*/^{206}Pb^*$	1 s.e.	$^{206}Pb/^{238}U$	1 s.e.	$^{207}Pb/^{235}U$	1 s.e.	$^{207}Pb/^{206}Pb$	1 s.e.	% Radiogenic ^{206}Pb	% Radiogenic ^{207}Pb	U/Th	U (ppm)
1	0.1896	0.00960	1.992	0.11100	0.07619	0.00052	1119	52	1113	37.7	1100	13.6	100	99.86	0.86	1216
2	0.1869	0.00377	1.953	0.03760	0.07580	0.00032	1104	20.5	1099	12.9	1090	8.53	100	99.9	0.56	533
3	0.1877	0.00395	1.950	0.04850	0.07537	0.00070	1109	21.5	1099	16.7	1078	18.6	100	99.51	0.60	453
4	0.1803	0.00652	1.907	0.06740	0.07674	0.00072	1068	35.6	1084	23.5	1115	18.8	100	99.48	0.65	423
5	0.1878	0.00375	1.962	0.04060	0.07579	0.00055	1109	20.3	1103	13.9	1090	14.4	100	99.56	1.07	467
6	0.1836	0.00392	1.915	0.04370	0.07564	0.00061	1087	21.3	1086	15.2	1086	16	100	99.83	0.82	534
7	0.1882	0.00369	1.974	0.03870	0.07606	0.00024	1112	20	1107	13.2	1097	6.24	100	99.77	0.64	1410
8	0.1826	0.00859	1.894	0.09300	0.07523	0.00048	1081	46.8	1079	32.6	1075	12.9	100	100	0.50	603
9	0.1896	0.00405	1.995	0.03990	0.07629	0.00039	1119	21.9	1114	13.5	1103	10.2	100	99.8	1.62	1241
10	0.1856	0.00353	1.957	0.03730	0.07644	0.00019	1098	19.2	1101	12.8	1107	4.97	100	99.88	1.41	1465
11*	0.1699	0.00316	1.771	0.03350	0.07560	0.00041	1012	17.4	1035	12.3	1084	10.7	99.7	96.59	0.95	1378
12	0.1849	0.00373	1.949	0.03890	0.07642	0.00028	1094	20.3	1098	13.4	1106	7.21	100	100	0.50	686
13	0.1795	0.00396	1.898	0.04460	0.07672	0.00039	1064	21.7	1080	15.6	1114	10.1	100	100	0.49	680
14	0.1860	0.00407	1.910	0.04490	0.07448	0.00051	1100	22.1	1085	15.7	1054	13.9	100	100	0.34	397
15	0.1831	0.00365	1.921	0.03870	0.07609	0.00035	1084	19.9	1088	13.4	1097	9.07	100	99.78	0.95	863
16	0.1837	0.00329	1.927	0.03510	0.07609	0.00027	1087	17.9	1091	12.2	1098	6.96	100	99.96	1.21	1488
17	0.1845	0.00448	1.934	0.04760	0.07602	0.00038	1092	24.4	1093	16.5	1096	9.97	100	99.7	0.39	621
18	0.1904	0.00491	1.987	0.05020	0.07568	0.00055	1124	26.6	1111	17.1	1087	14.6	100	99.81	0.51	517
19	0.1823	0.00417	1.897	0.04430	0.07545	0.00035	1080	22.7	1080	15.5	1080	9.18	100	99.78	0.77	818
20	0.1894	0.00458	1.975	0.04690	0.07562	0.00044	1118	24.8	1107	16	1085	11.7	100	99.97	0.91	1016
21	0.1912	0.00442	2.005	0.04650	0.07603	0.00030	1128	23.9	1117	15.7	1096	7.98	100	99.96	0.48	1092
22	0.1876	0.00373	1.969	0.04010	0.07612	0.00045	1108	20.3	1105	13.7	1098	11.7	99.9	98.79	0.56	1179

11* excluded because of high ^{204}Pb

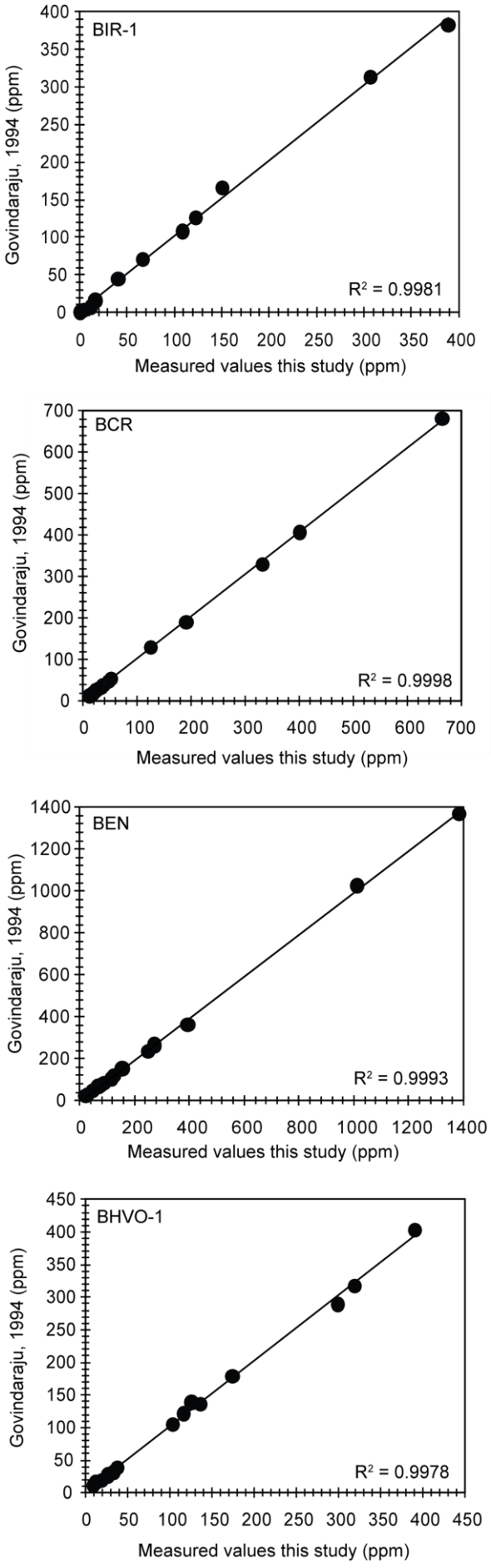

Fig. E.1. Comparison of average measured concentrations of elements (in ppm) stated in Table E.3 of the international standards BIR-1, BCR, BEN and BHVO-1 by XRF to accepted values (Govindaraju, 1994).

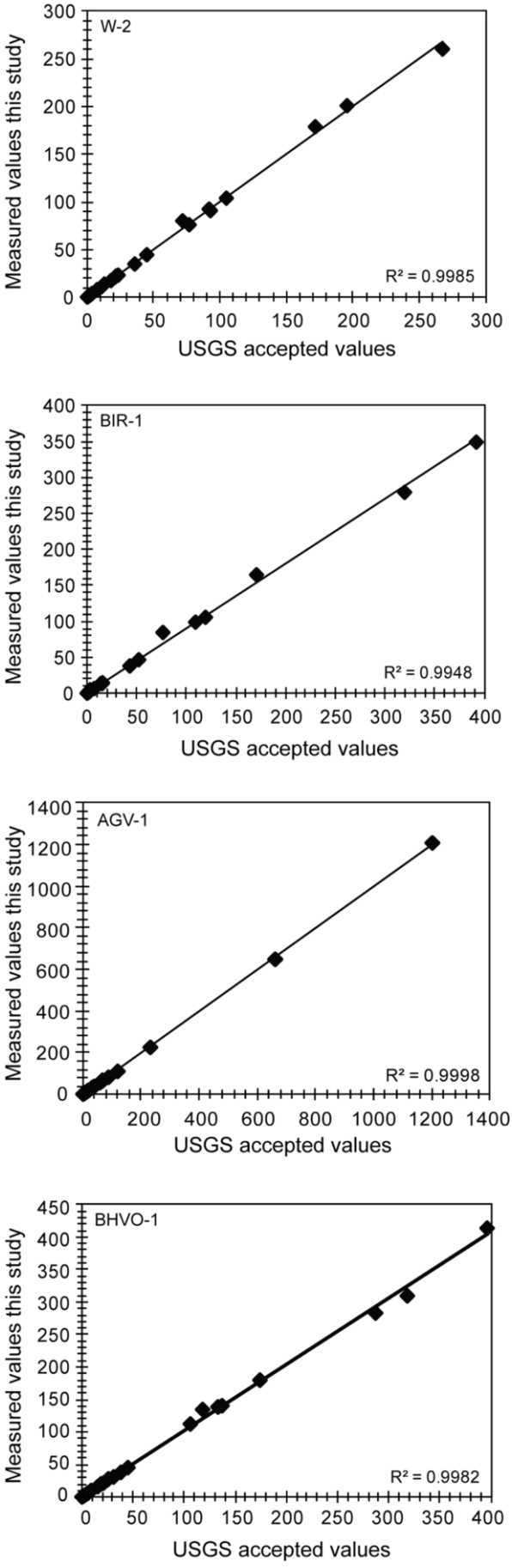

Fig. E.2. Comparison of average measured concentrations of elements of the international standards W-2, BIR-1, AGV-1 and BHVO-1 (in ppm stated in Table E.4, measured by ICPMS, ELAN 6000) to accepted values.

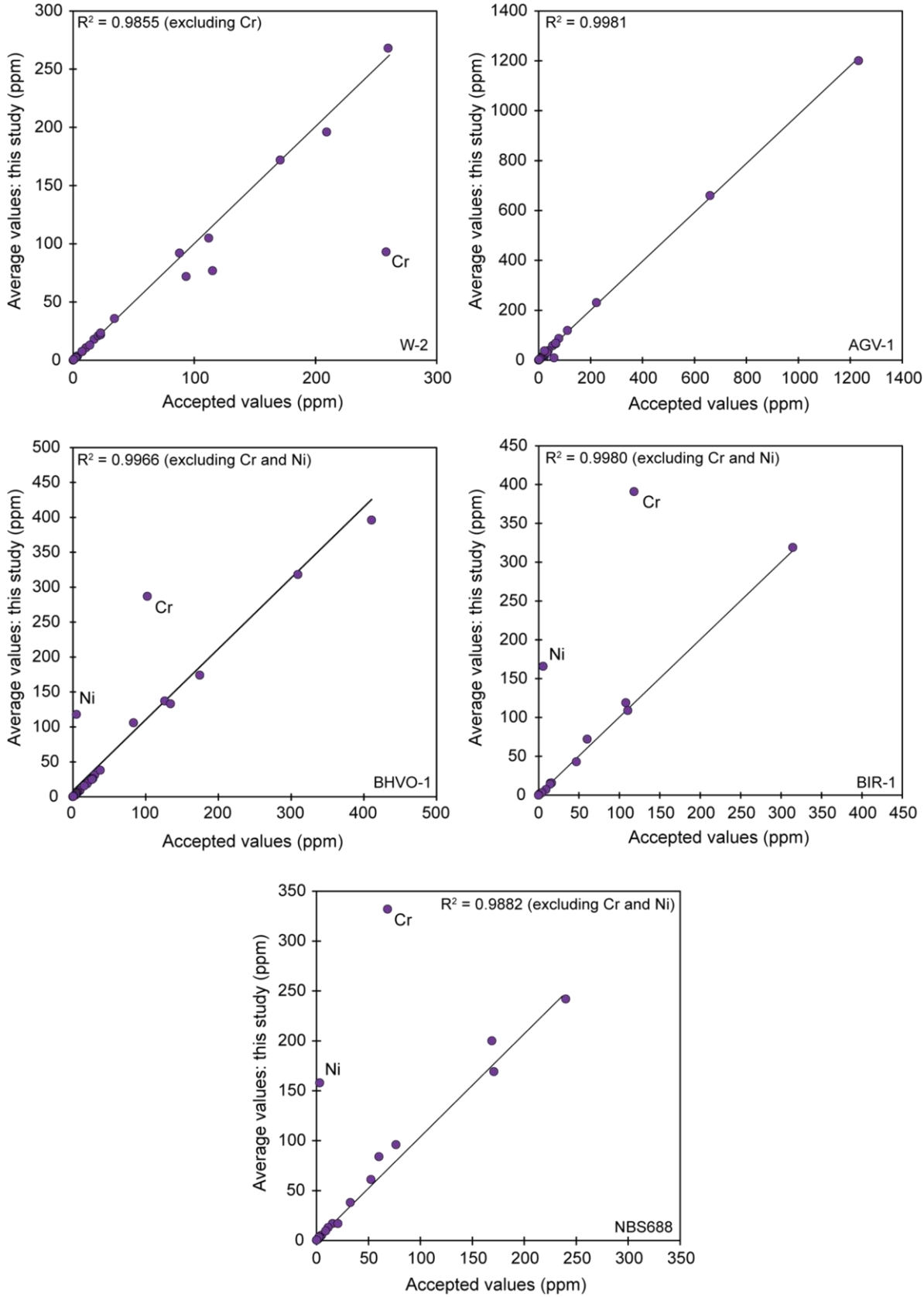

Fig. E.3. Comparison of average measured concentrations of elements of international standards (in ppm, stated in Table E.5, measured by ICPMS, X-Series 2) to accepted values.

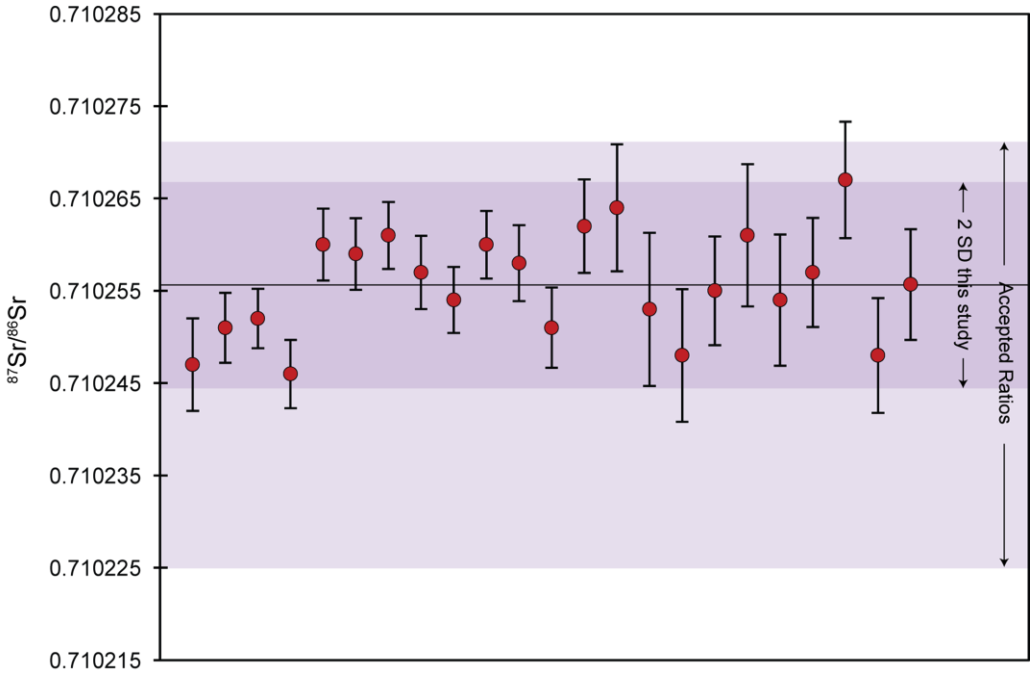

Fig. E.4. Graph showing reproducibility for the $^{87}Sr/^{86}Sr$ composition of NBS987 international standard during this study (during whole rock analyses, n=22, see Table E.6). Error bars show 2σ confidence. Shaded area represents accepted values as reported by Thirlwall, (1991). Dark shaded area represents 2 standard deviations on the average value of the NBS987 standard obtained by this study (n = 22).

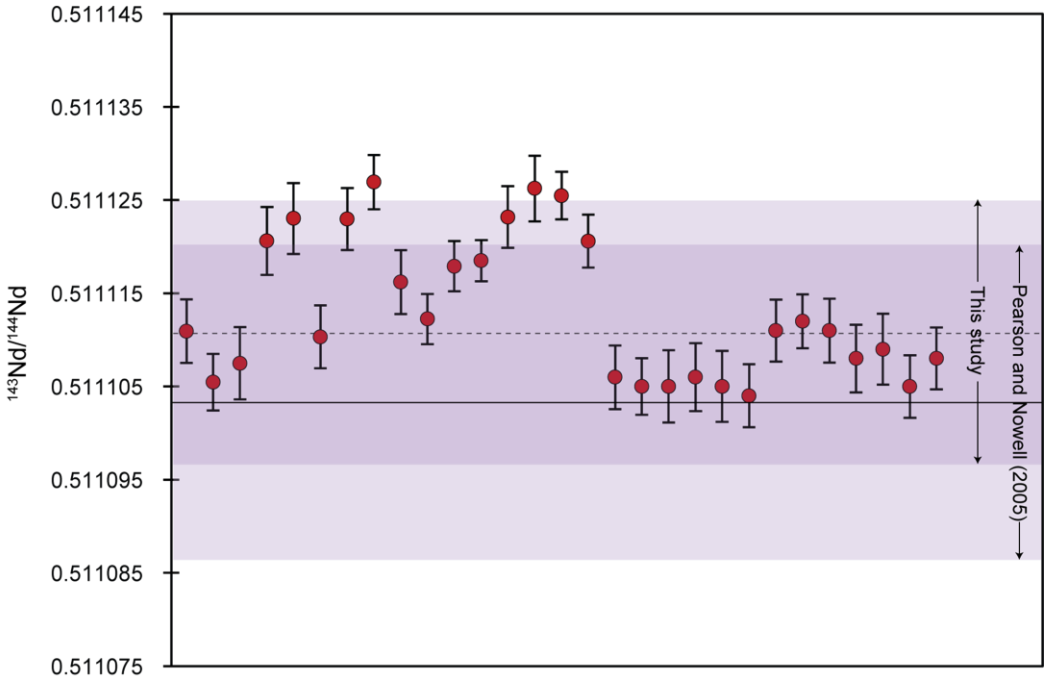

Fig. E.5. Graph showing reproducibility for the $^{143}Nd/^{144}Nd$ composition of in-house J&M standard during this study (during whole rock analyses, n=29, see Table E.6). Error bars show 2σ confidence. Values are within 2σ of the average $^{143}Nd/^{144}Nd$ J&M standard value from Pearson and Nowell (2005, n=562). Shaded areas represent 2 standard deviations.

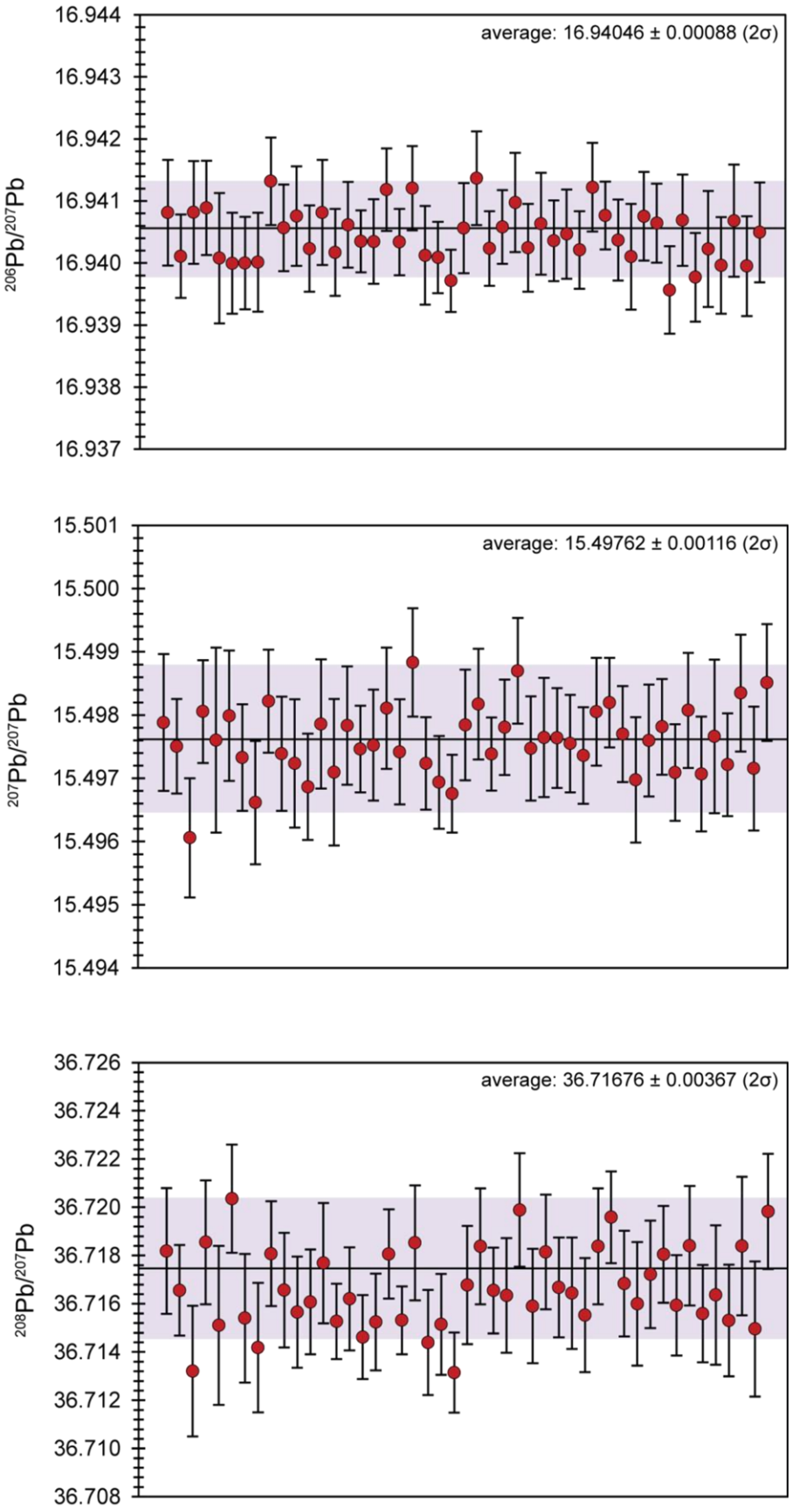

Fig. E.6. Graphs showing reproducibility for the ^{206}, ^{207} and ^{208}Pb/^{204}Pb composition of NBS981 international standard during this study (during whole rock analyses by PIMMS, n=48, see Table E.7). Error bars show 2σ confidence. Solid line represents average values, shaded region represent 2σ of this (n = 48).

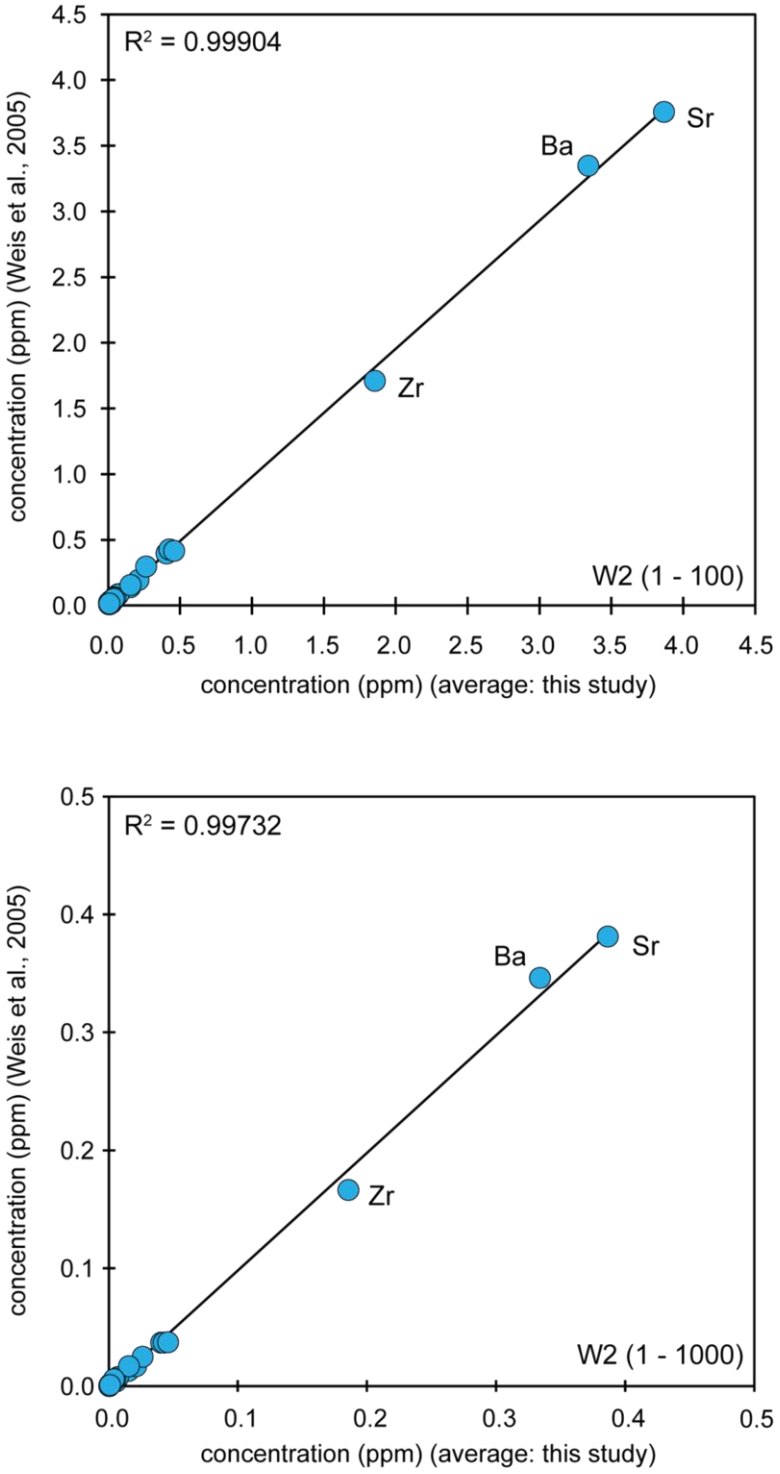

Fig. E.7. Comparison of average measured concentrations of elements (in ppm) stated in Table E.9 of the international standard W-2 to USGS accepted values. 1-100 denotes dilution by a factor of 100, 1-1000 by 1000.

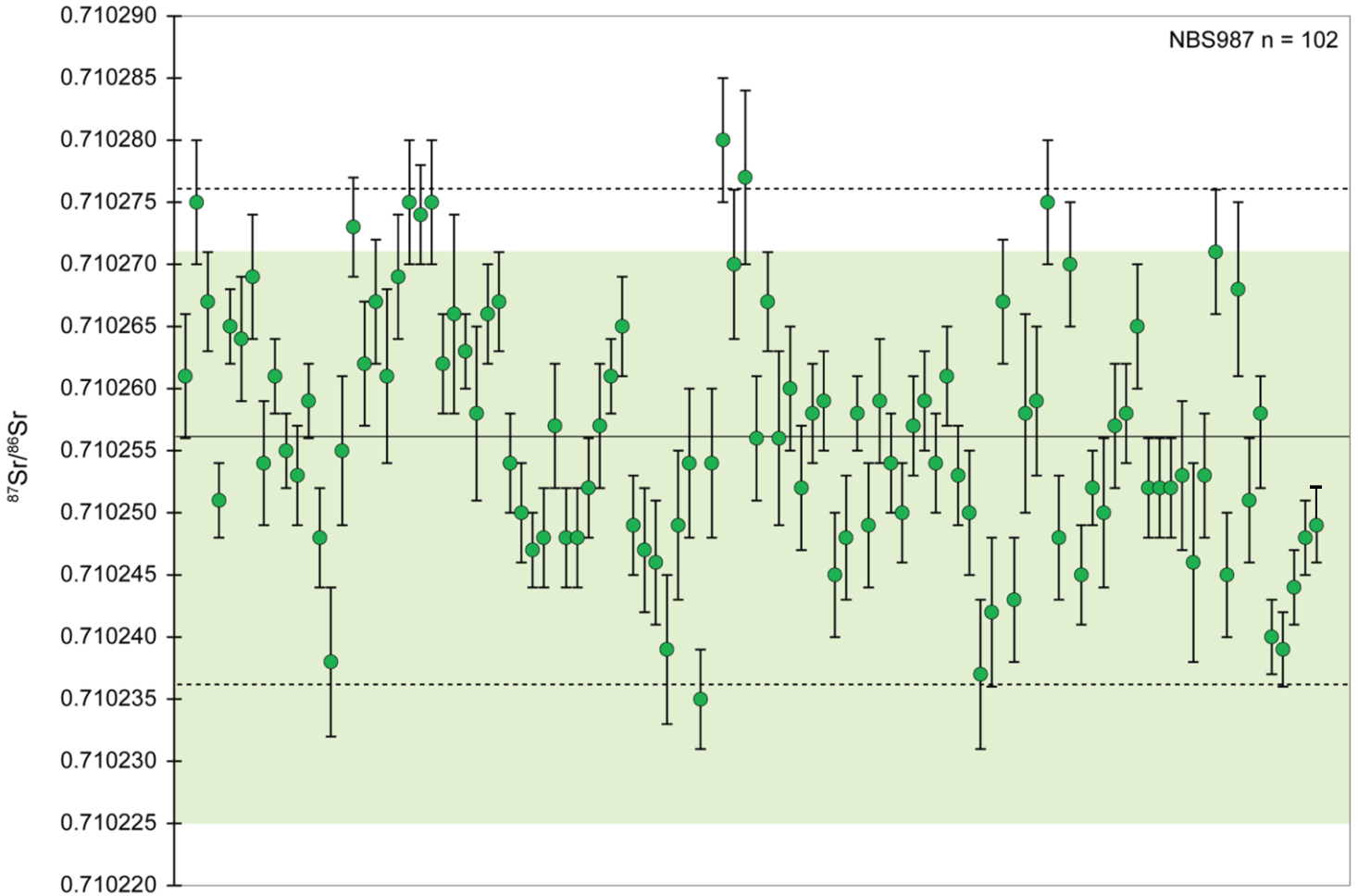

Fig. E.8. Graphs showing reproducibility on the $^{87}Sr/^{86}Sr$ composition of NBS987 international standard during this study (by TIMS, see Table E.10). Error bars show 2σ confidence. Shaded region represents range of accepted values (after Thirlwall, 1991). Solid line represents average value obtained during this work, dashed lines show 2σ on this value (0.710256 ± 0.000020).

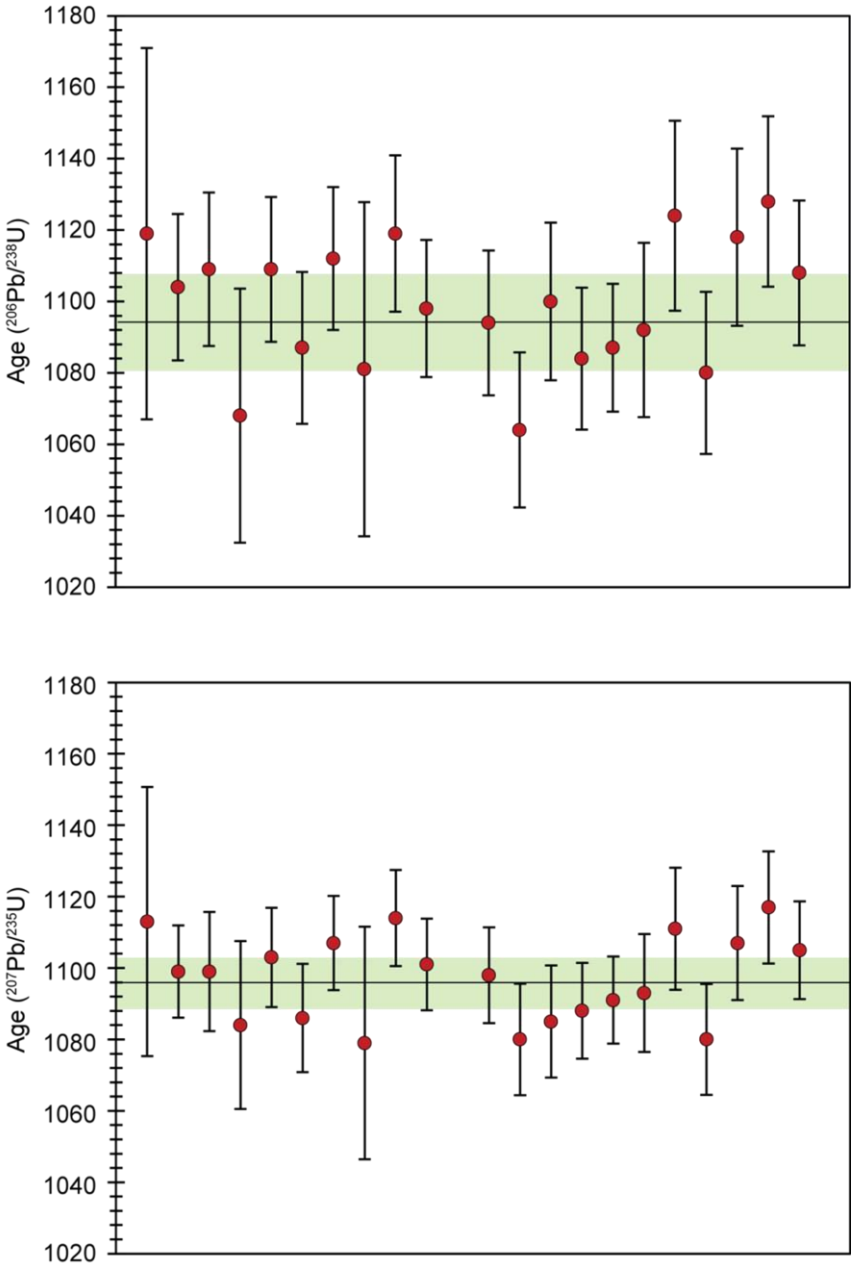

Fig. E.9. Comparison of measured ages ($^{206}Pb/^{238}U$ and $^{207}Pb/^{235}U$, n = 21) on zircon standard AS3 at UCLA to the average value (and 2σ of, represented by the shaded region) presented in Schmitz et al., (2003) (n = 27).